UNIVERSIDADE DE SÃO PAULO
INSTITUTO DE GEOCIÊNCIAS

"Geochemical characterization of the Equatorial Atlantic Magmatic Province and its correlation with other magmatic events related to the South Atlantic Opening"

ANTOMAT AVELINO DE MACEDO FILHO

Tese de apresentada ao Programa de Pós-Graduação em Geociências – Geoquímica e Geotectônica para obtenção do título de Doutor em Ciências.

Área de concentração: Geotectônica

Orientadora: Profª. Drª. Maria Helena Bezerra Maia de Hollanda

SÃO PAULO
2021

Autorizo a reprodução e divulgação total ou parcial deste trabalho, por qualquer meio convencional ou eletrônico, para fins de estudo e pesquisa, desde que citada a fonte.

Serviço de Biblioteca e Documentação do IGc/USP
Ficha catalográfica gerada automaticamente com dados fornecidos pelo(a) autor(a)
via programa desenvolvido pela Seção Técnica de Informática do ICMC/USP

Bibliotecários responsáveis pela estrutura de catalogação da publicação:
Sonia Regina Yole Guerra - CRB-8/4208 | Anderson de Santana - CRB-8/6658

Macêdo Filho, Antomat Avelino de
"Geochemical characterization of the Equatorial Atlantic Magmatic Province and its correlation with other magmatic events related to the South Atlantic Opening" / Antomat Avelino de Macêdo Filho; orientadora Maria Helena Bezerra Maia de Hollanda . -- São Paulo, 2021.
282 p.

Tese (Doutorado - Programa de Pós-Graduação em Geoquímica e Geotectônica) -- Instituto de Geociências, Universidade de São Paulo, 2021.

1. Tholeiitic magmatism. 2. Magmatic plumbing systems. 3. EM component. 4. West Gondwana breakup. 5. Large Igneous Provinces. I. Hollanda , Maria Helena Bezerra Maia de , orient. II. Título.

UNIVERSIDADE DE SÃO PAULO
INSTITUTO DE GEOCIÊNCIAS

"Geochemical characterization of the Equatorial Atlantic Magmatic Province and its correlation with other magmatic events related to the South Atlantic Opening"

ANTOMAT AVELINO DE MACEDO FILHO

Orientadora: Profª. Drª. Maria Helena Bezerra Maia de Hollanda

Tese de Doutorado

Nº 637

COMISSÃO JULGADORA

Drª. Maria Helena Bezerra Maia de Hollanda

Drª. Maria Irene Bartolomeu Raposo

Dr. Sergio de Castro Valente

Dr. Cleyton de Carvalho Carneiro

Dr. Valdecir de Assis Janasi

Drª. Luana Moreira Florisbal

SÃO PAULO
2021

To my family.

ACKNOWLEDGMENTS

I would not have achieved this PhD dissertation if I did not have the direct or indirect support from many people and institutions, for whom I feel the need to express my gratitude.

My first acknowledgments are to my supervisor, Prof. Dr. Maria Helena Hollanda, for the opportunity and guidance during these years. Maria Helena's criticism, comments, and general advice surely saved me from many mistakes, oversights and, undoubtedly, elevated this dissertation to a higher level.

It has been a pleasure to work with Prof. Dr. Carlos Archanjo. I am grateful for the knowledge shared in the fieldwork, structural geology, and, above all, for the guidance in the Crystal Size Distribution approaches.

I acknowledge Stephen Fraser, first for accepting to be my supervisor for a 1-year Research Internship Abroad Program (BEPE) at the W.H. Bryan Mining & Geology Research Centre (BRC) – The University of Queensland (UQ) – Australia; and second, by all contributions, guidance and experience in Self-Organizing Maps (SOM) shared with me.

I am indebted to Dr. Alanny Melo for her support from the first sampling works to the final discussions involving SOM applications. During our time at the UQ, we had the opportunity to conceptualize and write our first papers using SOM approach. One is already published. And it is just begun!

I would like to highlight the efforts of Carlos Á., Ms. Alisson O, and Ms. Daniel S. Thank you, guys, for helping me with the data collection (lab or field), reviewing my texts, and by the fruitful discussions. I hope that our scientific partnership remains unscathed!

I must not forget other colleagues from USP for the nice convivence and general support: Ms. Lucas L., Ms. Ney, Dr. Alice W., Ms. Juan C., Dr. Rodrigo I., Ms. José Renato, Ms. Alana D. I wish a promising career for everyone!

I give full recognition to professors from the USP and other Brazilian universities, who gave me the chance to expand my knowledge in Geosciences: Francisco F. (UFPR), Excelso R., Gaston R., Haakon F., Marly B., Valdecir J., Rogério A., Irene R.,Veridiana M., and Paulo B. Professors Cláudia P., Patrício M., and Alexandra S. are emphasized because they gave me the opportunity of an internship in their subjects under the Teaching Improvement Program (PAE/USP).

Many thanks to the staff from USP, for kindly assisting in several steps of my work: Alexandre B., Giselle E., Izabel R., Katherine K., Liliane P., Marcos M., Rodrigo A., Vasco L., Jordana Z., and Samuel E.

I am grateful to the people from the Sustainable Minerals Institute (SMI/UQ), who made me feel like I was in a second home in Australia: Prof. Dr. Rick V., Prof. Dr. Paul G., and other lab colleagues: Prof. Dr. Kate T., Torben W., Vahid V., Rocio V., Robin C., Shujaat A., and Dr. Pia L.

I thank to the #UQMagmaTeam for discussions and shared experiences in the world of Petrology/Volcanology. Especially the admirable professors who guided the meetings: Dr. Teresa Ubide and Dr. Carlos Spier.

I would like to say thank you to my housemates in Brisbane (Abhishek J., 徐子期, Tribute M., Nanthini J., and 陈宁智) and Brazilian colleagues (Nathalia R., Beatriz M., Bárbara M., Leonardo N., Paulo A.). People from many places of this world taught me about different ways to face life. Sure, you made my life abroad much easier!

I am very lucky to have a friendship with talented geoscientists Ms. Allyson Santos and Ms. Gabriel Lima. Thank you, guys, for the precious tips on using remote sensing products for geological mapping and macroscale structural analysis.

I thank to my (longtime) friends Emanuelly M. and Kennedy C., for precious support and conversations along the way (especially during the quarantine). Either by celebrating victories or by listening to my complaints, you have always been there!

I am deeply grateful to my parents (Rosa and Antomat), sister (Eugênia), and nephews (Joaquim and Duda). Thank you for always encouraging me and understanding my physical absence throughout the last four years. I have no words, and I cannot measure the gratitude I owe you. You are simply amazing!

I dedicate a special word of acknowledgment to the São Paulo Research Foundation (FAPESP) for sponsoring the EQUAMP project 2017/08423–9 in which my PhD is linked. I could not have undertaken this research without scholarships provided by FAPESP and Coordination for the Improvement of Higher Education Personnel (CAPES) at USP (grants 2017/13130–0 and 1643026, respectively) and UQ (grant 2018/24769–5).

Finally, I am indebted to locals from the countryside of Northeastern Brazil, for their support and hospitality during fieldwork campaigns. So many people crossed my path, throughout this challenging experience, teaching me about optimism, strength, and resilience: essential qualities for a PhD candidate. That’s why the laurels of this thesis are yours as well!

So many miles I've walked,
So many rivers I've crossed,
So many battles I've lost,
Make me who I am today,
And when tomorrow it comes,
There'll be a brand new sun,
This song is not over,
It's just begun...

(Stick Figure)

ABSTRACT

Macêdo Filho, A.A., 2021. Geochemical characterization of the Equatorial Atlantic Magmatic Province and its correlation with other magmatic events related to the South Atlantic Opening. [Ph.D. Dissertation], São Paulo, Institute of Geoscience, University of São Paulo.

This work aims to study tholeiitic magmatic events presently exposed in NE Brazil and related to the evolution of the Atlantic continental margin during the Mesozoic. This magmatism is also correlated to the break-up of the West Gondwana supercontinent and are represented by mafic dike swarms crosscutting the Precambrian Borborema Province and intrusions (sill complexes dominantly) hosted in the Paleozoic Parnaíba Basin. The mafic dikes in the Borborema Province were until the beginning of this research restricted to a 350 km-long EW Rio Ceará-Mirim Swarm. However, high-resolution airborne magnetic surveys carried out on the province have shown its continuation toward SW, extending for an extra >650 km, and making up a total of >1,000 km in length across the province. A second set of dikes herein studied are hosted in the northern Borborema Province, named as Canindé Dike Swarm, where they extend for 380 km on a WNW-trend. The sills are commonly referred as the Sardinha Formation and compose a wide multilayered sill complex on the eastern Paleozoic section of the Parnaíba Basin. The close spatial relationship, petrological signatures and previous Early Cretaceous ages support the hypothesis of both events belonging to one major intrusive magmatic province: the Equatorial Atlantic Magmatic Province (EQUAMP). The petrological approach developed over the Rio Ceará Mirim-Canindé dikes and Sardinha sills (petrography, mineral chemistry, whole-rock geochemistry, and Sr-Nd-Pb isotopes) enabled the discrimination of two major geochemical groups: (1) high-Ti tholeiites (HT; TiO_2 > 2.0 wt.%), rich incompatible elements with initial $^{87}Sr/^{86}Sr$ (~0.706) and $\varepsilon Nd_{(130)}$ (-3.0 av.), and moderately radiogenic $^{206}Pb/^{204}Pb_{(m)}$ ratios of ~18.3; The HT melts sometimes form evolved rocks such as trachyandesites and trachytes with lower TiO_2 (generally < 2.5 wt.%; MgO < 3 wt.%). (2) Low-Ti tholeiites composed by evolved basaltic andesites with MgO < 6 wt.% and less radiogenic Nd ($\varepsilon Nd_{(130)}$ -4.65 to -4.40). The HT tholeiites are prevalent in dikes and sills. However, the LT group is reported just on the Borborema Province. These magmas have different degrees of enrichments in large ion lithophiles and light rare-earth elements, coupled with depletion in high-field-strength elements (Nb-Ta) and isotopic (Sr-Nd-Pb) signatures compatible with enriched mantle sources (EM-like). Additionally, few sets of dikes and sills have geochemical signature akin to the Central Atlantic Magmatic Province (CAMP). They form subalkaline (to transitional) basalts and basaltic andesites with MgO > 6 wt.% and slightly more radiogenic Nd ($\varepsilon Nd_{(130)}$ -1.3 av.), as similarly observed in the low-Ti Prevalent CAMP group. Two restrict sites in the Parnaíba Basin present very radiogenic Nd ($\varepsilon Nd_{(130)}$ ~6.1-3.3) and trace element pattern analogous to High-Ti CAMP. The geochemical-isotopic modelling processed for EQUAMP magma groups suggest an EM composition, which may be explained by mixing of DMM (Depleted MORB Mantle) with SCLM (Sub-Continental Lithospheric Mantle)-derived melts, plus minor crustal assimilation or an involvement of OIB (Ocean Island Basalt)-EM or FOZO/HIMU (via mantle plumes) and lithospheric melts. A possible explanation for EM magmas in the EQUAMP would be the Tristan-Gough hotspot. These magmas could have flooded throughout Rio Ceará Mirim-Transminas dike swarms toward NE South America forming the widespread HT tholeiitic dikes and sill complexes. Finally, a classic petrological comparison based on diverse geochemical parameters, isotopic data, as well as a (semi-)automated analysis processed with Self-Organizing Maps finds strong similarity between EQUAMP magmas and contemporaneous other tholeiitic plumbing systems of the Paraná-Etendeka Magmatic Province (PEMP) such as Florianópolis, Ponta Grossa, Resende-Ilha Grande, Southern Espírito Santo, Transminas dike swarms and Bero Volcanic complex

(Angola). These aspects combined with the possible physical link between the Rio Ceará Mirim and Transminas (PEMP) swarm and Riacho do Cordeiro and Vitória-Colatina swarms (PEMP) indicate that both provinces share similar mantle sources and magmatic processes. Consequently, it can be assumed that EQUAMP and PEMP form together a continental scale tholeiitic event related to the early opening stage of the South Atlantic Ocean, therefore designed as one major single LIP of Lower Cretaceous age that should be collectively referred as the South Atlantic Magmatic Province (SAMP).

Keywords: Tholeiitic magmatism, Magmatic plumbing systems, EM component, West Gondwana breakup, Large Igneous Provinces.

RESUMO

Macêdo Filho, A.A., 2021. “Geochemical characterization of the Equatorial Atlantic Magmatic Province and its correlation with other magmatic events related to the South Atlantic Opening”. [Tese de Doutorado], São Paulo, Instituto de Geociências, Universidade de São Paulo.

Este trabalho teve como objetivo estudar os eventos magmáticos toleíticos atualmente expostos no Nordeste do Brasil e relacionados à evolução da margem continental Atlântica durante Mesozoico. Este magmatismo também está relacionado à fragmentação incial do supercontinente Gondwana Ocidental, sendo representado por enxames de diques máficos cortando os terrenos Pré-cambrianos da Província Borborema e intrusões (domiantemente complexos de soleiras) hospedadas nas camadas paleozócicas da Bacia do Parnaíba. Os diques máficos estavam até o início desta pesquisa restritos a um enxame de diques EW do magmatismo Rio Ceará-Mirim com cerca de 350 km de extensão. No entanto, levantamentos magnéticos aerogeofísicos de alta resolução realizados na Província de Borborema mostraram sua continuação SW, estendendo-se por mais de 650 km, e perfazendo um total de mais de 1.000 km em extensão. Um segundo conjunto de diques aqui estudado está localizado no norte da Província de Borborema, denominado como Enxame de Diques Canindé, onde se estendem por 380 km em uma orientação WNW. As soleiras são comumente referidas como Formação Sardinha e compõem um amplo complexo de intrusões de múltiplas camadas na seção leste da Bacia do Parnaíba. A próxima relação espacial, assinaturas petrológicas e as idades prévias do Cretáceo Inferior apoiam a hipótese de ambos os eventos pertencerem a uma importante província magmática intrusiva: a Província Magmática do Atlântico Equatorial (PMAE). A abordagem petrológica desenvolvida sobre os diques Rio Ceará Mirim-Canindé e soleiras Sardinha (petrografia, química mineral, geoquímica de rocha inteira e isótopos Sr-Nd-Pb) permitiu a discriminação de dois grandes grupos geoquímicos: (1) toleítos de alto-Ti (HT; TiO_2> 2,0% em peso) ricos em elementos incompatíveis com $^{87}Sr/^{86}Sr$ inicial (~0,706), εNd (-3,0 av.), e proporções moderadamente radiogênicas de $^{206}Pb/^{204}Pb$ (~18,3). Este grupo HT às vezes forma rochas evoluídas, como traquiandesitos e traquitos com TiO_2 geralmente < 2,5% em peso e MgO < 3% em peso. (2) Toleítos de baixo TiO_2 (LT; TiO_2< 2,0% em peso) compostos por andesitos basálticos evoluídos com MgO < 6% em peso e Nd menos radiogênico (εNd -4,65 a -4,40). Os HT são prevalentes em diques e soleiras. No entanto, o grupo LT é relatado apenas na Província de Borborema. Esses grupos têm diferentes graus de enriquecimento em maiores, traços litófilos e elementos terras raras leves, juntamente com empobrecimento em elementos de alta intensidade de campo (Nb-Ta) e assinaturas isotópicas (Sr-Nd-Pb) que são compatíveis com manto enriquecido (componente EM). Além disso, alguns conjuntos de diques e soleiras têm assinatura geoquímica semelhante à Província Magmática do Atlântico Central (PMAC). Eles formam basaltos subalcalinos (a transicionais) e andesitos basálticos com MgO > 6% em peso e Nd ligeiramente mais radiogênico (εNd -1,3 av.) que são semelhantes ao grupo de baixo TiO_2 chamado “Prevalent CAMP”. Dois locais restritos na Bacia do Parnaíba apresentam também amostras com Nd muito radiogênico (εNd ~ 6.1-3.3) e padrão de elementos traço análogo ao “High-Ti CAMP”. A modelagem geoquímica-isotópica processada para os grupos de magma da PMAE sugere uma composição EM, que pode ser explicada pela mistura de DMM (*Depleted MORB Mantle*) com fundidos derivados do SCLM (*Sub-Continental Lithospheric Mantle*), além de menor assimilação crustal ou um envolvimento de OIB(*Ocean Island Basalt*)-EM ou FOZO/HIMU (via plumas mantélicas) e fontes litosféricas. Uma possível explicação para magmas EMI na PMAE seria o ponto de quente de Tristão da Cunha-Gough. Esses magmas podem ter fluido ao longo dos enxames de diques Rio Ceará Mirim-Transminas em direção ao NE da América do Sul, onde formaram os complexos de intrusões toleíticas de alto TiO_2. Finalmente, uma comparação petrológica clássica baseada

em diversos parâmetros geoquímicos, dados isotópicos, bem como uma análise (semi)automatizada processada com Mapas Auto-Organizáveis indica forte similaridade entre magmas PMAE e outros sistemas intrusivos toleíticos contemporâneos da Província Magmática do Paraná-Etendeka (PMPE) como os enxames de diques de Florianópolis, Ponta Grossa, Resende-Ilha Grande, Sul do Espírito Santo, Transminas e complexo Vulcânico de Bero (Angola). Esses aspectos combinados com a possível ligação física entre os enxames do Rio Ceará Mirim e Transminas e os enxames de Riacho do Cordeiro e Vitória-Colatina (PMPE) indicam que ambas as províncias compartilham fontes de manto e processos magmáticos semelhantes. Consequentemente, pode-se presumir que PMAE e PMPE formam juntas um evento toleítico de escala continental relacionado ao estágio inicial de abertura do Oceano Atlântico Sul, portanto, compondo um uma única LIP do Cretáceo Inferior, que poderia ser coletivamente referida como Província Magmática do Atlântico Sul (PMAS).

Palavras-chave: Magmatismo toleítico, Sistemas de condutos magmáticos, Componente EM, Dispersão do Gondwana Oeste, Grandes províncias ígneas.

SUMMARY

ABSTRACT ..... **xiii**

RESUMO ..... **x**

1. INTRODUCTION **17**

1.1. Presentation **17**

1.2. Rationale **17**

1.3. Objectives **18**

1.4. Dissertation Structure **19**

2. THEORETICAL REVIEW **20**

2.1. Large Igneous Provinces **20**

2.2. Continental Flood Basalts and Plumbing Systems **23**

2.3. The Gondwana Breakup and the Associated Mesozoic LIPs **27**

2.4. Geochemical Classifications of Magmas Constituting LIPs **30**

2.5. Methodologic Approaches **31**

2.5.1. Petrographic analyses **31**

2.5.2. Crystal Size Distribution **33**

2.5.3. Geochemical classification and magma differentiation **35**

2.5.4. Fractional crystallization **36**

2.5.5. Sources, crustal assimilation, and mixing **37**

2.5.6. Self-Organizing Maps (SOM) **41**

2.6. Analytical Producers **42**

2.6.1. Major and trace element analysis **42**

2.6.2. Isotope analysis (Sr, Nd, Pb) **42**

2.6.3. Mineral chemistry **43**

2.6.4. Crystal Size Distribution **43**

3. MAPPING AND PHYSICAL ASPECTS OF MESOZOIC DIKE SWARMS AND SILL COMPLEXES IN NE BRAZIL **45**

3.1. Introduction **45**

3.2. Previous works **45**

3.3. Spatial distribution of igneous products 47
3.4. Sampling 52
3.5. Structural Trend of Dike Swarms 57
3.6. Discussion 59
3.6.1. Juro-Triassic event 59
3.6.2. Early Cretaceous event 61

4. MINERAL CHEMISTRY AND CRYSTAL SIZE DISTRIBUTIONS OF MAFIC DIKES AND SILLS ON THE EASTERN BORDER OF THE PARNAÍBA BASIN, NE BRAZIL 64
4.1. Abstract 64
4.2. Introduction 65
4.3. Geological Setting 66
4.4. Sampling and Methods 68
4.5. Results 70
4.5.1. Major oxide chemistry 70
4.5.2. Petrography and mineral chemistry 71
4.5.3. Crystal size distribution 74
4.6. Discussion 76
4.6.1. Crystal size distribution 76
4.6.2. Chemical fractionation 79
4.6.3. Crystallization timescales 80
4.7. Conclusions 81
4.8. Acknowledgements 82

5. GEOCHEMICAL-ISOTOPIC SIGNATURE OF THE MESOZOIC THOLEIITIC MAGMATISM EXPOSED ON THE EASTERN PARNAÍBA BASIN 83
5.1. Introduction 83
5.2. Field Aspects and Sampling 83
5.3. Geochemical Classification and Geographical Distribution of Magmas 84
5.4. Petrography Notes and Mineral Chemistry 87
5.5. Major oxides and Fractional Crystallization 90
5.6. Trace Element Geochemistry 93
5.7. Isotope Geochemistry 95

5.8. Geochemical Correlations with Mesozoic LIPs in the Parnaíba Basin **97**

6. PETROGENESIS OF A MESOZOIC GIANT DIKE SWARMS IN NE SOUTH AMERICA: INTEGRATION OF GEOCHEMICAL AND ISOTOPIC DATA **100**

6.1. Abstract **100**

6.2. Introduction **101**

6.3. Geological Setting **103**

6.4. Methods **104**

6.5. Results **106**

6.5.1. Classification and geographical distribution **106**

6.5.2. Petrography and mineral chemistry **108**

6.5.3. Major element chemistry **110**

6.5.4. Trace element chemistry **111**

6.5.5. Radiogenic isotopes **114**

6.6. Discussion **115**

6.6.1. Fractional crystallization **115**

6.6.2. Conditions of magma crystallization **117**

6.6.3. Causes of the variability in Sr isotopic compositions **119**

6.6.4. Assessing the magma sources **120**

6.6.4.1. Non-plume Test 123

6.6.4.2. Plume Test 124

6.7. Conclusions **129**

6.8. Acknowledgments **130**

7. CRYSTAL SIZE DISTRIBUTION OF RIO CEARÁ-MIRIM DIKES AND CORRELATIONS WITH MAFIC INTRUSIONS OF THE PARNAÍBA BASIN .. **131**

7.1. Introduction **131**

7.2. Geological Setting **131**

7.3. Sampling and Methods **132**

7.4. Magma Types, Petrography, and Mineral Chemistry **133**

7.5. CSD Results **137**

7.6. Discussion **138**

7.6.1. Assessing textures and CSD of plagioclase **138**

7.6.2. Correlations among RCM dikes and intrusions of the Parnaíba Basin .. **140**

7.6.3. Crystallization timescales 145
7.6.4. Thermal influence in the Parnaíba Basin 146

8. GEOCHEMICAL CORRELATIONS AMONG THOLEIITIC PLUMBING SYSTEMS OF SOUTH ATLANTIC-RELATED LIPs 148
8.1. Introduction 148
8.2. The South Atlantic-related LIPs 150
8.2.1. Paraná Magmatic Province 150
8.2.2. Etendeka Magmatic Province 151
8.2.3. Equatorial Atlantic Magmatic Province 152
8.3. Material and Methods 157
8.3.1. Sample selection and screening 157
8.3.2. Self-Organizing Maps 159
8.3.3. Geological mapping 160
8.4. Results 161
8.4.1. Classification of the geochemical dataset 161
8.4.2. SOM 166
8.4.2.1. Component (plane) Plots 166
8.4.2.2. Cluster Analysis 167
8.4.2.3. Trace Element Patterns 168
8.4.2.4. Geographical Distribution 171
8.4.3. Radiogenic isotopes (Sr-Nd-Pb) 171
8.5. Discussion 175
8.5.1. Simplified Ti-based classifications 175
8.5.2. SOM solutions and previous petrological classifications 177
8.5.3. Geodynamic considerations 178

9. SYNTHESIS AND CONCLUDING REMARKS 182

REFERENCES 186

SUPPLEMENTARY MATERIAL OF CHAPTER 4. MINERAL CHEMISTRY AND CRYSTAL SIZE DISTRIBUTIONS OF MAFIC DIKES AND SILLS ON THE EASTERN BORDER OF THE PARNAÍBA BASIN, NE BRAZIL 217

SUPPLEMENTARY MATERIAL OF CHAPTER 5. GEOCHEMICAL-ISOTOPIC SIGNATURE OF THE MESOZOIC THOLEIITIC MAGMATISM EXPOSED ON THE EASTERN FLANK OF THE PARNAÍBA BASIN 237

SUPPLEMENTARY MATERIAL OF CHAPTER 6. PETROGENESIS OF A MESOZOIC GIANT DIKE SWARMS IN NE SOUTH AMERICA: INTEGRATION OF GEOCHEMICAL AND ISOTOPIC DATA 250

SUPPLEMENTARY MATERIAL OF CHAPTER 7. CRYSTAL SIZE DISTRIBUTION OF RIO CEARÁ-MIRIM DIKES AND REGIONAL CORRELATIONS WITH PARNAÍBA BASIN INTRUSIONS 278

SUPPLEMENTARY MATERIAL OF CHAPTER 8. GEOCHEMICAL CORRELATIONS AMONG THOLEIITIC PLUMBING SYSTEMS OF SOUTH ATLANTIC-RELATED LIPs 281

1. INTRODUCTION

1.1. Presentation

This dissertation meets the requirements to obtain the degree of Doctor of Philosophy in the Graduate Program in Geochemistry and Geotectonics of the Institute of Geosciences - University of São Paulo. This project focus on the study of mafic magmatic events exposed in the NE Brazil that were related to the evolution of the Atlantic continental margin during the Early Cretaceous, represented by giant dike swarms hosted in the Borborema Province (Rio Ceará-Mirim Magmatism), and a sill complexes intruding the Parnaíba Basin (Sardinha Magmatism). The very close spatial relationship between these plumbing systems styles together with the synchronous ages led Hollanda et al. (2019) to consider them as a part of a single Large Igneous Province (LIP): the Equatorial Atlantic Magmatic Province - EQUAMP. In order to test this hypothesis, this work studied EQUAMP components on a geochemical perspective, charged with carrying out a complete geochemical (major and trace element) and isotopic (Sr, Nd, Pb) characterization of the dike swarms and sills based on a comprehensive sampling to integrate their evolutionary histories and mantle source(s) into a model of a single LIP. The new data still allowed to establish correlations with the Early Cretaceous Paraná-Etendeka Province and outline an integrative geodynamic model for the tholeiitic magmatism linked to the early stage of Equatorial/South Atlantic Ocean born.

1.2. Rationale

The beginning of the 1990s brought with it the recognition of two magmatic events exposed in NE Brazil that were emplaced time-related to the breakup of the West Gondwana continent and the consequent opening of the Equatorial/South Atlantic Ocean in the Early Cretaceous. They were described as: (i) a mafic dike swarm named Rio Ceará-Mirim dike swarm (RCM) intrusive in Precambrian terranes of the Borborema Province (Bellieni et al., 1992; Matos, 1992; Oliveira, 1992), and (ii) sills (and subordinate dikes) grouped as Sardinha Formation in the Paleozoic sedimentary succession of the eastern side of the Parnaíba Basin (Bellieni et al., 1990; Fodor et al., 1990). Dikes and sills whether outcropping in the basement or within the basin, are prevalently described as high TiO_2 tholeiitic diabases.

Defined as a 350 km-long E-trending linear dike swarm (Archanjo et al., 2000; Hollanda et al., 2006; Ngonge et al., 2016a), the extension and geometry of the RCM was

recently re-examined after high-resolution airborne magnetic data of the Borborema Province available by the Brazilian Geological Survey (CPRM). These data allowed to show that the RCM drastically turns from EW towards a NE-SW direction at approximately 38ºW, which continuously propagates for, at least, 600-700 km more in length. The current total size of about 1,000 km characterizes the RCM as a giant, arcuate dike swarm in the sense of Ernst and Buchan (1997). Despite this relevance, no geological study was carried out on the NE-trending segment of the RCM yet.

The Sardinha sills, in turn, are exposed along the eastern side of the Parnaíba Basin, i.e. adjacent to the outcrop area of the NE-trending RCM. Although sills are mapped from north to south along the entire eastern side of the basin, the groundbreaking works have restricted the sampling to a small central area ignoring much of the geographic (and maybe geochemical) representativeness of this magmatism. Supported by resources of the oil-gas industry, some scientific papers were recently published dealing on the geochemical aspects of these eastern sills (Silva et al., 2017; Oliveira, et al., 2018; Heilbron et al., 2018; Miloski et al., 2019, 2020). Despite the merits, important sampling gaps persist, especially in southeastern areas.

1.3. Objectives

This work brings a significant database of geochemical (major oxides and trace elements) and Sr-Nd-Pb isotope data obtained from the aforementioned igneous rocks – i.e., the dikes composing the NE-trending branch of the RCM and the intrusions that represent the Sardinha Magmatism. The data obtained for the NE-trending RCM were integrated with existing data for the dikes that constitute the E-trending branch of the RCM (Ngonge et al., 2016a) to discuss the petrogenesis of the entire dike swarm. A subordinate intrusive system named Canindé dike swarm was additionally investigated in a similar approach.

The specific objectives were:

- To map the area of occurrence of the dikes in the Borborema Province and sill complexes of the Parnaíba Basin;
- To identify the mineral assemblage and textures of studied events;
- To understand the history of magma crystallization using of the crystal size distribution (CSD) technique combined with mineral chemistry in plagioclase and pyroxene;

- To define geochemical groups, recognize which mechanisms had operated during the magma evolution (fractional crystallization, and crustal assimilation), and also infer about the nature of mantle source(s) by using of geochemical (major and trace elements) and Sr-Nd-Pb isotope data;
- To compare the geochemical signatures of the EQUAMP with other plumbing systems of the Paraná-Etendeka Magmatic Province using classical petrological classifications and machine learning-based tecnic of Self-Organizing Maps (SOM).

1.4. Dissertation Structure

The PhD dissertation is organized into nine chapters. Current **Chapter 1** presents the topic and aims of this work. **Chapter 2** includes a literature review on LIPs and the fundamentals of the analytical methods applied in this investigation. **Chapter 3** presents the mapping of the entire RCM and other minor dike swarms and the sill province within the Parnaíba Basin based on airborne magnetic anomalies, satellite remote sensing data and field checking. **Chapter 4** presents the paper "Mineral chemistry and crystal size distributions of mafic dikes and sills on the eastern border of the Parnaíba Basin, NE Brazil" published in the *Journal of Volcanology and Geothermal Research* (Macêdo Filho et al., 2019). Chapters **5** and **6** deal with the geochemical and isotopic characterization of the sills and RCM (plus the Canindé subswarm), respectively. **Chapter 7** brings the results of the crystal size distribution (CSD) study via a combination of image analysis and mineral chemistry by electron microprobe (EPMA) applied to the NE-trending RCM and the comparison with results published for the Sardinha sills. **Chapter 8** includes the results of geochemical comparison among the EQUAMP and Paraná-Etendeka plumbing systems explored via SOM. Finally, **Chapter 9** summarizes the concluding remarks of this research.

2. THEORETICAL REVIEW

2.1. Large Igneous Provinces

Firstly defined by Coffin and Eldholm (1994), a Large Igneous Province (LIP) is a massive emplacement of mafic rocks (mostly Fe-Mg rich ± felsic and intermediate types) occurring in intraplate settings and manifested as continental flood basalts (CFB), oceanic basin basalt outpourings, volcanic passive margins, oceanic plateaus, submarine ridges, and seamount groups. After 25 years, these authors maintained the original concept while incorporating two elements. LIPs would be events: (1) erupted over short-lived periods (10^5-10^6 years) or persistently erupted within a period of 10^7-10^8 years (Fig. 2.1), and (2) placed in an area extent of over 10^4 km² (Coffin and Eldholm, 2018).

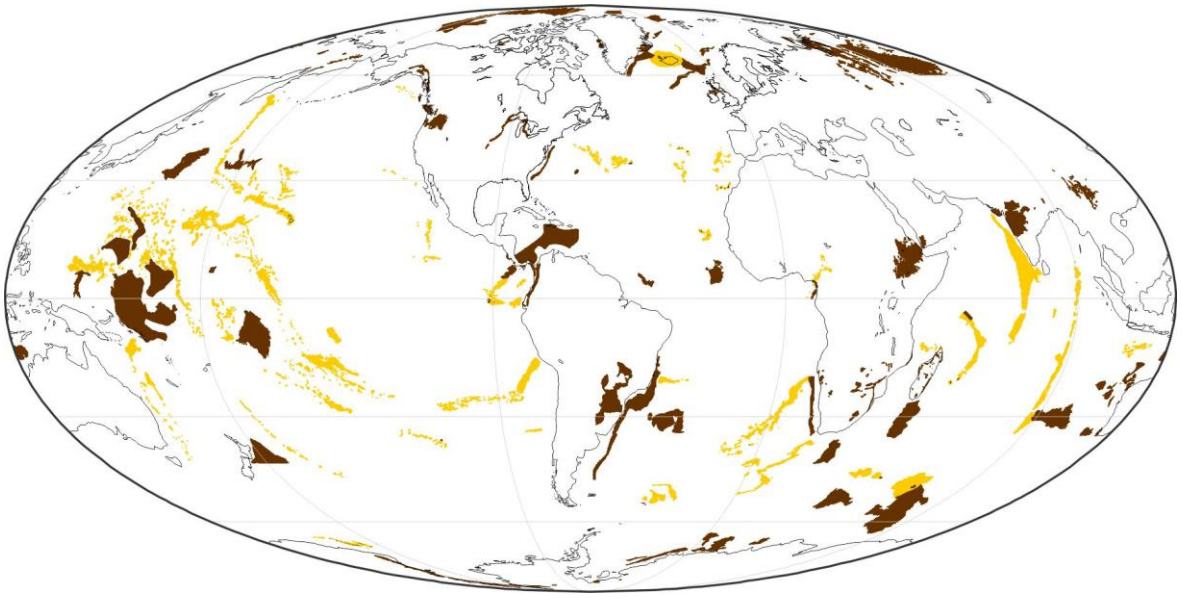

Figure 2.1. Distribution of main Phanerozoic LIPs on Earth. The brown areas represent transient events, whereas those in yellow color are persistent magmatic manifestations. Figure modified from Coffin and Eldholm (2018).

Sheth (2007) argues that the original Coffin and Eldholm's classification improperly excludes many of the igneous phenomena that differ from the classical continental flood basalts and oceanic manifestations. According to this author, a more comprehensive classification would also incorporate felsic provinces, layered intrusions, and even granitic batholiths (e.g., Tibet-Himalaya, Andes) with outcrop areas ≥ 50 × 10^3 km^2, which should be organized into *Large Volcanic Provinces* (LVP) and *Large Plutonic Provinces* (LPP) regardless their chemical affinity (Fig. 2.2). In this scheme, the LVPs should assemble Large Basaltic Provinces (LBPs),

Large Rhyolitic Provinces (LRPs), Large Andesitic Provinces (LAPs), and Large Basaltic–Rhyolitic Provinces (LBRPs). The LPPs should include, though, intrusive equivalents such as the Large Granitic Provinces (LGPs) and mafic intrusive components such as layered intrusions, giant dike swarms, anorthosite massifs, and deeper portions of oceanic plateaus. Thus, a LIP should not be restricted to mafic magmatism in intraplate settings, but contrarily would include any igneous manifestation even in convergent margins, which are normal sites of crustal growth and magma generation.

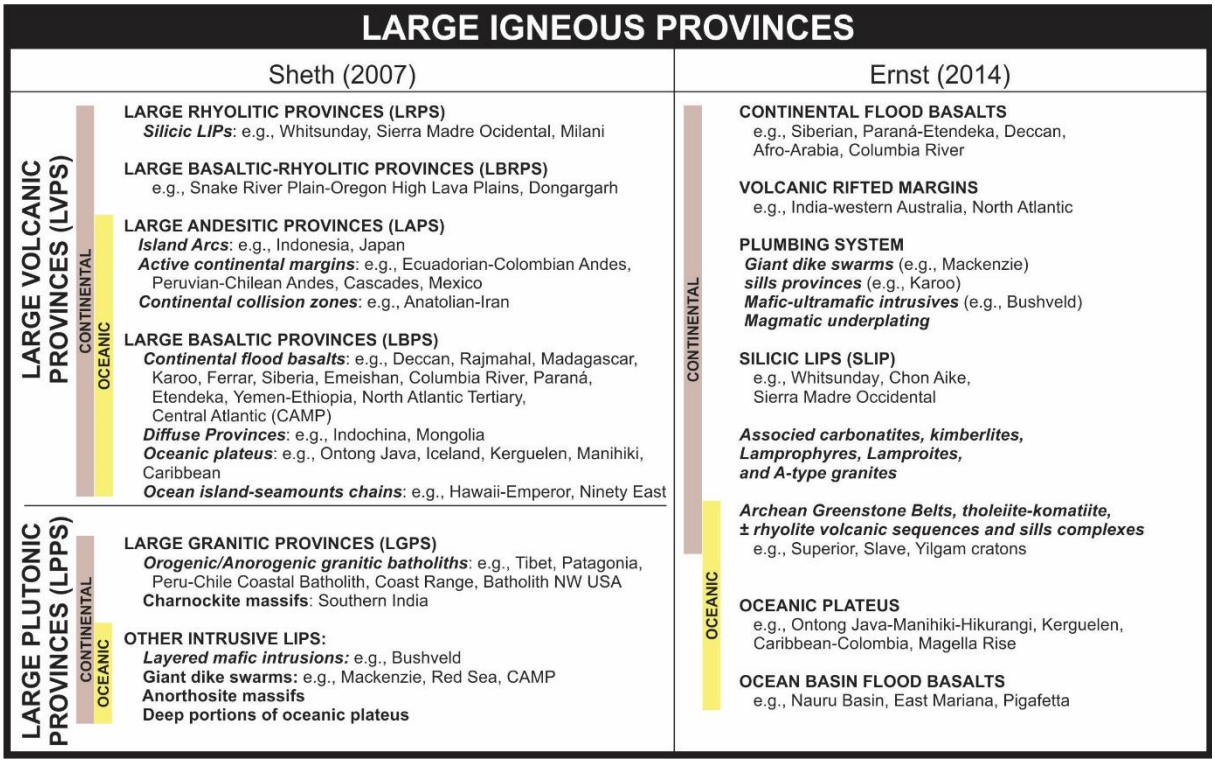

Figure 2.2. Large Igneous Provinces classifications according to Sheth (2007) and Ernst (2014). Both classifications encompass LIP components proposed in the previous classification of Coffin and Eldholm (1994).

Bryan and Ernst (2008) took back the LIP concept as defined by Coffin and Eldholm (1994) and included extrusive and intrusive silicic magmatic provinces (SiO_2 > 65 wt.%) that are not linked to "…*normal seafloor spreading or subduction, and massive Precambrian magmatic events*…", but, instead, represented by lava flows, giant dyke swarms, sill complexes and layered intrusions. Recently, Ernst (2014) has updated Bryan and Ernst's definition to also include carbonatites, kimberlites, lamprophyres and A-type granites associated with mafic provinces, besides Archean greenstone belts (Fig. 2.2). In this modern view, the volcanic and plutonic components of LIPs are described as 'anomalous' magmatic events that cover areas of over 0.1 Mkm² with a total volume ≥1 Mkm³ and are composed predominantly (but not

exclusively) of mafic igneous rocks definitely placed in intraplate settings. These are usually reported as short-lived events (< 5 million years) or events defined by multiple short pulses with a maximum duration of a few million years (Bryan et al., 2010; Bryan and Ferrari, 2013; Ernst, 2014; Ernst et al., 2019, 2021). This is the most comprehensive and consensual concept currently accepted for LIPs.

Passive and active triggering mechanisms have been evoked to explain the LIP emplacement. The active model necessarily assumes the participation of a mantle plume at the base of the lithosphere causing regional uplift, volcanism and rifting (e.g., Wilson, 1963, 1973; Morgan 1971; Richard and Griffiths, 1989; Campbell and Griffiths, 1990; White and McKenzie, 1995; Ernst and Buchan, 2001; Courtillot et al., 2003; Coltice et al., 2007, 2019). Passive models, in turn, require: (i) upwelling of the hot asthenosphere beneath a lithosphere under stretching and thinning (White and McKenzie, 1989); (ii) thermal insulation beneath (super)continents promoting melting of the subcontinental lithospheric mantle (SCLM) (Anderson, 1982; Coltice et al., 2007); (iii) edge-driven convection – i.e., small-scale convective flow induced by strong lateral contrasts of temperature and viscosity at the transition between older and thicker lithosphere (cratons) and young mobile belts (King and Anderson, 1995; King and Ritsema, 2000); or (iv) delamination of the thickened lithosphere and consequent ascent of the asthenosphere triggering melting of the eroded lithosphere left behind (e.g., Seber et al., 1996). Over the last decades, the plume theory has gained strength since global tomographic models showed a clear concurrence between the eruption sites of LIPs and marginal areas of “Large Low Shear–wave Velocity Provinces” (LLSVPs) (Fig. 2.3) existing beneath Africa and the mid-Pacific ocean (Torsvik et al., 2006; Doubrovine et al., 2016), which are global-scale features in the lower mantle derived from the accumulation over the Earth's history of the ancient subducted oceanic crust near the mantle-core boundary. After continuous accumulation through time, such slab cemeteries would act as a thermal insulator to channel heat flow from the outer core where plumes are expected to form (Niu, 2018).

Regardless of the triggering mechanisms involved to explain the anomalous melting of the mantle, LIPs have been a frontier theme in Geosciences due to its role in mantle geodynamics, continental breakup (timing of rifting process and paleocontinental reconstructions), climate changes and mass extinction events (i.e., impacts on biosphere, hydrosphere and atmosphere), mineral and energy exploration and interplanetary studies (Ernst et al., 2005; Bryan and Ferrari, 2013; Ernst et al., 2019). Since the dike swarm and sills that are the focus of this work are proposed to be a continental plumbing system LIP, the following

sections are dedicated to detailing some aspects of this theme in a modern perspective, taking into account the Mesozoic LIPs related to the breakup of Gondwana and, nowadays, located in the southern hemisphere.

2.2. Continental Flood Basalts and Plumbing Systems

Flood basalts linked to LIP events are huge volcanic accumulations of mafic rocks, usually of tholeiitic affinity, more expressive in oceanic realms than continental environments (Coffin and Eldholm, 1994). Such imbalance occurs due to a major efficiency of thermal anomalies ('plumes') in producing a higher volume of melts under thinner (oceanic) lithosphere (Courtillot and Renne, 2003). Except for some remnants of ophiolitic sections, the oceanic LIPs are barely preserved through time because of natural consumption along destructive plate margins (Doucet et al., 2020; Ernst et al., 2021).

Conversely, continental LIPs are usually well studied, with remarkable examples in Phanerozoic sections hosted within cratonic areas and continental shields, such as those in the Australian (Kalkarindji LIP of ~511 Ma; Ware et al., 2018) and Siberian (Siberian Traps of ~252 Ma; Augland et al., 2019) cratons; Pangea (Central Atlantic Magmatic Province of ~201 Ma; Marzoli et al., 1999, 2018); Africa-Antarctica (Karoo-Dronning Maud Land-Ferrar LIP of 184-183 Ma; Jourdan et al., 2005; Greber et al., 2020); South America-Africa (Paraná-Etendeka LIP of ~134 Ma; Thiede and Vasconcelos, 2010; Rocha et al., 2020; Gomes and Vasconcelos, 2021); India (Deccan Traps of ~66 Ma; Schoene et al., 2019) and East-African rift system (Afar LIP of 30 Ma to the present; Ebinger and Sleep, 1998; Riisager et al., 2005). They are thought to be the ultimate stage of a complex chain of processes that begins with partial melting and magma segregation from the mantle source and culminates with their eruption, generally associated with the disruption of (super)continents. The intermediate stages can be revealed by the plumbing systems, which record the history of the magma ascent through lithospheric discontinuities, structural weakness, or mechanical interfaces between rock layers forming dike swarms, sill complexes, mafic-ultramafic intrusions, magmatic underplating, and carbonatite and kimberlite bodies (Kavanagh et al., 2017). These plumbing system elements are not only recognized in Phanerozoic LIPs but are the exclusive remnants of vastly eroded Precambrian LIPs, the most dramatic and well-studied of them being the dike swarms and sill complexes (Ernst et al., 2019). Among the motivations in using dike swarms and sills to assess the magmatic diversity of the LIPs is because they tend to be less evolved than volcanic equivalents,

covering a major range of compositional diversity of magmas, also, their location and orientation provide evidence of magma ascent, feeder zones, and emplacement (Owen-Smith et al., 2021).

A dike is a tabular body crosscutting a rock layer at a high angle (> 50°), whereas a sill is a low-angle intrusion (< 10°) regarding a previous primary or tectonic orientation in the country rock (Galerne et al., 2008). Thus, sub-vertical intrusions are usually classified as dikes, and sub-horizontal intrusions as sills. Dikes usually intrude crystalline basement terrains and are often associated with extensional settings or crustal breakup. They are one of the keys to the interpretation of plate tectonics, preserving a record of ancient magnetic fields, widely used as paleostress indicators and in paleogeographic reconstructions, sometimes featuring mechanical anisotropies in the crust to localize strain in post-tectonic events (Geshi, 2005; Dineva et al., 2007; Peng, 2010; Ernst and Youbi, 2017; Magee et al., 2019). If dikes form a high concentration of intrusions (swarm) with a length greater than 300 km, they are classified as a giant dike swarm (Ernst and Buchan, 1997) displaying individual widths in the range of 10-40 m and recording horizontal magma flux for over hundreds to thousands of kilometers (e.g., Ernst and Baragar, 1992; Archanjo et al., 2000, 2002).

Based on the surface geometry, Ernst and Buchan (2001) proposed nomenclature for giant dike swarms (Fig. 2.4):

(i) the radiating swarms are interpreted as a result of the mantle plume impingement and can be classified as continuous fanning (type I), fanning subdivided into separate subswarms (type II), subswarms of subparallel dikes that radiate from a common point (type III);

(ii) the linear swarms consist of an array of subparallel and sparse dikes exposed over a broad area (type IV) or subparallel dikes forming a narrow zone (type V), and can represent distal sites of radiating swarm(s);

(iii) the arcuate swarms (type VI) display are usually part of a major radiating geometry in which the dikes (or dike swarms) converge towards a focal point in a domal uplift zone that are related either to the impingement of a mantle plume head or to a triple-junction region. The arcuate swarms can be considered a swinging pattern from a radial to the distal linear array, or partially (or completely) circumscribes a magmatic center.

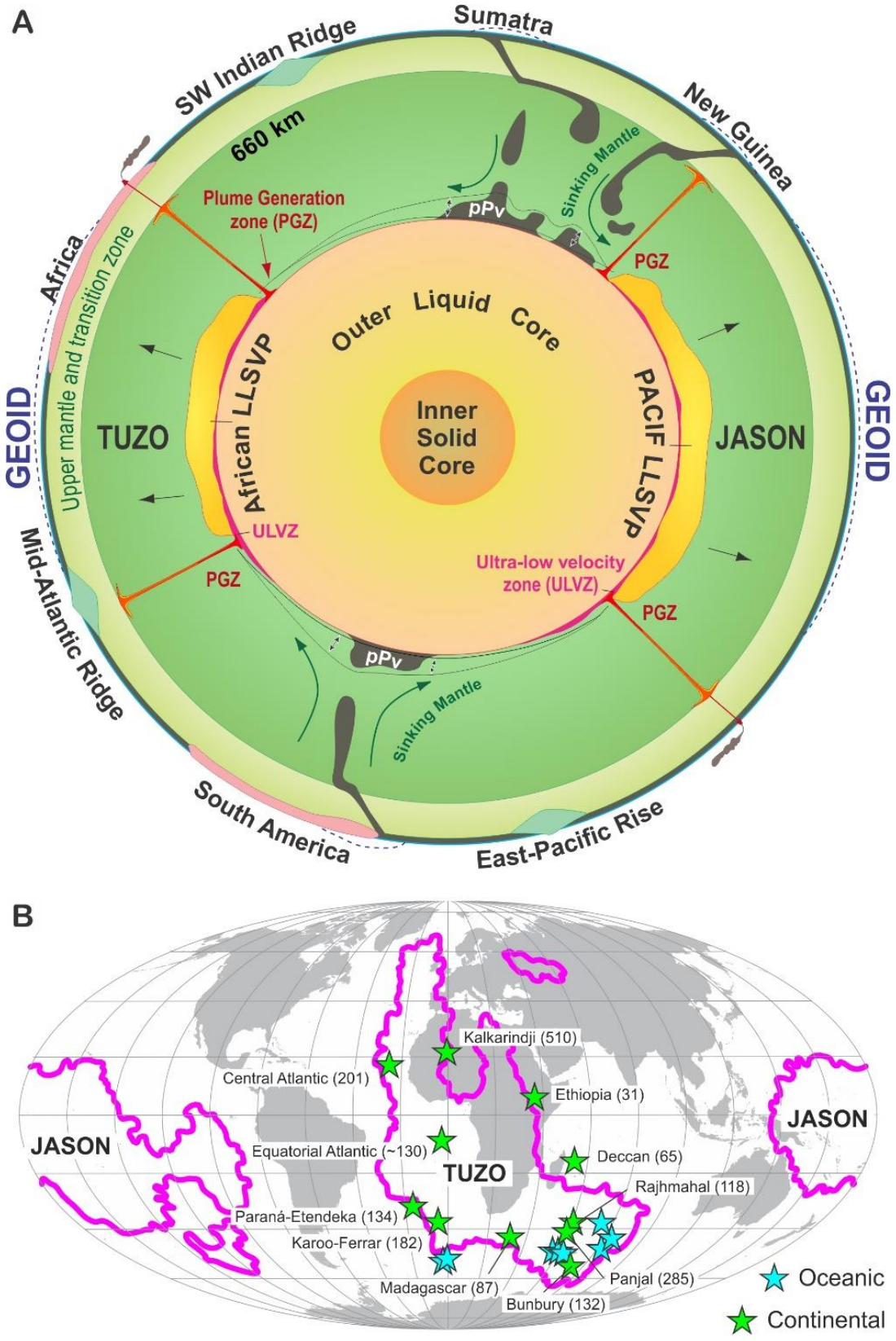

Figure 2.3. (A) Model of plume generation associated to LLSVPs according to Torvisk et al. (2006) and evidencing the TUZO/African and JASON/Pacific areas. *pPv* indicates lenses of post-perovskite according to Trønnes (2010). (B) Global tomographic model drawn on a planimetric global map highlighting the 2,800 km deep contour of the LLSVPs. Stars correspond to continental (green color) and oceanic (blue color) LIP centers preferentially anchored along the African LLSVPs margins. Numbers within parentheses represent the LIP age in Ma (based on Svensen et al., 2017).

Sills are sub-horizontal bodies widely hosted in sedimentary basins (or into deep supracrustal sequences) at variable depths (Muirhead et al., 2012). They can play a role as heat sources for the maturation of organic matter, consequently participating in the hydrocarbons genesis (Fjeldskaar et al, 2008) and greenhouse gases production, which can be possibly linked to paleoclimate shifts and mass extinction events (Svensen et al., 2007; Davies et al., 2017). According to Magee et al. (2016 and therein references), seismic data and field observations have shown that sill complexes form an interconnected network of saucer-shaped and inclined sheets that can extend laterally for tens to thousands of kilometers and therefore feed volcanic centers considerably far from the main feeder zone (Fig. 2.5A). These authors point out the coalescence of magma fingers or magma lobes (on a larger scale) as a common mechanism for sills emplacements (Fig. 2.5B).

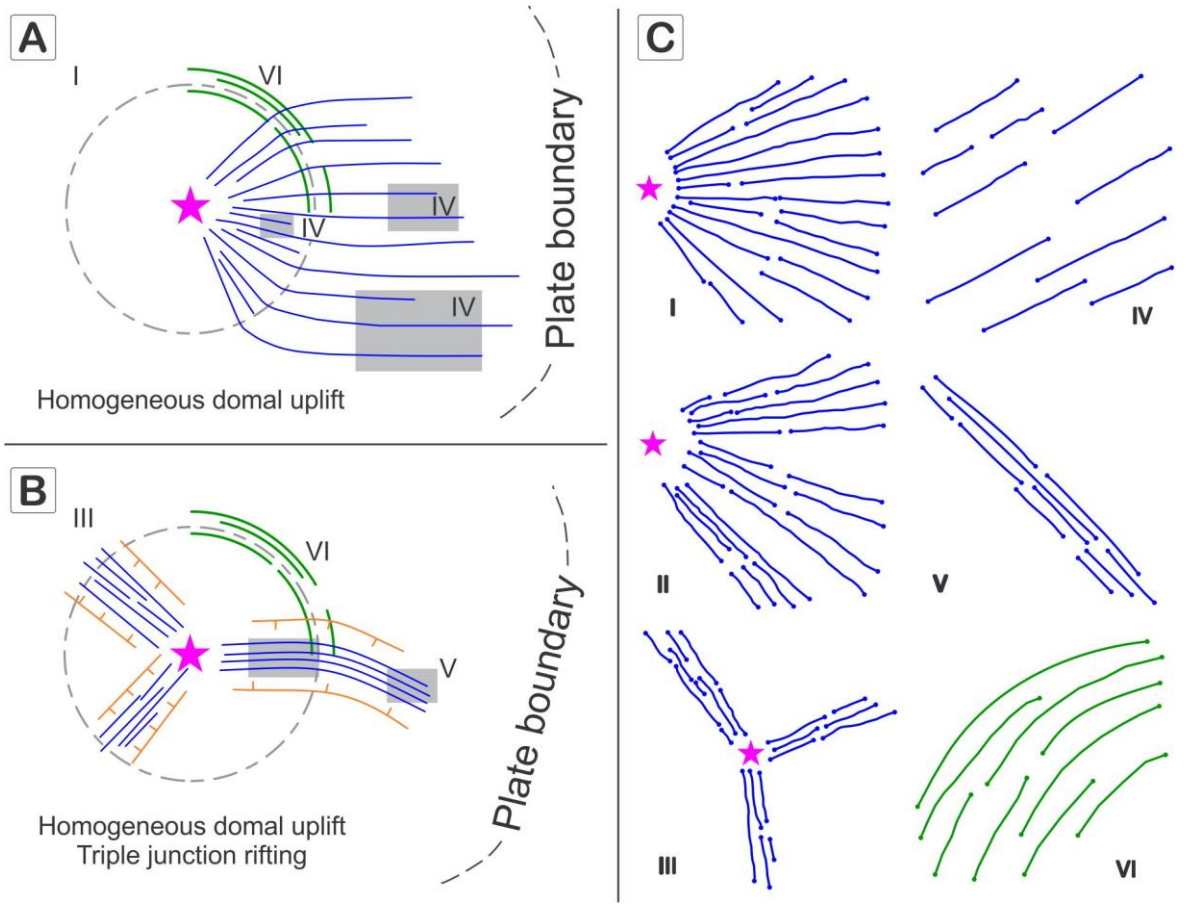

Figure 2.4. Geometry-based nomenclature for giant dike swarms according to Ernst and Buchan (2001). The pink star corresponds to a thermal anomaly/mantle plume center located at (A) the convergence of radiating dikes and (B) a triple-junction rift, both associated with a domal uplift zone. (C) Characteristic geometries of giant radiating dike swarms: I - continuous fanning swarm; II - fanning pattern subdivided into separate subswarms; III – subswarms of subparallel dikes that radiate from a common point; IV - subparallel dikes over a broad area; V - subparallel dikes in a narrow zone; VI - arcuate pattern. Blue lines are axial dikes and orange lines constitute the envelope for radial dike systems; the dotted circle is the domal uplifted center.

For Menand (2011), the reasons for (sub)vertical migrant magmas to be converted into sills are (1) buoyant control, where sills are formed into crustal levels when magmas reach neutral buoyant; (2) rheology control, when an intrusion across contrasting ductile and elastic horizons can convert a feeder dike into a sill; (3) rigidity anisotropy, which explain that if a propagating feeder dike finds a rigid layer it can be arrested encouraged sill formation; and (4) stress control, related to the rotation of minimum compressive stress axis to vertical leading the subhorizontal intrusion. Studies regarding numerical models and field observations support the idea that when a vertical intrusion like a dike reaches subhorizontal strata or discontinuities (bedding planes and/or compliant lithologies), it propagates parallel to the preferential orientation of the country-rock forming a sill, which can deflect in one or two directions along the contact (Gudmundsson, 2011; Magee et al., 2016).

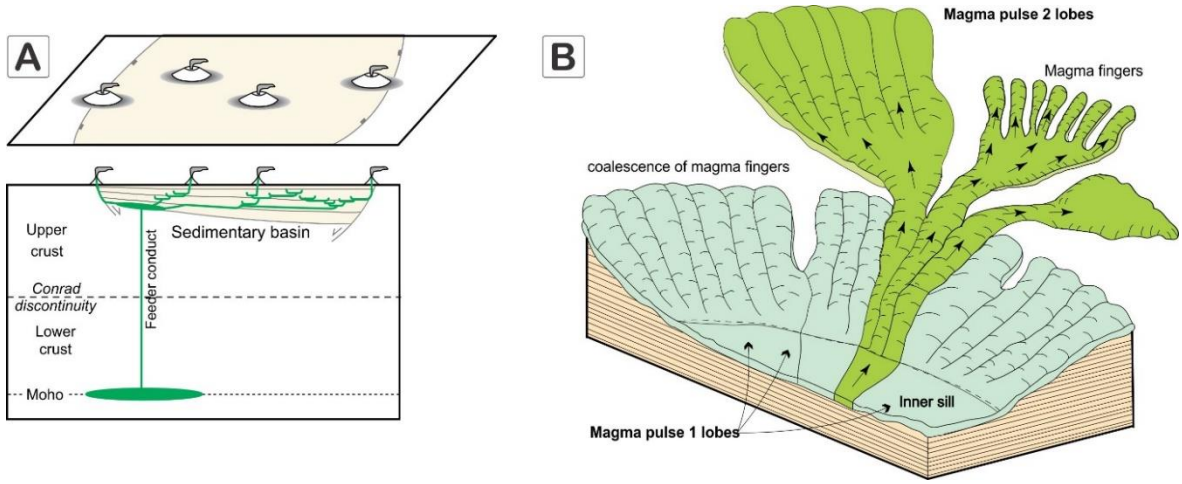

Figure 2.5. General features of sills. In (A) sill complexes emplacement within a sedimentary basin that can form flood basalts far from main feeder conduct. In (B) sketch of saucer-shaped sill formation in two magma pulses. Lobes are formed by the coalescence of propagating fingers. Source: Magee et al. (2016).

2.3. The Gondwana Breakup and the Associated Mesozoic LIPs

The diachronic assembly of continental masses to form the Gondwana occurred in the Neoproterozoic Era spanning from 690 to 530 Ma (Li et al., 2008). This supercontinent was originally formed by more than 2/3 of the present-day landmasses (South America, Africa-Arabia, India, Australia, Antarctica, and New Zealand) housing about 1/3 of all known LIPs in the world (Sensarma et al., 2017). At ca. 300 Ma, in the Paleozoic, Gondwana became part of the even larger Pangea supercontinent after its collision with Laurasia (North America, Europe, North Asia, Japan) (Bradley, 2011). Pangea remained consolidated as a single landmass until

the Triassic–Jurassic boundary (ca. 201.5 Ma), when deep mantle dynamics caused its disruption and, as a consequence, massive mafic (tholeiitic) magmatism was emplaced shortly before the opening of the Central Atlantic Ocean forming the well-known Central Atlantic Magmatic Province (Marzoli et al., 1999; Blackburn et al., 2013; Davies et al., 2017, 2021; Heimdal et al., 2018). The CAMP is perhaps the largest continental LIP on Earth (Fig. 2.6), covering ca. 11×10^6 km^2 (Marzoli et al., 2018), with remnants in west Africa (Knight et al., 2004; Verati et al., 2005, 2007), southwest Europe (Iberia and France; Callegaro et al., 2014; Jourdan et al., 2003), east coast of North America (Callegaro et al., 2013; Merle et al., 2014; Whalen et al., 2015), and South America (Marzoli et al., 1999; De Min et al., 2003; Deckart et al., 2005; Merle et al., 2011; Bertrand et al., 2014).

The Gondwana breakup started at the Lower Jurassic when rifting processes triggered the individualization of the West Gondwana (South America and Africa-Arabia) and East Gondwana (Antarctica, India/Sri Lanka, Madagascar, Australia, and other microcontinental blocks), giving place to the opening of the pre-Indian Ocean (Torsvik et al., 2012; Gibbons et al., 2013). The Jurassic rifting was followed by the emplacement of the Karoo-(Dronning Maud Land-)Ferrar tholeiitic magmas (~184-178 Ma; Fig. 2.6) covering an area of ca. 6×10^6 km^2 including Africa, Antarctica, Australia (Tasmania/Victoria) and minor extents in South America, India and New Zealand (Cox et al., 1992; Heimann et al., 1994; Encarnación et al., 1996; Duncan et al., 1997; Jourdan et al., 2005; Svensen et al., 2017; Greber et al., 2020). From the Jurassic onwards, the East Gondwana diachronically underwent other rifting episodes to dismember Madagascar-Seychelles-India from Australia-Antarctica (Royer and Coffin, 1992; White et al., 2013), resulting in the emplacement of the Bunbury (136-130 Ma) and Rajmahal (~118-115 Ma) traps preserved, respectively, in Western Australia and NE India (Kent et al., 2002; Olierook et al., 2016). In the K-T boundary, India started to separate from the East Gondwana remnant to begin its drifting towards Asia, at the time when the Deccan Traps erupted (Hooper et al., 2010; Renne et al., 2015). Rifting is still in progress to disconnect the Arabian Peninsula from the rest of Africa, generating continuous volcanism since 30 Ma ago (Riisager et al., 2005).

The extensional tectonics related to the West Gondwana breakup led to the separation of South America and Africa, and gave place to the opening of the South Atlantic Ocean (Torsvik et al., 2012; Matthews et al., 2016), during which the major igneous manifestation is surely the Paraná–Etendeka Magmatic Province (PEMP; Fig. 2.6) (~134 Ma; Janasi et al., 2011; Florisbal et al., 2014; Almeida et al., 2018; Rocha et al., 2020). This province covers an area of at least

1.5 × 10^6 km^2 including central-southern Brazil and the neighboring countries Argentina, Uruguay, and Paraguay, besides the African counterparts in western Namibia, Angola, and South Africa (Peate et al., 1992). The PEMP is composed of tholeiitic volcanics (flood basalts and silicic rocks) and intrusive bodies represented by dike swarms and sill complexes hosted either into the sedimentary layers of the Paraná Basin (Paleozoic) or crosscutting the Precambrian basement (Bellieni et al., 1986; Peate et al., 1992, 1997).

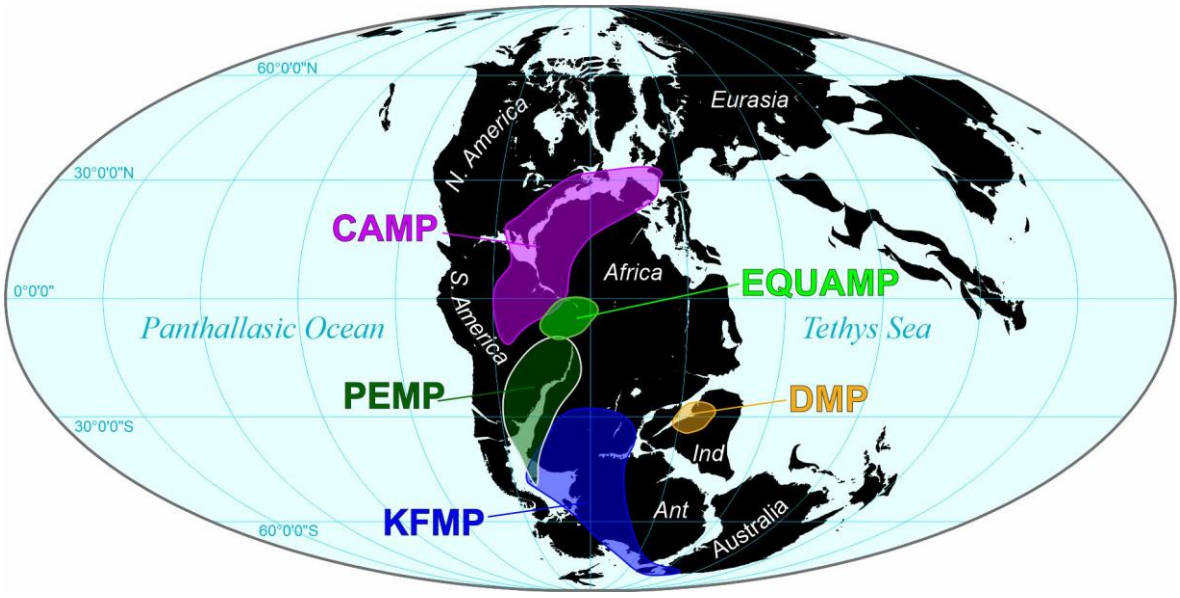

Figure 2.6. Earth at 201 Ma ago with rough boundaries of main Mesozoic LIPs recognized in the West Gondwana realm: Central Atlantic (CAMP; Triassic), Karoo-Ferrar (KFMP; Early Jurassic), Paraná-Etendeka (PEMP; Early Cretaceous) and Equatorial Atlantic (EQUAMP; Early Cretaceous), and Deccan (DMP; Late Cretaceous). The reconstruction was generated in GPlates software based on the model of Matthews et al. (2016).

The propagation of the South Atlantic rift towards the north was marked by a change in the tectonic regime from orthogonal to slightly oblique extension to transform or strike-slip faulting prevailing in the Equatorial Atlantic segment (Moulin et al., 2010; Heine et al., 2013; Frizon de Lamotte et al., 2015; Ye et al., 2017). In NE of Brazil and African counterpart, the extensional tectonics resulted in the development of several intracontinental rift basins and emplacement of mafic (tholeiitic) dike swarms and a sill complex as seen in the south. These igneous components are scattered over an area ca. 0.7 × 10^6 km^2 in NE of Brazil, gathered in a single entity, termed as the Equatorial Atlantic Magmatic Province (EQUAMP; Fig. 2.6) by Hollanda et al. (2019). The Sardinha sills and subordinate dikes are hosted by Paleozoic sedimentary rocks of the Parnaíba Basin, being especially exposed in its eastern side (Fodor et al., 1990; Bellieni et al., 1990; Silva et al., 2017; Mocitaiba et al., 2017; Oliveira et al., 2018; Heilbron et al., 2018; de Castro et al., 2018; Macêdo Filho et al., 2019; Fernandes et al., 2020),

whereas the dike swarms are identified as Rio Ceará–Mirim (Bellieni et al., 1992; Ernesto et al., 2003; Hollanda et al., 2006; Ngonge et al., 2016a) with at least 1,000 km in length, and two minor swarms (~350 km long) named Canindé and Riacho do Cordeiro, all intrusive in the Precambrian Borborema Province (Oliveira et al., 2021; Melo et al., 2021, 2022). The African counterpart of the EQUAMP is thought to be the tholeiitic lavas and intrusive rocks in the Benue Trough (Maluski et al., 1995; Coulon et al., 1996). Younger igneous activities in South America and Africa are associated with the continental drifting stages.

2.4. Geochemical Classifications of Magmas Constituting LIPs

Perhaps the most used geochemical distinction applied to tholeiitic magmas is that originally made by Cox et al. (1967) by studying the compositional variation of basalts of the Karoo province. In this groundbreaking work, these authors divided the Karoo basalts into two distinct provinces – one of them including rocks with abnormally higher Ti (also K, P, Sr and Zr) contents than expected for tholeiitic geochemistry. Since then, the Cox and coauthor's classification has become a first-order tool to discuss the petrogenesis of Gondwanan LIPs using the arbitrary (but consistent) threshold of 2 wt.% of TiO_2 to discriminate between low- and high-Ti tholeiites (e.g., Bellieni et al., 1984; Peate, 1992; Marzoli et al., 1999; Marsh et al., 2001; Sano et al., 2001; Ware et al., 2018).

Several incompatible elements (or incompatible/HFSE) ratios and other major element discriminants have been tested to strengthen the differences between these two major geochemical groups. For example, Peate et al. (1992) argued that the Ti/Y ratio would be a more efficient discriminant since Y is not as sensitive to fractional crystallization as TiO_2. By adopting the Ti/Y threshold of 310, and combining bivariate plots between major (SiO_2, TiO_2, P_2O_5, Fe_2O_{3T}) and trace element (Sr, Ba, Zr) or trace element ratios (Ti/Zr, Zr/Y, Sr/Y, Ba/Y), they identified six types of mafic magmas in the Paraná Province. These are the high-Ti/Y (> 310) Urubici, Pitanga, Paranapanema and Ribeira, and the low-Ti/Y (< 310) Esmeralda and Gramado, while the Palmas and Chapecó magma types are, respectively, the silicic equivalents of the low-Ti and high-Ti basaltic tholeiites.

When adopting the Ti/Y ratio for the Etendeka tholeiites, Marsh et al. (2001) found that some 'unequivocally low-Ti magmas' of this opposite province plot as high-Ti types, a reason why they preferred to use the original classification based on TiO_2 contents, besides the abundances of other major and trace elements and elemental ratios. There, eight tholeiitic

groups were individualized, the majority of low-Ti composition – Tafelberg, Kuidas, Horingbaai, Huab, Taefelkop, Albin and Esmeralda, prevailing in volume over the high-Ti Khumib tholeiites.

A similar approach was presented by Marzoli et al. (2018) to organize the CAMP rocks into six magma types using TiO_2 and MgO contents, the La/Yb value and a combination of isotope (Sr-Nd-Pb) signatures. Five of these types correspond to low-Ti variants – Tiourjdal, Prevalent-CAMP, Holyoke, Recurrent and Carolina, whereas only one type (named simply High-Ti) differs. The more recent studies made on the Karoo(-Ferrar) basalts follow the same line of reasoning of using Ti-based classification combined with incompatible element parameters (e.g., Jourdan et al., 2007; Luttinen, 2018).

2.5. Methodologic Approaches

2.5.1. Petrographic analyses

Microscopic petrographic analysis implies discriminating the mineral phases and their textural relationships. The minerals are identified through their optical properties in thin section, under a polarizing microscope, and the composition complemented with (semi)quantitative methods, Energy-Dispersive X-Ray Analysis (EDXA) or Electron Probe Micro-Analysis (EPMA). The EPMA technique consists in quantifying the concentration of chemical elements via interaction of a high-energy electron beam with the mineral to generate X-rays, with energy and wavelength characteristic of each chemical element (Gomes, 2015). The intensity of these rays is used to determine the concentration via Wavelength Dispersive Spectroscopy (WDS). In situ analyses are made on a polished surface of the mineral from a spot beam size not exceeding a few micrometers. The resulting multi-element spectrum is expressed as percentages of oxides.

The texture of a rock refers to the size and shape of the minerals, their distribution, orientation and mutual relationships, which are all key indicators of the cooling history of magmas. The cooling rate translates the history of nucleation and mineral growth, and they are strongly dependent on the degree of undercooling of the magma (e.g., Cashman, 1993). At the beginning of the magmatic evolution, rapid undercooling favors the increasing of rates of nucleation and dense population of crystals (Swanson, 1977) and they are gradually inhibited as the cooling progresses. Therefore, undercooling occurs when the temperature drops below

the melting point before crystallization starts. At higher temperature/small undercooling, the maximum rate of growth is greater than the maximum rate of nucleation as it is 'easier' to add an atom with high kinetic energy to a pre-existing crystalline structure than to form a new 'mineral nucleus'. Figure 2.7 illustrates (Winter, 2001) the behavior of the nucleation and mineral growth in a bivariate system between magmatic cooling rate and temperature: the influence of undercooling (T) on the nucleation and growth are expressed in three situations: T.1 – slow cooling of the magma and low undercooling, T.2 – rapid cooling of the magma and significant undercooling, and T.3 – ultra-fast cooling of the magma and high undercooling.

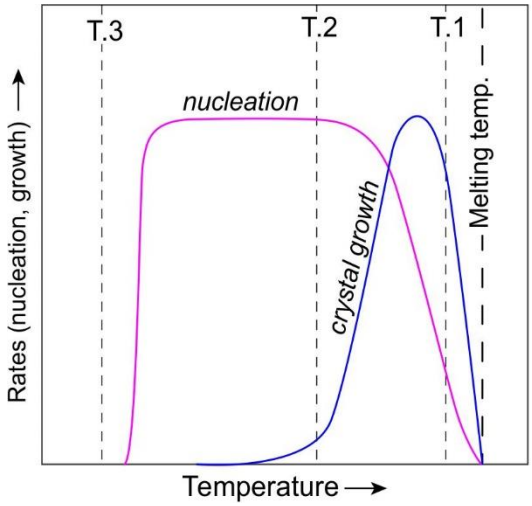

Figure 2.7. Diagram representing curves of nucleation rates (pink) and crystal growth (blue) in magmas in the function of temperature below the melting point. Source: Winter (2001).

In T.1, the nucleation rate is exceptionally low while the growth rate is high, this situation favors the formation of a few minerals that will grow a lot, resulting in the coarse texture of some plutonic rocks. In contrast, the rate of nucleation will be higher than the growth rate in T.2, thus favoring the formation of small crystals as seen in volcanic rocks. The extreme case of undercooling in very high degrees (T.3) favors extremely low rates of both nucleation and growth so that the liquid crystallizes like glass. In a situation in which the magma crystallization occurs in two stages, the result is a bimodal distribution of the size of the grains, with the co-existence of macrocrystals formed in T.1 and microcrystals representing T.2.

2.5.2. Crystal Size Distribution

Comprehensive textural analysis of an igneous rock must consider much more than the simple description of the individual aspects of each mineral phase in a thin section. The crystal size distribution (CSD) technique concerns to a quantitative way of describing the history of cooling magmas, including the rate of nucleation and mineral growth, and density. This technique was originally developed to understand crystallization models in chemical engineering (Randolph and Larson, 1971), and was later applied to igneous (Cashman and Marsh, 1988; Marsh 1988) and metamorphic (Cashman and Ferry, 1988) systems. Since then, it has been used to quantitatively measure the gain or removal of crystals (in number per volume unit) of a given size range and evaluate the relevance of fractional crystallization, accumulation and annealing in petrological systems.

In practice, the CSD data acquisition firstly consists of isolating the mineral of interest from a vectorized image that should be representative of the rock, whether outcrop, polished or thin section, to withdraw the 2D shape and size of it. The 2D-vectorized image needs to be treated to extract some morphometric parameters such as the intersection of crystals, width, length, area, and others. This process can be obtained manually, automatically using image analysis software, or a combination of both, being of utmost relevance pre-defining the minimum and maximum size intervals that will be considered to avoid misinterpretation associated with the specificities of the measurement (Higgins, 2000). In this study, the binary image was processed via the *IMAGE-J* software to generate an executable file in the *CSDcorrections* (v.1.6, M.D. Higgins) program, which dealt with each crystal as a single ellipse featured by its major and minor axes. The calculation of the size of the crystal distribution considers only the major axis. *CSDcorrections* still require an input of 3D-shape information of the crystal population, which was obtained via the Excel *CSDSlice* macro drawn by Morgan and Jerram (2006) through the stereological conversion of 2D (minor and major axes) to 3D (minor, intermediate, and major axes) measurements.

The graphic representation of a CSD analysis consists of illustrating the data in a bivariate diagram Ln (n = population density) versus L (crystal size, mm) (Marsh, 1988) (Fig. 2.8). In magmatic systems that evolve through simple crystallization, the results are distributed in a log-linear arrangement on the Ln(n)-L graph and interpreted as constant growth-nucleation rates. The slope of the line (m) is proportional to $-1/G\tau$, where G is the average growth rate and

τ the residence time (therefore, $m = -1/G\tau$), so that the slope of the line depends on the time required for the complete crystallization of the magma.

In more complex igneous systems, the geometry of the curve differs from the log-linear arrangement. Situations in which the textural characteristics of igneous rocks reflect the complexity of the magmatic processes are illustrated in Marsh (1988). The rapid undercooling generates an explosion of the fine crystals population, represented by curves with a greater inclination in the intervals of smaller fractions of the Ln(n)-L diagram. The removal of larger crystals from the system as a function of density can, in turn, generate stronger slopes in the interval that represents coarser crystals. On the other hand, the accumulation of larger crystals tends to flat the CSD curve with the increase of L. Finally, complex evolutions, for example, crystallization in two or more stages and mixtures of magmas with unlike crystalline populations, can generate irregular patterns in Ln(n)-L diagrams. Higgins (1996) demonstrates that the mixture of two magmas with populations described by log-linear systems individually can generate a resulting curve with a 'kinked' pattern.

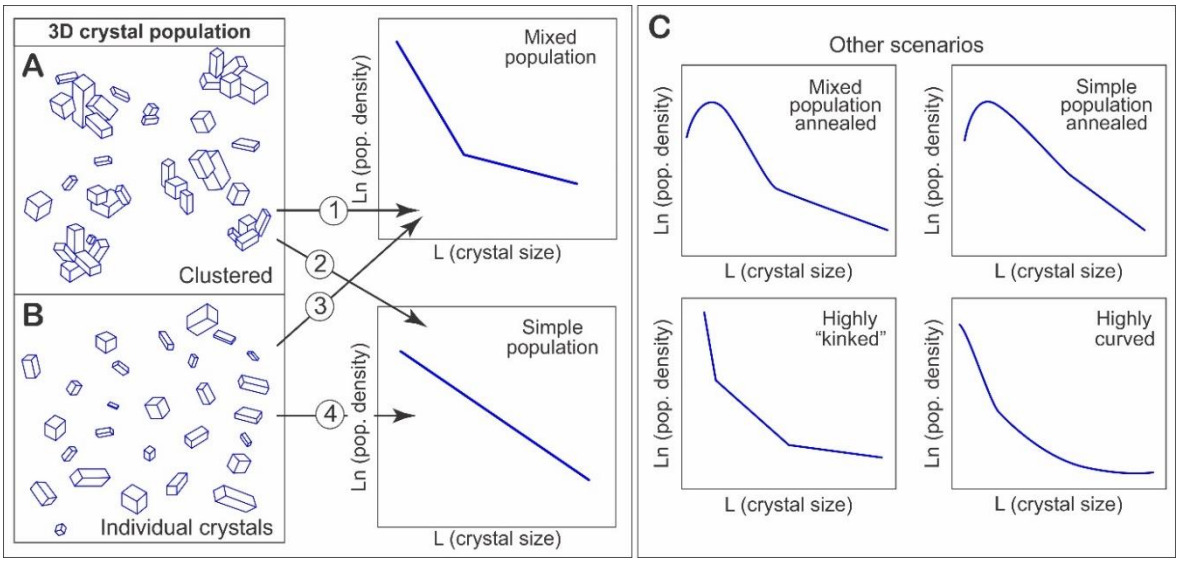

Figure 2.8. Examples of CSD patterns. (A): A theoretical population of agglomerated crystals (glomeroporphyritic texture) may represent a mixed population of different size crystals (1) or may have formed from a single size population (2). Same reasoning for (B): Patterns illustrating a single (4) or a more complex (3) size population taken from individual crystals. (C): Other examples of possible variations in CSD patterns. Source: Jerram et al. (2018).

Lofgren (1974) showed that at different degrees of undercooling (T.1 to T.3 in Fig. 2.7) the morphometry of plagioclase varies from acicular to tabular and then to equidimensional. Olivine also produces different forms at unlike degrees of undercooling (Donaldson, 1976), so both minerals are ideal for applying the CSD technique. Pyroxene can also be used. However,

in tholeiitic magmas where pigeonite and augite coexist as individual phases or solid solutions, it can be difficult to individualize one from the other by automatic (image) acquisition processes, thus requiring a semi-automatic or even manual extraction to avoid data misinterpretation. Further complexity in CSD studies involving pyroxene refers to the presence of inclusions of plagioclase in ophitic-subophytic textures, which can lead to the overestimation of the real size of the host pyroxene crystals.

2.5.3. Geochemical classification and magma differentiation

Bulk chemical analyses are firstly used to classify the rocks in terms of their major element compositions, from which the foremost schemes relate the total alkalis versus silica (TAS diagram) and total alkalis-iron-magnesium (AFM triangle) contents in igneous rocks, to respectively discriminate them into the alkaline and subalkaline series, and further subdivide the subalkaline series into tholeiitic and calc-alkaline affinities. The TAS classification was originally proposed for Hawaiian basalts by MacDonald and Katsura (1964), and later expanded to intermediate and acid compositions resulting from magma differentiation. The dividing line of Miyashiro (1978) encompasses this wide range of compositions; the basaltic rocks lying close to it, however, are often referred to as transitional (Figure 2.9A). Differentiation trends can also be illustrated by the distribution of rock compositions on the AFM diagram, in this case regarding Fe enrichment (tholeiitic) or depletion (calc-alkaline). Despite the reliability of this chemical classification, a simple identification of augite and a Ca-poor pyroxene coexisting in thin-section is sufficient to attest the tholeiitic affinity in basaltic rocks.

Given the typology of the rocks of interest, tholeiitic mafic rocks (augite-pigeonite), this work adopts the nomenclature based on the TAS diagram of Le Maitre (2002) (recommended by the International Union of Geological Sciences; IUGS), and the classification in magmatic series according to dividing line of Miyashiro (1978). Complementarily, the abundance of TiO_2 and incompatible elements (LILE, HFSE), as well as ratios between trace elements (Ti/Y, Ti/Zr) and isotopes (Sr-Nd-Pb), are adopted as useful parameters to divide geochemical groups. To assess sources and genetic processes, it is preferable the evaluation of isotopes and multi-elementary spider-diagrams normalized to chondrite (e.g., Boynton, 1984) or primitive mantle (e.g., Sun and McDonough, 1989).

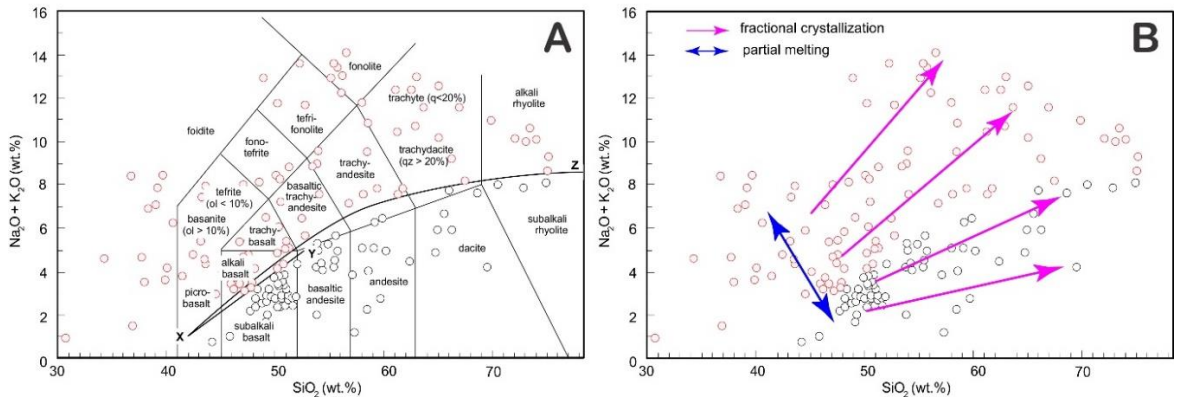

Figure 2.9. In (A) total alkali versus silica diagram (TAS) illustrates the subdivision between the alkaline and sub-alkaline series: the XY line refers to the division proposed by MacDonald and Katsura (1964), while the XZ line corresponds to the division of Miyashiro (1978). The fields and limits are those published in Le Maitre (2002). In (B) the arrows show the contributions of fractional crystallization and partial melting to magmatic differentiation. Source: Gill (2010).

2.5.4. Fractional crystallization

Magmatic differentiation is most commonly related to fractional crystallization, and it is likely the main mechanism influencing the compositional diversity of igneous rocks. More subtle variations may reflect the conditions under which parental magmas formed, such as partial melting degree, and depth and nature of the mantle source (Gill, 2010; pg. 144). The contribution of magmatic differentiation/fractional crystallization and partial melting for a suite of cogenetic rocks is qualitatively illustrated by inferred trends in the TAS diagram of Figure 2.9B. Similarly, this process can be evaluated in bivariate diagrams involving a differentiation index (MgO or SiO_2) against other oxides of major elements, or even trace element contents. The correlation between these variables is used to indicate whether the compositional spectrum of a given igneous suite results from either progressive removal or accumulation of a specific mineral as the magma crystallizes. Thus, the precise chemical composition of the mineral assemblage in a rock is essential to interpret probable trends in these diagrams. For basaltic rocks, MgO is preferred as a differentiation index rather than SiO_2 due to the minor dispersion of the silica contents in these rocks.

In a quantitative point of view, fractional crystallization (FC) is expressed through the equation:

$$C_l^{FC} = C_0 F^{(D-1)}$$

where C_l^{FC} is the concentration of elements in the remaining liquid during fractional crystallization, C_0 is the initial concentration of the element in the parental magma, F is the

fraction of liquid remaining, and D is the bulk partition coefficient of the elements for the fractional mineral phases (Rayleigh, 1896). Fractional crystallization modeling can be assessed using the Rhyolite-MELTS algorithm (Gualda et al., 2012). This software is designed to simulate magmatic differentiation processes considering equilibrium phase relationships under variable thermodynamic (P, T) conditions, fugacity, and hydration.

2.5.5. Sources, crustal assimilation, and mixing

Many of the isotopic characteristics of the terrestrial mantle have been discussed based on oceanic island records. Oceanic provinces have geochemical signatures compatible with Mid-Ocean-Ridge Basalt (MORB) or Ocean Island Basalts (OIB), whereas continental LIPs are more chemically diversified due to the expected role of the lithospheric mantle as source or contaminant during ascent. This makes the isotope signature of the continental basalts and derivatives very akin to that of crustal materials. Many studies on mantle geochemistry have been based on MORB and OIB basalts (Stracke et al., 2005 and references therein) because they occur far from the continental lithosphere that could contaminate parental melts (Greenough and McDivitt, 2018).

According to Stracke et al. (2005), five mantle endmembers would explain all isotope variability found in MORB (DMM; the Depleted MORB Mantle) and OIB (HIMU, EM-I, EM-II, and FOZO components) (Fig. 2.10). The OIB are typically richer in incompatible trace elements than most of the MORB, and they are easily discriminated into the three components – EMs and HIMU, by the classical Sr-Nd-Pb radiogenic isotopes (e.g., White, 1985; Zindler and Hart, 1986). When plotted in $^{87}Sr/^{86}Sr$, $^{143}Nd/^{144}Nd$, and Pb/Pb diagrams, all of them usually fan out from a common sector. Hart et al. (1992) named a fourth OIB reservoir as FOcal ZOne or simply FOZO (Fig. 2.10).

The HIMU is a simple expression for mantle with high time-integrated μ (High-μ) where 'μ' is the $^{238}U/^{204}Pb$ ratio showing the most radiogenic Pb isotope signatures among OIB. According to Stracke et al. (2005), it can be subdivided into a group with a very radiogenic Pb isotope signature ($^{87}Sr/^{86}Sr < 0.703$ and $^{206}Pb/^{204}Pb > 20.5$) and another one with slightly less radiogenic Pb isotope ratios and discretely more radiogenic Sr isotopes ($^{87}Sr/^{86}Sr$ 0.7028–0.7034 and $^{206}Pb/^{204}Pb$ 19.5–20.5). This rare endmember has the South Atlantic type locality in St. Helena Island, where lava sources are interpreted as a combination of hydrothermal alteration and subduction modified slab dehydration (e.g., Zindler et al., 1982; Zindler and Hart,

1986; Stracke et al., 2005; Hanyu et al., 2011; Kimura et al., 2016). Recently, Homrighausen et al. (2018b) proposed that a HIMU member is widely distributed worldwide, and its source could be explained by an Archean delaminated carbonatite-metasomatized SCLM. These authors argue that two potential regions on Earth could isolate a HIMU member from the convective mantle since Precambrian times: the shallow SCLM and a deep reservoir near the mantle-core boundary likely stored on the LLSVPs (also Homrighausen et al., 2018a, 2019).

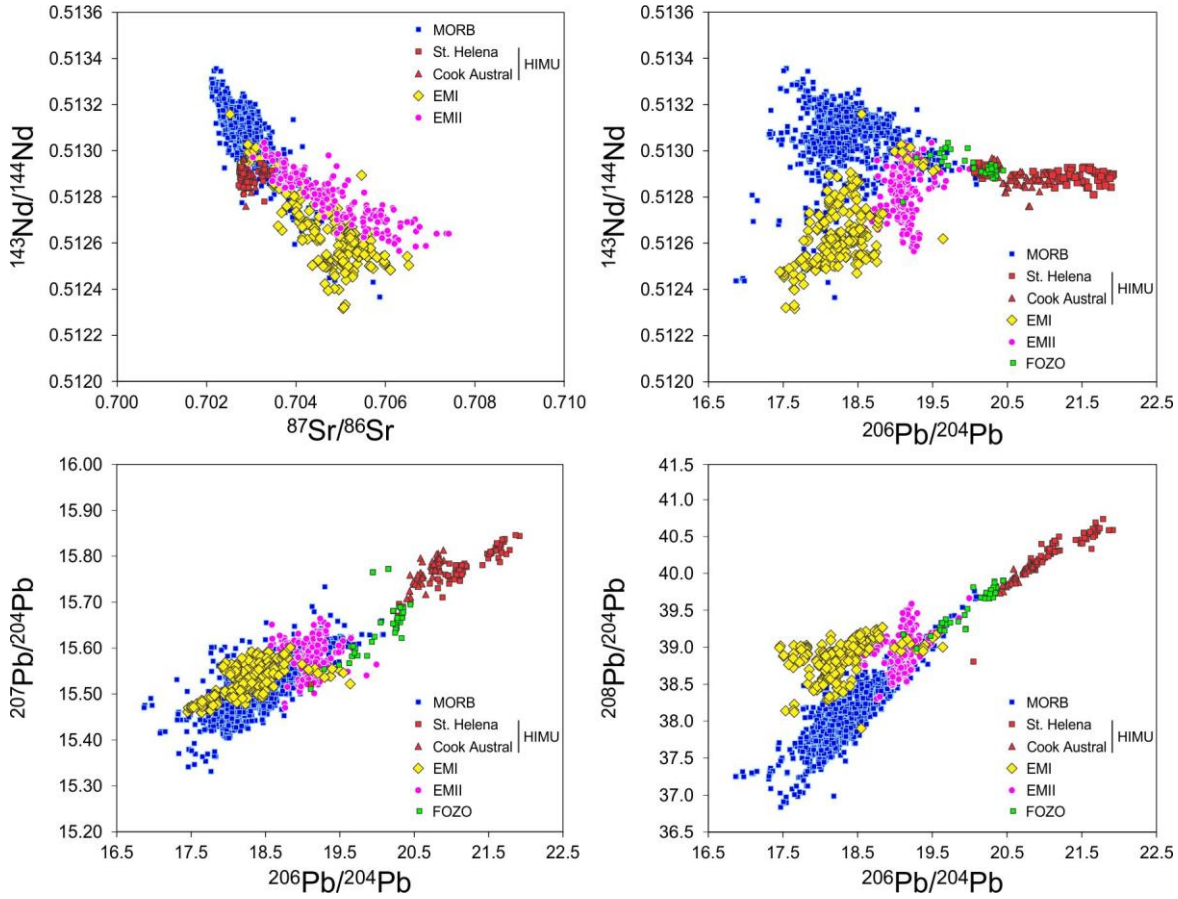

Figure 2.10. Binary plots of $^{87}Sr/^{86}Sr$ versus $^{143}Nd/^{144}Nd$, $^{206}Pb/^{204}Pb$ versus $^{143}Nd/^{144}Nd$, $^{206}Pb/^{204}Pb$ versus $^{207}Pb/^{204}Pb$ and $^{206}Pb/^{204}Pb$ versus $^{208}Pb/^{204}Pb$ for global MORB and OIB. Source: Stracke et al. (2003, 2005).

The Enriched Mantle (EM), in turn, is characterized by low $^{143}Nd/^{144}Nd$, variable $^{87}Sr/^{86}Sr$, and high $^{207}Pb/^{206}Pb$ and $^{208}Pb/^{204}Pb$. Processes such as melting of delaminated continental lithosphere, recycled metasomatized primitive mantle, metasomatized depleted oceanic lithosphere, recycled oceanic crust with sediments, and recycled oceanic plateaus have been evoked to explain the sources of EM components (e.g., Willbold and Stracke, 2010; Stracke, 2012). Homrighausen et al. (2019) argue that EMI material is sourced from the margin of LLSVPs, where it is formed by variable mixing proportions of the recycled lithosphere

(SCLM or lower crust), oceanic crust (FOZO) and sediments (EMII). Hoernle et al. (2015) achieved similar conclusions studying the Tristan-Gough hotspot - the type-locality of EMI members on the South Atlantic Ocean. They concluded that EMI-like magmas of PEMP would derive from an EMI source from the African LLSVP margin mixed with lithospheric components.

The FOZO has $^{87}Sr/^{86}Sr$ 0.7030, $^{143}Nd/^{144}Nd$ 0.51297, $^{206}Pb/^{204}Pb$ 20, $^{207}Pb/^{204}Pb$ 15.64, $^{208}Pb/^{204}$ Pb 39.51[176] and $^{176}Hf/^{177}Hf$ 0.28306 (Stracke et al., 2005), probably forming a ubiquitous component in the source of MORB and OIB, with isotopic ratios differing from HIMU for having lower $^{206, 207, 208}Pb/^{204}Pb$ ratio, and higher $^{208}Pb/^{206}Pb$ and $^{208}Pb^*/^{206}Pb^*$ ratios. FOZO can have primitive $^{3}He/^{4}He$ signatures compatible with common ancient reservoirs in the Earth's mantle; however, it lacks other primitive characteristics, being understood as a uniform mixture of other mantle endmembers (Kimura et al., 2016).

Precisely recognizing the extent of crustal contamination in continental mafic magmas is not a simple task once they naturally interact with the lithospheric mantle (SCLM) during ascent, or are generated from the partial melting of it. As a result, magmas that had involvement with the SCLM generally preserve chemical features akin to the crust, including enrichment in incompatible elements (Rb, Ba, Th, U, LREE) and depletion in refractory elements such as Nb, Ta and Ti, which are extensively recorded in many tholeiitic basalts that form the Mesozoic LIPs (e.g., Luttinen and Furnes, 2000; Jourdan et al., 2005; Rocha-Júnior et al., 2012). Such imbalance results from the combination of selective mobility into metasomatic fluids/melts and retention into eclogite-facies mineral assemblages following slab dehydration, respectively (Zheng, 2019). However, on the basis of mantle petrology, seismic tomography, and integrated lithospheric modeling, Griffin et al., (2009) observed that beneath Archean cratons, the SCLM tends to be possible residual compositions strongly depleted in comparison to that usually re-fertilized underling younger (Proterozoic) shields.

Crustal assimilation by magmas ascending to the surface or even during emplacement in crustal levels is perhaps the main mechanism acting to modify the original geochemical and isotopic signature of primary mafic melts. The effects of it are easily discernible because of the large differences in compositions between the two (mantle and crustal) endmembers. Isotopic ratios stand out as the most sensitive indicators of crustal assimilation, once they are relatively little affected (or unaffected) by fractional crystallization in comparison with major and even trace elements. The $^{87}Sr/^{86}Sr$ ratio is particularly useful because Rb is more strongly incompatible than Sr during the partial melting, leading to much higher Rb/Sr (and therefore

$^{87}Rb/^{86}Sr$ and $^{87}Sr/^{86}Sr$) ratios in crustal rocks than the values measured from mantle-derived rocks (average Rb/Sr ~ 0.028; Taylor and MacLennan, 1985). Consequently, any minimum degrees of contamination of mafic magmas with crust components would have the potential to change their original chemistry.

The observation of most evolved magmas of a given cogenetic suite would have, in general, higher, and inhomogeneous $^{87}Sr/^{86}Sr$ ratios than the primitive terms led De Paolo (1981) to model a combined petrogenetic mechanism involving fractional crystallization and crustal assimilation (AFC), expressed by:

$$C_l^{AFC} = C_0 \left[F^{-z} + \left(\frac{r}{r} - 1\right)\frac{C_a}{ZC_0}(1 - F^{-Z})\right] \qquad (2)$$

where C_l^{AFC} is the concentration of an element in the resulting magma, C_a corresponds to the assimilated material, r (m_a/m_b) is the relative ratio of assimilated material to crystallized material, where m_a is the amount of material assimilated and m_b is the amount of material crystallized, and $z = \frac{r+D-1}{\mathrm{r}-1}$. For isotope ratios, the AFC process can be modeled by applying the following expression:

$$IC_l^{AFC} = [\left(\frac{r}{r-1}\right)\left(\frac{C_a}{z}\right)(1 - F^{-z})IC_a + C_0F^{-z}IC_0]/[\left(\frac{r}{r-1}\right)\left(\frac{C_a}{z}\right)(1 - F^{-z}) + C_0F^{-z}] \qquad (3)$$

where IC_l^{AFC} is the isotopic ratio in the magma that underwent the AFC process, IC_a is the isotopic ratio of the assimilated material and IC_0 is the isotopic ratio in the parental magma.

According to De Paolo (1981), if the relative ratio of assimilated material to crystallized material r is small or near to zero, the AFC curves approach pure fractional crystallization. Contrarily, if r is large, the AFC curves approach a simple mixing process in which two magmas of contrasting composition physically mix to form a single (hybrid) magma of uniform composition (Anderson, 1976). For Powell (1984), the concentration of elements in mixed magmas (C_m) is the result of the mixture of two unlike components and can be expressed by the relationship:

$$C_m = \mathrm{X}(C_a - C_b) + C_b \qquad (4)$$

where, C_a e C_b are the concentrations of an element in magma a and b, respectively, and X means the degree of mixing. If the objective is to investigate the mixing process based on isotopic concentrations, the following expression can be applied:

$$I_{Cm} = I_{Ca}\left(\frac{C_aX}{C_m}\right) + I_{Cb}\left(\frac{C_b(1-X)}{c_m}\right) \qquad (5)$$

where, I_{Cm} is the isotopic ratio resulting from the mixture between the magmas a and b, and I_{ca} and I_{cb} are the isotopic ratios of magmas *a* and *b*, respectively.

2.5.6. Self-Organizing Maps (SOM)

The Self–Organizing Maps (SOM; Kohonen, 1982) is a non-traditional unsupervised data analysis approach that considers each input sample as a vector in a data space defined by the input variables. The approach then uses measures of vector similarity to find patterns and relationships between those vectors. The output of the process is typically a two-dimensional "map" that essentially represents the total input (nD) data set, with similar samples represented as "nodes" on the map, and the nodes themselves ordered and positioned by how similar or dissimilar they are to each other. Because of the vector quantization approach and the use of vector similarity measures, the SOM procedure may be used to examine populations that are both Gaussian and non-Gaussian in nature, and sample-variable relationships that are both linear and/or non-linear. The SOM approach considers both competitive and cooperative learning processes to train "seed-vectors" to represent the patterns within the data and eventually be represented as "nodes" on the self-organized map. Hence, the SOM processing has similarities to a neural network (Kohonen, 1982, 2001; Fraser and Dickson, 2007; Friedel, 2011).

The SOM has been extensively used as an analytical and visualization tool of high–dimensional multivariate datasets and in exploratory data mining applications to identify correlation patterns and clustering analysis to identify anomalies or trends. As such, it allows to integrate analysis of any multivariate spatial dataset with complex inputs, also improving the understanding of subtle and intricate relationships existing between dissimilar data sets (Penn, 2005; Kohonen, 2013; Hodgkinson et al., 2013). Many contributions of SOM have been noticed regarding the integration, interpretation, and visualization of geosciences and environmental datasets (e.g., Bação et al., 2005; Penn, 2005; Fraser et al., 2006; Fraser and Dickson, 2007; Li and Eastman, 2010; Carneiro et al., 2012; Mocitaiba et al., 2017), but fewer works dedicated to geochemical data (e.g., Lacassie et al., 2004, 2006; Löhr et al., 2010).

One of the first applications of SOM to study mafic rocks concern de Castro et al. (2018) that match major element compositions, magnetic airborne data, magnetic susceptibility measurements of the Jurassic and Cretaceous events exposed in the Parnaíba Basin. They observed positive correlations between TiO_2 content and magnetic susceptibility of tholeiitic

rocks confirming the value of previous classifications based on the content of TiO_2 to segment magmatic events in the Parnaíba Basin (low-Ti-high-MgO Mosquito/CAMP versus high-Ti-low-MgO Sardinha sills). Recently, Owen-Smith et al. (2021) constrained the magmatic diversity of the Etendeka Province with SOM considering major and few trace elements (Ni, Cr, Sc, Y, Zr, Nb, Rb, Sr, Ba) of mafic types observing a general good correspondence between the SOM clustering and prior petrological classifications. They conclude that the SOM method can be a useful tool if the analyst is interested in data-intensive regional comparisons.

2.6. Analytical Producers

2.6.1. Major and trace element analysis

The samples were crushed and powdered in an agate ring mill under ~300 mesh. Major elements were determined by X-ray fluorescence in the Technological Characterization Laboratory (LCT) of the University of São Paulo after fusion of 1 gram of powdered sample with 7 grams of lithium tetraborate. Accuracy and reproducibility were monitored by the GBW07105 basalt standard. The loss on ignition (LOI) was measured by weight differences after heating 2 g of powdered sample for 2 hours at a constant temperature of 1020°C and then cooling to room temperature. All major oxide compositions were recalculated to 100% on a volatile-free basis despite their negligible LOI values.

Trace element analyses were carried out by inductively coupled plasma mass spectrometry at Bureau Veritas Mineral Laboratories (ACME Labs, Canada) using the commercial package 'LF100–EXT '(LF100 + AQ200), in which 31 refractory+RE (rare earth) elements were measured after lithium fusion (LF100 code), while 14 metals (including Cu, Pb, Ni) had their concentrations quantified after sample dissolution with diluted aqua regia (1:1:1 HNO_3:HCl:H_2O) (AQ200 code).

2.6.2. Isotope analysis (Sr, Nd, Pb)

The isotope analyses were performed at the Isotope Geology Research Center (CPGeo) of the University of São Paulo. The process avoids possible sawed surfaces from the rock fragments and subjecting them to successive washing with deionized and then Milli-Q water before powdering in an agate mill, following the recommendations from Marques et al. (2016).

Approximately 50 mg of rock powder were dissolved in HF:HNO_3 (3:1) and then in concentrated HCl acid under sub-boiling conditions (100º C), for 5-7 days. Ion exchange chromatography was firstly performed by loading the whole sample solutions into Biorad AG1-X8® resin columns to isolate Pb, while the eluted matrix solution was loaded into Sr-Spec® columns to separate Sr and REE, and then Nd and Sm were purified throughout LN-Spec® columns.

The isotopic compositions were determined by thermal ionization mass spectrometry using a Finnigan MAT-262 machine for Pb, while a multicollector ThermoFisher Scientific Triton™ for Sr and Nd. During the analytical program, instrumental reproducibility was monitored throughout successive analyses of international standards. The initial Sr and Nd isotope compositions reported in the text were calculated using the elemental concentrations for Rb, Sr, Sm, and Nd obtained by ICP-MS, assuming an Early Cretaceous age (~130 Ma).

2.6.3. Mineral chemistry

Mineral chemistry of the major constituents was performed on 30 µm-thick carbon-coated thin sections using a JEOL probe equipped with five wavelength dispersive spectrometers at the Institute of Geosciences (GeoAnalítica Lab) of the University of São Paulo and Paulista University. The analytical conditions included Faraday current intensity of 20 nA with an acceleration voltage of 15 kV, and a beam spot size between range from 5 to 10 µm. Elements were quantified using the K_α line (and L_α, when required) considering the following mineral standards for calibration: TAP for Si and Al; TAPH for Mg and Na; PETJ for Ca, K and Sr; LIFL for Fe, Mn, Ti, Cr and Ba. Counting time was 20 s on the peak of all elements except Na with 10 s. ZAF matrix corrections were performed through the PC–EPMA software.

2.6.4. Crystal Size Distribution

Image capture of thin sections and a combination of them to form a .JPEG mosaic was performed on a Leica DN750P optical microscope operating with the Leica Application Suite software. The thresholds of the plagioclase and pyroxene crystals were manually checked using CorelDraw Graphics Suite X8, and refined by applying the SPO2003 software (Launeau, 2004), where lines of one pixel in width and aggregated of pixels smaller than 8 pixels were removed. The resulting binary images were analyzed in the ImageJ 1.51J8 software

(https://https://imagej.nih.gov/ij/) combined with the macro CSD_output for CSDcorrections v.1.6 software (Higgins, 2000). The CSD data were calculated after estimating the crystal (plagioclase) morphology (the short-intermediate-long axes) for each sample through the CSDslice5 spreadsheet of Morgan and Jerram (2006). In this procedure, we adopted a 'massive' rock fabric and a value of '0.1' for roundness as a priori assumptions.

3. MAPPING AND PHYSICAL ASPECTS OF MESOZOIC DIKE SWARMS AND SILL COMPLEXES IN NE BRAZIL

3.1. Introduction

The original size and areal extent estimation are important frontiers in LIP characterization (Ernst et al., 2005). Therefore, this chapter covers the general aspects of geological mapping, structural trends (in dikes), field features and sampling activities of the Mesozoic mafic intrusions in NE of Brazil. Additionally, a brief discussion based on macrostructures and previous bibliographic information is conducted to suggest possible tectonic mechanisms linked to the emplacement of the studied magmatic events. This information will eventually support further discussions in subsequent chapters.

3.2. Previous works

The lineament of dikes that crop out in the Rio Grande do Norte and eastern Ceará states (NE Brazil), running south of the Potiguar Basin and crosscutting regional structures recorded in the Precambrian basement, was named by Gomes et al. (1981) in reference to the Rio Ceará-Mirim hydrographic basin. Since then, the Rio Ceará-Mirim dikes have been collectively referred to as a ca. 350 km-long dike swarm displaying a dominant E-trending direction (Sial et al., 1976, 1987; Bellieni et al., 1992; Martins and Oliveira, 1992; Oliveira, 1994; Oliveira and Gomes, 1996; Archanjo et al., 2000, 2002; Ernesto et al., 2003; Hollanda et al., 2006; Ngonge et al., 2016a). Hollanda et al. (2019) re-interpreted the mapping of the RCM based on high-resolution aeromagnetic data of the Borborema Province made available from the Geological Survey of Brazil (CPRM) together with remote sensing products, to show that it is a larger geologic unit reaching more than 1,000 km and presenting an arcuate geometry that turns from an EW to NE-SW direction at approximately 38ºW. In that work, the authors reviewed data from the literature to propose that three dike swarms intrusive in the Borborema Province, from which the RCM is the most voluminous, with the Sardinha sills exposed in the eastern side of the Parnaíba Basin, would be part of a LIP of Early Cretaceous age; therefore, contemporaneous to the Paraná-Etendeka LIP in S-SE Brazil. Unlike the well-studied E-trending segment for which geochemical, geochronological, structural, and paleomagnetic data are published in Bellieni et al. (1992), Archanjo et al. (2000, 2002), Hollanda et al. (2006) and

Ngonge et al., 2016a, there is a paucity of geochemical information concerning the NE-trending segment of the RCM. Oliveira et al. (2021) applied a speedy unspiked K-Ar methodology to investigate age patterns in NE-RCM and Canindé dikes. This systematic analysis corroborates an Early Cretaceous age for high-Ti tholeiites and andesitic types, following $^{40}Ar/^{39}Ar$ results previously published for EW-RCM (Smith et al., 2001; Ngonge et al., 2016a). Overall, low-Ti tholeiites have less conclusive ages spanning from < 80 to > 200 Ma, and the possibility remains that few Juro-Triassic subswarms of the Central Atlantic LIP (CAMP) are interspersed with some Early Cretaceous dikes.

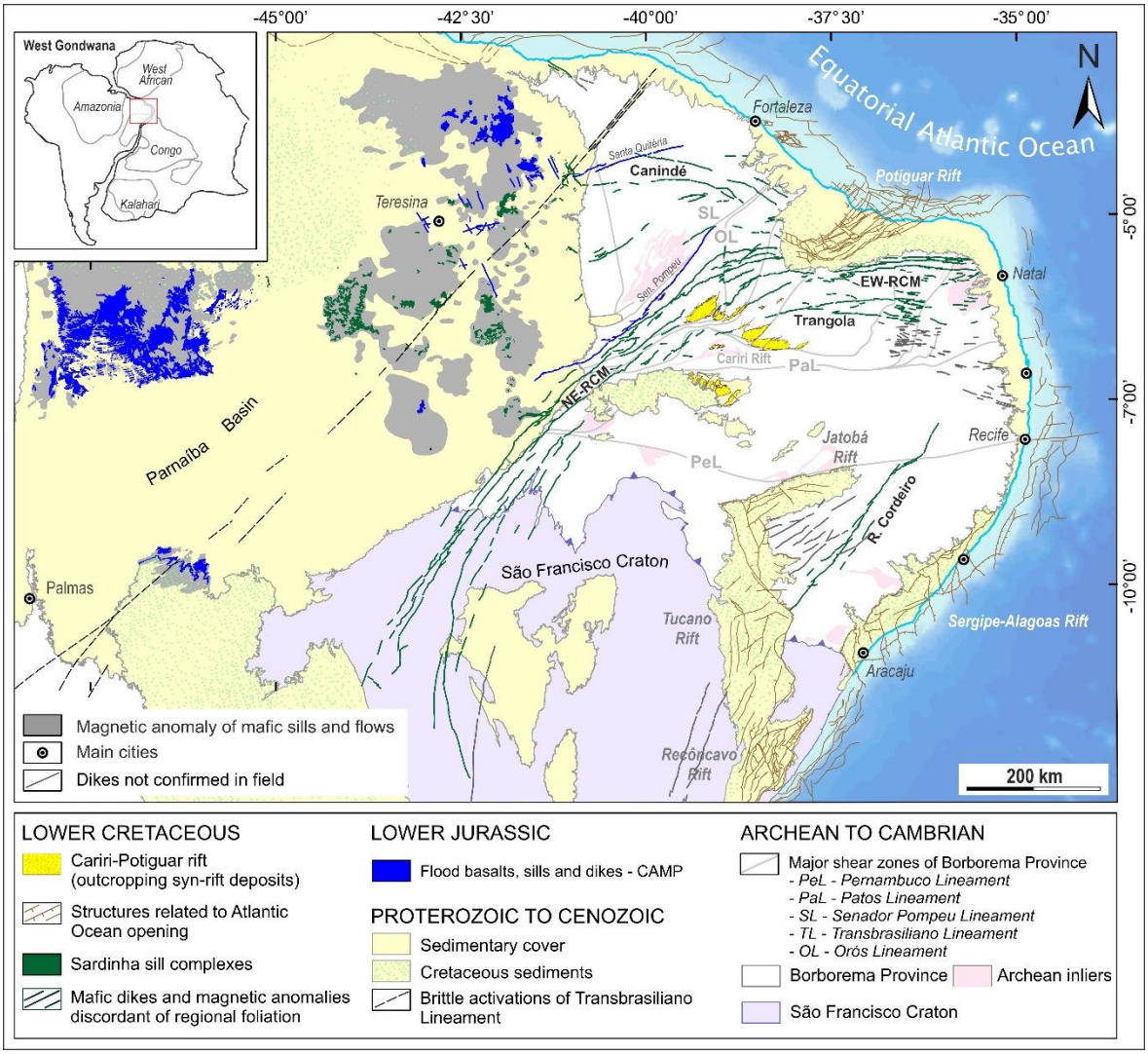

Figure 3.1. Geological map of NE Brazil highlighting the regional distribution of Mesozoic flood basalts, dikes and sill complexes. The Mosquito Formation (Central Atlantic LIP) occurs as flood basalts in the western side of the Parnaíba Basin, while sills and dikes are prevalent styles in the eastern flank, as observed in Early Cretaceous Sardinha magmatism (Equatorial Atlantic LIP). On the Precambrian basement of the Borborema Province and the São Francisco Craton, the plumbing systems manifest exclusively as regional dike swarms. The geophysical signature of sills is based on Mocitaiba et al. (2017). The geological mapping of dikes and sills have been remapped based on geophysical, remote sensing products and new fieldwork data.

The petrological aspects of the Sardinha sills, in turn, have been discussed since the 1970s (Sial et al., 1976, 1987; Fodor et al., 1990; Bellieni et al., 1990; Baksi et al., 1997; Ernesto et al., 2003), with additional input of data and interpretation provided by several recent publications (Silva et al., 2017; Oliveira et al., 2018; Heilbron et al., 2018; Klöcking et al., 2018; Macêdo Filho et al., 2019; Miloski et al., 2019, 2020). Advances in the local mapping and structural analysis of these igneous bodies, including a few dikes that can be mapped on the surface (e.g., Lima and Jardim de Sá, 2017; Santos et al., 2018; Silva et al., 2020; Fernandes et al., 2020), as well as surface and subsurface geophysical modeling (Mocitaiba et al., 2017; Trosdtorf et al., 2018; de Castro et al., 2018), have brought the knowledge about the mafic magmatism in the eastern Parnaíba basin to a higher level. Despite the entrenched idea that the basin hosts two magmatic events discriminated in terms of both age and geochemistry, some of these recent works suggest that there is no geographical provinciality, i.e., the Jurassic low-Ti magmatism represented as the Mosquito Formation would also be present in the eastern side (Fig. 3.1) coexisting with the Early Cretaceous high-Ti (Sardinha) magmas (e.g., Ernesto et al., 2003; de Castro et al., 2018; Klöcking et al., 2018; Miloski et al., 2020).

3.3. Spatial distribution of igneous products

The digital mapping of mafic sills and dikes (Fig. 3.1) was facilitated by the high compositional contrast relative to the surrounding sedimentary and granite-gneissic terrains in which they intrude, besides the flat and barren landscape and low vegetation. Mapping was performed from manual extraction of linear (assumed to be dikes) and contour (of sills) features using a basic combination of remote sensing tools (Fig. 3.2; Fig. 3.3) – Google Earth™ (e.g., Fig. 3.2A-C), 'free-cost' Spot Image scenes (2011-2012), Digital Globe Imagery (LANDSAT 5, 7, 8; Fig. 3.2D), airborne magnetic data (e.g., Fig. 3.2B; Fig. 3.3A-B-C-D) from Geological Survey of Brazil and data from published works (Mocitaiba et al., 2017; de Castro et al., 2018), thus providing a regional-scale distribution of dikes and sills of interest. Additionally, we compare the results with maps of dike swarms in the Borborema Province developed using the semi-automatic extraction of lines combined with the modeling of geophysical parameters using the Self-Organizing Maps technique (Melo et al., 2021).

Field campaigns were carried out along eighty-eight days to check the correspondence between magnetic anomalies and rock exposures, in addition to sampling. The field strategy consisted in navigating through all remote sensing products using the Avenza Maps™

application (Avenza Systems Inc.) and All-In-One Offline Maps (Psyberia Ltd). The satellite image resolution available in this study was typically 15 m per pixel, which is good enough to precisely locate the great majority of the dikes with mean widths exceeding 30 meters (Hollanda et al., 2019).

The dikes in the Borborema Province are grouped into four swarms (Fig. 3.1). The largest one is the arcuate RCM with at least 1,000 km, and the others include the 355 km-long NE-trending Riacho do Cordeiro Swarm, the 240 km-long EW-trending Trangola Swarm (southern swarm in EW-RCM), and the 380 km-long WNW-trending Canindé Swarm. The Riacho do Cordeiro and Trangola dike swarms have linear geometries, whereas the Canindé Swarm has a discrete arcuate array. Except for the Trangola Swarm, all others can be classified as giant dike swarms according to Ernst and Buchan (1997; also, Ernst, 2014). Although they visibly cut the regional basement structures, their main directions (EW and NE) are fairly parallel to the major Precambrian strike-slip shear zones, which suggest a strong control of the older crustal discontinuities on the diking processes during the Mesozoic.

The EW-trending RCM extends for ca. 350-400 km from the eastern Atlantic margin to the longitude 38º W, where it changes to a NE-SW direction (225º of azimuth). The NE-trending segment follows continuously the regional trend of the Cariri-Potiguar Rift System (Fig. 3.1) for 600-700 km until reaching the northwestern margin of the São Francisco Craton. The magnetic anomalies continue southwards into the craton for at least 200 km but the exposure in field is hard to follow due to the thick Cenozoic sedimentary cover in this region. The average width of the E-trending segment is variable between 18 to 30 km and can be up to 85 km in the NE-trending segment, making the entire swarm look like an in-splay geometry. The Canindé Swarm has an arcuate pattern that has an apparent focal zone centered at the Potiguar Rift, which together with the two segments of the RCM characterize a radial-like system.

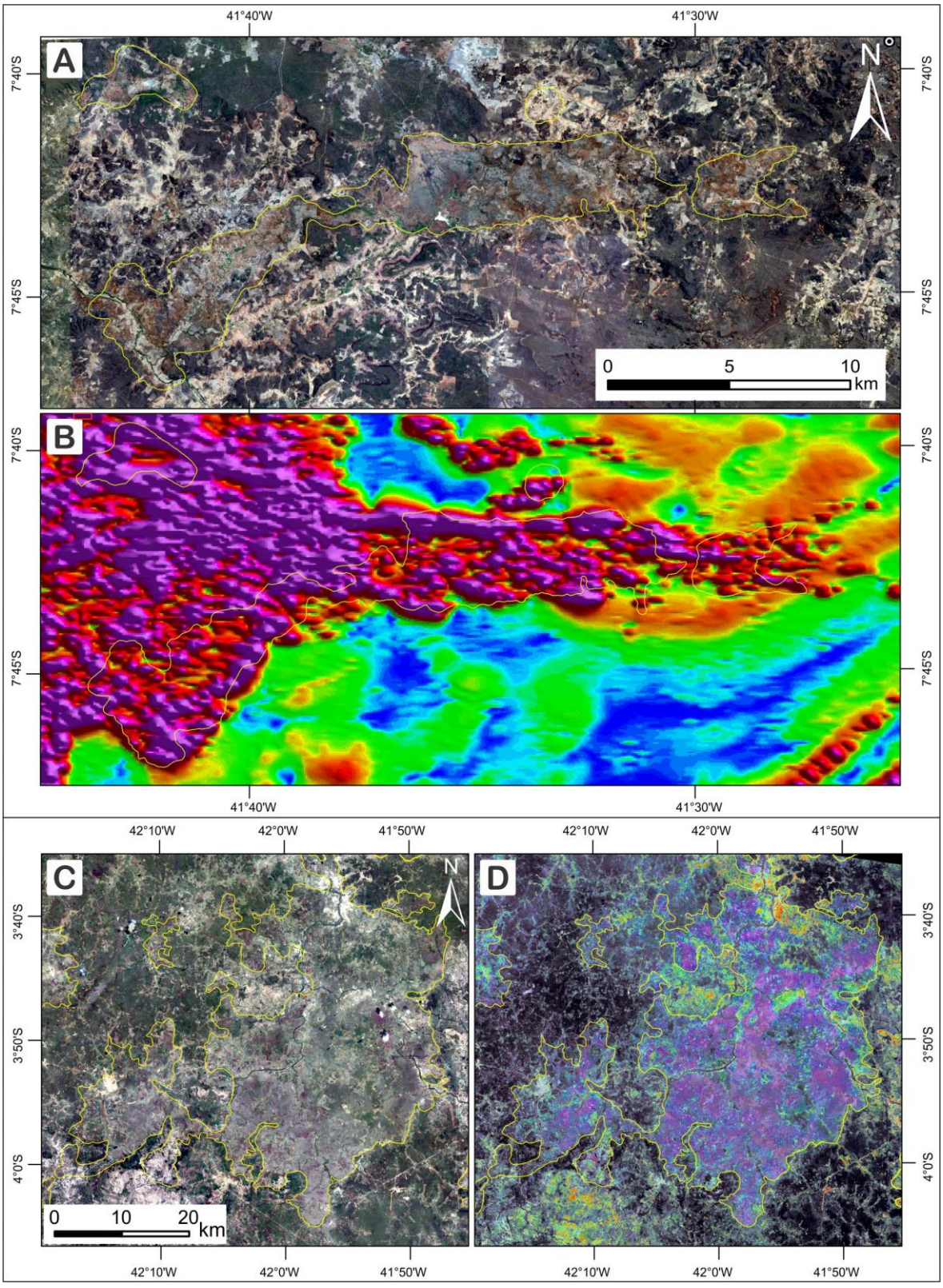

Figure 3.2. Sill exposures in the eastern side of the Parnaíba Basin as shown by different remote sensing products. (A) Google Earth image and (B) Analytic Signal Amplitude map (ASA) of airborne magnetic data of sills on the Isaias Coelho area. (C) Google Earth images and (D) Landsat-5 TM (e.g., RGB composite R[PC1/PC6]G[PC2]B[PC3]) of sill complexes on the Esperantina village region. The geological contact of sills is delineated by yellow contours.

The Trangola Swarm is exposed to the south of (and is parallel to) the E-trending RCM and has the particularity of also including alkaline (in addition to tholeiitic) basalts and andesite basalts not found in the other swarms (Hollanda et al., 2006; Ngonge et al., 2016a). The Riacho do Cordeiro swarm is exposed southeast of the Borborema Province along 235º azimuths. It propagates towards the São Francisco Craton to the south, and its north termination deviates slightly at the intersection with the Pernambuco Shear Zone (see also Dantas, 2021), which could indicate a brittle reactivation of the shear zone after the emplacement of the swarm or, alternatively, fracture refraction followed by dike intrusion due to stronger rocks in the Pernambuco Lineament. Even so, the geochemical characteristics of Trangola and Riacho do Cordeiro dike swarms are not detailed in this work; they are targets of two MSc projects that are being developed under the Graduate Program on Geochemistry and Geotectonics of the University of São Paulo as part of the EQUAMP project. Both dike swarms have linear trends.

Satellite images and anomalies from airborne magnetic surveys show that the dikes from all swarms consist of single bodies or arrays of two or more dike segments connected by steps, which show left- and right-lateral *en-echelon* arrangements (Fig. 3.3A-B-C-D). The morphological parameters, i.e. apparent length and width, are variable between the dikes, as already cited by Hollanda et al. (2019); they are reproduced in Table 3.1. Individual dikes in the RCM Swarm have lengths ranging from a few hundred meters to tens of kilometers, but not longer than 40 km, and widths that vary from 16.5 to 193 meters. The minimum dike lengths in the Canindé, Trangola and Riacho do Cordeiro swarms are 5.9, 2.4, and 5.5 km, whereas the maximum lengths, are 39, 23, and 39 km, respectively. The variation in width is in the same order as that in the RCM, although the Canindé swarm has a minimum dike width of 52 m. One particularity of the Riacho do Cordeiro is that the wider dikes occur south of the swarm, becoming progressively thinner as it approaches the Pernambuco Lineament, to the north.

The geographic distribution of the sills in the eastern side of Parnaíba Basin (Fig. 3.4) was determined based on the 1:500,000 geologic map published by Lima and Leite (1977), and their contours adjusted according to the sampling location performed for this study and other publications (when geographic coordinates were available) and interpretation of remote sensing products. Compared to the opposite side of the basin, the sill exposure on the eastern basin margin is remarkably smaller, over an area of ca. 7.225 km^2 (Macêdo Filho et al., 2019), although a combined integration of aeromagnetic (Mocitaiba et al., 2017), well-logs and seismic data (e.g., de Castro et al., 2018) indicate that the area under the influence of magmatic activity

can reach up to 85,400 km². This means that the major area of magma (roughly > 90%) is stored in the subsurface.

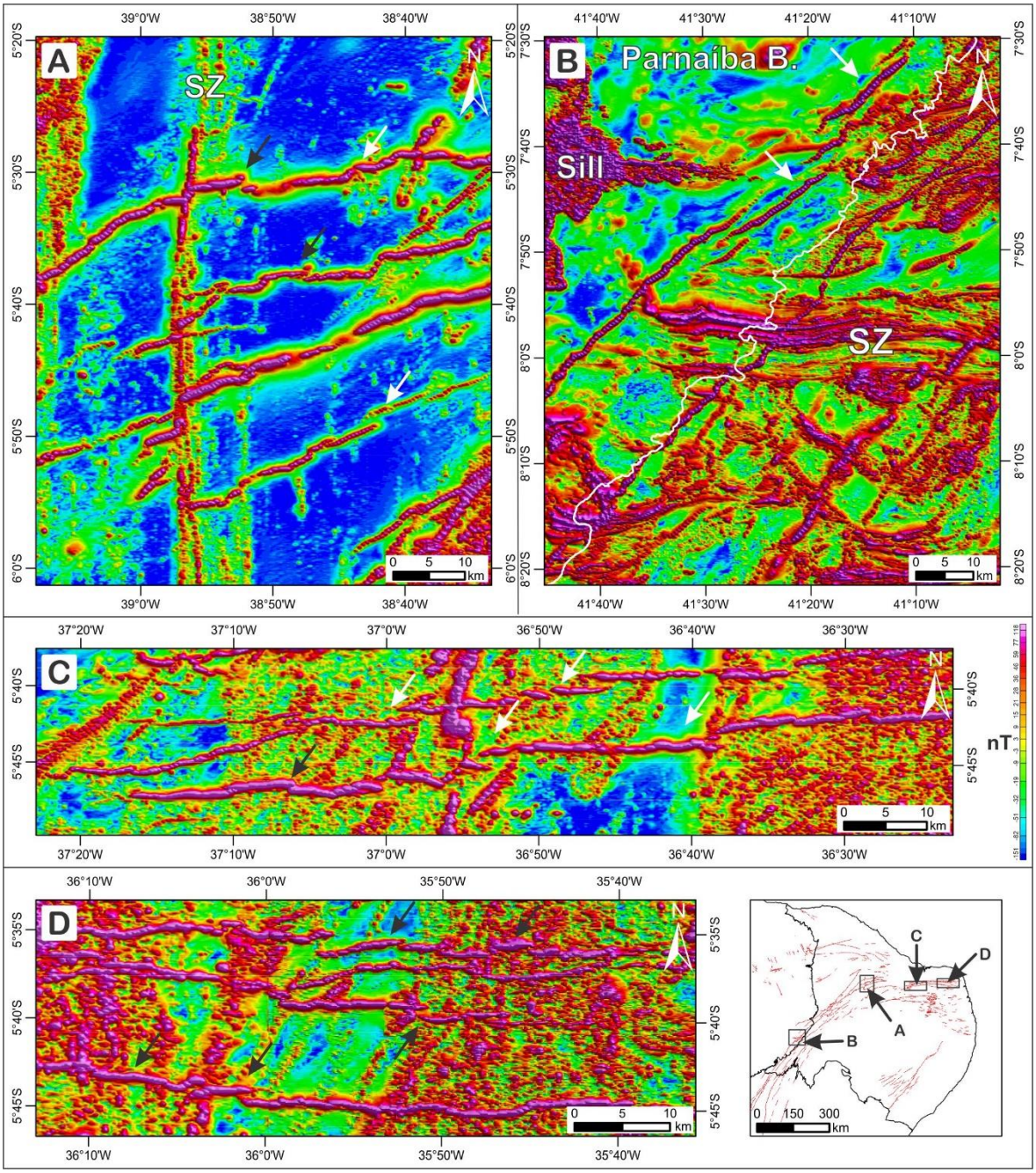

Figure 3.3. Analytic Signal Amplitude maps (ASA) of airborne magnetic data highlighting the RCM dikes in high amplitude linear anomalies (pink colors). The left-lateral and right-lateral *en-echelon* arrangements in (A, B) NE and (C, D) EW-RCM branches are pointed out by black and white arrows, respectively. The white line in B marks the contact between the Parnaíba Basin and the Precambrian Basement. The main shear zones crossed by dikes are represented as SZ in A (Orós Shear Zone) and B (Pernambuco Shear Zone) where dikes may undergo refraction. The inset in the bottom right shows the geographical location of each figure.

Samples were collected in the vicinity of Teresina City and Floriano town, as well as Elesbão Veloso, Picos-Wall Ferraz, Isaías Coelho, and Itaueira villages (see locations in Fig. 3.4), where the sills are emplaced preferentially along lithological (sandstone-siltstone) interfaces. The integrated surface and subsurface cartographies are illustrated in Figure 3.4. Due to the flat topography, outcrops are found along road cuts and a few quarries. Sills are usually layered-parallel bodies with slightly arched (laccoliths) to flat roofs, and thicknesses not exceeding a few meters. When exposed in quarries, they reach at least 20-30 meters of thickness, which agrees to minimum values estimated from well-log data (de Castro et al., 2018). Columnar joints resulting from shrinkage on cooling and stopped blocks (roof pendant) are relatively common in the quarries (Fig. 3.5A) or occur less frequently along drainages. Dikes are very subordinate relative to the sills in field exposures and show no clear preferential orientation, which implies that they could correspond to climbing edges (Fig. 3.5B-C) of saucer-shaped sills or, alternatively, simply magma-filled fractures linked to narrow sills not exposed at the surface.

Table 3.1. Physical measurements (length and width) of EQUAMP dike swarms. Length (L) was estimated by measuring the distance between the most extreme points of dike exposure. Width (W) was measured perpendicular to each dike segment. All values were extracted from satellite images; measurements of the RCM dikes are those published in Hollanda et al. (2019) which also considered the smaller dikes measured in fieldwork.

Dike swarm	Dominant Structural trend	Number of dikes	Length (km)		Width (m)		Average		Median	
			Min	Max	Min	Max	L (km)	W (m)	L (km)	W (m)
EW-RCM	EW	69	0.1	14.8	18.0	193	3.4	86.0	2.3	75.4
NE-RCM	NE-SW	39	0.4	37.7	16.5	193	8.6	57.1	2.7	59.8
Canindé	WNW	10	5.9	39.3	52.2	143	4.0	61.8	22.7	88.0
Trangola	EW	10	2.4	23.0	19.9	69.2	20.7	90.4	8.0	62.2
Riacho do Cordeiro	NE-SW	10	5.5	39.0	10.8	161	20.5	78.9	21.5	80.8

3.4. Sampling

The sampling of the sills was performed over the course of the 5-year PRO-PARNAÍBA project funded by Petrobras (2012-2017), while the dikes were part of the 2-year EQUAMP project funded by FAPESP (2016-2018), amounting to 228 samples of which 118 were from sills and 110 from dikes (NE-trending RCM and Canindé). The sampling of the dikes covered the NE-RCM swarms until approximately -8.5° latitude. The dikes outcrop mostly as residual rounded blocks dispersed on the ground or along drainages (Fig.3.6A-B).

Weathering effects are mainly discernible by the pervasive development of onion skin structure either in dikes or sills, thus favoring a common landscape of many of the outcrops that are the accumulation of rounded blocks dispersed on the ground or along drainages (Fig.3.6A-B; Fig. 3.7A-B). Even so, the majority of blocks are pristine and free of alteration when examined microscopically. Dikes and sills are medium-grained, melanocratic to mesocratic rocks (diabases). Chilled margins are rare to find. Country rock xenoliths are also rare and were notable only in a quarry in exploitation close to Teresina (Fig. 3.7C) or dikes crosscutting Paleozoic sandstones in the basin border (Fig. 3.7D) or in outcrops of a dike intruding the crystalline basement (Fig. 3.7E-F).

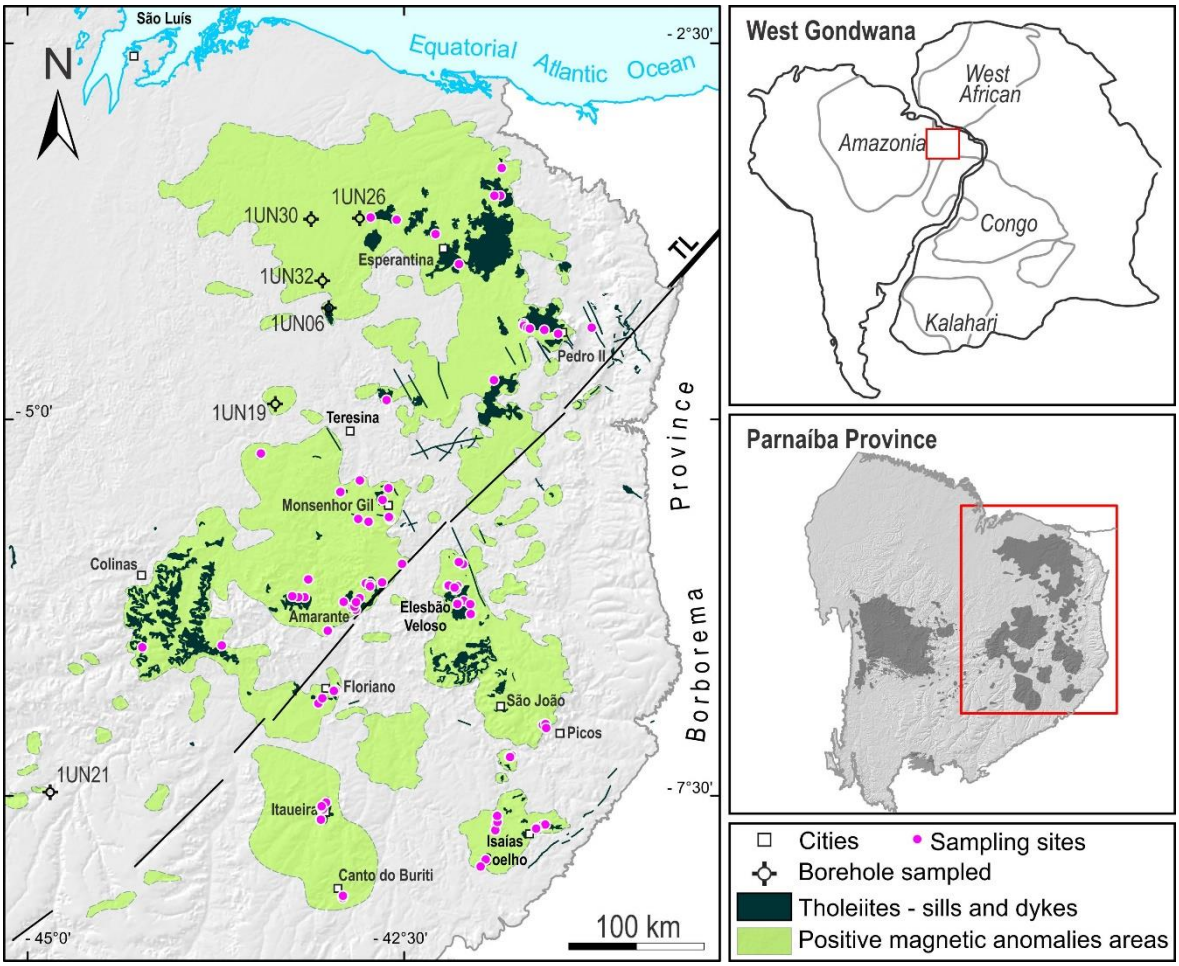

Figure 3.4. Simplified map of the eastern flank of the Parnaíba Basin with a focus on mafic rocks (modified from Macêdo Filho et al., 2019) and sampling sites. The intrusions exposed on the surface are represented by dark green colors, while pale green is the magnetic signature attributed to mafic rocks in the subsurface (Mocitaiba et al., 2017).

Intermediate rocks are subordinate in the dike swarms and sill province. They are coarse-grained feldspar-rich rocks only found near the Elesbão Veloso village, and no clear relationship with the diabases was found. In these rocks, sub-centimeter to centimeter-sized

acicular crystals of pyroxene occurs in a feldspar-rich matrix defining a “pegmatitic” texture (Fig. 3.7G-H). Amygdales are full to partially filled with carbonate or zeolite.

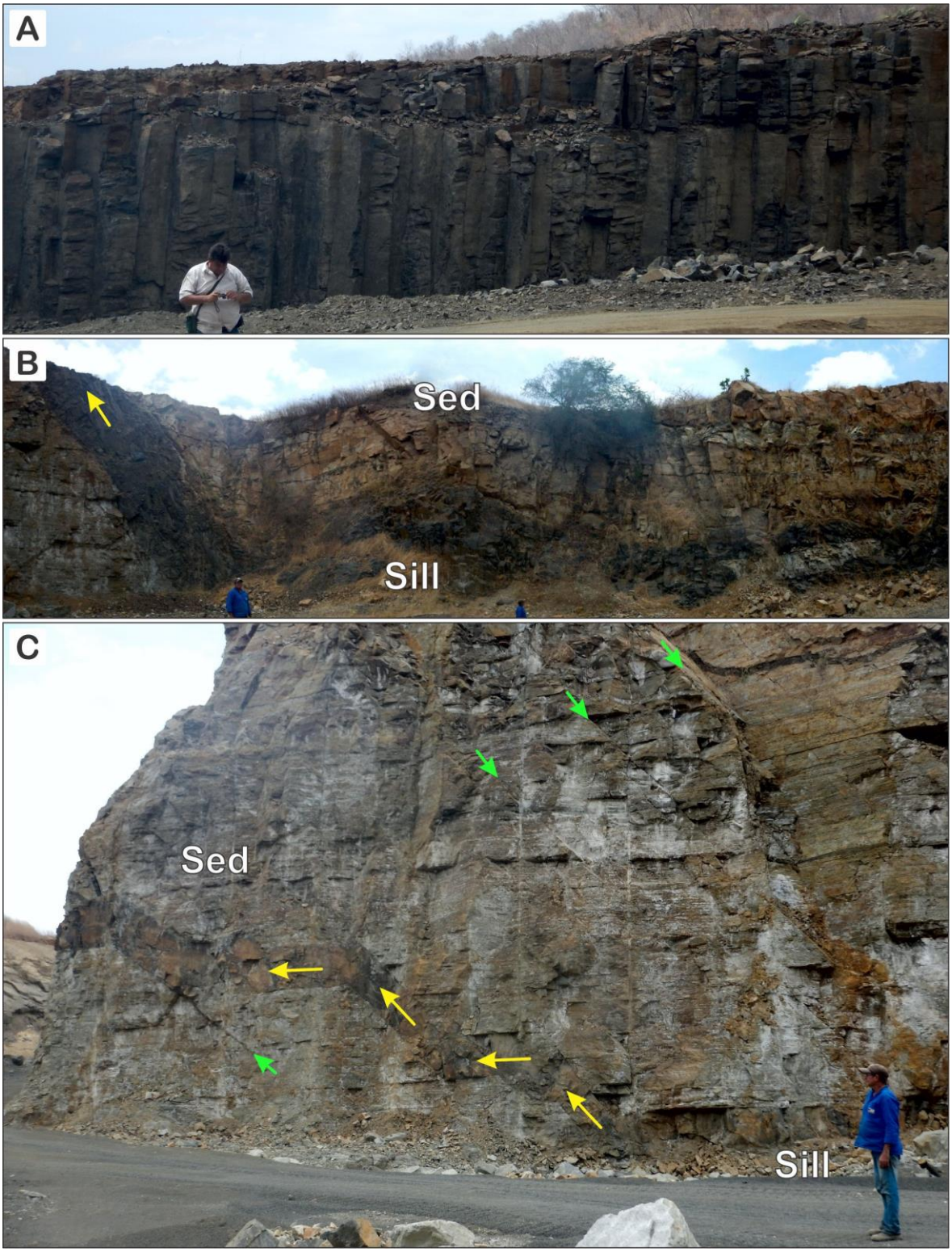

Figure 3.5. Field aspects of Sardinha intrusions. (A) columnar joints and a sill intrusive in a sedimentary sequence (sed). (B) A climbing edge (yellow arrow) structure is represented by dike/sheet and a similar feature is illustrated in (C) where, additionally, fractures/faults were used by the magma to move upward (green arrows).

Figure 3.6. Field aspects of the dikes. Common exposition pattern as rounded blocks (A) along drainages (e.g., NE-RCM) or (B) on flat topography (e.g., Canindé dikes). Sill complexes in the Parnaíba Basin also have similar erosive features.

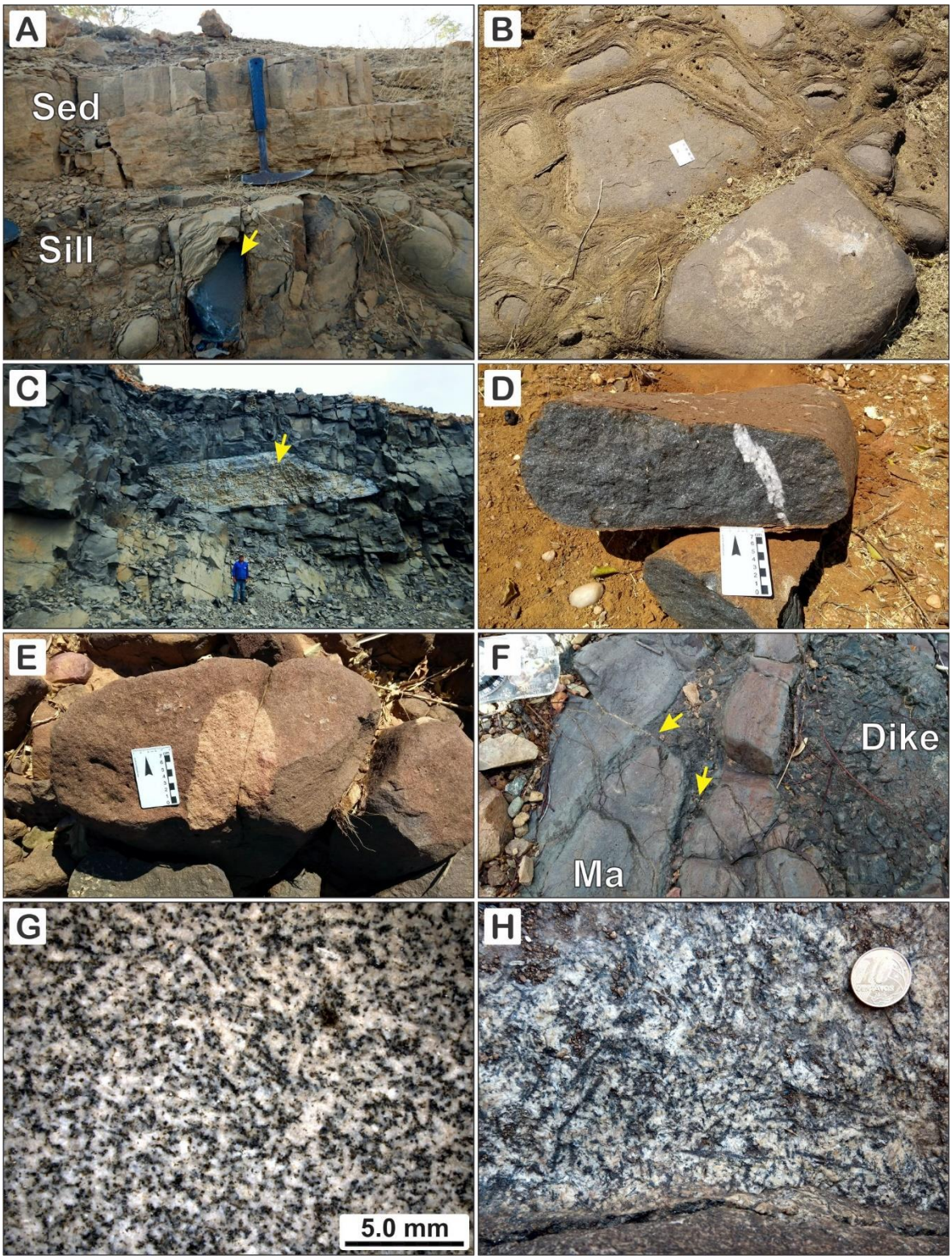

Figure 3.7. Field aspect of sampled rocks. Onion skin structure due to weathering affecting (A) sills (note pristine cores) and (B) dikes. Sandstone xenoliths in (C) sills and (D) dikes, where it can occur as recrystallized quartz-rich domains. In crystalline basement xenoliths of (E) granodioritic rocks or (F) metamorphic rocks forming rounded fragments. The yellow arrows in (F) represent the sense of propagation of apophysis from dikes to host marbles (Ma). The typical texture of (G) fine-grained intermediate composition rocks of the NE-Rio Ceará-Mirim dikes and (H) coarse-grained feldspar-rich sill showing centimeter-sized acicular pyroxene defining a “pegmatitic” texture samples on the central area of Elesbão Veloso laccolith.

3.5. Structural Trend of Dikes Swarms

Traces of faults and shear zones of the Precambrian basement of the Borborema Province were extracted from regional-scale geologic maps (CPRM) using the ESRI's ArcGIS 10.4.1 software. The vector data were used to generate rosette diagrams in the RockWare® software RockWorks17 (Revision 2020.2.26). The diagrams were made using the length (of lines) weighted frequency method (direction count). The methodology to identify mafic dikes was described in the previous section.

The Borborema Province can be divided into three major domains, separated by the EW-trending Patos and Pernambuco shear zones (e.g., Santos et al., 2017). The Northern Domain is composed of Paleoproterozoic, mainly gneissic migmatitic basement (including small inliers of Archaean age) and medium- to high-grade Ediacaran metasedimentary belts. The Central Domain consists of elongate terrains of different lithologies, ages (from Paleoproterozoic to Ediacaran), and metamorphic grades, all juxtaposed by NE-trending shear zones. It differs from the Northern Domain by the presence of bimodal volcanism and Tonian (1.0-0.93 Ga) plutonism (Santos et al., 2010). The Southern Domain, in turn, consists mostly of Ediacaran passive margin deposits thrusted over the São Francisco Craton as a result of a collision with the Pernambuco-Alagoas superterrane at 0.63-0.62 Ga (Oliveira et al., 2010). In the whole Borborema Province, the EW- to NE-trending strike-slip shear zones are several hundred kilometers long and up to 25 kilometers wide, usually displaying mylonitic fabrics formed at high-temperature conditions, where many Neoproterozoic granitic plutons intrude (Vauchez et al., 1995, 1997; Archanjo et al., 2013). Some of these structures still accommodated brittle activations (e.g., normal, strike-slip or locally reverse faults) related to extensional events that led to the development of intra-continental rifted basins at the Cambrian-Ordovician (e.g., Cococi and Jaibaras rifts; Françolin et al., 1994; Sénant and Popoff, 1991) and at the Mesozoic (e.g., Cariri-Potiguar, Sergipe-Alagoas, and Tucano-Jatobá rift systems; Matos, 1992, 2000). These weakness zones also accommodated the emplacement of dike swarms, since dikes follow the same structural trend of major lithospheric discontinuities of the basement (EW- to NE-trending).

Dikes are more common in the northern Borborema Province, and less frequently in the southern and central domains. Additionally, the minor occurrence of dikes is recognized in the eastern border of the Parnaíba Basin. The Rio Grande do Norte sector is typically structured by NE-SW lineaments (vector mean of ~46°) with a secondary frequency of EW structures related

to the Patos Shear Zone (Fig. 3.8). This area includes the EW-RCM Swarm which shows a mean dike trend at ca. 092°, therefore forming an angle of ca. 45° with the NE-trending structures. The EW-RCM keeps a similar orientation compared to the strike-slips faults from the Cariri-Potiguar Rift system and the adjacent continental Atlantic margin (Matos et al., 1992, 2000).

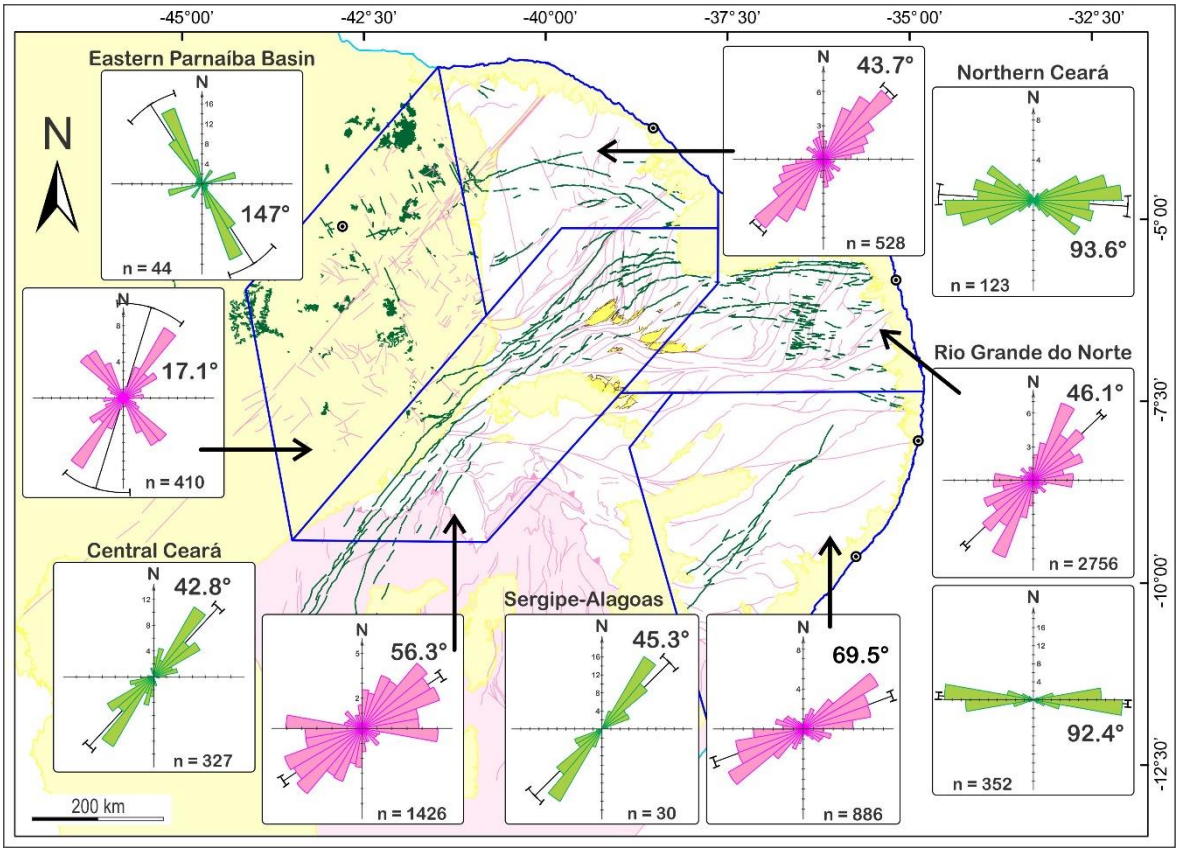

Figure 3.8. Rosette diagrams of Mesozoic dikes, faults, and Precambrian basement structures in the different sectors of Borborema Province and Parnaíba Basin. The main vector values are discriminated in each diagram. Pink colors represent ductile structures of the regional basement, except the Parnaíba Basin domain where it occurs exclusively as brittle structures (faults and fractures), while green colors indicate the dike swarms. The diagrams were made using the frequency weighted by the length of the lines method.

The lineaments between the Central Ceará and the northern margin of the São Francisco Craton show a mean trend of 56° Az (Fig. 3.8). This area contains the NE-RCM, from which the dikes have a mean orientation to 43° Az, hence subparallel to the NE- trending regional foliation and at a high angle to the EW Patos and Pernambuco shear zones. Curiously, when the whole arcuate RCM Swarm is considered, there is an exact angle of 130° between the main direction of EW and NE-trends. Additionally, the NE-RCM has the same structural trend of normal faults of the Cariri-Potiguar rift.

The main basement structures from the Northern Ceará sector display a NE-trending with a mean orientation at 44° Az (Fig. 3.8). Well-developed minor structures, although subordinate, are recorded to the NNW-SSE direction. The latter is related to the Santa Quitéria batholith and the N-trending Tauá Shear Zone (Ávila et al., 2019). This region is crossed by the Canindé dikes, which vary in orientation from NW-SE to EW as they approach the EW-RCM. Such an arcuate trend of the Canindé dikes is also coincident with the trace of the continental platform between the Rio Grande do Norte and Ceará states.

The Sergipe-Alagoas sector is sectioned by EW-trending structures, such as those of the Pernambuco lineament, as well as by high frequency NE-trending structures that yield a mean orientation in the rose diagram of 69° Az (Fig. 3.8). This sector hosts the Riacho do Cordeiro dikes which show mean orientation to 45° Az and are subparallel to the basement structures, the NE-RCM, and Sergipe-Alagoas Rift System.

Finally, faults and fractures with peculiar orientations are recognized in the eastern flank of the Parnaíba Basin (Fig. 3.8). They form two main trends to NE-SW and NW-SE. The NE-trending structures are brittle reactivations of the Transbrasiliano Lineament, while the NW-trending structures are coincident with the mean orientation of the dikes (147° Az) of that area. This dike orientation is completely distinct from the dikes identified in the Borborema Province.

3.6. Discussion

3.6.1. Juro-Triassic event

The N35W-trending dikes and faults of the NE Parnaíba Basin are analogous to the orientation of the continental platform adjacent to the western Maranhão State (~N30W), where NW-trending CAMP dikes are reported (Klein et al., 2013). The well-documented Mosquito Formation (CAMP basalts; Merle et al., 2011) situated in the western Parnaíba Basin exhibits an elongated (~330 × 210 km) magnetic anomaly (Mocitaiba et al., 2017) with the major axis oriented at ~N45W. This alignment is similar to NW-trending fractures found in the host rocks of the Mosquito Formation (Silva et al., 2020), as well as to Juro-Triassic NNW-trending dikes emplaced in the Araguaia Belt close to the field of the Mosquito flood basalts (Cruz and Gorayeb, 2020). Furthermore, NW-oriented (plus minor NE-oriented) CAMP dikes have been reported in further areas of northern Brazil, the Guiana Shield and its African counterpart (Sial et al., 1987; Reis et al., 2013; Teixeira et al., 2019; Marzoli et al., 1999; Deckart et al., 1997;

Callegaro et al., 2017; Davies et al., 2017) as seen in Late-Triassic-Early Jurassic continental reconstructions of Pangea (e.g., Ye et al., 2017; Figure 3.9).

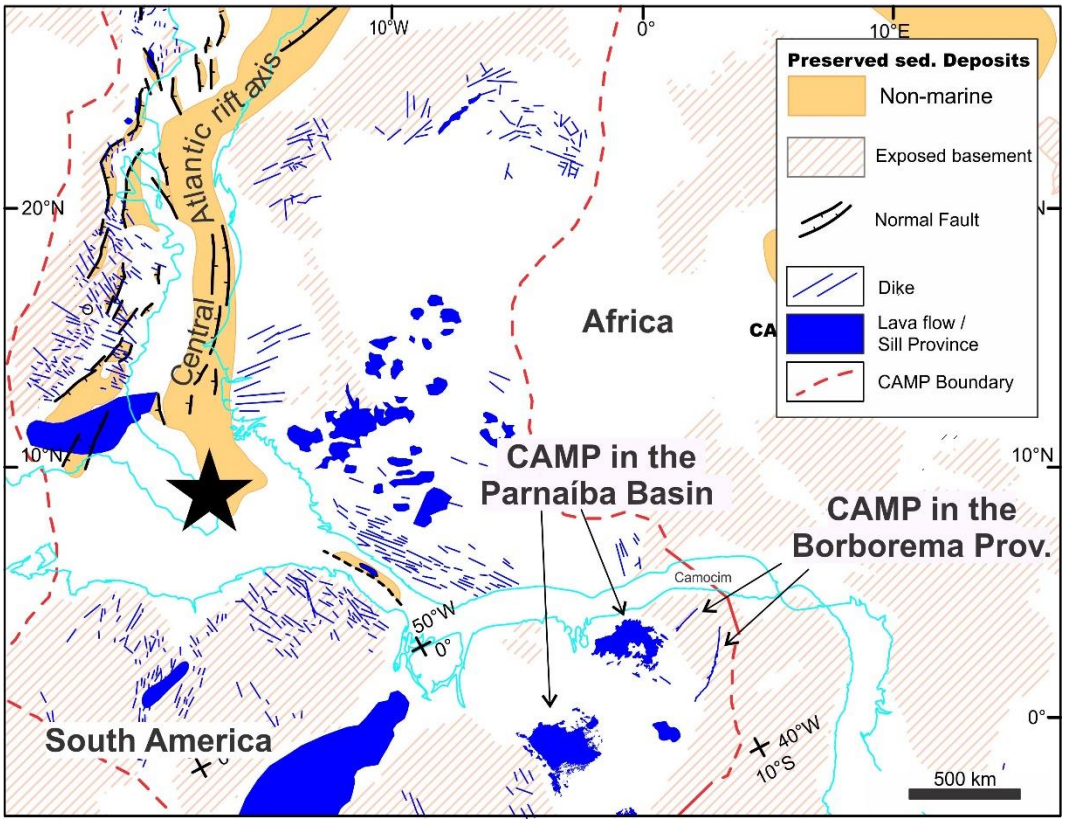

Figure 3.9. Paleoreconstruction model of part of Pangea at the Jurassic-Triassic (Ye et al., 2017) with updated CAMP cartography in NE Brazil. The general orientation of dike swarms and rough boundaries of the Central Atlantic magmatic province (CAMP) is shown. Jurassic-Triassic continental flood basalts and sill complexes in the Parnaíba Basin are likely related to the NW-trend of CAMP rocks propagating towards the West Gondwana (South American-African plates). The black star represents the plausive focal zone of CAMP in the Central Atlantic area.

Additional evidence of Juro-Triassic magmatic activity in NE Brazil concerns to paleomagnetic results of Ernesto et al. (2003), which investigated mafic rocks from the EW–RCM, Parnaíba Basin, Lavras da Mangabeira Rift, and "*some isolated dikes outcropping to the west of the Ceará–Mirim Swarm in the Ceará State*" (Ernesto et al., 2003). They suggested a Lower Jurassic remnant magnetization for intrusions on the NE Parnaíba and Lavras da Mangabeira basins (also reinforced by $^{39}Ar/^{40}Ar$ ages spanning from 180 to 208 Ma; e.g., DeMin et al., 2003; Heilbron et al., 2018; Fernandes et al., 2020), and an imprecise "site 3" located on the Santa Quitéria dikes. The Santa Quitéria Subswarm is a ~200 km–long structure oriented to N75E and discordant to the WNW-trending Canindé dikes (Fig. 3.1), but consistent with the orientation of the continental margin near the Piauí-Camocim segment (NW Ceará Basin). In the geochemical approach, we will see that these rocks are indeed akin to the CAMP.

The Santa Quitéria dikes and a NE-oriented subswarm (Fig. 3.1) subparallel to the Senador Pompeu Shear Zone tend to cluster near the Juro-Triassic age in K-Ar systematic supporting a CAMP filiation (Oliveira et al., 2021).

In conclusion, the NW-trending brittle faults and fractures associated with CAMP emplacement in NE Brazil coincidentally point to the focal zone of the Central Atlantic area and, therefore, they would be manifestations of the far-field stress linked to the Central Atlantic Rift attempt toward South American and African plates (Fig. 3.9).

3.6.2. Early Cretaceous event

The EW-RCM, Trangola, and Canindé swarms are oblique to the regional Precambrian structures. Thus, deformation and, consequently, dike emplacement were concentrated into thinner damaged zones of < 25-30 km in width. Conversely, the NE-RCM Swarm has lengths of 700 km and occurs in the same trend of the Early Cretaceous Cariri-Potiguar Rift, spread in a fractured area of ca. 100 km wide. This diffuse pattern may be formed by extensional NW-trending tectonics that reactivated an older NE-trending fabric of the basement where dikes were nucleated.

The magnetic anomalies trending to ~N45E allow us to define the Riacho do Cordeiro swarm between the eastern Pernambuco lineament and the NE margin of the São Francisco Craton. The dikes show the same orientation as Sergipe-Alagoas Rift, and likely reach the Recôncavo Rift vicinity as suggested by NE-SW-trending magnetic anomalies adding up to 700 km in length. Hence, similar in size and orientation to the NE-RCM. However, the basement structures in the Sergipe Microplate are in general N45-90E oriented. This pattern may have imposed some degree of obliquity to the dilatational structures related to the NW-SE extensional stress during the Early Cretaceous tectonics. Consequently, the Riacho do Cordeiro dikes concentrate the deformation in a single and well-developed N45E swarm. The width variation of the Riacho do Cordeiro became progressively thinner from SW to NE, and when it reaches the Pernambunco Lineament, it deviates and keeps the propagation just for ca. 55 km. Likewise, the Tucano Rift propagates northwards but, closer to the Pernambuco lineament, it changes in orientation to form the ENE Jatobá Rift. The syn-rift sequence filling the Pernambuco-Paraíba Basin is correlated to the Aptian (Córdoba et al., 2007), therefore younger than the syn-rift deposits in the Sergipe-Alagoas Rift dated from the Berriasian (Campos Neto et al., 2007). Again, the Sergipe-Alagoas Rift had its propagation hampered northwards. Hence,

dike swarms and rift basins indicate that the Central Domain of the Borborema Province, particularly the area between the EW-trending Patos and Pernambuco shear zones (also poorly crossed by EQUAMP dikes), worked as a shield for the propagation northwards of the rift system that evolved from the South Atlantic during the Lower Cretaceous.

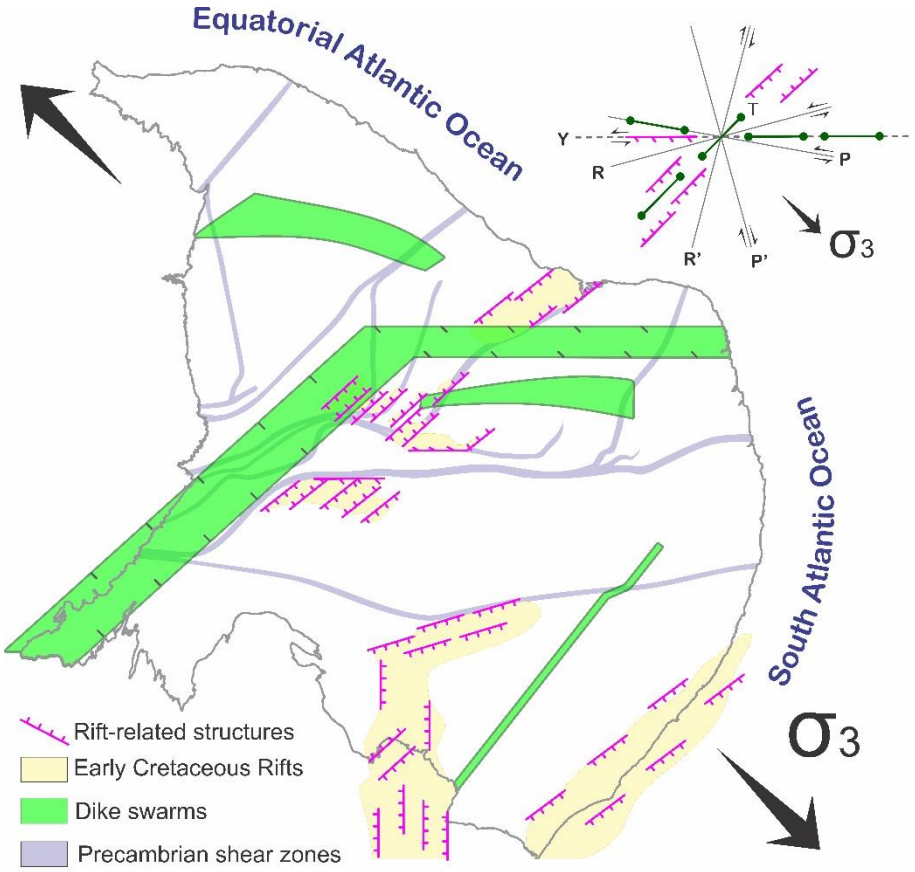

Figure 3.10. Schematic kinematic model correlating intrusion of dike swarms, rift basins development, and the initial stages of South Atlantic Ocean opening in NE Brazil (Early Cretaceous). In this model, an extentional vector (σ3) oriented NW-SE trigger the formation of NE-SE normal faults of rift basins and NE-dike swarms by activation of pre-existent weakness zones of Precambrina basement (prevalent NE-SW). The EW rift-related faults and dikes swarms may have a directional component associated.

Considering the mean angle of 130° between the EW-RCM (092°) and NE-RCM (222°), the extensional direction (σ3) should be oriented ~N45W (Fig. 3.10). Thus, the NE-RCM and Riacho do Cordeiro swarms may have nucleated into the shear dextral faults or dilatational fractures (~T type). While EW-RCM, Trangola, and Canindé dikes were emplaced into a shear sinistral zone (~Y type). Analogous kinematic models considered as extensional strain axis NW-SE-oriented with EW left-lateral component are proposed for the Cariri-Potiguar Rift (e.g., Matos, 1992; Françolin et al., 1994), and Benue Trough, where left

transtensional tectonics dominate (Guiraud and Maurin, 1992). Moreover, the NW-trending extension direction has been correlated to the opening of the South Atlantic Rift between the extreme NE of Brazil and Gabon-Nigeria segments (e.g., Heine et al., 2013).

Alternatively, a σ3 oriented N-S may be related to the generation of EW-RCM, whereas NE-RCM might have been formed by brittle activations of basement discontinuities (mainly NE-SW) with a transtensive dextral component. Oliveira (1992) and Melo et al. (2022) proposed another possible explanation to the arcuate geometry of the RCM swarm based on a regional variation of σ3 from NW-SE in central Borborema Province generating NE-RCM, to N-S near the Equatorial Atlantic margin forming the EW-RCM. Even so, all hypotheses raised here need to be better constrained by detailed structural and high-resolution geochronological approaches.

4. MINERAL CHEMISTRY AND CRYSTAL SIZE DISTRIBUTIONS OF MAFIC DIKES AND SILLS ON THE EASTERN BORDER OF THE PARNAÍBA BASIN, NE BRAZIL

Macêdo Filho, A.A., Archanjo, C.J., Hollanda M.H.B.M., and Negri, F.A.

Article published by Journal of Volcanology and Geothermal Research

4.1. Abstract

Crystal size distributions (CSDs) and mineral chemistry of plagioclase and clinopyroxene are used to quantify textures and estimate timescales of Mesozoic mafic sills and dikes exposed on the eastern margin of the Parnaíba Basin (NE Brazil). The diabases consist of plagioclase, clinopyroxene (augite and pigeonite) and Fe–Ti oxides and show textures that vary from holocrystalline, to locally porphyritic, glomerophyric and hypocrystalline. Plagioclase and clinopyroxene CSDs are similar in sills and dikes, with clinopyroxene slopes systematically steeper than plagioclase slopes. Plagioclase usually records nearly log-linear negative slopes that tend to steepen approaching the wall rock contact. Plagioclase typically shows normal zoning with anorthite contents varying (An_{84-25}) from the center to the grain margin. Calculated residence times for the log-linear segments vary from ca. one month ($\tau = 10^{-7}$ mm.s^{-1}) for samples situated 20 cm from the contact to ca. four months for samples ~3 m away from the contact. Clinopyroxene consists of augite (dominant) and pigeonite and shows relatively uniform compositions. Unlike plagioclase, clinopyroxene CSDs tend to be flat or slightly positive towards the finer grains suggesting that the texture was modified during the crystallization of the residual melt. Plagioclase microlites (L < 0.5 mm), in contrast, show kinked CSDs with the steeper negative slopes including minute crystals of sanidine (orthoclase component) and alkali-sodic feldspar in addition to Ca-Na plagioclase. The modified textures and high nucleation density of microlites in mostly static, deep-seated magmatic reservoirs therefore resulted from chemical disequilibrium between largely solidified tholeiitic magma and late, highly fractionated alkali-rich residual melts. The estimated time for the full crystallization of the largest sills is one and one-half years.

Keywords: Crystal Size Distribution, Mineral Chemistry, Diabase, Parnaíba Basin.

4.2. Introduction

Quantification of textures through crystal size distributions (CSDs) can provide important information about crystallization history and cooling of magmatic rocks (Marsh, 1988). CSD is a technique that relates nucleation, the average growth rate and the time the crystal grows (or resides) in the magma. The method is based on the balance in the number of crystals within a specific size range of a particular volume of magma, named the *population density*. One of the most striking features of CSD is that crystal populations in many magmatic systems often show an almost straight line with negative slope when plotted as population density against crystal size (Cashman and Marsh, 1988; Higgins, 1998; Higgins and Roberge, 2003; Archanjo et al., 2012; Fornaciai et al., 2015). Marsh (1988) and Cashman and Marsh (1988) show that such a log-linear relation is typical of steady continuous crystallization associated with a nearly constant growth rate irrespective of crystal size. CSD theory for a linear log-normal distribution, therefore, provides the nucleation density (n^o) when grain size approaches to zero, and the slope enables the measurement of the crystal growth rate (G) and residence time (τ). Moreover, fanning of log-linear CSDs of comagmatic rock suites is caused by different cooling rates, moving from the margin (steeper slope) to the interior (gentle slope) of a magmatic body (Zieg and Marsh, 2005), or even by closure (Higgins, 2002).

Several natural and experimental results, however, have shown that many CSDs deviate from a straight line. According to Marsh (1988), the modification of steady-state crystallization may derive from quenching which tends to steepen the curve for smaller grain sizes and crystal accumulations, or removal from the liquid promoting concave-up and concave-down curves and kinked CSDs, respectively. The kinked CSD slopes, in turn, may results from two different crystal populations crystallizing in the magma. Likewise, continuous to sudden changes in magmatic processes, such as heterogeneous nucleation (Špillar and Dolejš, 2015), textural coarsening (Higgins, 2011) and physical mixing of distinct magmas (Higgins 1996; Salisbury et al., 2008) can produce curved CSDs (Armienti et al., 1994; Ngonge et al., 2013; Preece et al., 2013; Fornaciai et al., 2015). Concave-up CSDs have also been documented in experimental studies as a result of the combination of two plagioclase populations, one formed during the annealing period and other formed during depressurization and rapid cooling (Brugger and Hammer, 2010; Vona and Romano, 2013). These CSD results, nevertheless, have been mostly applied to volcanic systems that are continuously refilled by new magma ("open model" of Marsh, 1988).

In this work, we combine crystal size distributions and mineral chemistry to investigate the magma crystallization and solidification history of mafic sills and dikes found intruding within Paleozoic sedimentary rocks of the Parnaíba Basin (NE Brazil). Contrasting with CSD patterns generated in open volcanic systems, the CSDs of the studied diabases evolved from melts solidified entirely at depth (closed systems), in which texture depends on the balance between nucleation and growth from a static magma chamber.

4.3. Geological Setting

The intracratonic Parnaíba sag-type basin covers an area of approximately 6.5 x 10^5 km^2 in northeast Brazil (Fig. 4.1). The basin is floored by Precambrian rocks and the sedimentary column has a mean thickness of approximately 3,000 m (Goes and Feijó, 1994; Vaz et al., 2007). Geophysical surveys reveal the presence of two intersecting, NE- and E-trending rift systems developed in the Precambrian basement, which have been interpreted as earlier structures relative to the deposition of the sag deposits (de Castro et al., 2014). The NE-trending rift system is parallel to one of the major basement structures – the Transbrasiliano Lineament– along which the thickness of the sedimentary pile reaches approximately 5,000 meters. This lineament can be traced from Ceará (northeast Brazil) to central Brazil and correlates, in a predrift reconstruction, with the Kandi Lineament in West Africa (Schobbenhauss et al., 1975; Fuck et al., 2011). The Transbrasiliano-Kandi Lineament, therefore, reaches more than 4,500 km in length constituting a fundamental structure of West Gondwana (Fairhead & Maus, 2003; Brito Neves and Fuck, 2014). This intercontinental structure has been reactivated several times in the Phanerozoic and was probably used for magmas derived from the mantle to move upward and be emplaced in the basin (e.g. Northfleet and Neves, 1966; Zalán et al., 1985; Destro et al., 1994; Amaral et al., 2017).

The sedimentary filling is dominated by siliciclastic sediments. Sandstone and subordinate shale and conglomerate, as well as local limestone and evaporite beds are grouped into three super-sequences that record successive transgressive-regressive cycles separated by regional erosive unconformities (Vaz et al., 2007). The older sequence, of Silurian age, is represented by the Serra Grande Group, which was followed by the deposition of Middle Devonian-Early Carboniferous sediments of the Canindé Group and, afterward, by the sediments of the Balsas Group accumulated during the Late Carboniferous-Early Triassic. The detrital zircon record indicates that the long-term sedimentation of ca. 250 m.y. was likely

resulted from a combination of continuous denudation of adjacent Precambrian rocks and intrabasinal recycling (Hollanda et al., 2018).

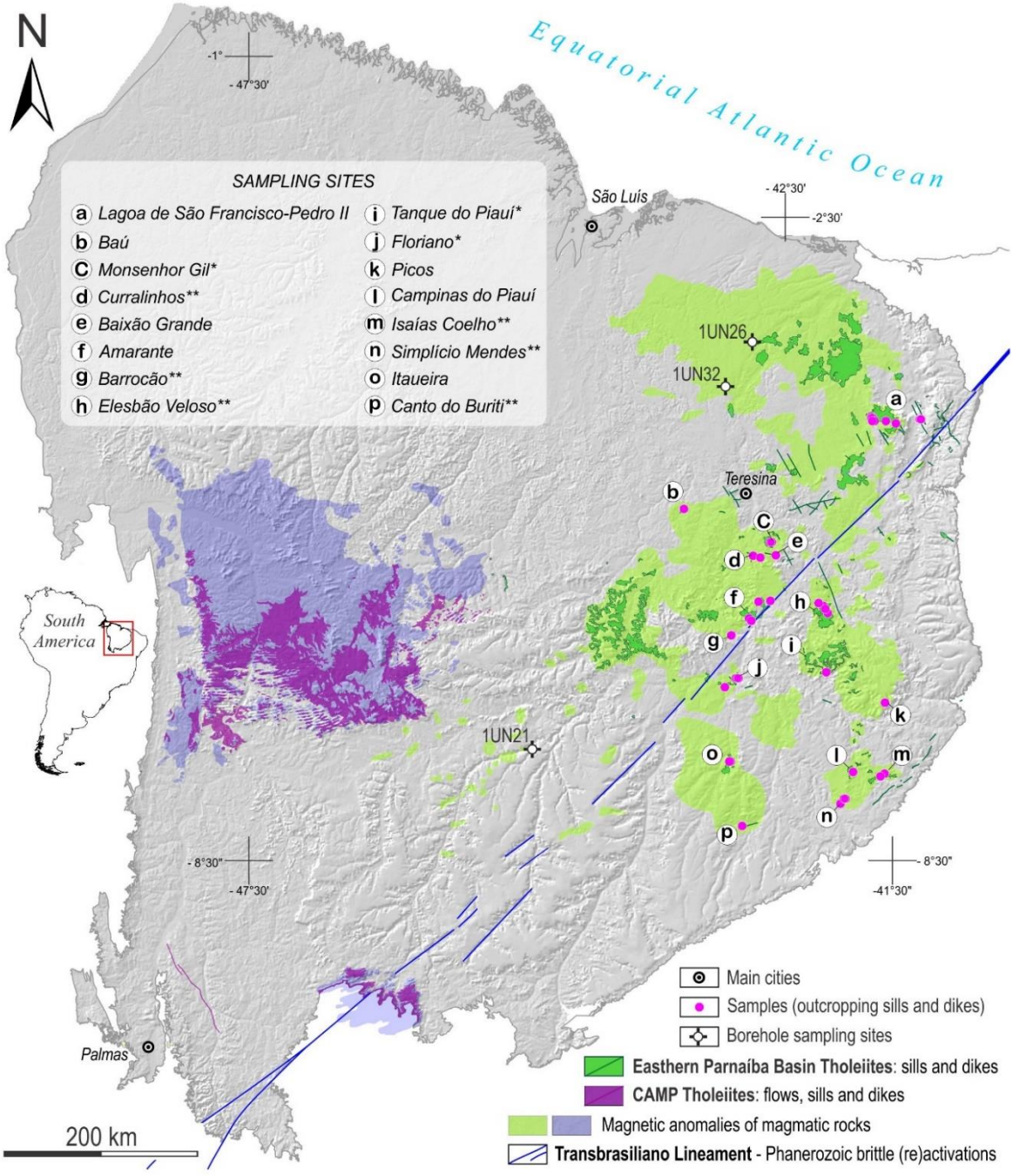

Figure 4.1. Simplified map with regional distribution of the Mesozoic magmatic rocks in the Parnaíba Basin (BP); note that the eastern magmatism consists of intrusive rocks. The light green and light purple areas illustrate the subsurface distribution of magmatic rocks based on geophysical data (after Mocitaiba et al., 2017 and de Castro et al., 2018). All sampling sites were analyzed by geochemistry (major elements). CSD analysis was applied to samples from sites highlighted with *, while those with ** were studied by combining CSDs and mineral chemistry. The regional relief was generated based on the images from the Shuttle Radar Topography Mission (SRTM).

At the Triassic-Jurassic transition, the basin was penetrated by mafic lava flows and sills. These rocks are regionally grouped into the Mosquito Formation and have been widely described as correlative with the Central Atlantic magmatic province (CAMP) (Bellieni et al., 1990; Fodor et al., 1990; Marzoli et al., 1999; De Min et al., 2003; Merle, 2011; Oliveira et al., 2018). A second magmatic event known as the Sardinha Formation is represented by mafic magmas emplaced as sills and dikes (Bellieni et al. 1990; Fodor et al. 1990; Silva et al., 2017; Heilbron et al., 2018; Oliveira et al., 2018). A striking aspect highlighted in all these works refers to the geographic distributions of the two magmatic events where Mosquito lava flows are restricted to the western side of the basin, while the Sardinha sills and dikes were emplaced only on the opposite (eastern) side. Recent studies involving aeromagnetic mapping and seismic and well log interpretation have shown that the volume of magma trapped within the Parnaíba sediments is much more extensive in subsurface than at the surface. Regardless of the location, sills have been described as dominantly layer-parallel bodies with lengths from tens to hundreds of kilometers and maximum thickness of approximately 250 meters (de Castro et al., 2018; Trosdtorf et al., 2018). Saucer-shaped, planar transgressive and fault block geometries are also cited decribed by these authors but of subordinate occurrence. Based on geophysical data, Mocitaiba et al. (2017) estimate that the area occupied by sills on the eastern side of the basin would reach ca. 85,400 km² (Fig. 4.1).

Major oxide geochemistry previously published for the mafic rocks shows that the compositions vary mostly from tholeiitic basalts to basaltic andesites. Similar to other Gondwanan igneous provinces, the Mosquito and Sardinha tholeiites have been classified into the high-Ti-P (TiO_2 > 2 wt%; P_2O_5 > 0.2 wt%) or low-Ti-P (TiO_2 < 2 wt%; P_2O_5 < 0.2 wt%) groups. MgO contents in these groups show that the low-Ti-P magmas are more primitive with values generally higher than 6–7 wt%. In this work, we present the major oxide compositions of the studied samples (mafic sills and dikes of the eastern side) only for magma affinity classification. A detailed study of the petrologic aspects of these intrusive rocks is in progress for further publication.

4.4. Sampling and Methods

Sampling was carried out at forty different sites. Thirty-five samples came from rock exposures on the surface, and five samples were recovered from three boreholes (1UN21, 1UN26 and 1UN32) drilled by the Parnaíba Basin Coal Project (DNPM/CPRM). The sills

drilled along the survey vary from 2 to > 42 m in thickness and were emplaced either in pelite-sandstone interfaces or entirely within the shale units of the middle- to early Carboniferous sequence (Canindé Group). Similar stratigraphic control was observed for the sills sampled on the surface.

Petrography and texture were investigated in ninety-five thin sections. After petrographic description, we chose forty pristine samples for determining major oxide compositions by conventional X-ray fluorescence (XRF) spectrometry at the *Laboratório de Caracterização Tecnológica* (www.lct.poli.usp.br) using the ROC–1 package. The analytical procedure employed fusion of the samples with lithium tetraborate flux and subsequent quantitative analysis using the calibration curve method with standards (XRF peak intensity *versus* concentration). The loss on ignition was measured after heating two grams of rock sample to 1,020 ºC for two hours and weighing. All major oxide results are listed in Table A1 (Appendix).

Plagioclase and pyroxene were analyzed for mineral chemistry in the *Laboratório de Microssonda Eletrônica* (www.igce.rc.unesp.br) using a JEOL JXA-8230 probe equipped with five wavelength dispersive spectrometers. The operation conditions were 15 kV, 20 nA beam current and 10 μm spot size. The elements were analyzed using the Kα line applying the following diffracting crystals and mineral microprobe standards: TAP for Si (orthoclase), Al (anorthite) and Na (albite); PETJ for Ca (wollastonite); PETL for K (orthoclase), Ti (ilmenite) and Cr (chromite); and LIFH for Fe (ilmenite) and Mn (rhodonite). ZAF matrix corrections were performed using the PC-EPMA software. For the classification of plagioclase and clinopyroxene we considered microprobe analyses with oxide totals of 100 ± 2%. All mineral chemistry data are listed in Table A2 and A3 (Appendix).

Fourteen thin sections from six dikes and four sills exposed at the surface were used for CSD analysis. As sills and dikes must form a plumbing system in which dikes would feed sills, we checked whether CSDs would record differences in their crystallization histories. In contrast, four samples from the boreholes were used to investigate CSDs from the contact towards the center of the intrusion. Finally, according to the CSD patterns and to check the evolution of the silicate chemical compositions, we investigated the mineral chemistry from cores to margins in eight thin-sections of plagioclase and clinopyroxene.

CSDs were studied under both plane- and cross-polarized light using a computer-assisted Leica DN750P microscope. Image capture and subsequent superposition were performed by using the *Leica Application Suite (LAS)* software that assembles multiple sequential images

from a thin section. The final (mosaic) image is scaled, and plagioclase and pyroxene are isolated by threshold filters from opaque grains and unclassified (mostly glass) material (Fig. 4.2). We applied *SPO2003* software (Launeau, 2004) to eliminate grains less than 8 pixels and lines with widths of 1 pixel and to remove grains that met the image edges. Finally, plagioclase and pyroxene are manually vectorized to define grain contacts. CSDs were calculated using the *CSDcorrections v.1.6* software (Higgins, 2000). The rock fabric was considered massive, with grain roundness close to blocks (0.1) and crystal habits (ratios of short, intermediate and long axes) of each sample estimated through the *CSDslice5* spreadsheet of Morgan and Jerran (2006). All CSD data are listed in Table A4 (Appendix).

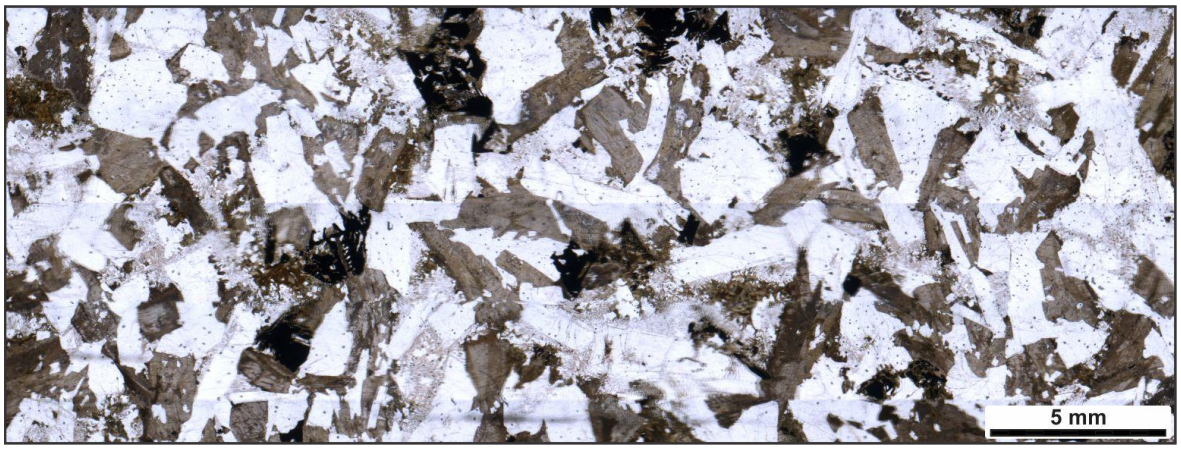

Figure 4.2. Holocrystalline diabase (plane-polarized light) consisting of plagioclase (white to light grey), clinopyroxene (grey) and Fe-Ti oxides (black). The colors and grain relief allow to isolate the mineral phases using image classification filters. The outlines of each crystal, however, are traced by hand assisted by the respective crossed-polar image (sample 1UN2680, see location on Figure 4.1).

4.5. Results

4.5.1. Major oxide chemistry

In geochemical classification diagrams (Fig. 4.3), all samples plot within the subalkaline field with tholeiitic compositions. The data group into two clusters, one comprising basalt to basaltic andesite and the other defining an evolutionary trachytic trend from basaltic towards trachyandesitic compositions. Taking into account the Ti-based classification, these two groups are classified as low-Ti (TiO_2 ~ 1.1-2 wt%, MgO ~ 5.5-7.7 wt%) and high-Ti (TiO_2 ~ 2.5–4.2 wt%, MgO ~2.6-5.8 wt%) tholeiites. The P contents are not distinctive between the low- and high-Ti magmas, varying from 0.3-1.1 wt% in both groups. A few samples lie outside of these Ti-Mg ranges and are characterized by not only low Ti (< 2 wt%) contents but also by very low

MgO (< 2.4 wt%), in addition to SiO_2 contents of 57-63% wt%, suggesting that these magmas evolved from fractional crystallization of the high-Ti tholeiites.

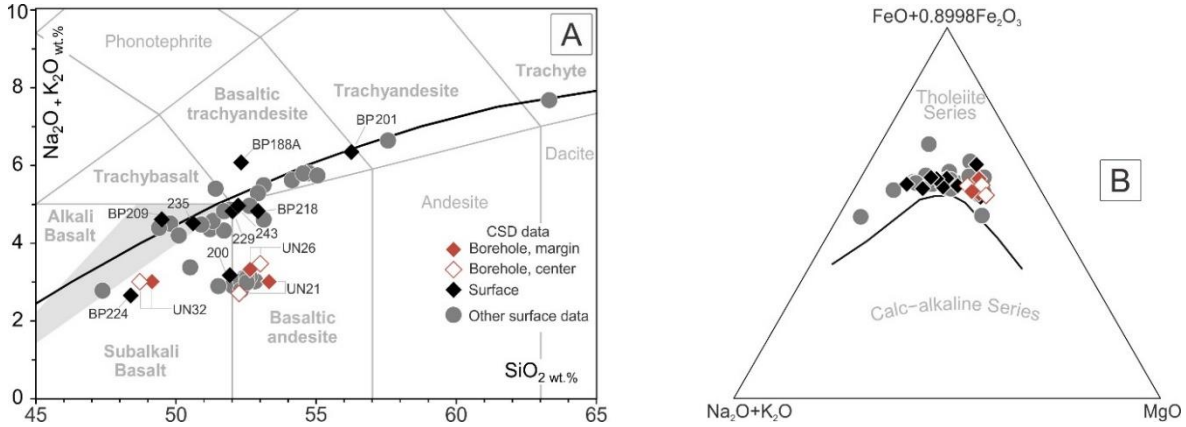

Figure 4.3. (A) TAS diagram (Le Maitre, 2002) showing the division line between alkaline and subalkaline magmatic suites. The gray field constitutes an overlapping zone between alkaline and subalkaline basalts. (B) AFM diagram (Irvine and Baragar, 1971) showing the tholeiitic signature of the eastern Parnaíba Basin magmatism. The borehole samples are available in Silva et al., (2017).

4.5.2. Petrography and mineral chemistry

Mafic sills and dikes are represented by pristine samples, dark colored in hand specimen, and usually show equigranular, fine- to medium-grained (< 1 to 1-5 mm) and, less often, coarse-grained (> 5 mm) textures. Plagioclase, clinopyroxene and Fe–Ti oxides constitute the essential mode in these diabases, whereas sulfides and apatite are the most evident accessory phases. Regardless of the grain size, plagioclase is always the dominant mineral totaling 50–75% of the mode, followed by clinopyroxene (20–45%) and Fe–Ti oxides (≤ 5%). Crystallinity in the diabases varies from holocrystalline to hypocrystalline. Textures in the holocrystalline diabases (Fig. 4.2) vary from subophitic to micrographic, intergranular and glomerophyric. In contrast, the hypocrystalline diabases contain (devitrified) glass and plagioclase microlites in the groundmass. Intersertal, seriate, vesicular/amygdaloidal and trachytoid textures are subordinate in these rocks.

Plagioclase is euhedral to anhedral in both holo- and hypocrystalline types. In the former, plagioclase grains are equidimensional to rectangular, sometimes defining glomerocrysts (Fig. 4.4A). In the holocrystalline diabases, plagioclase normally displays polysynthetic twinning and/or oscillatory (normal) zoning with compositions varying from labradorite to oligoclase ($An_{69}Ab_{30}Or_1$ to $An_{15}Ab_{68}Or_{17}$) (Fig. 4.5A and 6.6A). In sample BP224, however, plagioclase has bytownitic ($An_{85}Ab_{15}$ to $An_{70}Ab_{30}$; $Or_{<0.4}$) to labradoritic

($An_{69-53}Ab_{30-47}Or_{0-1}$) compositions indicating that this sample is a more primitive diabase than the other studied samples. Inclusions of clinopyroxene, apatite, glass and opaque minerals are common. In samples BP201 and 1UN26.80 (borehole) some large plagioclase grains (>1 mm) display well-developed outer shells in optical continuity with the inner zoning but dominated by intermixed sodic ($An_{2-0}Ab_{97-100}Or_{1-0}$) and alkali feldspar ($An_{0}Ab_{17-4}Or_{83-96}$) phases (Fig. 4.6B). Microlites of both holo- and hypocrystalline diabases have either calcic ($An_{61-25}Ab_{38-69}Or_{1-6}$) or sodic-alkali compositions ($An_{0}Ab_{51–41}Or_{49–59}$; BP209 and BP235). Quenching textures including sieve and micrographic types are common in the holocrystalline diabases, while intrafasciculate, swallowtail (Fig. 4.4B) and fanlike textures are more often found in the hypocrystalline rocks.

Equilibrium coexistence of two clinopyroxenes supports the tholeiitic affinity for the Parnaíba diabases. Augite is euhedral to anhedral and occurs either as single prismatic crystals or forming glomerophyric aggregates showing purple-brown to light green pleochroism typical of the Ti–Fe augite series (TiO_2 = 1.9-0.3 wt%, FeO_t = 24-7 wt%). Whatever the grain size, the compositions are relatively homogeneous (Fig. 4.6C) varying from $En_{51-27}Wo_{31-40}Fs_{18-33}$ in the large crystals (>0.5 mm) to $En_{49-23}Wo_{36-36}Fs_{15-41}$ in finer crystals (Fig. 4.5B). Subophitic to ophitic textures are common and sector ("hourglass", Fig. 4.4C) and concentric zonings are frequently observed. Pigeonite ($En_{65-43}Wo_{9-9}Fs_{26-48}$) occurs as euhedral to subhedral crystals, surrounding augite or as inclusion (Fig. 4.4D), varying from prismatic to acicular light brown crystals; the finest acicular crystals are usually present in the groundmass of the hypocrystalline diabases.

Opaque minerals are titanomagnetite or ilmenite occurring as rectangular, dendritic, skeletal and acicular shapes. EDS analysis indicates mainly Fe-Ti oxides (titanomagnetite or ilmenite) and sulfide (pyrite and chalcopyrite) minerals. Apatite is euhedral to subhedral and typically shows hexagonal (basal section) to acicular habits. Some apatite grains may reach 1.2 mm in length, forming swarms of needles hosted in the groundmass. Secondary phases, such as sericite, chlorite and calcite/zeolite filling amygdales are of minor importance but are common as a whole.

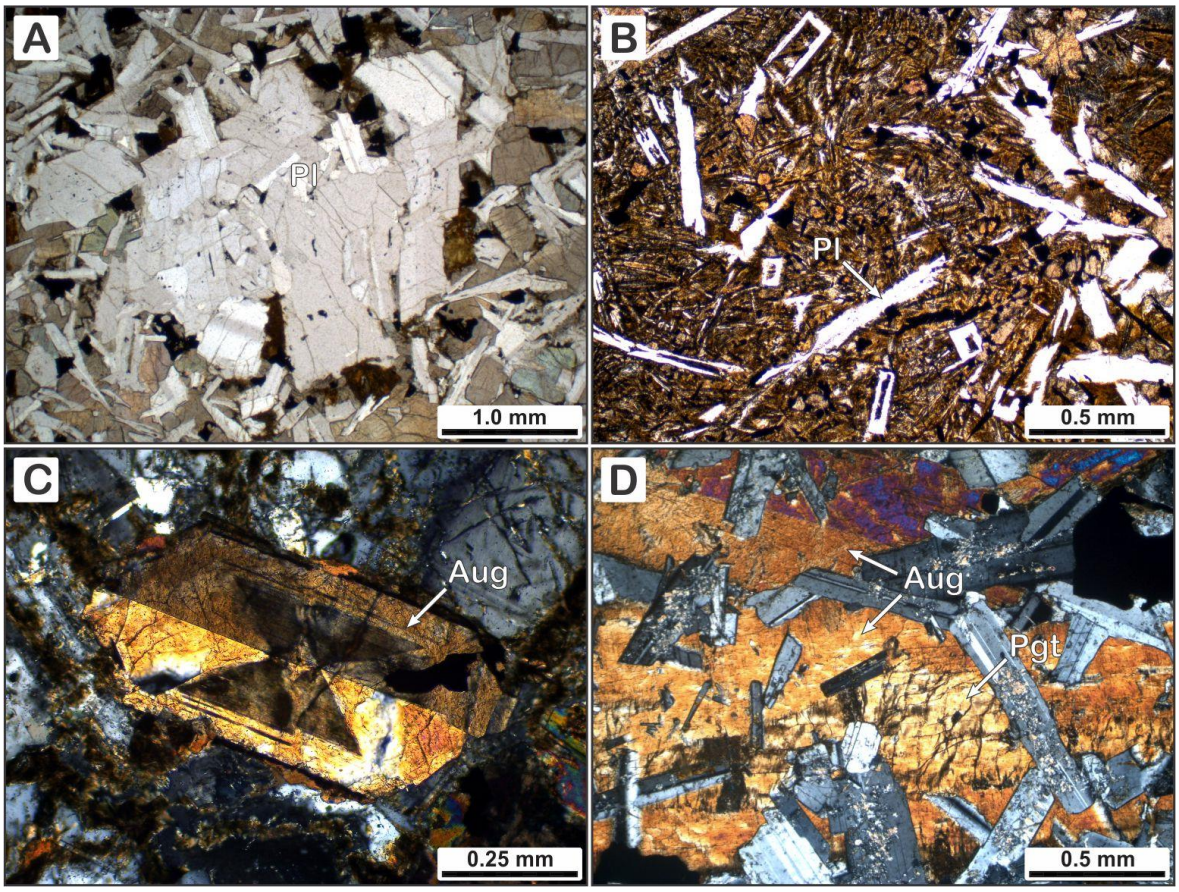

Figure 4.4. Typical textures in the Parnaíba diabases. (A) Plagioclase glomerocryst in a groundmass consisting of plagioclase, clinopyroxene and Fe-Ti oxides (BP224, PPL). (B) Plagioclase (Pl) laths displaying intrafasciculate, swallowtail to skeletal habits in a hypocrystalline groundmass (BP218, PPL). (C) Sector zoning (hourglass) in augite (Aug) phenocryst (29.04, XPL). (D) Large grain of clinopyroxene with pigeonite (Pgt) at center and augite at rims with inclusions of euhedral plagioclase forming an ophitic-subophitic microstructure (BP112, XPL). PPL, plane-polarized light; XPL, cross-polarized light.

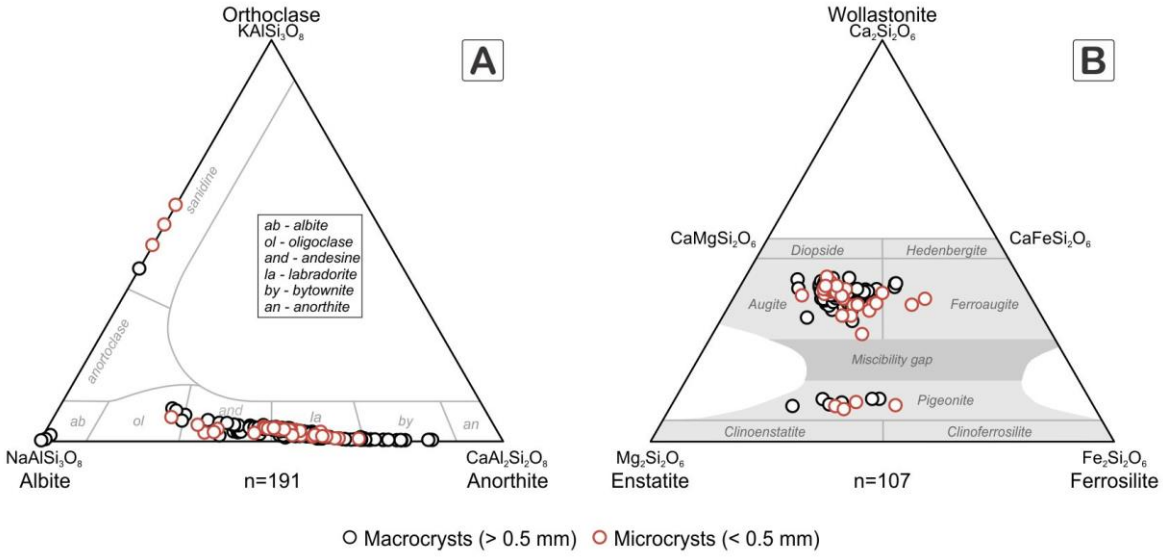

Figure 4.5. Range of solid solutions of (A) feldspar and (B) pyroxene measured in studies sills of the eastern border of Parnaíba basin.

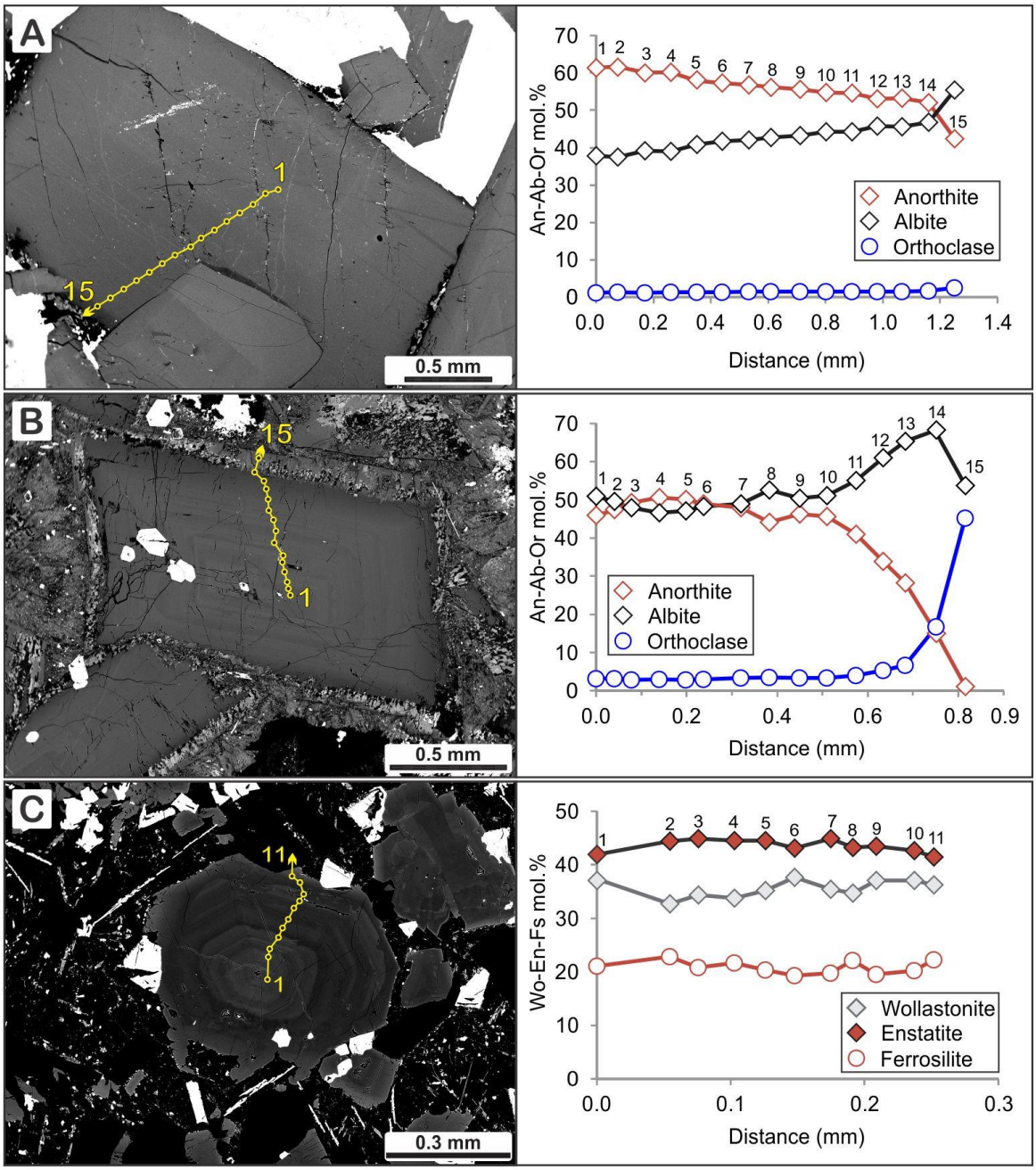

Figure 4.6. Compositional profiles (i.e., solid-solutions of anorthite-albite-orthoclase) across feldspar crystals. (A) Subtle normal zonation in plagioclase (1UN2680). (B) Normal zonation with an abrupt change in composition in the mantled rim (BP201). (C) Clinopyroxene subtle oscillatory zoning and relatively homogeneous endmember compositions (BP218).

4.5.3. Crystal size distribution

The results for CSDs are summarized in Table 1 and the respective data are plotted on a population density (ln(n), mm^{-4}) and size (L, mm) diagrams (Figs. 6.7 and 6.8). CSD parameters are calculated using the plagioclase population between approximately 0.020 mm (20 µm) and 6 mm and the clinopyroxene population between 0.024 mm and 3.2 mm. Grain

sizes less than 0.02 mm are not considered in the CSD results since crystals smaller than 8 pixels were removed during image processing. In addition, a few CSDs show a net downturn towards the finer grains, which we consider an artifact due to the combined effects of cleaning the binary image and sectioning for thin section preparation since coarse grains have more probability of being sectioned than fine grains. The results show great agreement between the mean volume calculated by the CSDs and the 2-D modal abundance, which confirms the estimation of the ratios between the short, intermediate and long crystal axes of plagioclase and clinopyroxene provided by *CSDslice5* (Morgan and Jerram, 2006).

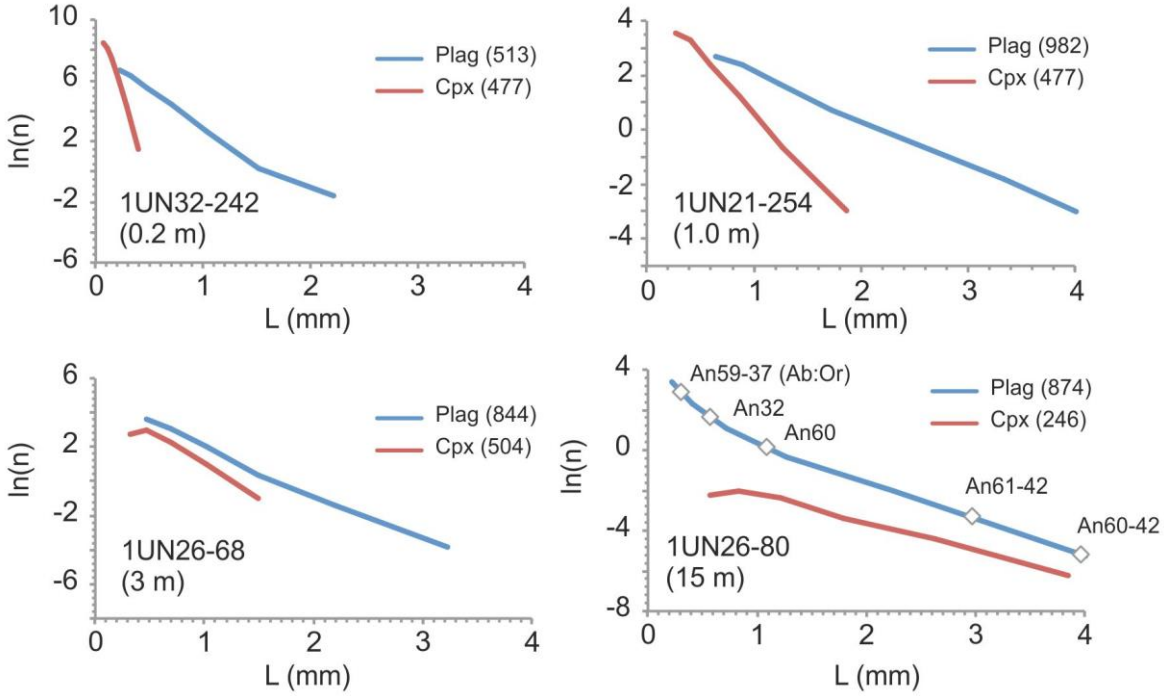

Figure 4.7. CSD diagrams from borehole samples collected at different distances from the wall-rock contact.

Plagioclase and clinopyroxene CSDs of the borehole samples show distinct slopes, usually higher in clinopyroxene, but in one sample (1UN26.80) the plagioclase and clinopyroxene CSDs depart from a log-linear distribution with goodness of fit ($Q < 0.01$) with parallel curves. Plagioclase CSDs at 20 cm from contacts with sandstones and up to 3 m from the contacts (Fig. 4.7) record slopes that fit or are very close to a straight line ($Q \geq 0.1$). The population density (n^o) ranges between 3.83 and 7.83 (mm^{-4}), with the sample nearest to the contact showing the highest intercept and slope values. One sample (1UN26.80) records a distinctly steeper slope towards the finer plagioclase grains, which contrasts with the clinopyroxene CSD that tend to be flat to slightly positive towards their finest grains.

CSDs from sills and dikes are similar with clinopyroxene slopes higher than plagioclase slopes in all samples (Fig. 4.8). Five plagioclase CSDs with L > 0.5 mm fit log-linear distributions (BP200, BP209, BP201, BP224 and BP235) with intercepts (n^o) between 1.00 and 5.20 and slopes between -1.44 and -3.53. Plagioclase microlites (L < 0.5 mm) of three samples (BP200F, BP209F and BP243F) show high density nucleation values ($n^o \geq 6.0$ mm^{-4}) associated with steeper slopes that however, depart from a log-linear distributions. In contrast, some clinopyroxene slopes tend to be flat (BP200 and BP209) or somewhat positive (BP229) towards their finer fractions, in agreement with the deficiency of small clinopyroxene crystals in these samples. In turn, three clinopyroxene CSDs fit straight lines (BP209, BP201 and BP243) with slopes between -2.8 and -4.7 (Table 1).

4.6. Discussion

4.6.1. Crystal size distribution

A common feature of all CSDs for the Parnaíba diabases is the steeper slopes for clinopyroxene and large maximum plagioclase crystal sizes, except in one borehole sample (1UN26.80) in which both plagioclase and clinopyroxene CSDs depart from a log-linear distributions. Assuming that crystal size results from the interplay among nucleation, growth rate and the time the crystal resides in the magma, the larger mean plagioclase sizes indicate that these grains formed early to have the opportunity to become larger than augite grains which formed late. The shorter clinopyroxene residence time in the magma is further documented by its steeper CSD slope, provided both phases had equivalent growth rates. These lines of evidence associated with (sub)ophitic textures between plagioclase and augite crystals agree with a crystallization at the eutectic of both minerals for most of the cooling history (Lofgren, 1974; Kirpatrick, 1977). The holo- and hypocrystalline textures recorded in the diabases would be related to the degree of undercooling experienced by the mafic magma, low and therefore growth-dominated to provide the holocrystalline types or fast and associated with rapid cooling for the hypocrystalline types (Vona and Romano, 2013). Alternatively, the coarser textures could be driven by temperature cycling i.e., the magma spends long periods of time oscillating at elevated temperatures (Mills and Glazner, 2013).

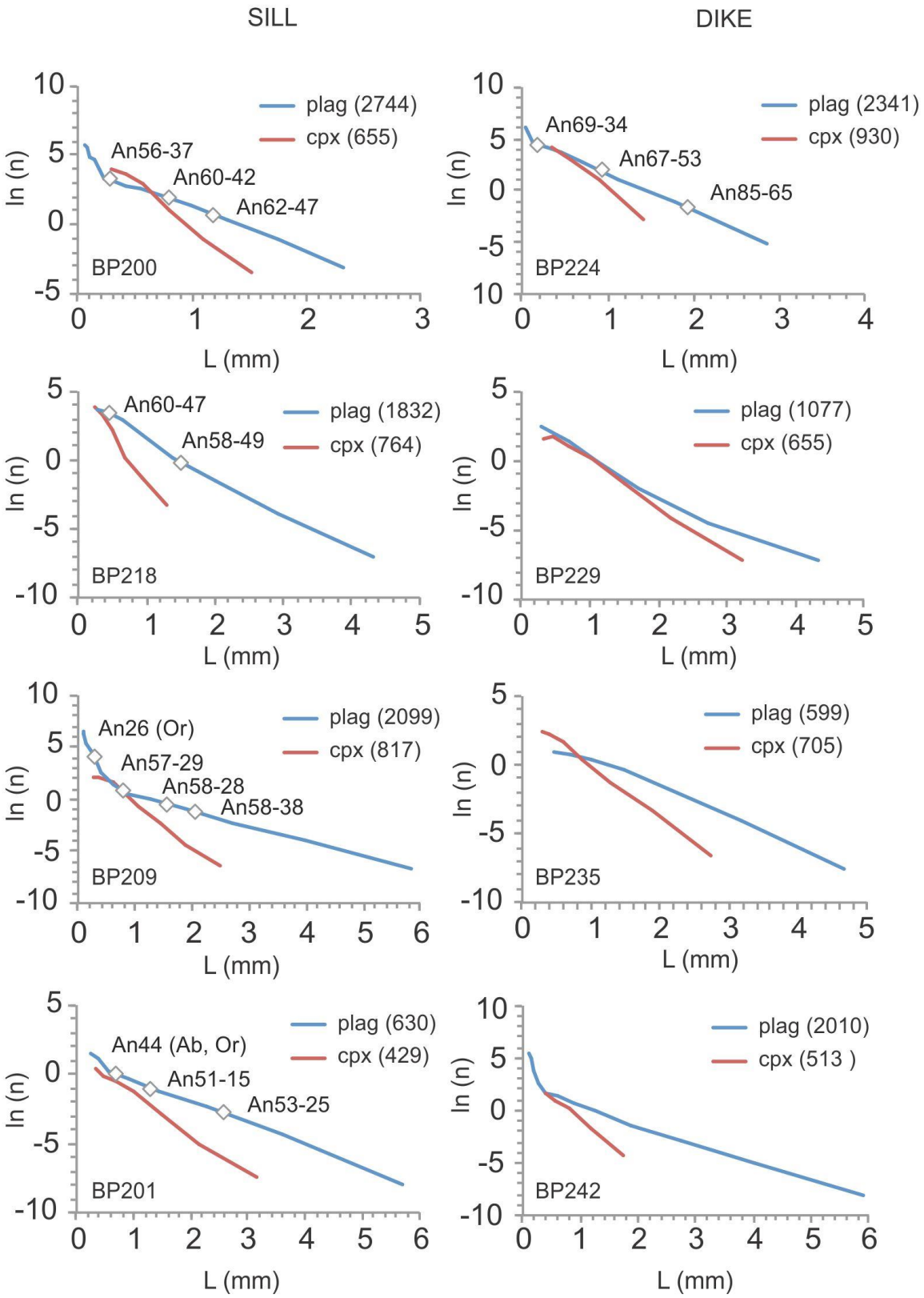

Figure 4.8. CSD diagrams of sill and dike samples indicating the composition of different plagioclase grain sizes. Sa, sanidine (orthoclase component); Olig, oligoclase; Ab, albite; An, anorthite.

Some plagioclase CSDs for grain sizes above approximately 0.5 mm show straight negative slopes. Furthermore, borehole samples display a fanlike geometry in that the straight segments close to the contact record higher slopes (and n° values) than those far from the contact. Assuming steady plagioclase growth rates, the shallower slopes towards the inner part of the sill indicate longer residence times in conformity with the CSD theory (Zieg and March, 2002; Resmini, 2007). However, the plagioclase characteristic lengths (CL = -1/slope) and the volumetric phase proportions show no clear relation (Fig. 4.9), although diabases with hypocristalline texture tend to have higher CL (and smaller volumes) than those with holocrystalline texture (but sample BP209). According to Higgins (2006), the high aspect ratio of plagioclase could be attributed to a greater growth rate of the tablet edge than that of the tablet side, perhaps associated to a high degree of undercooling. The holocrystalline texture, in turn, would record a larger population of plagioclase in the magma that grew slowly, perhaps under a lower degree of undercooling in that growth is more equal on the tablet edges and sides. One sample with high CL and volume phase (BP209), therefore different from the rest of the samples, might evidence some local mechanism of textural coarsening such as temperature cycling.

Most clinopyroxene CSDs, in turn, do not plot as straight lines probably due to nonuniform growth rates. Evidence for nonlinear growth rates in clinopyroxene is provided by "hourglass" microstructure in augite (Fig. 4C) in which different faces grow at slightly different rates and compositions (Gray, 1971; Watson and Liang, 1995). Likewise, some clinopyroxene CSDs show deficiencies in small crystals, which may indicate that the texture was modified during the crystallization of the residual melt. Nevertheless, a few CSDs fit straight lines suggesting that at least locally, clinopyroxene nucleation and growth rates were relatively homogeneous upon cooling.

A net change in crystallization parameters occurs in some CSDs evidenced by the steeper slopes for plagioclase grains less than 0.5 mm (microlites). Chemical analyses indicate that the microlites form isolated crystals consisting of alkali-sodic plagioclase (from albite to andesine), sanidine and anorthoclase, and occur as intergrowths of fine alkaline feldspar rimming coarser calcic plagioclase. These features therefore indicate that the residual melt crystallized at higher nucleation and growth rates compared to the older calcic plagioclase. Some studies in volcanic systems attributed these kinked CSDs to mixing of two magmas with different grain populations (Higgins, 1996; Morgan et al., 2007). Kinked concave-up CSDs with steeper slopes towards the finer grain population have also been produced in experimental

setups during decompression and quenching (Brugger and Hammer 2010; Vona and Romano, 2013) and documented in chilled margins of mafic dikes (Ngonge et al., 2013). As the mafic sills of Parnaíba record static magma chambers that crystallized at depth, the kinked CSDs are attributed to faster nucleation of microlites issued from a residual alkali-sodic melts in disequilibrium with earlier, largely solidified tholeiitic magma.

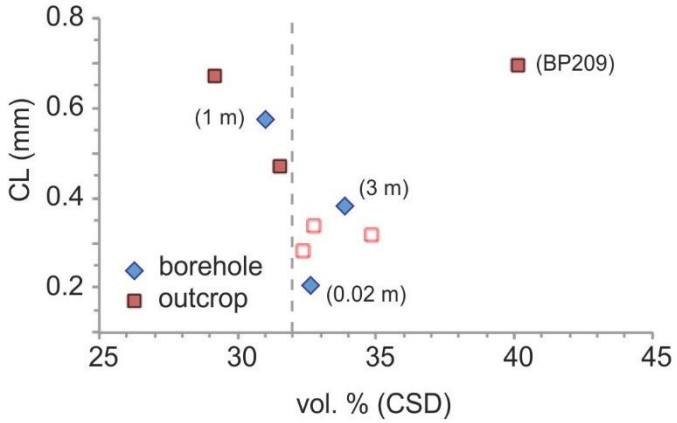

Figure 4.9. Characteristic length (CL) and volumetric phase proportion from plagioclase with straight CSD segments (see text). The dashed vertical line corresponds approximately to the limit between hypo- (left) and holocrystalline (right) diabases. The distance from the wall-rock contact of the borehole samples is indicated in parenthesis.

4.6.2. Chemical fractionation

Mineral chemistry obtained for plagioclase grains from sills and dikes show normal Ca-Na zoning suggesting evolution by fractional crystallization in a closed magmatic system. The development of mantles of intermixed Ab–Or components around calcic–sodic plagioclase indicates that the liquid became highly saturated in alkali components at the late stage of crystallization. This interpretation is also supported by the observation of similar sodic or alkali compositions in microlites of both holocrystalline and hypocrystalline diabases. According to Smith and Brown (1988), the coexistence of plagioclase and orthoclase is frequently observed in magmatic systems below 700 ºC. Such temperatures, however, are not compatible with the crystallization temperatures normally attributed to tholeiitic magmas. Applying the compositions obtained in this study to the clinopyroxene geothermometer of Putirka (2008) (P = 1 kbar), the crystallization temperatures would be from 1250-1195 ºC. The coexistence of two feldspars by fractional crystallization is possible only if the parental magma itself is

primarily potassic, which is not the case for the mafic magmatism of the Parnaíba Basin whose K_2O content varies ~0.85–0.34 wt% in the more primitive samples (MgO ~5.25-6.34 wt%). Therefore, we believe that such a peculiar texture might result from the reaction between the early-formed Ca-Na plagioclase and a sodic-alkali residual liquid crystallizing at fast to intermediate rates (Brown, 1993; Nakano, 1992).

Clinopyroxene, in turn, shows no obvious chemical zonation and has nearly homogeneous compositions irrespective of the grain size. According to Ubide and Kamber (2018), pyroxene crystallizing in a magma chamber continuously refilled by multiple injections of primary melts would record Cr (as well as Mg) zoning marked by alternation of Cr-rich (magma influx) and Cr-poor (normal fractionation) sectors. The analyzed grains usually contain from 2500-1500 ppm in the center to less than 200 ppm in the rim (see Table A3; Appendix). These results associated with CSD patterns agree with a normal crystallization trend for the magmatism and that the Parnaíba diabases did not experience multiple important magma injections throughout their evolution. Notably, only one pyroxene exhibits oscillatory zonation that includes variable Cr contents across the crystal, which in turn might represent a rare antecrystal. Additionally, no alkaline pyroxene composition was identified in the studied diabases. The chemical homogeneity of the clinopyroxene support the model that the sills and dikes would evolve in a closed system.

4.6.3. Crystallization timescales

The use of the log-linear segments of plagioclase CSDs to estimate residence time of the crystal in the magma requires caution since its growth rate (G) can vary several orders of magnitude between 10^{-6} and 10^{-12} mm.s^{-1} (Brugger and Hammer, 2010). Experimental data, for instance, provide G for plagioclase typically between 10^{-6} and 10^{-8} mm.s^{-1} (Pupier et al., 2008; Agostini et al., 2013; Vona and Romano, 2013), with the highest growth rates related to microlite crystallization. In natural systems, such as lava lakes in Hawaii and lavas erupted by Mount Etna, measurements of plagioclase growth rates range between 10^{-7} and 10^{-9} mm.s^{-1} (Cashman and Marsh, 1988; Forniciai et al., 2015). These variations suggest that different parameters may control plagioclase growth in magmas, such as melt composition, degree of undercooling, fluids and magmatic pressures.

Assuming a constant plagioclase growth rate of 10^{-6} mm.s^{-1} for the well sample closest to the wall-rock contact (1UN32.242), the residence time would be approximately two and one-

half days, whereas that at 3 m away from the contact (1UN26.68) would be approximately four and one-half days. Adopting a slower growth rate, say 10^{-7} mm.s^{-1}, residence times would increase to twenty-four days and three and one-half days, respectively. A lower plagioclase growth rate appears to be more reasonable if we consider the solidification rate recorded in the upper crust of the Makaopuhi lava lake (ca. 5 m/year; Cashman and Marsh, 1988). Residence times for log-linear segments of sills and dikes collected at the surface provide values between two and three months if G = 10^{-7} mm.s^{-1} and, for still slower G (5 x 10^{-7} mm.s^{-1}), approximately ten months and one and one-half years (BP235 and 209). More extended residence times determined for these samples probably record the wider and thicker mafic intrusions exposed at the surface.

Timescales from the steeper slopes of the microlites are not used since their growth rates were probably not constant. Since they correspond to the crystallization of the residual melt, we estimate very short residence times, probably not more than a few days in the sill closest to the wall rock. However, owing to the uncertainty in mineral growth rates in magmatic systems, these timescales based on CSDs must be taken merely as approximations.

4.7. Conclusions

The CSDs of plagioclase and clinopyroxene combined with the mineral chemistry of Parnaíba mafic sills and dikes record simple fractional crystallization in agreement with static, deep-seated magma chambers. Plagioclase grains show normal zoning with compositions that vary from labradorite in the grain cores to andesine and oligoclase, whereas clinopyroxene grains show relatively uniform composition. Plagioclase CSDs show log-normal distributions for grain sizes above 0.5 mm and slopes that are systematically gentler than those for clinopyroxene from the same sample. Subophitic texture and sector "hourglass" zoning in clinopyroxenes indicate that plagioclase crystallized earlier and that clinopyroxene grew at variable rates on cooling. These processes account for the steeper CSD slopes for clinopyroxene than those for plagioclase.

Plagioclase CSDs and their respective compositions change significantly at the end of crystallization when the residual liquid becomes more alkalic and sodic. The microlites show compositions that vary from alkali (K-Na) to calcic feldspars while the coarser plagioclase becomes locally rimmed by late intermixed albite-orthoclase components. Some plagioclase CSDs are kinked, with the finest grains defining the steeper slope segments related to unsteady

growth rates. As the high nucleation density of microlites cannot be linked to quenching due to rapid decompression, the kinked CSDs are attributed to disequilibrium between the residual alkalic melt and an earlier largely solidified tholeiitic magma. The fractional crystallization that provides alkali-enriched melts, in turn, accounts for the trachytic trend recorded in some diabase samples that plot along the transitional field on the total alkali-silica diagram. Based on the log-linear CSD segments and assuming constant growth rates for plagioclase, the chemical fractionation and full crystallization next to the contact and in the core of the largest sills would take, respectively, between days and a few years.

4.8. Acknowledgements

A.A. Macêdo Filho thanks FAPESP for his PhD scholarship (grant 2017/13130-0). CJA and MHBMH thank the Brazilian agencies CAPES and CNPq (grants 204979/2016-3 and 305824/2014-7) for providing direct and indirect support for this research. We would also like to thank Natalia G. A. Souza for collecting the borehole samples, Alisson L. Oliveira and Carlos R. Ávila for constructive discussions; José M. Sobrinho for his assistance with petrographic descriptions; and Daniel F. Godoy for his assistance with EPMA analyses. The authors are grateful to the contributions of Dr. Pavel Izbekov and an anonymous referee, as well as the editor-in-chief, Dr. J. Gardner, which surely improved the original manuscript. This paper is a scientific contribution funded by FAPESP (grant 2017/08423-9).

5. GEOCHEMICAL-ISOTOPIC SIGNATURE OF THE MESOZOIC THOLEIITIC MAGMATISM EXPOSED ON THE EASTERN PARNAÍBA BASIN

5.1. Introduction

This chapter brings the geochemical and isotopic characteristics of sills and dikes exposed in the eastern side of the Parnaíba Basin, where they are historically attributed to the Sardinha Formation (e.g., Vaz et al., 2007). The geochemical signature of these intrusions herein described will support further comparisons with the dike swarms intrusive on the Borborema Province in further chapters, thus providing a more comprehensive characterization of the igneous products constituting the EQUAMP. For further information about geochemical analytical procedures, the reader is referred to Chapter 2.

5.2. Field Aspects and Sampling

Airborne magnetic mapping, seismic and well-data published (Castro et al., 2018) were integrated with a 1:250,000-scale geologic map (Lima and Leite, 1978) and Google Earth imagery was used to assist the sampling campaigns at the eastern Parnaíba Basin. The sills have slightly arched to flat (laccolith) roofs not exceeding a few meters in thickness along road cuts, but they can reach up to 20-30 meters in quarries. The occurrence of dikes is subordinate relative to the sills and the former are featured by the accumulation of sub-spherical boulders of variable sizes, with an apparent width estimated as 50-70 meters. The difficulty of recognizing a preferential strike for the dikes led us to suppose that they could be climbing edges of deeper saucer-shaped sills presently exposed on the surface. Alternatively, dike may represent channels of magmas that had connected stacked sills in depth, as seen in some of the quarries in the study area. Field aspects are illustrated in Chapter 3.

A set of 116 samples was collected from sills and dikes (Fig. 5.1). Due to the regional scale of sampling, it is hard to individually label them in Figure 5.1. Instead, we classified the samples according to the TAS scheme and their Ti-based compositions (see section 5.2) and discriminated the main magma types as colors in the figure. From north to south we collected: (1) nineteen samples from different sites around Esperantina and Pedro II villages, (2) thirty-five samples within a polygon circumscribed by Teresina city and Monsenhor Gil, Amarante, Mimoso, Baú and Colinas villages, and (3) sixty-two samples in south-southeast areas of the

basin. The southernmost rock exposures come from sites close to Itaueira and Canto do Buriti villages. Most of the samples are represented by melanocratic to mesocratic, medium- to fine-grained pristine diabases. Exceptions are a few coarse-grained leucocratic rocks (andesite-like compositions) that occur in spatial association with the mafic diabases near the Elesbão Veloso village (Fig. 5.1).

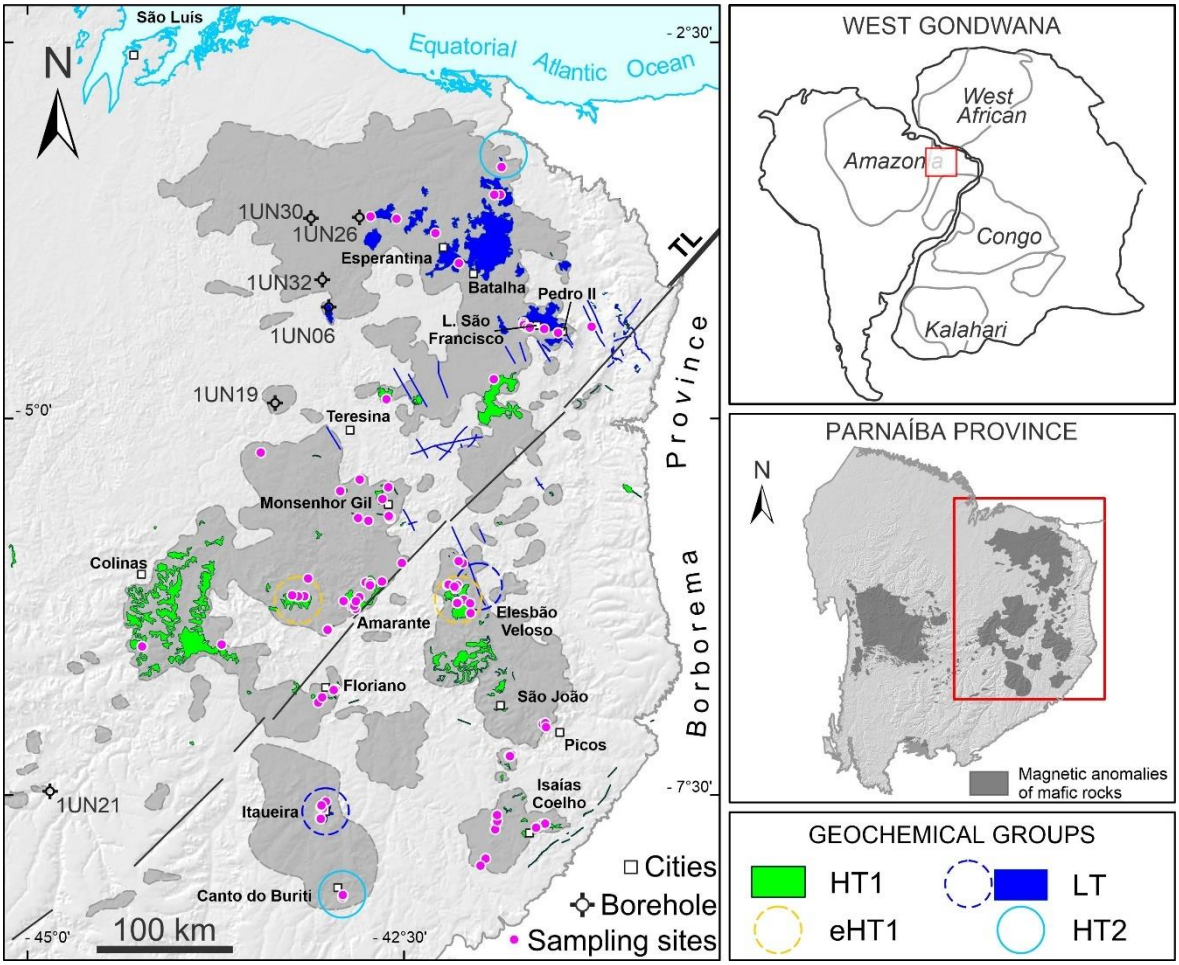

Figure 5.1. Simplified geological map of the eastern flank of the Parnaíba Basin with focus on the mafic magmatism and sampling sites (modified from Macedo Filho et al., 2019). The main geochemical groups are additionally represented as such: high-Ti tholeiites one (HT1), evolved high-Ti tholeiites one (eHT1), low-Ti tholeiites (LT) and high-Ti tholeiites two (HT2). The intrusions exposed on the surface are represented by green and blue colors while dark gray areas concern magnetic anomalies attributed to mafic rocks in subsurface according to Mocitaiba et al. (2017). The regional relief was generated based on the images from the Shuttle Radar Topography Mission (SRTM).

5.3. Geochemical Classification and Geographical Distribution of Magmas

The studied diabases comprise a transitional, tholeiitic series (Fig. 5.2A-B) consistent with the co-existence of a Ca-poor pyroxene (pigeonite) with sub-calcic augite combined with early crystallization of plagioclase relative to pyroxene as depicted by the petrography. As with

other Mesozoic tholeiitic rocks in South America, the intrusions in the eastern Parnaíba Basin can be discriminated in low- and high-Ti suites with a threshold line at TiO_2 = 2 wt.% (Fig. 5.2C).

In the TAS diagram, a group of 32 samples clusters below the divisor line (Miyashiro, 1978) representing sub-alkaline (total alkalis between 2.6 to 3.4 wt. %) basalts and basaltic andesites with TiO_2 < 2 wt.% (average of 1.45 ± 0.18 wt.%), P_2O_5 < 0.2 wt.% and MgO contents higher than 5.2 wt.% (average 6.2 ± 0.56 wt.%). Only the sample BP265 displays a total alkalis content of 5.38 wt.% (Na_2O = 4.36 wt.%, K_2O = 0.98 wt.%) for similar MgO content in the group, which probably relates to the alkali-rich overgrowths notably developed around plagioclase crystals. Diabases in this group have Ti/Y < 380 and Ti/Zr > 65, all of them plotting above the curve Ti/Zr = 0.15Ti/Y + 7.5 in the Ti/Y versus Ti/Zr diagram (Fig. 5.2D). Thus, this group will be further referred to as low-Ti tholeiites (or simply, LT). The LT diabases were mapped in three geographic sites as shown in Fig. 5.1: (1) at the north, close to the Batalha-Esperantina (samples 16.01, 16.02, 16.03, 18.01, 18.02 and 18.03) and Lagoa do São Francisco (samples BP109 to BP116) villages, (2) in a central region near the Elesbão Veloso village (BP200, BP253, BP256, BP264 to 266), and (3) at the south, in the vicinity of Itaueira village (23.07, 24.01, 24.02, BP227 and 228, BP275 and 276).

The second group of intrusions includes the majority of the studied diabases, i.e., 71 samples. They are basalts and basaltic andesites and andesites with sub-alkaline to transitional affinity (total alkalis > 3.3 wt. %). Although many of the samples have K_2O close to 2 wt.% (average of 1.97 ± 0.38), they are not potassic rocks, since Na_2O is also high, thus providing K/Na ratios < 1. The TiO_2 contents are higher than 2.36 wt.%, P_2O_5 > 0.45 wt.% (average of 0.71 ± 0.18 wt.%) and MgO < 6.2 wt.% (average of 4.32 ± 1.0 wt.%) except for two samples with MgO >7 wt.%. Differently from the LT, this group plots beneath the curve Ti/Zr = 0.15Ti/Y + 7.5 (Fig. 5.2D). These high-Ti diabases, hereafter labeled as HT1, were sampled in the central and southern areas of the eastern side of the basin. A group of nine HT1 basalts displays higher TiO_2, from 3.76 to 4.52 wt.% (average of 4.1 wt.%) and lower silica (< 50.6 wt.%) contents and are slightly different in some trace element concentrations (Table 5.1). When needed, their chemical characteristics will be highlighted in further sections. Intermediate compositions of the HT1 are described in eight trachytes to trachyandesites samples. For simplification, they will be henceforth named eHT1 (evolved HT1).

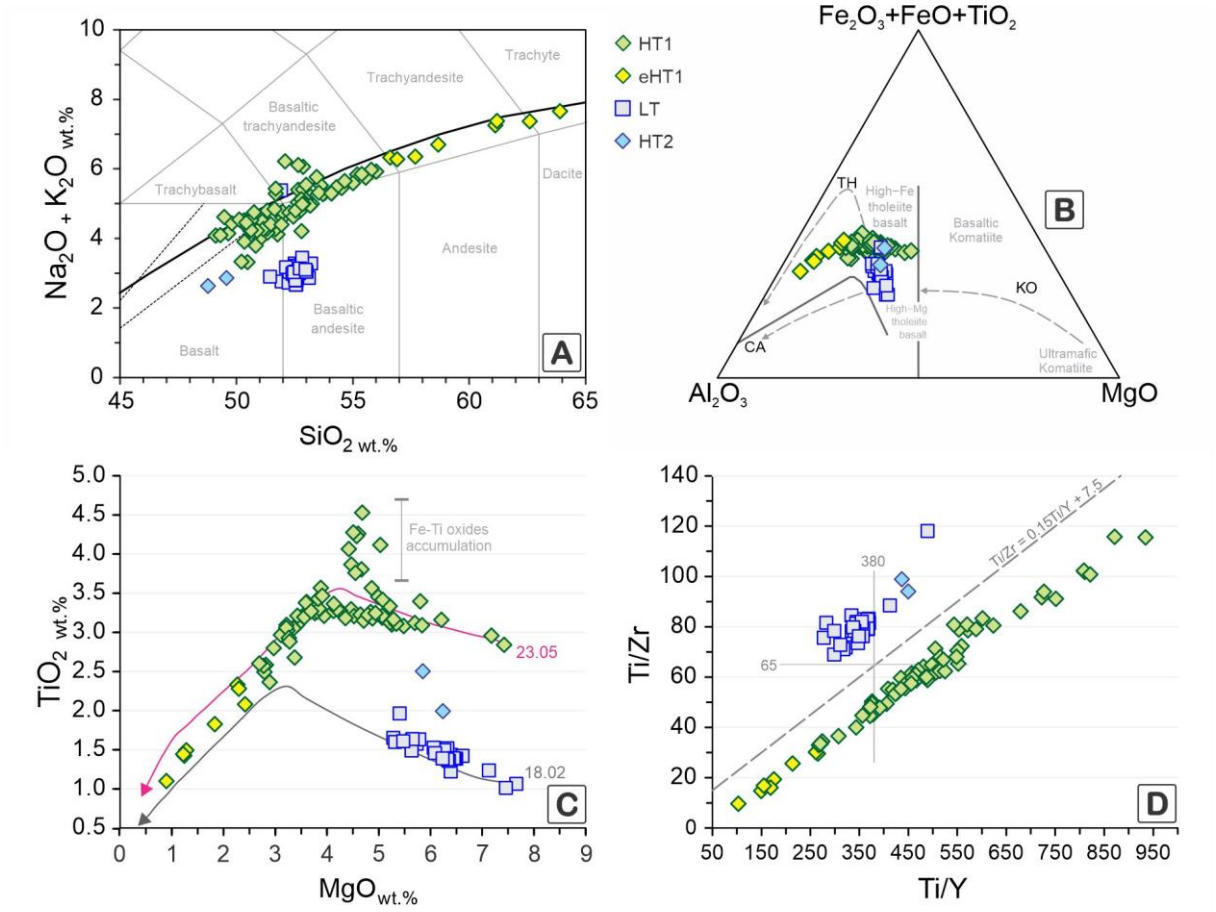

Figure 5.2. Classification and variation diagrams for intrusions on the eastern side of the Parnaíba Basin. (A) Part of TAS diagram (SiO_2 versus Na_2O+K_2O), where the compositional fields and dividing line are respectively from Le Maitre, (2002) and Miyashiro (1978); (B) Jensen cation plot (Jensen et al., 1976) used for discrimination of tholeiitic (TH), Calc-alkalic (CA), and komatiite (KO) fields; (C) MgO versus TiO_2 plot adopting a threshold of 2 wt.% to define high- and low-Ti magmas. The samples 23.05 (HT1) and 18.02 (LT) were chosen as starting compositions for modelling fractional crystallization in MELTS. (D) HT1 and LT-HT2 group discrimination in the Ti/Y versus Ti/Zr diagram. The discrimination line (dashed) and its respective function (Ti/Zr = 0.15Ti/Y + 0.75) are indicated.

Samples BP201 and BP257 plot close to the threshold line between the basaltic trachyandesite and trachyandesite fields (silica ~ 57 wt.%), but they were included in eHT1. Three of the intermediate rocks are coarse-grained, gabbroic-like rocks. In general, intermediate rocks have total alkalis contents ranging from 6.28 to 7.66 wt.% (average of 6.9 ± 0.5 wt.%) and TiO_2 and MgO contents much lower in comparison to the HT1 tholeiites. In all classification diagrams, they follow the HT1 plotting at the end of possible evolutionary trends, including in the Ti/Y (<270) versus Ti/Zr (<31) diagram (Fig. 5.2D).

Finally, two samples with high TiO_2 contents (TiO_2 > ~2 wt.%) differ from the HT1 for their lower SiO_2, K_2O and P_2O_5 (< 0.18 wt.%), and higher Fe_2O_3 (16.1-14.5 wt.%), Al_2O_3 and CaO contents for similar MgO contents. These rocks plot above the Ti/Zr = 0.15Ti/Y + 7.5 curve in the Ti/Y versus Ti/Zr diagram (Fig. 5.2D) and as it will be shown in further sections,

they also differ in terms of trace element (e.g., Sr < 240 ppm) and Sr-Nd-Pb isotope compositions. In terms of geographical distribution, these hereafter HT2 were collected in the southern side of the basin, near Canto do Buriti village and in the NE Parnaíba Basin, less than 50 km south the Itaueira LT (Fig. 5.1).

5.4. Petrography Notes and Mineral Chemistry

The mineral assemblage is similar in all studied samples, consisting of plagioclase, two pyroxenes (augite >> pigeonite) and Fe-Ti oxides as major constituents (Fig. 5.3). Devitrified glass generally occupies the interstices of minerals in hypocrystalline rocks, commonly representing a volumetrically important component (Fig. 5.3A). The hypocrystalline textures are frequently observed in the HT1 and eHT1, although, they can show holocrystalline specimens as well. Plagioclase is always dominant and is found as macro- (0.5 to 1 mm) and microcrystals (or microlites; < 0.5 mm), very often exhibiting sub-ophitic to ophitic relationships with augite, which is especially evident in the holocrystalline samples which are more common in the LT and HT2 groups (Fig. 5.3B and Fig. 5.3C, respectively). In these samples, interstitial augite characterizes the intergranular texture. Apatite, sulfides (pyrite and chalcopyrite) and quartz (Fig. 5.3D) are only occasionally modal phases. In the intermediate rocks, medium-grained acicular augite is present in a feldspar-rich matrix (Fig. 5.3E). Gabbroic-like textures were observed mainly in thicker sills sampled on boreholes from the Coal Project of the Parnaíba Basin (Geological Survey of Brazil/CPRM), also reported by Silva et al. (2017), Macedo Filho et al. (2019), and Miloski et al. (2019).

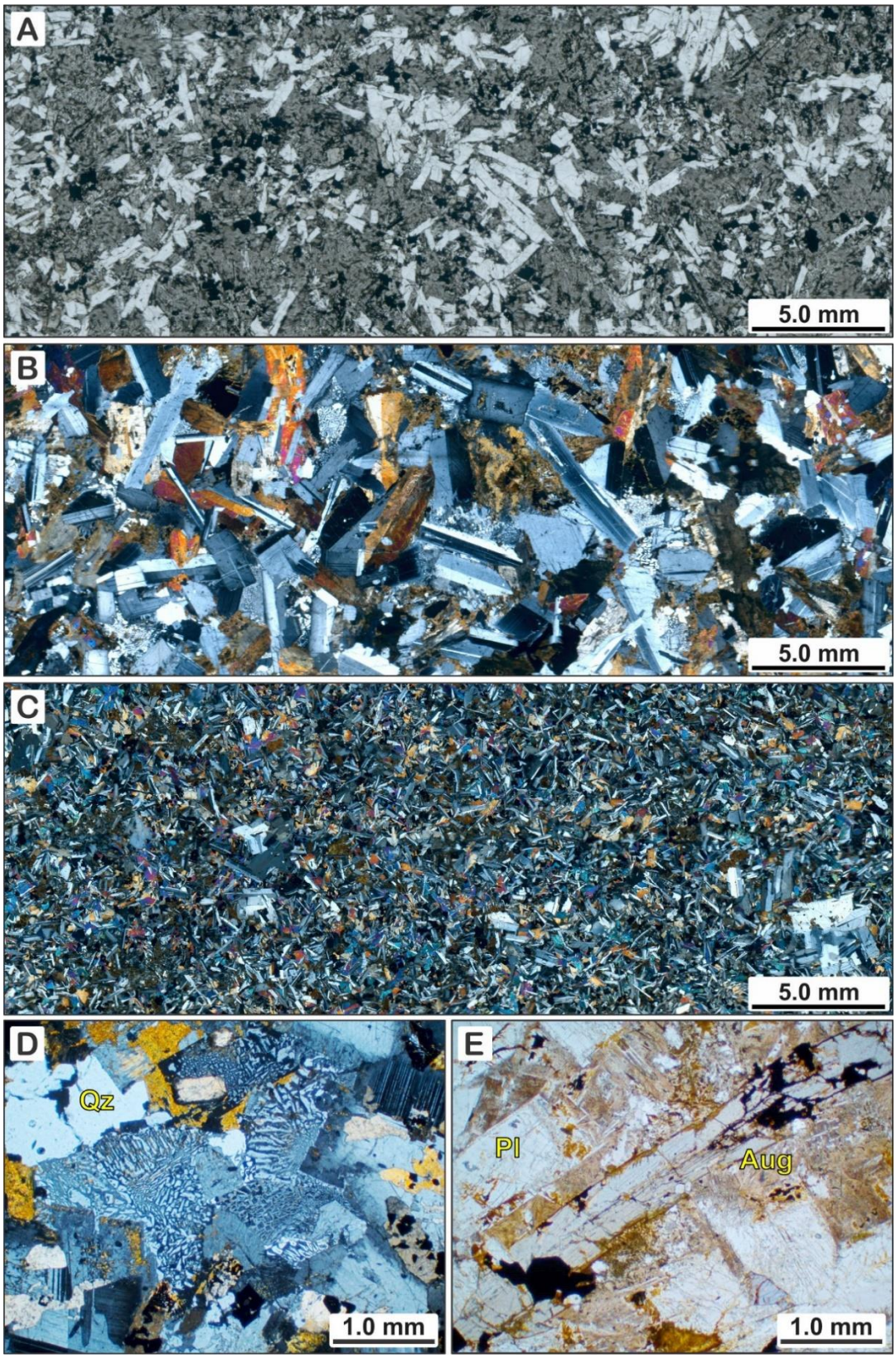

Figure 5.3. Photomicrographs of the studied intrusions in eastern Parnaíba Basin. (A) hypocrystalline diabase with medium-grained plagioclase and clinopyroxene crystals immersed on a matrix, as commonly seen in HT1 type; (B) holocrystalline medium- to coarse-grained diabase of the LT group; (C) holocrystalline fine- to medium-grained HT2 diabase from the southern Parnaíba Basin. (D) Quartz-bearing, granophyric texture and (E) acicular medium-grained augite crystal in andesites of the eHT1. Qz = quartz, Pl = plagioclase, Aug = augite.

Mineral chemistry of representative sills samples was previously published in Macedo Filho et al. (2019). Most of the samples of all geochemical groups have plagioclase macro-crystals with compositional zoning varying progressively from labradorite (core) to andesine (rim) (Fig. 5.4), while the microlites are of andesine composition. The exception is the BP-224 basalt (HT2) in which the core-rim zoning is dominated by a bytownite composition (Fig. 5.4). A singular texture in some of the hypocrystalline diabases is characterized by K-Na rims developed around plagioclase macro-crystals (Figure 5.5A). Clinopyroxene is dominantly augite, with a TiO_2 (usually > 0.7 wt.%) enrichment in samples of the HT1 group. Pigeonite is also reported in LT and HT1 groups, but it usually happens encapsulated by augite in LT, while in HT they form finer crystals or are precipitated on the augite crystal rims. Further information about textures and mineral chemistry of the Parnaíba Basin sill complexes is given in Macêdo Filho et al. (2019).

Plagioclase can also develop micrographic texture characterized by cuneiform to vermicular quartz intergrowths (Figure 5.5B). In such rocks, intersertal cryptocrystalline material is usually a modal component and is generally replaced by secondary minerals (Figure 5.5C). Secondary alteration includes variable degrees of sericitization of plagioclase and discrete to moderate hydration of pyroxene to form hornblende (Figure 5.5D) or chlorite. Although Fe-Ti oxides are mainly primary phases, they can also occur associated to the destabilization of augite, forming a “simplectite-like” texture. Calcite- (Figure 5.5E) or zeolite-filled (Figure 5.5F) vesicles are reported on a few samples.

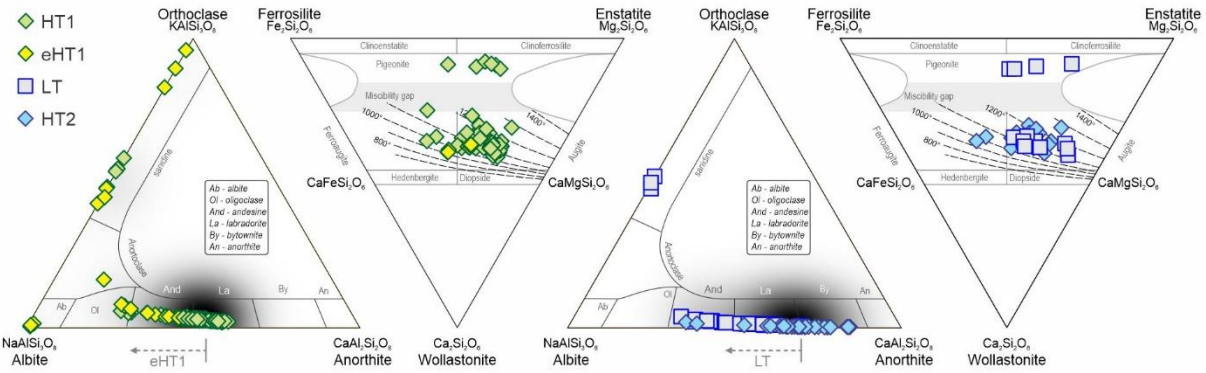

Figure 5.4. Range of solid solutions of feldspars and pyroxenes in high-Ti tholeiites (HT1, HT2), low-Ti tholeiites (LT) and evolved high-Ti tholeiites (eHT1) defined on the Parnaíba Basin intrusions. Dataset compiled from Macêdo Filho et al. (2019). Density maps in gray scale on feldspar ternary diagrams highlight the high frequency of labradorite-andesine fields for HT1 and eHT1, whereas LT and HT2 have major frequency in bytownite-labradorite members. The isotherms of Krentz (1982) are represented in the pyroxene diagrams.

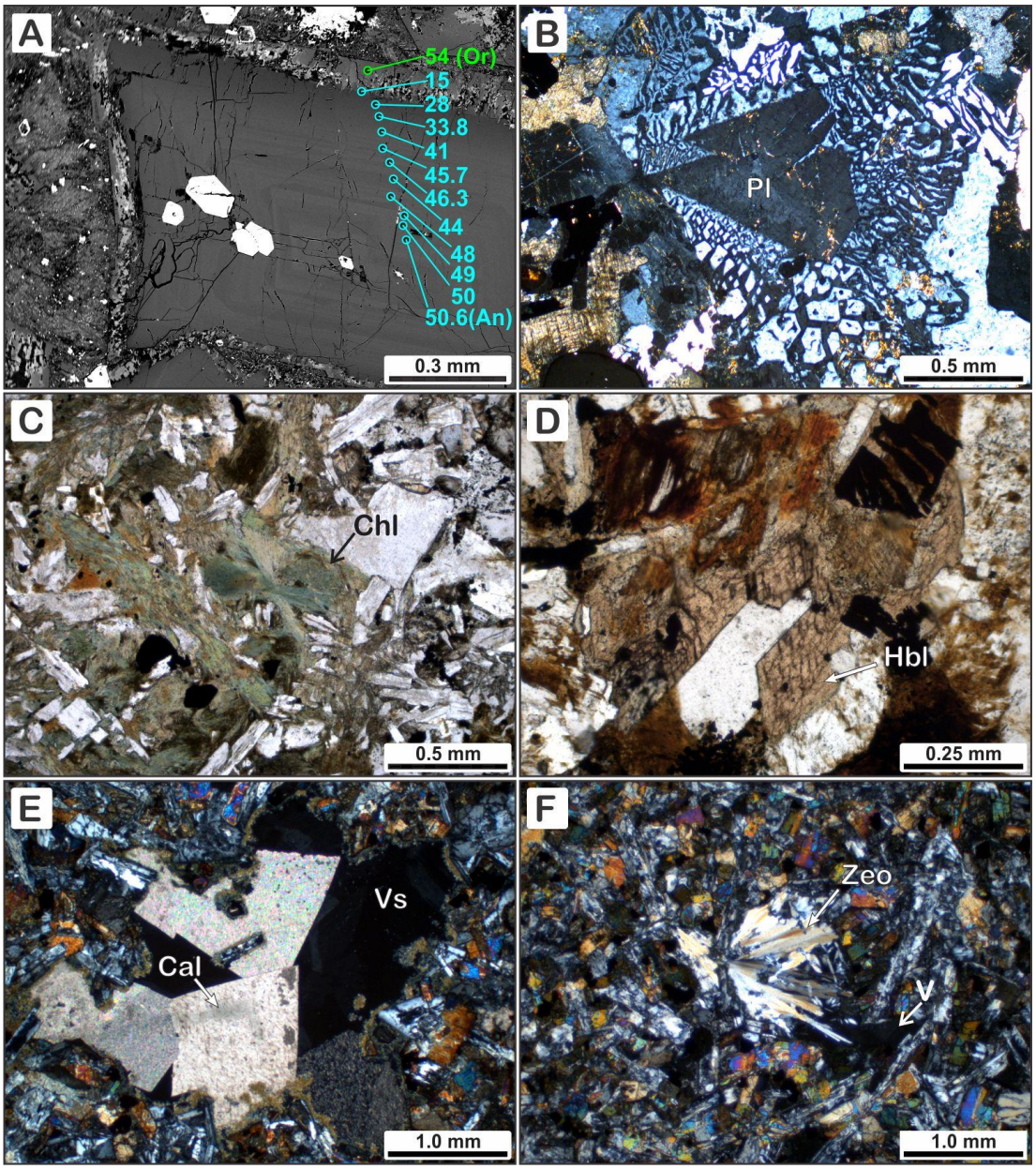

Figure 5.5. Some mineral features of intrusions on the eastern side of Parnaíba Basin. (A) Normal zoning in plagioclase crystal, characterized by progressive decreasing in An content and alkalic feldspar rims. (B) Micrographic intergrows in plagioclase. (C) Chlorite replacing glass. (D) Secondary or late magmatic hornblende replacing clinopyroxene. (E) Calcite crystal partially filling vesicle. (F) Amygdale filled with zeolite.

5.5. Major oxides and Fractional Crystallization

The LT and HT1 and HT2 groups cluster along distinctive evolutionary trends in bivariant plots that consider MgO as the differentiation index, and the eHT1 group represents liquids fractionated from the HT1 magmas (Fig. 5.6). Alkalis correlate negatively with MgO. Once there is no modal K-rich mineral in studied intrusions, the increase in total alkalis would reflect the high incompatibility and, therefore, accumulation of K and Na in later stages of the

crystallization, which is supported by the presence of sodic-potassic overgrowths surrounding plagioclases in HT1 and eHT1 diabases (Fig. 5.5A). In all groups, a positive correlation is noted between MgO and Ca contrasting with the random scattering of Sr indicating that plagioclase was not significantly removed during crystallization, but, instead, clinopyroxene was likely the main phase fractionating and controlling the Ca variability. Fe and Ti (Fig. 5.2C) increase in the LT group while they display no major variations evolution lines for the HT groups, sharply decreasing at MgO ~4 wt.%, which would indicate that Fe-Ti oxides were almost constant and only significantly fractionated when crystallization was in a very advanced stage. As expected, the samples with higher Ti (> 3.76 wt.%) cluster above the HT1 Ti-trend but are not distinguished in other plots (Fig. 5.2C). These are samples with the greater modal proportion of Fe-Ti oxides according to petrographic observations. Finally, even if olivine being rare as phenocrystals in these rocks, fractionation might have occurred in earlier stages of differentiation.

Rhyolite–MELTS 1.0.2 (melts.ofm–research.org; Gualda et al., 2012) was used to evaluate the closed-system differentiation of the studied diabases and test the interpretation from the bivariant plots. Fractional crystallization (FC) vectors were defined assuming the samples 18.02 and 23.05 as the starting liquids for the main groups: LT and HT1, respectively. The modeling adopted isobaric FC paths under the pressure of 1 kbar (i.e., shallow crustal level), thermal range of 1250-950°C, fO_2 along the quartz–fayalite–magnetite (QFM) oxygen buffer and H_2O of 0.2 wt.%. The resulting FC paths were drawn in the diagrams of Figure 5.6 (and Figure 5.2C). The MELTS models indicate that the geochemical diversity of LT diabases can be generated after 35% of FC, with greater prominence of clinopyroxene fractionation than plagioclase. The chemical variability of the HT1 diabases is explained by 5% to 45% of fractional crystallization with progressive removal of clinopyroxene from the parental melt, whereas the compositions of the eHT1 are formed within the window from 45% to 67% of fractionation. Such evolved compositions are by-products of the removal of pyroxene, plagioclase, and Fe-Ti oxides from parental tholeiitic magmas, where plagioclase and Fe-Ti oxides played a role just after melts reached a MgO content around 3-4 wt.%. The models, however, indicate an incompatible character for P_2O_5, as suggested by bivariant plot. This oxide appears to be compatible only when the system reaches about 3 wt.% in MgO, which might be due to apatite fractionation (possibly as inclusions in plagioclase phenocrysts).

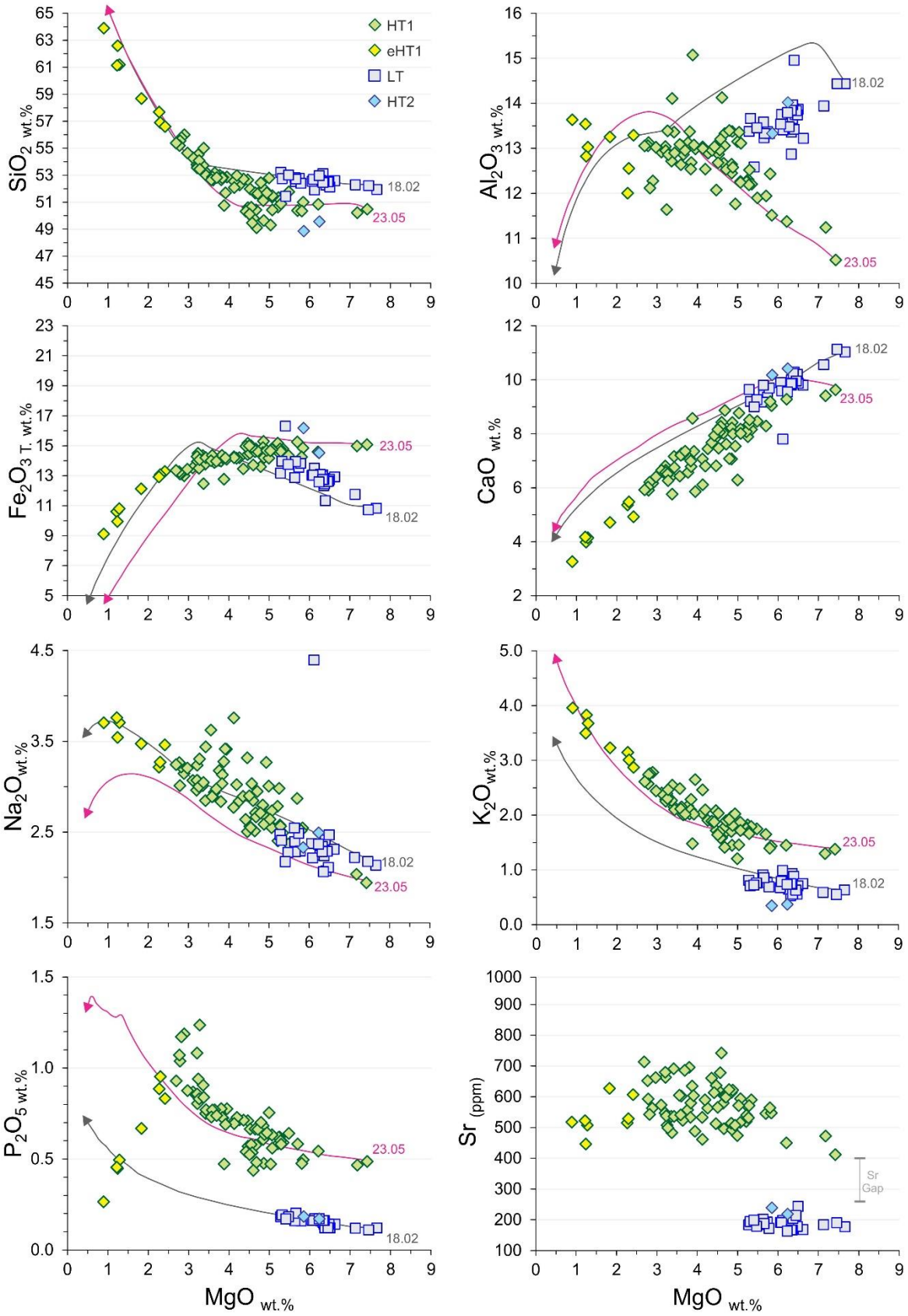

Figure 5.6. Binary plots showing major oxides (besides Sr) against MgO, used for characterizing the geochemical groups and respective evolutionary trends defined for the geochemical groups of the sills. Samples 23.05 (HT1) and 18.02 (LT) were chosen as the starting composition for modelling fractional crystallization (FC) in MELTS. The FC paths were calculated assuming isobaric conditions at 1 kbar and QFM (quartz-fayalite-magnetite) buffer.

5.6. Trace Element Geochemistry

The LT and HT1 (and eHT1) groups show common features on primitive mantle-normalized (Sun and McDonough, 1989) trace element diagrams (Fig. 5.7), including enrichment in incompatible elements (LILE and LREE) and depletion in Nb, Th-U, Sr, and P relative to their neighbors. However, they show differences in trace element abundances. The HT1 group is more enriched in LILE, HFSE and LREE compared to the LT, and the degree of enrichment greatly increases towards the evolved compositions as a result of differentiation. LILE and HFSE abundances in the LT are uniform and, except for Ba (128–306 ppm), Rb (14–27 ppm), Th (1.2–2.5 ppm) and U (0.2–1.4 ppm), they do not show evident correlation with MgO (not shown), whereas Zr (76–125 ppm), Nb (4.9–7.7 ppm), Hf (2.1– 3.4 ppm) and Y (17.8–32 ppm) are negatively correlated to MgO (not shown).

As already noted by the major element compositions, the HT1 diabases have widely variable trace element contents compatible with a high degree of differentiation. For instance, they have Ba (357–988 ppm), Rb (24–63 ppm), Th (2.6–6.8 ppm), U (0.5–1.5 ppm), Zr (208–456 ppm), Nb (17.3–37.3 ppm), Hf (5.2–11.8 ppm) and Y (26–56.6 ppm) correlating negatively with MgO, supporting fractionation of plagioclase and apatite as well as of some of the accessory minerals.

The HT2 is less enriched in LILE and HFSE contents, for instance, and have lower contents of Ba (<98 ppm), Rb (<7.2 ppm), Th (<0.8 ppm), U (<0.2 ppm), Zr (<157 ppm), Hf (<4.3 ppm) and Y (<32.8 ppm) when compared with HT1. These diabases are holocrystalline with ophitic/subophitic textures with no evidence of devitrified matrix or vesicles, being composed of plagioclase (bytownite-labradorite) and clinopyroxene (augite), minerals with low compatibility for these trace elements in basic melts. Even so, the evident depletion in Sr, even considering rocks with dominant calcic plagioclase, indicates that these types are derived from originally depleted sources.

Chondrite-normalized (Boynton, 1984) REE patterns are quite homogeneous and weakly fractionated in the LT group, with La varying from 25 to 44 times chondrite values and HREE (Er to Lu) 9–16 times chondrite values, with La_{CN}/Yb_{CN} = 2.6–3.6, La_{CN}/Sm_{CN} = 1.6–2.1 and Gd_{CN}/Yb_{CN} = 1.3–1.5 (Fig. 5.7).

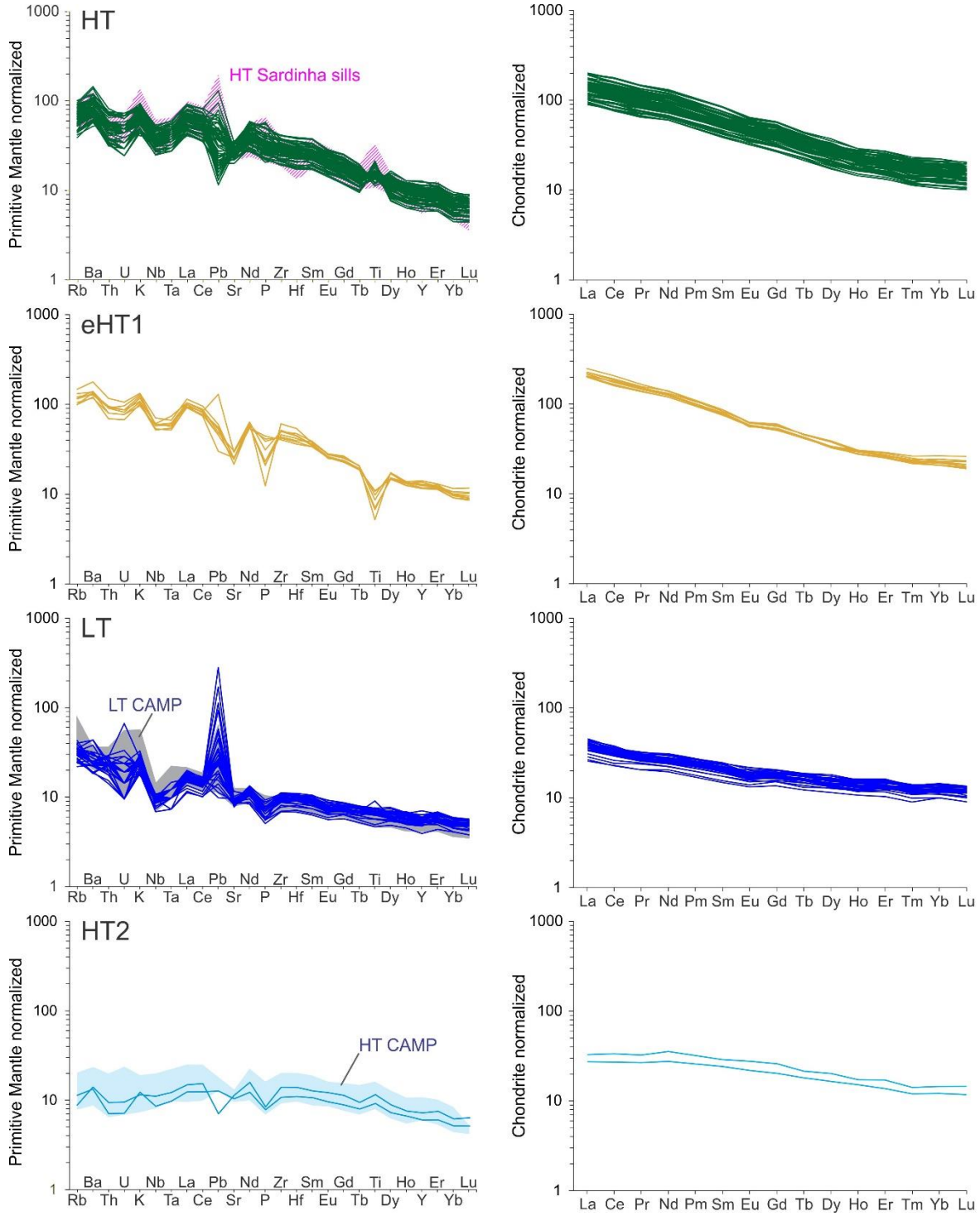

Figure 5.7. Multielement and REE patterns for geochemical groups of the sills normalized to the primitive mantle values of Sun and McDonough (1989) and the chondrite values of Boynton (1984), respectively. High-Ti tholeiites of the Sardinha sills and low- and high-Ti basalts of the Mosquito formation (Central Atlantic LIP) are represented for comparison (sources: Fodor et al., 1990; De Min et al., 2003; Merle et al., 2011; Oliveira et al., 2018; Heilbron et al., 2018).

The HT1 diabases, in turn, have variable La contents ranging from 88 to 200, and HREE ranging from 12–27 times the chondrite values, which results in moderately steep REE patterns with La_{CN}/Yb_{CN} = 6.7–9.8, La_{CN}/Sm_{CN} = 2.0–2.6, and Gd_{CN}/Yb_{CN} = 2.3–2.7 (Fig. 5.7). Neither

the LT nor the HT1 groups have evident Eu anomalies. The eHT1 have REE characteristics closely identical to the HT1 group. The slightly greater abundance of incompatible elements combined with the negative anomalies in Ti and P corroborate the genetic link between HT1 and eHT1 by differentiation. The HT2 diabases in turn are characterized by a flatter pattern with La varying from 27 to 33 times chondrite and HREE (Er to Lu) clustering at 12–17 times chondrite.

The wide variability in Ti contents shown by the HT1 diabases is also expressed in the development of positive (> 1) to negative (<1) Ti/Ti* ($Ti_{PM}/\sqrt{[Tb_{PM}\cdot Dy_{PM}]}$) anomalies vs. Mg# as shown in Figure 5.8, denoting the effects of Fe-Ti oxide fractionation. Samples with Ti/Ti* > 1.5 are, generally, those impacted by a particular accumulation of Fe-Ti oxides during the magmatic evolution of the group. Minor variations in Ti/Ti* are found in the HT2, while the LT displays no Ti anomalous.

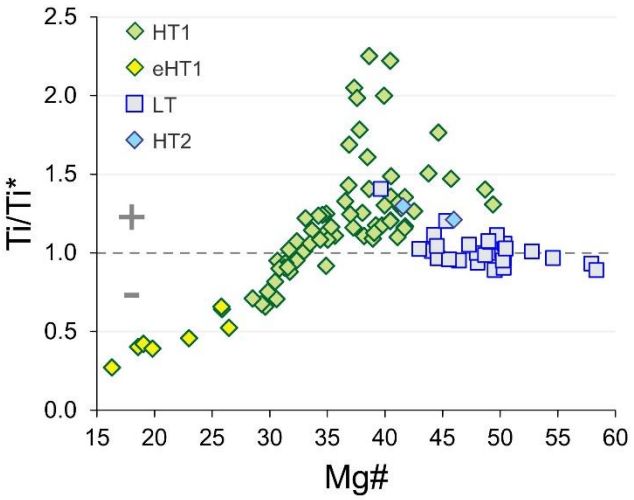

Figure 5.8. Ti/Ti* anomalies versus Mg# for Parnaíba Basin intrusions. HT1 range from stronger positive anomalies in higher Ti rocks to negative in more evolved samples (as also observed in eHT1). The LT data display values close to 1, while HT2 is positive.

5.7. Isotope Geochemistry

Seventy-four samples were selected from the geochemical groups for Sr and Nd isotope analyses (Table A1; Appendix of Chapter 5), as such: 23 samples from the LT group, 48 from the HT1 and eHT1 and, 2 from the HT2 group. Pb isotope compositions were obtained for fewer samples, being 7 from the LT, 13 from the HT1 (plus eHT1), and 2 from the HT2 groups. Sr

and Nd isotopic ratios were recalculated back to 130 Ma assuming the published ages for the Sardinha magmatism in the Parnaíba Basin (e.g., Baksi and Archibald, 1997), while Pb isotopes ratios are reported as measured values.

As already noted by the elemental geochemistry, the isotopic characteristics of the groups are also distinct, confirming that they are not genetically related, except for the HT1 and eHT1. In Figure 5.9, the isotopic compositions are plotted with published data for the Sardinha sills and Mosquito (CAMP) lava flows (Fodor et al., 1990; De Min et al., 2003; Merle et al., 2011; Klein et al., 2013; Oliveira et al., 2018). The $^{87}Sr/^{86}Sr$ ratios are comparable between groups, clustering from 0.705862 to ~0.707 in the LT, and 0.705564 to 0.706441 in the HT1-evolved HT1. The LT samples have uniform initial εNd values ranging between -0.98 and -1.71, but two samples present more unradiogenic Nd (BP256, BP264; εNd -3.0 and -7.6, respectively). Even so, the general tendency of LT types in all isotope diagrams is plot akin low-Ti CAMP basalts (Marzoli et al., 2018) around the Enriched Mantle endmembers. On the other hand, the HT1 and its evolved examples show initial εNd values ranging between -2.1 and -3.0 (Fig. 5.9), therefore preserving Sr-Nd-Pb isotope ratios as those previously defined to high-Ti Sardinha tholeiites (Fodor et al., 1990; Oliveira et al., 2018) which have isotopic ratios comparable to Enriched Mantle I (EM-I member).

Finally, the two samples of the HT2 group have initial unradiogenic Sr (0.703430 and 0.703520) and radiogenic Nd (eNd of 6.1 and 3.3) isotopic compositions. Together with Pb (especially $^{208}Pb/^{204}Pb$) they are comparable with the isotopic signature defined for the high-Ti tholeiites of the CAMP (Marzoli et al., 2018) in the western Parnaíba Basin, and have compositions as depleted mantle (e.g., E-MORB member).

The $^{207}Pb/^{204}Pb$ ratios are very radiogenic for both the LT ($^{207}Pb/^{204}Pb$ = 15.593 to 15.706) and HT1 ($^{207}Pb/^{204}Pb$ = 15.495 to 15.561) for relatively similar, low to moderate $^{206}Pb/^{204}Pb$ ratios (18.184 to 18.510). While not exactly discernible by their ^{206}Pb (U/Pb) and ^{208}Pb (Th/Pb) compositions, these two groups are set apart from each other by their ^{207}Pb, which is more radiogenic in the LT diabases than in the HT1, suggesting that an older crustal component would be involved in the genesis of the low-Ti magmas. This component would exist either in the source itself or as a contaminant during ascent through the lithosphere and/or emplacement at crustal levels.

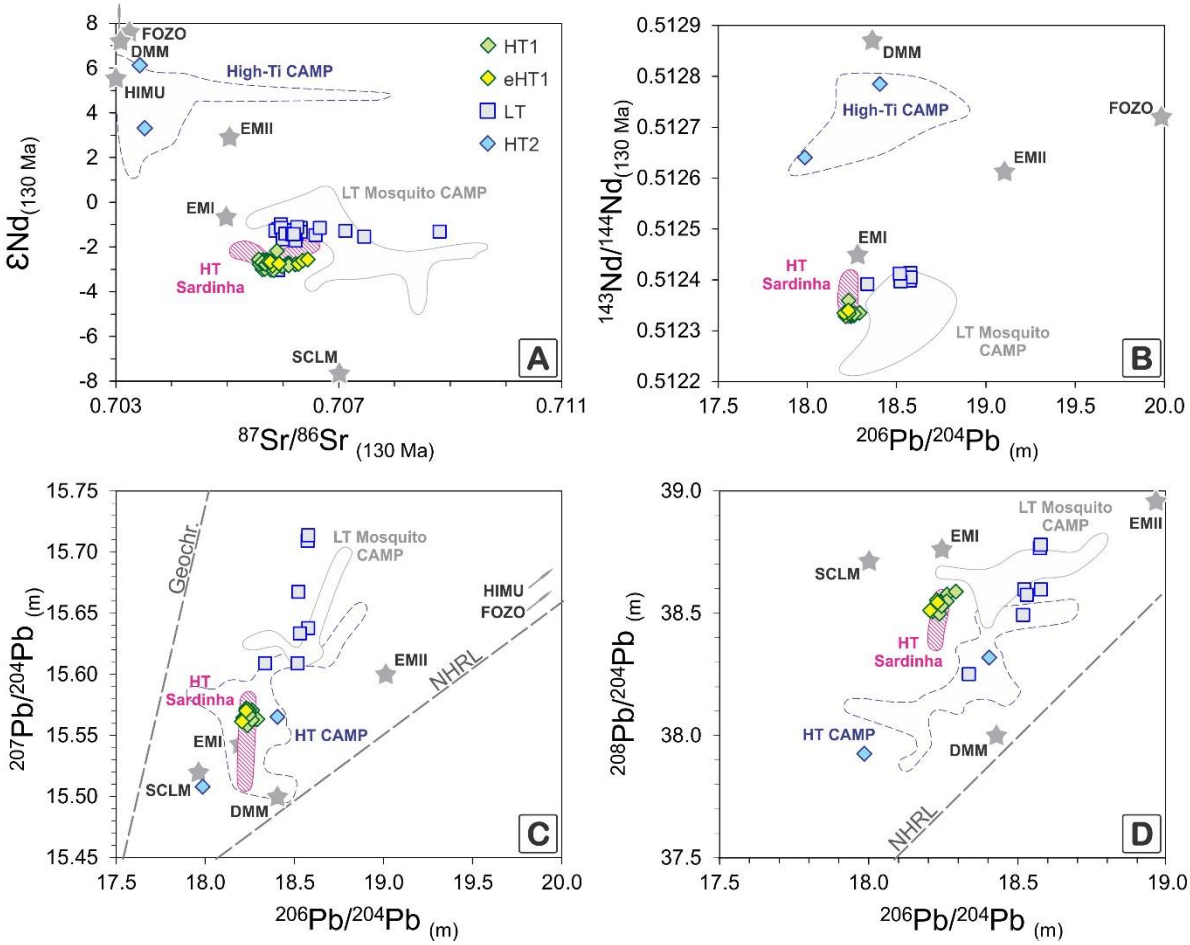

Figure 5.9. Isotope data of sill complexes. (A) $^{87}Sr/^{86}Sr_{(130\ Ma)}$ versus $\varepsilon Nd_{(130\ Ma)}$. (B) $^{206}Pb/^{204}Pb_{(m)}$ versus $^{143}Nd/^{144}Nd_{(130\ Ma)}$. (C) $^{206}Pb/^{204}Pb_{(m)}$ versus $^{207}Pb/^{204}Pb_{(m)}$ and (D) $^{206}Pb/^{204}Pb_{(m)}$ versus $^{208}Pb/^{204}Pb_{(m)}$ plots. The NHRL concern the Northern Hemisphere reference line (Hart, 1984) and is represented in both diagrams. Fields of high- and low-Ti basalts of the Central Atlantic LIP (CAMP) in western Parnaíba Basin (Mosquito formation) and high-Ti tholeiites of the Sardinha sills are represented for comparison (sources: Fodor et al., 1990; De Min et al., 2003; Merle et al., 2011; Klein et al., 2013; Oliveira et al., 2018). Centroid values of MORB and OIB members (Stracke et al., 2005) and a SCLM composition represented by alkalic magmatism of the Alto Paranaíba (Araujo et al., 2001) are plotted for comparison.

5.8. Geochemical Correlations with Mesozoic LIPs in the Parnaíba Basin

Since geochronological data for the samples described in this chapter are not available, the comparisons with other magmatic events exposed in the Parnaíba Basin are herein processed based on geochemical-isotopic constraints. To better illustrate these correlations, we performed a principal component analysis (PCA) considering the whole-rock dataset of major oxides, trace elements (V, Cr, Co, Ni, Cu, Pb, Zn, Rb, Sr, Cs, Y, Zr, Nb, Ba, Hf, Ta, Th, U), REE and isotopes (Sr-Nd-Pb) of LT, HT1-eHT1 and HT2 groups in combination with those previously published in the literature for the Mosquito/CAMP basalts and the Sardinha sill complexes. The motivation in the use of PCA analysis lies in the reduction of the dimensionality of a

considerable dataset formed of many interrelated variables, improving the interpretability, and minimizing information loss, since it retains as much as possible of the variation present in the dataset (Jolliffe, 2002; Jolliffe and Cadima, 2016).

The scatter diagram in Figure 5.10 shows that all data plotted in the coordinate system given by principal component 1 (PC1) versus principal component 2 (PC2), with the percentage of variance at 61.6% and 16.8%, respectively. The LT presents major contributions of Mg, Ca, Al, Ni, LOI, and Sr-Pb isotope ratios analogous to low-Ti basalts of the CAMP/Mosquito Formation, whereas the HT1-eHT1 presents a high contribution of Si, Ti, Na, K, P, and incompatible elements (LILE, HFSE and REE) overlapping the convex hull of the Early Cretaceous (high-Ti) Sardinha sills. The HT2 occurs on quadrants of the major contribution of Mg, Ca, Fe, Mn, Ni, Co, Cu, V, and $^{143}Nd/^{144}Nd$, highlighting the depleted character of this group similarly plotted for high-Ti CAMP basalts.

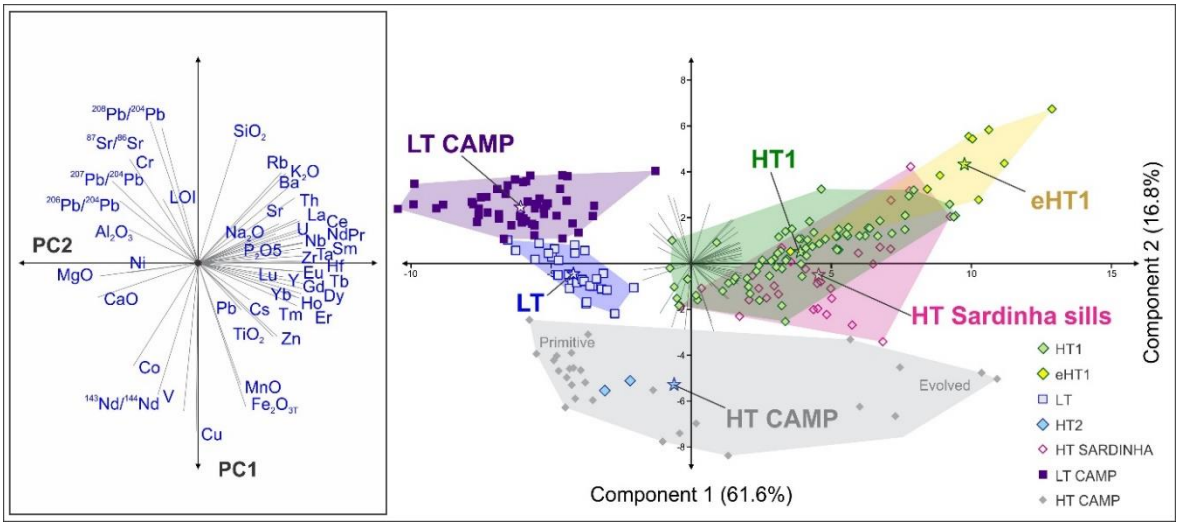

Figure 5.10. Principal components analysis (PCA) of major oxides and trace elements, REE and isotopes (Sr-Nd-Pb). The scatter plot displays the LT, HT1, eHT1 and HT2 samples of the Mosquito formation (low- and high-Ti CAMP basalts), and high-Ti Sardinha magmatism (sources: Fodor et al., 1990; De Min et al., 2003; Merle et al., 2011; Klein et al., 2013; Oliveira et al., 2018; Heilbron et al., 2018). Average values of each geochemical group are indicated as stars within the respective convex hull. The inset represents a biplot with vector contributions of each geochemical-isotopic parameter.

These results indicate that the paradigm of geographic provinciality of magmatic events in the Parnaíba Basin, *i.e.*, that the CAMP magmas would be restricted to the western side of the Parnaíba Basin, while the mafic magmatism on the eastern side would be addressed to the Sardinha Formation, must be reviewed. The new sampling showed low-Ti tholeiites comparable to "Prevalent low-Ti CAMP" (cf. Marzoli et al., 2018) on the Batalha-Esperantina-Pedro II, Elesbão Veloso, and Itaueira areas. Accordingly, the presence of Juro-Triassic

intrusions (181-210 Ma) sharing the same geographical space of Early Cretaceous Sardinha sills is further supported by recent $^{39}Ar/^{40}Ar$ geochronological data (Heilbron et al., 2018; Fernandes et al., 2020) and low-Ti tholeiites have been described in previous geochemical works but in a more restricted sampling (Fodor et al., 1990; Baksi and Archibald, 1997; Ernesto et al., 2003; Silva et al., 2017; de Castro et al., 2018; Oliveira et al., 2018; Heilbron et al., 2018; Macêdo Filho et al., 2019; Miloski et al., 2019, 2020).

Another novelty achieved in this study concern the high-Ti CAMP group, for the first time reported on the east side of the Parnaíba Basin. Such compositions are rare in the global context of the Central Atlantic LIP, being reported just on the equatorial margin surroundings of South America (Brazil and Guyanas; De Min et al., 2003; Deckart et al., 2005; Merle et al., 2011; Klein et al., 2013; Heimdal et al., 2019) and Africa (Liberia and Sierra Leone; Dupuy et al., 1988; Mauche et al., 1989; Callegaro et al., 2017) related to the extensional tectonics of Central Atlantic rift towards the West Gondwana continent, as already discussed in Chapter 3.

6. PETROGENESIS OF A MESOZOIC GIANT DIKE SWARMS IN NE SOUTH AMERICA: INTEGRATION OF GEOCHEMICAL AND ISOTOPIC DATA

Macêdo Filho, A.A. and Hollanda, M.H.B.M

Article submitted to Lithos

6.1. Abstract

The Rio Ceará-Mirim magmatism produced Mesozoic giant arcuate dike swarms during the initial stage of the West Gondwana breakup near the Equatorial Atlantic Ocean (NE Brazil), where they assemble tholeiites and subordinate intermediate rocks. A multi-data approach based on petrography, mineral chemistry, whole-rock geochemistry, and Sr-Nd-Pb isotopes enables the discrimination of four geochemical groups (two high-Ti and two low-Ti). High-Ti groups are composed of: (1) basalts and basaltic andesites with TiO_2 generally higher than 2.0 wt.%, MgO > ~3 wt.% (named as HT group) and incompatible elements, and (2) evolved high-Ti tholeiites composed of (trachy)andesites and trachytes with lower TiO_2 (generally < 2.5 wt.%; Mg < 3 wt.%) interpreted as fractionated magmas from the HT group. Therefore, both have similar $^{87}Sr/^{86}Sr_{(127)}$ (~0.706) and $\varepsilon Nd_{(127)}$ (-2.90 to -2.56), and moderately radiogenic $^{206}Pb/^{204}Pb_{(m)}$ ratios between 18.66-18.21. Conversely, low-Ti tholeiites (TiO_2 < 2 wt.%) are (3) LT1 composed by evolved basaltic andesites, with ~Ti/Zr < 70, MgO <6 wt.%, and Al_2O_3 >15 wt.%; and (4) LT2 with subalkaline (to transitional) basalts and basaltic andesites but ~Ti/Zr >70, and MgO >6 wt.%. These two low-Ti groups are, respectively, less radiogenic (LT1 $\varepsilon Nd_{(127)}$ -4.65 to -4.40) and slightly more radiogenic (LT2 $\varepsilon Nd_{(127)}$ -1.44 to -1.08) in Nd relative to the HT group. The geochemical groups present different degrees of enrichment in large ion lithophile and light rare-earth elements coupled with depletion in high-field-strength elements (Nb-Ta) combined with isotopic (Sr-Nd-Pb) signatures compatible with enriched mantle sources. We showed that EM compositions of RCM magmatism may be explained by mixing of DMM with SCLM-derived melts plus minor crustal assimilation, or by the involvement of OIBs derived from mantle plumes of the South Atlantic area mixed with lithospheric sources.

Keywords: Continental tholeiites, Early Cretaceous, enriched mantle sources, mantle plume, South Atlantic Ocean

6.2. Introduction

The early stage of the breakup of the West Gondwana supercontinent in the Lower Cretaceous was connected to an impressive volume of tholeiitic magmas along the South Atlantic Rift, notably emplaced as lava flows and plumbing systems at the present-day southern region of the South America and Africa continents. There, the igneous activity converged to form the Paraná-Etendeka Magmatic Province (PEMP) (Peate, 1997; Peate et al., 1992, 1999). In the northern extension of this rift systems, nowadays the Equatorial Atlantic margin, the igneous activity is manifested in the form of dike swarms and sill complexes that altogether characterize a plumbing system-type large igneous province (LIP), defined by Hollanda et al. (2019) as the Equatorial Atlantic Magmatic Province (EQUAMP).

The most important component of the EQUAMP is the Rio Ceará-Mirim Dike Swarm (RCM), an arcuate structure nearly 1,000 km-long intrusive in Precambrian terranes formed by a EW-trending segment of 350-400 km that shifts to a NE-trending direction and continues for at least 600 km more (Fig. 6.1). The 380 km-long Canindé dike swarm extends towards W-NW from the inflection point between the EW- and NE-trending RCM segments forming a kind of ‘focal zone’ whose placed at the southern tip of the Potiguar Rift. In spite of the giant dimension, the knowledge of the geochemical aspects of the RCM is only available for its EW-trending segment (Bellieni et al., 1992; Hollanda et al., 2006; Ngonge et al., 2016a). Therefore, the NE-trending RCM and the Canindé dike swarms lack of any geological/petrological information (even field aspects).

In this chapter, we followed the guidelines of classical studies on the petrology of Gondwana-related LIPs to provide a comprehensive outline on mineral and whole-rock (major oxide, trace element and Sr-Nd-Pb isotope) geochemistry of the EQUAMP plumbing system focused on the NE-trending RCM (hereinafter NE-RCM) and Canindé swarms. Our aims included: (1) to determine the Ti-based and elemental classification of the magmas to understand the crystallization (pressure-temperature) history and mechanisms involved in their petrogenesis, and (2) to use trace element and isotope data to make inferences about the mantle source(s). Although non-geochemical evidence is also required to propose a reliable model that explains the generation of mafic magmatism in continental settings, especially geophysics and numerical modeling, the dataset herein presented could certainly contribute to the classical discussion on the plume *versus* non-plume models. In line to provide an integrated petrological comprehension of the EQUAMP igneous products, we incorporated

the available dataset of Ngonge et al. (2016a) for the EW-trending segment (EW-RCM) alongside the presentation of our new results.

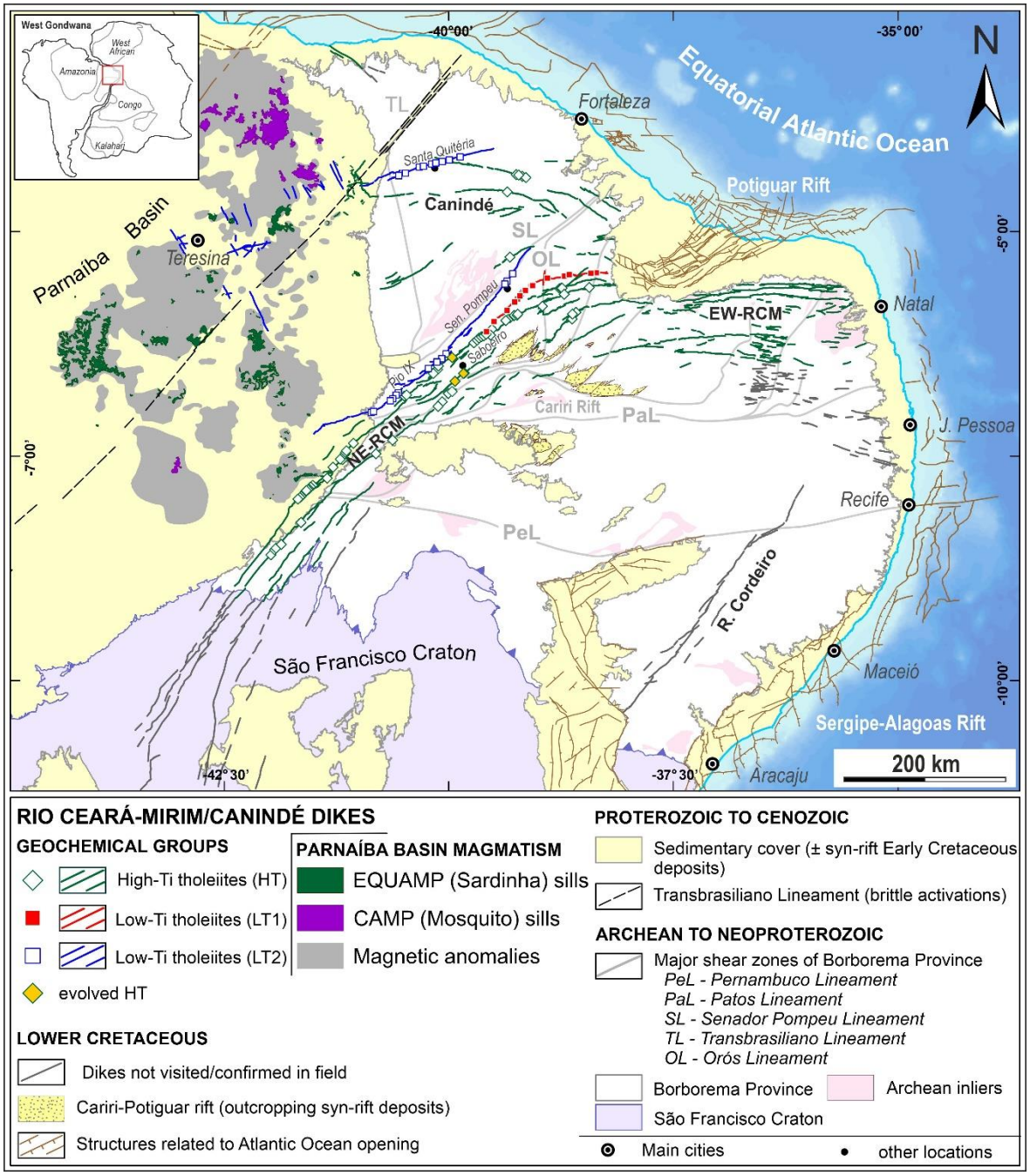

Figure 6.1. Simplified geological map of extreme NE Brazil illustrating the EQUAMP igneous products; CAMP event in the Parnaíba Basin is also shown. Dikes swarms map was updated combining magnetic airborne data with field work verification. The Rio Ceará-Mirim (RCM) and Canindé dike swarms are colored according to the geochemical suites defined in this work. Geological contacts and geophysical signatures of sill complexes are based on Macêdo Filho et al. (2019) and Mocitaiba et al. (2017), respectivelly.

6.3. Geological Setting

The entire RCM and the Canindé dike swarms are intrusive in the Precambrian Borborema Province (Fig. 6.1), one of the several crustal blocks deeply involved in the Brasiliano/Pan-African tectonics to form the West Gondwana supercontinent at the end of the Neoproterozoic (Brito Neves et al., 2014; Ávila et al., 2020). It presently covers an area of approximately 436,000 km^2 in northeastern South America bounded by the São Francisco Craton to the south and the Paleozoic Parnaíba Basin to the west, with the northern and eastern limits made with the Atlantic Ocean. The province shares many aspects with its counterpart in the NW Africa including the prevalence of large Paleoproterozoic (mostly Rhyacian-aged) domains including Archean inliers strongly reworked in amphibolite to granulite facies during the Brasiliano orogeny; Neoproterozoic foreland-type sedimentary successions (nowadays schist fold belts) preserved in discontinuity over the older basement rocks; and spatial-and-temporal connection between Neoproterozoic continental-scale shear zones and granite (*sensu lato*) suites (e.g., Van Schmus et al., 2008). Some of these shear zones show evidence of late activation in brittle regime in response to far-field stresses at the margins of the then formed Gondwana, leading to the development of extensional tectonics and subsequent formation of Paleozoic intra-continental rift (and after sag-type) basins (Sénant and Popoff, 1991; Françolin et al., 1994).

In the Early Cretaceous, the West Gondwana started to accommodate closely contemporaneous lithospheric thinning and rifting to give way to the present-day Atlantic Ocean (Matos et al., 1992, 2000; Granot and Dyment, 2015). As in southern South America and Africa, the EQUAMP dike swarms are understood as products of the early stages of the continental breakup at ca. 125-134 Ma as estimated from ^{40}K decay-based dating (Bellieni et al., 1992; Smith et al., 2001; Mizusaki et al., 2002; Ngonge et al., 2016a; Oliveira et al., 2021). A similar time interval was determined for a sill complex exposed in the eastern edge of the adjacent Parnaíba Basin (the Sardinha Formation; Baksi and Archibald, 1997; Fernandes et al., 2020) that are interpreted as cogenetic magmas of the dike swarms in the basement, all of them part of the EQUAMP (Hollanda et al., 2019). By considering its 1,000 km of length, the RCM is the main component of this province running parallel to the equatorial margin for 350-400 km to then it shifts the direction to 225° azimuth at longitude 39° west, a curving zone that roughly coincides with the Cariri-Potiguar Rift axis (Melo et al., 2021, 2022). From this point, the RCM extends for 600 km (or even more) until reaches the

northwestern edge of the São Francisco Craton (Fig. 6.1).

The physical aspects of the giant RCM dike swarm are described in Hollanda et al. (2019). The dikes consist dominantly of melanocratic medium-grained diabases with lengths of 4–21 kilometers and widths ranging in 57–90 meters; dikes as wide as 150–200 meters have been mapped. The undeformed and unmetamorphosed nature of the dikes fan-shaped geometry constitutes a strong indication for a change in the paleostress trajectories at the time of intrusion. According to Oliveira (1992), the trajectories likely change from N-S along the EW-RCM to NW-SE in its western termination, a condition that certainly has continued during the emplacement of the NE-RCM (also Melo et al., 2022).

Chemical characteristics of the EW-RCM diabases include the coexistence of high- and low-Ti basalts and basaltic andesites, with the former being far the dominant compositional types. Such magmatic suites share enrichment in incompatible elements and depletion in high field strength elements combined, combined with radiogenic Sr and non-radiogenic Nd isotope signatures in distinct magnitudes (Ngonge et al., 2016a). These authors argued that: (1) fractional crystallization was the main mechanism to explain the chemical variability recorded by the dikes, even though they do not discard some effects of low-pressure crustal contamination, and (2) an old enriched lithospheric (spinel lherzolite) mantle was the prevailing source to generate both high- and low-Ti suites. Inferences on possible mechanisms to induce mantle melting had not been taken into account by Ngonge and co-workers, but will be introduced in this paper.

6.4. Methods

One hundred and twelve bulk rock samples collected from the NE-RCM and the Canindé dikes were analyzed for major elements, in addition to seventy-four of those samples were also analyzed for trace elements. A set of forty samples was selected for Sr-Nd isotope analysis and thirteen samples were selected for Pb isotope analysis. The complete results are provided as Supplementary Material (Table A1).

The samples were all collected from apparently fresh outcrops. The altered surfaces were removed, and samples were crushed and further powdered in an agate ring mill to c. ~300 mesh. Major elements were determined by X-ray fluorescence in the Technological Characterization Laboratory (LCT) of the University of São Paulo after fusion of 1 gram of powdered sample with 7 grams of lithium tetraborate. Accuracy and reproducibility were

monitored by the GBW07105 basalt standard. The loss on ignition (LOI) was measured by weight differences after heating 2 g of powdered sample for 2 hours at a constant temperature of 1020°C and then cooling to room temperature. All major oxide compositions were recalculated to 100% on a volatile-free basis despite their negligible LOI values (0.3 to 1.6 wt.%; only two samples have LOI > 2.5 wt.%).

Trace element analyses were carried out by inductively coupled plasma mass spectrometry at Bureau Veritas Mineral Laboratories (ACME Labs, Canada) using the commercial package 'LF100–EXT '(LF100 + AQ200), in which 31 refractory+RE (rare earth) elements were measured after lithium fusion (LF100 code), while 14 metals (including Cu, Pb, Ni) had their concentrations quantified after sample dissolution with diluted aqua regia (1:1:1 HNO_3:HCl:H_2O) (AQ200 code).

A second aliquot of whole-rock powder was prepared for perform the isotope analyses taking some of the recommendations from Marques et al. (2016), which concerns carefully avoiding possible sawed surfaces from the rock fragments and subjecting them to successive washing with deionized and then Milli-Q water before powdering in an agate mill. Isotopic analyzes were done at the Isotope Geology Research Center of the University of São Paulo. Approximately 50 mg of rock powder were dissolved in HF:HNO_3 (3:1) and then in concentrated HCl acid under sub-boiling conditions (100º C), for 5-7 days. Ion exchange chromatography was firstly performed by loading the whole sample solutions into Biorad AG1-X8® resin columns to isolate Pb, while the eluted matrix solution was loaded into Sr-Spec® columns to separate Sr and REE, and then Nd and Sm were purified throughout LN-Spec® columns. Total procedure blanks during the analytical program were 45-136 pg for Sr, 35-197 pg for Nd, and 72 pg for Pb.

Isotopic compositions were determined by thermal ionization mass spectrometry using a Finnigan MAT-262 machine for Pb, while a multicollector ThermoFisher Scientific Triton™ was used to measure Sr and Nd. During the course of the analytical program the instrumental reproducibility was monitored throughout successive analyses of international standards and the range of the measured ratios and 2σ-uncertainties were: $^{87}Sr/^{86}Sr$ 0.710248 ± 0.000016 to 0.710252 ± 0.000017, for NBS987; $^{143}Nd/^{144}Nd$ 0.512093 ± 0.000004 to 0.512105 ± 0.000005, for JNdi; and $^{206}Pb/^{204}Pb$ 16.893 ± 0.004 (0.13% a.m.u.$^{-1}$), $^{207}Pb/^{204}Pb$ 15.432 ± 0.004 (0.12% a.m.u.$^{-1}$) and $^{208}Pb/^{204}Pb$ 36.512 ± 0.013 (0.13% a.m.u.$^{-1}$) for NBS981. All measured $^{87}Sr/^{86}Sr$ and $^{143}Nd/^{144}Nd$ ratios were normalized to $^{86}Sr/^{88}Sr$ = 0.1194 and $^{146}Nd/^{144}Nd$ = 0.7219, respectively. The initial Sr and Nd isotope compositions reported in the

text were calculated using the elemental concentrations for Rb, Sr, Sm, and Nd obtained by ICP-MS, assuming an $^{40}Ar/^{39}Ar$ age of c. 127 Ma obtained by Ngonge et al. (2016a).

Mineral chemistry of the major constituents was performed on 30 µm-thick carbon-coated thin sections of seven representative samples of the NE-RCM dikes using a JEOL JXA-FE-8530 probe equipped with five wavelength dispersive spectrometers at the GeoAnalítica Lab in the Institute of Geosciences (University of São Paulo). The analytical conditions included Faraday current intensity of 20 nA with an acceleration voltage of 15 kV, and a beam spot size between range from 5 to 10 µm. Elements were quantified using the K_α line (and L_α, when required) considering the following mineral standards for calibration: TAP for Si (anorthoclase and diopside) and Al (anorthite); TAPH for Mg (diopside) and Na (albite); PETJ for Ca (wollastonite), K (orthoclase) and Sr (strontianite); LIFL for Fe (fayalite), Mn (fayalite), Ti (rutile), Cr (chromite) and Ba (benitoite). Counting time was 20 s on the peak of all elements except Na with 10 s. ZAF matrix corrections were performed through the PC–EPMA software. All results are listed in the Supplementary Material (Tables A2, A3).

6.5. Results

6.5.1 Classification and geographic distribution

The distribution of the oxides plotted in the TAS diagram shows that most of the NE-RCM and Canindé diabases are dominated by basalt and basaltic andesite compositions (Fig. 6.2A) of tholeiitic affinity (Fig. 6.2B), with a small set of fine-grained feldspar-rich diabases plotting within the (trachy)andesite-trachyte fields. Basalts and basaltic andesites display either hypocrystalline (Fig. 6.3A) or holocrystalline textures (6.3B-C), which are directly correlated with the Ti-based chemistry, i.e. the hypocrystalline diabases are high-Ti tholeiites while the holocrystalline diabases are low-Ti tholeiites (Fig. 6.2C). As in the EW-RCM swarm, the high-Ti tholeiites (further simply dealt as HT) prevail over the low-Ti (LT) compositions, with the discriminant boundary of TiO_2 at 2 wt.% instead of the limit of 1.5 wt.% proposed by Ngonge et al. (2016a).

There is a striking linear correspondence between the HT tholeiites and the (trachy)andesites and trachytes suggesting that these magmas would be linked by magmatic differentiation. For simplification, these intermediate tholeiites will be hereinafter included as

part of the HT suite although we have kept them individualized in all diagrams as eHT (evolved HT).

In the MgO *versus* Ti/Zr diagram proposed by Peate et al. (1992) to discriminate the low-Ti suites of the Paraná LIP, the low-Ti samples from NE-RCM and Canindé swarms are grouped in separate clusters. We designated them as LT1 (0.94 < TiO_2 < 1.52 wt.%; MgO < 6wt.%; Ti/Zr < 70) and LT2 (1.13 < TiO_2 < 1.76 wt.%; MgO > 6 wt.%; Ti/Zr > 70) (Fig. 6.2D). Part of the low-Ti tholeiites of the EW-RCM (DCO04 and DCO08) with lower MgO contents clusters close to the LT1 suite, and the others (samples DCO03, DCO06 and DCO14) with higher MgO have compositions akin to the LT2.

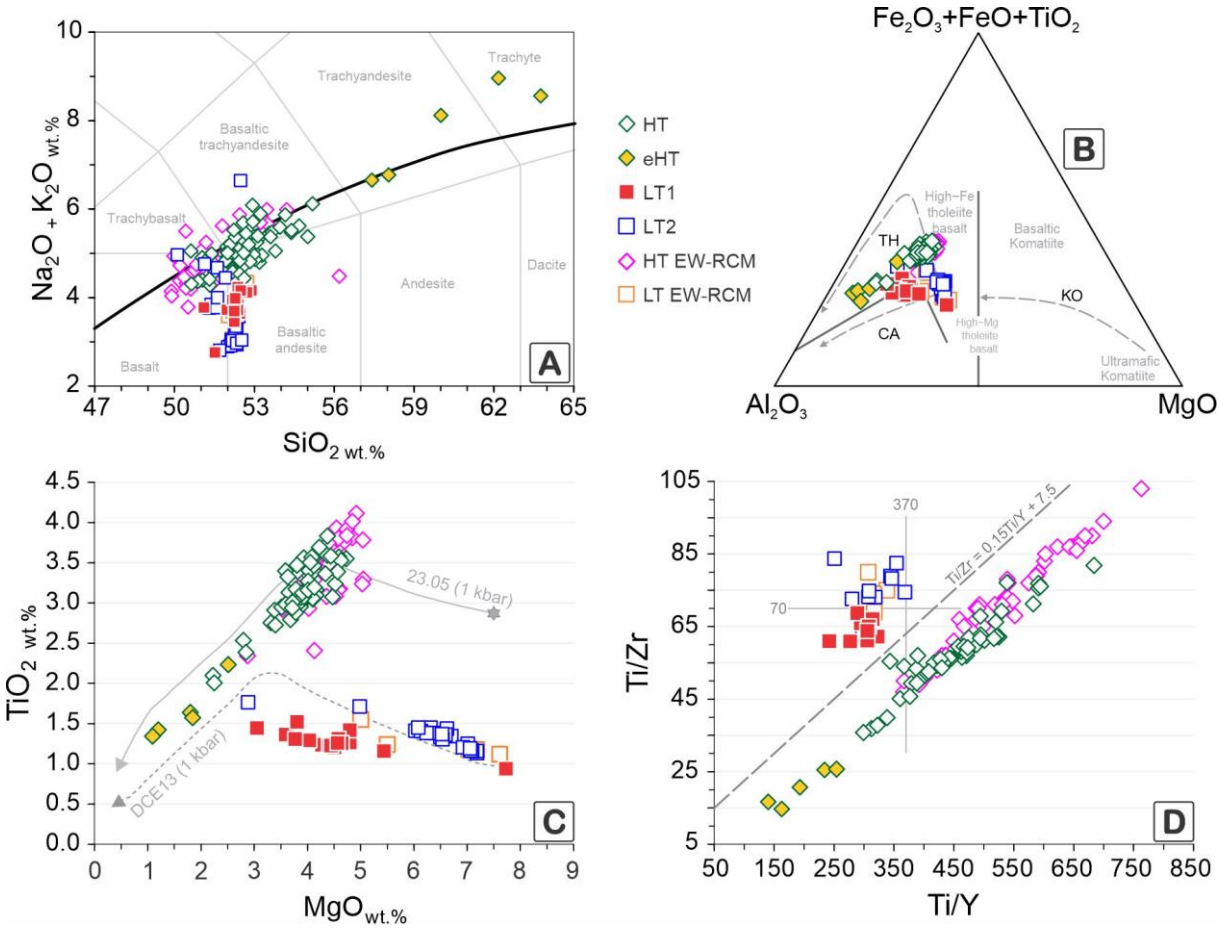

Figure 6.2. Geochemical classifications and discriminations for the Rio Ceará-Mirim and Canindé dikes: (A) TAS total - alkalis *versus* SiO_2, where the compositional fields and dividing line are referred from Le Maitre (2002) and Miyashiro (1978); (B) Cation plot (Jensen et al., 1976) with discrimination of tholeiitic (TH), calc-alkalic (CA), and komatiite (KO) fields; (C) TiO_2 *versus* MgO diagram. The gray-colored paths are calculated assuming isobaric FC (fractional crystallization) at 1 kbar adopting the H_2O = 0.2 wt.%, QFM buffer and 23.05 and DCE13 as starting melts; (D) Discrimination of HT1-eHT and LT1-LT2 in the Ti/Y *versus* Ti/Zr diagram. The diving line (dashed) and its respective function (Ti/Zr = 0.15Ti/Y+0.75) are represented. In all diagrams, samples from the EW-RCM tholeiites (Ngonge et al., 2016a) are plotted for comparison.

While HT magmas are distributed in the entire (EW- and NE-) RCM and Canindé swarms, the intermediate compositions are only identified in the central area of the NE-RCM within a radius of 17 km around the Saboeiro village (Fig. 6.1). Their relationship with the mafic rocks is not easily recognized in the field, and a suggestive occurrence as small-scale (evolved) melt from the HT basalts or basaltic andesites must be considered. The low-Ti tholeiites, in turn, are more restricted in the area. For instance, those with LT1 composition were sampled close to the curving area among the two RCM branches, while the LT2 were identified only in the NE-RCM along a first-order anomaly parallel to the Senador Pompeu shear zone and in the set of ENE-oriented dikes nearby the Santa Quitéria village (Fig. 6.1).

6.5.2. Petrography and mineral chemistry

The mineral assemblage of the HT and LT tholeiites of the NE-RCM does not differ from that described for the EW-RCM tholeiites. It is dominated by plagioclase, two clinopyroxenes and opaque minerals, likely Ti-magnetite. Apatite, a secondary opaque (possibly ilmenite) and primary sulfides are identified as accessory phases; ilmenite usually develops at the expense of augite destabilization. In the hypocrystalline HT tholeiites, the interstices between the crystals are mainly occupied by brownish (devitrified) glass typifying intersertal arrays, while in the holocrystalline LT tholeiites augite and plagioclase crystals develop subophitic-ophitic relationships and augite usually occur as interstitial microcrysts characterizing intergranular textures.

Plagioclase is normally zoned ranging from bytownite to labradorite compositions in both the HT (An_{74-23}) and LT (An_{81-66}) suites (Fig. 6.4), while alkali-rich overgrowths in plagioclase in the HT tholeiites exhibit compositions in $Ab_{1-40}Or_{99-55}$ coexisting with interstitial microgranophyres (Fig. 6.3D-E). The more extreme alkalic overgrowths are observed in plagioclase of the (trachy)andesites and trachytes including both pure albite (Ab_{97-89}) and K-rich feldspar (Or_{98-85}) (Fig. 6.4).

Augite and pigeonite are a little more magnesian in the LT ($En_{53-18}Wo_{31-26}$ and $En_{69-28}Wo_{9-17}$) than in the HT ($En_{44-29}Wo_{33-35}$ and $En_{43-37}Wo_{12-6}$) tholeiites (Fig. 6.4). In all tholeiites, the augite macrocrysts display an increase in FeO_T (and MnO) coupled with a decrease in MgO (plus Cr_2O_3), TiO_2 and CaO from the cores towards the rims. TiO_2 contents in augite and pigeonite are always higher than 0.7 wt.% in the HT tholeiites and lower than this value in the LT tholeiites, regardless of whether the measurements were made on cores or

rims. Differently, the TiO_2 compositions in augite from the trachyandesites and trachytes plot along a continuum from 1.0 to 0.4 wt%, with the higher values also measured on the cores.

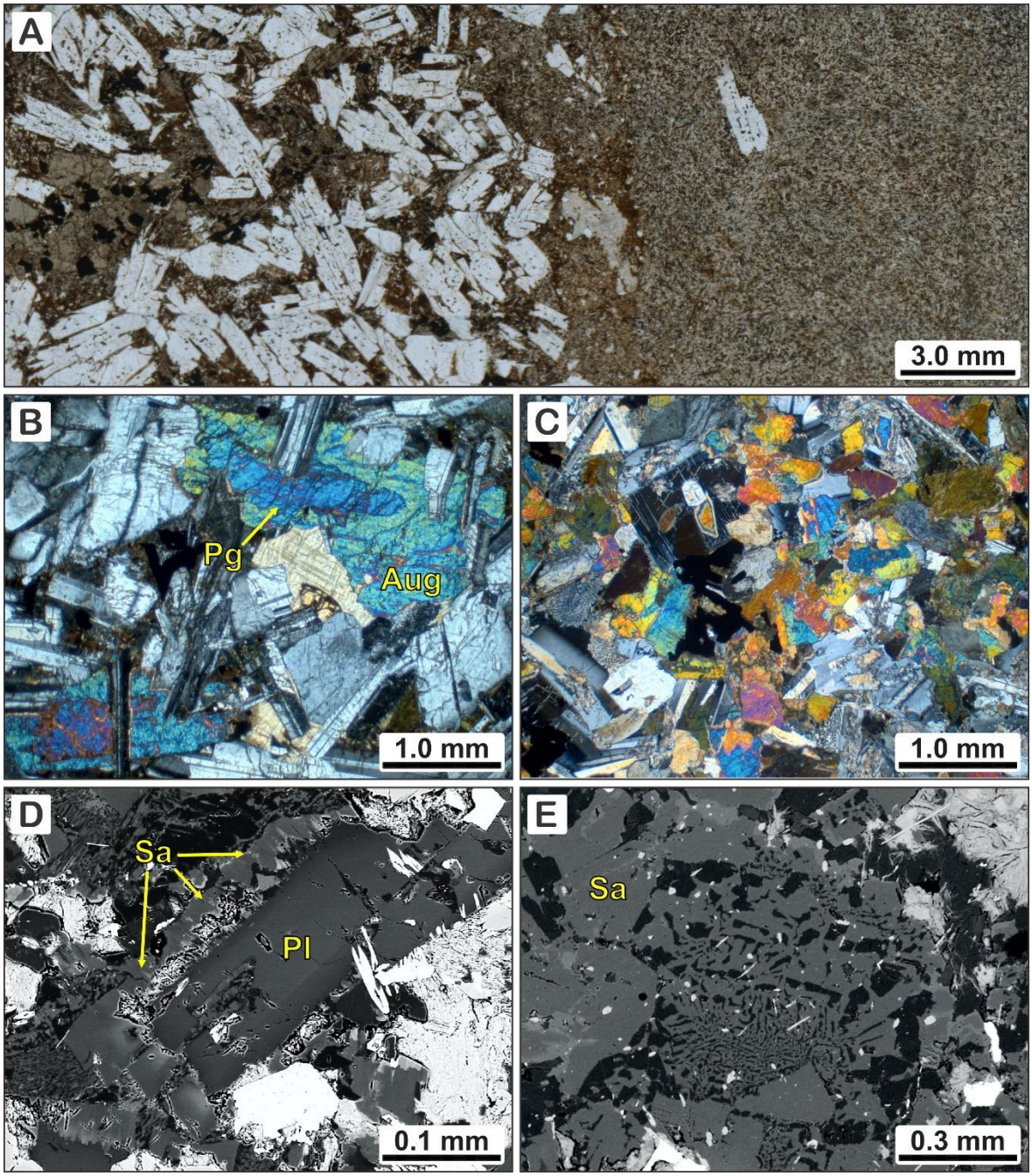

Figure 6.3. Textural aspects of Rio Ceará-Mirim-Canindé dikes: (A) medium-grained plagioclase and augite crystals immersed in a matrix (feldspar and pyroxene) is representative of the HT tholeiites, shown in left side. In the right side, a fine-grained light color rock of the evolve HT group. Holocrystalline subophitic diabases are frequent in the (B) LT1 and (C) LT2 groups, where plagioclase [Pl], augite [Aug] and pigeonite [Pg] form the main crystallizing phases. Detail of (D) plagioclase with sanidine [Sa] shell and (E) granophyre in late sanidine of HT tholeiites.

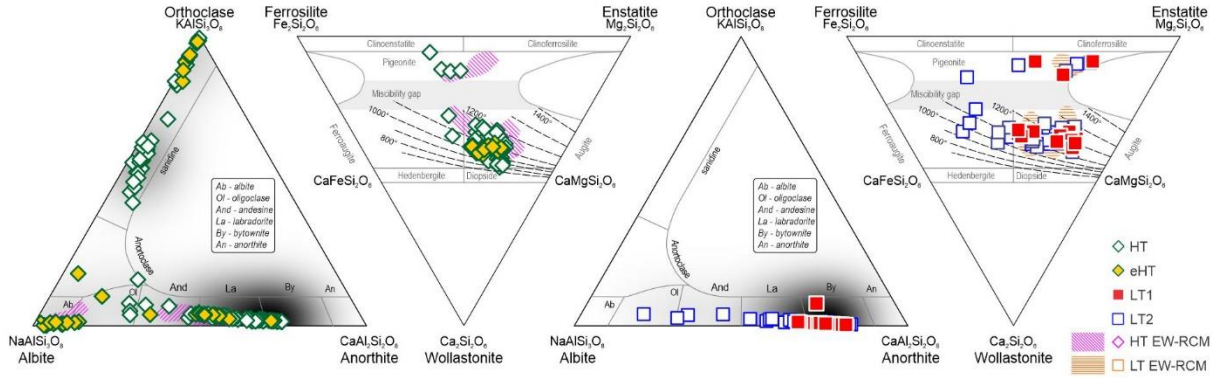

Figure 6.4. Mineral chemistry data obtained from plagioclase and clinopyroxene of the NE-RCM: (A) An-Ab-Or (mol%) for feldspars, and En-Wo-Fs (mol%) for clinopyroxenes. An: anorthite, Ab: albite, Or: orthoclase, En: enstatite, Wo: wollastonite, Fs: ferrosilite. The isotherms of Krentz (1982) are represented in the pyroxene diagrams. The shaded grayscale areas represent a density map highlighting the most frequent feldspar compositions of the analyzed crystals. Field of EW-RCM according to Ngonge et al. (2016a) is shown by comparison.

6.5.3. Major element chemistry

The HT tholeiites define general evolutionary trends marked by a decrease in CaO, TiO_2 and Fe_2O_3 and an increase in Al_2O_3 and K_2O as MgO decreases (Fig. 6.5). Moreover, the low MgO contents characterize the HT tholeiites with values generally < 5 wt.% (as also described for the EW-RCM) for basaltic andesites evolve up to 2.3 wt.% and the trachyandesites and trachytes have values as low as 1.1 wt.%. The positive correlation between MgO and CaO combined with an apparent negative correlation with Al_2O_3 (and lack with Sr) suggests that plagioclase fractionation had no important role in the HT magmatic differentiation. Instead, the decrease in CaO can be attributed to the continuous removal of augite as the magmas evolve. Decrease in TiO_2 and Fe_2O_3 indicates progressive removal of opaque minerals, while the increase in K_2O (not as clear in Na_2O) is explained by the accumulation of alkalis in the residual liquids as evidenced by the development of alkalic overgrowths in plagioclase and interstitial granophyres.

The P_2O_5 behavior is a bit complex. When considering the entire RCM dataset, two sub-groups are discriminated at similar MgO contents, with a gap in P_2O_5 between 0.6–0.7 wt.%. The samples that cluster at lower P_2O_5 values, which include those of the EW-RCM and a minor group of the NE-RCM, are distributed alongside an accumulation trend. The sub-group of higher P_2O_5 contents does not define (alone) any tendency, but it appears that they represent the primary compositions from where the evolved trachytic samples are derived. If that is true, apatite would have strongly fractionated when MgO reaches about 3.5 wt.%. In

the absence of a plausible cause to explain the P_2O_5 behavior for the HT magmas (not observed by other oxides), we attempt to say that the existing gap may be an effect of sub-sampling.

The oxide distribution patterns of the two LT suites are generally similar (Fig. 6.5) except in Al_2O_3, which certainly increases in the LT1 and decreases in the LT2 tholeiites (R^2=0.56, if the two more evolved samples are excluded). Pronounced decreasing in CaO in both LT suites contrasts with discrete accumulation in Sr indicating that even for the LT2 magmas plagioclase fractionation must have been minor participation than augite during magma differentiation. Fe_2O_3, TiO_2 and P_2O_5 accumulate in the LT2, while the Fe_2O_3 behavior in the LT1 group is not conclusive, suggesting that opaque minerals and apatite also had no relevance as fractionating phases. The low-Ti EW-RCM samples are in part akin to the LT2 tholeiites, and part to the LT1.

6.5.4. Trace element chemistry

All three tholeiite suites share common features on the primitive mantle-normalized multielementary diagrams (Fig. 6.6) including enrichment in highly incompatible elements (LILEs = Rb, Ba, Th, and U) and depletion in Nb (and Ta), Sr, P, and Ti, but the magnitude of enrichment and depletion differs among them. In the HT suite there is a continuous increase in the ΣLILE from the basalts to the intermediate rocks, but the magnitude of Nb (average $[Nb/Nb^*]_{PM}$ = 0.70±0.05), Sr ($[Sr/Sr^*]_{PM}$ = 0.79±0.22) and P ($[P/P^*]_{PM}$ = 0.85±0.14) depletion is generally consistent for the entire suite regardless the MgO content. Ti anomaly is either negative or positive, but its good correlation with MgO and SiO_2 (not shown) indicates that such variation reflects the effect of magmatic differentiation. Th and U also are depleted relative to their neighbors. The LT1 and LT2 suites have similar trace element contents (respectively, 201-400 ppm and 139-611 ppm), but lower in relation to the HT. Notwithstanding, two LT2 samples (DCE01B and DPI05) show total contents as high as those of the HT suite, and at least for a few samples, U displays a positive peak relative to Th and K. Depletion in Nb (0.59±0.08), Sr (0.56±0.15) and P (0.72±0.10) are slightly more accentuated than in the HT tholeiites, while depletion in Ti is absent. Ni, Co and Cr have very low contents, especially in the tholeiites of the HT suite.

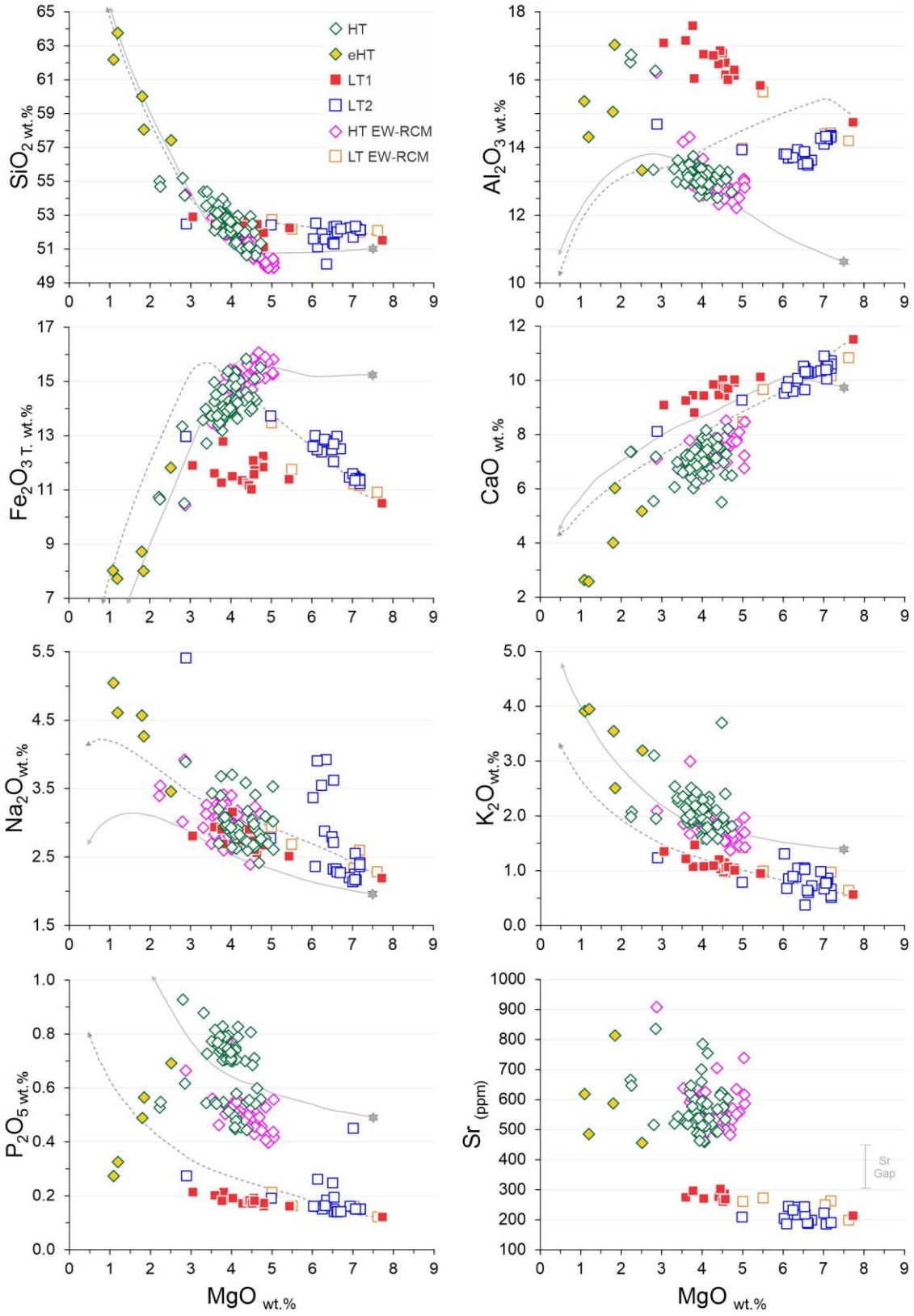

Figure 6.5. Binary plots involving MgO *versus* oxides (and Sr). Basalts 23.05 (gray star; Supplementary Material; Table A4) and DCE13 are the starting melts in the FC (MELTS) modelling, assumed to respectively the HT and LT1 suites. The gray-colored lines represent the calculated MELTS paths.

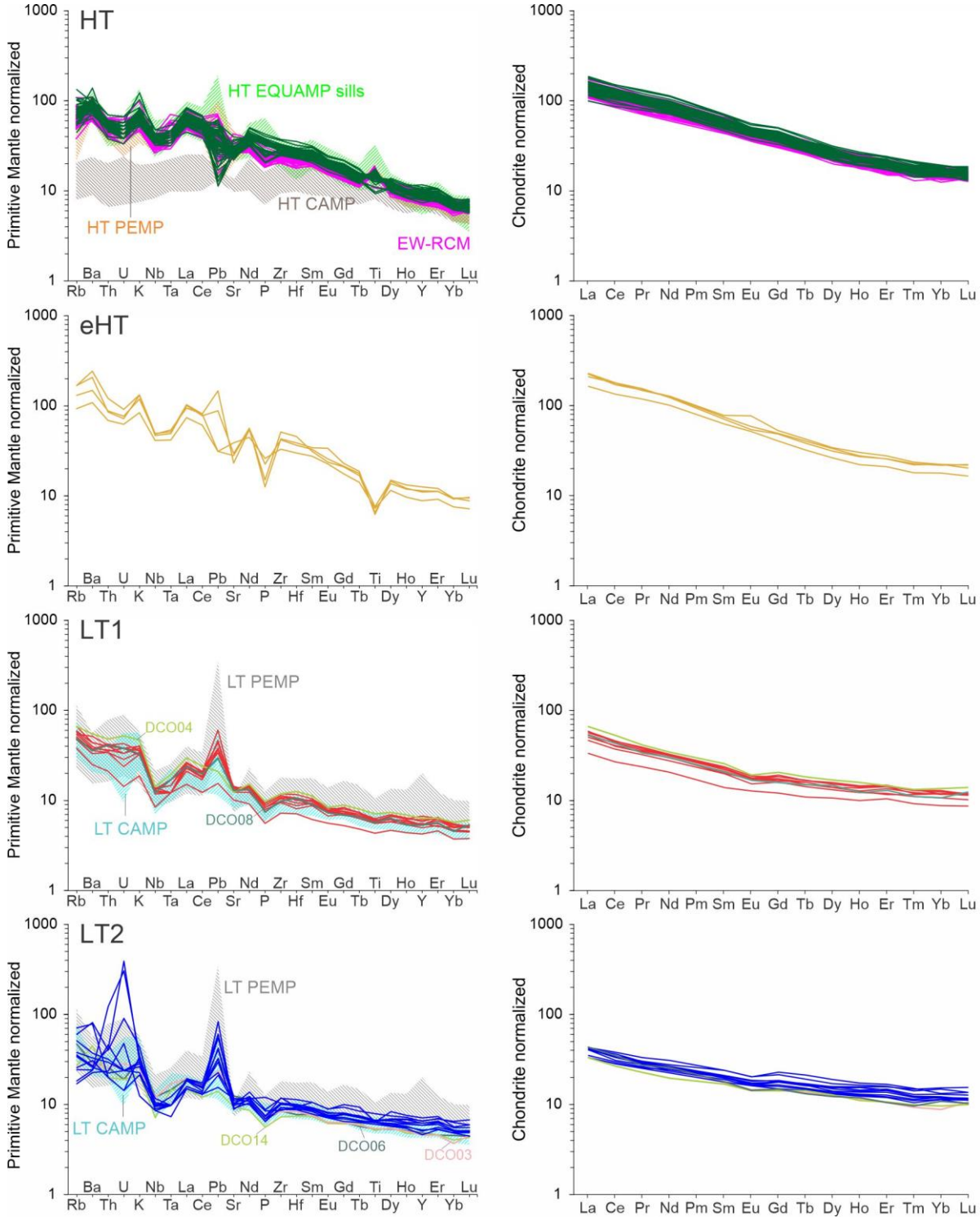

Figure 6.6. Multielementary diagrams and REE patterns normalized to the Primitive Mantle of Sun and McDonough (1989) and Chondrite of Boynton (1984), respectively. Data for comparison are: EW-RCM (Ngonge et al., 2016a); high-Ti EQUAMP (Sardinha) tholeiites of the eastern border of Parnaíba Basin (Fodor et al., 1990; Oliveira et al., 2018; Heilbron et al., 2018); low-Ti (Mosquito) CAMP field of the western Parnaíba Basin (Merle et al., 2011; Oliveira et al., 2018); and low- and high-Ti tholeiites of the Paraná Province (De Min et al., 2018).

In Figure 6.6, fields of other high- and low-Ti tholeiitic magmas related to Mesozoic LIPs in South America are shown for comparison. HT overlap compositions as such high-Ti EQUAMP sill complexes and PEMP, while LTs present ambiguous behavior plotting over low-Ti suites of the CAMP and PEMP.

The chondrite-normalized rare earth element (REE) patterns are strongly to moderately fractionated (Fig. 6.6) with average $(La/Yb)_{CN}$ ratios ranging from 10-8.7 (for HT), to 4.5-3.8 (LT1) and 3.0-2.7 (LT2). This difference is mainly determined by the variation in the heavy REE contents once the average $(La/Sm)_{CN}$ ratios are consistently identical in the HT and LT1 (2.5±0.1), while somewhat less pronounced (1.9±0.1) for the LT2 tholeiites. In the trachyandesites and trachyte the average $(La/Sm)_{CN}$ ratio is a bit higher (2.9±0.2). Eu anomalies are negligible in all groups in accordance with the overall minor relevance of plagioclase fractionation.

6.5.5. Radiogenic isotopes

Sr, Nd and Pb isotope ratios were determined for forty samples selected from those studied for whole-rock geochemistry. Sr and Nd measurements were calculated back 127 Ma according to the $^{40}Ar/^{39}Ar$ age published by Ngonge et al. (2016a) for one high-Ti dike of the EW-RCM. Pb isotope ratios are presented as measured values.

HT, LT1 and LT2 have all enriched initial Sr and Nd isotope compositions (Fig. 6.7A), distinguishing from each other by their Nd rather than Sr signatures. For instance, the HT tholeiites have εNd ranging from -3.3 to -2.4 coupled with $^{87}Sr/^{86}Sr$ ratios ranging from 0.705540 up to as radiogenic values as 0.708969 (for the trachytic samples), while the LT1 and LT2 have, respectively, more and less negative ε_{Nd} values in the ranges of -4.7 to -4.5 (LT1) and -1.44 to -1.08 (LT2). As a group, the LT1 tholeiites are more radiogenic in Sr (0.708501 to 0.710455) than the LT2 (0.706452 to 0.709522), and the low-Ti EW-RCM magmas again resemble one and another. However, the isotopic compositions of the high-Ti EW-RCM tholeiites randomly scatter in the enriched quadrant, part of them nearby our results for the HT magmas including with even less radiogenic $^{87}Sr/^{86}Sr$ ratios. Those very negative Nd compositions were explained by Ngonge et al. (2016a) as a likely effect of selective contamination related to magma ascent through diking and/or isotopic imbalance related to the mantle source(s).

Present-day Pb isotope compositions plot all above the Northern Hemisphere reference line (NHRL; Hart, 1984) with consistent compositions within each suite (Fig. 6.7B-C). The $^{206}Pb/^{204}Pb$ ratios group generally between 18.2 and 18.8, the LT tholeiites presenting more radiogenic values (18.416-18.477 for LT2, and 18.740-18.758 for LT1) comparative to the HT tholeiites (18.208-18.366; one trachyandesite has 18.664). In the HT, the $^{207}Pb/^{204}Pb$ and $^{208}Pb/^{204}Pb$ compositions cluster closer to the EMI-OIB component while those of the LT tholeiites deviate towards more radiogenic values suggesting a major contribution of old crust in these magmas. The high-Ti EW-RCM tholeiites mimic the NE-RCM equivalents, but the low-Ti tholeiites (especially those akin to the LT1: DCO04 and DCO08) are even more radiogenic than the LT compositions.

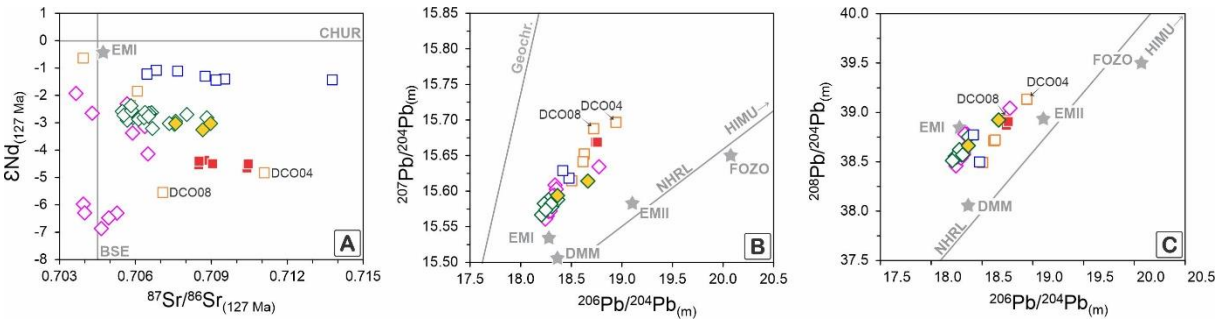

Figure 6.7. Isotopic compositions of the NE-RCM and Canindé tholeiites. (A) Initial $^{87}Sr/^{86}Sr$ *versus* εNd; (B) Measured $^{206}Pb/^{204}Pb$ *versus* $^{207}Pb/^{204}Pb$ and (C) $^{206}Pb/^{204}Pb$ *versus* $^{208}Pb/^{204}Pb$. Northern Hemisphere reference line (NHRL; Hart, 1984) and average of MORB and OIB endmembers according to Stracke et al. (2005) are plotted for comparison.

6.6. Discussion

6.6.1. Fractional crystallization

To test the relevance of fractional crystallization (FC) mechanisms in producing the chemical variability recorded in the RCM magmas, we applied the algorithm rhyolite–MELTS 1.0.2 (melts.ofm–research.org; Gualda et al., 2012) adopting two real samples as starting liquids (Fig. 6.5). The sample 23.05 (Supplementary Material; Table A4) consists of a high-Ti (TiO_2 2.84 wt.%) tholeiitic basalt collected from a mafic sill of the Parnaíba Basin and considered as part of the EQUAMP and, therefore, interpreted as cogenetic magma of the RCM dikes (Hollanda et al., 2019). This sample is herein dealt with as the more primitive melt (MgO of 7.4 wt.%) representing the HT tholeiite suite. The low-Ti basalt DCE13 (MgO

of 7.7 wt.%) was chosen as the common starting melt of the LT tholeiites. We assumed isobaric FC modeling considering fO_2 along the quartz–fayalite–magnetite (QFM) oxygen buffer and H_2O at 0.2 wt.% and pressure at 1 kbar consistent with hypabyssal (< 5 km-deep) systems, as the case of the dikes. These conditions are compatible with the continuous fractionation of opaque (Ti-magnetite–ilmenite) minerals observed for the HT tholeiites which are suggestive of low H_2O and fO_2 during magmatic differentiation. Furthermore, experiments with higher H_2O (i.e., > 1.5%) tend to suppress plagioclase crystallization because of the decrease in temperature stability in mafic melts (Tatsumi and Suzuki, 2009).

From the basalt 23.05, MELTS simulation indicated that the HT suite would be generated within a range of 15-45% of fractional crystallization dominated by removal of clinopyroxene (augite) at temperatures of 1140-1090°C; the intermediate trachytic compositions would be easily produced as augite continuously fractionates (45-65% of FC) up to temperatures of 1090-1020°C. The simulation also indicated that the opaque assemblage would be dominated by the magnetite($FeFe_2O_4$)-ulvospinel($TiFe_2O_4$) solid solution, which greatly agrees with descriptions reported from anisotropy of magnetic susceptibility (AMS) investigations performed on the EW-RCM (Archanjo et al., 2000). However, MELTS did not predict crystallization/fractionation of alkali-sodic feldspar. The commonly observed presence of micrometer-scale granophyric overgrowths (as well as interstitial blobs) enclosing plagioclase crystals in the HT magmas would reflect, therefore, K-Na enrichment in the residual liquids after (quasi) complete crystallization of the main mineral assemblage. Another possible explanation for the presence of alkaline compositions related to the final stages of crystallization would be the phenomenon of silicate liquid immiscibility (Philpotts, 1982), where Ca, Mg, and Ti prefer a poorly polymerized (Fe-rich) melt, while K and Na concentrate in the highly polymerized (Si-rich) melt.

The FC modelling failed in producing conclusive results for the LT1 tholeiites using the basalt DCE13 as the parental liquid, even by varying the *a priori* parameters (pressure, H_2O). Contrarily, for the LT2 tholeiites the results were reliable for CaO, TiO_2 and Fe_2O_3 while partially for SiO_2, P_2O_5 and K_2O pointing out for majority of compositions formed within the range of 9-44% of FC of augite together with plagioclase, under temperature conditions range of 1185-1145°C. Opaque minerals start to crystallize at MgO ~3 wt.% as indicated by the Fe_2O_3 and TiO_2 evolutionary trends that inflect to adjust the most evolved basaltic andesite DCE86 (see back Fig. 6.5), which compositions correspond to ~68% of FC at ~1085°C. Regardless of the shortcomings in applying FC modeling when parental liquids

are not available for the investigated suites, the MELTS modeling has proved that fractional crystallization was the major petrogenetic mechanism controlling the chemical variability observed in the RCM and Canindé dikes.

6.6.2. Conditions of magma crystallization

Thermodynamic inferences were estimated by using geothermobarometry based on the chemistry of clinopyroxene (augite) because it is an early liquidus phase with a continuous history of fractionation in the investigated magmas. Here, we applied the clinopyroxene-only temperature-dependent equation [32b] of Putirka (2008) by inputting temperature values obtained from the equation [T1] of Putirka et al. (1996) as recommended by Hammer et al. (2016) to efficiently constrain pressure conditions in basic melts. We parameterized Putirka's equation to H_2O in the melt at 0.2 wt.% in line with the value adopted for the MELTS modeling. The calculations only considered the chemical analyses in equilibrium with melts, i.e. those plotting within the dashed line field in an Mg#(mineral-liquid) diagram (Rhodes et al., 1979; Fig. 6.8A). There, the Mg# (Mg# = 100×MgO+/MgO+FeO) obtained from individual augite crystals and their corresponding bulk rocks (or liquids) are plotted together with a Fe-Mg distribution coefficient of 0.28±0.08 for clinopyroxene (Putirka, 2008). Exceptions concern to P-T calculations cores from the evolved HT (DCE32C and DCE33), LT1 (DCE03), and LT2 (DPI03) recalculated for melts with MgO# of ~36-29.5, 48, and 33.5, respectively.

Core-to-rim variation as marked by decrease in the Mg#, is conspicuous in augite crystals of the three geochemical suites analyzed by EMPA (Fig. 6.8A). The Mg# from cores of the HT tholeiites are in equilibrium with their host magmas (DCE10, DPI12B and DPI23), but the Mg# values measured from augite cores of the trachytes DCE32C and DCE33 do not, indicating that they must have started crystallization from melts originally mafic in composition and ended when the liquids evolved up to andesite-dacite compositions. Higher Mg# values were obtained from augite of the LT1 and LT2 suites which are in equilibrium with their host magma compositions, respectively represented by the basalts DCE03 and DCE44. This suggests that the bulk rock compositions well represent the parental magmas from which these magmatic crystals have grown up. The augite compositions of the basalt DPI03 (LT2), however, failed in showing equilibrium with the liquid, a behavior that would be expected from cumulatic rocks. Although not cumulate, DPI03 is a holocrystalline

subophitic basalt with a high amount of augite, an aspect that would somewhat increase the Mg# of the basaltic melt and produce the compositional imbalance between mineral and the bulk rock system.

In Figure 6.8B we plotted the temperature ranges of clinopyroxene crystalization of HT and LTs calculated from MELTS assuming 1 and 5 kbar. The augite compositions indicate that the HT magmas would have evolved at maximum pressures of approximately 3.0-3.5 kbars, and temperatures of 1140º-1070°C, with the trachytic magmas evolving under pressures not exceeding 2 kbars and lower temperatures. Similar temperature range was calculated from oxide (Ti, Al, Mg) compositions of augite of the high-Ti EW-RCM tholeiites (Ngonge et al., 2016a). The pressure conditions for the LT1 and LT2 magmas, in turn, are roughly similar. The LT1 magmas are generally hotter (1220-1150°C) than the LT2 (1240-1070°C), but they would have crystallized under pressures of 4.0-4.5 kbars (a few data indicated > 5.5 kbars).

A progressive decrease in temperature and pressure conditions as estimated for all three geochemical suites is compatible with a history of transcrustal crystallization, when the magmas start cooling in intermediate-depth chambers within the crust to progressivelly move up towards the final emplacement sites, at shallower levels. Paleodepth estimation was performed by considering a geostatic pressure gradient of 3.64 km/kbar used as a multiplying factor for those clinopyroxene-based pressures. The HT tholeiitic magmas would have started crystallization at 15-10 km of depth continuing to segregate (and differentiate) towards upper crustal levels, until reach shallower (<7 km) depths and crystallize the trachytic magmas. Pressure-dependent paleodepths calculated for the LT tholeiites, in turn, range from 30–28 km to near 5 km indicating that these hotter (more magnesian) magmas must have started to crystallize 2-3 times deeper than the HT tholeiites although the main crustal domain indicated by the augite compositions is comparable to that of the HT tholeiites.

The crustal thickness of about 30-35 km has been estimated for the northern Borborema Province as a result of continental stretching related to the West Gondwana rifting and breakup during the Early Cretaceous (de Lima et al., 2015; Luz et al., 2015), contrasting with the estimate of 42±2 km for the top of Moho beneath the cratonic Parnaíba Basin (Almeida et al., 2015; Tozer et al., 2017). A peculiar feature detected in such thinned Borborema domain concerns the presence of a 9-18 km deeper seismic discontinuity interpreted as a sub-horizontal detachment zone left after the Mesozoic extension that culminated with the Atlantic Ocean, and which is not present (or is very weak) in other domains of the province

(Almeida et al., 2015). This feature coincides geographically with the region where the EW-RCM and Canindé dike swarms occur, leading us to suppose that magma zones that fed the EQUAMP plumbing system might have a connection with lithospheric domains affected by pronounced stretching.

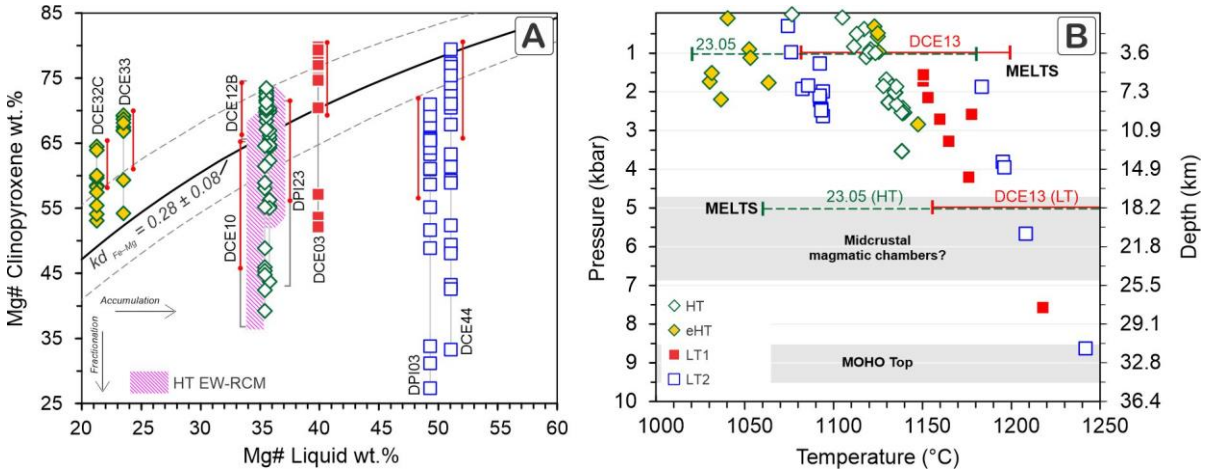

Figure 6.8. (A) Rhodes's diagram showing equilibrium compositions between mineral (cpx) and liquid using the $Kd_{[Fe\text{-}Mg]}$ of 0.28±0.08 for clinopyroxene according to Putirka (2008). Red lines indicate the analytical set measured on clinopyroxene cores. Field of the high-Ti augite compositions of the EW-RCM is illustrated for comparison (Ngonge et al., 2016a). (B) P-T-Depth diagram based on geothermobarometers calculated from clinopyroxene analyses in equilibrium with melt. The thermal range obtained from MELTS modelling was plotted assuming pressure of 1 and 5 kbar (dashed green line for the HT basalt 23.05, and red line for the LT basalt DCE13).

6.6.3. Causes of the variability in Sr isotopic compositions

The $^{87}Sr/^{86}Sr$ ratios of the three magmatic suites (HT, LT1 and LT2) shown in Figure 6.7A scatter from compositions nearby the Bulk Silicate Earth towards more radiogenic values and are accompained by decreasing in εNd values. Because $^{87}Sr/^{86}Sr$ ratios are not modified by fractional crystallization, differing radiogenic values could be explained by either low-pressure crustal contamination or alteration. The dikes intrude country rocks that are well known strongly radiogenic in Sr and non-radiogenic in Nd (e.g., Souza et al., 2016; Hollanda et al., 2003). Any small degree of contamination would not only shift the Sr but also the Nd isotopic compositions towards more enriched values. Furthermore, $^{87}Sr/^{86}Sr$ ratios should correlate with other indicators of crustal input like, for instance, K_2O/P_2O_5 ratio (Hart et al, 1997) or LILE contents. Despite the LT tholeiites have generally high K_2O/P_2O_5 values (average of 5.9±0.5 for LT1, and 4.8±1.4 for LT2), the feeble correlation between this chemical indicator and the $^{87}Sr/^{86}Sr$ ratios (r^2 value < 0.3) does not support relevant crustal

contamination. The same occurs regarding the LILE contents (not shown). Correlation is even weaker for the HT tholeiites asserting that their transitional to potassic signature is rather an original attribute than an effect of extensive assimilation of crustal material.

Mafic rocks are also very sensitive to weathering leading to mineral breakdown and element (especially LILE) mobility. In field, the dike outcrops are featured by accumulation of rounded boulders as a result of severe spheroidal exfoliation, even though the rocks are virtually pristine and the LOI contents are relatively low (generally <1.5%). In thin section, the effects of alteration are seen by a variable degree of plagioclase sericitization and chloritization of the groundmass. As sericite is usually introduced during open-system alteration, its presence announces that some aqueous fluids had interacted with the mineral assemblage. An expected consequence is the selective leaching of Sr relative to REE causing deviation of the $^{87}Sr/^{86}Sr$ ratios towards more radiogenic values, and likely negligible shift in Nd isotopic compositions. The dike DCE01 (LT2) is an example. Sampling was made in two sites: one at the medium-grained center (DCE01A) and other at the fine-grained margin (DCE01B). Stronger alteration in the marginal sample is evidenced by severe replacement of plagioclase by sericite/saussurite and of groundmass by clay minerals. The initial $^{87}Sr/^{86}Sr$ ratio of the marginal basalt is 0.713778 contrasting with the inner basalt with 0.709181, this one visibly less altered. Interestingly, they share the same Nd isotopic composition ($^{143}Nd/^{144}Nd$ of 0.512401; εNd -1.4). Unfortunately, Pb isotope data are not available for these two samples, but positive spikes of U and Th in a few LT2 samples (including the marginal DCE01 sample) suggest some additional degree of assimilation of regional country rocks. Irrespective of this, we argue for an origin from enriched mantle source(s) for the tholeiitic magmas of the EQUAMP plumbing system.

6.6.4. Assessing the magma source(s)

Although being mantle-derived magmas, continental (tholeiitic) basalts forming LIPs are usually affected by AFC processes instead of representing primitive melts, a reason that limits their use to constrain a definite chemical signature (plume or non-plume) of their mantle reservoirs. The recent work of Pearce et al. (2021) proposes to combine the Th/Nb (representing crustal input proxy) against Ti/Yb (representing residual garnet proxy, i.e. depth of melting) ratios as a way to look back at the geochemistry of mantle sources of LIP basalt suites through a plume *versus* lithospheric-influenced perspective.

Th/Nb values of the HT tholeiites cluster in the range of 0.14-0.22 (average of 0.17±0.02, 1s.d.) and their TiO_2/Yb are generally > 0.8, while the LT tholeiites have Th/Nb of 0.25-0.55 and lower and more restricted TiO_2/Yb (0.5-0.6); an anomalously high Th/Nb value of 1.53 corresponds to the basalt DPI01 that shows a spike in Th of 10.4 ppm (i.e. Th_N ~100 times PM; Fig. 6.6). These compositions are plotted in Figure 6.9A, from which two aspects are highlighted. First, the two broad geochemical groups - HT and LT, are very distinct. The HT tholeiites plot within the narrow field defined by EM-OIB basalt compositions with Th/Nb greater than those of typical OIBs, which would be a result of a higher proportion of deep-recycled crustal components into the asthenosphere. Contrarily, the LT tholeiites cluster entirely within the lithosphere-dominated field (SZLM in the diagram). According to Pearce et al. (2021), basalts plotting in this field are derived from subduction-modified mantle and the magnitude of the data dispersion would indicate variable interaction with crustal contaminants during magma ascent and/or emplacement. The second aspect is that, although LT1 and LT2 distinguish in several compositional features, notably by their Sr and Nd isotope compositions, they plot at similar Th/Nb and TiO_2/Yb compositions.

When we compare the average composition of geochemical groups with Mesozoic LIPs of South America is possible to observe that HT group is akin to high-Ti basalts of the PEMP, whereas LT1 and LT2 resemble signatures of low-Ti tholeiites of the PEMP and CAMP (Fig. 6.9B). Recently, Oliveira et al. (2021) conducted an investigative K-Ar study across the NE-RCM dike swarm in which LT2 samples defined a regression line (not exactly an isochron) estimated age of ca. 199 Ma. Although precise dating is required to prove the provinciality of the LT2, the current evidence does not preclude a Jurassic-Triassic age for this group.

Regardless of the age provinciality proposed for LT groups, both present Th/Nb and TiO_2/Yb indicating a strong influence of metasomatism in their mantle source(s). In fact, metasomatic enrichment and melting depletion in the lithosphere of the northern Borborema Province are vastly reported in the literature from a suite of peridotite (lherzolites and harzburgites) xenoliths (Rivalenti et al., 2000, 2007; Fodor et al., 2002; Ngonge et al., 2016b, 2019). Re-Os data and platinum group element patterns indicate a complex and multi-stage history of melt depletion and LILE enrichment (refertilization) events from the Proterozoic to Meso-Cenozoic (Ngonge et al., 2019). The Proterozoic history of the Borborema Province records convergent/collisional tectonics that led to pervasive crustal reworking and accretion at the Rhyacian (Souza et al., 2007) and Ediacaran (Hollanda et al., 2003) periods, implying in the printing of subduction-like features to the mantle beneath. From the Neoproterozoic-

Cambrian transition onwards, the province underwent a long-lasting period of tectonic quiescence during which the continental lithospheric mantle was apparently preserved from any chemical modification until it suffers partial melting and contributing to the EQUAMP magmatism as a result of extension and rifting at the Mesozoic.

Nd model ages recorded by the RCM tholeiitic magmas are systematically consistent around 1.5 Ga (the LTs) and 1 Ga (the HT) (Hollanda et al., 2006; Ngonge et al., 2016a; this work), together with Sm/Nd between 0.135-0.155 which, in turn, are much lower than those values reported for the depleted mantle and BSE (or chondrites) (e.g., Amelin and Rotenberg, 2004). The combination of low Sm/Nd ratios and Proterozoic model ages suggests a mantle with a long-lived history of Nd enrichment relative to Sm, prior melting. The fraction of contribution of this enriched (and old) component in each HT and LT groups is non-identical and, at least for the HT tholeiites, another component with OIB-type characteristics (contamined asthenosphere or deep plume) would be required. We simulated two simple scenarios (non-plume and plume) that could explain the chemical and isotope signatures of the EQUAMP magmas.

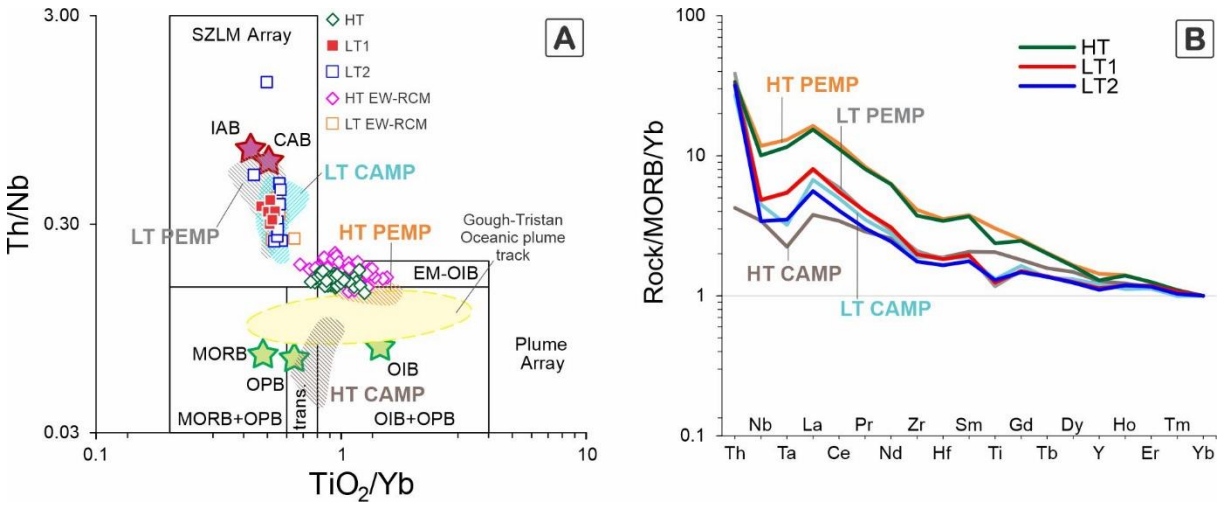

Figure 6.9. (A) Two-proxy projection of Th/Nb *versus* TiO_2/Yb and (B) geochemical patterns based on Pearce et al. (2021) with of HT and LT of the Rio Ceará-Mirim dikes. Fields and average values of HT and LT (Mosquito) CAMP tholeiites of the western Parnaíba Basin (Merle et al., 2011; Oliveira et al., 2018), Paraná Province (cf. De Min et al., 2018) and Gough-Tristan hotspot are also illustrated in both graphs. Normalizing factors are from Sun and McDonough (1989). Acronyms: Mid-Ocean Ridge Basalt (MORB); Ocean Island Basalt (OIB); Enriched Mantle-rich OIB (EM-OIB); Oceanic Plateau Basalt (OPB); Island Arc Basalt (IAB); Continental Arc Basalt (CAB); Subduction-modified Mantle (SZLM).

6.6.4.1. Non-plume Test

Non-plume models invoke the mechanisms of either passive upwelling (Mckenzie, 1978) or edge-convection (e.g., King and Ritsema, 2000) of the asthenosphere in response to, respectively, far-field stress forces or small-scale convective flow, to explain continental intraplate mafic magmatism. In both scenarios, the magma composition is controlled by the main source(s) involved, i.e. lithosphere *versus* asthenosphere, while the production of magma is conditioned to how much of the convective asthenosphere (i.e. the thermal energy) ascends to decompress and melt (Saunders, 2005).

In Figure 6.10 we modeled single mixing curves between a MORB type component (plausible for depleted upper mantle) and enriched SCLM-derived melts in order to examine if this simulation mimics the compositions of the HT and LT magmas. Here, the Sr-Nd-Pb depleted mantle (DMM) signature is an average value extracted from Stracke et al. (2005), while trace elements are those from Sun and McDonough (1989). The SCLM, in turn, is represented by a real alkaline composition of Alto Paranaíba magmatism – sample TR-84 (Araujo et al., 2001). In the same diagrams, we also simulate the AFC influence on either DM-SCLM or DM curves, both cases assuming contamination with local Precambrian felsic and intermediate/mafic crusts (samples ZEF28B and ZEF8A+ES543B respectively; Table A4; Souza et al., 2016) with *r*-values (ratio of assimilated material to crystallized material) of 0.25, compatible for tholeiitic intrusions (Tegner et al., 2005).

The Sr-Nd isotope compositions of the HT tholeiites cluster around mixing of $DM_{90\%}SCLM_{10\%}$ with a proportion of 2.5-5% of assimilation with either a felsic or mafic crustal component especially observed for the EW-RCM samples (Fig. 6.10A-B), while a higher proportion of SCLM-derived melts relatively to the DM contribution (~$DMM_{80-70\%}SCLM_{20-30\%}$) is required to match the Pb isotope ratios (Fig. 6.10C-D). The Sr-Nd isotope compositions of the LT1 tholeiites would simply be achieved by mixing DM with approximately 10% of the old granodioritic crust (Fig. 6.10A). However, when combining Nd and Pb compositions, the influence of AFC processes does not overcome 12.5% of assimilation (Fig. 6.10B).

Looking at trace element budgets, a $DMM_{90-70\%}SCLM_{10-30\%}$ mixing would produce spectra that reasonably fit to the LILE average abundances of the HT tholeiites (Fig. 6.10E), but that fails in reproducing their HFSE and HREE concentrations, which tend to be more enriched in these magmas. Roughly, a parental melt DMM enriched with 2.5% of SCLM is

enough to produce a trace element abundance of an enriched MORB (Fig. 6.10F) as those defined by Sun and McDonough (1989). Such enriched MORB-like melts mixed with 10-20% of Paleoproterozoic crust (ZEF28B) (Fig. 6.10F) or even many crustal endmembers (e.g., Rudnick and Fountain, 1995) exhibit a spectrum of trace elements akin to LT magmas. Alternatively, the magma genesis of LT tholeiites would also be explained in the context of a mantle plume as an enrichment agent, since enriched MORB basalts are attributed to a DM source interacting with plume material (e.g., Schilling et al., 1985).

In conclusion, the non-plume model did not generate such a suitable fit for HT magmas, but it seems to work well for LT. The lithospheric/crustal contribution in the latter case could have occurred *en route* to the shallower crust. As previously seen, clinopyroxene cores showing deeper transcrustal crystallizing patterns in LT magmas, may be additional evidence of AFC within the crust pile. Otherwise, crustal contribution would have occurred within mantle environment, due to previous subduction events related to Precambrian orogenies that may strongly affect the mantle wedges in the West Gondwana supercontinent.

6.6.4.2. Plume Test

Despite not being consensual, some plate reconstruction models indicate that the location of the Ascension and St. Helena plumes at the Lower Cretaceous would have been beneath the region currently shared by the NE Brazil and African counterpart (e.g., Matthews et al., 2016; Zahirovic et al., 2016). The Ascension lavas have OIB-like trace element compositions (sample AI-66; Jicha et al., 2013) and Sr-Nd-Pb-Hf isotope ratios (GEOROC) plotting within the FOZO field as the defined by Stracke et al. (2005). St. Helena in turn is typically a HIMU-OIB hotspot, here represented by sample 149 for Sr-Nd-Pb isotopic ratios (Chaffey et al., 1989) and SH-86 for trace elements (Kawabata et al., 2011).

These chemical signatures are distinguished from the EM-like compositions of the RCM dikes, but it is found in a small set of olivine-bearing tholeiitic (diabase) dikes that sparsely outcrop to the south of the EW-RCM (Archanjo et al., 2000). Four samples collected from different dikes provided Sr-depleted and Nd-Pb radiogenic isotope ratios comparable with those of HIMU-FOZO (Hollanda et al., 2006; Ngonge et al., 2016a). Although not precisely dated, the supposed distribution of these dikes along an EW trend parallel to the main RCM leads these authors to establish a temporal correspondence between them.

Contemporaneous tholeiitic and alkaline transitional (G1-G2) basalts dated at Jurassic-

Early Cretaceous (147-106 Ma; Maluski et al., 1995) are also identified in the northern Benue Trough, the African counterpart of the RCM magmatism (Bellieni et al., 1992). For the African alkaline basalts, Coulon et al., 1996 proposed the involvement of a HIMU-type component (or a mixing between N-MORB and HIMU – St. Helena plume) based on a Pb-Sr isotope approach, while the SCLM was assumed as a source for the tholeiitic basalts.

Despite eventual effects of selective contamination variably shifting the isotope compositions, the geochemical data of the olivine-bearing dikes with the G1-G2 basalts indicate that these magmas can be originated from an interaction between a Pb-radiogenic source and a Sr-Nd enriched (lithospheric) component. Mixing between an OIB-FOZO endmember and SCLM-derived melts (sample TR-84) is shown in Figure 6.11. About 20-30% of SCLM melts in a dominant FOZO source explain the isotope compositions of the HT tholeiites constituting the RCM dikes (Fig. 6.11A-B-C-D), in agreement with Gibson et al. (2005) that argued that a FOZO-type plume interacting with old SCLM would generate EMI-type melts. A mixing of $FOZO_{80\%}SCLM_{20\%}$ melt with continental crust resembles LILEs and REE abundances akin to those observed in HT magmas (Fig. 6.11E).

Similar results can be achieved with a HIMU-OIB as a source. But trace element patterns of a $HIMU_{80\%}SCLM_{20\%}$ melt with some continental crust contribution resemble HT magmas just in terms of few LILEs (not shown). Such misfitting may be because a HIMU source would require additional contributions (plus lithosphere) to generate HT magmas. An indication of this is that most radiogenic Pb magmas of the EW-RCM and Benue (Ngonge et al., 2016a; Coulon et al., 1996): if they were derived from HIMU source, they would require c. 10-20% of a DMM component to generate FOZO-like signatures as those of Ascension plume (Fig. 6.11).

Another alternative in favor of a plume contribution includes thinking in a far-off mantle source. In this case, it is mandatory to consider the physical connection of plumbing systems to the north (EQUAMP) and south (those related to the PEMP) of the São Francisco craton, implying in understanding what would have been the mechanism to feed such large-scale area across the West Gondwana supercontinent. In this scenario, the concept of Large Low Shear-Velocity Province (LLSVP) interpreted at the base of the lower mantle (e.g., Torsvik et al., 2006) should be invoked. According to Homrighausen et al. (2019), the margins of LLSVPs (where the PEMP is centered) are geochemically featured by variable mixing proportions of the recycled subcontinental lithosphere, oceanic crust (representing the FOZO/PREMA component) and sediments (i.e., an enriched component), thus representing

sites favorable to generate EM-type magmas.

There is a good correlation between the present-day isotope compositions of Gough and those constrained for the SCLM beneath South America (according to Carlson et al., 1996; Araujo et al., 2001), as well as with our HT data (Fig. 6.11A-B-C-D). Similarly, RCM and Paraná high-Ti tholeiites have comparable geochemistry. Taking advantage of this geochemical correspondence and following Hoernle et al. (2015), who argued that LLSVP-derived (EMI-Gough) material was mixed with lithosphere to originate the Paraná lavas, we found that the EQUAMP HT would result from a negligible amount (<5%) of crustal contamination with primary magmas like the tholeiite SO233DR3-1 of those authors (Fig. 6.11). In terms of trace elements, HT magmas resemble the spectrum of Gough tholeiites (SO233DR3-1; Fig. 6.11F), but the hotspot derived melts tend to present slightly higher values in HFSE (Nb-Ta) combined with lower abundances of HREE which may be explained by lower degrees of melting (e.g., Jicha et al., 2013), once Gough plume has been progressively diminishing it potential of melting since the Early Cretaceous (Hoernle et al., 2015).

The ability of mantle plumes in feeding dike swarms with an extension of hundreds of kilometers is already reported in the literature and it can be taken as real examples of theoretical assumptions that show that magma can achieve long distances without freezing (e.g., Fialko and Rubin, 1999). Ernst and Baragar (1992) have shown by magnetic anisotropy susceptibility that magmas traveled along the fan-shaped Mackenzie dike swarm (1.3 Ga-old) for more than 2,000 km from its focal feeder zone. Even longer distances are proposed for the Ferrar LIP, where Leat (2008) based on the aeromagnetic trends and homogeneity of geochemical data proposed that lateral flows had spread from a single source for at least 4,000 km along the Antarctica-Australia rifted margin.

The massive set of dikes that characterizes the RCM swarm can be easily (and continually) traced on the field from the Equatorial Atlantic margin up to the northwest edge of the São Francisco Craton (Melo et al., 2022). From this point on, the magnetic anomalies assume an arcuate pattern until connect with a c. 850 km-long NNW-trending structure named Transminas dikes (Coelho and Chaves, 2017). The southern end of Transminas dikes consists of high-Ti tholeiites dated at 135–128 Ma (Rosset et al., 2007; Coelho and Chaves, 2017) with isotope geochemistry (e.g., $^{206}Pb/^{204}Pb$ 18.202-18.343; $^{207}Pb/^{204}Pb$ 15.563-15.593, $^{208}Pb/^{204}Pb$ 38.499-38.633; Marques et al., 2016) identical to that of the RCM dikes (Fig. 6.11C-D). Therefore, the physical continuity between these two mega-swarms is feasible and

must be considered in further geodynamical models on the evolution of the Early Cretaceous Atlantic Rift.

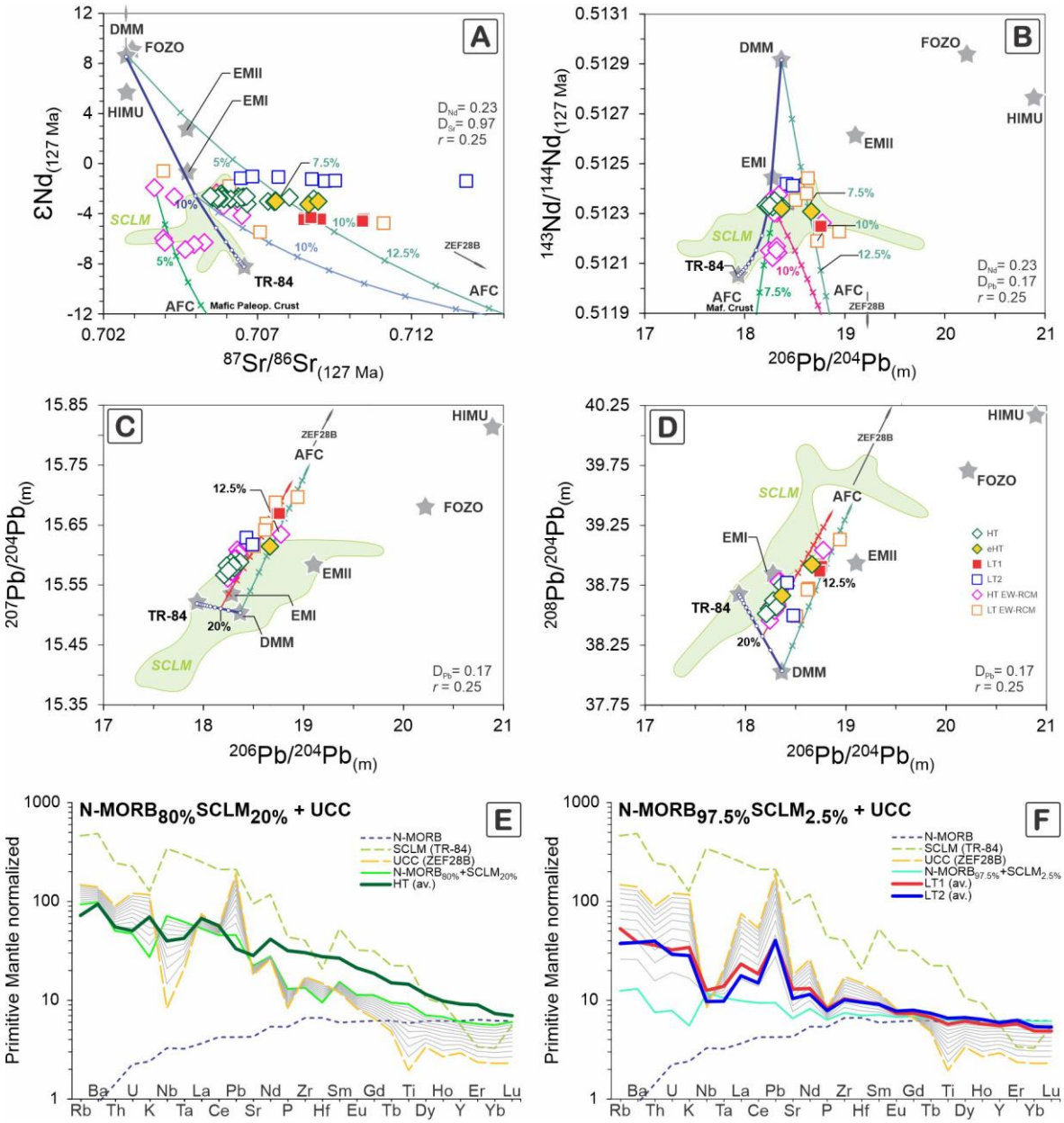

Figure 6.10. Mixing models on (A) $^{87}Sr/^{86}Sr_{(127)}$ *versus* $\varepsilon Nd_{(127)}$, (B) $Nd/Nd_{(127)}$ *versus* $^{206}Pb/^{204}Pb_{(m)}$, (C) $^{206}Pb/^{204}Pb_{(m)}$ *versus* $^{207}Pb/^{204}Pb_{(m)}$ and (D) $^{206}Pb/^{204}Pb_{(m)}$ *versus* $^{208}Pb/^{204}Pb_{(m)}$ considering a Depleted MORB Mantle (DMM) as primary source of magmatism (Strack et al., 2005) mixed with lithospheric mantle component represented by ultrakaline rocks (TR-84) of the Alto Paranaíba Magmatism (Green field; Araujo et al., 2001; Carlson et al., 1996). Each dot represents 10% of mixing. Assimilation paths adopt Precambrian components of the Borborema Province (Souza et al., 2016) and r-*values* (ratio of assimilated material to crystallized material) at 0.25, where each × represents 2.5% of assimilated material. The percentual values represent the amount of crustal component assimilated. Trace element mixing models are shown in (E) and (F). The gray lines represent 10% of mixing between two members. The values were normalized to primitive mantle of Sun and McDonough (1989). The centroid mantle endmembers are from Stracke et al. (2005). Further information about the members used in the models are given in Supplementary Material (Table A4).

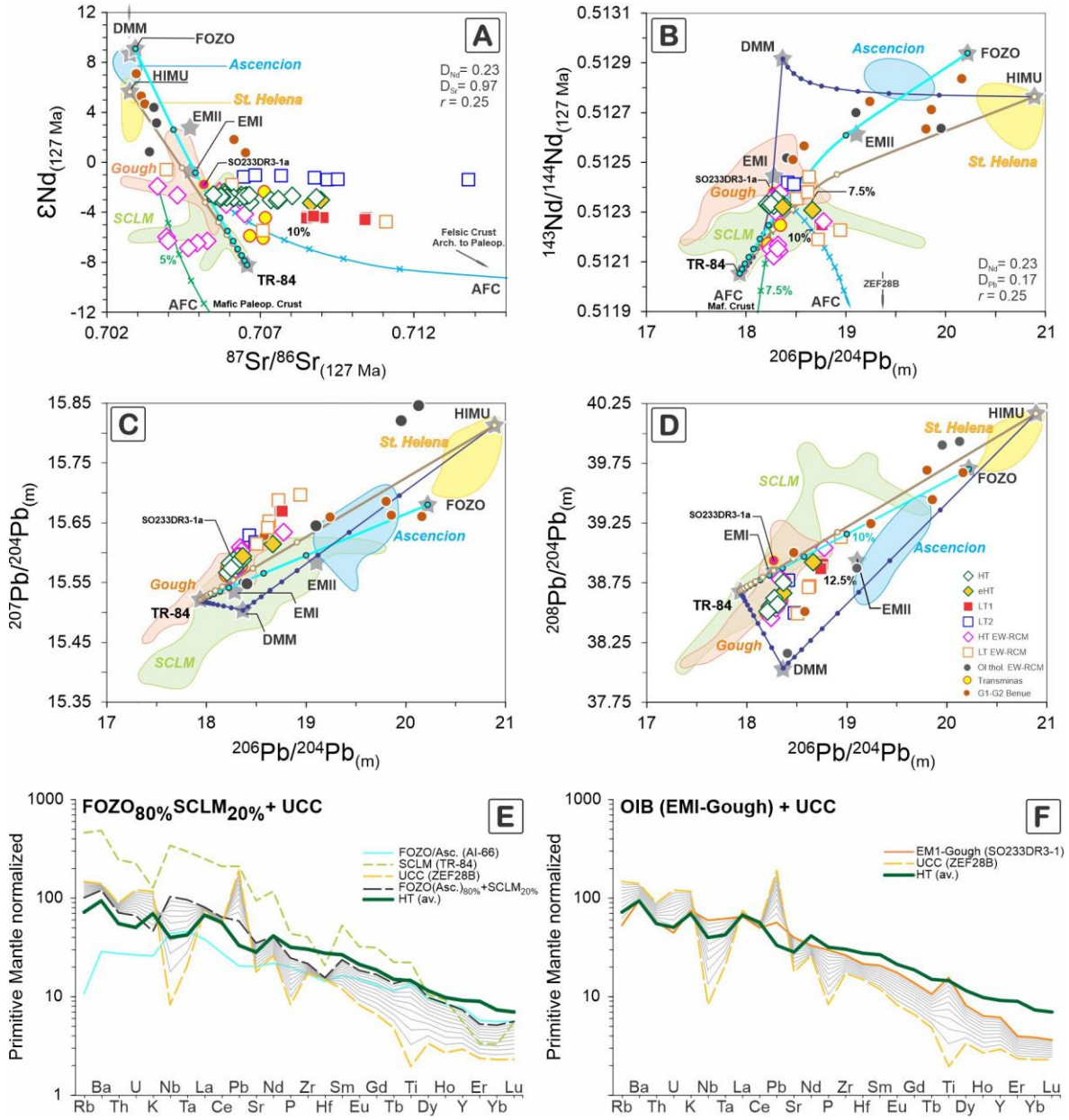

Figure 6.11. Mixing models on (A) $^{87}Sr/^{86}Sr_{(127)}$ *versus* $\varepsilon Nd_{(127)}$, (B) $Nd/Nd_{(127)}$ *versus* $^{206}Pb/^{204}Pb_{(m)}$, (C) $^{206}Pb/^{204}Pb_{(m)}$ *versus* $^{207}Pb/^{204}Pb_{(m)}$ and (D) $^{206}Pb/^{204}Pb_{(m)}$ *versus* $^{208}Pb/^{204}Pb_{(m)}$ considering FOZO member mantle as the primary source of magmatism mixed with subcontinental lithospheric mantle (SCLM) component represented by ultrakaline rocks of Alto Paranaíba (Green field; Araujo et al., 2001; Carlson et al., 1996). The EM-1 dataset of the Gough-Walvis Ridge (Hoernle et al., 2015), Ascension (GEOROC) and St. Helena (Stracke et al., 2005) are represented as orange, blue and yellow fields, respectively. Assimilation paths adopt Precambrian components of the Borborema Province (Souza et al., 2016) and r-*values* (ratio of assimilated material to crystallized material) at 0.25, where each × represents 2.5% of assimilated material. Trace element mixing models are shown in (E) and (F). The gray lines represent 10% of mixing between two members. Trace elements were normalized to primitive mantle of Sun and McDonough (1989). The centroid mantle endmembers are from Stracke et al. (2005). Further information about the members used in the models are given in Supplementary Material (Table A4).

6.7. Conclusions

Our geochemical data of the NE-RCM and Canindé dike swarms, integrated with those available for the EW-RCM, allowed us to make the following brief comments.

(1) The RCM and Canindé dikes consist of three geochemical groups. High-Ti (HT) tholeiites (higher in incompatible element contents) are prevalent in the RCM and Canindé swarms, eventually exhibiting intermediate (andesites and dacite) compositions denoting the strong influence of fractional crystallization. Low-Ti (LT) tholeiites (lower in incompatible element contents) form two well-defined clusters based on their major and trace element, as well as isotope compositions: LT1 and LT2. LT1 is characterized by Ca depletion and Al enrichment, and less radiogenic Nd isotope ratios; in the LT2, in turn, both CaO and Al_2O_3 decrease with fractionation, and they have more radiogenic Nd isotope compositions.

(2) The RCM-Canindé plumbing system is characterized by a transcrustal crystallization history. Clinopyroxenes in the HT tholeiite group start to crystallize in shallow magma chambers likely forming as a result of the rifting processes, while those clinopyroxenes of the LT1 and LT2 groups record crystallization under higher P-T conditions.

(3) The geochemical data of both HT and LT1 tholeiites require the involvement of variable proportions of an enriched component that can be either the subcontinental metasomatized mantle itself (case of LT1) or a deep plume (case of HT). By assuming the involvement of a plume, Ascension-St. Helena and Tristan-Gough are likely candidates. Crustal contamination must have occurred to some extent.

(4) If a FOZO-type (Ascension) plume is involved, the role of the SCLM is required as a 'subordinate' component with proportions not greater than 30%. The SCLM is not (or negligibly) needed if an EM-Gough plume was involved.

(5) Even if the EM-Gough hotspot is considered as the source of HT magmas, few compositions reported in EW-RCM and Benue Rift still require the involvement of FOZO/HIMU component. It might suggest that northern (Ascencion-St. Helena) and southern (Tristan-Gough) hotspots played a role in the tectonomagmatic activity of South Atlantic rifting.

(6) Given the narrow similarity of RCM compositions with those reported for the EM-Gough type, and with the high-Ti magmas of Paraná LIP, a physical connection

between the northern and southern plumbing systems formed during Atlantic rifting must be considered.

6.8. Acknowledgments

A.A.M.F. thanks the São Paulo Research Foundation (FAPESP) and the Coordination for the Improvement of Higher Education Personnel (CAPES) for his PhD scholarships at the University of São Paulo (grants 2017/13130–0 and 1643026, respectively). M.H.B.M.H. thanks the National Council for Scientific and Technological Development (CNPq) for her research fellowship. We would like to thank Carlos J. Archanjo, Carlos R. Ávila, Daniel V.L. Santos, Alanny C.C. Melo and Alisson L. Oliveira for their help with the data collection. Odirney Silva is thanked for the assistance with part of geochemical sample preparation. This article is part of A.A.M.F's PhD dissertation and corresponds to contribution No. 6 for the EQUAMP project (FAPESP 2017/08429-9).

7. CRYSTAL SIZE DISTRIBUTION OF RIO CEARÁ-MIRIM DIKES AND CORRELATIONS WITH MAFIC INTRUSIONS OF THE PARNAÍBA BASIN

7.1. Introduction

Crystal Size Distribution (CSD) is a methodology based on the quantification of textures that provide information about the crystal growth rate, nucleation, and crystallization history of the magmas. This chapter deal with CSD aspects of the NE-trending segment of the Rio Ceará-Mirim dike swarm (RCM) combined with mineral chemistry information to investigate the crystallization history of dikes intruding Precambrian basement of Borborema Province. For further information about CSD data and mineral chemistry of sill complexes of the Parnaíba Basin, the reader is referred to the article "Mineral chemistry and crystal size distributions of mafic dikes and sills on the eastern border of the Parnaíba Basin, NE Brazil" transcribed in Chapter 4 and already published by the Journal of Volcanology and Geothermal Research (Macêdo Filho et al., 2019).

7.2. Geological Setting

The RCM intrudes prevalently the Borborema Province (Fig. 7.1), one of the largest crustal blocks (Archean to Proterozoic) that formed the West Gondwana Supercontinent because of the Brasiliano/Pan-African collision (Brito Neves et al., 2014). This province covers c. 436,000 km^2 in NE South America being limited by the Archean-Paleoproterozoic São Francisco craton and the Paleozoic Parnaíba Basin to the south and west, respectively, while its northern and eastern borders are bounded by the Atlantic Ocean.

The rifting of West Gondwana and initial drifting between South America and Africa took place in the Early Cretaceous, with progressive seafloor spreading onward into the Late Cretaceous (Granot and Dyment, 2015). Mafic magmatism was pervasive across the entire Atlantic Rift System. In that context, the RCM along with its volcanic equivalents in the Benue Trough (Nigeria and Cameroon) were emplaced when the rifting processes reached the area of the Equatorial Atlantic Ocean segment (e.g., Matos, 2000), peaking roughly between 150 and 100 Ma (e.g., Bellieni et al., 1992; Maluski et al., 1995).

In the present-day configuration, the RCM swarm initiates on the eastern Atlantic margin and extends approximately 400 km parallel to the equatorial coastline, close to longitude 39°

west; it dramatically changes to 225° azimuth in the Cariri-Potiguar Rift (Fig. 7.1). Following this NE azimuth, the RCM extends another 550-600 km, crossing the SE flank of the Parnaíba Basin, until it reaches the northwestern border of the São Francisco Craton (Hollanda et al., 2019; Oliveira et al., 2021; Melo et al., 2021, 2022). Some physical aspects of this arcuate, giant dike swarm are described by Hollanda et al. (2019), who proposed joining it with other minor swarms (Canindé and Riacho do Cordeiro) as well as mafic sills exposed in the eastern Parnaíba Basin (the Sardinha sills; Fodor et al., 1990; Baksi and Archibald, 1997) in a single magmatic province coined the Equatorial Atlatic Magmatic Province - EQUAMP. In this new LIP, only the dikes belonging to the E-W-trending branch of the RCM swarm and few sills sites in the Parnaíba Basin were investigated for their geological and petrological properties (Bellieni et al., 1992; Archanjo et al., 2000, 2002; Hollanda et al., 2006; Ngonge et al., 2016a). In contrast, the 600 km-long NE-trending RCM swarm and many sites of sills in southeastern areas of the Parnaíba Basin have never been studied for geochemistry, geochronology or simply by textural aspects. Therefore, we investigate the magma crystallization and solidification history of the RCM dikes combining crystal size distribution (CSD), mineral chemistry, whole-rock geochemistry and general geological information. Such information allowed to establish correlations with the mafic intrusions from the eastern side of the Parnaíba Basin, already studied by Macêdo Filho (2019) in a similar approach.

7.3. Sampling and Methods

Thirteen thin sections of different sites (Fig. 7.1) were studied for crystal size distribution following the methodology described in Macêdo Filho et al. (2019). Since pyroxene is often associated with plagioclase in ophitic/subophytic texture or can have opaque minerals as inclusions, which would lead to overestimation of the real size of individual crystals, the CSD analysis was only applied to plagioclase crystals in the dikes. Furthermore, the co-existence of augite and pigeonite have different thermodynamic growth conditions (e.g, Krentz, 1982), which makes the use of pyroxene CSD unsuitable to understand the crystallization history of the dikes. Image capture of parts of the thin section, and a combination of them to form a .JPEG mosaic was performed on a Leica DN750P optical microscope operating with the Leica Application Suite software. The thresholds of the plagioclase crystals were manually checked using CorelDraw Graphics Suite X8, and refined by applying the SPO2003 software (Launeau, 2004), where lines of one pixel in width and aggregated of pixels smaller than 8 pixels were

removed. The resulting binary images were analyzed in the ImageJ 1.51J8 software (https://https://imagej.nih.gov/ij/) combined with the macro CSD_output for CSDcorrections v.1.6 software (Higgins, 2000). The CSD data were calculated after estimating the crystal (plagioclase) morphology (the short-intermediate-long axes) for each sample through the CSDslice5 spreadsheet of Morgan and Jerram (2006). In this procedure, we adopted a 'massive' rock fabric and a value of '0.1' for roundness as a priori assumptions.

The CSD results of plagioclase crystals are plotted in bivariant diagrams of population density (ln(n), mm^{-4}) *versus* size (L, mm), with plotting parameters are summarized in Table 7.1. The plagioclase populations considered for this study were preferentially those between 0.1 and 5 mm since finer crystal sizes tend to break the CSD curve down. The deficiency of finer plagioclase may be limited by the resolution of the device used to image acquisition or can be related to the Ostwald ripening when the smaller crystals are dissolved in the melt and incorporated in the larger crystals (Voorhees, 1992). Likewise, plagioclase grains that sometimes occupy the larger bins of the CSD distribution as single crystals and tend to distort the slope upward were removed from the CSD calculations. These "anomalously" large crystals may correspond to antecrysts with a nucleation and growth distinct from the groundmass (Cashman and Marsh, 1988).

7.4. Magma Types, Petrography, and Mineral Chemistry

The RCM dikes have a bimodal composition in terms of Ti content (TiO_2 threshold of 2 wt.%) with prevalent high-Ti tholeiites (HT), less frequent low-Ti tholeiites (LT), and intermediate composition rocks (see Chapter 6). These dikes are intrusive in a highly heterogeneous crust of the Borborema Province that consists of numerous basement complexes, metavolcanosedimentary fold belts and intermediate to felsic plutonic suites as indicated in regional geological maps of the Geological Survey of Brazil (CPRM). On the SE flank of Parnaíba Basin, the RCM crosscut sedimentary Paleozoic sequences, where they coexist with HT sill complexes (Macêdo Filho et al., 2019).

The RCM dikes are formed by plagioclase (± alkali feldspar), clinopyroxene (augite ± pigeonite), opaque minerals (Fe-Ti oxides), apatite, and rare olivine (usually pseudomorphs). The HT tholeiites are dominantly hypocrystalline, whereas the LT tholeiites are often holocrystalline with ophitic/subophidic textures. The modal composition depends on the crystallinity degree, but overall, plagioclase forms ca. 15–50% of the mode, followed by 10–

30% of clinopyroxene and ≤ 5% of opaque minerals plus other accessories. The crystalline or glassy, usually devitrified, matrix comprises less than 45% of the rock modal composition.

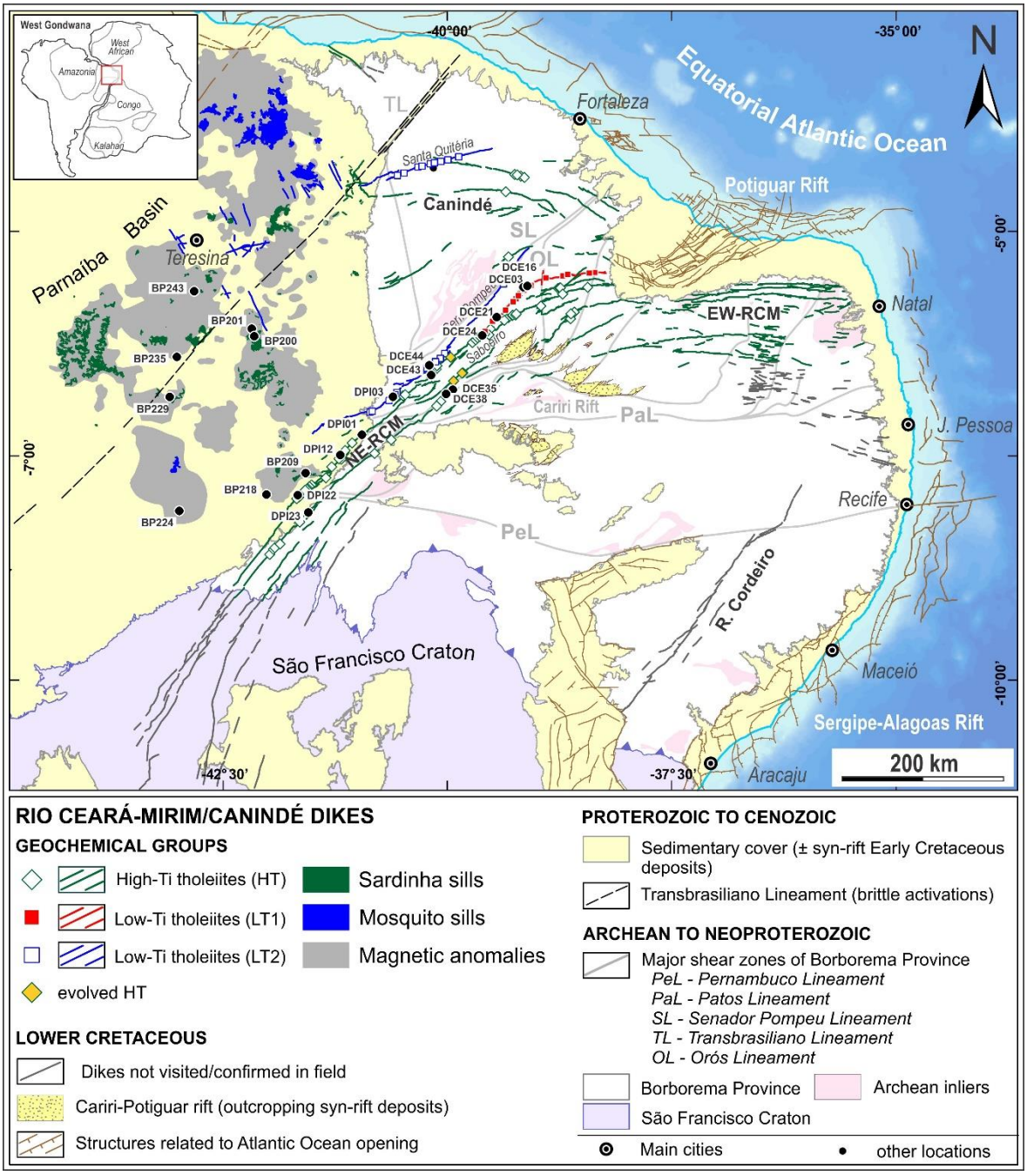

Figure 7.1. Regional map of dike swarms with sites investigated by CSD represented with respective labels. Information about geochemical group discrimination is given in previous chapters. Outcropping sills characterized by CSD (Macêdo Filho et al., 2019) are additionally represented.

Plagioclase macrocrysts are lath–shaped in hypocrystalline types to slightly equidimensional in holocrystalline diabases. Micrographic and subophitic textures are frequently observed in the holocrystalline tholeiites, while plagioclase laths are enclosed into

devitrified glass or clinopyroxene (subophidic texture) in the hypocrystalline types. Often, macrocryts contain groundmass inclusions, giving a sieve–textured to sponge–like aspect. In the matrix, plagioclase crystals have a chaotic orientation. Intermediate rocks have coarser plagioclase frequently fractured, likely composing antecrysts. Clinopyroxene forms prismatic crystals or glomerocrysts. Ophitic to subophitic textures is a feature in holocrystalline tholeiites, while augite glomerocrysts, in common association to opaque minerals and pigeonite, are frequently observed in holocrystalline types.

Mineral chemistry of plagioclase and clinopyroxene phenocrysts was examined along core-to-rim profiles, whereas the microlitic laths (≤ 0.5 mm) were analyzed as individual crystals or along short (2-3 points) profiles. The results from seven representative samples are summarized in Chapter 5. The variability in the Ca-Na compositions within the plagioclase phenocrysts and laths is essentially the same. Generally, plagioclase ranges largely in composition from bytownite An_{83} to oligoclase An_{18}, with a marked frequency at the labradorite-bytownite range (Fig. 7.2, 7.3A). The most primitive plagioclase (An >80%) compositions are found in the LT samples (DCE03, DCE44 and DPI03). Overall, zoning is normal (Fig. 7.3A, 7.4). In some of these crystals, the composition of the rim grades toward oligoclase $An_{13\text{-}12}$. Alkaline feldspars occur as finer crystals and mainly as overgrowths in plagioclase, where the compositions are albite ($Ab_{97\text{-}89}$) to high-K sanidine ($Or_{98\text{-}85}$) (Fig. 7.3A), but also occur as microlites. Alkaline feldspar occurs in four samples (DCE10, DCE32C, DCE33, and DCE12B) that were classified as HT diabases or associated with evolved (from HT) rocks of intermediate composition.

Augite (macro and microcrysts) has compositions that range between $En_{69}Wo_{8}Fs_{23}$ to $En_{18}Wo_{33}Fs_{49}$ (Fig. 7.2, 7.3B). This variation includes the entire set of compositions measured on macro and microcrysts. The geochemical pattern observed in RCM points to augite crystals enriched in Ti (TiO_2 > 0.7 wt.%) for HT tholeiites, while LT tholeiites present augite crystals with TiO_2 < 0.7 wt.% similar to that observed in sills of the Parnaíba Basin. The normal zoning is recorded by a Mg and Cr decrease accompanied by Ti and Mn increase attributed to an evolution in a closed system (Streck, 2008). Pigeonite ($En_{69.5\text{-}37.5}Wo_{8.5\text{-}11.5}Fs_{22\text{-}51}$) encapsulated by augite can be observed in holocrystalline diabases, although a late generation of smaller acicular crystals have been found in the rock matrix or surrounding augite crystals (Fig. 7.3B). Augite crystals are scarce in rocks of intermediate composition and, when present, often have sieve texture.

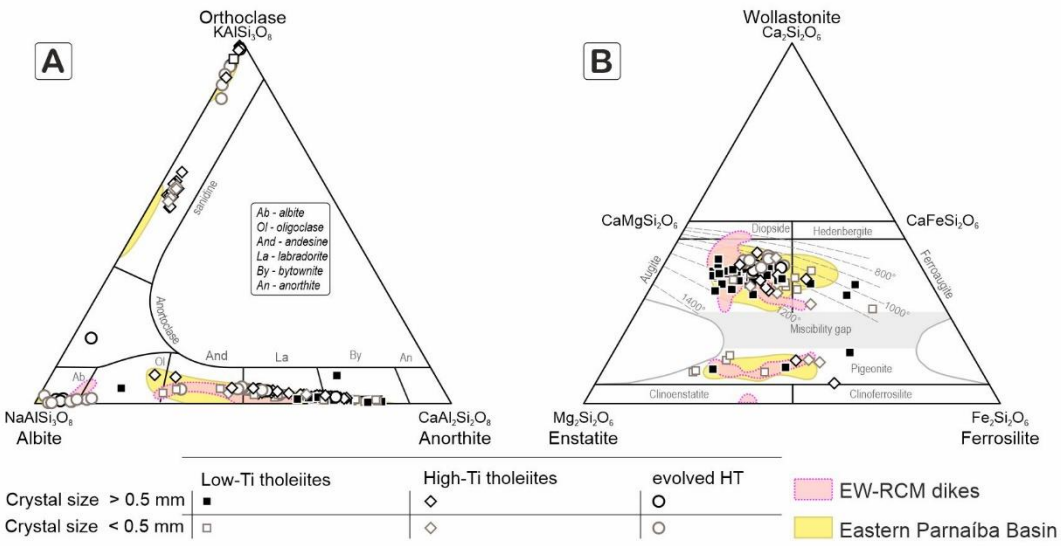

Figure 7.2. Chemical composition of feldspars and clinopyroxenes of NE-Rio Ceará-Mirim dike swarm, showing the compositional fields of intrusions of the eastern border of Parnaíba Basin (Macêdo Filho et al., 2019) and EW-Rio Ceará-Mirim dikes (Ngonge et al., 2016).

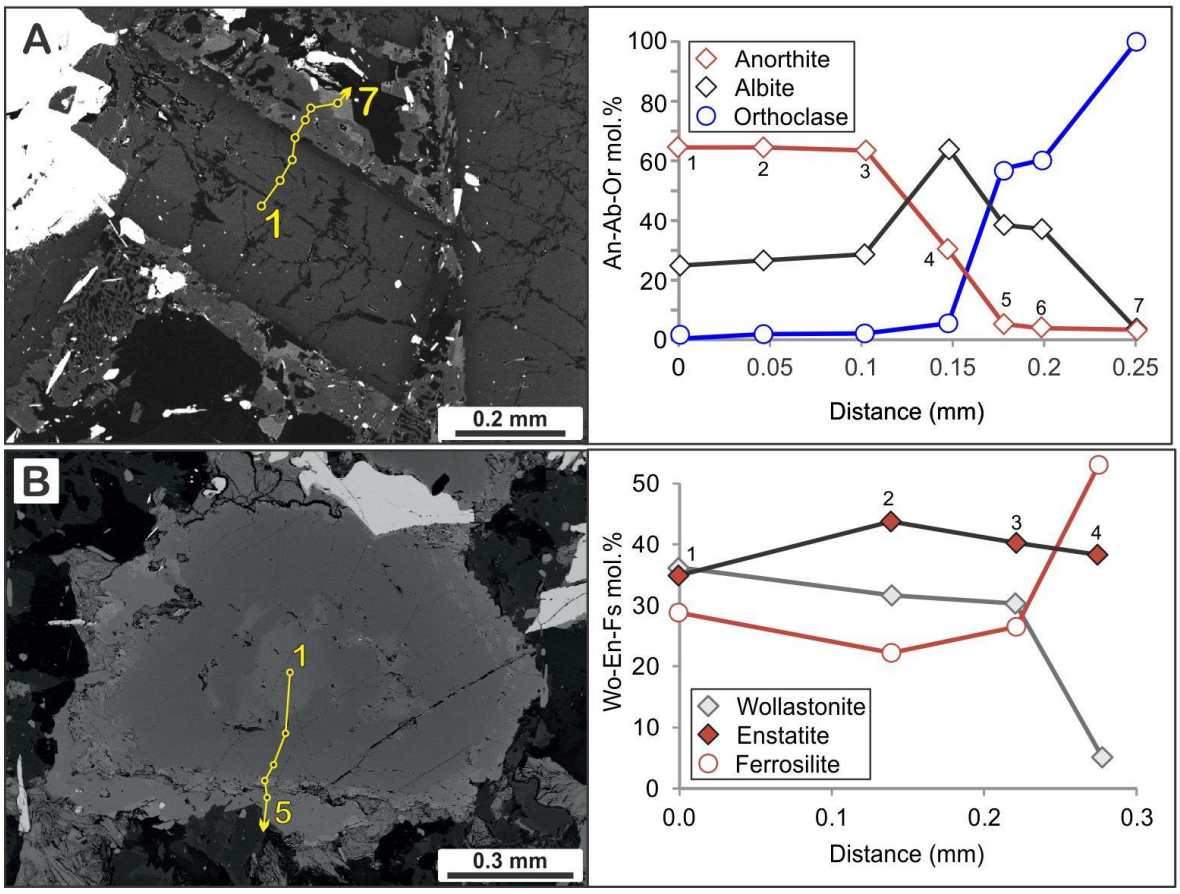

Figure 7.3. Textural aspects of plagioclase and clinopyroxene in NE-Rio Ceará-Mirim dikes. In (A) plagioclase showing normal zoning and rim of K-feldspar. In (B) Augite crystal with suggestive inverse zoning and pigeonite on the rims.

7.5. CSD Results

The results of CSD are plotted on a population density (ln(n), mm−4) and size (L, mm) diagrams (Fig. 7.4). Seven samples show log-linear slopes characterized by the goodness of fit above 0.01 (Higgins, 2006), whereas five samples record curved CSDs with the highest slopes towards the finer grain population and more gentle slopes towards the coarser grains (Table 7.1). The samples with well-defined log-linear distribution (DCE 21, DCE 38, DCE 44 and DPI3 and DPI22) were characterized by 455 to 634 crystals (av. 538 ± 50 grains) that compose from 16.2 to 41.8% (av. 30.1 ± 8.0%) of modal composition in diabases. The log-linear samples have mean size ranging from 0.22 to 1.48 mm (0.83 ± 0.38 mm), intercepts varying from 1.92 to 7.72 mm^{-4} (av. 4.13 ± 1.88 mm^{-4}), slope from -9.83 to -1.28 (av. -3.39 ± 2.77) and characteristic length from 0.1 to 0.78 mm (av. 0.45 ± 0.23 mm).

Curved CSDs are recorded in the samples DCE03, DCE16, DCE35, DPI01, DPI12, and DPI23 (Fig. 7.4) which were constrained by 468 to 613 crystals (av. 521 ± 49 grains). These samples have modal plagioclase from 22.8 to 47.3% (av. 35 ± 9.3%) which is slightly higher than values observed in log-linear diabases. The mean size in curved CSD range from 0.29 to 0.97 mm (av. 0.59 ± 0.2 mm), intercepts are from 2.75 to 5.8 mm^{-4} (4.05 ± 0.95 mm^{-4}), slopes range from -4.61 to -1.66 (-2.7 ± 0.9) for characteristic lengths between 0.21-0.60 mm (av. 0.41 ± 0.1 mm).

Table 7.1. CSD parameters for plagioclase of the RCM.

Sample	N	Mean size (mm)	Error	Intercept* (mm^{-4})	Error	Slope*	Error	Goodness of fit (Q)	Characteristic length (mm)	Plagioclase modal** (%)
Log-linear										
DCE21	525	0.77	0.10	2.69	0.10	-1.74	0.07	0.53	0.57	41.8
DCE24	547	0.72	0.08	3.20	0.09	-2.19	0.07	0.01	0.46	16.2
DCE38	634	1.48	0.15	1.92	0.10	-1.28	0.05	0.55	0.78	35.7
DCE43	515	0.48	0.05	4.70	0.10	-3.57	0.12	0.001	0.28	25.4
DCE44	539	1.06	0.12	2.99	0.10	-1.48	0.05	0.86	0.68	33.2
DPI03	455	0.73	0.07	5.66	0.15	-3.65	0.17	0.95	0.27	24.0
DPI22	554	0.22	0.02	7.72	0.12	-9.83	0.41	0.70	0.10	34.9
Curved										
DCE03	557	0.48	0.06	3.78	0.09	-2.73	0.09	<0.001	0.37	47.3
DCE16	613	0.71	0.09	2.75	0.08	-1.66	0.05	<<0.001	0.60	45.0
DCE35	516	0.46	0.06	3.47	0.08	-2.14	0.06	<<0.001	0.47	39.4
DPI01	483	0.97	0.09	4.53	0.14	-2.41	0.12	0.06	0.41	28.2
DPI12	468	0.29	0.04	5.80	0.09	-4.61	0.14	<<0.001	0.22	27.5
DPI23	492	0.60	0.06	3.97	0.09	-2.59	0.09	<0.001	0.39	22.8

N - number of grains. *Average values. **Modal composition corresponds to crystals with L > 0.2 mm.

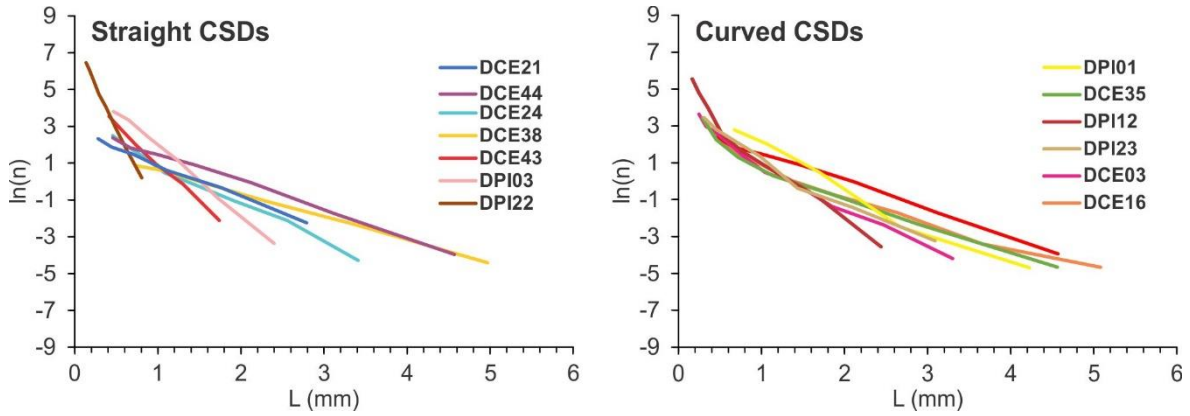

Figure 7.4. CSD of plagioclase obtained in the Rio Ceará-Mirim diabases, recording straight and curved patterns.

7.6. Discussion

7.6.1. Assessing textures and CSD of plagioclase

Compositional zoning in magmatic feldspars represents a potentially useful record of changes in the chemical and physical environment during crystallization. The plagioclase normal zoning usually reflects a progressively evolving composition of the melt during the solidification process, *i.e.*, fractional crystallization in a closed system. Nevertheless, oscillatory zoning observed in some crystals could be evidence of (1) slow growth rates (Shore and Fowler, 1996) that could be linked to crystallizing in the central portion of intrusions or (2) as a by-product of magma convection into the magmatic chambers (Elardo and Shearer, 2014).

The common presence of sieve texture in plagioclase crystals in hypocrystalline tholeiites and the graphic intergrow in holocrystalline tholeiites may be evidence of decompression at a shallow crustal level. Indirect evidence of geothermobarometer in clinopyroxene supports lower T-P crystallizing conditions to HT magmas in comparison to LT (Chapter 6). Moreover, alkali feldspars among microlites and or as phenocrysts shells suggest highly saturated alkali melts present at the late stage of crystallization (Macêdo Filho et al., 2019). These characteristics are found ubiquitously in the intermediate rocks and sometimes in the high–Ti tholeiites. A possible explanation for the presence of alkaline compositions related to the final stages of crystallization would be the phenomenon of silicate liquid immiscibility, where Ca, Mg, and Ti prefer a poorly polymerized (Fe-rich) melt, while K and Na prefer the highly polymerized (Si-rich) melt (Philpotts et al., 2017).

Similar CSDs have been recorded in plagioclase populations with grain sizes above 0.5 mm in the sills (Macêdo Filho et al., 2019). Log-linear CSDs are attributed to a simple crystallization history with plagioclase growing at uniform rates, where crystallinity would be associated with the undercooling rates, *i.e.* the holocrystalline texture is usually related to low undercooling whereas the hypocrystalline texture to high undercooling conditions (Higgins, 1998; Chakraborti et al., 2015). This is supported by the normal chemical fractionation of plagioclase in which cores of coarser crystals tend to present higher An contents than crystal rims and finer grains (Fig. 7.5).

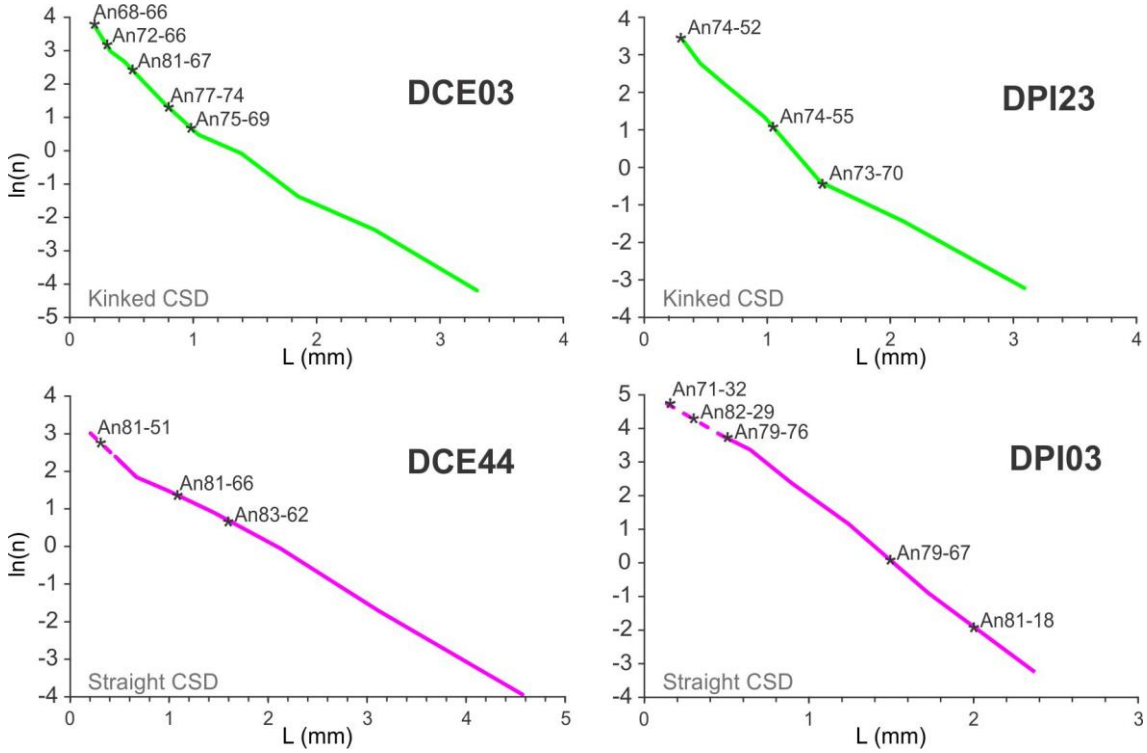

Figure 7.5. Examples of compositional range of plagioclase represented according to grain size in straight and curved CSDs.

Curved CSD indicate a more complex crystallization history that could result from (i) non-uniform crystal growth rates, (ii) blend of at least two crystal size populations, and/or (iii) fast nucleation of microliths at the final stages of magmatic crystallization (Marsh, 1988; Higgins, 1996). Assessing the regional distribution of CSD, it is possible to observe that the RCM dikes intruding along the edge of the Parnaíba Basin tend to exhibit curved patterns (DPI01, DPI12) or finer crystal size populations (DPI22), which may be an indicator of faster undercooling. The single evidence of magma mixing/mingling in our sampling is addressed to the site DCE35 (Fig. 7.4), where the curved CSD would be better explained by mixing distinct

plagioclase populations of HT tholeiitic magma (SiO_2 < 55 wt.%) and intermediate composition melts (SiO_2 > 57 wt.%).

In holocrystalline LT diabases, such as samples DCE03 and DCE16 (Fig. 7.4), the curved CSDs seem to be derived from more complex processes, since seven analysed plagioclase showed monotonous/normal zoning, which would suggest a simple crystallization history. Nonetheless, the samples DCE03 have few finer crystals at L ~ 0.4 mm with the highest An content (Fig. 7.5). Moreover, indirect evidence from augite antecrysts with anomalous high TiO_2 cores in a context of low TiO_2 augites indicates that part of the early crystals of pyroxene would have grown in a different compositional environment. This is an indication that inherited crystal populations would coexist in the holocrystalline diabase deforming the CSDs or it would be evidence of disturbance in the magma chamber (e.g., local recharge events).

Curved CSD patterns comparable to the RCM are reported in the Parnaíba Basin sills in which slopes of the straight segments become steeper towards the finer (< 0.5 mm) plagioclase grains. In both intrusive styles, curved/concave-up is preferentially recorded in the hypocrystalline diabases that are typified by fine intergrowths of alkali-sodic feldspar rimming coarser plagioclase crystals or even forming isolated microlitic crystals. Macêdo Filho et al. (2019) attributed concave-up CSDs to the disequilibrium between a late residual alkalic melt and an earlier solidified tholeiitic magmas. A similar phenomenon may have occurred in RCM dikes.

7.6.2. Correlations among RCM dikes and intrusions of the Parnaíba Basin

Figure 7.6 illustrates the CSDs of NE-RCM and Parnaíba Basin intrusions segmented into HT and LT tholeiites. The LT tholeiites generate straight or curved CSDs. Few specimens were sampled by boreholes in thicker sills from NE Parnaíba Basin (1UN samples) or massive first-order dikes of RCM swarm (e.g., DCE16). Some CSDs forming kinked patterns for L > 3 mm (e.g., 1UN32442, DCE16) may be additional evidence of accumulation of coarser plagioclase crystals. The HT tholeiites tend to exhibit straight CSDs, sometimes forming steeper curves for populations with L < 0.5 mm. This indicates that HT magmas experienced higher undercooling rates that were responsible for triggering an explosion of microlites populations, commonly seem in hypocrystalline textures.

In the Parnaíba Basin, a remarkable example of textural coarsening with granophyric textures, acicular spinifex-like augites and quartz as modal phase are observed in

trachyandesites from central portions of the Elesbão Veloso sill (e.g., BP201). On that area, fine-grained LT tholeiites (BP200; L < 3 mm) occur along with the contact with sedimentary sequences (Canindé Group) and are stratigraphically below the prevalent HT laccolith that coexists with intermediate composition rocks (Fig. 7.7). Such relationship suggests a major role of fractional crystallization in the center of magmatic chambers and/or storage of later evolved magmas on the rooftop of a laccolith where less dense melts (enriched in silica) and fluids (catalyst agent for textual coarsening) were supposedly stagnated. Similar textural features have been reported in the upper central zone of tholeiitic sill-like chambers of the Paraná Province (Lino and Vlach, 2021).

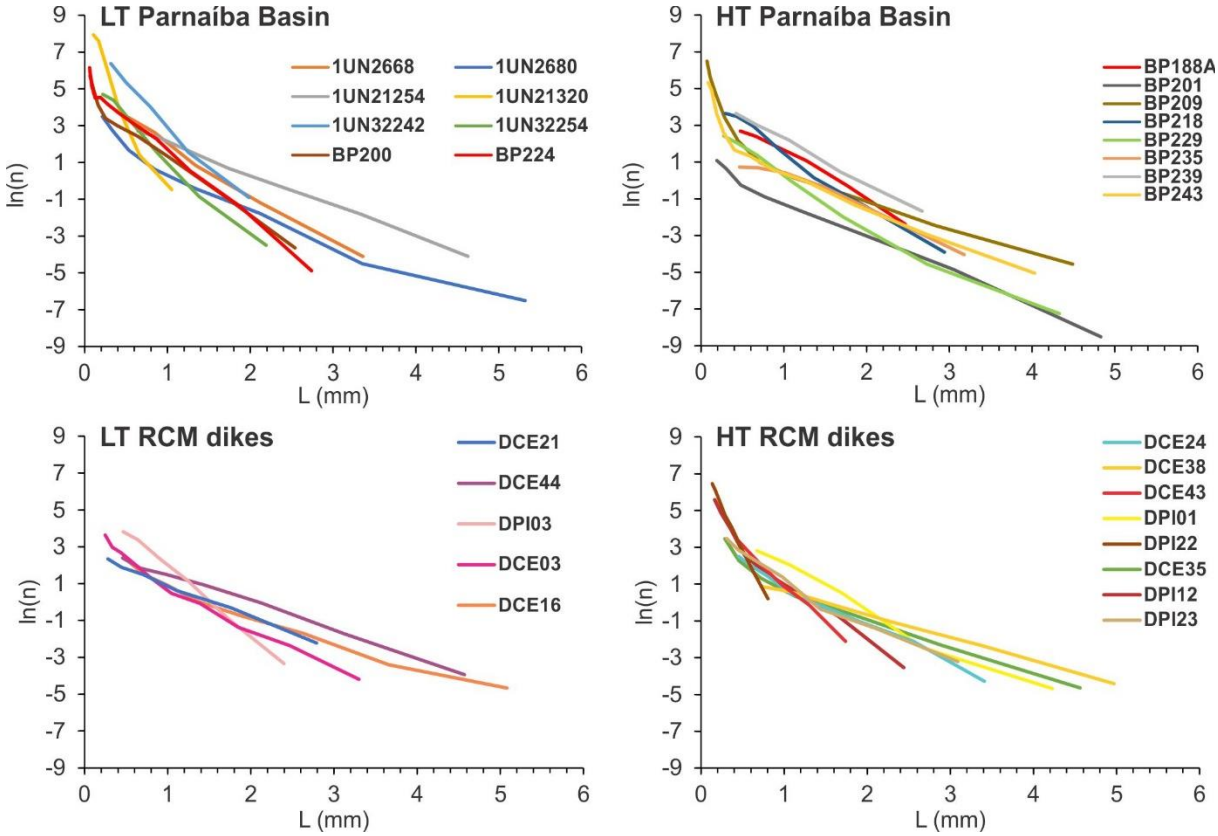

Figure 7.6. CSD comparisons among by high-Ti (HT) and low-Ti (LT) intrusions of the Parnaíba Basin and Rio Ceará-Mirim Dike Swarm (RCM). The samples BP224 (TiO_2 > 2wt.%) are shown with LT types because its high-MgO contents and holocrystalline texture. The trachyandesite BP201 is shown together with HT types. Unrepresentative populations of coarse-grained crystals were not regarded.

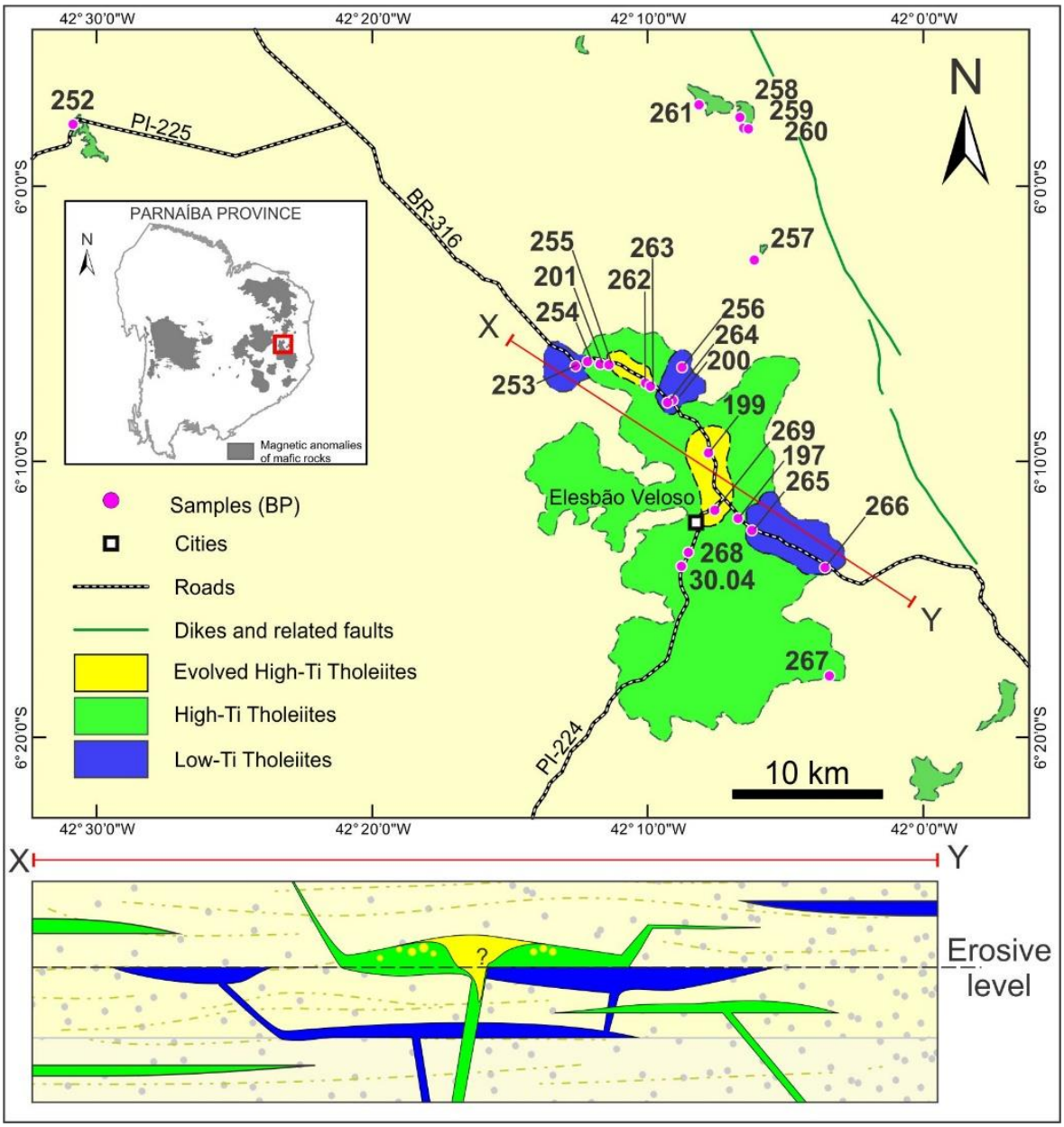

Figure 7.7. Distribution of magma types on the Elesbão Veloso area. Sampling sites are represented by magenta circles. The numbers with values from 197 and above have a BP prefix as shown in the supplementary material of Chapter 5. The schematic geological profile from X to Y represents the sill emplacement model. The evolved magmas (SiO_2 > 56%) are in the central part of the laccolite where the major role of differentiation and/or storage of less dense silicate melts might be predicted. The low-Ti tholeiites concentrate along with contact stratigraphically below to the prevalent HT chamber.

The similarities between dikes and sills are confirmed by mineral chemistry composition, whole-rock geochemistry, and isotopic data (chapters 5 and 6). The LT tholeiites (MgO > 6 wt.%) presenting low-incompatible elements content (e.g., 1UN samples and BP200) are commonly reported in NE Parnaíba Basin (Silva et al., 2017; de Castro et al., 2018; Oliveira et al., 2018; Heilbron et al., 2018; Macedo Filho et al., 2019; Miloski et al., 2019, 2020) sharing

similar composition and paleomagnetic data (Ernesto et al., 2003) to the Central Atlantic Magmatic Province (CAMP). The similarity is supported by geochronological investigations in Esperantina (~199 Ma; Sial et al., 1976), and Lagoa do São Francisco-Pedro II areas (~203 Ma; Rodrigues et al., 2015). The LT of southern Parnaíba Basin outcropping near Itaueira and HT tholeiites of Canto do Buriti villages (e.g., BP224; TiO_2 < 3 wt.%; MgO > 6 wt.%) were constrained on an interval of 189 Ma and 175 Ma (K-Ar; Sial et al., 1976), respectively, thus belonging to CAMP event.

In the Borborema Province, LT with high-MgO content, classified as LT2 type (e.g., DCE44, DPI03; Chapter 6) also present geochemical-isotopic similarities with the CAMP basalts. This information is supported by K-Ar ages clustering in the Juro-Triassic interval (Oliveira et al., 2021). On the other hand, LT tholeiites presenting MgO < 6 wt.% (LT1) such as the case of DCE03, DC16, DCE21 (Chapter 6) are magma types with suggestive Early Cretaceous age (Oliveira et al., 2021) restricted to the NE-RCM.

The HT tholeiites (MgO < 5 wt.%) classically ascribed to the Sardinha Magmatism have a major frequency of Early Cretaceous age (Sial et al., 1976, 1987; Fodor et al., 1990; Bellieni et al., 1990; Baksi and Archibald, 1997; Ernesto et al., 2003; Heilbron et al., 2018; Fernandes et al., 2020) and share geochemical-isotopic and textural similarities with RCM dikes (this thesis). Therefore, they are appropriately allocated within the Equatorial Atlantic LIP event.

In Figure 7.8 values of magnetic susceptibility (MS), TiO_2 content and K-Ar age indication of geochemical groups forming dike swarms in Borborema Province are plotted together with the dataset from Mosquito (CAMP) flood basalts and Sardinha (EQUAMP) sills. In the Parnaíba Basin, de Castro et al. (2018) observed direct correspondence between MS and composition of tholeiites, where LT basalts have MS overall < 25×10^{-3} SI (Mosquito basalts), whereas HT (Sardinha) diabases present MS usually > 25×10^{-3} SI. This general trend is also observed in magmas forming dikes swarms in the Borborema Province, where HT overlaps the field of Sardinha HT tholeiites. Even for low-Ti magmas such as the LT1 group (possibly Cretaceous age; Oliveira et al., 2021), the magnetic susceptibilities tend to exhibit values > 20×10^{-3} SI than those observed in the LT2 (e.g., Santa Quitéria dikes) and Jurassic-Triassic Mosquito basalts. According to Dunlop and Özdemir (1997), the MS of natural rocks depends on factors such as ferromagnetic mineral content, amount of Ti substitution for Fe, or oxidation of magnetic minerals. Therefore, the simple measurement of this parameter in fieldwork should be used as the first screening for different events or rocks compositions (high- *versus* low-Ti tholeiites).

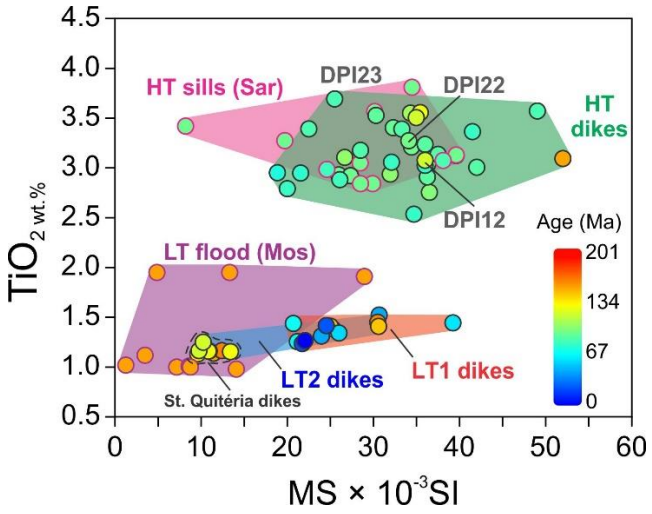

Figure 7.8. Relationship among magnetic susceptibility (MS), TiO_2 wt.% content, and K-Ar ages of Rio Ceará-Mirim dikes (Oliveira et al., 2021) according to geochemical groups discussed in chapters 5 and 6. Range of LT Mosquito basalts (dots with purple rims) and HT Sardinha sills (dots with magenta rims) are represented for comparison (de Castro et al., 2018). The MS measurements of Sardinha and Mosquito (CAMP) events were compiled from de Castro et al. (2018) and Mocitaiba et al. (2017) Ages of Mosquito and Sardinha events were considered at 201 Ma and 130 Ma (Merle et al., 2011; Baksi and Archibald, 1997), respectively. The highlighted samples DPI12, DPI22, and DPI23 were constrained by CSD.

Evaluating if RCM dikes are feeder agent of Sardinha sills can be better constrained in the region where the NE-RCM dikes crosscut the SE margin of Parnaíba Basin, near the Conceição do Canindé and Isaías Coelho villages (Figure 7.9A). The N45E-trending dikes of Conceição do Canindé (DPI01, DPI12B, DPI22) are intrusive in sandstones of the Serra Grande Group (Silurian age; Vaz et al., 2007) along ca. 200 km. These dikes host fine to medium-grained hypocrystalline HT diabases with curved CSDs that present K/Ar ages at Early Cretaceous (136 Ma; Sial, 1976; also Oliveira et al., 2021) and MS ca. 37 × 10^{-3} SI (see back Fig. 7.6). The Isaías Coelho sill (BP209, BP218), in turn, is hosted in shales and sandstones of the Cabeças and Pimenteiras formations (Canindé Group; Middle Devonian-Early Carboniferous age; Vaz et al., 2007) located ca. 5 km westward from the Conceição do Canindé dikes. The outcropping area of this sill is ca. 78 km², with but the bulk of magmatic rocks stored in the subsurface (> 2.500 km²), as indicated by the magnetic anomalies (Figure 7.9B).

The Isaias Coelho sill display fine to medium-grained hypocrystalline texture, HT compositions and CSD patterns of plagioclase concave-up (Macêdo Filho et al., 2019), where the K/Ar age is ca. 134 Ma (Sial, 1976), and values of MS are ca. 41 × 10^{-3} SI. Therefore, such evidence support that Parnaíba Basin sills and RCM dikes have similar composition, age, and crystallization histories. In this case, the geometry of intrusions seems to be purely controlled by the rheology of the host rock, since sandstones accommodate the deformation akin to the crystalline basement, enabling the formation of dikes, whereas sheets of shales interlayered with sandstones of the Canindé Group arrested magmas as sills.

Sedimentary Paleozoic units have been reported on the floor of many interior rift basins

in NE Brazil, as indicated by regional geological maps of the Brazilian Geological Survey (CPRM), where they remained protected from erosion. It is possible that at the Early Cretaceous, the sedimentary sequences of the Parnaíba Basin have covered a much larger area than the present-day boundaries. Thus, the RCM dikes could have feed sills within overlying sedimentary sequences where magmas flooded laterally (Fig. 7.9C). Even so, we do not exclude the additional possibility that non-outcropping dikes beneath the basin may have fed sills since magnetic anomalies (although weaker) seem to connect the RCM dikes to the sill complexes in the Isaías Coelho site.

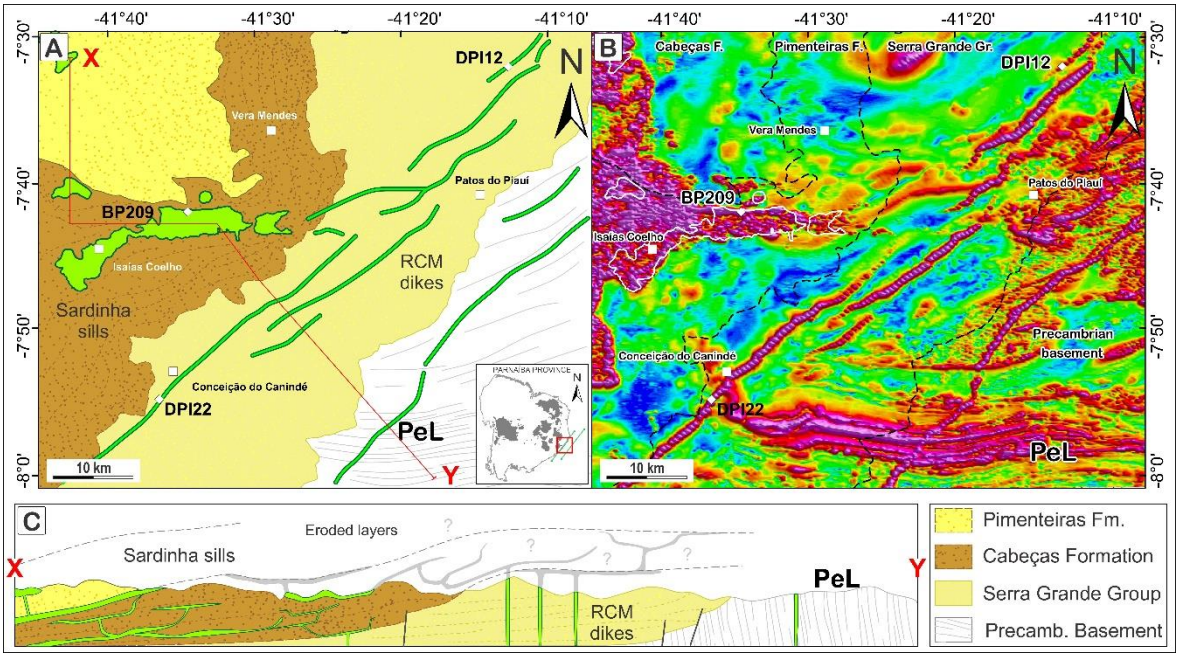

Figure 7.9. (A) Simplified geological map of the SE border of Parnaíba Basin, where the Rio Ceará-Mirim dikes crosscut the Silurian sandstones of the Serra Grande Group sandstones, while the Sardinha sills are hosted in the Pimenteiras and Cabeças formations (Canindé Group). The inset in represents the boundaries of the Parnaíba Basin with the location of the represented on the regional map (red square). (B) Analytic signal amplitude (ASA) of same area generated based on magnetic airborne data from the Brazilian Geological Survey (CPRM). The EW-oriented lineaments represent the Pernambuco shear zone (PeL) on the Precambrian Borborema Province. (C) Schematic geological section with possible sill feeding model from Rio Ceará-Mirim dikes. Magmas may have acquired lateral flow through the pelites-sandstones layers of the Canindé Group. The sills in shaded in gray constitute likely eroded bodies.

7.6.3. Crystallization timescales

Residence times of the interval between the aphyric mafic magma and the respective *solidus* can be estimated through the log-linear segment of the plagioclase CSD (Cashman and Marsh, 1988). If we assume that plagioclase from coarser diabase crystallizes at a slow growth

rate of about 10^{-8} mm·s^{-1} (e.g., Pupier et al., 2008), the residence times for RCM is between 2 and 2.5 years (e.g., DCE38, DCE44; Table 7.2). On the other hand, assuming similar crystallization histories for the coarser tholeiitic basalts emplaced in sedimentary strata of the Parnaíba Basin, residence times of sills returned values between 10 months and 1.5 years (samples BP235, BP209; Macêdo Filho et al., 2019).

The slightly longer residence times of the RCM may indicate that dikes would consist of deeper intrusions than the Parnaíba Basin sills, the former hosted in the basement of the basin. A deeper plumbing system, therefore, would have slower undercooling rates which, accordingly, leads to larger plagioclase grain sizes compared to those from the sills emplaced in the shallower crust. Fission track apatite data and numerical models support a remarkable regional uplift in the Borborema Province after the continental breakup (Sacek et al., 2019). Therefore, dikes intercepted by the present-day erosional level on the basement domain could be representatives of deeper sections in comparison to those intrusions hosted within overlying sequences of the Parnaíba Basin.

Table 7.2. Residence times of RCM calculated for representative populations of plagioclase with log-linear CSDs (goodness of fit - Q > 0.01).

Sample	Residence time (years)	
	Slow cooling (10^{-8}mm/s)	Rapid cooling (10^{-6}mm/s)
Log-linear		
DCE21	1.82	0.10
DCE38	2.48	0.14
DCE44	2.14	0.12
DPI03	0.87	0.05
DPI22	0.32	0.02

7.6.4. Thermal influence in the Parnaíba Basin

Temperatures reaching ca. 1250°C were estimated by pyroxene geothermometer in tholeiitic intrusions of the eastern Parnaíba Basin (Macêdo Filho et al., 2019). Considering residence time of plagioclase reach ca. 1.5 years and that tholeiitic magmas might be solidified at ca. 1100°C, we could estimate a loss of heat of mafic intrusions ca. 100°C/year in the initial stages of emplacement. However, thermal diffusion rates within sedimentary sequences could have been much lower over geological time. Models for saucer-shaped sills (5 km width and 100 m thick) showed that they cool down to approximately 200°C in 1.5×10^3 years,

accompanied by hydrothermal venting, gas releases, change of permeability, and porosity of host rocks (Iyer et al., 2013).

Mafic intrusions in sedimentary sequences containing high total organic carbon (TOC) can promote the generation of hydrocarbons and other greenhouse gases. For instance, sill complexes in Vøring and Møre and western Karoo basins were responsible for the generation of 2.2×10^3 and 1.3×10^3 Gt of methane, respectively (Aarnes et al., 2015; Iyer et al., 2013; Svensen et al., 2004; Svensen et al., 2007). In recent studies, Davies et al. (2017) and Heimdal et al. (2018) suggest that Juro–Triassic mass extinction event should be a consequence of gas releases (~88×10^3 Gt CO_2) related to thermal influence of CAMP sills over TOC-rich sedimentary units in the Paleozoic intracratonic basins (Amazonas and Solimões).in northern Brazil.

Geophysical data of the Parnaíba Basin indicate an area of sills totalizing ca. 85.4×10^3 km² on its eastern side (Mocitaiba et al., 2017; de Castro et al., 2018), where several intrusions are in contact with some sedimentary layers of the Pimenteiras Formation (TOC ~2–4%; Abelha et al., 2018). Consequently, such intrusions may have acted as catalysts for hydrocarbon generation (e.g., Daly et al. 2014; Miranda et al., 2018). However, we must stress that the Parnaíba Basin hosts not only CAMP flood basalts in the western, but its intrusive counterpart, also reported in the eastern areas. In that context, CAMP intrusions could have affected carbon-rich units of the Parnaíba Basin (together with Amazonas and Solimões basins) releasing greenhouse gases that triggered the Juro-Triassic global crisis. Hence, at the Early Cretaceous, the EQUAMP intrusions found a carbon-exhausted basin, where the volume of gases released was probably negligible for the generation of greenhouse effects. Rather, EQUAMP magmatism hosted in deeply eroded areas of NE of Brazil, together with the synchronous Paraná-Etedeka flood basalts, might have contributed to the (global cooling) Weissert event (e.g., Carvalheiro et al., 2021).

8. GEOCHEMICAL CORRELATIONS AMONG THOLEIITIC PLUMBING SYSTEMS OF SOUTH ATLANTIC-RELATED LIPs

8.1. Introduction

The breakup of continents and formation of new ocean basins is almost always associated with the formation of Large Igneous Provinces (LIP). LIPs are produced by massive magmatic events of predominantly mafic composition emplaced in pulses with brief duration (Coffin and Eldholm, 1994; Ernst, 2014). These geological entities were first defined for well-preserved Meso-Cenozoic flood basalts; however, in ancient LIPs or even for younger events hosted in areas strongly affected by erosion, many volcanic components are lost, and intrusive forms are therefore the only way of retrieving geological information (Ernst, 2014). These plumbing systems rather than lavas may offer major magmatic diversity and less evolved or altered rocks and giving direct information about magma ascent and emplacement (Owen-Smith et al., 2021).

In the Early Cretaceous, the West Gondwana Supercontinent was marked by a dramatic dispersal event, when the extensional tectonics of the South Atlantic Rift led to the formation of present-day South America and Africa (Matthews et al., 2016). The early stage of continental breakup started roughly before 134 Ma (Rocha et al., 2020) and was accompanied by the formation of the Paraná-Etendeka Magmatic Province (PEMP), which comprises bimodal volcanic rocks and related plumbing systems covering an area of approximately 1.5×10^6 km^2 in SE South America and central-southern Africa (Peate et al., 1992). Works concerning the geochemical/petrological characterization of the PEMP were published between the 1980s and 2000s, most focusing on continental flood basalts (CFBs) (e.g., Bellieni et al., 1984, 1986; Mantovani et al., 1985, 1988; Petrini et al., 1987; Piccirillo et al., 1988; Hawkesworth et al., 1988; Mantovani and Hawkesworth, 1990; Peate et al., 1992, 1999; Peate and Hawkesworth, 1996; Peate, 1997; Ewart et al., 1998, 2004; Marsh et al., 2001; Marques et al., 1999). In the past 20 years, the geochemical database of the PEMP has notably increased, not only for extrusive magmatism (e.g., Marsh et al., 2001; Ewart et al., 2004; Rocha-Júnior et al., 2012, 2013, 2020; De Min et al., 2018) but also for dike swarms and sills (e.g., Thompson et al., 2001; Trumbull et al. 2004, 2007; Santos et al., 2006; Rosset et al., 2007; Corval et al., 2008; Valente et al., 2009; BackeBerg et al., 2011; Keiding et al., 2011, 2013; Muzio et al., 2012, 2017; Almeida et al., 2013, 2021; Will et al., 2016; Marques et al., 2016, 2018; Guedes et al., 2016; Florisbal et al., 2018; Marsh and Swart, 2018; McMaster et al., 2019; Santiago et al., 2019;

Almeida et al., 2021; Owen-Smith et al., 2021).

Near the Equatorial (South) Atlantic margin, Early Cretaceous extensional tectonics led to the development of the northeast Brazilian Rift System, Benue Trough/Nigeria (Matos, 1992, 2000), and emplacement of mafic dike swarms and sill complexes that together represent the Equatorial Atlantic Magmatic Province (EQUAMP; Hollanda et al., 2019). The main elements of the EQUAMP, namely, the Rio Ceará-Mirim (RCM) dikes and Sardinha sills, have been studied since the 1990s (Fodor et al., 1990; Bellieni et al., 1990, 1992), but only recently has there been some increase in geochemistry-focused publications (Ernesto et al., 2003; Hollanda et al., 2006; Ngonge et al., 2016a; Oliveira et al., 2018; Heilbron et al., 2018; de Castro et al., 2018; Macêdo Filho et al., 2019, submitted).

The evaluation of geochemical databases and the determination of areal extent through geological cartography of igneous rocks are among the crucial parameters for LIP characterization (www.largeigneousprovinces.org/record). Analyzing massive amounts of data by classic methodologies, however, can be very laborious, depending on the complexity of the database. This limitation can be overcome by using (semi)automated methods such as Self-Organizing Maps (SOM; Kohonen, 1982). The SOM is a nontraditional unsupervised data analysis approach that treats each input sample as a vector in a data space defined by the input variables, then uses measures of vector similarity to find patterns and relationships between the vectors. This computational technique allows an integrated analysis of any multivariate spatial dataset with complex inputs; the method also improves the understanding of the subtle and intricate relationships between disparate datasets (Penn, 2005; Kohonen, 2013; Hodgkinson et al., 2013). The SOM have been extensively applied as an analytical (and visualization) tool for high-dimensional data and in exploratory data mining applications such as identifying correlation patterns and clustering analysis to determine anomalies or trends (e.g., Löhr et al., 2010; Friedel, 2011; Carneiro et al., 2012; Melo et al., 2021).

In this study, we explore SOM application to organize the EQUAMP and PEMP datasets, making use of major oxides and trace and rare earth elements combined with a qualitative revaluation of isotope data (Sr, Nd, and Pb); we investigate the general geological aspects of these provinces to process a complete characterization of mafic tholeiitic plumbing systems related to the early opening stage of South Atlantic Ocean.

8.2. The South Atlantic-related LIPs

The South Atlantic area portray diverse igneous manifestations including volcanic and intrusive products of the PEMP, alkaline carbonatites and kimberlites, the Rio Grande Rise-Walvis Ridge, and the Tristan archipelago and guyot track (Foulger, 2018). In NE Brazil and western/central Africa, the mafic igneous manifestations were firstly named (or genetically correlated) after the nearby Equatorial Atlantic Ocean (e.g., Maluski et al., 1995; Coulon et al., 1996; Marzoli et al., 2000; Segev, 2002). Recently, Hollanda et al. (2019) reviewed the available information about tholeiitic Early Cretaceous magmatism in NE Brazil, combined with an updated LIP classification, to propose the EQUAMP. Since the targets considered herein concern intrusive tholeiitic magmatism associated with the PEMP and EQUAMP, a brief overview of these provinces, their components, and geochemical-geochronological aspects is provided.

8.2.1. Paraná Magmatic Province

The magmatism in the Paraná Magmatic Province (PMP) is dominantly fissural with bimodal components, as observed on similar rifted continental margins (White and McKenzie, 1989). The CFBs, silicic volcanism, and intrusive bodies are spread in central–southern Brazil, northern Argentina, Uruguay, and eastern Paraguay (Peate et al., 1992). Flood basalts and sills are mainly reported in northern (e.g., Janasi et al., 2007; Rocha Júnior et al., 2013; Machado et al., 2015, 2018) and southern Paraná (intracratonic) Basin (e.g., Petersohn and Gouvea, 2009; Hartman et al., 2012, 2013; Sarmento et al., 2014, 2017; Santos Barreto et al., 2014, 2016; Ramo et al., 2016; De Min et al., 2018; Baggio et al., 2018), but also from 19° to 47° latitude adjacent to the South American continent as a volcanic rifted margin (Stica et al., 2014). CFBs and sills of the PMP were recently reported in the Parecis Basin (13°S, 54.5°W) (Rubert et al., 2019), augmenting its coverage inland toward central South America.

Geochronological data of CFBs of the Paraná, based on $^{40}Ar/^{39}Ar$ data, indicate age clustering within a 134–132 Ma interval (Gomes and Vasconcelos, 2021, for a review). This range overlaps with zircon U–Pb (sensitive high-resolution ion microprobe, SHRIMP) ages of c. 134 Ma obtained for bimodal volcanic rocks (e.g., Pinto et al., 2011; Hartmann et al., 2019) and with high-resolution geochronology (thermal ionization mass spectrometry, TIMS) ages of c. 133–134 Ma obtained on silicic lavas from northern Paraná Province (Janasi et al., 2011;

Rocha et al., 2020).

The results point to compositional zoning in the PMP (Bellieni et al., 1984, 1986), with low-Ti tholeiites (TiO_2 < 2 wt.%) more frequent in the southern portion (plus silicic magmatism; SiO_2 > 64 wt.%), while high-Ti tholeiites dominate in the northern domain (TiO_2 > 2 wt.%). In Paraná CFBs, Peate (1997) and Peate et al. (1992, 1999) recognized six tholeiitic groups (high-Ti/Y > 310: Urubici, Pitanga, Paranapanema, and Ribeira; and low-Ti/Y < 310: Esmeralda and Gramado) and two silicic volcanic/volcaniclastic suites (low-Ti dacite-rhyolitic Palmas type; high-Ti trachydacitic Chapeco type); these magma types were identified by analyzing numerous bivariate plots based on major oxide contents (SiO_2, TiO_2, P_2O_5, and Fe_2O_{3T}), trace elements (Sr, Ba, and Zr) and element ratios (Ti/Zr, Ti/Y, Zr/Y, Sr/Y, and Ba/Y).

The most prominent dike swarms of the PMP are found in the Falklands, Uruguay, Florianópolis, Ponta Grossa, eastern Paraguay, Resende–Ilha Grande, Serra do Mar, Southern Espírito Santo, Transminas, Vitória–Colatina and other less studied locales (e.g., West Bodoquena and Serra do Caiapó; Ernst and Buchan, 1997). All these swarms are composed of clinopyroxene, plagioclase, opaque minerals (Fe-Ti oxides and sulfides) and olivine (usually altered) as the main mineral phases, where high- and low-Ti tholeiites form the most common mafic types, with subordinate occurrences of silicic-trachyandesitic rocks. Further information about the location, structural trend, geochemical composition based on first-order Ti classification and geochronological aspects is provided in Table 8.1. The spatial distribution of all plumbing systems is illustrated in Figure 8.1, which presents the updated cartographic result of all the igneous manifestations related to the Equatorial/South Atlantic Ocean margin.

8.2.2. Etendeka Magmatic Province

The Etendeka Magmatic Province (EMP) comprises CFBs, sills, dikes, silicic volcanism, high-MgO basalt-picrite suites, and alkaline to tholeiitic ring complexes and offshore breakup volcanism occurring from the coast of South Africa to Gabon (Ewart et al., 2004; Fernandez et al., 2020). The main dike swarms (Fig. 8.1) are those at the False Bay, south of the Orange River systems (Saldanha Bay, Piketberg–Ceres, Cedarberg, Knersvlakte, Doring–Tanqua, Garies, Mehlberg, and Meob–Conception Bay; Trumbull et al., 2007), Henties Bay Outjo (HOD), the Skeleton Coast, SW Angola, and several swarms near the Atlantic margin not constrained by geochronology (Trumbull et al., 2004, 2007; Backeberg et al., 2011; Will et al., 2016; McMaster et al., 2019).

However, the geochronological results for the EMP have shown ages similar to those reported for the PMP, but some magmas on the African side yield a slightly older age of 135 Ma (Gomes and Vasconcelos, 2021 for a review). According to Marsh et al. (2001), the EMP may be subdivided into southern (dominantly low-Ti basalts) and northern domains (dominantly high-Ti basalts), with the E-W boundary at latitude 19°21.6′ S crossing Mowe Bay (Namibia). These authors point out that EMP has a larger variety of silicic and low-Ti mafic magmatism than that observed in South American examples, and is composed of 8 mafic groups including high-Ti (Khumib) tholeiites, low-Ti tholeiites (Tafelberg, Kuidas, Horingbaai, Huab, Taefelkop, Albin and Esmeralda), high-MgO basalts/picrites (MgO ≥ 13%), and 17 silicic magmas based on parameters such as major elements (e.g., SiO_2, TiO_2, P_2O_5, alkalis, and MgO), large ion lithophile element (LILEs) and high field strength element (HFSE) abundances (e.g., Zr, Sr, Rb, and Nb), element ratios (e.g., Zr/Y and Ti/Y), and isotopes (Sr-Nd). These magmas are also identified in sill and dike swarms of the Etendeka area; however, the dominant group is associated with low-Ti tholeiites (Table 8.1).

8.2.3. Equatorial Atlantic Magmatic Province

The main EQUAMP components are the RCM, Canindé, and Riacho do Cordeiro dike swarms and the Sardinha sills (and dikes) (Fig. 8.1). In the EQUAMP, previous geochemical classifications are extensively based on TiO_2 content (prevalent threshold ~2 wt.%) (Fodor et al., 1990; Bellieni et al., 1990, 1992; Ernesto et al., 2003; Hollanda et al., 2006, 2019; Ngonge et al., 2016a; Oliveira et al., 2018; Heilbron et al., 2018; de Castro et al., 2018; Macêdo Filho et al., 2019), trace element abundances (plus element ratios; e.g., Ti/Y and Ti/Zr) and isotopes (Sr-Nd-Pb) to distinguish dominant high- and low-Ti tholeiites and evolved rocks (Macêdo Filho et al., submitted). The reported $^{40}Ar/^{39}Ar$ ages of the RCM and Sardinha intrusions are between 126–132 Ma (Smith et al., 2001; Souza et al., 2003; Ngonge et al., 2016a) and 119–136 Ma (Baksi and Archibald, 1997; Heilbron et al., 2018; Fernandes et al., 2020), respectively (Table 8.1).

The RCM propagates toward the São Francisco Craton (Hollanda et al., 2019; Pessano et al., 2021; Melo et la., 2021, 2022; Oliveira et al., 2021) as far as Barreiras city (12°S, 44.9°W); this trend suggests lateral continuation with the Transminas dikes, which is also supported by geochemical-isotopic data (Macêdo Filho et al., submitted). This single plumbing system has a total length of at least 2,200 km and hence represents the largest dike swarm related to the South

Atlantic Ocean opening. The Riacho do Cordeiro is a coast-parallel strike swarm (N45°E) essentially composed of low-Ti tholeiites (TiO_2 < 2 wt.%; Dantas, 2021) showing K–Ar ages between 119 and 105 Ma (Misuzaki et al., 1991; Hollanda et al., 2019) and $^{39}Ar/^{40}Ar$ at ~132 Ma (Dantas, 2021), therefore supporting an Early Cretaceous derivation. The Riacho do Cordeiro is covered by rift sequences from the Tucano Basin; however, magnetic anomalies reappear near Araci town (11.3°S, 38.9°W) and propagate until to the surroundings of Amargosa (13°S, 39.3°W). Notwithstanding, approximately 180 km to the south, a couple of anomalies reappear; these anomalies mark the northernmost Vitória-Colatina dikes. Thus, we assume that Riacho do Cordeiro and Vitória-Colatina likely form a single plumbing system that is at least 1,600 km long and parallel to subparallel to the eastern coastline of South America in the adjacent segment.

The Benue Trough in Nigeria is the most magmatically active area of the west and central African Rift System (Wilson and Guiraud, 1992), where Early Cretaceous magmatism has been reported (e.g., Benkhelil et al., 1988; Guiraud and Maurin, 1991; Maluski et al., 1995; Coulon et al., 1996; Loule and Popsill, 2013). In Satellite images, mafic dike swarms can be mapped until the Plateau State in Central Nigeria. According to Maluski et al. (1995), the Mesozoic bimodal igneous activity of the Benue Rift erupted in the Tithonian–Aptian interval with $^{40}Ar/^{39}Ar$ ages between 123 and 147 Ma, with an additional younger pulse of Albian age (~106 Ma). Considering the area of occurrence of EQUAMP elements in NE Brazil and Nigeria, the total area in which remnants are present exceeds 1×10^6 km² on prebreak up maps. Unfortunately, the paucity of geochemical and geological information about Early Cretaceous tholeiites in the Nigeria region precludes accurate correlations between the two sides of the Equatorial Atlantic Ocean. Therefore, we do not further discuss west/central African magmatism in this work.

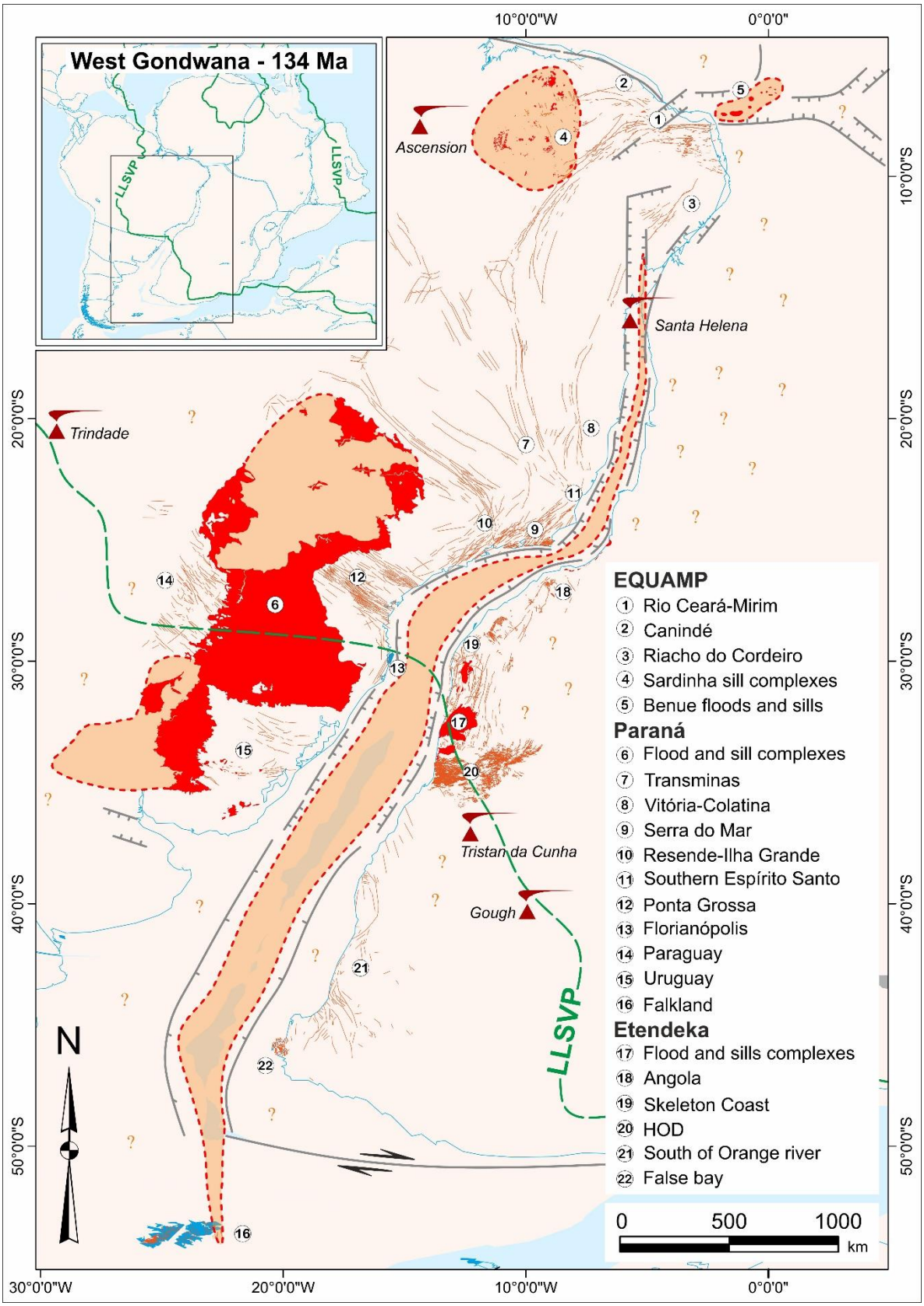

Figure 8.1. Predrift West Gondwana reconstruction, with focus on Early Cretaceous tholeiitic magmatism. The red dashed polygons represent regions hosting not crop out or offshore magmatism. The boundaries of African large low shear velocity provinces (LLSVP; Torvisk et al., 2006) are shown by green dashed lines. The reconstruction model at 134 Ma is fully illustrated in the inset (Matthews et al., 2016). Present-day South Atlantic hotspot locations and major structural features are indicated.

Table 8.1. Geochemical and geochronological synthesis of Paraná, Etendeka, and Equatorial Atlantic tholeiitic plumbing systems. Geochemical groups are classified according TiO_2 content and degree of fractionation as high-Ti tholeiites (HT; TiO_2 > ~2 wt.%), low-Ti tholeiites (LT; TiO_2 < ~2 wt.%) and evolved rocks (ER; SiO_2 > 56.5-63 wt.%).

Dike warms, sills, or flood basalts	Location	Geochemical groups	General orientation	Geochronology			
				Age (Ma)	Method	Analysed material	Source
Paraná							
Falkland DS	Eastern Falkland Islands	LT[1]	N05–15W	~135	$^{40}Ar/^{39}Ar$	plagioclase	Richards et al. (2013)
				121.3 ±1.2	$^{40}Ar/^{39}Ar$	plagioclase	Stone et al. (2008)
Uruguay DS	Central Uruguay	LT[2]	N45–75W	131.6 ± 1.3	$^{40}Ar/^{39}Ar$	–	Ures et al. (1997) apud Masquelin et al. (2009)
Florianópolis DS	Coastal area of Santa Catarina state (BR)	HT, LT, ER[3, 4]	N15–55E	129.4 ± 0.3	$^{40}Ar/^{39}Ar$	plagioclase	Deckart et al. (1998)
				119.0 ± 0.9 to 128.3±0.5	$^{40}Ar/^{39}Ar$	plagioclase	Raposo et al. (1998)
				134.1 ± 0.9	U–Pb, TIMS	zircon, baddeleyite	Florisbal et al. (2014)
Ponta Grossa DS	Paraná and southern São Paulo states (BR)	HT, LT, ER[5]	N60W	131.4 ± 0.4 to 129.2 ± 0.4	$^{40}Ar/^{39}Ar$	plagioclase	Renne et al. (1996a)
				133.9 ± 0.2 133.4 ± 0.2	U–Pb, TIMS	zircon, baddeleyite	Almeida et al. (2018)
Resende–Ilha Grande DS	Easten São Paulo state (BR)	HT[6]	N30W to N70–20W	156.5 ± 7.4 to 144 ± 3.2	$^{40}Ar/^{39}Ar$	Total whole rock (wt)	Guedes et al. (2016)
Serra do Mar DS	Rio de Janeiro state (BR)	HT, LT[7, 8, 9, 10, 11]	N30–50E	132.23 ± 0.6 to 132.1 ± 1.5	$^{40}Ar/^{39}Ar$	amphibole	Carvas (2016)
				131.4 ± 0.5 to 129.2 ± 0.4	$^{40}Ar/^{39}Ar$	plagioclase	Deckart et al. (1998)
				133.3–129.4	$^{40}Ar/^{39}Ar$	plagioclase, wt	Turner et al. (1994)
				130.2 ± 4.6 130.3 ± 2.9 135.9 ± 8.4 128.4 ± 6.5 122.4 ± 9.1 134.5 ± 1.7 110.0 ± 6.6 130.3 ± 1.6 120.4 ± 2.5 122.1 ± 3.5 116.7 ± 3.1 124.3 ± 0.8 120.6 ± 3.0	$^{40}Ar/^{39}Ar$	plagioclase	Almeida et al. (2021)
Southern Espírito Santo DS	Espirito Santo state (BR)	LT, HT[12]	N65W	141.9 ± 1.9	U–Pb, LA–ICP–MS	zircon	Santiago et al. (2019)
Transminas DS	Minas Gerais state (BR)	HT[13, 14]	N05–60W	135.72 ± 4.35 128.43 ± 8.46	$^{40}Ar/^{39}Ar$	plagioclase	Coelho and Chaves (2017)

				130.3 ± 0.6 129.8 ± 0.3	$^{40}Ar/^{39}Ar$	plagioclase	Rosset et al. (2007)
Vitória–Colatina DS	Espirito Santo and eastern Minas Gerais (BR)	LT[15]	N05–20W	134.92 ± 0.26 133.5 ± 0.40	$^{40}Ar/^{39}Ar$	plagioclase, wt	Belém (2015)
Etendeka							
False Bay DS	SW coast of South Africa	LT, HT[16, 17]	N40–70W	131.3 ± 1.3	$^{40}Ar/^{39}Ar$	plagioclase	Stewart et al. (1996)
Cedarberg DS	Africa-SW Namibia	LT[16]	N40–70W	–	–	–	–
Piketberg–Ceres DS			NS	–	–	–	–
Mehlberg DS			NS and N10W	134 ± 3	–	–	Reid and Rex (1994)
Meob–Conception Bay DS			NS	–	–	–	–
HOD DS	Namibia	LT, HT, ER[18, 19]	N40–70W and N30–70E	~125–130	$^{40}Ar/^{39}Ar$	plagioclase	Ewart et al. (1984)
HOD (Huab sills)	Namibia	LT[18, 19]	–	132.0 ± 0.7 Ma	$^{40}Ar/^{39}Ar$	plagioclase	Renne et al. (1996b)
Etendeka Gabbro	Namibia	LT[20]	–	130.5 ± 0.8	$^{40}Ar/^{39}Ar$	plagioclase	Kirstein et al. (2001)
Möwe Bay DS	Namibia-Angola	LT, HT, ER[21]	NS and N10W [a]	135.2 ± 0.7 130.5 ± 0.3 124.1 ± 0.8 113.0 ± 0.5	$^{40}Ar/^{39}Ar$	wt	Will et al. (2016)
Skeleton Coast DS	Namibia-Angola	LT, HT, ER[22, 23, 24]	NS and N10W; N25W	129.5 ± 1.5	$^{40}Ar/^{39}Ar$	plagioclase	Kirstein et al. (2001)
Kwanza basin basalts	Western Angola	HT, LT[25]	NS and N60–80W	126.1 ± 4	$^{40}Ar/^{39}Ar$	plagioclase	Marzoli et al. (1999a)
Bero Volcanic complex	SW Angola	LT, HT, ER[26]	-	-	-	-	-
Equatorial Atlantic							
Rio Ceará–Mirim DS	Rio Grande do Norte, Ceará, Piauí and Bahia (northern) states. BR	HT, LT, ER [27, 28, 29, 30]	E–W	130.9 ± 2.9 129.8 ± 1.8	$^{40}Ar/^{39}Ar$	amp, pyrite	Smith et al. (2001)
				132.2 ± 1.0	$^{40}Ar/^{39}Ar$	amp	Souza et al. (2003)
				126.9 ± 4	$^{40}Ar/^{39}Ar$	plagioclase	Ngonge et al. (2016)
			N45E	136	K–Ar	wt	Sial (1976)
				134–120	K–Ar	wt	Oliveira (1992)
Canindé DS	Ceará (BR)	HT [30]	N70E	–	–	–	–
Riacho do Cordeiro DS	Pernambuco, Alagoas, Sergipe and (NE) Bahia. (BR)	LT[31]	N35E	105.4 ± 9.5	K–Ar	wt	Misuzaki et al. (1991)
				119 ± 2	K–Ar	wt	Hollanda et al. (2019)
				~132	$^{40}Ar/^{39}Ar$	plagioclase	Dantas (2021)
Sardinha sill complexes (eastern Parnaíba Basin)	Piauí and eastern Maranhão (BR)	HT, ER[30, 32, 33, 34, 35, 36, 37]	–	~ 129–124	$^{40}Ar/^{39}Ar$	wt	Baksi and Archibald (1997)
				119.6 ± 0.8 128.0 ± 1.3 126.0 ± 2.7 128.8 ± 2.3 125.7 ± 2.7 128.3 ± 0.7 128.9 ± 1.3	$^{40}Ar/^{39}Ar$	plagioclase, wt	Heilbron et al. (2018)

				132.07 ± 0.43 136.86 ± 0.35 133.79 ± 0.30	$^{40}Ar/^{39}Ar$ (Isochrons age)	wt	Fernandes et al. (2020)
Benue bimodal volcanics	Nigeria	HT, LT[38]	–	106.0 ± 1.5 123.1 ± 1.6 146.7 ± 1.6 138.0 ± 1.8 130.7 ± 2.7 143.1 ± 1.5 137.8 ± 1.9	$^{40}Ar/^{39}Ar$	plagioclase, K-feldspar	Maluski et al. (1995)

Geochemical/geological information sources: Paraná: 1 - Stone et al. (2008); 2 - Muzio et al. (2012, 2017); 3 - Marques et al. (2018); 4 - Florisbal et al. (2018); 5 - Piccirillo et al. (1990); 6 - Guedes et al. (2016); 7 - Santos et al. (2006); 8 - Corval et al. (2008, 2009); 9 - Ngonge et al. (2013); 10 - Carvas (2016); 11 - Almeida et al. (2021); 12 - Santiago et al. (2019); 13 - Rosset et al. (2007); 14 - Marques et al. (2016); 15 - Valente et al. (2009). Etendeka: 16 - Trumbull et al. (2007); 17 - Backeberg et al. (2011); 18 - Trumbull et al. (2004); 19 - Ewart et al. (2004); 20 - Kirstein et al. (2001); 21 - Ewart et al. (1984); 22 - Will et al., 2016; 23 - Will and Frimmel et al. (2016); 24 - McMaster et al. (2019); 25 - Marzoli et al. (1999a); 26 - Marsh and Swart (2018). Equatorial Atlantic: 27 – Bellieni et al. (1992); 28 - Hollanda et al. (2003); 29 - Ngonge et al. (2016); 30 – Macêdo Filho (submitted); 31 – Dantas (2021); 32 – Fodor et al. (1990); 33 - Bellieni et al. (1990); 34 – Ernesto et al. (2003); 35 - Heilbron et al. (2018); 36 - Oliveira et al. (2018); 37 - Macêdo Filho et al., (2019). Benue: 38 – Coulon et al. (1996).

8.3. Material and Methods

8.3.1. Sample selection and screening

This work was developed based on whole-rock major oxides (SiO_2, Al_2O_3, Fe_2O_{3T}, MnO, MgO, CaO, Na_2O, K_2O, TiO_2, and P_2O_5), trace elements (V, Cr, Co, Ni, Cu, Pb, Zn, Rb, Sr, Cs, Y, Zr, Nb, Ba, Hf, Ta, Th, and U) and rare earth elements (REEs – La, Ce, Pr, Nd, Sm, Eu, Gd, Tb, Dy, Ho, Er, Tm, Yb, and Lu) from published literature clustering from 2004 to 2021 (Piccirilo et al., 1990; Renne et al., 1996; Zhou et al., 2000; Ewart et al., 2004; Trumbull et al., 2004, 2007; Janasi et al., 2007; Thompson et al., 2007; Machado et al., 2007; Corval, 2008; Corval et al., 2009; Valente et al., 2009; Petersohn and Gouvea, 2009; Renner, 2010; Backeberg, 2011; Hartmann et al., 2012; Keiding et al., 2011, 2013; Stone, 2013; Ngonge et al., 2013; Guedes et al., 2016; Will et al., 2016; Carvas, 2016; Muzio et al., 2017; Sarmento et al., 2017; Florisbal et al., 2018; Marques et al., 2018; Marsh et al., 2018; McMaster et al., 2019; Santiago et al., 2019; Owen-Smith et al., 2021; Almeida et al., 2021). The nature of compiled datasets includes X-ray fluorescence (XRF) for major oxide determination (and some trace elements in a few publications) and other more precise techniques, as such inductively coupled plasma (mass spectrometry (MS), atomic emission spectrometry (AES), optical emission spectrometry (OES), and emission spectrometry (ES)) and instrumental neutron activation analysis (INAA) for the determination of major oxides, trace elements and REEs.

Highly magnesian samples (MgO > 10.5 wt.%) are not considered in this study since picritic magmas are virtually absent in the EQUAMP and PMP. This filtering criteria also

eliminate samples potentially affected by ferromagnesian crystal accumulation. We reject potentially altered rocks by removing samples with loss on ignition (LOI) > 3.5 wt.% and correct all samples to a volatile-free basis. The contemporaneous silicic (SiO_2 > 65.5 wt.%) and alkaline magmas are also deleted from the database, first because they are virtually absent in the EQUAMP and, second because they are beyond the scope of tholeiitic magmatism. Nevertheless, we consider evolved rocks (SiO_2 = 57–65.5 wt.%) usually interpreted as fractional crystallization products from tholeiitic parental melts that are recognized in both areas. Outliers that are not explained in their original publications are also deleted. Moreover, as the EQUAMP is an exclusively intrusive LIP, we consider only data from dikes and sill complexes of the PEMP to make a proper comparison, adding up 956 samples (Supplementary material).

For data compilation in the EQUAMP, we integrate datasets of the EW-RCM (Hollanda et al. 2006; Ngonge et al., 2016a), NE-RCM, Canindé (Macêdo Filho et al., submitted) and Riacho do Cordeiro dike swarms (Dantas, 2021) because they apply the same sampling strategy and analytical protocols adopted in the EQUAMP Project. Similarly, Sardinha sills samples are available in the supplementary material of this work. We also integrate in the dataset other samples with high-Ti compositions available in Macêdo Filho et al. (2019), Heilbron et al. (2018) and Oliveira et al. (2018). Additionally, we considered six samples of Lower Cretaceous mafic rocks from northern Benue compiled from Coulon et al. (1996), but only to observe geochemical behavior and regional distribution of magma types.

The Mesozoic magmatic activity in NE Brazil encompasses an older, Jurassic event associated with CFBs and intrusions of the Central Atlantic Magmatic Province (CAMP) and Lower Cretaceous (EQUAMP) sills and dikes. Consequently, a mandatory step for validation of the EQUAMP database consists of recognizing and removing samples potentially belonging to the Central Atlantic LIP that can promote ‘noise’ in the EQUAMP dataset. The database was processed by a thorough revaluation and comparison of the overall geochemical and isotopic compositions with those from previous works published for the CAMP in NE Brazil (Fodor et al., 1990; Bellieni et al., 1992; De Min et al., 2003; Ernesto et al., 2003; Merle et al., 2011; Klein et al., 2013; Heilbron et al., 2018; Oliveira et al., 2018). This age provinciality screening is also supported by recent geochronological approaches in EQUAMP dike swarms (Oliveira et al., 2021). In summary, a total of 254 samples contributed to the geochemical characterization of the EQUAMP.

8.3.2. Self-Organizing Maps

The SOM approach uses both competitive and cooperative learning processes to train "seed vectors" to represent patterns within the data and eventually be represented as "nodes" on the self-organized map. The output of the process is typically a two-dimensional "map" that essentially represents the total input (nD) dataset, with similar samples represented as "nodes" on the map, and the nodes themselves ordered and positioned by their degree of similarity or dissimilarity to each other. Because of the vector quantization approach and the use of measures of vector similarity, SOM modeling may be used to examine populations that are both Gaussian and non-Gaussian in nature and sample–variable relationships that are linear and/or nonlinear. Hence, the SOM process resembles a neural network (Kohonen, 1982, 2001; Fraser and Dickson, 2007; Friedel, 2011).

This study used the SiroSOM© package (Version 2.20.20190411.121434), an advanced computation tool developed by the Commonwealth Scientific and Industrial Research Organization (CSIRO). Parameters considered as input to a SiroSOM© analysis (apart from the data) include the size of the map described by the number of nodes as rows down (X) and the number of nodes as columns across (Y), which also dictates the total number of nodes used (i.e., X*Y); the training length (number of iterations) for both the "rough" and "fine" cycles; and the shape of the search window with its initial and final sizes.

SiroSOM© offers analysis and "map" creation using either a rectangular (each node has 4 neighboring nodes) or hexagonal (each node has six neighboring nodes) lattice, with a sheet, cylinder or toroid as the projection surface to transform from multidimensional (nD) space to 2D space. For instance, in the case of a toroid, the final 2D surface map is a flat surface with continuity (wrap-around) between opposite edges on the 2D map representation.

One advantage of the SOM approach is that the output "self-organized map" data can be visualized, displayed or analyzed in many ways. The "unified distance matrix", or simply U-matrix (Ultsch and Vetter, 1994), is a particularly useful 2D display, as it allows one to visualize patterns, similarities, and differences between the nodes in terms of the Euclidian distances between the nodes. Hence, one can visualize and interpret the significance of natural domains or clusters within the dataset. Displaying the nodes using a color–temperature scale, for instance, blue representing closeness between adjacent nodes and red representing dissimilarity or distance, would further enhance the data visualization.

Component (plane) plots provide another 2D visualization of the "self-organized" map nodes that is particularly effective. These plots display, for each node, a plane or projection over the "map" that gives the contributions for any given variable (component) used in the analysis. Component (plane) plots can also be coded using a color–temperature scale, with blue nodes indicating a low contribution for a variable and red indicating a high contribution. Another useful SOM output that is calculated and recorded for each input sample is the quantization error, which is ideally less than one, and the smaller the value is, the better. This error represents a measure of the distance between a sample and its representative node–vector.

If the user has a large dataset, the quantitative analysis of such data can be more readily facilitated by k–means (Davies and Bouldin, 1979) clustering of the SOM nodes (Vesanto and Alhoniemi, 2000). The estimation of the best number of clusters is an unsupervised process calculated through the Davies–Bouldin criterion (Davies and Bouldin, 1979) and considers the best subdividing scheme for each number of clusters in terms of Euclidian distances within and between the proposed numbers of clusters.

The similarity index in SiroSOM© is based on a cross–plot visualization of the first and second components of principal component analysis (PCA; Christophersen and Hooper, 1992). To gauge the correlations between the components (variables), this process involves the calculation of a PCA and then the display of the individual component planes on a PC#1 *versus* PC#2 cross-plot (using their calculated eigenvalue contributions). On this similarity index plot, components (variables) that are positively correlated parameters tend to plot closer together on one side of the diagram, whereas inversely correlated components tend to plot on opposing sides of the axes (Löhr et al., 2010; García and González, 2004).

We must emphasize that the intention in SOM use is not to replace expert petrological knowledge or to challenge previous geochemical classifications that are well established in these provinces. Rather, we use this approach to make a data-intensive regional comparison, since in the SOM method, it is possible to attribute an equal weight to all variables, as similarly concluded by Owen-Smith et al. (2021).

8.3.3. Geological mapping

The mapping of EQUAMP and PEMP mafic rocks combines aeromagnetic data from the Geological Survey of Brazil (CPRM) and Bahia Mineral Research Company (CBPM), previous geological maps and Google Earth images.

Because dikes are spread in a continental-scale area, each aeromagnetic survey was processed individually. The geophysical data were previously corrected from diurnal variations and the International Geomagnetic Reference Field (IGRF). The processing routine was the same as that successfully used in part of the study area (de Castro et al., 2018; Melo et al., 2021, 2022). Geophysical processing started with a reduction to the magnetic pole (RTP) to correctly position the anomaly over its source. In addition, a pseudo-inclination was applied to stabilize the results of this filter, followed by the amplitude of the analytical signal (AAS) to highlight the edges of magmatic bodies and directional enhancement filters applied to highlight magnetic anomalies that constitute dikes.

The magnetic map interpretations were compared with previously published geologic maps (Geological Survey of Brazil) and high spatial-temporal resolution Google Earth images to improve the mapping of mafic dikes. Linear (high-amplitude) magnetic anomalies commonly reflect shear zones, dikes and regional faults. To sort out such ambiguities, we thoroughly assessed the anomalies, observing that dikes are represented on maps by strong positive and negative anomalies, with high amplitude in the AAS maps with well-marked orientations and are usually arranged in swarms that are parallel to subparallel, forming *en echelon* geometries and frequently crosscutting the regional fabric at high angles. On the other hand, shear zones are structures concordant with regional fabric, with magnetic anomalies wider than those of dikes. Last, regional faults may eventually stand out on magnetic maps, presenting a structural pattern similar to that of dikes, albeit fault anomaly patterns are discontinuous and more attenuated than those of both dikes and shear zones.

We additionally used GPlates 2.2.0 (https://www.gplates.org/) to manipulate plate reconstruction models and paleogeographic features of Early Cretaceous magmatism and South Atlantic-related hotspots through geological time. For this purpose, we assumed a stationary hotspot under a constantly moving plate. The result of all this cartographic work is shown in Figure 8.1.

8.4. Results

8.4.1. Classification of the geochemical dataset

In the total alkali-silica (TAS) classification diagram (Fig. 8.2), the high-Ti tholeiitic (HT) suite (TiO_2 > ~2 wt.%) of the EQUAMP and PEMP has SiO_2 < 56 wt.% and total alkalis ≤ 6.8

wt.%, plotting below the Miyashiro divisor (Miyashiro, 1978), with a few scattered samples above this limit due to higher alkali/silica ratios. Consequently, HT compositions indicate subalkaline basalts, basaltic andesites and basaltic trachyandesites. In the MgO *versus* TiO_2 diagram, the HT cluster above the line defined by the equation $TiO_2 = -0.1MgO + 3.3$ for samples with MgO > 4 wt.%. For samples with MgO < 4 wt.%, the ascendant curve $TiO_2 = 0.725MgO$ better separates the HT group from other suites. In the EQUAMP tholeiites, the Ti/Y parameter forms a continuous trend from 250–325 and overlaps among high- and low-Ti magmas. In the Etendeka, Marsh et al. (2001) also reported difficulties in using the Ti/Y discriminator of Peate et al. (1992). Even so, HT present high Ti/Y contents, usually above ~330, and are divided from other suites by the line defined by the equation $Ti/Zr = 0.4Ti/Y – 90$ in the Ti/Y *versus* Ti/Zr plot. Incompatible elements are abundant (e.g., Sr > 400 ppm), and La/Yb >10.

Evolved rocks (ER) have SiO_2 contents from 57–65 wt.%, with TiO_2 < 2.5 wt.%, and are mainly constrained within the trachyandesite-trachyte field in the TAS diagram. In the Ti/Y *versus* Ti/Zr diagram, the plot of ER is similar to that of low-Ti tholeiite (LT) magmas in terms of Ti/Y, but ER have lower Ti/Zr. In terms of incompatible elements and REE contents, ER are akin to HT magmas (e.g., Sr > 400 ppm; La/Yb > 10). The stark contrast between ER and HT is perfectly identified by the influence of low TiO_2 contents in conjunction with high incompatible element amounts, as expected for very fractionated rock types. Previous petrological work on the PEMP and EQUAMP interpreted ER as assimilation and fractional crystallization (AFC) products derived from HT magmas (e.g., Florisbal et al., 2018; Macêdo Filho et al., submitted).

The LT (TiO_2 < 2 wt.%) have lower alkali/silica ratios than HT rocks and are composed of subalkaline basalts and basaltic andesites with a smaller group in the andesite field of the TAS diagram in the case of PEMP. The LT present low TiO_2/MgO and they are thus arranged below the $TiO_2 = -0.1MgO + 2.5$ line in the MgO *versus* TiO_2 diagram for MgO > 3 wt.%. A particularity of PEMP magmas is basalts to basaltic andesites with transitional TiO_2 contents. Here, the transitional-TiO_2 tholeiites (TT) are those samples with TiO_2 from 2.7 to 1.7 wt.%. In the MgO *versus* TiO_2 diagram, TT differ from the dominant HT and LT groups because they tend to cluster within the area defined by the curves $TiO_2 = -0.1MgO + 3.3$ and $TiO_2 = -0.1MgO + 2.5$ (for MgO > 4 and 3 wt.%, respectively). However, in terms of incompatible element contents, TT are generally akin to the LT suites (i.e., Sr < 400 ppm; La/Yb < 10). In the EQUAMP, only a small number of samples plot within the TT field, but other geochemical

parameters, such as trace elements and REEs, show that the samples belong to either the HT or LT groups. The LT and TT suites tend to plot above the curve defined by the equation Ti/Zr = 0.4MgO – 90 in the Ti/Y *versus* Ti/Zr diagram, controlled by low incompatible element and REE contents. Notably, samples from False Bay and Saldanha Bay in the southern Etendeka province present a TiO_2 range of 3.6–2.2 wt.% but low incompatible element contents compared to those observed in the LT (Trumbull et al., 2007; Backeberg et al., 2011). The SOM results show that these samples are allocated with LT clusters and do not affect HT correlations between provinces.

In an exploratory step, we evaluated EQUAMP and PEMP dataset using Principal Component Analysis (PCA) considering the whole-rock dataset of major oxides, trace elements (V, Cr, Co, Ni, Cu, Pb, Zn, R, Sr, Cs, Y, Zr, Nb, Ba, Hf, Ta, Th, U) and REE to reduce the dimensionality of the dataset and minimize the information loss (Figure 8.3). The PCA for the EQUAMP targets only (Fig. 8.3A), where the HT make major contributions of Fe, Ti, P, Sr, HFSEs and REE. The ER from the RCM and Sardinha sills have a higher contribution of Si, alkalis (K and Na) and incompatible elements. The LT samples of the RCM and Riacho do Cordeiro dikes presented high correlation between then, plotting on the pole of samples depleted in trace elements. The correlation between these events is strongly confirmed by isotopic data validating the interpretation of Equatorial Atlantic units as a single LIP.

The broad HT-ER geochemical groups of EQUAMP are plotted together with the groups of the PEMP, where the convex hull of the EQUAMP is completely included in the PEMP range, which indicates analogous compositions for both domains (Fig. 8.3B). The LT samples of EQUAMP are generally evolved, therefore presenting plotting near the pole rich in Al-Si, but still, the convex hull is completely inserted in the compositional range of the PEMP (Fig. 8.3C). TTs presents a better correlation with the evolved LT group.

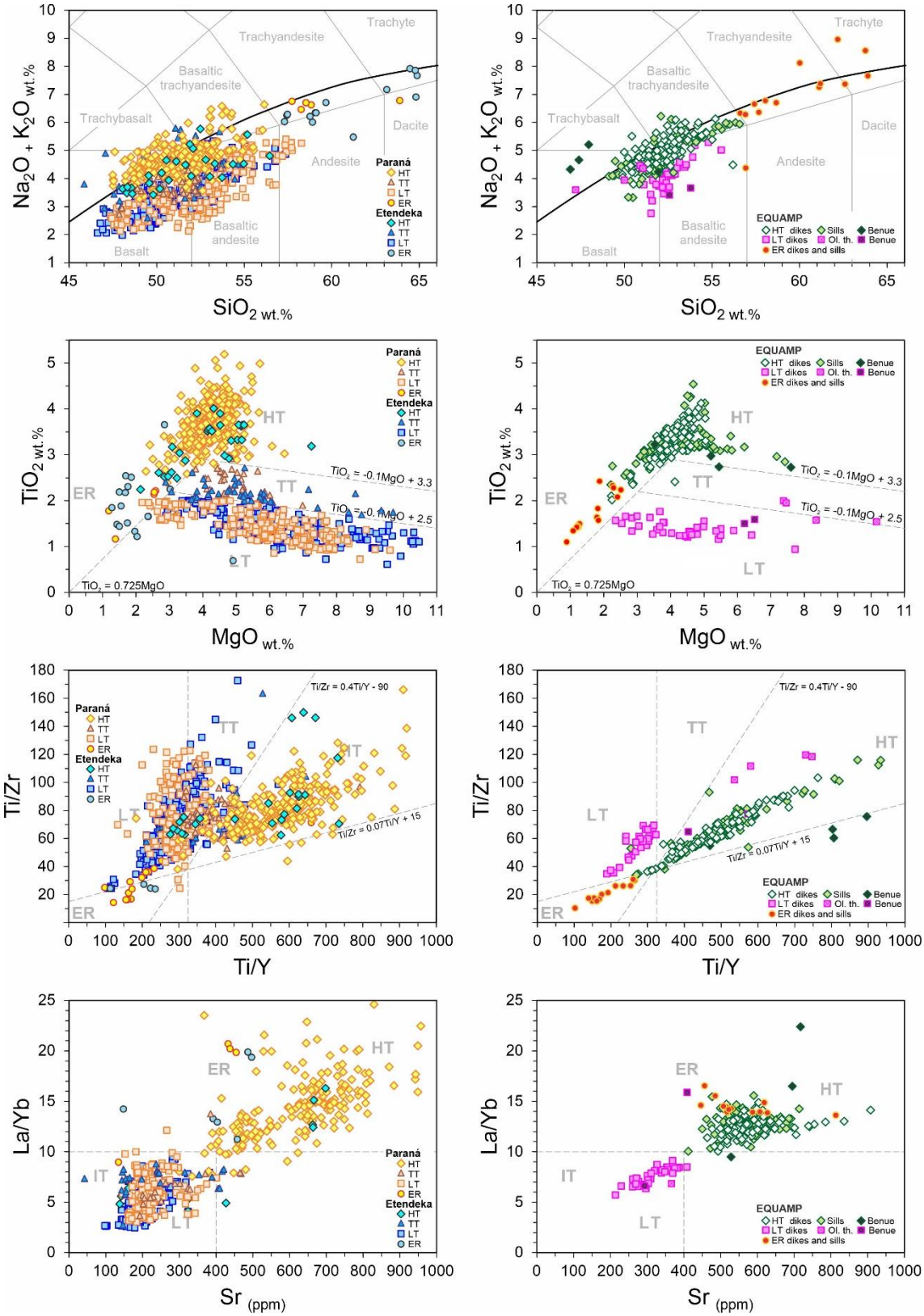

Figure 8.2. Geochemical dataset of intrusive rocks of the Paraná-Etendeka Magmatic Province (PEMP) and Equatorial Atlantic Magmatic Province (EQUAMP) used for SOM analysis. Samples are classified based on TiO_2 contents as high-Ti tholeiites (HT), transitional-Ti tholeiites (TT), and low-Ti tholeiites (LT). A minor population of evolved rocks (ER) is related to the evolution of mafic magmas by AFC processes. All bivariant plots consider LOI-free recalculation.

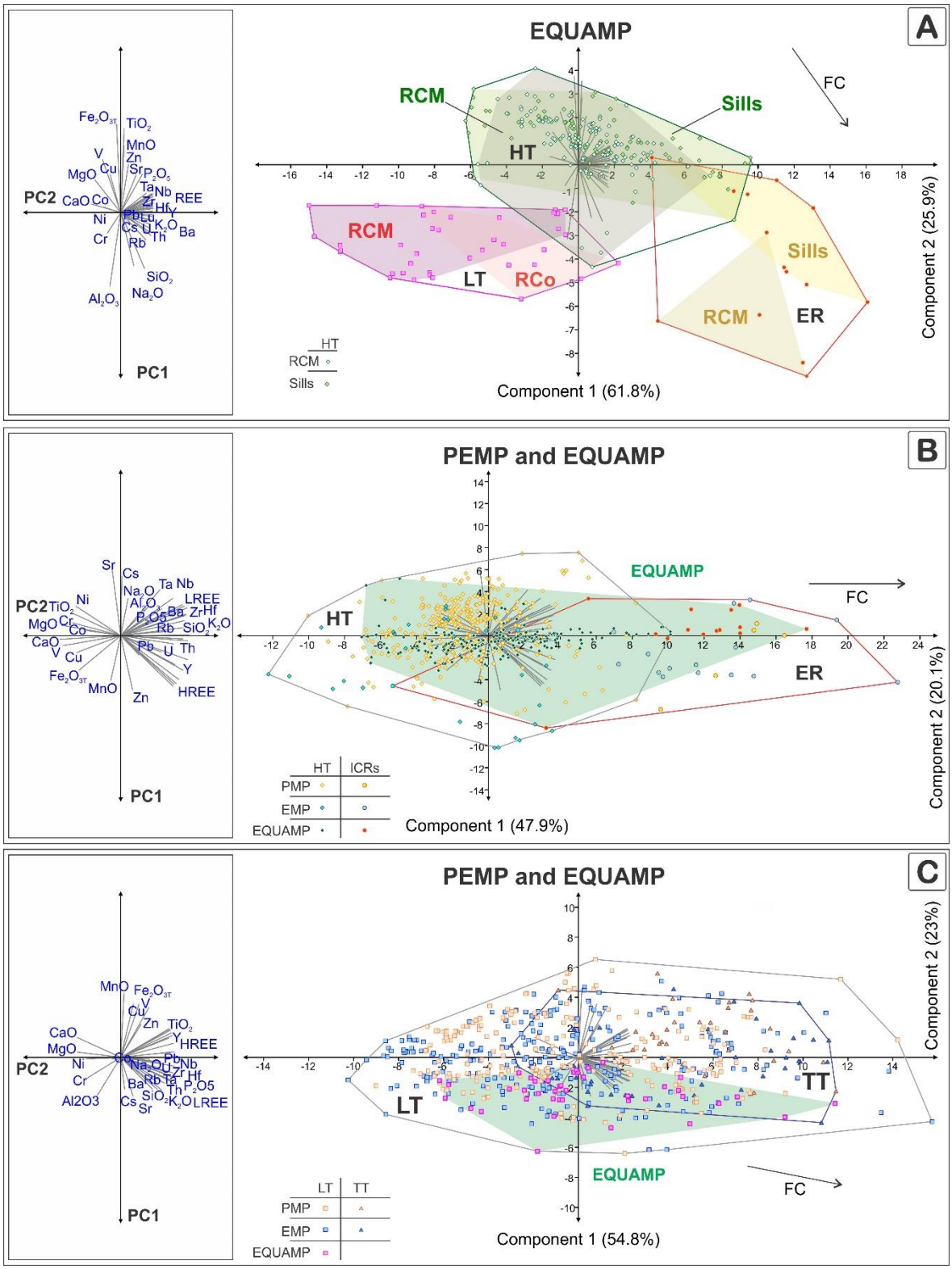

Figure 8.3. Principal component analysis (PCA) plots. (A) PCA applied to the EQUAMP dataset: RCM (Rio Ceará-Mirim dikes), RCo (Riacho do Cordeiro dikes), and Sardinha sills. The high-Ti tholeiites (HT) and evolved rocks (ER) of sills and dikes present comparable behavior, as similarly observed in low-Ti tholeiites (LT) of the RCM and RCo. (B) HT and ER for the combination of PEMP and EQUAMP rocks. (C) LT and TT from a combination of PEMP and EQUAMP rocks. Note that the EQUAMP convex hull is completely included in the convex hull of the PEMP.

8.4.2. SOM

In the processing of the PEMP and EQUAMP datasets on SiroSOM, we adopted an SOM map size of 58 (rows) × 52 (columns) with a total of 3,016 nodes. This map size was chosen to minimize the final quantization error and topologic error (both < 1). Unless indicated otherwise, the initialization (initiation, lattice, shape, and map size) and training parameters (neighbor, rough training, fine training, and errors) used for calculating the SOM computations reported in the studies in this chapter are listed in the Supplementary material.

8.4.2.1. Component (plane) Plots

Assessing the component plots of the PEMP and EQUAMP (Fig. 8.4), HT nodes have positive correlations with Fe_2O_3, P_2O_5, and to a lesser extent with SiO_2, Na_2O, K_2O, MnO, and incompatible elements (Sr, Rb, Zn, Y, Nb, Ba, Zr, Hf, U, Th, Ta and REEs) in a similar pattern, which is displayed by high P_2O_5 nodes. However, the latter P_2O_5 is better grouped with K_2O, Sr, Ba, Rb and REEs. The low-TiO_2 nodes are distributed between LT and ER. The LT reveal positive correlations with MgO, CaO, Al_2O_3, Cr, Co, Ni, and to a lesser extent with Y, V, Ni, Cr, Co, and Cu; meanwhile, ER are equivalent to high-SiO_2 nodes and positively correlated with Na_2O, K_2O, Rb, Y, Zr, Nb, Ba, Hf, Ta, Th and REEs.

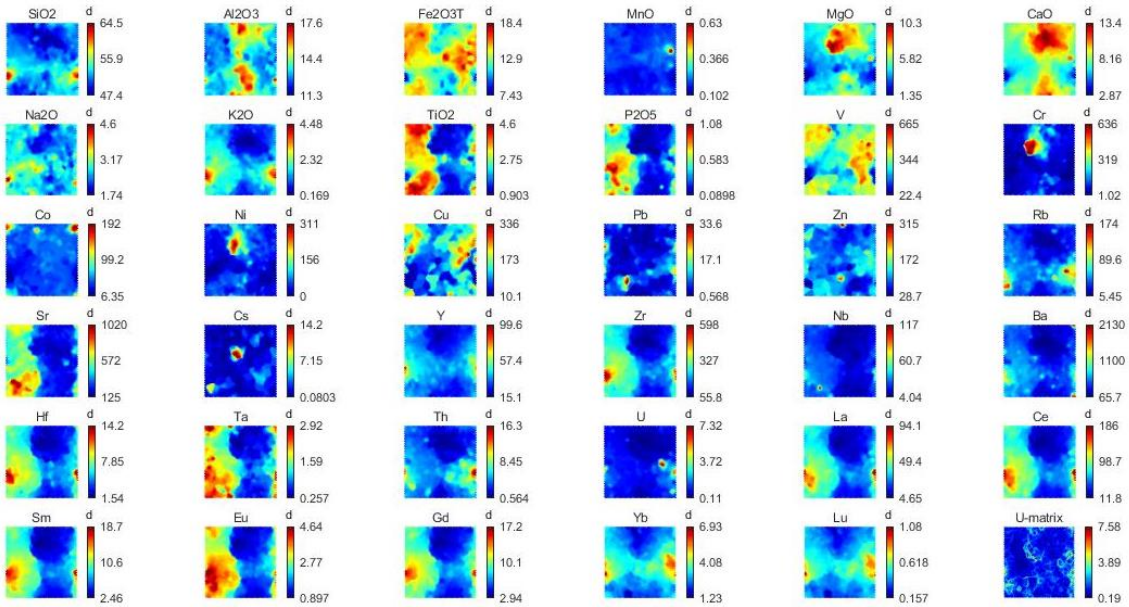

Figure 8.4. Component plane plots for major oxides (wt.%), trace elements, REEs and the U-matrix of the PEMP and EQUAMP magmas. The numbers next to the color bars represent the maximum, average, and minimum values for each geochemical parameter. Some REEs are not shown, but they present component plane plots similar to those of neighbors.

These observations are also supported by the similarity index based on PCA (PC1 *versus* PC2), where component plots of HFSEs, LILEs, and REEs have tight relationships with high-TiO_2 and high-SiO_2 nodes (Fig. 8.5). The heavy REEs (HREEs) are grouped with Y, whereas light REEs (LREEs) are positively correlated with Zr, Hf, Ba, and Nb. Parameters such as Fe_2O_{3T} remain in an intermediate PC position and plot on the side of the diagram with the incompatible elements, where its component plots together with other metals such as Mn, Zn, Cu and V. The pole enriched in incompatible elements is better constrained by the HT and ER groups than by the LT group. Finally, the component plots of MgO, CaO, Al_2O_3, Ni, Cr and to a lesser extent Co are interrelated in the TiO_2-poor pole of the PC plot.

8.4.2.2. Cluster Analysis

Combining the EQUAMP and PEMP datasets, the best K-means clustering yields 4 SOM-classified groups (Fig. 8.6; Table 8.2) for a Davies–Bouldin index value of 1.17: SA1, SA2, SA3, SA4. Overall, the centroid values of clusters show high contributions of MgO, CaO, K_2O, TiO_2, P_2O_5, and trace elements form four populations (supplementary material). However, Pb is a good discriminant for only the SA3 group, whereas Sr separates groups SA1-SA2 from SA3-SA4. The positions of the centroids of the four predefined geochemical groups plot very close to the centroids of the clusters suggested by the SOM in the similarity index plot (Fig. 8.5), corroborating the high correlation between the two classifications.

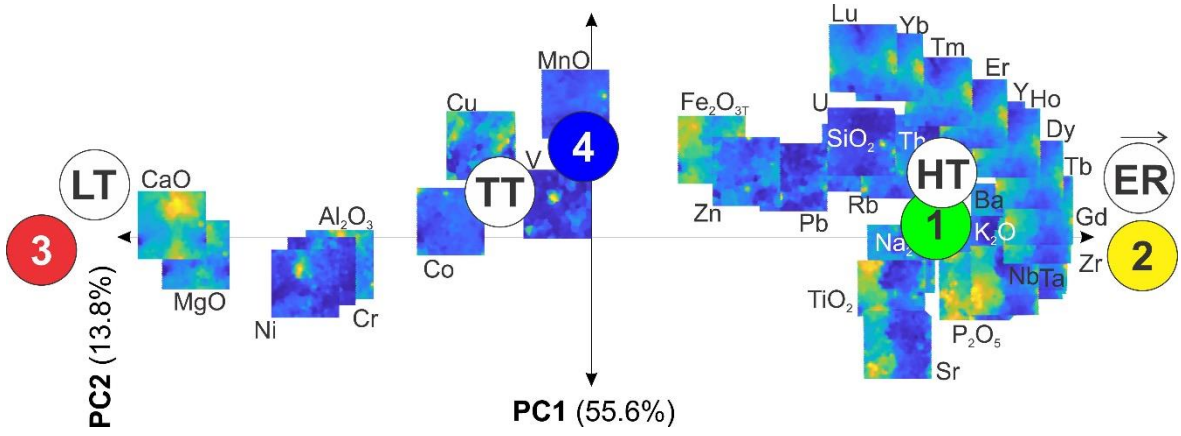

Figure 8.5. Similarity index plot based on principal component analyses in SiroSOM for major oxides, trace, and rare earth elements of the PEMP and EQUAMP samples. Average positions of geochemical groups (HT, TT, LT, and ER) and clusters SA (1, 2, 3, and 4) are also represented.

SA1 is composed of 83.2% samples from the HT group. SA2 is portrayed by 94.4% of ER compositions. Interestingly, this cluster groups magmas in a wider silica range (52–64 wt.%) than that previously classified as ER (SiO_2 = 57–64 wt.%), assimilating 10.3% more of the evolved HT samples. This means that SA2 should be a better indicator for separating basaltic andesitic-trachyandesitic fractionated samples from strict HT basaltic rocks. Cluster SA3 has a wide range of MgO from 3 to 10 wt.%, comprising 68.8% of all LT samples and 34.7% of TT tholeiites. On the other hand, SA4 comprises 58.7% of all TTs, followed by 30.3% of evolved LT compositions. In general, we observe that fractionation has a strong ability to modify the whole-rock geochemistry, which is well expressed in the HT-ER trend. Cluster SA4 is generated due to the strong similarity that exists between evolved LT and evolved TT samples. In the same way, some least evolved TT samples are allocated to SA3.

Table 8.2. Degrees of correlation among geochemical groups and K-means cluster analysis obtained in SiroSOM for the EQUAMP and PEMP.

Magma groups	N	Clusters			
		SA1	**SA2**	**SA3**	**SA4**
HT	561	**83.2%**	10.3%	1.24%	5.2%
ER	36	2.7%	**94.4%**	2.8%	2.8%
LT	542	0.2%	0.7%	**68.8%**	30.3%
TT	75	4%	2.8%	34.7%	**58.7%**

8.4.2.3. Trace Elements Patterns

Evaluating samples whose PEMP and EQUAMP petrological groups coincide with the SOM cluster analysis (Fig. 8.7). Primitive mantle (PM)-normalized incompatible element diagrams (Sun and McDonough, 1989) show that the HTs in the EQUAMP and PEMP are very similar, displaying enrichment in LILEs over HFSEs and LREEs. Values for LILEs are approximately 30–270 times greater than the normalization parameters, while the HFSEs are enriched by factors of 15–75 (Fig. 8.7). The most striking differences between the two subprovinces are related to Pb and Nb-Ta anomalies. The Pb anomalies are mostly negative in EQUAMP magmas, whereas the PEMP tends to display positive spikes with a paucity of negative Pb anomalies. Nb-Ta anomalies are present in both provinces; however, in the EQUAMP, they are more uniform, generating an inverted trapezoidal pattern, while many samples in the PEMP present barely noticeable Ta anomalies.

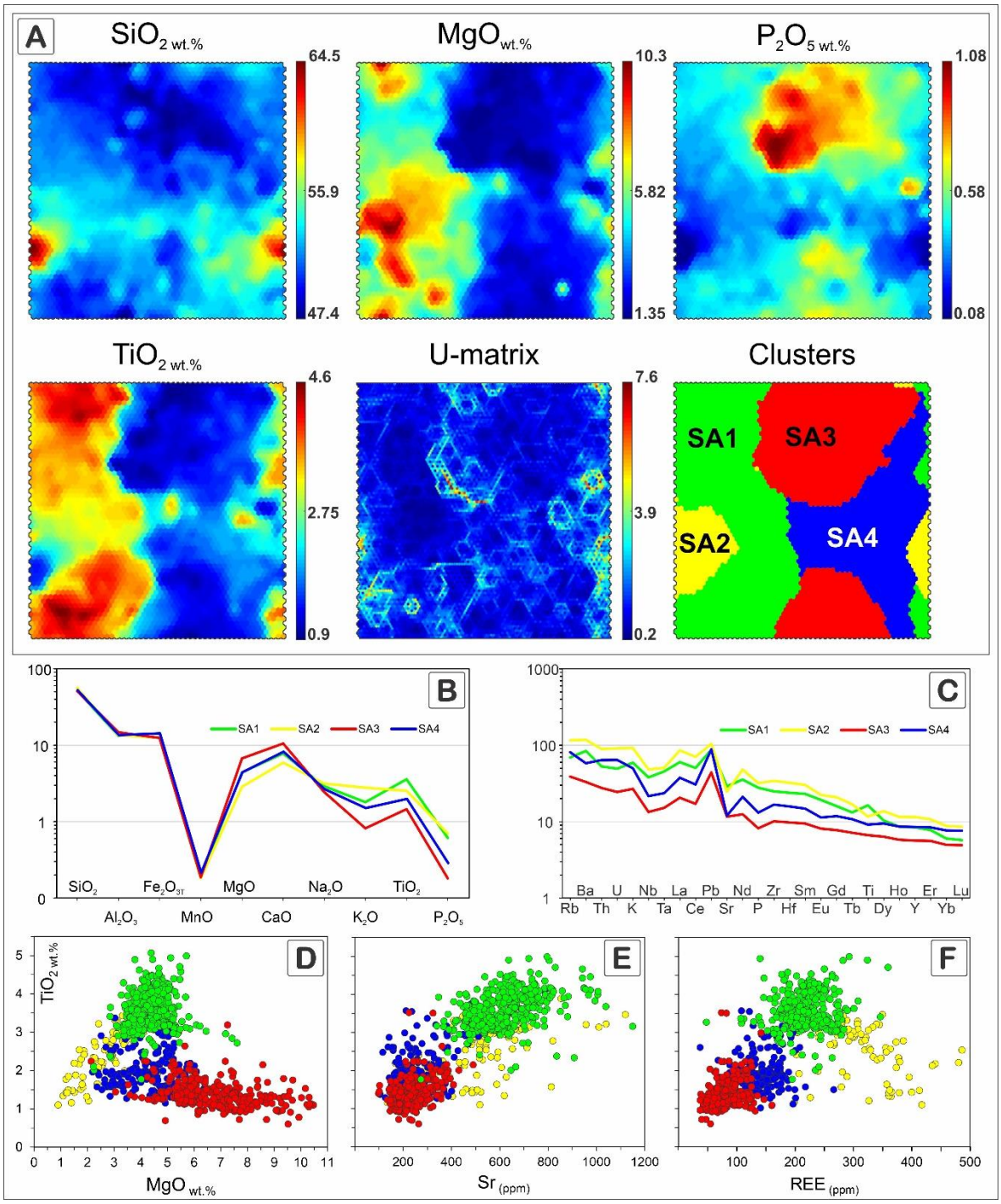

Figure 8.6. Details of component plane plots of (A) SiO_2, MgO, P_2O_5 and TiO_2, U-matrix, and K-means clusters obtained by the SiroSOM processing combining PEMP and EQUAMP: SA1, SA2, SA3, SA4. The spider plots represent the centroids of clusters for (B) major and (C) trace elements. Trace elements are normalized to the primitive mantle (Sun and McDonough, 1989). Clusters in (D) MgO *versus* TiO_2 diagram. (E) Sr *versus* TiO_2. (F) REE total *versus* TiO_2.

The ER are enriched 80–350 times the normalization parameters for LILEs and 20–80 times for HFSEs but form a distribution of incompatible elements akin to that of the HT group. Remarkable differences in comparison to mafic suites may be seen in LILE and HFSE enrichments coupled to prominent troughs at Ti-P; these features are completely plausible since

evolved magmas can be enriched in incompatible elements. Moreover, P-Ti can dimmish as a function of fractionation of Fe-Ti oxides, pyroxenes and apatite in parental tholeiitic melts.

The distribution of PM-normalized incompatible elements in LT magmas from the EQUAMP is homogeneous, with marked negative Nb-Ta anomalies (also P and Ti) and positive Pb, La, Nd, and Zr-Hf anomalies. In PEMP magmas, however, the greatest differences involve LILE contents that show heterogeneous behavior, varying 7–200 times the normalization parameters, while HFSEs are less than 20 times enriched.

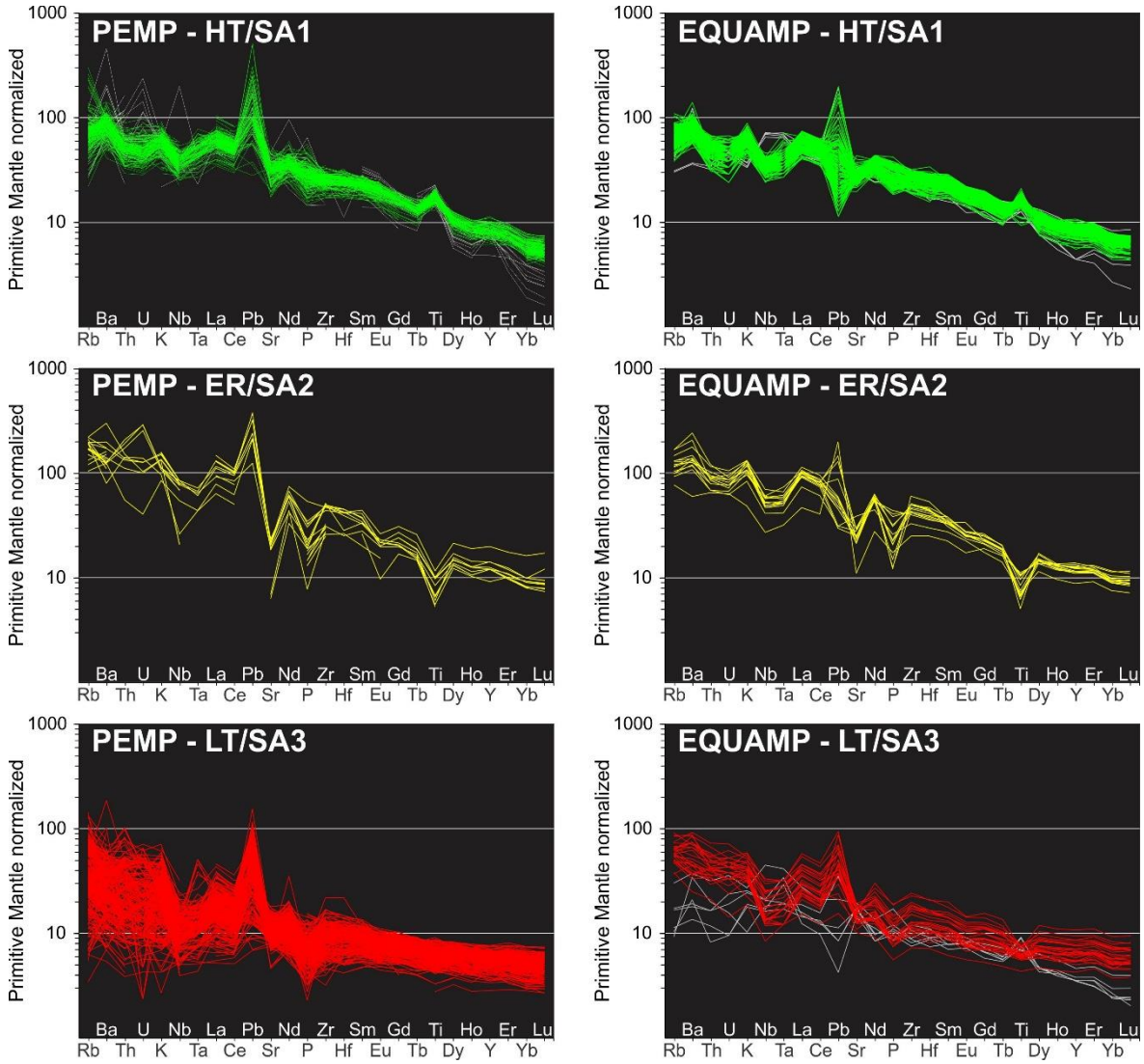

Figure 8.7. Primitive mantle-normalized (Sun and Donough, 1989) incompatible trace elements of the Equatorial Atlantic (EQUAMP) and Paraná-Etendeka (PEMP) provinces: high-Ti tholeiites (HT) in cluster SA1, evolved rocks (ER) in cluster SA2 and low-Ti tholeiites (LT) in cluster SA3. Gray lines for the PEMP are outlier samples, whereas in the EQUAMP diagrams, gray lines represent transitional basalts and olivine tholeiites of the EW-Rio Ceará-Mirim and northern Benue, which are plotted for comparison

8.4.2.4. Geographical Distribution

Figure 8.8 exhibits the geographical distribution of petrological groups and respective comparisons with SOM clusters. In the PMP, SA1 (HT) occurs in the Transminas, Resende-Ilha Grande, Serra do Mar, and Florianópolis dike swarms and in central/northern Paraná sill complexes. In the EMP, SA1 (HT) is rare and occurs on the northern side of the main lava field and in the Angola area. In the EQUAMP, SA1 (HT) is the most common type found in both the RCM and Sardinha sills. SA2 (ER) is usually observed in association with SA1 (HT) in all three provinces. The LT observed in SA3 and SA4 are the most common types in the southern PEMP and are found in the Vitória-Colatina and Serra do Mar dike swarms. The LT of the SA3 type occur in a single first-order dike at the intersection between the EW-RCM and NE-RCM swarms and in the Riacho do Cordeiro dikes. The TT of SA4 and SA3 are common in the central PMP.

8.4.3. Radiogenic isotopes (Sr-Nd-Pb)

In this section, the isotopic relationships are exclusively explored according to intrusive systems based on geochemical groups. The Sr-Nd-Pb isotope ratios of EQUAMP and PEMP dike swarms, sill complexes and Paraná basalt types (fields) are presented in Figure 8.9. All Sr and Nd isotope-dependent parameters are calculated at 130 Ma, considered an average age for the Early Cretaceous magmatism in the South Atlantic area. However, Pb isotope compositions are plotted as present ratios because several compiled works did not measure Pb concentrations, which precludes the correction for initial ratios.

HT tholeiites of the EQUAMP and PEMP present high frequencies of $^{87}Sr/^{86}Sr_{(130\ Ma)}$ at ~0.705–0.706 (Fig. 8.9), and all samples have $\varepsilon Nd_{(130\ Ma)} < -1$. A few tholeiitic samples and ER present a diffuse pattern toward radiogenic Sr, which may be suggestive of some degree of crustal assimilation. HT tholeiites of the RCM dikes and Sardinha sills have high concentrations of $\varepsilon Nd_{(130\ Ma)}$ between -1 and -3, as do HT samples of the Florianópolis, Ponta Grossa, Resende-Ilha Grande, and southern Espírito Santo dike swarms. Another striking resemblance concerns HT tholeiites from the Bero volcanic complex in Angola/Etendeka province that show the same Sr-Nd range as that observed in the RCM dikes and Sardinha sills. Moreover, the EQUAMP HT tholeiites plot over the HT Urubici/Khumib and Pitanga basalt fields for the PEMP.

The LT tholeiites display a large range of Sr isotopes, forming a diffuse (fanlike) pattern,

where less radiogenic Nd samples tend to show the most radiogenic Sr compositions. Such a feature outlines a contamination trend toward lithospheric/crustal sources. The most primitive (asthenosphere-derived) samples concern the HOD, Möwe Bay and Serra do Mar dikes, where $\varepsilon Nd_{(130\ Ma)}$ values concentrate between +1 and +6 coupled with $^{87}Sr/^{86}Sr_{(130\ Ma)}$ from 0.704 to 0.705. The second set of samples with $^{87}Sr/^{86}Sr_{(130\ Ma)}$ plotting from ~0.705 to 0.708 and $\varepsilon Nd_{(130\ Ma)}$ from +0.5 to -3.5 is observed in the Florianópolis, Ponta Grossa, Serra do Mar, Cedarbeg, False Bay, and Möwe Bay areas, and samples showing less radiogenic Nd ($\varepsilon Nd_{(130\ Ma)} < -4$) are diffuse. LT tholeiites of the RCM and Riacho do Cordeiro have an isotopic signature ($\varepsilon Nd_{(130\ Ma)} < -4$) similar to those of dikes from the Möwe Bay, Uruguay, southern Espírito Santo, and Vitória-Colatina and the Southern Paraná sills. Nonetheless, they still plot at the intersection between the fields of the Esmeralda and Gramado basalt types.

Pb isotope data of all compiled samples from the EQUAMP and PEMP plot far above the Northern Hemisphere reference line (NHRL; Hart, 1984). The $^{206}Pb/^{204}Pb$ *versus* $^{207}Pb/^{204}Pb$ and $^{206}Pb/^{204}Pb$ *versus* $^{208}Pb/^{204}Pb$ diagrams (Fig. 8.9) support more radiogenic Pb compositions for LT tholeiites of the RCM, Riacho do Cordeiro, Florianópolis, Cedarberg, HOD, and PMP sills, overlapping with the LT rocks of the Gramado and Esmeralda types. Exceptions are some LT samples from the Serra do Mar dikes with $^{206}Pb/^{204}Pb < 18$. In the HT, less radiogenic Pb predominates, as observed in the Florianópolis, Urubici/Khumib and Pitanga basalts. The EQUAMP rocks exhibit many values of $^{206}Pb/^{204}Pb$ within an ~18.2–18.4 interval, which is also supported by narrow intervals of $^{207}Pb/^{204}Pb$ (~15.56–15.61) and $^{208}Pb/^{204}Pb$ (~38.50–38.80). These Pb isotope compositions are quite similar to those of several Florianópolis, Transminas, and Bero volcanic complex intrusions that plot within the Urubici/Khumib and Pitanga basalt fields. Broadly, a significant portion of HT-ER and LT rocks of the EQUAMP and PEMP plot around the enriched mantle components (mainly EMI).

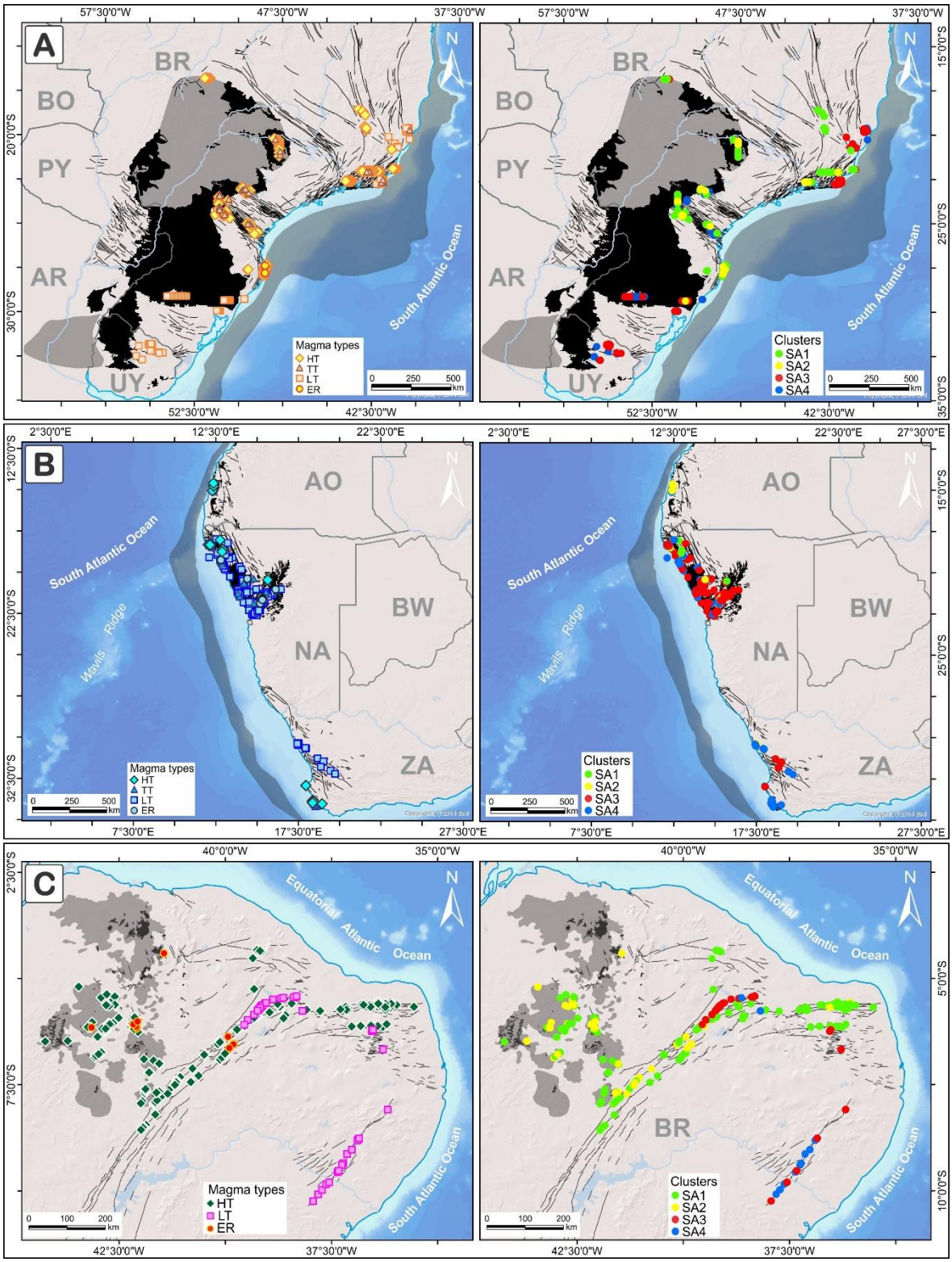

Figure 8.8. Geographical distribution of magma groups and respective clusters obtained in the SOM solutions for (A) Paraná, (B) Etendeka, and (C) Equatorial Atlantic provinces. Countries are represented by respective abbreviations: Brazil (BR), Argentina (Ar), Uruguay (UY), Paraguay (PY), Bolivia (BO), South Africa (ZA), Namibia (NA), Angola (AO), Botswana (BW).

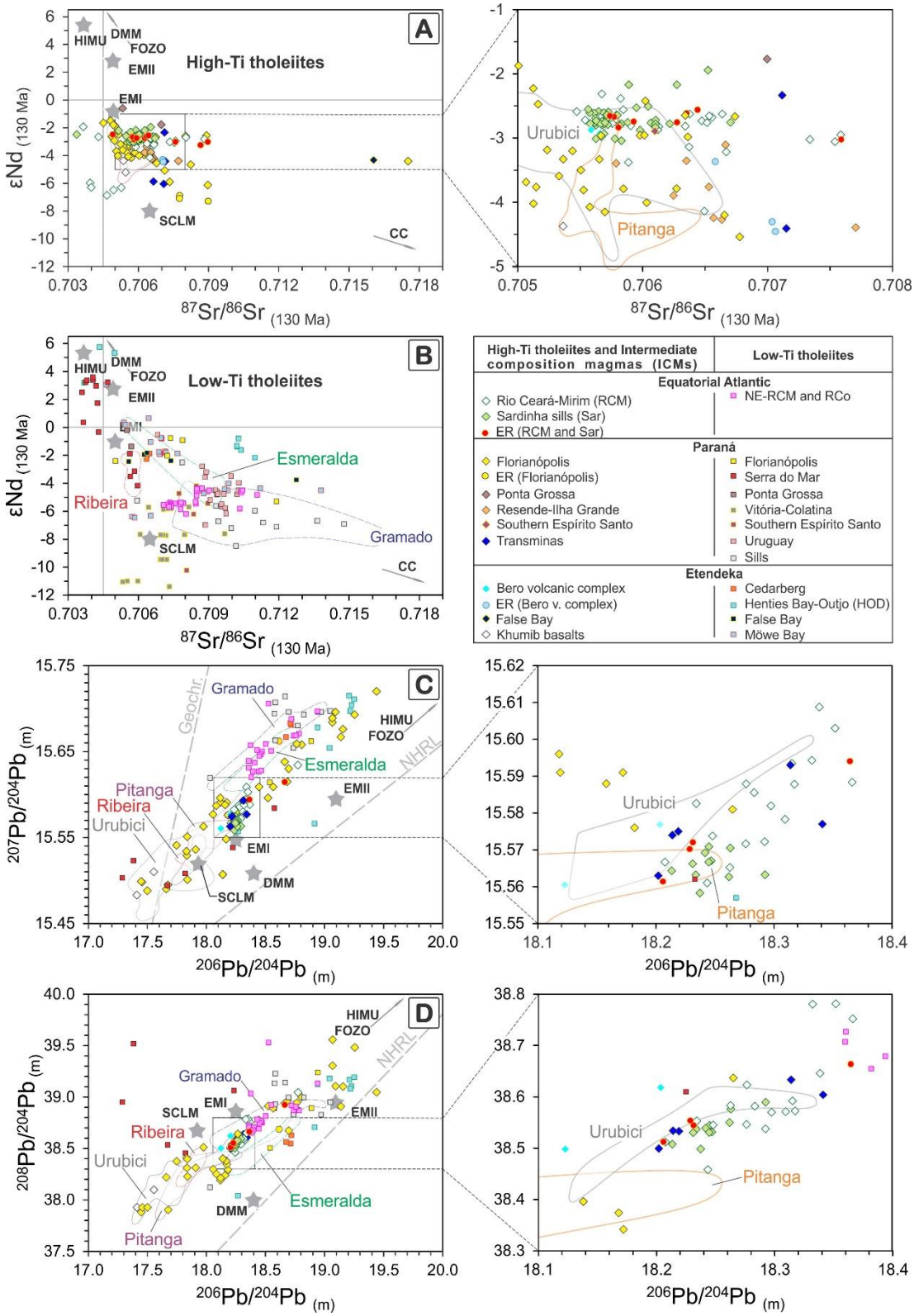

Figure 8.9. Isotopic dataset (Sr, Nd, and Pb) of intrusive rocks from the Equatorial Atlantic, Paraná (with main basalt types plotted as fields) and Etendeka provinces. The $\varepsilon Nd_{(130)}$ *versus* $^{87}Sr/^{86}Sr_{(130)}$ plots for (A) high-Ti and (B) low-Ti tholeiites. Intrusive forms and magma type fields are also plotted in (C) $^{206}Pb/^{204}Pb_{(m)}$ *versus* $^{207}Pb/^{204}Pb_{(m)}$ and (D) $^{206}Pb/^{204}Pb_{(m)}$ *versus* $^{208}Pb/^{204}Pb_{(m)}$ plots and displayed in an adjacent closeup diagram. Centroid values of mantle endmember were got from Stracke et al. (2005). The SCLM is represented by alkalic melts of Alto Paranaíba Province (Araujo et al., 2001).

8.5. Discussion

8.5.1. Simplified Ti-based classifications

The clustering results for the PEMP and EQUAMP exhibit a high correlation with the Ti-based classification. In Figure 8.10, we plot these data on different petrological/geochemical diagrams used to discriminate geochemical groups in Paraná (Peate et al., 1992) and Etendeka mafic volcanic rocks (Marsh et al., 2001). Peate et al. (1992) proposed TiO_2 at 2.8 wt.% to distinguish the Pitanga/Urubici magmas. Overall, this limit is useful for rocks with MgO between 6 and 3 wt.%. Fractionated or slightly primitive type plots beneath or above this limit, respectively. This limitation can be overcome by the combination of $TiO_2 = -0.1MgO + 3.3$ and $TiO_2 = 0.725MgO$ in the MgO *versus* TiO_2 plot. The line defined by $TiO_2 = -0.1MgO + 2.5$ in the MgO *versus* TiO_2 binary plot can resolve ambiguities with HT and TT samples. In the diagram of Sr *versus* TiO_2, Marsh et al. (2001) proposed limits of 400 ppm and 2.2 wt.%, respectively, to separate HT and LT magmas. However, these straight limits exclude some Sr-poor HT types observed in other regions of the PEMP. Therefore, we believe that a curve defined by $TiO_2 = -0.02Sr + 10$ is a better alternative to divide HTs and LTs in this plot.

The Ti/Y *versus* Ti/Zr diagram has been extensively applied in the PEMP, where Peate et al. (1992) proposed an arbitrary limit of $Ti/Y < 310$ for distinguishing HT and LT rocks, which worked well for flood basalts and available samples at the time. Nevertheless, a very large amount of data produced since then indicates a wide overlap between two broad groups. Moreover, the EQUAMP samples form a continuous trend from HTs to ER. Herein, we prefer to use the curves defined by the equations $Ti/Zr = 0.4Ti/Y - 90$ and $Zr/Y = -0.045Ti/Zr + 9$ in the Ti/Zr *versus* Zr/Y and Ti/Zr *versus* Zr/Y plots, respectively, to minimize the overlap of HT and LT compositions.

Another useful parameter to divide HT and LT is based on REE element abundances. For instance, the limit between LT and HT with respect to La/Yb ratios is usually defined at 10. Furthermore, high La/Yb values may be a proxy for the source (e.g., mantle rich in garnet) or indicate that La is more compatible than Yb and lower degrees of melting yield mafic compositions with higher La/Yb (Greenough and McDivitt, 2018).

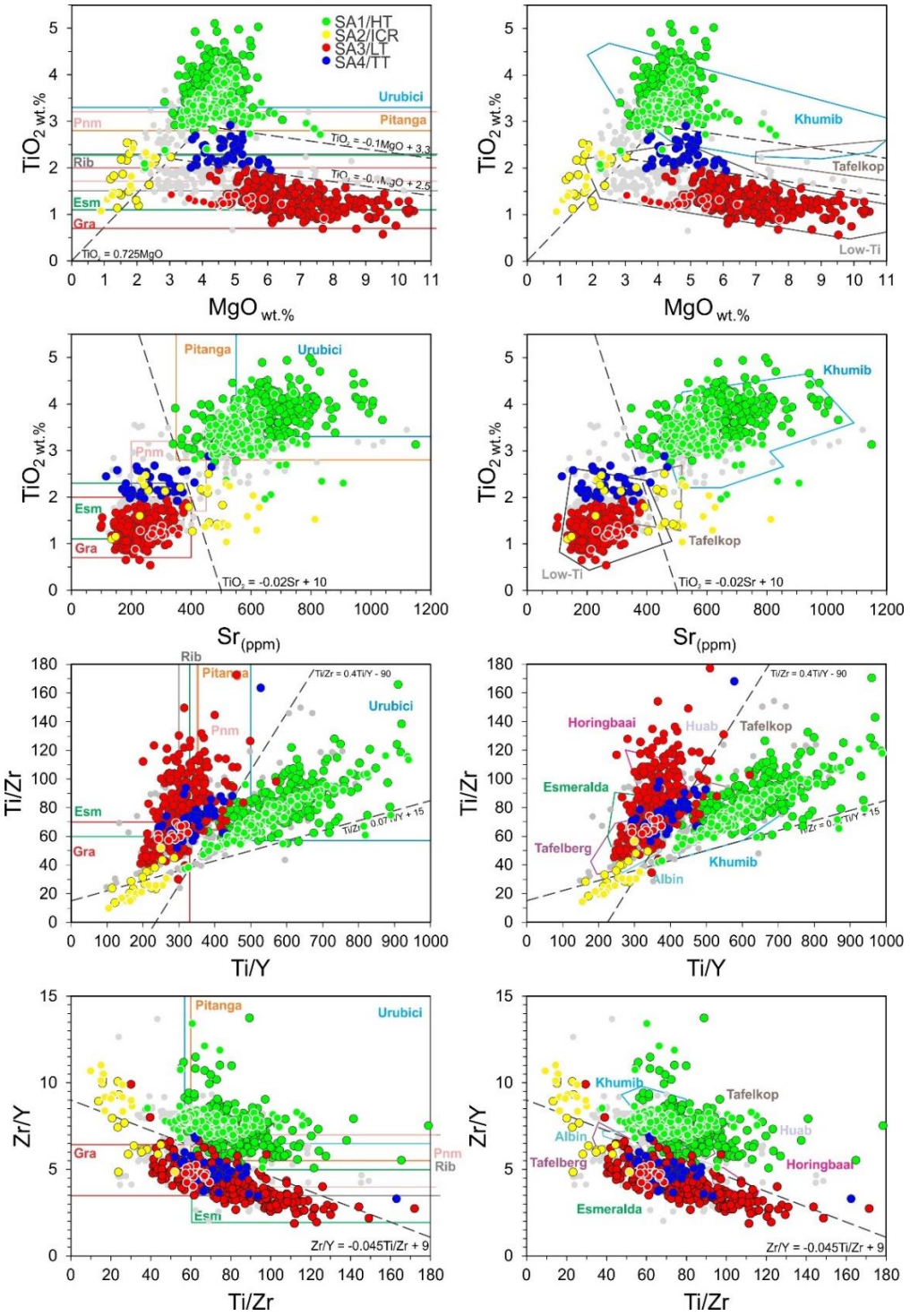

Figure 8.10. Classification diagrams for mafic magma discrimination based on geochemical parameters in Paraná-Etendeka province. Paraná magma types according Peate et al. (1992): Urubici, Pitanga, Paranapanema (Pnm), Ribeira (Rib), Gramado (Gra), and Esmeralda (Esm). Etendeka magma types cf. Marsh et al. (2001): Khumib, Talfelkop, Huab, Horingbaai, Talfelberg, and Esmeralda. Dots with white rims represent EQUAMP samples that are simplified as high-Ti tholeiites (HT), low-Ti tholeiites (LT) and evolved rocks (ER). Gray dots represent samples that do not exhibit correlation between clusters and Ti-based classification. The black dashed lines and respective equations represent proposed limits for dividing the broad compositional groups in the EQUAMP and PEMP.

8.5.2. SOM solutions and previous petrological classifications

The TiO_2 contents of HT/SA1 overlap the compositions of Urubici/Khumib and Pitanga types in the PEMP (Fig. 8.10). However, EQUAMP samples plot beyond the limits defined by Urubici/Khumib and Pitanga. HT/SA1 present very similar patterns in PM-normalized (Sun and Donough, 1989) incompatible trace element diagrams, and isotopic data for Sr-Nd-Pb are much more cohesive, which means that HT rocks had same/similar sources (or underwent similar petrogenetic processes) plus a lower degree of contamination than those observed for the other groups. Nevertheless, the more dispersed behavior of the PEMP tholeiites implies more important crustal contamination than in the EQUAMP. An indication of such a process is the ubiquitous positive Pb anomalies and comparative enrichments in LILEs.

The ER/SA2 in the EQUAMP and PMP magmas are interpreted as derived by AFC from HT types (Florisbal et al., 2018; Macêdo Filho et al., submitted). There are no specific groups for these rocks. Some of the ER from the EMP plot near LT types in the Zr/Y *versus* Ti/Zr diagram (Fig. 8.10). We are aware that these diagrams were developed to classify mafic types; thus, this behavior may even suggest that HT and LT may generate very similar magma compositions after strong degrees of fractional crystallization. ER are those with SiO_2 from 57 to 63% wt.%, but the SOM solutions allocate intermediate rocks with $SiO_2 > 52.5$ wt.% in SA2. Intermediate compositions are typically assigned to types with SiO_2 from 52 to 63 wt.% (Le Maitre, 2002); therefore, SA2 can be a better solution to separate andesitic rocks from strictly mafic melts (SiO_2 from 45 to 52 wt.%).

The LT/SA3 generate a massive amount of data that overlap many petrological groups of Peate et al. (1992) and Marsh et al. (2001). In general, the Esmeralda and Gramado types are well correlated with LT types, and a broad classification as LTs can be used if analysts are interested in simplistic models. However, when looking at PM-normalized (Sun and Donough, 1989) incompatible trace element diagrams, it is possible to recognize a wide variety of behaviors with enrichment in LILEs, from those observed for lithosphere-influenced magmatism to flat patterns that resemble melts produced under high degrees of melting like E-MORB (Trumbull et al., 2007). Therefore, local predefined petrological groups play a role in the regional characterization of low-Ti types and diverse petrogenetic evolution. We should stress that many of these magmas underwent variable degrees of crustal assimilation processes, as suggested by isotopes, assimilating very heterogeneous crust/lithospheric mantle, which significantly modified the composition of the original magmas. This may even justify the fact

that SOM solutions present less than 70% of correlation for LT types.

Finally, The TT/SA4 present TiO_2 > ~2 wt.% but are better correlated to LT types than to HT types. In Paraná, Peate et al. (1992) proposed the Paranapanema (high-Ti) and Ribeira (low-Ti) groups to explain magmas with transitional Ti contents. However, these classifications are successfully applied only to flood basalts. For intrusive forms, TT are rare, and the limits proposed by Peate et al. (1992) generate overlap in several binary plots, which leads to ambiguities.

8.5.3. Geodynamic considerations

Plate reconstruction models have suggested an outstanding spatial interplay among the focal zones of LIPs and the margins of Large Low Shear-wave Velocity Provinces (LLSVPs) (Torsvik et al., 2006). Accordingly, the Tristan-Gough (TG) hotspot located on the margin of African LLSVPs has been one of the most invoked mechanisms to explain anomalous igneous activity in the South Atlantic realm (e.g., Courtillot et al., 2003). The drifting of West Gondwana over the LLSVPs transported central Namibia to reach TG at 134 Ma (Fig. 8.11), where it caused regional uplift and dramatic magmatism associated with the PEMP event (Cox, 1989). High-MgO basalt-picrites are not mapped in the PMP and EQUAMP but are common in the EMP (e.g., El Dien et al., 2019; Trumbull et al., 2004a, 2007; Keiding et al., 2011, 2013; Stroncik et al., 2017) which registers the initial eruptive stage of the PEMP (Gomes and Vasconcelos, 2021). All these findings suggest that if a plume was present in the pre-South Atlantic area at the Lower Cretaceous, it could be reasonably located it beneath the African plate.

Nevertheless, the geochemical contribution of the Tristan Plume as a source of PEMP basalts has been widely questioned in the literature (e.g., Rocha-Júnior et al., 2012), because the Tristan member does not resemble PEMP melts. Alternatively, majority of Sr-Nd-Pb isotope data for the PEMP, in special HT magmas, overlap with the fields of the Gough-EMI member. Rohde et al. (2013) observed bilateral chemical zonation between the Tristan and Gough tracks traced for 70 Ma. Peate et al. (1999) and Gibson et al. (2005) explained Gough-EMI magmas with a delaminated subcontinental lithospheric mantle (SCLM) mixed with plume components. In a recent view, Hoernle et al. (2015) and Homrighausen et al. (2019) proposed a deep source in the lower mantle derived from the African LLSVP margin.

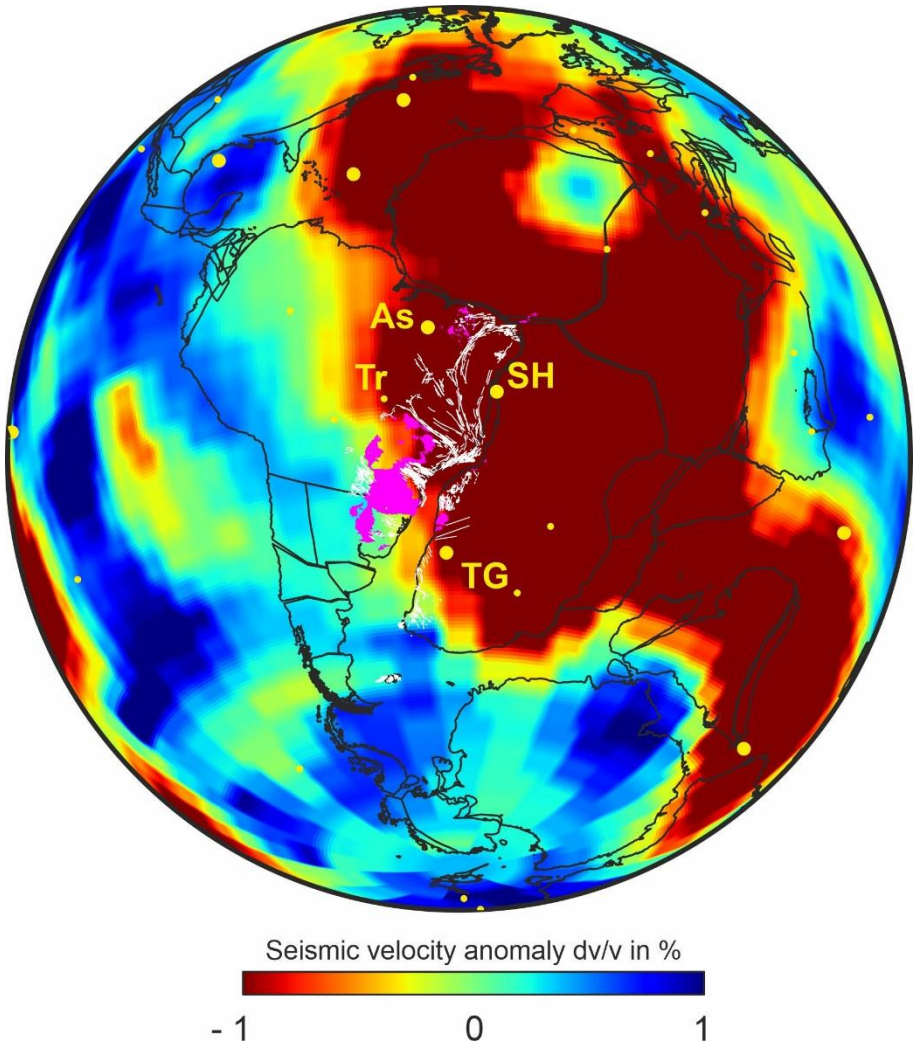

Figure 8.11. Tomographic slice at 2,800 km depth beneath the South Atlantic Ocean region (TX2019slab-s model; Lu et al., 2019) combined to plate reconstruction model at 134 Myr (Matthews et al., 2016). The high-temperature colors (brown to red) concern the African/Tuzo LLSVP (Large Low-shear Velocity Province). Early Cretaceous igneous provinces represented as dikes (white traces) and sills and flood (magenta polygons). Hotspots are represented as yellow-black dots with respective acronyms: Tristan-Gough (TG), Saint Helena (SH), Trindade (Tr), Ascension (As). Seismic tomography and plate reconstruction models were generated using the SubMachine tools (Hosseini et al., 2018).

Overall, the LT dikes of PEMP and EQUAMP outline a major role of lithospheric assimilation, which is reinforced by increasing in $^{87}Sr/^{86}Sr_{(130\ Ma)}$ accompanied by decreasing in MgO and $^{143}Nd/^{144}Nd_{(130\ Ma)}$. This agrees with other works which evoke lithospheric mantle source and/or mixing of the enriched SCLM and asthenospheric sources with some crustal input (e.g., Muzio et al., 2017; Marques et al., 2018; Trumbull et al., 2007; Pearce et al., 2021). Asthenosphere-derived melts have been suggested in HOD tholeiites for which Trumbull et al. (2007) interpreted enriched mid-ocean ridge basalt (E-MORB) as the primary source. In the PMP, isotopically depleted melts are identified only in the Serra do Mar dikes (Carvas, 2016;

Almeida et al., 2021) that was mostly emplaced on the coastal area projected toward Etendeka. Therefore, an asthenospheric component such MORB (or even E-MORB) may be reasonably selected as the parental source of LT magmas. In this case, LT would require a major amount of assimilation of heterogeneous lithospheric components to explain the compositional/isotopic heterogeneity. For instance, assimilation of the Paleoproterozoic basement of Borborema Province (Macêdo Filho et al., submitted) or many other Precambrian components of West Gondwana have been adopted as contaminant representatives in AFC models (e.g., Peate et al., 1999; Hoernle et al., 2015; Marques et al., 2018; Beccaluva et al., 2020).

A plausive model triggered by a plume impingement may be outlined if the upper asthenosphere had been melted (MORB-like) and mixed with minor plume component (to form a E-MORB member) and/or SCLM-derived melts (Fig. 8.12). These hotter and magnesian magmas would be subsequently contaminated with crustal materials, while fractionate and upwelling in the crust, to generate the wide geochemical-isotopic range of low-Ti magmas (Beccaluva et al., 2020). In the case of the main component forming dike swarms of South America, the high-Ti tholeiites, taking an asthenospheric component (~DMM) as the source is required up to 10% of alkalic SCLM-derived melts to enrich the basalts with minor involvement of continental crust (Macêdo Filho et al., submitted). On the other hand, if an OIB-EMI member is elected as a source of high-Ti tholeiites, just small degrees of crustal assimilation is required to explain their isotopic diversity (Macêdo Filho et al., submitted) in agreement with De Min et al. (2018) and Pearce et al. (2021) that proposed a mantle plume as a source of high-Ti tholeiites with insignificant crustal contamination in the PEMP.

An alternative reconstruction model located the Tristan plume head beneath the Florianópolis dikes at 134 Ma (Seton et al., 2012). These intrusions are commonly taking as the feeder system of the Urubici/Khumib basalts in PEMP (Peate et al., 1999; Florisbal et al., 2018; McMaster et al., 2019). If TG is the source of high-Ti tholeiites of the South Atlantic area, then distal magmatic manifestations such as EQUAMP may represent remnants of effective plumbing systems able to transport magmas over long distances. One remarkable piece of evidence of this is the high-Ti dikes of the Transminas and NE-RCM systems that show identical geochemical-isotopic and geochronological signatures (Macêdo Filho et al., submitted) and magnetic airborne data suggest that both swarms form a single plumbing system of up 2,300 km long. A similar correspondence exists among low-Ti dikes of the Riacho do Cordeiro e Vitória-Colatina swarm totalizing at least 1,600 km-long, still supports the correspondence between EQUAMP and PEMP. Expanding these correlations for other dike

swarms of the PEMP, then set of dike swarms related to the South Atlantic margin have c. 3550 km-long in South America, forming one of the largest sets of plumbing systems on Earth.

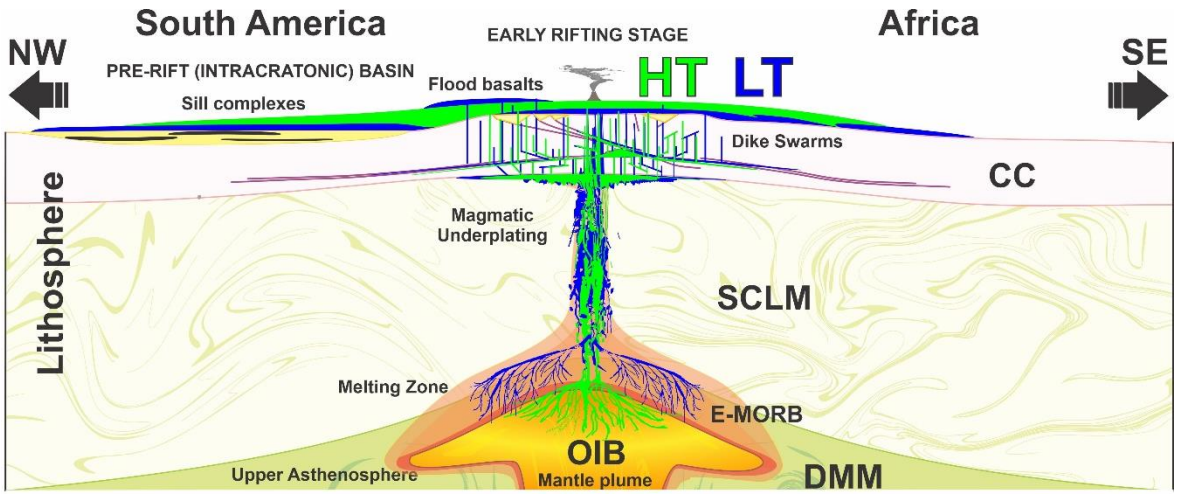

Fig 8.12. Schematic illustration with mantle plume as trigger mechanism and partial source of magmatism. In this case, the LT magmas would be generated by mixing asthenospheric mantle melts (DMM) with enriched lithospheric mantle-derived melts (SCLM) subsequently contaminated with crustal materials. Magmas rich in incompatible elements, such as the HT magmas in turn would be explained by a OIB (EMI) that melts from the mantle plume with some assimilation of lithospheric materials.

In global a context, EQUAMP should integrate the framework of subprovinces related to the Lower Cretaceous, in addition to Paraná and Etendeka provinces, forming a major single LIP related to the early stage of South Atlantic born: The South Atlantic Magmatic Province (SAMP). In pre-breakup reconstructions, the Early Cretaceous magmatism dispersed from West/Central African Rift System (Coulon et al., 1996; Loule and Popsill, 2013) to Falkland Islands (Richards et al., 2013; Stone et al., 2008) have an influence zone totalizing more than 9.5×10^6 km², therefore composing one of the largest LIP on Earth, not only in volume, but also in area of spread remnants. Such suggestion simplifies the understanding about the Atlantic Ocean evolution with three major LIPs (CSN): **C**entral Atlantic (CAMP; Juro-Triassic), **S**outh Atlantic (SAMP; Early Cretaceous) and **N**orth Atlantic (NAMP; Paleogene).

9. SYNTHESIS AND CONCLUDING REMARKS

A petrogenetic and geodynamical model to the Mesozoic magmatism in NE Brazil is proposed based on geological mapping, crystal size distribution analysis, mineral chemistry, and geochemical-isotopic characteristics of sills and dikes. Additionally, the data-intensive comparison using a Self-Organizing Maps approach allowed to establish geochemical correlation between Early Cretaceous tholeiitic plumbing systems of the Equatorial Atlantic and Paraná-Etendeka provinces. Considering the results arising from the combined different methodologies, the main conclusions of this work are highlighted:

- Dike swarms in the Borborema Province show high parallelism with the adjacent Atlantic margin. These intrusions also develop abundantly where they have an orientation analogous to the ductile fabric of the Precambrian basement. Therefore, the new map resultant from this study reinforces the intimate relationship of dike swarm emplacement, Precambrian basement structure control, and South Atlantic rift tectonics with extensional axis NW-SE oriented in NE Brazil.
- In the Parnaíba Basin, NNW-SSE-oriented dikes odd with trend of other swarms in the Borborema Province. Rather, these NW-dikes should better address to the Central Atlantic Magmatic Province (CAMP). Since they point to the CAMP focal zone in the Central Atlantic area as other Juro-Triassic dikes around the Equatorial margins of South America and Africa.
- The mafic sill complexes hosted in the eastern side of the Parnaíba Basin make ca. 7.500 km^2, which means that over 90% of magmatic rocks are stored in the subsurface as indicated on geophysical maps (Mocitaiba et al., 2017). The sills also exhibit evidence of Mosquito (CAMP) magmatism, predominantly hosted in the NE border of the basin, and few occurrences in SE side, while the central-eastern portion presents a high frequency of the Sardinha (EQUAMP) event.
- The CSD method combined with mineral chemistry of plagioclase and (eventually) clinopyroxene were used to better understand the crystallization history of intrusions on the eastern side of the Parnaíba Basin and RCM dikes. In both environments, diabases are holocrystalline to hypocrystalline formed by plagioclase (bytownite-andesine), augite, pigeonite, Fe–Ti oxides and late alkali-feldspar (on hypocrystalline types).

- EQUAMP intrusions record simple crystallization histories combined with high nucleation density of microlites in the final stage of crystallization. Residence estimated time for the full crystallization of sills reached one and one-half years, whereas for dikes in the Borborema Province two and a half years, suggesting that exposed sections of dikes are deeper intrusions than Parnaíba Basin sills.
- In the SE border of the Parnaíba Basin, where RCM dikes intercept the basal Silurian sequence, Sardinha sills and RCM dikes are apart from each other by 5 km. In that region, whole-rock geochemical-isotopic compositions, mineral chemistry, magnetic susceptibility, textural aspects, geochronological data and crystal size distribution patterns are basically the same. Therefore, the RCM dikes may have been the feeder system of sills complexes.
- In a possible model, the area covered by the Parnaíba Basin at the Early Cretaceous could have been much larger than present-day boundaries, and the dikes could be the remnants of a complex system feeding sills on the sedimentary layer above at the Mesozoic. Additionally, the hypothesis of feeder dikes beneath the basin must not be ruled out, since the RCM and Canindé swarms tend to form a diffuse arrangement from the Borborema Province towards the Parnaíba Basin, where dikes give way to sill complexes.
- The sampling achieved in this work allowed to greatly expand the knowledge about magmatic events in the eastern side of the Parnaíba Basin. Elementary geochemistry and radiogenic isotopes were applied to classify geochemical groups and as a first-order screening tool to segment different magmatic events, since two LIPs share the same geographic area in the basin.
- The new data showed the predominance of HT tholeiites (HT1; TiO_2 >2 wt.%; MgO < ~6 wt.%) enriched in incompatible elements which are reported on the central-southeastern areas with major oxides, trace elements and isotopic characteristics (εNd -2.1 to -3.0) and moderately radiogenic $^{206}Pb/^{204}Pb$ ratios (~18.25) analogous to the reported values of the HT Sardinha magmatism.
- On a few sites, such as Elesbão Veloso, HT tholeiites coexist with trachyandesites to trachytes wich show the same isotopic characteristics; therefore, they were interpreted as a fractionated product from HT melts. The Sardinha magmatism has been age constrained at the Early Cretaceous (e.g., Baksi and Archibald, 1997; Heilbron et al., 2018; Fernandes et al., 2020) and, therefore, addressed to the EQUAMP event.

- A second more important group concern to LT tholeiites (TiO_2 < 2 wt.%; MgO > 5 wt.%), poor in incompatible elements and reported on the NE border of the basin, with subordinate occurrences in the central and southern sections of the basin. LT showed geochemical-isotopically (εNd -0.98 to -1.71) signatures akin to the Prevalent low-Ti CAMP (Marzoli et al., 2018), age constrained around at ~201 Ma by the $^{39}Ar/^{40}Ar$ method (e.g., Merle et al., 2011; Heilbron et al., 2018; Fernandes et al., 2020; Davies et al., 2017).
- An additional geochemical group of HT tholeiites (HT2), presenting more primitive characteristics (εNd 6.1-3.3), were correlated to high-Ti CAMP basalts. Consequently, the paradigm in segmenting LIP influence areas as Mosquito event/CAMP in the western side, and Sardinha event/EQUAMP on the eastern side must be reviewed, since both LIPs coexist in the eastern section of the Parnaíba Basin.
- The RCM and Canindé dikes showed HT (TiO_2 > 2.0 wt.%) compositions, associated with evolved HT (trachyandesites and trachytes). These diabases present εNd between -2.90 to -2.56, and moderately radiogenic $^{206}Pb/^{204}Pb$ ratios (~18.3). The geochemical-isotopic signature of HT RCM resembles those of the Sardinha Sills in the Parnaíba Basin. These results, in conjunction with geochronological data available in the literature, support a single LIP event, confirming the hypothesis of Hollanda et al. (2019).
- Two groups of low-Ti tholeiites (TiO_2 < 2 wt.%) were characterized in the RCM swarm, an evolved group (LT1) presenting MgO < 6 wt.% and less radiogenic Nd (εNd -4.6 to -4.4), and another more magnesian (LT2, MgO >6 wt.%) with slightly more radiogenic Nd (εNd -1.4 to -1.0).
- In the regional context, HT melts of the EQUAMP have similar composition of contemporaneous HT magma types of the PEMP, whereas LT tholeiites have geochemical signatures analogous to CAMP and or PEMP low-Ti magmas (e.g., Esmeralda type). A K-Ar approach led by Oliveira et al. (2021) outlined an Early Cretaceous age to the evolved LT magmas (LT1), these results did not preclude the possibility of a CAMP provinciality to more magnesian tholeiites (LT2).
- The geochemical data of both HT and LT tholeiites require the involvement of variable proportions of an enriched component that can be either the subcontinental metasomatized mantle itself (case of LT) or a deep plume (case of HT). By assuming

the involvement of a plume, Ascension-St. Helena and Tristan-Gough are likely candidates. Crustal contamination must have occurred to some extent.

- If a FOZO-type (Ascension) plume is involved, the role of the SCLM is required as a 'subordinate' component with proportions not greater than 30%. The SCLM is not (or negligibly) needed if an EM-Gough plume was involved.
- A plausive hypothesis to justify the presence of HT Gough-type next to the Equatorial Atlantic would be the physical link between the NE-RCM and the Transminas dike swarms, which have the same geochemical-isotopic signature and suggestive lateral continuity in aeromagnetic maps. Therefore, magmas would be generated in the Tristan-Gough plume, and subsequently migrate to NE Brazil via this up to 2,300 km-long plumbing system. A similar link between EQUAMP and PEMP is outlined by Vitória-Colatina and Riacho do Cordeiro dikes swarms, totalizing at least 1,600 km-long, which present comparable geochemical-isotopic compositions and age.
- Even if the EM-Gough hotspot is considered as the source of HT magmas, few compositions reported in EW-RCM and Benue Rift still require the involvement of FOZO/HIMU components. It might suggest that northern (Ascencion-St. Helena) and southern (Tristan-Gough) hotspots played a role in the tectonomagmatic activity of South Atlantic rifting.
- The revaluation of the geochemical database of the PEMP and the EQUAMP, through classical petrological approach as well as through Self-Organizing Maps, indicates that the compositional diversity of EQUAMP rocks is completely encompassed in the PEMP compositional range. These relationships are even clearer for the HT group, which has a lower degree of crustal contamination than LT magmas, as suggested by isotopic data and patterns of trace elements.
- In conclusion, the EQUAMP integrate the framework of Lower Cretaceous LIPs in the West Gondwana realm, in addition to Paraná and Etendeka provinces, where they form one major single LIP ($> 9.5 \times 10^6$ km²) related to the early stage of South Atlantic Rift. Rather, these igneous manifestations should be collectively referred as the South Atlantic Magmatic Province (SAMP). Such model simplifies the genesis of the Atlantic Ocean with three major magmatic provinces: Central Atlantic (CAMP; Juro-Triassic), South Atlantic (SAMP; Early Cretaceous) and North Atlantic (NAMP; Paleogene).

REFERENCES

Aarnes, I., Planke, S., Trulsvik, M., Svensen, H., 2015. Contact metamorphism and thermogenic gas generation in the Vøring and Møre basins, offshore Norway, during the Paleocene–Eocene thermal maximum. J. Geol. Soc. London. 172, 588–598. https://doi.org/10.1144/jgs2014-098

Abelha, M., Petersohn, E., Bastos, G., 2018. New insights into the Parnaíba Basin: results of investments by the Brazilian National Petroleum Agency. In: Daly, M. C., Fuck, R. A., Julià, J., Macdonald, D.I.M., Watts, A. B. (eds) cratonic basin formation: a case study of the Parnaíba Basin of Brazil. Geological Society, London, Special Publications 472. https://doi.org/10.1144/SP472.9

Agostini, C., Fortunati, A., Arzilli, F., Landi, P., Carroll, M. R., 2013. Kinetics of crystal evolution as a probe to magmatism at Stromboli (Aeolian Archipelago, Italy). Geochimica et Cosmochimica Acta 110, 135–151. https://doi.org/10.1016/j.gca.2013.02.027

Almeida, J., Heilbron, M., Guedes, E., Neubauer, F., Manfred, B., Klausen, M. B., … Tetzner, W., 2021. Pre-to-syn-rift tholeiitic magmatism in a transtensive hyperextended continental margin: Onshore and offshore magmatism of the Campos Basin, SE Brazil. Journal of South American Earth Sciences, 108(October 2020). https://doi.org/10.1016/j.jsames.2021.103218

Almeida, J.C.H., da Costa P. L., Heilbron, M., Da Silva Schmitt, R., De Morisson Valeriano, C., Rubim, I.N., Mohriak, W.U., De Lima Machado Júnior, D., Tetzner, W., 2013. Guia de campo na Área Continental do Alto de Cabo Frio. Bol. Geociências da Petrobras 21, 325–355.

Almeida, V.V., Janasi, V.A., Heaman, L.M., Shaulis, B.J., Hollanda, M.H.B.M., Renne, P.R., 2018. Contemporaneous alkaline and tholeiitic magmatism in the Ponta Grossa Arch, Paraná-Etendeka Magmatic Province: Constraints from U–Pb zircon/baddeleyite and $^{40}Ar/^{39}Ar$ phlogopite dating of the José Fernandes Gabbro and mafic dykes. Journal of Volcanology and Geothermal Research, 355, 55–65. https://doi.org/10.1016/j.jvolgeores.2017.01.018

Almeida, Y.B., Julià, J., Frassetto, A., 2015. Crustal architecture of the Borborema Province, NE Brazil, from receiver function CCP stacks: Implications for Mesozoic stretching and Cenozoic uplift. Tectonophysics 649, 68-80. https://doi.org/10.1016/j.tecto.2015.03.001

Amaral, W.S., Kraus, R.K., Dantas, E.L., Fuck, R.A., Pitombeira, J.P.A., 2017. Sinistral reactivation of the Transbrasiliano Lineament: Structural and geochronological evidences in the Cariré Granulite Zone, Borborema Province – NE Brazil. Journal of South American Earth Sciences, 79, 409–420. https://doi.org/10.1016/j.jsames.2017.08.022

Amelin, Y., Rotenberg, E., 2004. Sm-Nd systematics of chondrites. Earth Planet. Sci. Lett. 223, 267–282. https://doi.org/10.1016/j.epsl.2004.04.025

Anderson, D. L., 1982. Isotopic evolution of the mantle: the role of magma mixing. Earth and Planetary Science Letters, 57(1), 1–12. https://doi.org/10.1016/0012-821X(82)90168-6

Araujo, A.L.N., Carlson, R.W., Gaspar, J.C., Bizzi, L.A. Petrology of kamafugites and kimberlites from the Alto Paranaíba Alkaline Province, Minas Gerais, Brazil. Contributions to Mineralogy and Petrology, 142(2), 163–177. https://doi.org/10.1007/s004100100280

Archanjo, C.J., 2002. Fabric of the Rio Ceará–Mirim mafic dike swarm (northeastern Brazil) determined by anisotropy of magnetic susceptibility and image analysis. Journal of Geophysical Research, 107(0). https://doi.org/10.1029/2001JB000268

Archanjo, C.J., Campanha, G.A., Salazar, C.A., Launeau, P., 2012. Using AMS combined with mineral shape preferred orientation analysis to understand the emplacement fabrics of the Apiaí gabbro–norite (Ribeira belt, SE Brazil). International Journal of Earth Sciences 101, 731–745. https://doi.org/10.1007/s00531–011–0659–x

Archanjo, C.J., Trindade, R.I., Macedo, J.W.P., Araújo, M.G., 2000. Magnetic fabric of a basaltic dyke swarm associated with Mesozoic rifting in northeastern Brazil. Journal of South American Earth Sciences 13(3), 179-189. https://doi.org/10.1016/S0895-9811(00)00023-7

Archanjo, C.J., Viegas, L.G.F., Hollanda, M.H.B.M., Souza, L.C., Liu, D., 2013. Timing of the HT/LP Transpression in the Neoproterozoic Seridó Belt (Borborema Province, Brazil): Constraints from U-Pb (SHRIMP) Geochronology and Implications for the Connections Between NE Brazil and West Africa. Gondwana Research 23(2), 701–714. https://doi:10.1016/j.gr.2012.05.005

Armienti, P., Pareschi, M.T., Innocenti, F., Pompilio, M., 1994. Effects of magma storage and ascent on the kinectis of crystal growth. Contributions to Mineralogy and Petrology 115 (4), 402–414.

Augland, L. E., Ryabov, V. V., Vernikovsky, V. A., Planke, S., Polozov, A. G., Callegaro, S., D. A. Jerram, Svensen, H. H., 2019. The main pulse of the Siberian Traps expanded in size and composition. Scientific Reports, 9(1), 1–12. https://doi.org/10.1038/s41598-019-54023-2

Ávila, C.F., Archanjo, C., Fossen, H., Hollanda, M.H.B.M., 2019. Zipperedshear Zone Model for Interacting Shear zones in the Borborema Province, Brazil, as Constrained by U-Pb Dating. Tectonics 38, https://doi.org/10.1029/2019TC005547

Ávila, C.F., Archanjo, C.J., Hollanda, M.H.B.M., Macêdo Filho, A.A. d., Lemos-Santos, D. do V., 2020. Shear zone cooling and fabrics of synkinematic plutons evidence timing and rates of orogenic exhumation in the northwest Borborema Province (NE Brazil). Precambrian Res. 350, 105940. https://doi.org/10.1016/j.precamres.2020.105940

Bação, F., Lobo, V., Painho, M., 2005. The self-organizing map, the Geo-SOM, and relevant variants for geosciences. Computers and Geosciences, 31(2), 155–163. https://doi.org/10.1016/j.cageo.2004.06.013

Backeberg, N. R., Reid, D. L., Trumbull, R. B., Romer, R. L., 2011. Petrogenesis of the false bay dyke swarm, Cape Peninsula, South Africa: Evidence for basement assimilation. South African Journal of Geology, 114(3–4), 335–352. https://doi.org/10.2113/gssajg.114.3-4.335

Baggio, S.B., Hartmann, L.A., Lazarov, M., Massonne, H.J., Opitz, J., Theye, T., Viefhaus, T., 2018. Origin of native copper in the Paraná volcanic province, Brazil, integrating Cu stable isotopes in a multi-analytical approach. Miner. Depos. 53, 417–434. https://doi.org/10.1007/s00126-017-0748-2

Baksi, A.K., Archibald, D.A., 1997. Mesozoic Igneous Activity in the Maranhão Province, Northern Brazil - $^{40}Ar/^{39}Ar$ Evidence for Separate Episodes of Basaltic Magmatism. Earth and Planetary Science Letters 151, 139–153. https://doi.org/10.1016/S0012-821X(97)81844-4

Barreto, C.J.S., de Lima, E.F., Scherer, C.M., Rossetti, L. de M.M., 2014. Lithofacies analysis of basic lava flows of the Paraná igneous province in the south hinge of Torres Syncline, Southern Brazil. J. Volcanol. Geotherm. Res. 285, 81–99. https://doi.org/10.1016/j.jvolgeores.2014.08.008

Barreto, C.J.S., Lafon, J.M., De Lima, E.F., Sommer, C.A., 2016. Geochemical and Sr-Nd-Pb isotopic insight into the low-Ti basalts from southern Paraná Igneous Province, Brazil: The role of crustal contamination. Int. Geol. Rev. 58, 1324–1349. https://doi.org/10.1080/00206814.2016.1147988

Beccaluva, L., Bianchini, G., Natali, C., Siena, F., 2020. Plume-related Paranà-Etendeka igneous province: An evolution from plateau to continental rifting and breakup. Lithos 362–363, 105484. https://doi.org/10.1016/j.lithos.2020.105484

Belém, J., 2015. Geoquímica, Geocronologia e Contexto Geotectônico do Magmatismo Máfico Associado ao Feixe de Fraturas Colatina, Estado do Espírito Santo. PhD dissertation. Universidade Federal de Minas Gerais, Belo Horizonte, Brazil, 134 pg.

Bellieni G, Comin-Chiaramonti P., Marques L.S., Martínez L.A., Melfi A.J., Nardy A.J.R., Piccirillo E.M., Stolfa D., 1986. Continental flood basalt from the central-western regions of the Paraná plateau (Paraguay and Argentina): petrology and petrogenetic aspects. Neues Jahrbuch.

Bellieni, G., Comín, P., Marques, L., Melfi, a, Piccirillo, E., Nardy, A., Rosemberg, A., 1984. High- and low-TiO_2 flood basalts from the Paraná plateau (Brasil): Petrology and geochemical aspects bearing on thier mantle origin. Neues Jahrbuch Für Mineralogie Abhandlungen, 150(January), 273–306.

Bellieni, G., Macedo, M.H.F., Petrini, R., Piccirillo, E.M., Cavazzini., G., Comin-Chiaramonti, P., Ernesto, M., Macedo, J.W.P., Martins, G., Melfi, A.J. Pacca, I.G., De Min, A., 1992. Evidence of Magmatic Activity Related to Middle Jurassic and Early Cretaceous Rifting from Northeastern Brazil (Ceará-Mirim): K/Ar age, Palaeomagnetism, Petrology and Sr-Nd Isotope Characteristics. Chemical Geology 97, 9-32.

Bellieni, G., Piccirillo, E.M., Cabazzini, G., Petrini, R., Comin-Chiaranmonti, P., Nardy, A.J.R., Civetta, L., Melfi, A.J., Zantedeschi, P., 1990. Low- and High-TiO_2 Mesozoic Tholeiitic Magmatism of the Maranhão Basin (NE-Brazil): K/Ar age, Geochemistry, Petrology, Isotope Characteristics and Relationships with Mesozoic Low- and High-TiO_2 Flood Basalts of the Paraná basin (SE-Brazil). Neues Jahrbuch Mineralogischer Abhandlungen 162(1), 1–33.

Benkhelil, J., Dainelli, P., Ponsard, J.F., Popoff, M., Saugy, L., 1988. The Benue trough: Wrench-fault related basin on the border of the equatorial Atlantic, Developments in Geotectonics. Elsevier B.V. https://doi.org/10.1016/B978-0-444-42903-2.50037-3

Bertrand, H., Fornari, M., Marzoli, A., García-Duarte, R., Sempere, T., 2014. The Central Atlantic Magmatic Province extends into Bolivia. Lithos, 188, 33–43. https://doi.org/10.1016/j.lithos.2013.10.019

Blackburn, T. J., Olsen, P. E., Bowring, S. A., McLean, N. M., Kent, D. V., Puffer, J., … Et-Touhami, M., 2013 . Zircon U-Pb geochronology links the end-triassic extinction with the central Atlantic magmatic province. Science, 340(6135), 941–945. https://doi.org/10.1126/science.1234204

Boynton, W.V., 1984. Cosmochemistry of the Rare Earth Elements: Meteorite Studies, in: Henderson, P., (Eds.), Developments in Geochemistry, Elsevier 2, 63–114. doi:10.1016/b978-0-444-42148-7.50008-3

Bradley, D.C., 2011. Secular trends in the geologic record and the supercontinent cycle. Earth-Science Reviews, 108(1–2), 16–33. https://doi.org/10.1016/j.earscirev.2011.05.003

Brito Neves, B.B., Fuck, R.A., 2014. The basement of the South American platform: Half Laurentian (N–NW) + half Gondwanan (E–SE) domains. Precambrian Research 244(1), 75–86. https://doi.org/10.1016/j.precamres.2013.09.020

Brown, W.L., 1993. Fractional crystallization and zoning in igneous feldspars: ideal water–buffered liquid fractionation lines and feldspar zoning paths. Contributions to Mineralogy and Petrology 113(1), 115–125. https://doi.org/10.1007/BF00320835

Brugger, C., Hammer, J., 2010. Crystal size distribution analysis of plagioclase in experimentally decompressed hydrous rhyodacite magma. Earth and Planetary Science Letters 300, 246–254. https://doi.org/10.1016/j.epsl.2010.09.046

Bryan, S.E., Ferrari, L., 2013. Large igneous provinces and silicic large igneous provinces: Progress in our understanding over the last 25 years. Bull. Geol. Soc. Am. 125, 1053–1078. https://doi.org/10.1130/B30820.1

Bryan, S.E., Peate, I.U., Peate, D.W., Self, S., Jerram, D.A., Mawby, M.R., Marsh, J.S., Miller, J. A., 2010. The largest volcanic eruptions on Earth. Earth-Science Reviews, 102(3–4), 207–229. https://doi.org/10.1016/j.earscirev.2010.07.001

Callegaro, S., Marzoli, A., Bertrand, H., Blichert-Toft, J., Reisberg, L., Cavazzini, G., Jourdan, F., Davies, J.H.F.L., Parisio, L., Bouchet, R., Paul, A., Schaltegger, U., Chiaradia, M., 2017. Geochemical Constraints Provided by the Freetown Layered Complex (Sierra Leone) on the Origin of High-Ti Tholeiitic CAMP Magmas. Journal of Petrology 58(9), 1811–1840. https://doi.org/10.1093/petrology/egx073

Callegaro, S., Marzoli, A., Bertrand, H., Chiaradia, M., Reisberg, L., Meyzen, C., Weems, R.E., Merle, R., 2013. Upper and lower crust recycling in the source of CAMP basaltic dykes from southeastern North America. Earth and Planetary Science Letters, 376, 186–199. https://doi.org/10.1016/j.epsl.2013.06.023

Callegaro, S., Rapaille, C., Marzoli, A., Bertrand, H., Chiaradia, M., Reisberg, L., Bellieni, G., Martins, L., Madeira, J., Mata, J., Youbi, N., De Min, A., Azevedo, M.R., Bensalah, M.K., 2014. Enriched mantle source for the Central Atlantic magmatic province: New supporting evidence from southwestern Europe. Lithos, 188, 15–32. https://doi.org/10.1016/j.lithos.2013.10.021

Campbell, I.H., Griffiths, R.W., 1990. Implications of mantle plume structure for the evolution of flood basalts. Earth and Planetary Science Letters, 99(1–2), 79–93. https://doi.org/10.1016/0012-821X(90)90072-6

Campos Neto, O.P.A., Lima, W.S., Gomes Cruz, F.E., 2007. Bacia de Sergipe-Alagoas. Boletim de Geociencias Da Petrobras 15(2), 405–415.

Carlson, R.W., Esperança, S., Svisero, D.P., 1996. Chemical and Os isotopic study of Cretaceous potassic rocks from Southern Brazil. Contributions to Mineralogy and Petrology, 125(4), 393–405. https://doi.org/10.1007/s004100050230

Carneiro, C. de C., Fraser, S.J., Crósta, A.P., Silva, A.M., Barros, C.E. de M., 2012. Semiautomated geologic mapping using self-organizing maps and airborne geophysics in the Brazilian Amazon. Geophysics 77, K17–K24. https://doi.org/10.1190/geo2011-0302.1

Carvas, K.Z., 2016. Diques mesozoicos subalcalinos de baixo titânio da Região dos Lagos (RJ): geoquímica e geocronologia 40Ar/39Ar. MSc thesis. Universidade de São Paulo, Instituto de Astronomia, Geofísica e Ciências Atmosféricas, São Paulo, Brazil.

Cashman, C. V, Marsh, B.D., 1988. Crystal size distribution (CSD) in rocks and the kinetics and dynamics of crystallisation. Contrib. to Mineral. Petrol. 99, 277–291. https://doi.org/10.1007/BF00371933

Cashman, K. V., Ferry, J.M., 1988. Crystal size distribution (CSD) in rocks and the kinetics and dynamics of crystallization III: Metamorphic crystallization. Contrib. to Mineral. Petrol. 99, 292–305. https://doi.org/10.1007/bf00371933

Cashman, K.V., 1993. Relationship between plagioclase crystallization and cooling rate in basaltic melts. Contributions to Mineralogy and Petrology, 113(1), 126–142. https://doi.org/10.1007/BF00320836

Cavalheiro, L., Wagner, T., Steinig, S., Bottini, C., Dummann, W., Esegbue, O., Gambacorta, G., Giraldo-gómez, V., Farnsworth, A., Flögel, S., Hofmann, P., Lunt, D.J., Rethemeyer, J., Torricelli, S., Erba, E., 2021. Impact of global cooling on Early Cretaceous high p CO 2 world during the Weissert Event. Nat. Commun. https://doi.org/10.1038/s41467-021-25706-0

Chaffey, D.J., Cliff, R.A., Wilson, B.M., 1989. Characterization of the St Helena magma source. Geol. Soc. Spec. Publ. 42, 257–276. https://doi.org/10.1144/GSL.SP.1989.042.01.16

Chakraborti, T.M., Ray, A., Deb, G.K., 2015. Crystal Size Distribution Analysis of Plagioclase from Gabbro-Anorthosite Suite of Kuliana, Orissa, Eastern India: Implications for Textural Coarsening in a Static Magma Chamber. Geological Journal, 52(2), 234–248. doi:10.1002/gj.2752

Christophersen, N., Hooper, R.P., 1992. Multivariate Analysis of Stream Water Chemical Data' The Use of Principal Components Analysis for the End-Member Mixing Problem. EM-space 28, 99–107.

Coelho, R.M., Chaves, A.O., 2017. Diques Máficos de Minas Gerais do Cretáceo Inferior: Idades Ar-Ar e correlação com a Província Ígnea Paraná-Etendeka, Geociências, v. 36, n. 4, p. 613 – 622.

Coffin, M. F., Eldholm, O., 2018. Large Igneous Provinces. Reference Module in Earth Systems and Environmental Sciences. https://doi.org/10.1016/b978-0-12-409548-9.11329-6

Coffin, M.F., Eldholm, O., 1994. Large Igneous Provinces: Crustal Structure, Dimensions, (93), 1–36.

Coltice, N., Husson, L., Faccenna, C., & Arnould, M., 2019. What drives tectonic plates? Science Advances, 5(10), 1–10. https://doi.org/10.1126/sciadv.aax4295

Coltice, N., Phillips, B. R., Bertrand, H., Ricard, Y., & Rey, P., 2007. Global warming of the mantle at the origin of flood basalts over supercontinents. Geology, 35(5), 391–394. https://doi.org/10.1130/G23240A.1

Corval, A., 2009. Petrogênese e Contexto Geodinâmico das Suítes Basálticas Toleíticas (de alto-TiO2 e baixo-TiO2) do Cretáceo Inferior da Porção Centro-oriental do Enxame de Diques da Serra do Mar. Rio de Janeiro. PhD thesis. Universidade Estadual do Rio de Janeiro. Centro de Tecnologia e Ciências. Faculdade de Geologia. 245 p.

Corval, A., Valente, S. C., Duarte, B.P., Famelli, N., Zanon, M., 2008. Geochimica Brasiliensis. Geochimica Brasiliensis, 22(3), 159–177.

Coulon, C., Vidal, P., Dupuy, C., Baudin, P., Popoff, M., Maluski, H., & Hermitte, D., 1996. The mesozoic to early cenozoic magmatism of the Benue Trough (Nigeria); geochemical evidence for the involvement of the St Helena Plume. Journal of Petrology, 37(6), 1341–1358. https://doi.org/10.1093/petrology/37.6.1341

Courtillot, V., Davaille, A., Besse, J., Stock, J., 2003. Three distinct types of hotspots in the Earth's mantle. Earth and Planetary Science Letters, 205(3–4), 295–308. https://doi.org/10.1016/S0012-821X(02)01048-8

Courtillot, V.E., Renne, P.R., 2003. On the ages of flood basalt events. Comptes Rendus - Geosci. 335, 113–140. https://doi.org/10.1016/S1631-0713(03)00006-3

Cox, K.G., 1989. The role of mantle plumes in the development of continental drainage patterns. Nature 342, 873–877. https://doi.org/10.1038/342873a0

Cox, K.G., 1992. Karoo igneous activity, and the early stages of the break-up of Gondwanaland. Magmatism and the Causes of Continental Break-Up, (68), 137–148.

Cox, K.G., MacDonald, R., Hornung, G., 1967. Geochemical and petrographic provinces in the Karoo basalts of southern Africa. American Mineralogist 52, 1451-1474.

Cruz, J.N.D., Gorayeb, S.S.P., 2020. Geology and Petrology of the Mafic Dike Swarms of the Araguaia Belt: Evidence for Distinct Events of Intracontinental Magmatism in Central-northern Brazil and Correlations with Large Igneous Provinces. Journal of South American Earth Sciences, 102563. doi:10.1016/j.jsames.2020.102563

Daly, M.C., Andrade, V., Barousse, C.A., Costa, R., McDowell, K., Piggott, N., Poole, A.J., 2014. Brasiliano crustal structure and the tectonic setting of the Parnaíba basin of NE Brazil: Results of a deep seismic reflection profile. Tectonics 33, 2102–2120. https://doi.org/10.1002/2014TC003632

Dantas, A.R., 2021. Caracterização geoquímica-isotópica e geocronologia do enxame de diques máficos Riacho do Cordeiro: extensão meridional da Província Magmática do Atlântico Equatorial. Msc thesis. Universidade de São Paulo, Instituto de Geociências São Paulo, Brazil.

Davies, D.L., Bouldin, D.W. 1979. A Cluster Separation Measure. IEEE Transactions on Pattern Analysis and Machine Intelligence, PAMI-1(2), 224–227. https:// doi.org/10.1109/tpami.1979.4766909

Davies, J.H.F.L., Marzoli, A., Bertrand, H., Youbi, N., Ernesto, M., Schaltegger, U. 2017. End-Triassic mass extinction started by intrusive CAMP activity. Nature Communications, 8(May), 1–8. https://doi.org/10.1038/ncomms15596

Davies, J.H.F.L., Marzoli, A., Bertrand, H., Youbi, N., Ernesto, M., Greber, N.D., Acherson, M., Simpson, G., Bouvier, A.S., Baumgartner, L., Pettke, T., Farina, F., Ahrenstedt, H.V., Schaltegger, U., 2021. Zircon petrochronology in large igneous provinces reveals upper crustal contamination processes: new U–Pb ages, Hf and O isotopes, and trace elements from the Central Atlantic magmatic province (CAMP). Contributions to Mineralogy and Petrology, 176(1), 1–24. https://doi.org/10.1007/s00410-020-01765-2

de Castro, D.L., Fuck, R.A., Phillips, J.D., Vidotti, R.M., Bezerra, F.H.R., Dantas, E.L., 2014. Crustal structure beneath the Paleozoic Parnaíba Basin revealed by airborne gravity and magnetic data, Brazil. Tectonophysics 614, 128–145. https://doi.org/10.1016/j.tecto.2013.12.009

de Castro, D.L., Oliveira, D.C., Hollanda, M.H.B.M., 2018. Geostatistical Interplay Between Geophysical and Geochemical Data: Mapping Litho-Structural Assemblages of Mesozoic Igneous Activities in the Parnaíba Basin (NE Brazil). Surveys in Geophysics, 39(4), 1–31. https://doi.org/10.1007/s10712-018-9463-5

De Min, A., Callegaro, S., Marzoli, A., Nardy, A. J., Chiaradia, M., Marques, L. S., Gabbarrini, I., 2018. Insights into the petrogenesis of low- and high-Ti basalts: Stratigraphy and geochemistry of four lava sequences from the central Paraná basin. Journal of Volcanology and Geothermal Research 355, 232–252. https://doi.org/10.1016/j.jvolgeores.2017.08.009

De Min, A., Piccirillo, E.M., Marzoli, A., Bellieni, G., Renne, P.R., Ernesto, M., Marques, L., 2003. The Central Atlantic Magmatic Province (CAMP) in Brazil: petrology, geochemistry, 40Ar/39Ar ages, paleomagnetism and geodynamic implications. In: Hames, W.E., Mchome, J.G., Renne, P.R., Ruppel, C. (Eds.). The Central Atlantic Magmatic Province: insights from fragments of Pangea. American Geophysical Union Geophysical Monograph Series 136, 209–226. https://doi.org/10.1029/136GM06

De Paolo, D.J., 1981. Trace element and isotopic effects of combined wall-rock assimilation and fractional crystallization. Earth and Planetary Science Letters 53(2), 189–202. https://doi.org/10.1016/0012821x(81)90153-9

Deckart, K., Bertrand, H., Liégeois, J. P., 2005. Geochemistry and Sr, Nd, Pb isotopic composition of the Central Atlantic Magmatic Province (CAMP) in Guyana and

Guinea. Lithos, 82(3-4 SPEC. ISS.), 289–314. https://doi.org/10.1016/j.lithos.2004.09.023

Deckart, K., Féraud, G., Bertrand, H., 1997. Age of Jurassic Continental Tholeiites of French Guyana, Surinam and Guinea: Implications for the Initial Opening of the Central Atlantic Ocean. Earth and Planetary Science Letters 150(3–4), 205–220. https://doi.org/10.1016/s0012-821x(97)00102-7

Deckart, K., Feraud, G., Marques, L.S., Bertrand, H., 1998. New Time Constraints On Dyke Swarms Related to the Parana-Etendeka Magmatic Province, and Subsequent South Atlantic Opening, Southeastern Brazil. J. Volcanol. Geotherm. Res. 80, 67–83.

Destro, N., Szatmari, P., Ladeira, E. A., 1994. Post-Devonian transpressional reactivation of a Proterozoic ductile shear zone in Ceará, NE Brazil. Journal of Structural Geology, 16(1), 35–45. https://doi.org/10.1016/0191-8141(94)90016-7

Dineva, S., Eaton, D., Ma, S., Mereu, R., 2007. The October 2005 Georgian Bay, Canada, earthquake sequence: Mafic dykes and their role in the mechanical heterogeneity of Precambrian crust. Bulletin of the Seismological Society of America, 97(2), 457–473. https://doi.org/10.1785/0120060176

Donaldson, C. H. 1976. An experimental investigation of olivine morphology. Contributions to Mineralogy and Petrology, 57(2), 187–213. https://doi.org/10.1007/BF00405225

Doubrovine, P.V., Steinberger, B., Torsvik, T.H., 2016. A failure to reject: Testing the orrelation between large igneous provinces and deep mantle structures with EDF statistics, Geochem. Geophys. Geosyst., 17, 1130–1163, https://doi.org/10.1002/2015GC006044

Doucet, L.S., Li, Z.X., Ernst, R.E., Kirscher, U., Dien, H.G.El, Mitchell, R.N., 2020. Coupled supercontinent-mantle plume events evidenced by oceanic plume record. Geology, 48(2), 159–163. https://doi.org/10.1130/G46754.1

Duncan, R.A., Hooper, P.R., Rehacek, J., Marsh, J.S., Duncan, A.R., 1997. The timing and duration of the Karoo igneous event, southern Gondwana. Journal of Geophysical Research B: Solid Earth, 102(B8), 18127–18138. https://doi.org/10.1029/97jb00972

Dunlop D.J., Özdemir Ö. 1997. Rock magnetism. Fundamentals and frontiers. Cambridge studies in mag- netism series. Cambridge University Press, Cambridge, 573p.

Dupuy, C., Marsh, J., Dostal, J., Michard, A., Testa, S., 1988. Asthenospheric and lithospheric sources for Mesozoic dolerites from Liberia (Africa): trace element and isotopic evidence. Earth and Planetary Science Letters, 87(1–2), 100–110. https://doi.org/10.1016/0012-821X(88)90067-2

Ebinger, C., Sleep, N. Cenozoic magmatism throughout east Africa resulting from impact of a single plume. 1998. Nature 395, 788–791. https://doi.org/10.1038/27417

Elardo, S.M., Shearer, C.K., 2014. Magma chamber dynamics recorded by oscillatory zoning in pyroxene and olivine phenocrysts in basaltic lunar meteorite Northwest Africa 032. Am. Mineral. 99, 355–368. https://doi.org/10.1515/am.2014.4552

Encarnacion, J., Fleming, T.H., Elliot, D.H., Eales, H.V., 1996. Synchronous emplacement of Ferrar and Karoo dolerites and the early breakup of Gondwana. Geology, 24(6), 535–538

Ernesto, M., Bellieni, G., Piccirillo, E.M., Marques, L.S., de Min, A., Pacca, I.G., Martins, G., Macedo, J.W.P., 2003. Paleomagnetic and geochemical constraints on the timing and duration of the CAMP activity in northeastern Brazil. Geophysical Monograph Series, 136, 129–149. https://doi.org/10.1029/136GM07

Ernst, R. E., Buchan, K. L., 1997. Giant Radiating Dyke Swarms: Their Use in Identifying Pre-Mesozoic Large Igneous Provinces and Mantle Plumes. Geophysical Monograph Series 100, 297–333. https://doi.org/10.1029/GM100p0297

Ernst, R. E., Buchan, K.L., 2001. The use of mafic dike swarms in identifying and locating mantle plumes. Special Paper of the Geological Society of America, 352, 247–265. https://doi.org/10.1130/0-8137-2352-3.247

Ernst, R. E., Youbi, N., 2017. How Large Igneous Provinces affect global climate, sometimes cause mass extinctions, and represent natural markers in the geological record. Palaeogeography, Palaeoclimatology, Palaeoecology, 478, 30–52. https://doi.org/10.1016/j.palaeo.2017.03.014

Ernst, R.E., 2014. Large Igneous Provinces. ttps://doi.org/10.1017/cbo9781139025300.011

Ernst, R.E., Baragart, W.R.A., 1992. Evidence from magnetic, 356(April), 511–513. https://doi.org/10.1016/j.jsames.2014.10.007

Ernst, R.E., Bond, D.P.G., Zhang, S., Buchan, K.L., Grasby, S.E., Youbi, N., El Bilali, H., Bekker, A., Doucet, L.S., 2021. Large Igneous Province Record Through Time and Implications for Secular Environmental Changes and Geological Time-Scale Boundaries, (January), 1–26. https://doi.org/10.1002/9781119507444.ch1

Ernst, R.E., Buchan, K.L., 1997. Giant radiating dyke swarms: Their use in identifying pre-Mesozoic large igneous provinces and mantle plumes. Geophysical Monograph Series, 100, 297–333. https://doi.org/10.1029/GM100p0297

Ernst, R.E., Buchan, K.L., Campbell, I.H., 2005. Frontiers in Large Igneous Province research. https://doi.org/10.1016/j.lithos.2004.09.004

Ernst, R.E., Liikane, D.A., Jowitt, S.M., Buchan, K.L., Blanchard, J.A., 2019. A new plumbing system framework for mantle plume-related continental large igneous provinces and their mafic-ultramafic intrusions. Journal of Volcanology and Geothermal Research, 384, 75–84

Ewart, A., 1998. Etendeka Volcanism of the Goboboseb Mountains and Messum Igneous Complex, Namibia. Part I: Geochemical Evidence of Early Cretaceous Tristan Plume Melts and the Role of Crustal Contamination in the Parana-Etendeka CFB. J. Petrol. 39, 191–225. https://doi.org/10.1093/petrology/39.2.191

Ewart, A., Marsh, J.S., Milner, S.C., Duncan, A.R., Kamber, B.S., Armstrong, R.A., 2004. Petrology and geochemistry of early cretaceous bimodal continental flood volcanism of the NW Etendeka, Namibia. part 1: Introduction, mafic lavas and re-evaluation of mantle source components. Journal of Petrology, 45(1), 59–105. https://doi.org/10.1093/petrology/egg083

Ewart, A.J., Marsh, J.S., Duncan, A.R., Miller, R.M., Hawkesworth, C.J., Betton, P.J., Rex, D.C., 1984. Geochemistry and petrogenesis of the Etendeka volcanic rocks from SWA/ Namibia. In: Erlank, A.J. (Ed.), Petrogenesis of Volcanic Rocks of the Karoo Province, Geological Society of South Africa Special Publication 13, Johannesburg, pp. 195–245.

Fairhead, J. D., Maus, S., 2003. CHAMP satellite and terrestrial magnetic data help define the tectonic model for South America and resolve the lingering problem of the pre-break-up fit of the South Atlantic Ocean. The Leading Edge 22, 779–783. DOI:10.1190/1.1605081

Fernandes, L.B.M., Jardim de Sá, E.F., Vasconcelos, P.M.P., Córdoba, V.C., 2020. Structural controls and $^{40}Ar/^{39}Ar$ geochronological data of basic dike swarms in the eastern domain of the Parnaíba Basin, northeast Brazil. Journal of South American Earth Sciences, 101(March), 102601. https://doi.org/10.1016/j.jsames.2020.102601

Fernandez, O., Olaiz, A., Cascone, L., Hernandez, P., Pereira, A. de F., Tritlla, J., Ingles, M., Aida, B., Pinto, I., Rocca, R., Sanders, C., Herrá, A., Tur, N., 2020. Geophysical evidence for breakup volcanism in the Angola and Gabon passive margins. Mar. Pet. Geol. 116, 104330. https://doi.org/10.1016/j.marpetgeo.2020.104330

Fialko, Y.A., Rubin, A.M., 1999. Thermal and mechanical aspects of magma emplacement in giant dike swarms. J. Geophys. Res. Solid Earth 104, 23033–23049. https://doi.org/10.1029/1999jb900213

Fjeldskaar, W., Helset, H. M., Johansen, H., Grunnaleite, I., Horstad, I., 2008. Thermal modelling of magmatic intrusions in the Gjallar Ridge, Norwegian Sea: Implications for vitrinite reflectance and hydrocarbon maturation. Basin Research, 20(1), 143–159. https://doi.org/10.1111/j.1365-2117.2007.00347.x

Florisbal, L.M., Heaman, L.M., de Assis Janasi, V., Bitencourt, M.F., 2014. Tectonic significance of the Florianópolis Dyke Swarm, Paraná-Etendeka Magmatic Province: A reappraisal based on precise U-Pb dating. Journal of Volcanology and Geothermal Research, 289, 140–150. https://doi.org/10.1016/j.jvolgeores.2014.11.007.

Florisbal, L.M., Janasi, V.A., Bitencourt, M.F., Nardi, L.V.S., Marteleto, N.S., 2018. Geological, geochemical and isotope diversity of ~ 134 Ma dykes from the Florianópolis Dyke Swarm, Paraná Magmatic Province: Geodynamic controls on petrogenesis. Journal of Volcanology and Geothermal Research, 355, 181–203. https://doi.org/10.1016/j.jvolgeores.2017.08.002

Fodor, R. V., Sial, A.N., Gandhok, G., 2002. Petrology of spinel peridotite xenoliths from northeastern Brazil: Lithosphere with a high geothermal gradient imparted by Fernando de Noronha plume. J. South Am. Earth Sci. 15, 199–214. https://doi.org/10.1016/S0895-9811(02)00032-9

Fodor, R.V., Sial, A.N., Mukasa, S.B., McKee, E.H., 1990. Petrology, isotope characteristics, and K-Ar ages of the Maranhão, northern Brazil, Mesozoic basalt province. Contributions to Mineralogy and Petrology 104(5), 555–567. https://doi.org/10.1007/BF00306664

Forniciai, A., Perinelli, C., Armienti, P., Favalli, M., 2015. Crystal size distributions of plagioclase in lavas from July–August 2001 Mount Etna eruption. Bulletin of Volcanology 77, 70. https://doi.org/10.1007/s00445–015–0953–8

Foulger, G.R., 2018. Origin of the South Atlantic igneous province. J. Volcanol. Geotherm. Res. 355, 2–20. https://doi.org/10.1016/j.jvolgeores.2017.09.004

Françolin, J.B.L., Cobbold, P.R., Szatmari, P., 1994. Faulting in the Early Cretaceous Rio do Peixe basin (NE Brazil) and its Significance for the Opening of the Atlantic. Journal of Structural Geology 16(5), 647–661. https://doi.org/10.1016/0191-8141(94)90116-3

Fraser, S.J., Dickson, B.L., 2007. A new method for data integration and integrated data interpretation: self-organizing maps. Proceedings of Exploration 07: Fifth Decennial International Conference on Mineral Exploration, 7, 907–910.

Fraser, S.J., Mikula, P. A., Lee, M.F., Dickson, B.L., Kinnersly, E., Snowden., 2006. Data mining mining data - Ordered vector quantisation and examples of its application to mine geotechnical data sets. 6th International Mining Geology Conference, Rising to the Challenge, (August), 259–268.

Friedel, M.J., 2011. Modeling hydrologic and geomorphic hazards across post-fire landscapes using a self-organizing map approach. Environmental Modelling and Software, 26(12), 1660–1674. https://doi.org/10.1016/j.envsoft.2011.07.001

Frizon De Lamotte, D., Fourdan, B., Leleu, S., Leparmentier, F., De Clarens, P., 2015. Style of rifting and the stages of Pangea breakup. Tectonics, 34(5), 1009–1029. https://doi.org/10.1002/2014TC003760

Fuck, R.A., Dantas, E.L., Vidotti, R.M., Roig, H.L., Almeida, T., 2011. Transbrasiliano lineament: a review and new data from airborne surveys and SRTM data. In: Gondwana 14 Reuniting Gondwana: The East Meets the West, Búzios. Abstracts. Rio de Janeiro: SBG, p.117.

Galerne, C.Y., Neumann, E.R., Planke, S., 2008. Emplacement mechanisms of sill complexes: Information from the geochemical architecture of the Golden Valley Sill Complex, South Africa. Journal of Volcanology and Geothermal Research, 177(2), 425–440. https://doi.org/10.1016/j.jvolgeores.2008.06.004

Gamal EL Dien, H., Doucet, L.S., Li, Z.X., 2019. Global geochemical fingerprinting of plume intensity suggests coupling with the supercontinent cycle. Nat. Commun. 10, 1–7. https://doi.org/10.1038/s41467-019-13300-4

García, H.L., González, I.M. 2004. Self-organizing map and clustering for wastewater treatment monitoring. Engineering Applications of Artificial Intelligence. https://doi.org/10.1016/j.engappai.2004.03.004

Geshi, N., 2005. Structural development of dike swarms controlled by the change of magma supply rate: The cone sheets and parallel dike swarms of the Miocene Otoge igneous complex, Central Japan. Journal of Volcanology and Geothermal Research, 141(3–4), 267–281. https://doi.org/10.1016/j.jvolgeores.2004.11.002

Gibbons, A.D., Whittaker, J.M., Müller, R.D., 2013. The breakup of East Gondwana: Assimilating constraints from Cretaceous ocean basins around India into a best-fit tectonic model. Journal of Geophysical Research: Solid Earth, 118(3), 808–822. https://doi.org/10.1002/jgrb.50079.

Gibson, S.A., Thompson, R.N., Day, J.A., Humphris, S. E., Dickin, A. P., 2005. Melt-generation processes associated with the Tristan mantle plume: Constraints on the origin of EM-1. Earth and Planetary Science Letters, 237(3–4), 744–767. https://doi.org/10.1016/j.epsl.2005.06.015

Gill, R., 2010. Igneous Rocks and Processes A Practical Guide.

Góes, A.M.O.; Feijó, F.J., 1994. Bacia do Parnaíba. Boletim de Geociências da Petrobras 8(1), 57-68.

Gomes, A.S., Vasconcelos, P.M., 2021. Geochronology of the Paraná-Etendeka large igneous province. Earth-Science Rev. 220, 103716. https://doi.org/10.1016/j.earscirev.2021.103716

Gomes, C.B., 2015. A Microssonda Eletrônica na Geologia. Editora da Universidade de São Paulo. 248 pp.

Gomes, J.R.C.; Gatto, C.M.P.P.; Souza, G.M.C.DE; Luz, D.S. DA; Pires, J.L.; Teixeira, W.; Franca, F.A.B.DE; Cabral, E.M.A.; Menor, E.A.; Monteiro, N.; Barros, M.J.G.; Ribeiro, E.G.; Lima, E.A.DE; Fonseca, R.A.DA., 1981. Geologia. In: PROJETO RADAMBRASIL. Folhas SB.24/25 Jaguaríbe e Natal; geologia, geomorfologia, pedologia, vegetação e uso potencial da terra. Rio de Janeiro.

Granot, R., Dyment, J., 2015. The Cretaceous opening of the South Atlantic Ocean. Earth and Planetary Science Letters 414, 156–163. https://doi.org/10.1016/j.epsl.2015.01.015

Gray, N.H., 1971. A parabolic hourglass structure in titanaugite. American Mineralogist 56, 952–958.

Greber, N.D., Davies, J.H.F.L., Gaynor, S.P., Jourdan, F., Bertrand, H., Schaltegger, U. 2020. New high precision U-Pb ages and Hf isotope data from the Karoo large igneous province; implications for pulsed magmatism and early Toarcian environmental perturbations. Results in Geochemistry, 1(August), 100005. https://doi.org/10.1016/j.ringeo.2020.100005

Greenough, J.D., McDivitt, J.A., 2018. Earth's evolving subcontinental lithospheric mantle: inferences from LIP continental flood basalt geochemistry. International Journal of Earth Sciences, 107(3), 787–810. https://doi.org/10.1007/s00531-017-1493-6

Griffin, W.L., O'Reilly, S.Y., Afonso, J.C., Begg, G.C., 2009. The composition and evolution of lithospheric mantle: A re-evaluation and its tectonic implications. Journal of Petrology, 50(7), 1185–1204. https://doi.org/10.1093/petrology/egn033

Gualda, G.A.R., Ghiorso, M. S., Lemons, R.V., Carley, T.L., 2012. Rhyolite-MELTS: A modified calibration of MELTS optimized for silica-rich, fluid-bearing magmatic systems. Journal of Petrology, 53(5), 875–890. https://doi.org/10.1093/petrology/egr080

Gudmundsson, A., 2011. Deflection of dykes into sills at discontinuities and magma-chamber formation. Tectonophysics, 500(1–4), 50–64. https://doi.org/10.1016/j.tecto.2009.10.015.

Guedes, E., Heilbron, M., de Morisson Valeriano, C., de Almeida, J.C.H., Szatmari, P. 2016. Evidence of Gondwana early rifting process recorded by Resende-Ilha Grande Dike Swarm, southern Rio de Janeiro, Brazil. Journal of South American Earth Sciences, 67, 11–24. https://doi.org/10.1016/j.jsames.2016.01.004

Guiraud, R., Maurin, J.C., 1992. Early Cretaceous rifts of Western and Central Africa: an Overview. Tectonophysics 213(1–2), 153–168. https://doi.org/10.1016/0040-1951(92)90256-6

Hammer, J., Jacob, S., Welsch, B., Hellebrand, E., Sinton, J., 2016. Clinopyroxene in postshield Haleakala ankaramite: 1. Efficacy of thermobarometry. Contributions to Mineralogy and Petrology 171(1). https://doi.org/10.1007/s00410-015-1212-x

Hanyu, T., Tatsumi, Y., Kimura, J.I., 2011. Constraints on the origin of the HIMU reservoir from He-Ne-Ar isotope systematics. Earth Planet. Sci. Lett. 307, 377–386. https://doi.org/10.1016/j.epsl.2011.05.012

Hart, S.R., 1984. The DUPAL anomaly: A large-scale isotopic anomaly in the southern hemisphere. Nature 309, 753–756.

Hart, W.K., Carlson, R.W., Shirey, S.B., 1997. Radiogenic Os in primitive basalts from the northwestern U.S.A.: Implications for petrogenesis. Earth Planet. Sci. Lett. 150, 103–116. https://doi.org/10.1016/s0012-821x(97)00075-7

Hartmann, L.A., Arena, K.R., Duarte, S.K., 2012. Geological relationships of basalts, andesites and sand injectites at the base of the Paraná volcanic province, Torres, Brazil. Journal of Volcanology and Geothermal Research, 237–238, 97–111. https://doi.org/10.1016/j.jvolgeores.2012.05.017

Hartmann, L.A., Arena, K.R., Duarte, S.K., Pertille, J., 2013. Long-distance lava correlation in the Paraná volcanic province along the Serra Geral cuesta, southeastern Brazil. Int. J. Earth Sci. 102, 1655–1669. https://doi.org/10.1007/s00531-013-0899-z

Hartmann, L.A., Baggio, S.B., Brückmann, M.P., Knijnik, D.B., Lana, C., Massonne, H.J., Opitz, J., Pinto, V.M., Sato, K., Tassinari, C.C.G., Arena, K.R., 2019. U-Pb geochronology of Paraná volcanics combined with trace element geochemistry of the zircon crystals and zircon Hf isotope data. J. South Am. Earth Sci. 89, 219–226. https://doi.org/10.1016/j.jsames.2018.11.026

Hawkesworth, C., Mantovani, M., Peate, D., 1988. Lithosphere remobilization during parana cfb magmatism. J. Petrol. Special_Vo, 205–223. https://doi.org/10.1093/petrology/Special_Volume.1.205

Heilbron, M., Guedes, E., Mane, M., Valeriano, C.M., Tupinambá, M., Almeida, J., Silva, L.G.E., Duarte, B.P., Dela Favera, J.C., Viana, A., 2018. Geochemical and temporal provinciality of the magmatism of the eastern Parnaíba Basin, NE Brazil. In: Daly, M. C., Fuck, R. A., Julià, J., Macdonald, D.I.M., Watts, A. B. (eds) cratonic basin formation: a case study of the Parnaíba Basin of Brazil. Geological Society, London, Special Publications 472. https://doi.org/10.1144/SP472.11

Heimann, A., Fleming, T. H., Elliot, D. H., Foland, K. A., 1994. A short interval of Jurassic continental flood basalt volcanism in Antarctica as demonstrated by 40Ar39Ar geochronology. Earth and Planetary Science Letters, 121(1–2), 19–41. https://doi.org/10.1016/0012-821X(94)90029-9

Heimdal, T.H., Callegaro, S., Svensen, H.H., Jones, M.T., Pereira, E., Planke, S., 2019. Evidence for magma–evaporite interactions during the emplacement of the Central Atlantic Magmatic Province (CAMP) in Brazil. Earth and Planetary Science Letters, 506, 476–492. https://doi.org/10.1016/j.epsl.2018.11.018

Heimdal, T.H., Svensen, H.H., Ramezani, J., Iyer, K., Pereira, E., Rodrigues, R., … Callegaro, S., 2018. Large-scale sill emplacement in Brazil as a trigger for the end-Triassic crisis. Scientific Reports, 8(1), 1–12. https://doi.org/10.1038/s41598-017-18629-8

Heine, C., Zoethout, J., Müller, R.D., 2013. Kinematics of the South Atlantic rift. Solid Earth, 4(2), 215–253. https://doi.org/10.5194/se-4-215-2013

Higgins, M. D., 2002. Closure in crystal size distributions (CSD), verification of CSD calculations, and the significance of CSD fans. American Mineralogist, 87(1), 171-175. https://doi.org/10.2138/am-2002-0118

Higgins, M.D., 1996. Magma dynamics beneath Kameni volcano, Thera, Greece, as revealed by crystal size and shape measurements. Journal of Volcanology and Geothermal Research, 70(1–2), 37–48. https://doi.org/10.1016/0377-0273(95)00045-3.

Higgins, M.D., 1998. Origin of Anorthosite by Textural Coarsening: Quantitative Measurements of a Natural Sequence of Textural Development. Journal of Petrology 39 (7), 1307–1323.https://doi.org/10.1093/petroj/39.7.1307.

Higgins, M.D., 2000. Measurement of crystal size distributions. American Mineralogist, 85(9), 1105–1116. https://doi.org/10.2138/am-2000-8-901

Higgins, M.D., 2006. Verification of ideal semi-logarithmic, lognormal or fractal crystal size distributions from 2D datasets. J. Volcanol. Geotherm. Res. 154, 8–16. https://doi.org/10.1016/j.jvolgeores.2005.09.015

Higgins, M.D., 2011. Textural coarsening in igneous rocks. International Geology Review 53, 354–376. https://doi.org/10.1080/00206814.2010.496177

Higgins, M.D., Roberge J., 2003. Crystal size distribution of plagioclase and amphibole from Soufriere Hills Volcano, Montserrat: evidence for dynamic crystallization–textural coarsening cycles. Journal of Petrology 44 (8), 1401–1411. https://doi.org/10.1093/petrology/44.8.1401

Higgins, M.D., Verification of ideal semi-logarithmic, lognormal or fractal crystal size distributions from 2D datasets. J. of Volcanol. and Geotherm. R., 154(1–2), 2006, 8–16. https://doi.org/10.1016/j.jvolgeores.2005.09.015

Hodgkinson, J. H., Fraser, S. J., Donchak, P., 2013. Using self-organising maps to derive lithological boundaries from geophysically-derived data in the Mt. Isa region, Queensland. ASEG Extended Abstracts, 2012(1), 1–4. https://doi.org/10.1071/aseg2012ab359.

Hoernle, K., Rohde, J., Hauff, F., Garbe-Schönberg, D., Homrighausen, S., Werner, R., Morgan, J.P., 2015. How and when plume zonation appeared during the 132 Myr evolution of the Tristan Hotspot. Nature Communications 6. https://doi.org/10.1038/ncomms8799

Hollanda, M.H.B.M., Archanjo, C.J., Macedo Filho, A.A., Fossen, H., Ernst, R.E., de Castro, D.L., Melo, A.C.C., Oliveira, A.L., 2019. The Mesozoic Equatorial Atlantic Magmatic Province (EQUAMP), in Srivastava, R.K., Ernst, R.E., Peng (Eds.), Dyke

Swarms of the World: A Modern Perspective, Springer, Singapore. pp. 87–110. https://doi.org/10.1007/978-981-13-1666-1

Hollanda, M.H.B.M., Góes, A.M., Negri, F.A., 2018. Provenance of sandstones in the Parnaíba Basin through detrital zircon geochronology. In: Daly, M. C., Fuck, R. A., Julià, J., Macdonald, D.I.M., Watts, A. B. (eds) cratonic basin formation: a case study of the Parnaíba Basin of Brazil. Geological Society, London, Special Publications 472. https://doi.org/10.1144/SP472.16

Hollanda, M.H.B.M., Martins Pimentel, M., Jardim de Sá, E.F., 2003. Paleoproterozoic subduction-related metasomatic signatures in the lithospheric mantle beneath NE Brazil: Inferences from trace element and Sr-Nd-Pb isotopic compositions of Neoproterozoichigh-K igneous rocks. J. South Am. Earth Sci. 15, 885–900. https://doi.org/10.1016/S0895-9811(03)00014-2

Hollanda, M.H.B.M., Pimentel, M.M., Oliveira, D.C., de Sá, E.F.J., 2006. Lithosphere-asthenosphere interaction and the origin of Cretaceous tholeiitic magmatism in Northeastern Brazil: Sr-Nd-Pb isotopic evidence. Lithos 86, 34–49. https://doi.org/10.1016/j.lithos.2005.04.004

Homrighausen, S., Hoernle, K., Geldmacher, J., Wartho, J. A., Hauff, F., Portnyagin, M., …Garbe-Schönberg, D., 2018. Unexpected HIMU-type late-stage volcanism on the Walvis Ridge. Earth and Planetary Science Letters, 492, 251–263. https://doi.org/10.1016/j.epsl.2018.03.049.

Homrighausen, S., Hoernle, K., Hauff, F., Geldmacher, J., Wartho, J. A., van den Bogaard, P., & Garbe-Schönberg, D., 2018. Global distribution of the HIMU end member: Formation through Archean plume-lid tectonics. Earth-Science Reviews, 182(June 2017), 85–101. https://doi.org/10.1016/j.earscirev.2018.04.009.

Homrighausen, S., Hoernle, K., Hauff, F., Wartho, J.A., van den Bogaard, P., Garbe-Schönberg, D., 2019. New age and geochemical data from the Walvis Ridge: The temporal and spatial diversity of South Atlantic intraplate volcanism and its possible origin. Geochim. Cosmochim. Acta 245, 16–34. https://doi.org/10.1016/j.gca.2018.09.002

Hooper, P., Widdowson, M., Kelley, S. 2010. Tectonic setting and timing of the final Deccan flood basalt eruptions. Geology, 38(9), 839–842. https://doi.org/10.1130/G31072.1

Hosseini, K., Matthews, K. J., Sigloch, K., Shephard, G. E., Domeier, M. and Tsekhmistrenko, M., 2018, SubMachine: Web-Based tools for exploring seismic tomography and other models of Earth's deep interior. Geochemistry, Geophysics, Geosystems, 19. doi:10.1029/2018GC007431

Irvine, T.N., Baragar, W.R.A., 1971. A guide to the chemical classification of the common volcanic rocks. Canadian Journal of Earth Sciences 8, 523–548.

Iyer, K., Rüpke, L., Galerne, C.Y., 2013. Modeling fluid flow in sedimentary basins with sill intrusions: Implications for hydrothermal venting and climate change. Geochemistry, Geophys. Geosystems 14, 5244–5262. https://doi.org/10.1002/2013GC005012

Janasi, V. de A., de Freitas, V.A., Heaman, L.H., 2011. The onset of flood basalt volcanism, Northern Paraná Basin, Brazil: A precise U-Pb baddeleyite/zircon age for a Chapecó-type dacite. Earth and Planetary Science Letters, 302(1–2), 147–153. https://doi.org/10.1016/j.epsl.2010.12.005.

Janasi, V. de A., Negri, F. de A., Montanheiro, T. J., Freitas, V.A. de, Rocha, B.C., Reis, P.M., 2007. Geochemistry of the eocretacic basalt magmatism in the Piraju-Ourinhos region, SE Brazil, and implications to the stratigraphy of the Serra Geral Formation.

Revista Brasileira de Geociências, 37(01), 148–162. https://doi.org/10.25249/0375-7536.2007371148162

Jensen, L.S., 1976. A New cation plot for classifying subalkalic volcanic rocks. Ontario Geological Survey Miscellaneous Paper 66.

Jerram, D. A., Dobson, K. J., Morgan, D. J., & Pankhurst, M. J., 2018. The petrogenesis of magmatic systems: Using igneous textures to understand magmatic processes. Volcanic and Igneous Plumbing Systems: Understanding Magma Transport, Storage, and Evolution in the Earth's Crust. https://doi.org/10.1016/B978-0-12-809749-6.00008-XJicha, B.R., Singer, B.S., Valentine, M.J., 2013. $^{40}Ar/^{39}Ar$ geochronology of subaerial Ascension island and a Re-evaluation of the temporal progression of basaltic to rhyolitic volcanism. Journal of Petrology, 54(12), 2581–2596. https://doi.org/10.1093/petrology/egt058

Jolliffe I.T., Cadima J., 2016. Principal component analysis: a review and recent developments. Phil. Trans. R. Soc. A 374: 20150202. http://dx.doi.org/10.1098/rsta.2015.0202

Jolliffe, I.T., 2002. Principal component analysis. 2nd edition. Springer. New York, New York, USA. 502 pp.

Jourdan, F., Bertrand, H., Schärer, U., Blichert-Toft, J., Féraud, G., Kampunzu, A.B., 2007. Major and trace element and Sr, Nd, Hf, and Pb isotope compositions of the Karoo large igneous province, Botswana - Zimbabwe: Lithosphere vs Mantle Plume Contribution. Journal of Petrology 48(6), 1043–1077. https://doi.org/10.1093/petrology/egm010.

Jourdan, F., Féraud, G., Bertrand, H., Kampunzu, A.B., Tshoso, G., Watkeys, M.K., Le Gall, B., 2005. Karoo large igneous province: Brevity, origin, and relation to mass extinction questioned by new 40Ar/39Ar age data. Geology 33, 745–748. https://doi.org/10.1130/G21632.1

Jourdan, F., Marzoli, A., Bertrand, H., Cosca, M., Fontignie, D., 2003. The Northernmost CAMP: $^{40}Ar/^{39}Ar$ age, petrology and Sr-Nd-Pb isotope geochemistry of the Kerforne Dike, Brittany, France. Geophysical Monograph Series, 136, 209–226. https://doi.org/10.1029/136GM011.

Kavanagh, J.L., Rogers, B.D., Boutelier, D., Cruden, A.R., 2017. Controls on sill and dyke-sill hybrid geometry and propagation in the crust: The role of fracture toughness. Tectonophysics, 698, 109–120. https://doi.org/10.1016/j.tecto.2016.12.027

Kawabata, H., Hanyu, T., Chang, Q., Kimura, J.I., Nichols, A.R.L., Tatsumi, Y., 2011. The petrology and geochemistry of St. Helena alkali basalts: Evaluation of the oceanic crust-recycling model for HIMU OIB. J. Petrol. 52, 791–838. https://doi.org/10.1093/petrology/egr003

Keiding, J.K., Frei, O., Renno, A.D., Veksler, I.V., Trumbull, R.B., 2013. Conditions of magma crystallization in the henties bay-outjo dyke swarm, namibia: Implications for the feeder system of continental flood basalts. Lithos, 179, 16–27. https://doi.org/10.1016/j.lithos.2013.07.018

Keiding, J.K., Trumbull, R.B., Veksler, I.V., Jerram, D.A., 2011. On the significance of ultra-magnesian olivines in basaltic rocks. Geology, 39(12), 1095–1098. https://doi.org/10.1130/G32214.1

Kent, R.W., Pringle, M.S., Müller, R.D., Saunders, A.D., Ghose, N.C., 2002. $^{40}Ar/^{39}Ar$ geochronology of the Rajmahal Basalts, India, and their relationship to the Kerguelen plateau. Journal of Petrology, 43(7), 1141–1153. https://doi.org/10.1093/petrology/43.7.1141.

Kimura, J., Gill, J.B.G., Skora, S., Keken, P.E.V., Kawabata, H., 2016. Origin of geochemical mantle components: Role of subduction filter. Geochemistry Geophysics Geosystems, 17, 1312–1338. https://doi.org/10.1002/2015GC006205.

King, S.D., Anderson, D.L., 1995. An alternative mechanism of flood basalt formation. Earth and Planetary Science Letters, 136(3–4), 269–279. https://doi.org/10.1016/0012-821X(95)00205-Q.

King, S.D., Ritsema, J., 2000. African hot spot volcanism: Small-scale convection in the upper mantle beneath cratons. Science, 290(5494), 1137–1140. https://doi.org/10.1126/science.290.5494.1137

Kirpatrick, R.J., 1977. Nucleation and growth of plagioclase, Makaopuhi and Alac lava lakes, Kilauea Volcano, Hawaii. Geological Society of America Bulletin 88, 78–84. https://doi.org/10.1130/0016-7606(1977)88<78:nagopm>2.0.co;2

Kirstein, L.A., Kelley, S., Hawkesworth, C., Turner, S., Mantovani, M., Wijbrans, J., 2001. Protracted felsic magmatic activity associated with the opening of the South Atlantic. J. Geol. Soc. London. 158, 583–592. https://doi.org/10.1144/jgs.158.4.583

Klein, E.L., Angélica, R.S., Harris, C., Jourdan, F., Babinski, M., 2013. Mafic dykes Intrusive into Pre-Cambrian Rocks of the São Luís Cratonic Fragment and Gurupi Belt (Parnaíba Province), North-northeastern Brazil: Geochemistry, Sr-Nd-Pb-O isotopes, $^{40}Ar/^{39}Ar$ geochronology, and relationships to CAMP magmatism. Lithos (172–173), 222–242. https://doi.org/10.1016/j.lithos.2013.04.015

Klöcking, M., White, N., Maclennan, J., 2018. Role of Basaltic Magmatism within the Parnaíba Cratonic Basin, NE Brazil. Geological Society, London, Special Publications, SP472.4. doi:10.1144/sp472.4.

Knight, K.B., Nomade, S., Renne, P.R., Marzoli, A., Bertrand, H., Youbi, N., 2004. The Central Atlantic Magmatic Province at the Triassic-Jurassic boundary: Paleomagnetic and $^{40}Ar/^{39}Ar$ evidence from Morocco for brief, episodic volcanism. Earth and Planetary Science Letters, 228(1–2), 143–160. https://doi.org/10.1016/j.epsl.2004.09.022

Kohonen, T., 1982. Self-organized formation of topologically correct feature maps. Biological Cybernetics, 43(1), 59–69. https://doi.org/10.1007/BF00337288

Kohonen, T., 2001. Self-Organizing Maps. Third Edition. Springer Series in Information Berlin; Heidelberg; New York; Barcelona; Hong Kong; London; Milan; Paris; Singapore; Tokyo: Springer.

Kohonen, T., 2013. Essentials of the self-organizing map. Neural Networks, 37, 52–65. https://doi.org/10.1016/j.neunet.2012.09.018.

Krentz, O., 1982. Zum Charakter der Metamorphose und zur Altersstellung Pelitischer Metamorphite des Westlichen Erzgebirges. Dr rer nat thesis Bergakademie Freiberg, pp. 176.

Lacassie, J.P., McClung, C.R., Bailie, R.H., Gutzmer, J. and Ruiz-Del-Solar, J., 2006. Geochemical patterns of schists from the Bushmanland Group: An artificial neural networks approach. Journal of Geochemical Exploration, 91, 81-98.

Lacassie, J.P., Roser, B., Del Solar, J.R. and Herve, F., 2004. Discovering geochemical patterns using self-organizing neural networks: a new perspective for sedimentary provenance analysis. Sedimentary Geology, 165, 175-191.

Launeau, P., 2004. Mise en évidence des écoulements magmatiques par analyse d'image 2–D des distributions 3–D d'orientations préférentielles de formes. Bulletin de la Société géologique de France 175(4): 331–350. https://doi.org/10.2113/175.4.331

Le Maitre, R.W., 2002. Igneous rocks – a classification and glossary of terms. Recommendations of the IUGS subcommission on the systematics of igneous rocks. Cambridge: Cambridge University Pres. 2nd edn.

Leat, P.T., 2008. On the long-distance transport of Ferrar magmas. Geol. Soc. Spec. Publ. 302, 45–61. https://doi.org/10.1144/SP302.4

Li, Z., Eastman, J.R. 2010. Commitment and typicality measures for the Self-Organizing Map. International Journal of Remote Sensing, 31(16), 4265–4280. https://doi.org/10.1080/01431160903246725

Li, Z.X., Bogdanova, S.V., Collins, A.S., Davidson, A., De Waele, B., Ernst, R.E., Fitzsimons, I.C.W., Fuck, R.A., …Vernikovsky, V. 2008. Assembly, configuration, and break-up history of Rodinia: A synthesis. Precambrian Research, 160(1–2), 179–210. https://doi.org/10.1016/j.precamres.2007.04.021

Lima, E.A., Leite J.F., 1978. Projeto Estudo Global de Recursos Minerais da Bacia do Parnaíba: Integração Geológica-metalogenética. Relatório Final da Etapa III, DNPM/CPRM, Recife.

Lima, F.G.F., Jardim de Sá, E. F., 2017. Controle Estrutural da Borda Eudeste da Bacia do Parnaíba, Nordeste do Brasil: Relação com Eventos Geodinâmicos no Gondwana. Geologia USP - Serie Cientifica 17(3–4), 3–21. https://doi.org/10.11606/issn.2316-9095.v17-125909.

Lima, M.V.A.G. d., Berrocal, J., Soares, J.E.P., Fuck, R.A., 2015. Deep seismic refraction experiment in northeast Brazil: New constraints for Borborema province evolution. J. South Am. Earth Sci. 58, 335–349. https://doi.org/10.1016/j.jsames.2014.10.007

Lino, L.M., Vlach, S.R.F. 2021. Textural and Geochemical Evidence for Multiple, Sheet-like Magma Pulses in the Limeira Intrusion, Paraná Magmatic Province, Brazil. Journal of Petrology, 62(3), 1–38. https://doi.org/10.1093/petrology/egab011

Lofgren, G., 1974. An experimental study of plagioclase crystal morphology: isothermal crystallization. Journal of Science 274, 243–273. https://doi.org/10.2475/ajs.274.3.243

Löhr, S.C., Grigorescu, M., Hodgkinson, J.H., Cox, M.E., Fraser, S.J., 2010. Iron occurrence in soils and sediments of a coastal catchment. A multivariate approach using self organising maps. Geoderma, 156(3–4), 253–266. https://doi.org/10.1016/j.geoderma.2010.02.025.

Loule, J.P., Pospisil, L., 2013. Geophysical evidence of Cretaceous volcanics in Logone Birni Basin (Northern Cameroon), Central Africa, and consequences for the West and Central African Rift System. Tectonophysics 583, 88–100. https://doi.org/10.1016/j.tecto.2012.10.021

Lu, C., Grand, S.P., Lai, H., Garnero, E.J., 2019. TX2019slab: A New P and S Tomography Model Incorporating Subducting Slabs. Journal of Geophysical Research: Solid Earth. doi:10.1029/2019jb017448

Luttinen, A.V. 2018. Bilateral geochemical asymmetry in the Karoo large igneous province. Scientific Reports, 8(1), 1–11. https://doi.org/10.1038/s41598-018-23661-3.

Luttinen, A.V., Furnes, H. 2000. Flood basalts of Vestfjella: Jurassic magmatism across an Archaean-Proterozoic lithospheric boundary in Dronning Maud Land, Antarctica. Journal of Petrology, 41(8), 1271–1305. https://doi.org/10.1093/petrology/41.8.1271.

Luz, R.M.N., Julià, J., do Nascimento, A.F., 2015. Bulk crustal properties of the Borborema Province, NE Brazil, from P-wave receiver functions: Implications for models of intraplate Cenozoic uplift. Tectonophysics 644, 81–91. https://doi.org/10.1016/j.tecto.2014.12.017

Macdonald, G. A., Katsura, T., 1964. Chemical Composition of Hawaiian Lavas. Journal of Petrology, 229(62), 82–133. https://doi.org/10.1016/j.precamres.2012.04.001.

Macêdo Filho, A. A., Archanjo, C. J., Hollanda, M. H. B. M., Negri, F. A., 2019. Mineral Chemistry and Crystal Size Distributions of Mafic Dikes and Sills on the Eastern Border of the Parnaíba Basin, NE Brazil. Journal of Volcanology and Geothermal Research 377, 69–80.

Machado, F.B., Nardy, A.J.R., Oliveira, M.A.F. de. 2007. Geologia e aspectos petrológicos das rochas intrusivas e efusivas mesozóicas de parte da borda leste da bacia do Paraná no estado de São Paulo. Revista Brasileira de Geociências, 37(1), 64–80. https://doi.org/10.25249/0375-7536.20073716480

Machado, F.B., Rocha-Júnior, E.R.V., Marques, L.S., Nardy, A.J.R., 2015. Volcanological aspects of the northwest region of Paraná continental flood basalts (Brazil). Solid Earth 6, 227–241. https://doi.org/10.5194/se-6-227-2015

Machado, F.B., Rocha-Júnior, E.R.V., Marques, L.S., Nardy, A.J.R., Zezzo, L.V., Marteleto, N.S., 2018. Geochemistry of the northern paraná Continental Flood Basalt (PCFB) province: Implications for regional chemostratigraphy. Brazilian J. Geol. 48, 177–199. https://doi.org/10.1590/2317-4889201820180098

Magee C., Ernst R.E., Muirhead J., Phillips T., Jackson C.AL., 2019. Magma Transport Pathways in Large Igneous Provinces: Lessons from Combining Field Observations and Seismic Reflection Data. In: Srivastava R., Ernst R., Peng P. (eds) Dyke Swarms of the World: A Modern Perspective. Springer Geology. Springer, Singapore. https://doi.org/10.1007/978-981-13-1666-1_2

Magee, C., Muirhead, J. D., Karvelas, A., Holford, S.P., Jackson, C.A.L., Bastow, I. D., … Shtukert, O., 2016. Lateral magma flow in mafic sill complexes. Geosphere, 12(3), 809–841. https://doi.org/10.1130/GES01256.1

Maluski, H., Coulon, C., Popoff, M., Baudin, P., 1995. $^{40}Ar/^{39}Ar$ chronology, petrology and geodynamic setting of Mesozoic to early Cenozoic magmatism from the Benue Trough, Nigeria. Journal of the Geological Society 152(2), 311–326. https://doi.org/10.1144/gsjgs.152.2.0311

Maluski, H., Coulon, C., Popoff, M., Baudin, P., 1995. $^{40}Ar/^{39}Ar$ chronology, petrology and geodynamic setting of Mesozoic to early Cenozoic magmatism from the Benue Trough, Nigeria. Journal of the Geological Society 152(2), 311–326. https://doi.org/10.1144/gsjgs.152.2.0311

Mantovani, M.S.M., Hawkesworth, C.J., 1990. An inversion approach to assimilation and fractional crystallisation processes. Contrib. to Mineral. Petrol. 105, 289–302. https://doi.org/10.1007/BF00306540

Mantovani, M.S.M., Marques, L.S., De Sousa, M.A., Civetta, L., Atalla, L., Innocenti, F., 1985. Trace element and strontium isotope constraints on the origin and evolution of paraná continental flood basalts of Santa Catarina state (Southern Brazil). J. Petrol. 26, 187–209. https://doi.org/10.1093/petrology/26.1.187

Mantovani, S.M., Peate, D.W., Hawkesworth, C.J., 1988. Geochemical stratigraphy of Parana continental flood basalts: a contribution from boreholes samples. Mesozoic Flood Volcanism Parana Basin 15–24.

Marques, L.S., De Min, A., Rocha-Júnior, E.R.V., Babinski, M., Bellieni, G., Figueiredo, A.M.G., 2018. Elemental and Sr-Nd-Pb isotope geochemistry of the Florianópolis Dyke Swarm (Paraná Magmatic Province): crustal contamination and mantle source constraints. Journal of Volcanology and Geothermal Research 355, 149–164. https://doi.org/10.1016/j.jvolgeores.2017.07.005

Marques, L.S., Dupré, B., Piccirillo, E.M., 1999. Mantle source compositions of the Parana Magmatic Province (southern Brazil): Evidence from trace element and Sr-Nd-Pb isotope geochemistry. J. Geodyn. 28, 439–458. https://doi.org/10.1016/S0264-3707(99)00020-4

Marques, L.S., Rocha-Júnior, E.R.V., Babinski, M., Carvas, K.Z., Petronilho, L.A., De Min, A., 2016. Lead isotope constraints on the mantle sources involved in the genesis of Mesozoic high-Ti tholeiite dykes (Urubici type) from the São Francisco Craton (Southern Espinhaço, Brazil). Brazilian Journal of Geology 46, 105–122. https://doi.org/10.1590/2317-4889201620150010

Marsh, B. D., 1988. Crystal size distribution (CSD) in rocks and the kinetics and dynamics of crystallisation. Contributions to Mineralogy and Petrology 99, 277–291. https://doi.org/10.1007/BF00371933

Marsh, J.S., Ewart, A., Milner, S.C., Duncan, A.R., Miller, R.M.G., 2001. The Etendeka Igneous Province: Magma types and their stratigraphic distribution with implications for the evolution of the Paraná-Etendeka flood basalt province. Bulletin of Volcanology, 62(6–7), 464–486. https://doi.org/10.1007/s004450000115

Marsh, J.S., Swart, R., 2018. The Bero Volcanic Complex: Extension of the Paraná-Etendeka Igneous Province into SW Angola. Journal of Volcanology and Geothermal Research, 355, 21–31. https://doi.org/10.1016/J.JVOLGEORES.2016.10.011

Martins, G., Oliveira, D.C., 1992. O Enxame e Diques Rio Ceará-Mirim (EDCM) no Contexto da Abertura do Atlântico. Revista de Geologia 5, 51–78.

Marzoli, A, Renne, PR, Piccirillo, EM, Ernesto, M, Bellieni, G, De Min, A., 1999. Extensive 200–million–year old continental flood basalts of the Central Atlantic Magmatic Province. Science 284:616–618. DOI: 10.1126/science.284.5414.616

Marzoli, A, Renne, PR, Piccirillo, EM, Ernesto, M, Bellieni, G, De Min, A., 1999. Extensive 200–million–year old continental flood basalts of the Central Atlantic Magmatic Province. Science 284:616–618. https://doi.org/10.1126/science.284.5414.616

Marzoli, A., Callegaro, S., Dal Corso, J., Davies, J. H. F. L., Chiaradia, M., Youbi, N., … Jourdan, F. 2018. The Central Atlantic Magmatic Province (CAMP): A Review. https://doi.org/10.1007/978-3-319-68009-5_4

Marzoli, A., Melluso, L., Morra, V., Renne, P.R., Sgrosso, I., D'Antonio, M., Duarte Morais, L., Morais, E.A.A., Ricci, G., 1999. Geochronology and petrology of Cretaceous basaltic magmatism in the Kwanza basin (western Angola), and relationships with the Parana-Etendeka continental flood basalt province. J. Geodyn. 28, 341–356. https://doi.org/10.1016/S0264-3707(99)00014-9

Marzoli, A., Renne, P.R., Piccirillo, E.M., 2000. Ar/Ar geochronology of Mesozoic continental basaltic magmatism, and the open- ing of the central, equatorial and southern Atlantic Ocean. Penrose 2000, Volcanic Rifted Margins. University of London, p. 54.

Masquelin, H., Aïfa, T., Muzio, R., Hallot, E., Veroslavsky, G., Bonnevalle, L., 2009. The Cuaró Mesozoic doleritic dyke swarm, southern Paraná basin, Uruguay: Examples of superimposed magnetic fabrics? Comptes Rendus - Geosci. 341, 1003–1015. https://doi.org/10.1016/j.crte.2009.07.004

Matos, R.D., 1992. The Northeast Brazilian Rift System. Tectonics 11(4), 766–791. https://doi.org/10.4324/9780429496073-6

Matos, R.M., 2000. Tectonic Evolution of the Equatorial South Atlantic the Brazilian and West African Equatorial Margins Comprise America. Atlantic Rifts and Continental Margins, 331–354. https://doi.org/10.1029/GM115p0331

Matthews, K.J., Maloney, K.T., Zahirovic, S., Williams, S.E., Seton, M., Müller, R.D., 2016. Global plate boundary evolution and kinematics since the late Paleozoic. Global and Planetary Change, 146, 226–250. https://doi.org/10.1016/j.gloplacha.2016.10.002

Mauche, R., Faure, G., Jones, L. M., Hoefs, J., 1989. Anomalous isotopic compositions of Sr, Ar and O in the Mesozoic diabase dikes of Liberia, West Africa. Contributions to Mineralogy and Petrology, 101(1), 12–18. https://doi.org/10.1007/BF00387197

McKenzie, D., 1978. Some remarks on the development of sedimentary basins. Earth Planet. Sci. Lett. 40, 25–32. https://doi.org/10.1016/0012-821X(78)90071-7

McMaster, M., Almeida, J., Heilbron, M., Guedes, E., Mane, M. A., Linus, J.H. 2019. Characterisation and tectonic implications of the Early Cretaceous, Skeleton Coast Dyke Swarm, NW Namibia. Journal of African Earth Sciences, 150(May 2018), 319–336. https://doi.org/10.1016/j.jafrearsci.2018.11.010

Melo, A.C.C., de Castro, D., Oliveira, D.C., Hollanda, M.H.B.M., 2022. Mesozoic dike swarms in Borborema Province (NE Brazil): A structural analysis based on airborne geophysical data and field work. Journal of South American Earth Sciences, 113. https://doi.org/10.1016/j.jsames.2021.103650

Melo, A.C.C., de Castro, D.L., Fraser, S.J., de Macêdo Filho, A.A., 2021. Using self-organizing maps in airborne geophysical data for mapping mafic dyke swarms in NE Brazil. J. Appl. Geophys. 192, 104377. https://doi.org/10.1016/j.jappgeo.2021.104377

Menand, T., 2011. Physical controls and depth of emplacement of igneous bodies: A review. Tectonophysics, 500(1–4), 11–19. https://doi.org/10.1016/j.tecto.2009.10.016

Merle, R., Marzoli, A., Bertrand, H., Reisberg, L., Verati, C., Zimmermann, C., Chiaradia, M., Belienni, G., Ernesto, M., 2011. 40Ar/39Ar ages and Sr–Nd–Pb–Os geochemistry of CAMP tholeiites from western Maranhão Basin (NE Brazil). Lithos 122, 137–151. https://doi.org/10.1016/j.lithos.2010.12.010

Merle, R., Marzoli, A., Reisberg, L., Bertrand, H., Nemchin, A., Chiaradia, M., Callegaro, S., Jourdan, F., Bellieni, G., Kontak, D., Puffer, J., Gregory McHone, J., 2014. Sr, Nd, Pb and Os isotope systematics of CAMP tholeiites from Eastern North America (ENA): Evidence of a subduction-enriched mantle source. J. Petrol. 55, 133–180. https://doi.org/10.1093/petrology/egt063

Mills, R.D., Glazner, A.F., 2013. Experimental study on the effects of temperature cycling on coarsening of plagioclase and olivine in alkali basalt. Contributions to Mineralogy and Petrology 166, 97–111. https://doi.org/10.1007/s00410=013–0867–4

Miloski, P., Castro, S., Julio, V., Mendes, C., Neysi, C., 2020. Petrogenesis of the Low- TiO_2 Batalha Suite in the Eastern Parnaíba basin, Northeastern Brazil. International Journal of Earth Sciences. https://doi.org/10.1007/s00531-020-01829-5

Miloski, P., Cezar, J., Neysi, C., Almeida, D., Castro, S., Regina, S., Medeiros, D., 2019. Journal of South American Earth Sciences Petrogenesis of Continental Flood Basalts in Eastern Parnaiba Basin, Brazil: A Singular Sill Occurrence with Low- and High-TiO_2 Tholeiites. Journal of South American Earth Sciences 94, 102192. https://doi.org/10.1016/j.jsames.2019.05.008

Miranda, F.S.D.E., Vettorazzi, A.N.A.L., Cunha, R.D.A.C., Aragão, F.B., Michelon, D., Caldeira, J.L., Porsche, E., Martins, C., Ribeiro, R.B., Vilela, A.F., Corrêa, J.R., Silveira, L.S., Andreola, K., Janeiro, E.S.A.R. De, 2018. Atypical igneous-sedimentary petroleum systems of the Parnaíba Basin , Brazil : seismic , well logs and cores.

Miyashiro, A., 1978. Nature of alkalic volcanic rock series. Contributions to Mineralogy and Petrology, 66(1), 91–104. https://doi.org/10.1007/BF00376089

Mizusaki, A.M.P., Saracchini, F.E., 1991. Cataálogo geral de dados geocronológicos da Petrobras. Internal Report, p. 24.

Mizusaki, A.M.P., Thomaz-Filho, A., Milani, E.J., De Césero, P., 2002. Mesozoic and Cenozoic igneous activity and its tectonic control in northeastern Brazil. J. South Am. Earth Sci. 15, 183–198. https://doi.org/10.1016/S0895-9811(02)00014-7

Mocitaiba, L.S.R., De Castro, D.L., De Oliveira, D.C., 2017. Cartografia geofísica regional do magmatismo mesozoico na Bacia do Parnaíba. Geologia USP - Serie Cientifica, 17(2), 169–192. https://doi.org/10.11606/issn.2316-9095.v17-455

Morgan, D.J., Jerram, D.A., 2006. On estimating crystal shape for crystal size distribution analysis. Journal of Volcanology and Geothermal Research 154, 1–7. https://doi.org/10.1016/j.jvolgeores.2005.09.016

Morgan, D.J., Jerram, D.A., Chertkoff, D.G., Davidson, J.P., Pearson, D.G., Kronz, A., Nowell, G.M., 2007. Combining CSD and isotopic microanalysis: Magma supply and mixing processes at Stromboli Volcano, Aeolian Islands, Italy Earth and Planetary Science Lettters 260, 419–431. https://doi.org/10.1016/j.epsl.2007.05.037

Morgan, W.J., 1971. Convection plumes in the lower mantle. Nature, 230(5288), 42–43. https://doi.org/10.1038/230042a0

Moulin, M., Aslanian, D., Unternehr, P., 2010. A new starting point for the South and Equatorial Atlantic Ocean. Earth-Science Reviews, 98(1–2), 1–37. https://doi.org/10.1016/j.earscirev.2009.08.001

Muirhead, J.D., Airoldi, G., Rowland, J. V., White, J.D.L., 2012. Interconnected sills and inclined sheet intrusions control shallow magma transport in the Ferrar large igneous province, Antarctica. Bull. Geol. Soc. Am. 124, 162–180. https://doi.org/10.1130/B30455.1

Muzio, R., Peel, E., Porta, N., Scaglia, F., 2017. Mesozoic dykes and sills from Uruguay: Sr – Nd isotope and trace element geochemistry. Journal of South American Earth Sciences, 77, 92–107. https://doi.org/10.1016/j.jsames.2017.04.016

Muzio, R., Scaglia, F., Masquelin, H., 2012. Petrochemistry of mesozoic mafic in- trusions related to the Paran?a magmatic province, Uruguay. Int. Geol. Rev. 54, 844e860 nº7.

Nakano, S., 1992. Internal textures and chemical compositions of anti–rapakivi mantled feldspars from Oki–Dogo Island, Japan. Mineralogy and Petrology 46(2), 123–135. https://doi.org/10.1007/BF01160182

Ngonge, E.D., Archanjo, C.J., Hollanda, M.H.B.M., 2013. Plagioclase crystal size distribution in some tholeiitic mafic dikes in Cabo Frio–Búzios, Rui de Janeiro, Brazil. Journal of Volcanology and Geothermal Research 255, 26–42. https://doi.org/10.1016/j.jvolgeores.2013.01.009

Ngonge, E.D., de Hollanda, M.H.B.M., Archanjo, C.J., de Oliveira, D.C., Vasconcelos, P.M.P., Muñoz, P.R.M., 2016a. Petrology of continental tholeiitic magmas forming a 350-km-long Mesozoic dyke swarm in NE Brazil: Constraints of geochemical and isotopic data. Lithos 258–259, 228–252. https://doi.org/10.1016/j.lithos.2016.04.008

Ngonge, E.D., de Hollanda, M.H.B.M., Pimentel, M.M., de Oliveira, D.C., 2016b. Petrology of the alkaline rocks of the Macau Volcanic Field, NE Brazil. Lithos 266–267, 453–470. https://doi.org/10.1016/j.lithos.2016.10.008

Ngonge, E.D., de Hollanda, M.H.B.M., Puchtel, I.S., Walker, R.J., Archanjo, C.J., 2019. Characteristics of the lithospheric mantle beneath northeastern Borborema Province, Brazil: Re–Os and HSE constraints on peridotite xenoliths. Journal of South American Earth Sciences 96, 102371. https://doi.org/10.1016/j.jsames.2019.102371

Niu, Y., 2018. Origin of the LLSVPs at the base of the mantle is a consequence of plate tectonics – A petrological and geochemical perspective. Geoscience Frontiers, 9(5), 1265–1278. https://doi.org/10.1016/j.gsf.2018.03.005

Northfleet, A.A., Neves, S.B., 1966. Semidetalhe da região sudoeste do Alto Parnaíba. Relatório Petrobrás, Belém.

Olierook, H.K.H., Jourdan, F., Merle, R.E., Timms, N.E., Kusznir, N., Muhling, J.R., 2016. Bunbury Basalt: Gondwana breakup products or earliest vestiges of the Kerguelen mantle plume? Earth Planet. Sci. Lett. 440, 20–32. https://doi.org/10.1016/j.epsl.2016.02.008

Oliveira, A.L., Hollanda, M.H.B.M., Siqueira, R., A.A. Macêdo Filho. 2021. Geological Society, London, Special Publications, 518, 5 May 2021, https://doi.org/10.1144/SP518-2020-250

Oliveira, A.L., Pimentel, M.M., Fuck, R.A., Oliveira, D.C., 2018. Petrology of Jurassic and Cretaceous basaltic formations from the Parnaíba Basin, NE Brazil: correlations and associations with large igneous provinces. In: Daly, M. C., Fuck, R. A., Julià, J., Macdonald, D.I.M., Watts, A. B. (eds) cratonic basin formation: a case study of the Parnaíba Basin of Brazil. Geological Society, London, Special Publications 472. https://doi.org/10.1144/SP472.9

Oliveira, D.C. 1994. Novas considerações sobre a evolução tectônica do enxame de diques Rio Ceará-Mirim – Nordeste oriental do Brasil. Revista da Escola de Minas, Ouro Preto, 47 (3)223-27.

Oliveira, D.C., 1992. O papel do Enxame de Diques Rio Ceará Mirim na evolução tectônica do nordeste oriental (Brasil): implicações na formação do Rifte Potiguar. MSc thesis, Universidade Federal de Ouro Preto, Ouro Preto, Brazil.

Oliveira, D.C., Gomes, C.J.S., 1996. A Expressão de Reativações Pós-intrusão do Enxame de Diques Rio Ceará Mirim (Mesozóico): Implicações na Evolução Tectônica da Bacia Potiguar. Boletim de Geociências da Petrobras.

Owen-Smith, T.M., Trumbull, R.B., Bauer, K., Keiding, J.K., Will, T.M., 2021. A neural network application to assess magma diversity in the Etendeka igneous province, Namibia, 124. https://doi.org/10.25131/sajg.124.0034/5323446/0034

Pearce, J.A., Ernst, R.E., Peate, D.W., Rogers, C., 2021. LIP printing: Use of immobile element proxies to characterize Large Igneous Provinces in the geologic record. Lithos, 392–393, 106068. https://doi.org/10.1016/j.lithos.2021.106068

Peate, D.W., 1997. The Paraná-Etendeka province. Geophys. Monogr. Ser. 100, 217–245. https://doi.org/10.1029/GM100p0217

Peate, D.W., Hawkesworth, C.J., 1996. Lithospheric to asthenospheric transition in low-Ti flood basalts from southern Paraná, Brazil. Chem. Geol. 127, 1–24. https://doi.org/10.1016/0009-2541(95)00086-0

Peate, D.W., Hawkesworth, C.J., Mantovani, M.M.S., Rogers, N.W., Turner, S.P., 1999. Petrogenesis and stratigraphy of the high-Ti/Y Urubici magma type in the Parana Flood Basalt Province and implications for the nature of 'Dupal'-type mantle in the South Atlantic Region. Journal of Petrology 40(3), 451–473. https://doi.org/10.1093/petroj/40.3.451

Peate, D.W., Hawkesworth, C.J., Mantovani, M.S.M., 1992. Chemical stratigraphy of the Paraná lavas (South America): classification of magma types and their spatial distribution. Bulletin of Volcanology, 55(1–2), 119–139. https://doi.org/10.1007/BF00301125.

Peng, P., 2010. Reconstruction and interpretation of giant mafic dyke swarms: A case study of 1.78 Ga magmatism in the North China craton. Geological Society Special Publication, 338, 163–178. https://doi.org/10.1144/SP338.8.

Penn, B.S., 2005. Using self-organizing maps to visualize high-dimensional data. Comput. Geosci. 31, 531–544. https://doi.org/10.1016/j.cageo.2004.10.009

Petersohn, E., Gouvea, E.M. 2009. Geologia e geoquímica da soleira de Reserva, estado do Paraná. Revista Brasileira de Geociências, 39(4), 740–750. https://doi.org/10.25249/0375-7536.2009394740750

Petrini, R., Civetta, L., Piccirillo, E.M., Bellieni, G., Comin-chiaramonti, P., Marques, L.S., Melfi, A.J., 1987. Mantle heterogeneity and crustal contamination in the genesis of low-ti continental flood basalts from the paranà plateau (brazil): Sr-nd isotope and geochemical evidence. J. Petrol. 28, 701–726. https://doi.org/10.1093/petrology/28.4.701

Philpotts, A.R., 1982. Compositions of immiscible liquids in volcanic rocks. Contrib. to Mineral. Petrol. 80, 201–218. https://doi.org/10.1007/BF00371350

Piccirillo, E.M., 1988. Continental flood volcanism from the Parana basin (Brazil), Continental flood basalts. https://doi.org/10.1007/978-94-015-7805-9_6

Piccirillo, E.M., Bellieni, G., Cavazzini, G., Comin-Chiaramonti, P., Petrini, R., Melfi, A.J., Pinese, J.P.P., Zantadeschi, P., De Min, A., 1990. Lower Cretaceous tholeiitic dyke swarms from the Ponta Grossa Arch (southeast Brazil): Petrology, Sr-Nd isotopes and genetic relationships with the Paraná flood volcanics. Chem. Geol. 89, 19–48. https://doi.org/10.1016/0009-2541(90)90058-F

Pinto, V.M., Hartmann, L.A., Santos, J.O.S., McNaughton, N.J., Wildner, W., 2011. Zircon U-Pb geochronology from the Paraná bimodal volcanic province support a brief eruptive cycle at ~135Ma. Chem. Geol. 281, 93–102. https://doi.org/10.1016/j.chemgeo.2010.11.031

Powell, R., 1984. Inversion of the assimilation and fractional crystallization (AFC) equations; characterization of contaminants from isotope and trace element relationships in volcanic suites. Journal of the Geological Society 141(3), 447–452. doi:10.1144/gsjgs.141.3.0447

Preece, K., Barclay, J., Gertisser, R., Herd, R.A., 2013. Textural and micropetrological variations in the eruptive products of the 2006 dome–forming eruption of Merapi volcano, Indonesia: implications for sub–surface processes. Journal of Volcanology and Geothermal Research 261, 98–120. https://doi.org/10.1016/j.jvolgeores.2013.02.006

Pupier, E., Duchene, S., Toplis, M.J., 2008. Experimental quantification of plagioclase crystal size distribution during cooling of a basaltic liquid. Contributions to Mineralogy and Petrology 155, 555–570. https://doi.org/10.1007/s00410007–0258–9

Putirka, K., Johnson, M., Kinzler, R., Longhi, J., Walker, D., 1996. Thermobarometry of mafic igneous rocks based on clinopyroxene-liquid equilibria, 0-30 kbar. Contributions to Mineralogy and Petrology volume 123, 92-108. https://doi.org/10.1007/s004100050145

Putirka, K.D., 2008. Thermometers and barometers for volcanic systems. Reviews in Mineralogy and Geochemistry 69(1), 61–120. https://doi.org/10.2138/rmg.2008.69.3

Putirka, K.D., 2008. Thermometers and barometers for volcanic systems. Reviews in Mineralogy and Geochemistry 69(1), 61–120. https://doi.org/10.2138/rmg.2008.69.3

Rämö, O.T., Heikkilä, P.A., Pulkkinen, A.H., 2016. Geochemistry of Paraná-Etendeka basalts from Misiones, Argentina: Some new insights into the petrogenesis of high-Ti continental flood basalts. J. South Am. Earth Sci. 67, 25–39. https://doi.org/10.1016/j.jsames.2016.01.008

Randolph, A.D., Larson, M.A., 1971. Theory of Particulate Processes. Academic Press, New York.

Raposo, M.I.B., Ernesto, M., Renne, P.R., 1998. Paleomagnetism and 40Ar/39Sr dating of the early Cretaceous Florianopolis dike swarm (Santa Catarina Island), Southern Brazil. Phys. Earth Planet. Inter. 108, 275–290. https://doi.org/10.1016/S0031-9201(98)00102-2

Rayleigh, Lord. 1896. L. Theoretical considerations respecting the separation of gases by diffusion and similar processes. Philosophical Magazine Series 5, 42(259), 493–498. https://doi.org/10.1080/14786449608620944

Reid, D.L., Rex, D.C., 1994. Cretaceous dykes associated with the opening of the South Atlantic: the Mehlberg dyke, northern Richtersveld. South African J. Geol. 97, 135–145.

Reis, N.J., Teixeira, W., Hamilton, M.A., Bispo-Santos, F., Almeida, M.E., D'Agrella-Filho, M.S., 2013. Avanavero Mafic Magmatism, a Late Paleoproterozoic LIP in the Guiana Shield, Amazonian Craton: U-Pb ID-TIMS Baddeleyite, Geochemical and Paleomagnetic Evidence. Lithos 174, 175–195. https://doi.org/10.1016/j.lithos.2012.10.014

Renne, P.R., Deckart, K., Ernesto, M., Féraud, G., & Piccirillo, E. M. 1996a. Age of the Ponta Grossa dike swarm (Brazil), and implications to Paraná flood volcanism. Earth and Planetary Science Letters, 144(1–2), 199–211. https://doi.org/10.1016/0012-821x(96)00155-0

Renne, P.R., Glen, J.M., Milner, S.C., Duncan, A.R., 1996b. Age of Etendeka flood volcanism and associated intrusions in southwestern Africa. Geology 24, 659–662. https://doi.org/10.1130/0091-7613(1996)024<0659:AOEFVA>2.3.CO;2

Renne, P.R., Sprain, C.J., Richards, M.A., Self, S., Vanderkluysen, L., Pande, K. 2015. State shift in Deccan volcanism at the Cretaceous-Paleogene boundary, possibly induced by impact. Science, 350(6256), 76–78.

Renner, L.C. 2010. Geoquímica de Sills basálticos da Formação Serra Geral, Sul do Brasil, com base em rocha total e micro-análise de minerais. Universidade Federal do Rio Grande do Sul, Instituto de Geociências, Porto Alegre, Brazil.

Resmini, R.G., 2007. Modeling of crystal size distributions in sills. Journal of Volcanology and Geothermal Research 161,118–130. https://doi.org/10.1016/j.jvolgeores.2006.06.023

Richards, M. A., Griffiths, R. W., 1989. Thermal entrainment by deflected mantle plumes. Nature, 342(6252), 900–902. https://doi.org/10.1038/342900a0

Richards, P.C., Stone, P., Kimbell, G.S., McIntosh, W.C., Phillips, E.R., 2013. Mesozoic magmatism in the Falkland Islands (South Atlantic) and their offshore sedimentary basins. J. Pet. Geol. 36, 61–73. https://doi.org/10.1111/jpg.12542

Riisager, P., Knight, K.B., Baker, J.A., Ukstins Peate, I., Al-Kadasi, M., Al-Subbary, A., Renne, P.R., 2005. Paleomagnetism and $^{40}Ar/^{39}Ar$ Geochronology of Yemeni Oligocene volcanics: Implications for timing and duration of Afro-Arabian traps and geometry of the Oligocene paleomagnetic field. Earth and Planetary Science Letters, 237(3–4), 647–672. https://doi.org/10.1016/j.epsl.2005.06.016

Rivalenti, G., Mazzucchelli, M., Girardi, V.A.V., Vannucci, R., Barbieri, M.A., Zanetti, A., Goldstein, S.L., 2000. Composition and processes of the mantle lithosphere in northeastern Brazil and Fernando de Noronha: Evidence from mantle xenoliths. Contrib. to Mineral. Petrol. 138, 308–325. https://doi.org/10.1007/s004100050565

Rivalenti, G., Zanetti, A., Girardi, V. A. V., Mazzucchelli, M., Tassinari, C.C.G., Bertotto, G.W., 2007. The effect of the Fernando de Noronha plume on the mantle lithosphere in north-eastern Brazil. Lithos 94(1–4), 111–131. https://doi.org/10.1016/j.lithos.2006.06.012

Rocha-Júnior, E.R.V., Marques, L.S., Babinski, M., Machado, F.B., Petronilho, L.A., Nardy, A.J.R., 2020. A telltale signature of Archean lithospheric mantle in the Paraná continental flood basalts genesis. Lithos 364–365. https://doi.org/10.1016/j.lithos.2020.105519

Rocha-Júnior, E.R.V., Marques, L.S., Babinski, M., Nardy, A.J.R., Figueiredo, A.M.G., Machado, F.B., 2013. Sr-Nd-Pb isotopic constraints on the nature of the mantle sources involved in the genesis of the high-Ti tholeiites from northern Paraná Continental Flood Basalts (Brazil). J. South Am. Earth Sci. 46, 9–25. https://doi.org/10.1016/j.jsames.2013.04.004

Rocha-Júnior, E.R.V., Puchtel, I.S., Marques, L.S., Walker, R.J., Machado, F.B., Nardy, A.J.R., Babinski, M., Figueiredo, A.M.G., 2012. Re-Os isotope and highly siderophile element systematics of the Paraná continental flood basalts (Brazil). Earth and Planetary Science Letters 337–338, 164–173. https://doi.org/10.1016/j.epsl.2012.04.050

Rodrigues, J.B. 2015. Relatório interno. Projeto Opala. Serviço Geológico do Brasil (CPRM), Brasília. 83p

Rosset, A., De Min, A., Marques, L.S., Macambira, M.J.B., Ernesto, M., Renne, P.R., Piccirillo, E.M., 2007. Genesis and geodynamic significance of Mesoproterozoic and Early Cretaceous tholeiitic dyke swarms from the São Francisco craton (Brazil). Journal of South American Earth Sciences, 24(1), 69–92. https://doi.org/10.1016/j.jsames.2007.02.002

Royer, J.Y., Coffin, M.F., 1992. Jurassic to Eocene plate tectonic reconstructions in the Kerguelen Plateau region. Proc., Scientific Results, ODP, Leg 120, Central Kerguelen Plateau, (September), 917–928. https://doi.org/10.2973/odp.proc.sr.120.200.1992

Rubert, R.R., Mizusaki, A.M.P., Martinelli, A.G., 2019. Mesozoic tectonic in the deposition and evolution of Cretaceous sedimentary packages of the Parecis Basin, center-western Brazil. J. South Am. Earth Sci. 93, 140–154. https://doi.org/10.1016/j.jsames.2019.05.002

Rudnick, R.L., Fountain, D.V., 1995. Nature Crust: and Composition of the Continental Perspective. Physics of the Earth and Planetary Interiors, 145(95), 267–309

Salisbury, M.J., Bohrson, W.A., Clynne, M.A., Ramos, F.C., Hoskin, P., 2008. Multiple plagioclase crystal population identified by crystal size distribution and in situ chemical data: Implications for timescales of magma chamber processes associated with the 1915 eruptions of Lassen Peak, CA. Journal of Petrology, 49(10), 1755-1780. DOI:10.1093/petrology/egn045

Sano, T., 2001. Differentiation Processes of Deccan Trap Basalts: Contribution from Geochemistry and Experimental Petrology. J. Petrol. 42, 2175–2195. https://doi.org/10.1093/petrology/42.12.2175

Santiago, R., de Andrade Caxito, F., Aparecida Neves, M., Luiz Dantas, E., Batista de Medeiros Júnior, E., Nascimento Queiroga, G., 2019. Two generations of mafic dyke swarms in the southeastern brazilian coast: reactivation of structural lineaments during the gravitational collapse of the araçuaí-ribeira orogen (500 ma) and west gondwana breakup (140 ma). Precambrian Research, (January), 105344. https://doi.org/10.1016/j.precamres.2019.105344

Santos, C.H.O., Jardim de Sá, E.F., Alves da Silva, F.C., Antunes, A.F., 2018. Reativações pós-silurianas do Lineamento Transbrasiliano na porção sul da Bacia do Parnaíba. Geologia USP. Série Científica, 18(2), 71-86. https://doi.org/10.11606/issn.2316-9095.v18-134712

Santos, E.J., Schmus, W.R. Van, Kozuch, M., Neves, B.B.B., 2010. The Cariris Velhos Tectonic Event in Northeast Brazil. Journal of South American Earth Sciences 29(1), 61–76. https://doi.org/10.1016/j.jsames.2009.07.003

Santos, L.C.M. d. L., Dantas, E.L., Vidotti, R.M., Cawood, P.A., dos Santos, E.J., Fuck, R.A., Lima, H.M., 2017. Two-stage terrane assembly in Western Gondwana: Insights

from structural geology and geophysical data of central Borborema Province, NE Brazil. J. Struct. Geol. 103, 167–184. https://doi.org/10.1016/j.jsg.2017.09.012

Santos, T.D. dos, 2006. Petrogênese dos basaltos de baixo-TiO_2 do Enxame de Diques da Serra do Mar na Região dos Lagos, RJ. MSc thesis. Universidade do Estado do Rio de Janeiro. Rio de Janeiro, Brazil.

Sarmento, C.C.T., Sommer, C. A., De Lima, E. F., De Oliveira, D.S. 2014. Corpos hipabissais correlacionados à Formação Serra Geral na região do Cerro do Coronel, RS: Geologia e petrologia. Geologia USP - Serie Cientifica, 14(2), 23–44. https://doi.org/10.5327/Z1519-874X201400020002

Sarmento, C.C.T., Sommer, C. A., Lima, E.F., 2017. Mafic subvolcanic intrusions and their petrologic relation with the volcanism in the south hinge Torres Syncline, Paraná-Etendeka Igneous Province, southern Brazil. Journal of South American Earth Sciences, 77, 70–91. https://doi.org/10.1016/j.jsames.2017.04.017

Saunders, A.D., 2005. Large Igneous Provinces: Origin and Enviromental Consequences. Elements 1, 259–263. https://doi.org/10.2113/gselements.1.5.265

Schilling, J.G., Thompson, G., Kingsley, R., Humphris, S., 1985. Hotspot-migrating ridge interaction in the South Atlantic. Nature, 313(5999), 187–191. https://doi.org/10.1038/313187a0

Schobbenhaus, C., Ribeiro, C.L., Oliva, L.A., Takanohashi, J.T., Lindenmayer, A.G., Vasconcelos, J.C., Orlandi, V., 1975. Carta Geológica do Brasil ao Milionésimo, Folha Goiás (SD–22). DNPM, Brasília.

Schoene, B., Eddy, M.P., Samperton, K.M., Keller, C.B., Keller, G., Adatte, T., Khadri, S.F. R., 2019. U-Pb constraints on pulsed eruption of the Deccan Traps across the end-Cretaceous mass extinction. Science, 363(6429), 862–866. https://doi.org/10.1126/science.aau2422

Seber, D., Barazangi, M., Ibenbrahim, A., Demnati, A., 1996. Geophysical evidence for lithospheric delamination beneath the alboran sea and rif-betic mountains. Nature 379, 785–790. https://doi.org/10.1038/379785a0

Segev, A., 2002. Flood basalts, continental breakup and the dispersal of Gondwana: evidence for periodic migration of upwelling mantle flows (plumes). Stephan Mueller Spec. Publ. Ser. 2, 171–191. https://doi.org/10.5194/smsps-2-171-2002

Sénant J., Popoff, M., 1991. Early Cretaceous Extension in Northeast Brazil Related to the South Atlantic Opening. Tectonophysics 198:35-46

Sensarma, S., Storey, B.C., Malviya, V.P., 2017. Gondwana Large Igneous Provinces (LIPs): distribution, diversity and significance. Geological Society, London, Special Publications, 463, 1–16. https://doi.org/10.1144/SP463.11

Seton, M., Müller, R.D., Zahirovic, S., Gaina, C., Torsvik, T., Shephard, G., Talsma, A., Gurnis, M., Turner, M., Maus, S., Chandler, M., 2012. Global continental and ocean basin reconstructions since 200Ma. Earth-Science Reviews, 113(3–4), 212–270. https://doi.org/10.1016/j.earscirev.2012.03.002

Sheth, H.C., 2007. Large Igneous Provinces (LIPs)': Definition, recommended terminology. https://doi.org/10.1016/j.earscirev.2007.07.005.

Shore, M., Fowler, A.D., 1996. Oscillatory zoning in minerals: A common phenomenon. Can. Mineral. 34, 1111–1126.

Sial, A.N., 1976. The post-paleozoic volcanism of northeast Brazil and its tectonic significance. An. Acad. Bras. Cienc. 48, 299–311.

Sial, A.N., Oliveira, E.P., Choudhuri, A., Mafic dyke swarm of Brazil. 1987. in Mafic dyke swarms, Editors: Halls, H.C. and Fahrig, W.F., Geological Association of Canada Special Paper 34., p. 467-481.

Silva, A.G., Almeida, C.N., Valente, S.C., Almeida, L.F.B., 2017. The petrogenesis of tholeiitic diabases in eastern Parnaíba Basin: evidence for geochemical heterogeneities in the subcontinental lithospheric mantle in NE Brazil. Brazilian Journal of Geology 47(2), 275–299. https://doi.org/10.1590/2317

Silva, P.H.M., Jardim de Sá, E.F., Souza, Z.S. de, Córdoba, V.C., 2020. Structural Controls and Stratigraphic Setting of Sills: Example of the Central Atlantic Magmatic Province in the Parnaíba Basin, Northeast Brazil. Journal of South American Earth Sciences 101, 102606. https://doi.org/10.1016/j.jsames.2020.102606

Smith J.V., Brown W.L., 1988. Feldspar minerals, vol 1. Springer, Berlin Heidelberg, New York.

Smith, P.E., Evensen, N.M., York, D., Szatmari, P., Oliveira, D.C., 2001. Single-crystal ^{40}Ar-^{39}Ar Dating of Pyrite: No Fool's Clock. Geology 403–406. https://doi.org/10.1130/0091-7613(2001)029<0403:SCAADO>2.0.CO;2

Souza, S.Z., Vasconcelos, P.M., Nascimento, M.A.L., Silveira, F.V., Paiva, H.S., Dias, L.G.S., Thiede, D., Carmo, I.O., 2003. 40Ar /39Ar geochronology of Mesozoic and Cenozoic magmatism in NE Brazil. Short Pap. - IV South Am. Symp. Isot. Geol. 691–694

Souza, Z.S., Kalsbeek, F., Deng, X.D., Frei, R., Kokfelt, T.F., Dantas, E.L., Li, J., Pimental, M.M., Galindo, A.C., 2016. Generation of continental crust in the northern part of the Borborema Province, northeastern Brazil, from Archaean to Neoproterozoic. Journal of South American Earth Sciences 68, 68–96. https://doi.org/10.1016/j.jsames.2015.10.006

Špillar, V., Dolejš, D., 2015. Melt extraction from crystal mushes: Numerical model of texture evolution and calibration of crystallinity–ordering relationships. Lithos 239, 19–32. https://doi.org/10.1016/j.lithos.2015.10.001

Stewart, K., Turner, S., Kelley, S., Hawkesworth, C., Kirstein, L., Mantovani, M., 1996. 3-D, 40Ar-39Ar geochronology in the Paraná continental flood basalt province. Earth Planet. Sci. Lett. 143, 95–109. https://doi.org/10.1016/0012-821x(96)00132-x

Stica, J.M., Zalán, P.V., Ferrari, A.L., 2014. The evolution of rifting on the volcanic margin of the Pelotas Basin and the contextualization of the Paraná-Etendeka LIP in the separation of Gondwana in the South Atlantic. Mar. Pet. Geol. 50, 1–21. https://doi.org/10.1016/j.marpetgeo.2013.10.015

Stone, P., 2013. Mesozoic dyke swarms of the Falkland Islands (South Atlantic). Keyworth, Nottingham, British Geological Survey, 11p.

Stone, P., Richards, P.C., Kimbell, G.S., Esser, R.P., Reeves, D. 2008. Cretaceous dykes discovered in the Falkland Islands: implications for regional tectonics in the South Atlantic. Journal of the Geological Society, 165(1), 1–4. https://doi.org/10.1144/0016-76492007-072

Stracke, A., 2012. Earth's heterogeneous mantle: A product of convection-driven interaction between crust and mantle. Chemical Geology, 330–331, 274–299. https://doi.org/10.1016/j.chemgeo.2012.08.007

Stracke, A., Hofmann, A.W., Hart, S.R., 2005. FOZO, HIMU, and the rest of the mantle zoo. Geochemistry, Geophysics, Geosystems 6(5). https://doi.org/10.1029/2004GC000824

Streck, M.J., 2008. Mineral Textures and Zoning as Evidence for Open System Processes. Rev. Mineral. Geochemistry 69, 595–622. https://doi.org/10.2138/rmg.2008.69.15

Stroncik, N.A., Trumbull, R.B., Krienitz, M.S., Niedermann, S., Romer, R.L., Harris, C., Day, J.M.D., 2017. Helium isotope evidence for a deep-seated mantle plume involved in South Atlantic breakup. Geology 45, 827–830. https://doi.org/10.1130/G39151.1

Sun, S.S., McDonough, W.F., 1989. Chemical and isotopic systematics of oceanic basalts: implications for mantle composition and processes. Geological Society, London, Special Publications 42(1), 313–345. https://doi.org/10.1144/GSL.SP.1989.042.01.19

Svensen, H. H., Torsvik, T. H., Callegaro, S., Augland, L., Heimdal, T. H., Jerram, D. A., … Pereira, E. 2017. Gondwana Large Igneous Provinces: Plate reconstructions, volcanic basins and sill volumes. Geological Society Special Publication, 463(1), 17–40. https://doi.org/10.1144/SP463.7

Svensen, H., Planke, S., Chevallier, L., Malthe-Sørenssen, A., Corfu, F., & Jamtveit, B., 2007. Hydrothermal venting of greenhouse gases triggering Early Jurassic global warming. Earth and Planetary Science Letters, 256(3–4), 554–566. https://doi.org/10.1016/j.epsl.2007.02.013

Svensen, H., Planke, S., Malthe-Sørenssen, A., Jamtveit, B., Myklebust, R., Rasmussen Eidem, T., & Rey, S. S. 2004. Release of methane from a volcanic basin as a mechanism for initial Eocene global warming. Nature, 429(6991), 542–545. https://doi.org/10.1038/nature02566

Swanson, S.E., 1977. Relation of nucleation and crystal-growth rate to the development of granitic textures. American Mineralogist, 62(9–10), 966–978.

Tatsumi, Y., Suzuki, T., 2009. Tholeiitic vs calc-alkalic differentiation and evolution of arc crust: Constraints from melting experiments on a basalt from the Izu-Bonin-Mariana arc. Journal of Petrology 50(8), 1575–1603. https://doi.org/10.1093/petrology/egp044

Tegner, C., Wilson, J.R., Robins, B., 2005. Crustal assimilation in basalt and jotunite: Constraints from layered intrusions. Lithos 83, 299–316. https://doi.org/10.1016/j.lithos.2005.03.007

Teixeira, W., Hamilton, M. A., Girardi, V. A. V., Faleiros, F. M., & Ernst, R. E., 2019. U-Pb Baddeleyite Ages of Key Dyke Swarms in the Amazonian Craton (Carajás/Rio Maria and Rio Apa areas): Tectonic Implications for events at 1880, 1110 Ma, 535 Ma and 200 Ma. Precambrian Research 329, 138–155. https://doi.org/10.1016/j.precamres.2018.02.008

Thiede, D.S., Vasconcelos, P. M. 2010. Paraná flood basalts: Rapid extrusion hypothesis confirmed by new $^{40}Ar/^{39}Ar$ results. Geology, 38(8), 747–750. https://doi.org/10.1130/G30919.1

Thompson, R.N., Gibson, S.A., Dickin, A.P. and Smith, P.M., 2001. Early Cretaceous Basalt and Picrite Dykes of the Southern Etendeka Region, NW Namibia: Windows into the Role of the Tristan Mantle Plume in Paraná–Etendeka Magmatism. Journal of Petrology, 42, 2049-208

Thompson, R.N., Riches, A.J.V., Antoshechkina, P.M., Pearson, D.G., Nowell, G.M., Ottley, C.J., Dickin, A.P., Hards, V.L., Nguno, A.-K. and Niku-Paavola, V., 2007. Origin of CFB Magmatism: Multi-tiered Intracrustal Picrite-Rhyolite Magmatic Plumbing at Spitzkoppe, Western Namibia, during Early Cretaceous Etendeka Magmatism. Journal of Petrology, 48, 1119-1154

Torsvik, T.H., Smethurst, M.A., Burke, K., Steinberger, B., 2006. Large igneous provinces generated from the margins of the large low-velocity provinces in the deep mantle. Geophysical Journal International, 167(3), 1447–1460. https://doi.org/10.1111/j.1365-246X.2006.03158.x

Torsvik, T.H., Van der Voo, R., Preeden, U., Mac Niocaill, C., Steinberger, B., Doubrovine, P. V., … Cocks, L.R.M., 2012. Phanerozoic Polar Wander, Palaeogeography and Dynamics. Earth-Science Reviews, 114(3–4), 325–368. https://doi.org/10.1016/j.earscirev.2012.06.007

Tozer, B., Watts, A.B., Daly, M.C., 2017. Crustal structure, gravity anomalies, and subsidence history of the Parnaíba cratonic basin, Northeast Brazil. J. Geophys. Res. Solid Earth 122, 5591–5621. https://doi.org/10.1002/2017JB014348

Trønnes, R.G., 2010. Structure, mineralogy and dynamics of the lowermost mantle. Mineralogy and Petrology, 99(3–4), 243–261. https://doi.org/10.1007/s00710-009-0068-z

Trosdtorf, I., Neto, J.M.M., Santos, S.F., Filho, C.V.P., Oglio, T.A.D., Galves, A.C.M., Silva, A.M., 2018. Phanerozoic magmatism in the Parnaíba Basin: characterization of igneous bodies (well logs and 2D seismic sections), geometry, distribution and sill emplacement patterns. In: Daly, M. C., Fuck, R. A., Julià, J., Macdonald, D.I.M., Watts, A. B. (eds) cratonic basin formation: a case study of the Parnaíba Basin of Brazil. Geological Society, London, Special Publications 472. https://doi.org/1144/SP472.10

Trumbull, R. B., Vietor, T., Hahne, K., Wackerle, R., Ledru, P., 2004. Aeromagnetic mapping and reconnaissance geochemistry of the Early Cretaceous Henties Bay-Outjo dike swarm, Etendeka Igneous Province, Namibia. Journal of African Earth Sciences, 40(1–2), 17–29. https://doi.org/10.1016/j.jafrearsci.2004.07.006

Trumbull, R.B., Reid, D.L., de Beer, C., van Acken, D., Romer, R.L., 2007. Magmatism and continental breakup at the west margin of southern Africa: A geochemical comparison of dolerite dikes from northwestern Namibia and the Western Cape. South African Journal of Geology, 110(2–3), 477–502. https://doi.org/10.2113/gssajg.110.2-3.477

Turner, S.J., Langmuir, C.H., Dungan, M.A., Escrig, S., 2017. The importance of mantle wedge heterogeneity to subduction zone magmatism and the origin of EM1. Earth Planet. Sci. Lett. 472, 216–228. https://doi.org/10.1016/j.epsl.2017.04.051

Ubide, T., Kamber, B.S., 2018. Volcanic crystals as time capsules of eruption history. Nature Communications 9:236. https://doi.org/10.1038/s41467–017–02274–w

Ultsch, A., Vetter, C., 1994. Self-Organizing-Feature-Maps versus statistical clustering methods: a benchmark. Univ. Marburg, FG 1–14.

Ures, C., Feraud, G., Bertrand, H., Bossi, J. 1997. New age and geochemical constraints on the Parand flood volcanism: Additional data on Uruguay extrusive and intrusive formations.

Valente, S., Dutra, T., Heilbron, M., Szatmari, P. 2009. Litogeoquímica de diques de diabásio da Faixa Colatina, ES, 23(2), 177–192.

Van Schmus, W. R., Oliveira, E. P., Da Silva Filho, A. F., Toteu, S. F., Penaye, J., Guimarães, I. P. 2008. Proterozoic links between the Borborema Province, NE Brazil, and the Central African fold belt. Geological Society Special Publication, 294, 69–99. https://doi.org/10.1144/SP294.5

Vauchez, A., Barruol, G., Tommasi, A., 1997. Why do Continents Break-up Parallel to Ancient Orogenic Belts? Terra Nova 9(2), 62–66. https://doi.org/10.1111/j.1365-3121.1997.tb00003.x

Vauchez, A., Neves, S., Caby, R., Corsini, M., Egydio-Silva, M., Arthaud, M., Amaro, V., 1995. The Borborema Shear Zone System, NE Brazil. Journal of South American Earth Sciences 8(3–4), 247–266. https://doi.org/10.1016/0895-9811(95)00012-5

Vaz, P.T., Rezende, N.G.A.M., Wanderley Filho, J.R., Silva Travassos, W.A., 2007. Bacia do Parnaíba. Boletim de Geociências da Petrobras 15(2), 253–263.

Verati, C., Bertrand, H., Féraud, G., 2005. The farthest record of the Central Atlantic Magmatic Province into West Africa craton: Precise $^{40}Ar/^{39}Ar$ dating and geochemistry of Taoudenni basin intrusives (northern Mali). Earth and Planetary Science Letters, 235(1–2), 391–407. https://doi.org/10.1016/j.epsl.2005.04.012

Verati, C., Rapaille, C., Féraud, G., Marzoli, A., Bertrand, H., Youbi, N. 2007. $^{40}Ar/^{39}Ar$ ages and duration of the Central Atlantic Magmatic Province volcanism in Morocco and Portugal and its relation to the Triassic-Jurassic boundary. Palaeogeography, Palaeoclimatology, Palaeoecology, 244(1–4), 308–325. https://doi.org/10.1016/j.palaeo.2006.06.033

Vesanto, J., Alhoniemi, E., 2000. Clustering of the self-organizing map. IEEE Trans. Neural Networks 11, 586–600. https://doi.org/10.1109/72.846731

Vona, A., Romano, C., 2013. The effects of undercooling and deformation rates on the crystallization kinetics of Stromboli and Etna basalts. Contributions to Mineralogy and Petrology 166, 491–509. https://doi.org/10.1007/s00410–013–0887–0

Voorhees, P.W., 1992. Ostwald Ripening of Two-Phase Mixtures. Annual Review of Materials Science, 22(1), 197–215. https://doi.org/10.1146/annurev.ms.22.080192.001213

Ware, B.D., Jourdan, F., Merle, R., Chiaradia, M., Hodges, K., 2018. The Kalkarindji Large Igneous Province, Australia: Petrogenesis of the oldest and most compositionally homogenous province of the Phanerozoic. Journal of Petrology, 59(4), 635–666. https://doi.org/10.1093/petrology/egy040

Watson, E.B., Liang, Y., 1995. A simple model for sector zoning in slowly grown crystals: Implications for growth rate and lattice diffusion, with emphasis on accessory minerals in crustal rocks. American Mineralogist 80, 1179–1187. https://doi.org/10.2138/am-1995-11-1209

Whalen, L., Gazel, E., Vidito, C., Puffer, J., Bizimis, M., Henika, W., Caddick, M. J., 2015. Supercontinental inheritance and its influence on supercontinental breakup: The Central Atlantic Magmatic Province and the breakup of Pangea. Geochemistry, Geophysics, Geosystems, 1–23. https://doi.org/10.1002/2015GC005885

White, L.T., Gibson, G.M., Lister, G.S., 2013. A reassessment of paleogeographic reconstructions of eastern Gondwana: Bringing geology back into the equation. Gondwana Research, 24(3–4), 984–998. https://doi.org/10.1016/j.gr.2013.06.009

White, R., McKenzie, D., 1989. Magmatism at rift zones: the generation of volcanic continental margins and flood basalts. Journal of Geophysical Research, 94(B6), 7685–7729. https://doi.org/10.1029/JB094iB06p07685

White, R.S., McKenzie, D., 1995. Mantle plumes and flood basalts. Journal of Geophysical Research, 100(B9). https://doi.org/10.1029/95jb01585

White, W.M., 1985. Sources of oceanic basalts: radiogenic isotopic evidence. Geology, 13(2), 115–118. https://doi.org/10.1130/0091-7613(1985)13<115:SOOBRI>2.0.CO;2

Will, T.M., Frimmel, H. E., & Pfänder, J. A., 2016. Möwe Bay Dykes, Northwestern Namibia: Geochemical and geochronological evidence for different mantle source regions during the Cretaceous opening of the South Atlantic. Chemical Geology, 444, 141–157. https://doi.org/10.1016/j.chemgeo.2016.08.040

Willbold, M., Stracke, A., 2010. Formation of enriched mantle components by recycling of upper and lower continental crust. Chemical Geology, 276(3–4), 188–197. https://doi.org/10.1016/j.chemgeo.2010.06.005

Wilson, J.T., 1973. Plumes and Plate Motions; Tectonophysics, 19(2), 149–164.

Wilson, M., Guiraud, R., 1992. Magmatism and rifting in Western and Central Africa, from Late Jurassic to Recent times. Tectonophysics 213, 203–225. https://doi.org/10.1016/0040-1951(92)90259-9

Winter, J.D., 2001. An Introduction to Igneous and Metamorphic Petrology. Prentice-Hall, New Jersey. 697 pp.

Ye, J., Chardon, D., Rouby, D., Guillocheau, F., Dall'asta, M., Ferry, J.N., Broucke, O., 2017. Paleogeographic and structural evolution of northwestern Africa and its Atlantic margins since the early Mesozoic. Geosphere, 13(4), 1254–1284. https://doi.org/10.1130/GES01426.1

Zahirovic, S., Matthews, K.J., Flament, N., Müller, R.D., Hill, K.C., Seton, M., Gurnis, M., 2016. Tectonic evolution and deep mantle structure of the eastern Tethys since the latest Jurassic. Earth-Science Reviews, 162, 293–337. https://doi.org/10.1016/j.earscirev.2016.09.005

Zalán, P.V., Conceição, J.C.J., Wolf, S., Astolfi, M.A.M., Appi, V.T., Wolff, S., Vieira, I.S., Marques, A., 1985. Estilos estruturais relacionados a intrusões magmáticas básicas em rochas sedimentares. Boletim Técnico da Petrobras 28(4), 221–230.

Zeig, M.J., Marsh, B.D., 2002. Crystal size distribution and scaling laws in the quantification of igneous textures. Journal of Petrology 43(1), 85–101. https://doi.org/10.1093/petrology/43.1.85

Zheng, Y.F., 2019. Subduction zone geochemistry. Geosci. Front. 10, 1223–1254. https://doi.org/10.1016/j.gsf.2019.02.003

Zhou, H., Hoernle, K., Geldmacher, J., Hauff, F., Homrighausen, S., Garbe-Schönberg, D., Jung, S., 2020. Geochemistry of Etendeka magmatism: Spatial heterogeneity in the Tristan-Gough plume head. Earth and Planetary Science Letters, 535, 116123. https://doi.org/10.1016/j.epsl.2020.116123

Zieg, M.J., Marsh, B.D., 2005. The Sudbury Igneous Complex: viscous emulsion differentiation of a superheated melt sheet. Geological Society of America Bulletin 117, 1427–1450. https://doi.org/10.1130/B25579.1

Zindler, A., Hart, S., 1986. Chemical geodynamics. Annual Review of Earth and Planetary Sciences. Vol. 14, (c), 493–571. https://doi.org/10.1146/annurev.ea.14.050186.002425

Zindler, A., Jagoutz, E., Goldstein, S., 1982. Nd, Sr and Pb isotopic systematics in a three-component mantle: A new perspective. Nature, 298(5874), 519–523. https://doi.org/10.1038/298519a0

APPENDIX – SUPPLEMENTARY MATERIAL

CHAPTER 4. MINERAL CHEMISTRY AND CRYSTAL SIZE DISTRIBUTIONS OF MAFIC DIKES AND SILLS ON THE EASTERN BORDER OF THE PARNAÍBA BASIN, NE BRAZIL

Table A1. Geochemical data of some representative samples of the eastern Parnaíba Basin magmatism. *Samples analyzed by CSD. **Samples analyzed combining CSD and micropobre.

Sampling sites	Latitude	Longitude	Sample	SiO_2	TiO_2	Al_2O_3	Fe_2O_3	MnO	MgO	CaO	Na_2O	K_2O	P_2O_5	LOI	SUM
Amarante	-6.084674	-42.644406	BP232	51.5	3.14	12.5	14.6	0.20	4.70	7.60	2.94	1.89	0.66	0.49	100.22
	-6.248918	-42.842601	BP233	51.3	3.11	12.2	14.8	0.20	5.34	8.16	2.49	1.79	0.59	0.90	100.88
	-6.267883	-42.820553	BP234	51.3	3.10	12.3	14.5	0.19	5.25	7.89	2.98	1.82	0.62	0.38	100.33
	-6.805663	-42.965297	BP237	52.5	3.00	12.7	14.0	0.21	3.15	6.44	3.01	2.21	0.84	1.15	99.21
	-6.090931	-42.752787	BP231	52.7	3.04	12.7	13.7	0.21	3.16	6.53	3.18	2.25	0.79	1.00	99.26
Baixão Grande	-5.664936	-42.591077	BP240	50.9	3.14	12.6	14.2	0.19	4.43	7.31	2.51	1.99	0.65	1.32	99.24
	-5.657513	-42.590557	BP241	50.5	3.16	12.3	14.7	0.19	4.79	8.12	2.76	1.68	0.60	0.70	99.50
Barrocão	-6.402763	-43.001935	BP235**	50.2	3.11	11.9	15.2	0.21	5.68	8.26	2.86	1.64	0.58	0.21	99.85
	-6.406480	-43.006954	BP236	49.7	3.80	12.8	14.9	0.21	4.39	7.73	2.46	1.69	0.56	0.99	99.23
Baú	-5.227315	-43.450689	BP186	52.2	3.23	12.8	13.8	0.20	3.65	7.27	2.94	1.99	0.73	0.53	99.34
Campinas do Piauí	-7.689491	-41.885325	BP216	49	4.19	13.9	13.5	0.18	4.53	8.29	2.8	1.56	0.43	0.63	99.01
Canto do Buriti	-8.183425	-42.906194	BP224 **	48	2.46	13.1	15.9	0.23	5.75	10	2.29	0.34	0.18	0.75	99.00
Curralinhos	-5.661832	-42.803959	BP243 **	51.8	3.01	13.0	13.4	0.20	3.33	6.97	2.77	2.09	0.73	2.00	99.30
	-5.680652	-42.735747	BP242	54.6	2.45	12.9	12.9	0.21	2.74	5.81	2.96	2.69	1.02	1.50	99.78
Elesbão Veloso	-6.129379	-42.152877	BP200 **	51.5	1.37	13.7	12.6	0.19	6.42	9.75	2.44	0.7	0.12	0.85	99.64
	-6.106329	-42.193981	BP201 **	55.8	2.05	13.1	13.1	0.22	2.38	4.86	3.41	2.83	0.82	1.59	100.16
	-6.199554	-42.110748	BP197	57.1	1.78	12.9	11.8	0.2	1.78	4.59	3.38	3.14	0.65	1.71	99.03
	-6.160122	-42.128592	BP199	62.8	1.08	13.4	8.95	0.17	0.88	3.21	3.64	3.89	0.26	1.86	100.14
Floriano	-6.888731	-43.068797	BP229 *	51.6	3.20	13.1	13.7	0.19	3.73	6.95	2.78	1.98	0.76	1.15	99.14
	-6.802368	-42.953417	BP230A	54.3	2.55	12.8	13.1	0.20	2.64	5.81	3.18	2.56	0.91	0.99	99.04
	-6.802368	-42.953417	BP230B	54.1	2.52	12.8	13.0	0.21	2.72	5.91	3.20	2.52	1.05	1.20	99.23
Isaías Coelho	-7.695982	-41.577020	BP209 **	49.1	4.20	13.1	14.8	0.19	4.54	8.21	3.01	1.57	0.53	0.59	99.84
	-7.718913	-41.616386	BP215	49.4	3.99	12.8	14.7	0.2	4.34	7.79	2.59	1.84	0.53	1.57	99.75
Itaueira	-7.593610	-43.037400	BP227	51.6	1.37	13.6	12.4	0.19	6.34	9.79	2.25	0.62	0.12	1.01	99.29
	-7.593606	-43.037444	BP228	51.9	1.35	13.7	12.3	0.18	6.29	10.1	2.21	0.55	0.12	0.67	99.37
Lagoa de São Francisco	-4.390720	-41.251336	BP-109A1	51.1	1.95	12.5	16.2	0.23	5.37	8.94	2.16	0.72	0.17	0.33	99.67
	-4.390720	-41.251336	BP-109B1	52.0	1.38	13.7	12.5	0.19	6.19	9.49	2.35	0.73	0.17	0.53	99.23

	-4.363552	-41.703676	BP-111	52.4	1.59	13.3	13.6	0.20	5.41	9.16	2.25	0.75	0.18	0.58	99.42
	-4.377477	-41.701385	BP-112	52.2	1.62	13.2	13.8	0.20	5.60	9.08	2.26	0.85	0.20	0.45	99.46
	-4.378301	-41.701064	BP-113	51.9	1.36	13.7	12.6	0.20	6.26	9.75	2.26	0.74	0.16	0.46	99.39
	-4.393402	-41.678367	BP-114A1	51.9	1.34	13.8	12.6	0.19	6.28	9.75	2.04	0.73	0.16	0.52	99.31
	-4.396412	-41.662910	BP-115	52.1	1.58	13.5	13.8	0.19	5.25	9.09	2.38	0.70	0.19	0.59	99.37
	-4.406087	-41.566576	BP-116	52.1	1.44	13.6	12.9	0.20	6.02	9.48	2.19	0.78	0.16	0.42	99.29
Pedro II	-4.430912	-41.474218	BP108	52.7	2.65	11.5	17.2	0.22	2.60	7.17	3.35	1.16	0.28	1.99	100.82
Monsenhor Gil	-5.536260	-42.641923	BP188A *	51.9	3.15	12.9	13.8	0.21	3.51	6.34	3.57	2.45	0.72	0.79	99.34
	-5.536260	-42.641923	BP188B	53.7	2.75	12.8	13.2	0.2	2.92	6.29	3.15	2.4	0.86	1.12	99.39
Simplício Mendes	-7.973886	-41.990105	BP218 **	52.5	3.17	12.9	13.4	0.17	4.34	7.64	2.88	1.88	0.71	1.18	100.77
	-7.926744	-41.955196	BP217A	50.9	3.13	13	13.2	0.13	4.65	6.87	2.63	1.86	0.68	1.95	99.00
	-7.926744	-41.955196	BP217B	50.8	3.11	12.3	13.9	0.18	4.77	7.82	2.53	1.77	0.62	1.25	99.05
Picos	-7.033269	-41.575292	BP190	51.0	3.42	12.9	14.0	0.19	3.86	7.25	3.37	1.99	0.68	0.65	99.31
Tanque do Piauí	-6.749614	-42.121263	BP239 *	49.6	1.13	13.3	10.5	0.16	7.59	7.33	4.84	0.91	<0.10	4.07	99.43

Table A2. Microprobe analysis data for feldspars of the eastern Parnaíba Basin magmatism. Abrev.: C - core, I - intermediate position, R - rim and MR - mantled rim. *Results not considered for classification of feldspars.

Sample	Crystal	Crystal size (mm)	Position	Analyzed Spot	Analyzed elements (%)								SUM	End-members (% mol)		
					SiO_2	Al_2O_3	TiO_2	Fe_2O_3	MgO	CaO	Na_2O	K_2O		An	Ab	Or
BP200	BP200PL1	1	C	BP200_1_1	51.03	30.44	0.03	0.97	0.18	14.04	3.41	0.17	100.27	68.80	30.22	0.98
			I	BP200_1_2	50.53	31.05	0.03	0.97	0.12	14.43	3.40	0.12	100.64	69.61	29.68	0.71
			R	BP200_1_3	58.03	26.25	0.05	0.64	0.04	8.37	6.48	0.42	100.29	40.62	56.93	2.44
	BP200PL7	1.23	C	BP200_7_1	52.74	29.48	0.04	1.05	0.15	12.85	4.22	0.18	100.72	62.08	36.90	1.02
			I	BP200_7_2	53.34	28.84	0.05	1.00	0.13	12.16	4.73	0.20	100.45	58.02	40.82	1.16
			R	BP200_7_3	56.61	27.33	0.05	0.73	0.05	9.60	5.87	0.31	100.54	46.61	51.59	1.80
	BP200PL5	0.645	I	BP200_5_1	54.84	28.28	0.07	0.80	0.09	11.30	5.13	0.24	100.74	54.14	44.48	1.38
			C	BP200_5_2	53.13	28.93	0.07	1.11	0.09	12.26	4.47	0.19	100.24	59.59	39.29	1.12
			I	BP200_5_3	53.37	28.94	0.07	1.09	0.10	12.11	4.54	0.19	100.39	58.94	39.97	1.09

			R	BP200_5_4	54.56	28.01	0.06	0.99	0.06	10.86	5.05	0.24	99.83	53.55	45.04	1.41
			I	BP200_5_5	57.83	26.04	0.03	0.60	0.03	8.50	6.32	0.38	99.73	41.68	56.10	2.22
	BP200PL5A	0.254	C	BP200_5A_6	54.00	28.46	0.06	1.03	0.10	11.51	4.89	0.22	100.26	55.81	42.94	1.25
			R	BP200_5A_7	58.42	25.96	0.01	0.75	0.03	7.62	6.85	0.50	100.13	36.98	60.14	2.88
BP224	BP224PL1	> 3.4	C	BP224_1_1	48.81	32.36	0.02	0.77	0.17	15.76	2.58	0.04	100.50	76.97	22.79	0.24
			I	BP224_1_2	50.85	31.10	0.05	0.76	0.18	14.09	3.36	0.07	100.46	69.57	30.02	0.42
			I	BP224_1_3	48.53	32.70	0.05	0.74	0.15	16.05	2.36	0.04	100.63	78.76	20.99	0.25
			I	BP224_1_4	48.64	32.45	0.04	0.79	0.15	15.90	2.46	0.04	100.44	77.96	21.82	0.22
			I	BP224_1_5	50.56	31.40	0.04	0.84	0.17	14.49	3.17	0.07	100.73	71.36	28.23	0.42
			I	BP224_1_6	48.59	32.47	0.02	0.78	0.14	15.84	2.47	0.05	100.36	77.80	21.92	0.27
			I	BP224_1_7	50.95	30.00	0.05	0.94	0.19	13.88	3.58	0.08	99.66	67.84	31.69	0.47
			R	BP224_1_8	59.33	26.09	0.04	0.94	0.03	7.90	6.94	0.25	101.53	38.08	60.48	1.45
	BP224PL2	> 4	C	BP224_2_1	50.29	31.19	0.03	0.78	0.18	14.57	3.22	0.07	100.33	71.14	28.45	0.40
			I	BP224_2_2	49.64	31.41	0.04	0.81	0.17	14.93	2.87	0.05	99.92	74.00	25.72	0.28
			I	BP224_2_3	50.10	31.26	0.06	0.82	0.16	14.66	3.27	0.05	100.38	71.02	28.69	0.29
			I	BP224_2_4	49.46	31.82	0.05	0.83	0.15	15.11	2.89	0.06	100.35	74.02	25.64	0.34
			I	BP224_2_5	50.13	31.19	0.04	0.83	0.15	14.72	3.09	0.07	100.22	72.16	27.42	0.43
			I	BP224_2_6	50.25	30.91	0.05	0.83	0.17	14.56	3.39	0.07	100.21	70.11	29.51	0.38
			I	BP224_2_7	49.07	31.63	0.05	0.82	0.16	15.35	2.77	0.06	99.90	75.10	24.56	0.34
			R	BP224_2_8	50.39	30.66	0.06	0.87	0.17	14.17	3.45	0.06	99.83	69.16	30.48	0.35
	BP224PL3	1.84	C	BP224_3_1	46.96	33.80	0.01	0.35	0.14	17.35	1.78	0.05	100.44	84.10	15.59	0.31
			I	BP224_3_2	46.79	33.90	0.01	0.34	0.14	17.27	1.71	0.05	100.20	84.56	15.14	0.30
			I	BP224_3_3	46.96	33.60	0.01	0.42	0.14	16.86	1.77	0.05	99.81	83.74	15.94	0.32
			I	BP224_3_4	51.94	30.26	0.06	0.75	0.20	13.54	3.90	0.09	100.73	65.41	34.09	0.50
			I	BP224_3_5	50.53	30.41	0.05	0.86	0.18	14.22	3.45	0.07	99.77	69.21	30.39	0.40
			I	BP224_3_6	50.74	30.68	0.05	0.88	0.20	14.19	3.52	0.08	100.32	68.74	30.82	0.44
			R	BP224_3_7	51.41	29.85	0.07	1.00	0.18	13.25	3.83	0.08	99.67	65.34	34.17	0.49
	BP224PL3A.8	< 0.5	C	BP224_3A_8	50.89	30.71	0.05	0.93	0.19	14.01	3.49	0.07	100.34	68.67	30.92	0.41

	BP224PL3A.9	< 0.5	R	BP224_3A_9	52.12	29.47	0.09	1.09	0.19	13.14	3.97	0.09	100.17	64.28	35.17	0.55
	BP224PL4	1	C	BP224_4_1	51.40	29.75	0.07	1.04	0.23	13.22	3.93	0.11	99.74	64.61	34.78	0.62
			I	BP224_4_2	51.38	30.04	0.04	0.82	0.20	13.54	3.81	0.07	99.90	65.96	33.62	0.42
			I	BP224_4_3	51.63	30.35	0.05	0.88	0.19	13.76	3.69	0.07	100.61	67.08	32.54	0.39
			I	BP224_4_4	52.76	29.03	0.08	1.03	0.16	12.30	4.34	0.11	99.81	60.61	38.75	0.65
			R	BP224_4_5	54.89	27.87	0.07	0.90	0.11	10.84	5.30	0.16	100.14	52.56	46.50	0.94
	BP244PL4A		C	BP224_4A_6	51.46	29.83	0.06	0.97	0.19	13.43	3.83	0.09	99.85	65.64	33.86	0.51
			R	BP224_4A_7	52.97	28.88	0.08	1.18	0.15	12.28	4.52	0.11	100.17	59.62	39.72	0.66
	BP224PL4B8	< 0.5	C	BP224_4B_8	51.93	29.71	0.06	0.89	0.14	13.14	4.12	0.09	100.09	63.46	36.03	0.51
	BP224PL4B9	< 0.5	R	BP224_4B_9	59.14	25.22	0.04	0.60	0.03	7.05	7.14	0.33	99.56	34.61	63.45	1.95
BP218	BP218PL1	1.44	C	BP218_1_1	55.10	27.43	0.10	0.78	0.13	10.31	5.21	0.57	99.62	50.49	46.20	3.31
			I	BP218_1_2	54.85	27.84	0.10	0.72	0.10	10.58	5.05	0.56	99.79	51.93	44.83	3.24
			I	BP218_1_3	54.99	27.65	0.11	0.78	0.11	10.54	5.10	0.51	99.79	51.73	45.31	2.96
			I	BP218_1_4	54.91	27.90	0.09	0.70	0.10	10.63	4.98	0.55	99.86	52.40	44.39	3.21
			I	BP218_1_5	55.42	27.42	0.10	0.73	0.09	10.13	5.37	0.61	99.87	49.26	47.21	3.53
			I	BP218_1_6	53.31	28.61	0.12	0.91	0.13	11.74	4.51	0.40	99.73	57.63	40.04	2.34
			R	BP218_1_7	54.00	27.66	0.14	0.96	0.12	10.71	5.02	0.44	99.06	52.72	44.70	2.58
	BP218PL1A	1	C	BP218_1A_8	54.88	27.56	0.09	0.75	0.10	10.31	5.12	0.55	99.36	50.98	45.81	3.21
			I	BP218_1A_9	55.66	27.47	0.07	0.73	0.11	9.88	5.45	0.56	99.92	48.42	48.32	3.26
			I	BP218_1A_10	54.47	27.42	0.11	0.79	0.09	10.45	5.08	0.53	98.93	51.55	45.34	3.11
			I	BP218_1A_11	56.43	26.71	0.08	0.71	0.11	9.30	5.52	0.68	99.53	46.29	49.70	4.01
			I	BP218_1A_12	55.29	27.21	0.08	0.66	0.09	9.87	5.39	0.58	99.17	48.57	48.01	3.42
			R	BP218_1A_13	53.61	27.76	0.11	0.88	0.13	11.09	4.72	0.42	98.72	55.08	42.43	2.49
	BP218PL1B	< 0.5	R	BP218_1B_14	54.70	27.22	0.12	0.83	0.11	10.20	5.24	0.51	98.93	50.26	46.75	2.99
	BP218PL1C	< 0.5	C	BP218_1C_15	54.81	27.46	0.11	0.85	0.11	10.21	5.41	0.50	99.46	49.61	47.52	2.87
	BP218PL1D	< 0.5	R	BP218_1D_16	52.35	28.73	0.09	0.87	0.12	12.25	4.35	0.37	99.13	59.58	38.27	2.14
	BP218PL3	0.78	C	BP218_3_1	53.73	28.09	0.12	0.80	0.12	11.33	4.81	0.42	99.42	55.18	42.41	2.41

			R	BP218_3_2	55.11	26.93	0.11	0.86	0.11	10.16	5.29	0.52	99.09	49.93	47.05	3.02
	BP218PL3A	< 0.5	C	BP218_3A_3	56.28	26.71	0.14	0.89	0.12	9.49	5.60	0.59	99.80	46.69	49.86	3.45
	BP218PL3B	< 0.5	C	BP218_3B_4	53.95	28.15	0.12	0.90	0.12	11.07	4.91	0.45	99.66	54.02	43.38	2.60
	BP218PL3C	< 0.5	C	BP218_3C_5	54.65	27.49	0.14	0.94	0.10	10.53	5.17	0.48	99.50	51.47	45.72	2.81
BP243	BP243PL1	1.72	C	BP243_1_1	53.40	28.61	0.08	0.74	0.12	11.46	4.62	0.39	99.42	56.50	41.24	2.26
			I	BP243_1_2	53.77	28.18	0.09	0.73	0.12	11.26	4.69	0.41	99.24	55.66	41.91	2.44
			I	BP243_1_3	53.81	28.27	0.08	0.75	0.13	11.18	4.78	0.42	99.42	55.00	42.57	2.43
			R	BP243_1_4	55.15	27.49	0.07	0.67	0.09	10.13	5.30	0.51	99.41	49.87	47.16	2.96
	BP243PL1B	0.41	C	BP243_1B_5	54.24	28.54	0.09	0.75	0.11	11.36	4.87	0.41	100.36	54.99	42.65	2.36
	BP243PL1C	0.68	C	BP243_1C_6	54.83	27.63	0.08	0.67	0.11	10.38	5.17	0.47	99.35	51.12	46.11	2.77
	BP243PL1D7	0.63	C	BP243_1D_7	54.18	28.12	0.07	0.71	0.10	10.87	4.94	0.44	99.43	53.47	43.95	2.57
	BP243PL1D8		I	BP243_1D_8	55.52	27.40	0.08	0.62	0.08	9.77	5.41	0.51	99.40	48.43	48.53	3.03
	BP243PL2	1.1	C	BP243_2_1	53.98	28.17	0.07	0.71	0.10	11.20	4.78	0.42	99.42	55.04	42.48	2.48
			I	BP243_2_2	54.31	28.05	0.07	0.69	0.09	11.00	5.06	0.44	99.69	53.21	44.26	2.53
			I	BP243_2_3	54.01	28.48	0.08	0.72	0.12	11.41	4.92	0.42	100.15	54.84	42.77	2.39
			R	BP243_2_4	53.79	28.11	0.09	0.69	0.11	10.96	5.00	0.43	99.17	53.43	44.09	2.48
	BP243PL2A	< 0.5	C	BP243_2A_5	54.22	28.18	0.08	0.74	0.12	10.87	5.04	0.46	99.71	52.93	44.43	2.64
	BP243PL2B	< 0.5	R	BP243_2B_6	55.70	27.08	0.06	0.68	0.07	9.72	5.67	0.55	99.51	47.13	49.71	3.16
	BP243PL2C	< 0.5	R	BP243_2C_7	55.59	27.37	0.07	0.73	0.06	9.92	5.64	0.52	99.91	47.82	49.22	2.96
	BP243PL5	0.3744	C	BP243_5_1	55.39	27.38	0.08	0.70	0.11	9.99	5.36	0.54	99.54	49.12	47.73	3.15
			I	BP243_5_2	54.93	27.31	0.08	1.00	0.17	9.99	5.16	0.52	99.15	50.08	46.84	3.08
			I	BP243_5_3	54.46	28.22	0.08	0.68	0.09	10.77	5.05	0.45	99.80	52.67	44.71	2.62
			R	BP243_5_4	54.89	27.90	0.12	1.43	0.16	10.37	5.32	0.46	100.65	50.45	46.89	2.65
1UN2680	1UN2680PL3	0.77	C	1UN2680_plg_3	53.68	28.23	0.05	0.86	N.A.	11.33	4.85	0.22	99.21	55.66	43.08	1.26
	1UN2680PL4	0.68	C	1UN2680_plg_4_1	52.91	29.37	0.04	0.86	N.A.	12.28	4.51	0.17	100.14	59.49	39.51	1.00
			I	1UN2680_plg_4_2	52.70	29.32	0.06	0.89	N.A.	12.23	4.28	0.18	99.65	60.58	38.34	1.07

			I	1UN2680_plg_4_3	52.52	29.39	0.05	0.66	N.A.	12.09	4.40	0.16	99.27	59.73	39.31	0.96
			R	1UN2680_plg_4_4	54.44	28.08	0.05	0.83	N.A.	10.26	5.27	0.25	99.18	51.09	47.45	1.46
	1UN2680PL5	0.44	C	1UN2680_plg_5_1	52.57	29.26	0.04	0.80	N.A.	12.38	4.20	0.17	99.41	61.35	37.64	1.01
			R	1UN2680_plg_5_2	53.26	28.70	0.06	0.84	N.A.	11.84	4.54	0.16	99.40	58.48	40.58	0.93
	1UN2680PL6	1.05	C	1UN2680_plg_6_1	52.54	29.08	0.06	0.88	N.A.	12.11	4.29	0.17	99.12	60.29	38.68	1.03
	1UN2680PL4A	0.2	C	1UN2680_plg_4a_1	52.58	29.55	0.04	0.70	N.A.	11.93	4.48	0.23	99.52	58.74	39.90	1.37
			I	1UN2680_plg_4a_2	55.24	27.35	0.03	0.74	N.A.	9.32	5.98	0.32	98.98	45.40	52.73	1.87
			R	1UN2680_plg_4a_3	57.82	25.49	0.02	0.53	N.A.	7.35	6.81	0.35	98.38	36.58	61.33	2.09
	1UN2680PL7A*	-	C	1UN2680_plg_7a_1*	65.01	19.55	0.03	0.14	N.A.	0.19	5.28	7.60	97.81	1.03	50.82	48.14
			I	1UN2680_plg_7a_2*	64.77	19.45	0.01	0.14	N.A.	0.00	5.18	7.94	97.50	0.00	49.81	50.19
			R	1UN2680_plg_7a_3*	65.00	19.39	0.01	0.15	N.A.	0.00	5.00	8.35	97.90	0.00	47.64	52.36
	1UN2680PL7	< 0.5	C	1UN2680_plg_7_1	59.28	24.82	0.00	0.58	N.A.	6.51	7.15	0.66	99.00	32.17	63.94	3.89
	1UN2680PL8	< 0.5	C	1UN2680_plg_8_1	54.30	28.19	0.07	0.79	N.A.	11.00	5.05	0.22	99.62	53.91	44.81	1.28
			R	1UN2680_plg_8_2	52.71	29.08	0.06	0.94	N.A.	12.28	4.31	0.18	99.55	60.49	38.46	1.05
	1UN2680PL1	4.2	C	1UN2680_plg_1_1	53.67	28.79	0.04	0.88	N.A.	12.14	4.39	0.18	100.09	59.79	39.14	1.07
			I	1UN2680_plg_1_2	53.38	28.79	0.07	0.93	N.A.	12.13	4.43	0.20	99.91	59.54	39.31	1.15
			I	1UN2680_plg_1_3	53.14	29.02	0.06	0.85	N.A.	12.10	4.29	0.19	99.64	60.26	38.63	1.11
			I	1UN2680_plg_1_4	53.42	29.02	0.04	0.90	N.A.	12.06	4.31	0.19	99.93	60.07	38.82	1.11
			I	1UN2680_plg_1_5	53.27	29.12	0.04	0.86	N.A.	12.13	4.29	0.18	99.88	60.32	38.63	1.05
			I	1UN2680_plg_1_6	53.30	28.99	0.06	0.88	N.A.	12.15	4.43	0.18	99.98	59.65	39.31	1.04
			I	1UN2680_plg_1_7	53.28	29.10	0.04	0.84	N.A.	12.26	4.39	0.19	100.09	60.00	38.92	1.08
			I	1UN2680_plg_1_8	53.25	28.86	0.08	0.90	N.A.	12.05	4.49	0.18	99.82	59.09	39.84	1.06
			I	1UN2680_plg_1_9	53.75	29.00	0.08	0.86	N.A.	11.73	4.41	0.20	100.02	58.78	40.04	1.18
			R	1UN2680_plg_1_10	57.20	26.66	0.04	0.61	N.A.	8.42	6.18	0.41	99.52	41.91	55.66	2.43
	1UN2680PL2	3	C	1UN2680_plg_2_1	52.74	29.25	0.04	0.84	N.A.	12.49	4.25	0.17	99.79	61.26	37.72	1.02
			I	1UN2680_plg_2_2	52.90	29.24	0.04	0.89	N.A.	12.42	4.18	0.18	99.84	61.49	37.45	1.07
			I	1UN2680_plg_2_3	53.07	28.75	0.04	0.88	N.A.	12.08	4.36	0.17	99.35	59.89	39.10	1.01
			I	1UN2680_plg_2_4	53.14	28.89	0.05	0.95	N.A.	12.04	4.31	0.19	99.58	59.99	38.88	1.13

			I	1UN2680_plg_2_5	53.42	28.68	0.05	0.84	N.A.	11.79	4.59	0.20	99.57	58.02	40.82	1.16
			I	1UN2680_plg_2_6	53.72	28.78	0.03	0.82	N.A.	11.77	4.75	0.21	100.09	57.11	41.68	1.21
			I	1UN2680_plg_2_7	53.98	28.63	0.05	0.78	N.A.	11.71	4.80	0.22	100.18	56.70	42.01	1.29
			I	1UN2680_plg_2_8	54.06	28.38	0.05	0.87	N.A.	11.35	4.77	0.23	99.72	56.02	42.61	1.37
			I	1UN2680_plg_2_9	54.24	28.21	0.04	0.77	N.A.	11.29	4.86	0.22	99.62	55.52	43.21	1.27
			I	1UN2680_plg_2_10	54.20	28.00	0.07	0.90	N.A.	11.12	4.98	0.21	99.47	54.58	44.17	1.24
			I	1UN2680_plg_2_11	54.68	28.17	0.04	0.72	N.A.	11.09	4.96	0.23	99.89	54.53	44.12	1.35
			I	1UN2680_plg_2_12	54.49	28.03	0.05	0.71	N.A.	10.75	5.13	0.23	99.38	52.97	45.71	1.32
			I	1UN2680_plg_2_13	55.08	28.00	0.06	0.72	N.A.	10.77	5.10	0.24	99.96	53.11	45.50	1.40
			I	1UN2680_plg_2_14	54.67	27.99	0.03	0.75	N.A.	10.47	5.20	0.24	99.36	51.89	46.68	1.42
			R	1UN2680_plg_2_15	57.19	26.45	0.01	0.59	N.A.	8.67	6.28	0.41	99.59	42.25	55.38	2.37
BP201	BP201PL1	1.4	MR	BP201_plg_1_1*	65.03	19.62	0.03	0.19	N.A.	0.19	5.55	7.09	97.71	1.03	53.80	45.17
			R	BP201_plg_1_2*	62.60	22.03	0.06	0.27	N.A.	2.87	7.21	2.67	97.72	15.03	68.31	16.66
			I	BP201_plg_1_3	60.07	23.90	0.04	0.32	N.A.	5.67	7.26	1.11	98.37	28.16	65.30	6.54
			I	BP201_plg_1_4	58.80	25.20	0.05	0.36	N.A.	6.80	6.77	0.87	98.84	33.86	60.98	5.16
			I	BP201_plg_1_5	56.95	26.24	0.06	0.45	N.A.	8.26	6.14	0.67	98.77	40.94	55.12	3.93
			I	BP201_plg_1_6	55.99	27.22	0.06	0.44	N.A.	9.14	5.65	0.55	99.05	45.67	51.05	3.28
			I	BP201_plg_1_7	55.69	27.07	0.05	0.47	N.A.	9.33	5.62	0.55	98.77	46.28	50.48	3.25
			I	BP201_plg_1_8	56.51	26.79	0.06	0.53	N.A.	8.97	5.90	0.59	99.35	44.06	52.49	3.45
			I	BP201_plg_1_9	55.10	27.33	0.07	0.52	N.A.	9.56	5.39	0.53	98.49	47.95	48.89	3.15
			I	BP201_plg_1_10	54.99	27.56	0.05	0.57	N.A.	9.88	5.38	0.48	98.91	48.97	48.20	2.83
			I	BP201_plg_1_11	54.62	27.89	0.06	0.54	N.A.	9.99	5.20	0.47	98.77	50.05	47.16	2.79
			I	BP201_plg_1_12	54.98	27.85	0.06	0.46	N.A.	10.09	5.14	0.48	99.06	50.55	46.61	2.84
			I	BP201_plg_1_13	54.82	27.48	0.07	0.56	N.A.	9.77	5.25	0.47	98.41	49.29	47.91	2.80
			I	BP201_plg_1_14	56.07	27.36	0.09	0.53	N.A.	9.56	5.52	0.53	99.66	47.37	49.52	3.12
			C	BP201_plg_1_15	55.81	27.30	0.07	0.49	N.A.	9.25	5.65	0.53	99.11	46.00	50.88	3.12
	BP201PL2	2.5	C	BP201_plg_2_1	55.52	27.59	0.08	0.54	N.A.	9.96	5.33	0.50	99.52	49.32	47.75	2.93

			I	BP201_plg_2_2	54.50	27.42	0.08	0.56	N.A.	10.21	5.02	0.49	98.27	51.40	45.67	2.92
			I	BP201_plg_2_3	54.99	27.85	0.07	0.58	N.A.	10.23	5.35	0.48	99.54	49.96	47.24	2.80
			I	BP201_plg_2_4	54.61	27.89	0.06	0.57	N.A.	10.53	4.94	0.46	99.05	52.61	44.68	2.71
			I	BP201_plg_2_5	54.78	27.80	0.07	0.58	N.A.	10.10	5.17	0.45	98.96	50.51	46.78	2.70
			I	BP201_plg_2_6	55.69	27.21	0.06	0.55	N.A.	9.49	5.53	0.52	99.05	47.19	49.75	3.07
			I	BP201_plg_2_7	54.98	27.83	0.07	0.51	N.A.	10.13	5.20	0.48	99.19	50.41	46.77	2.83
			I	BP201_plg_2_8	55.42	27.44	0.06	0.50	N.A.	9.49	5.58	0.51	98.99	47.01	49.99	3.00
			I	BP201_plg_2_9	55.44	27.16	0.05	0.49	N.A.	9.31	5.36	0.54	98.35	47.37	49.33	3.30
			I	BP201_plg_2_10	56.38	26.75	0.06	0.51	N.A.	8.77	5.86	0.64	98.97	43.54	52.68	3.78
			I	BP201_plg_2_11	55.92	26.76	0.06	0.47	N.A.	9.09	5.73	0.55	98.57	45.20	51.55	3.25
			I	BP201_plg_2_12	57.12	26.24	0.06	0.43	N.A.	8.11	6.29	0.66	98.90	40.02	56.13	3.85
			R	BP201_plg_2_13	60.84	23.56	0.03	0.28	N.A.	4.88	7.38	1.36	98.33	24.59	67.26	8.14
			MR	BP201_plg_2_14*	63.80	18.71	0.00	0.11	N.A.	0.00	0.41	14.68	97.71	0.00	4.03	95.97
			MR	BP201_plg_2_15*	64.86	19.15	0.07	0.23	N.A.	0.00	5.37	7.60	97.27	0.00	51.80	48.20
	BP201PL3	0.83	MR	BP201_plg_3_1	56.17	26.90	0.05	0.42	N.A.	8.87	5.91	0.60	98.92	43.73	52.72	3.55
			MR	BP201_plg_3_2*	61.93	18.85	0.00	0.12	N.A.	0.00	1.02	13.50	95.42	0.00	10.33	89.67
			C	BP201_plg_3_3	66.05	19.16	0.04	0.29	N.A.	0.00	5.98	6.85	98.37	0.00	56.99	43.01
	BP201PL4	0.83	C	BP201_plg_4_1	55.41	27.21	0.07	0.55	N.A.	9.32	5.78	0.53	98.87	45.66	51.27	3.06
			R	BP201_plg_4_2	66.49	20.29	0.01	0.18	N.A.	0.33	11.15	0.26	98.71	1.58	96.91	1.50
	BP201PL5	1.52	C	BP201_plg_5_1	56.02	27.14	0.03	0.45	N.A.	8.99	5.78	0.58	98.99	44.64	51.92	3.44
			I	BP201_plg_5_2	56.15	26.77	0.05	0.45	N.A.	8.79	5.82	0.59	98.61	43.89	52.63	3.48
			I	BP201_plg_5_3	57.19	26.22	0.05	0.41	N.A.	8.11	6.28	0.71	98.96	39.90	55.97	4.13
			I	BP201_plg_5_4	58.64	25.31	0.03	0.38	N.A.	6.86	6.86	0.90	98.97	33.72	61.04	5.24
			R	BP201_plg_5_5	60.40	23.81	0.02	0.33	N.A.	5.15	7.39	1.28	98.38	25.67	66.70	7.63
	BP201PL6	0.7	C	BP201_plg_6_1	56.14	26.85	0.06	0.48	N.A.	8.80	5.90	0.57	98.80	43.65	53.01	3.34
			MR	BP201_plg_6_2*	67.60	20.05	0.00	0.10	N.A.	0.21	11.57	0.09	99.62	0.98	98.49	0.53
			MR	BP201_plg_6_3	63.73	18.92	0.00	0.38	N.A.	0.00	1.71	12.84	97.59	0.00	16.86	83.14
	BP201PL7	> 1.4	C	BP201_plg_7_1	57.79	25.40	0.04	0.44	N.A.	7.25	6.47	0.76	98.15	36.51	58.93	4.57

			C	BP201_plg_7_2	67.29	19.73	0.00	0.06	N.A.	0.05	11.58	0.04	98.75	0.23	99.56	0.21
BP209	BP209PL1	2.2		BP209_1_1*	21.06	12.65	0.06	0.55	N.A.	5.85	3.88	0.36	34.33	43.95	52.80	3.25
			C	BP209_1_2	54.34	28.06	0.09	0.65	N.A.	10.52	5.11	0.43	99.19	51.85	45.63	2.52
			I	BP209_1_3	53.51	28.42	0.10	0.66	N.A.	11.25	4.65	0.37	98.94	55.99	41.85	2.16
			I	BP209_1_4	54.32	28.20	0.09	0.67	N.A.	10.44	5.16	0.43	99.31	51.47	45.99	2.55
			I	BP209_1_5	52.86	28.94	0.10	0.74	N.A.	11.72	4.48	0.34	99.18	57.94	40.03	2.02
			R	BP209_1_6	56.79	25.83	0.25	0.80	N.A.	7.60	6.30	0.76	98.33	38.19	57.29	4.53
	BP209PL2	0.82	C	BP209_2_1	54.54	28.08	0.09	0.63	N.A.	10.57	5.03	0.46	99.40	52.29	44.99	2.72
			I	BP209_2_2	53.33	28.59	0.10	0.71	N.A.	11.18	4.74	0.39	99.04	55.27	42.42	2.31
			I	BP209_2_3	54.20	28.10	0.09	0.63	N.A.	10.73	4.84	0.44	99.02	53.62	43.78	2.60
			I	BP209_2_4	55.05	27.91	0.08	0.57	N.A.	10.09	5.19	0.50	99.40	50.24	46.79	2.97
			I	BP209_2_5	53.32	28.99	0.11	0.67	N.A.	11.35	4.56	0.36	99.36	56.65	41.20	2.16
			I	BP209_2_6	54.67	28.32	0.06	0.69	N.A.	10.20	5.20	0.42	99.55	50.74	46.80	2.46
			R	BP209_2_7	60.25	24.16	0.05	0.46	N.A.	5.71	7.17	0.88	98.69	28.95	65.74	5.31
	BP209PL2.8	< 0.5	C	BP209_2_8	65.61	19.04	0.04	0.42	N.A.	0.00	4.31	9.32	98.74	0.00	41.29	58.71
	BP209PL3	1.3	C	BP209_3_1	53.46	28.65	0.10	0.72	N.A.	11.00	4.87	0.38	99.19	54.28	43.48	2.24
			I	BP209_3_2	53.33	28.95	0.08	0.68	N.A.	11.58	4.49	0.33	99.45	57.59	40.44	1.97
			I	BP209_3_3	55.86	27.10	0.07	0.51	N.A.	9.02	5.79	0.57	98.92	44.70	51.93	3.37
			R	BP209_3_4	59.93	24.38	0.05	0.42	N.A.	5.72	7.49	0.87	98.87	28.16	66.72	5.11
			MR	BP209_3_5*	64.96	19.10	0.06	0.28	N.A.	0.00	4.73	8.79	97.91	0.00	44.99	55.01
	BP209PL4	< 0.5	C	BP209_4_1	60.32	24.01	0.04	0.43	N.A.	5.20	7.72	0.99	98.71	25.55	68.64	5.81
		< 0.5	R	BP209_4_2*	64.26	19.31	0.06	0.31	N.A.	0.00	5.31	7.67	96.92	0.00	51.30	48.70
BP235	BP235PL1	1.98	C	BP235_1_1	54.06	28.23	0.09	0.66	N.A.	11.00	4.82	0.39	99.26	54.49	43.20	2.31
			I	BP235_1_2	54.61	27.98	0.08	0.67	N.A.	10.69	5.07	0.45	99.54	52.42	44.99	2.60
			I	BP235_1_3	52.97	29.18	0.09	0.67	N.A.	11.78	4.39	0.35	99.42	58.50	39.45	2.05
			I	BP235_1_4	54.78	28.04	0.08	0.60	N.A.	10.47	5.06	0.46	99.48	51.91	45.40	2.69

			R	BP235_1_5	56.10	27.00	0.06	0.52	N.A.	9.36	5.80	0.58	99.42	45.54	51.11	3.34
	BP235PL2	0.38	C	BP235_4_1	54.92	28.35	0.09	0.63	N.A.	10.53	5.19	0.46	100.17	51.41	45.90	2.69
			I	BP235_4_2	55.17	27.83	0.06	0.60	N.A.	9.78	5.28	0.51	99.24	49.02	47.92	3.06
			MR	BP235_4_3	65.95	18.90	0.06	0.28	N.A.	0.00	4.93	8.72	98.84	0.00	46.19	53.81

Table A3. Microprobe analysis data for pyroxenes of the eastern Parnaíba Basin magmatism. Abrev.: C - core, I - intermediate positions, R - rim and MR - mantled rim. *Results not considered for classification of pyroxenes.

Sample	Crystal	Crystal size (mm)	Position	Analysed Spot	Analyzed elements (%)										SUM	End-members (% mol)		
					SiO_2	Al_2O_3	TiO_2	FeOt	MnO	MgO	CaO	Na_2O	K_2O	Cr_2O_3		Wo	En	Fs
BP200	BP200CPX1	1.5	C	BP200_CPX_1_1	51.87	2.58	0.47	7.18	0.13	17.00	19.85	0.16	0.00	0.25	99.51	40.34	48.05	11.60
			I	BP200_CPX_1_2	52.18	2.17	0.40	7.95	0.19	17.37	18.79	0.18	0.00	0.17	99.40	38.11	49.00	12.90
			R	BP200_CPX_1_3	49.77	1.93	0.69	16.15	0.41	13.35	16.11	0.36	0.15	0.01	98.91	33.84	39.01	27.15
	BP200CPX1A	< 0.5 mm	C	BP200_CPX_1A_4	52.18	1.80	0.37	8.97	0.24	17.46	18.00	0.16	0.01	0.06	99.25	36.38	49.09	14.52
			R	BP200_CPX_1A_5	50.02	1.37	0.57	18.41	0.41	11.87	16.24	0.20	0.00	0.00	99.08	34.22	34.81	30.98
	BP200CPX1B	< 0.5 mm	C	BP200_CPX_1B_6	50.47	1.82	0.67	14.43	0.34	14.13	17.21	0.23	0.00	0.01	99.31	35.56	40.61	23.83
	BP200CPX9	0.8	C	BP200_CPX_9_1	52.74	0.93	0.26	16.36	0.37	23.22	4.39	0.05	0.00	0.00	98.33	8.83	64.91	26.26
			R	BP200_CPX_9_2	49.94	0.74	0.39	26.13	0.60	15.40	5.02	0.10	0.00	0.01	98.31	10.60	45.28	44.12
BP224	BP224CPX1	0.4	C	BP224_CPX_1_1	49.22	3.39	1.12	11.30	0.24	14.03	18.79	0.28	0.00	0.14	98.52	39.71	41.24	19.05
			I	BP224_CPX_1_2	48.93	3.11	1.22	12.81	0.26	14.00	17.79	0.29	0.00	0.08	98.49	37.47	41.03	21.50
			R	BP224_CPX_1_3	50.13	2.07	0.93	15.58	0.35	14.89	15.11	0.20	0.00	0.00	99.26	31.31	42.92	25.77
	BP224CPX1A	< 0.5 mm	C	BP224_CPX_1A_4	49.03	2.66	1.21	13.85	0.31	13.29	18.06	0.27	0.00	0.02	98.71	37.93	38.85	23.22
	BP224CPX1B	< 0.5 mm	C	BP224_CPX_1B_5	49.66	1.47	0.88	18.27	0.48	12.39	15.40	0.20	0.02	0.01	98.77	32.57	36.47	30.96
	BP224CPX1C	< 0.5 mm	C	BP224_CPX_1C_6	49.47	3.55	1.10	11.42	0.28	15.08	17.49	0.28	0.00	0.22	98.89	36.73	44.07	19.20
	BP224CPX1D	< 0.5 mm	C	BP224_CPX_1D_7	49.48	3.30	1.04	11.82	0.28	14.72	18.11	0.27	0.01	0.14	99.15	37.71	42.64	19.66
	BP224CPX4	0.7	C	BP224_CPX_4_1	51.69	1.72	0.54	11.23	0.31	17.90	15.13	0.17	0.00	0.22	98.90	30.85	50.77	18.38

			I	BP224_CPX_4_2	49.22	3.70	1.11	11.39	0.25	15.50	16.93	0.28	0.00	0.27	98.65	35.58	45.31	19.11
			I	BP224_CPX_4_3	49.64	2.44	1.25	16.17	0.38	13.81	15.58	0.22	0.00	0.01	99.51	32.66	40.26	27.08
			R	BP224_CPX_4_4	49.02	1.52	0.88	17.72	0.42	10.98	17.98	0.21	0.00	0.01	98.73	37.92	32.22	29.86
	BP224CPX4A	0.6	C	BP224_CPX_4A_5	49.52	2.79	1.12	14.53	0.35	14.97	15.83	0.27	0.00	0.07	99.44	32.78	43.14	24.08
			R	BP224_CPX_4B_6	49.72	2.36	1.10	16.99	0.41	14.17	14.28	0.22	0.00	0.02	99.28	30.01	41.43	28.56
	BP224CPX4C	< 0.5 mm	C	BP224_CPX_4C_7	49.43	2.14	1.11	15.98	0.37	13.39	16.06	0.21	0.00	0.01	98.67	33.85	39.26	26.89
	BP224CPX5	< 0.5 mm	C	BP224_CPX_5_1	50.09	2.07	0.98	16.39	0.41	13.03	16.14	0.22	0.00	0.01	99.34	34.06	38.26	27.68
			I	BP224_CPX_5_2	50.28	1.40	0.76	18.86	0.47	11.70	16.46	0.23	0.00	0.01	100.17	34.41	34.04	31.55
			R	BP224_CPX_5_3	48.84	1.08	0.56	24.28	0.58	7.73	16.61	0.20	0.00	0.00	99.88	35.51	22.99	41.50
	BP224CPX5A	< 0.5 mm	C	BP224_CPX_5A_4	49.66	2.19	1.10	16.55	0.37	14.13	14.97	0.22	0.01	0.00	99.20	31.30	41.08	27.62
			R	BP224_CPX_5A_5	49.21	1.56	0.65	22.87	0.57	8.87	15.81	0.17	0.03	0.01	99.75	34.04	26.56	39.39
	BP224CPX5B	< 0.5 mm	C	BP224_CPX_5B_6	50.11	2.14	0.96	15.33	0.38	14.73	14.96	0.21	0.00	0.01	98.83	31.35	42.93	25.72
BP218	BP218CPX1	1.7	C	BP218_CPX_1_1	50.21	2.97	1.14	10.36	0.27	15.26	18.44	0.29	0.01	0.22	99.17	38.45	44.25	17.30
			I	BP218_CPX_1_2	49.53	3.43	1.21	11.20	0.27	14.64	17.85	0.39	0.00	0.08	98.59	37.84	43.19	18.97
			I	BP218_CPX_1_3	48.92	3.68	1.27	12.47	0.26	14.15	17.01	0.43	0.01	0.05	98.23	36.49	42.21	21.30
			I	BP218_CPX_1_4	50.12	2.51	1.23	11.45	0.28	14.96	18.10	0.26	0.00	0.00	98.91	37.65	43.30	19.05
			R	BP218_CPX_1_5	49.48	2.69	1.38	12.22	0.30	14.01	18.36	0.26	0.01	0.00	98.72	38.55	40.92	20.53
	BP218CPX1A		C	BP218_CPX_1A_6	49.68	3.54	1.20	11.63	0.31	15.04	16.82	0.32	0.01	0.15	98.70	35.74	44.45	19.80
	BP218CPX1B	0.6	C	BP218_CPX_1B_7	48.39	4.81	1.79	9.98	0.20	14.74	18.20	0.37	0.00	0.21	98.69	39.02	43.95	17.03
			R	BP218_CPX_1B_8	48.42	5.07	1.69	9.86	0.22	14.47	18.58	0.39	0.00	0.21	98.91	39.89	43.21	16.90
	BP218CPX1C		C	BP218_CPX_1C_9	48.54	3.01	1.90	13.22	0.34	12.40	19.12	0.32	0.02	0.00	98.88	40.71	36.74	22.55
	BP218CPX2	0.6	C	BP218_CPX_2_1	49.40	3.07	1.31	12.47	0.29	14.30	17.58	0.31	0.02	0.06	98.81	37.05	41.94	21.00
			I	BP218_CPX_2_2	49.79	2.95	1.23	13.66	0.35	15.32	15.72	0.30	0.01	0.06	99.39	32.77	44.42	22.81
			I	BP218_CPX_2_3	50.09	2.81	1.07	12.42	0.30	15.46	16.43	0.25	0.00	0.11	98.93	34.32	44.93	20.75
			I	BP218_CPX_2_4	50.09	2.78	1.18	12.94	0.33	15.33	16.18	0.30	0.00	0.06	99.20	33.80	44.55	21.65
			I	BP218_CPX_2_5	49.21	3.77	1.40	11.99	0.27	15.12	16.58	0.34	0.00	0.18	98.85	35.14	44.58	20.28
			I	BP218_CPX_2_6	49.25	3.58	1.27	11.33	0.28	14.57	17.70	0.37	0.00	0.09	98.43	37.64	43.09	19.27

			I	BP218_CPX_2_7	49.78	3.21	1.10	11.72	0.28	15.39	16.92	0.30	0.00	0.13	98.82	35.48	44.88	19.65
			I	BP218_CPX_2_8	48.82	4.01	1.30	12.87	0.31	14.48	16.19	0.45	0.00	0.04	98.47	34.72	43.21	22.07
			I	BP218_CPX_2_9	50.48	2.22	1.09	11.72	0.28	15.04	17.87	0.24	0.00	0.03	98.99	37.11	43.44	19.46
			I	BP218_CPX_2_10	49.93	2.61	1.32	12.10	0.30	14.69	17.75	0.24	0.00	0.01	98.95	37.09	42.68	20.23
			R	BP218_CPX_2_11	49.31	2.60	1.48	13.17	0.38	14.20	17.30	0.27	0.00	0.01	98.72	36.31	41.47	22.22
	BP218CPX2A		C	BP218_CPX_2A_12	50.26	2.53	1.22	11.74	0.28	15.09	17.70	0.28	0.00	0.00	99.09	36.81	43.67	19.52
			R	BP218_CPX_2A_13	48.95	3.15	1.56	11.60	0.30	14.06	18.71	0.28	0.01	0.02	98.63	39.35	41.12	19.53
	BP243CPX1	1.2	C	BP243_CPX_1_1	50.59	1.94	0.94	12.74	0.33	14.16	18.37	0.24	0.00	0.01	99.33	38.05	40.80	21.14
			I	BP243_CPX_1_2	50.73	1.74	0.90	12.98	0.33	14.33	18.20	0.22	0.00	0.00	99.44	37.51	41.08	21.42
			I	BP243_CPX_1_3	50.14	2.33	1.17	12.77	0.37	13.95	18.22	0.27	0.02	0.02	99.26	38.04	40.52	21.44
			I	BP243_CPX_1_4	50.75	1.64	0.86	12.62	0.34	14.65	17.85	0.22	0.01	0.00	98.93	36.91	42.16	20.93
			I	BP243_CPX_1_5	51.29	1.51	0.82	13.05	0.38	14.75	17.48	0.22	0.01	0.00	99.50	36.05	42.32	21.63
			R	BP243_CPX_1_6	50.63	1.60	0.83	15.62	0.42	13.65	16.66	0.21	0.01	0.00	99.63	34.58	39.42	26.00
	BP243CPX1A	< 0.5 mm	C	BP243_CPX_1A_7	52.47	0.70	0.43	21.69	0.56	19.59	4.30	0.07	0.00	0.00	99.82	8.80	55.69	35.51
	BP243CPX1B	< 0.5 mm	MR	BP243_CPX_1B_8	50.21	1.61	0.83	19.06	0.55	13.95	12.67	0.19	0.01	0.01	99.08	26.73	40.95	32.32
BP243	BP243CPX1C	< 0.5 mm	R	BP243_CPX_1C_9	49.36	1.75	0.84	18.38	0.54	10.57	17.30	0.21	0.01	0.00	98.96	36.98	31.44	31.57
	BP243CPX2	2.0	C	BP243_CPX_2_1	50.83	1.89	0.95	13.27	0.37	14.50	17.13	0.27	0.00	0.00	99.20	35.73	42.07	22.21
			I	BP243_CPX_2_2	50.87	1.96	0.94	13.30	0.40	14.58	17.17	0.25	0.00	0.01	99.48	35.65	42.13	22.22
			I	BP243_CPX_2_3	50.47	1.76	0.90	13.23	0.34	14.44	17.54	0.22	0.00	0.02	98.90	36.37	41.65	21.98
			R	BP243_CPX_2_4	50.68	1.69	0.83	13.23	0.37	14.45	17.51	0.24	0.00	0.01	99.00	36.31	41.67	22.02
	BP243CPX2A	< 0.5 mm	C	BP243_CPX_2A_5	50.56	1.77	0.91	12.65	0.34	14.48	18.04	0.23	0.00	0.00	98.98	37.32	41.69	20.98
	BP243CPX2B	0.5	C	BP243_CPX_2B_6	51.13	1.81	0.89	12.99	0.37	14.26	18.07	0.21	0.00	0.00	99.73	37.38	41.05	21.57
			C	BP243_CPX_2B_7	50.68	1.76	0.89	12.98	0.34	14.39	17.93	0.25	0.01	0.00	99.22	37.09	41.41	21.51
	BP243CPX2C	< 0.5 mm	C	BP243_CPX_2C_8	50.72	1.82	0.95	12.92	0.37	14.29	17.91	0.23	0.00	0.00	99.21	37.17	41.28	21.55
1UN2680	1UN2680CPX1	3.0	C	1UN2680_cpx_1_1	50.57	2.18	0.69	12.83	0.29	14.17	18.11	0.19	0.00	0.01	99.04	37.67	41.02	21.31
			R	1UN2680_cpx_1_2	50.39	1.56	0.67	16.34	0.36	12.64	16.90	0.20	0.00	0.00	99.05	35.56	37.01	27.43

	1UN2680CPX2	1.8	I	1UN2680_cpx_2_1	50.21	1.59	0.68	15.54	0.33	12.49	17.71	0.21	0.00	0.01	98.77	37.31	36.59	26.10
	1UN2680CPX2.2	1.9	I	1UN2680_cpx_2_2	50.61	0.87	0.39	25.31	0.60	16.01	5.04	0.07	0.00	0.00	98.88	10.59	46.84	42.56
	1UN2680CPX6	0.6	C	1UN2680_cpx_6_1	51.22	1.01	0.38	22.12	0.48	18.72	4.69	0.03	0.00	0.02	98.67	9.68	53.84	36.47
BP201	BP201CPX1	1.4	C	BP201_cpx_1_1	50.55	1.25	0.69	16.38	0.51	12.22	17.53	0.18	0.00	0.01	99.32	36.74	35.63	27.63
			I	BP201_cpx_1_2	50.18	1.49	0.81	16.17	0.44	11.76	17.84	0.22	0.01	0.00	98.92	37.83	34.67	27.50
			R	BP201_cpx_1_3	49.66	1.00	0.64	19.29	0.54	9.21	18.35	0.22	0.01	0.00	98.91	39.33	27.48	33.19
	BP201CPX2	1.1	C	BP201_cpx_2_1	50.31	1.34	0.70	16.71	0.42	11.67	17.68	0.21	0.00	0.00	99.03	37.39	34.32	28.28
			R	BP201_cpx_2_2	49.65	1.08	0.63	19.52	0.55	9.44	18.00	0.22	0.00	0.01	99.10	38.47	28.05	33.48
	BP201CPX6	1.5	C	BP201_cpx_6_1	50.04	1.53	0.78	16.13	0.45	11.96	17.54	0.21	0.01	0.00	98.64	37.22	35.32	27.46
			R	BP201_cpx_6_2	49.60	1.04	0.67	19.40	0.57	9.19	18.42	0.24	0.00	0.00	99.12	39.37	27.30	33.33
BP209	BP209CPX1	1.4	C	BP209_cpx_1_1	50.35	2.51	1.24	11.16	0.26	14.75	18.64	0.26	0.00	0.00	99.16	38.77	42.69	18.54
			I	BP209_cpx_1_2	50.42	2.57	1.27	10.73	0.26	14.65	19.36	0.30	0.00	0.00	99.55	40.07	42.17	17.76
			I	BP209_cpx_1_3	50.58	2.16	1.12	10.68	0.28	14.77	19.02	0.27	0.00	0.01	98.88	39.53	42.70	17.78
			I	BP209_cpx_1_4	51.04	1.92	1.01	11.67	0.31	14.59	18.47	0.23	0.00	0.02	99.24	38.40	42.17	19.43
			R	BP209_cpx_1_5	50.96	1.61	0.81	13.88	0.37	13.48	18.00	0.23	0.00	0.01	99.35	37.59	39.17	23.23
	BP209CPX1A6	< 0.5 mm	I	BP209_cpx_1A_6	51.37	0.72	0.44	23.66	0.64	17.52	4.71	0.05	0.00	0.00	99.10	9.80	50.70	39.49
	BP201CPX1A7	< 0.5 mm	I	BP209_cpx_1A_7	50.20	0.35	0.42	27.91	0.82	14.20	4.18	0.06	0.00	0.01	98.15	9.02	42.59	48.39
	BP209CPX2	0.9	C	BP209_cpx_2_1	50.15	2.52	1.22	11.50	0.29	14.54	18.53	0.30	0.00	0.00	99.03	38.63	42.17	19.19
			I	BP209_cpx_2_2	50.51	2.28	1.16	11.25	0.26	14.83	18.54	0.24	0.00	0.02	99.10	38.49	42.85	18.66
			I	BP209_cpx_2_3	50.32	2.21	1.13	11.41	0.30	14.93	18.32	0.25	0.00	0.01	98.87	37.99	43.05	18.96
			R	BP209_cpx_2_4	50.97	1.28	0.69	14.72	0.42	13.24	17.72	0.22	0.01	0.01	99.27	36.95	38.40	24.64
	BP209CPX2A	0.4	C	BP209_cpx_2A_5	51.02	1.84	0.93	11.12	0.28	15.14	18.31	0.23	0.00	0.02	98.88	37.93	43.63	18.44
			R	BP209_cpx_2A_6	51.00	1.42	0.73	13.81	0.41	13.98	17.37	0.25	0.01	0.02	98.99	36.25	40.58	23.17
BP235	BP235CPX1	1.5	C	BP235_cpx_1_1	50.91	2.13	1.01	10.99	0.28	15.26	18.27	0.24	0.00	0.06	99.14	37.83	43.95	18.21
			I	BP235_cpx_1_2	50.95	2.26	1.10	10.87	0.27	15.06	18.80	0.24	0.01	0.07	99.64	38.79	43.24	17.96

			I	BP235_cpx_1_3	50.58	2.42	1.03	10.95	0.26	15.43	17.97	0.25	0.00	0.06	98.96	37.29	44.55	18.16
			R	BP235_cpx_1_4	51.29	1.77	0.93	12.52	0.35	14.94	17.65	0.24	0.00	0.01	99.69	36.41	42.86	20.73
			R	BP235_cpx_1_5	50.91	1.33	0.68	14.41	0.40	13.41	17.70	0.22	0.00	0.00	99.06	36.93	38.93	24.14
	BP235CPX1A	0.8	C	BP235_cpx_1A_1	51.65	0.92	0.55	19.53	0.54	20.31	5.18	0.08	0.00	0.02	98.76	10.54	57.54	31.92
			R	BP235_cpx_1A_2	52.24	0.81	0.49	20.60	0.55	19.82	4.48	0.05	0.01	0.00	99.05	9.22	56.78	34.01
	BP235CPX2	0.6	C	BP235_cpx_2_1	48.59	4.56	1.69	11.12	0.25	13.51	18.97	0.31	0.00	0.18	99.18	40.67	40.29	19.04
			I	BP235_cpx_2_2	50.59	2.36	1.03	12.20	0.30	14.63	17.94	0.21	0.01	0.12	99.39	37.34	42.35	20.31
			I	BP235_cpx_2_3	51.19	2.27	1.05	11.41	0.28	15.17	18.21	0.24	0.01	0.05	99.87	37.60	43.57	18.83
			R	BP235_cpx_2_4	51.51	1.08	0.58	15.22	0.45	12.49	18.13	0.23	0.02	0.00	99.69	37.98	36.40	25.63
			MR	BP235_cpx_2_5*	45.22	4.98	0.97	23.62	0.45	8.24	10.03	2.06	0.88	0.00	96.45	24.89	28.45	46.66
	BP235CPX4	0.3	C	BP235_cpx_4_1	50.11	2.35	1.16	12.36	0.32	13.77	18.37	0.25	0.01	0.03	98.72	38.74	40.40	20.86
			I	BP235_cpx_4_2	50.54	2.62	1.34	10.50	0.29	14.24	19.64	0.22	0.00	0.00	99.39	41.02	41.39	17.59
			R	BP235_cpx_4_3	50.76	2.08	1.11	11.11	0.31	14.87	18.71	0.27	0.00	0.00	99.22	38.73	42.82	18.45
	BP235CPX4A	< 0.5 mm	I	BP235_cpx_4A_4	51.46	0.58	0.46	22.88	0.59	18.94	3.91	0.06	0.00	0.02	98.89	8.05	54.23	37.73

Table A4. CSD dataset of plagioclase and pyroxene of the eastern Parnaíba Basin magmatism.

	Plagioclase						Clinopyroxene					
	Mid Inter	ln(pop den)	ln(min PD)	ln(max PD)	Cry Num	Vol%	Mid Inter	ln(pop den)	ln(min PD)	ln(max PD)	Cry Num	Vol%
1UN2668	3.36	-4.11	-4.72	-3.74	0.03	7.69	1.44	-0.56	-0.72	-0.41	0.38	22.39
	2.12	-1.19	-1.37	-1.03	0.30	22.75	0.91	1.27	1.17	1.37	1.49	22.06
	1.34	0.84	0.74	0.93	1.43	27.44	0.57	2.75	2.67	2.82	4.12	15.29
	0.84	2.63	2.56	2.69	5.39	25.97	0.36	2.93	2.80	3.04	3.12	2.90
	0.53	3.44	3.37	3.50	7.63	9.22	-	-	-	-	-	-
	0.34	3.24	3.09	3.37	3.97	1.20	-	-	-	-	-	-
1UN2680	Mid Inter	ln(pop den)	ln(min PD)	ln(max PD)	Cry Num	Vol%	Mid Inter	ln(pop den)	ln(min PD)	ln(max PD)	Cry Num	Vol%
	5.32	-6.51	-7.20	-6.10	0.00	3.13	4.41	-6.79	-7.27	-6.46	0.00	12.79
	3.35	-4.50	-4.85	-4.25	0.02	3.69	3.18	-5.29	-5.58	-5.05	0.01	15.39

	2.12	-1.77	-1.90	-1.66	0.17	8.98	2.29	-4.10	-4.32	-3.91	0.01	13.56
	1.34	-0.41	-0.51	-0.32	0.41	5.55	1.65	-3.09	-3.28	-2.93	0.02	9.95
	0.84	0.63	0.53	0.72	0.73	2.49	1.18	-2.27	-2.45	-2.12	0.04	6.06
	0.53	1.67	1.57	1.75	1.29	1.11	0.85	-2.06	-2.32	-1.86	0.04	2.00
	0.34	2.74	2.65	2.82	2.39	0.51	0.61	-2.01	-2.43	-1.71	0.03	0.57
	0.21	3.49	3.39	3.57	3.18	0.17	-	-	-	-	-	-
	0.13	2.44	2.05	2.72	0.70	0.01	-	-	-	-	-	-
	0.08	1.66	0.50	2.19	0.21	0.00	-	-	-	-	-	-
1UN21254	Mid Inter	ln(pop den)	ln(min PD)	ln(max PD)	Cry Num	Vol%	Mid Inter	ln(pop den)	ln(min PD)	ln(max PD)	Cry Num	Vol%
	4.63	-4.10	-4.54	-3.79	0.03	6.81	1.917	-2.86	-3.45	-2.49	0.0361	2.991
	3.34	-1.81	-1.98	-1.66	0.18	18.01	1.38	-1.07	-1.36	-0.84	0.156	4.83
	2.40	-0.36	-0.48	-0.26	0.55	20.48	0.993	0.55	0.37	0.69	0.564	6.494
	1.73	0.69	0.60	0.78	1.14	15.85	0.715	1.95	1.84	2.06	1.66	7.126
	1.24	1.66	1.58	1.73	2.14	11.11	0.514	2.63	2.51	2.74	2.35	3.759
	0.90	2.36	2.28	2.43	3.11	6.03	0.37	3.5	3.39	3.6	4.03	2.401
	0.64	2.70	2.61	2.79	3.16	2.28	0.266	3.49	3.32	3.63	2.87	0.639
	0.46	2.58	2.43	2.72	2.02	0.54	-	-	-	-	-	-
1UN21320	Mid Inter	ln(pop den)	ln(min PD)	ln(max PD)	Cry Num	Vol%	Mid Inter	ln(pop den)	ln(min PD)	ln(max PD)	Cry Num	Vol%
	1.05	-0.47	-1.34	-0.02	0.30	5.92	-	-	-	-	-	-
	0.66	1.39	0.93	1.70	1.23	6.06	-	-	-	-	-	-
	0.42	3.86	3.67	4.01	9.10	11.29	-	-	-	-	-	-
	0.26	6.18	6.09	6.26	58.70	18.30	-	-	-	-	-	-
	0.17	7.61	7.54	7.67	155.00	12.11	-	-	-	-	-	-
	0.11	7.93	7.82	8.02	134.00	2.64	-	-	-	-	-	-
1UN32242	Mid Inter	ln(pop den)	ln(min PD)	ln(max PD)	Cry Num	Vol%	Mid Inter	ln(pop den)	ln(min PD)	ln(max PD)	Cry Num	Vol%
	1.99	-0.91	-1.61	-0.51	0.37	12.66	0.40	1.80	1.10	2.20	1.11	2.68
	1.25	1.55	1.29	1.76	2.72	23.62	0.25	5.10	4.94	5.25	19.10	11.58
	0.79	4.03	3.91	4.13	20.40	44.49	0.16	7.24	7.15	7.32	102.00	15.47
	0.50	5.34	5.25	5.43	48.00	26.30	0.10	8.25	8.16	8.33	177.00	6.77

	0.31	6.37	6.28	6.45	84.90	11.67	0.06	7.85	7.62	8.04	74.50	0.72
	0.20	6.33	6.16	6.48	51.50	1.78	-	-	-	-	-	-
	0.13	6.17	5.85	6.41	27.50	0.24	-	-	-	-	-	-
1UN32254	Mid Inter	ln(pop den)	ln(min PD)	ln(max PD)	Cry Num	Vol%	Mid Inter	ln(pop den)	ln(min PD)	ln(max PD)	Cry Num	Vol%
	2.19	-3.50	-4.25	-3.08	0.03	3.71	2.37	-3.37	-3.96	-3.00	0.04	9.16
	1.38	-0.85	-1.09	-0.65	0.27	8.36	1.50	-1.53	-1.88	-1.28	0.15	9.07
	0.87	1.55	1.44	1.65	1.89	14.49	0.94	0.18	-0.04	0.35	0.52	7.93
	0.55	3.28	3.21	3.35	6.74	13.01	0.60	1.76	1.61	1.89	1.59	6.14
	0.35	4.38	4.31	4.44	12.70	6.16	0.38	3.52	3.42	3.61	5.86	5.66
	0.22	4.70	4.60	4.79	11.10	1.35	0.24	4.42	4.31	4.51	9.04	2.20
	0.14	3.53	2.94	3.89	2.16	0.07	0.15	5.04	4.91	5.15	10.60	0.65
	-	-	-	-	-	-	0.09	3.72	2.73	4.20	1.79	0.03
	-	-	-	-	-	-	0.06	4.14	3.45	4.54	1.72	0.01
BP188A	Mid Inter	ln(pop den)	ln(min PD)	ln(max PD)	Cry Num	Vol%	Mid Inter	ln(pop den)	ln(min PD)	ln(max PD)	Cry Num	Vol%
	2.47	-2.38	-2.71	-2.13	0.08	6.74	0.70	-1.63	-2.15	-1.29	0.06	0.95
	1.78	-0.32	-0.47	-0.19	0.42	14.13	0.44	1.38	1.22	1.51	0.81	3.03
	1.28	1.06	0.96	1.16	1.22	15.20	0.28	3.53	3.45	3.61	4.41	4.14
	0.92	1.83	1.74	1.92	1.89	8.81	0.18	4.73	4.65	4.80	9.19	2.17
	0.66	2.40	2.29	2.49	2.39	4.14	0.11	4.06	3.81	4.26	2.98	0.18
	0.48	2.68	2.54	2.80	2.28	1.47	-	-	-	-	-	-
	0.34	1.24	0.43	1.69	0.39	0.09	-	-	-	-	-	-
BP200	Mid Inter	ln(pop den)	ln(min PD)	ln(max PD)	Cry Num	Vol%	Mid Inter	ln(pop den)	ln(min PD)	ln(max PD)	Cry Num	Vol%
	2.54	-3.64	-3.89	-3.44	0.03	8.56	2.27	-3.50	-3.76	-3.29	0.03	7.88
	1.60	-0.56	-0.64	-0.48	0.42	29.63	1.43	-0.35	-0.43	-0.28	0.46	29.01
	1.01	1.30	1.25	1.35	1.71	30.05	0.90	1.49	1.44	1.53	1.84	28.83
	0.64	2.43	2.39	2.48	3.35	14.80	0.57	2.60	2.55	2.65	3.53	13.93
	0.40	2.98	2.92	3.03	3.64	4.04	0.36	3.13	3.06	3.18	3.77	3.74
	0.25	3.38	3.30	3.45	3.43	0.96	0.23	3.56	3.48	3.64	3.67	0.91
	0.16	4.12	4.03	4.20	4.54	0.32	0.14	4.28	4.18	4.36	4.74	0.30

	0.10	5.04	4.95	5.12	7.17	0.13	0.09	5.20	5.11	5.28	7.54	0.12
	0.06	5.71	5.61	5.80	8.85	0.04	0.06	5.91	5.81	6.00	9.65	0.04
BP201	Mid Inter	ln(pop den)	ln(min PD)	ln(max PD)	Cry Num	Vol%	Mid Inter	ln(pop den)	ln(min PD)	ln(max PD)	Cry Num	Vol%
		-8.51	-9.73	-7.97	0.000713	4.231	3.15	-7.44	-8.87	-6.88	0.000707	0.976
	4.83	-4.85	-5.05	-4.68	0.0174	25.96	2.15	-5.14	-5.56	-4.84	0.00484	2.111
	3.05	-2.89	-3	-2.79	0.0781	29.25	1.46	-2.93	-3.11	-2.77	0.03	4.137
	1.923	-1.68	-1.78	-1.59	0.165	15.48	0.997	-1.28	-1.4	-1.18	0.106	4.626
	1.214	-0.89	-1	-0.79	0.229	5.424	0.679	-0.51	-0.63	-0.4	0.157	2.162
	0.766	-0.26	-0.4	-0.14	0.272	1.613	0.463	-0.12	-0.28	0.02	0.157	0.685
	0.483	0.65	0.51	0.77	0.425	0.633	0.315	0.4	0.21	0.56	0.18	0.248
	0.305	1.08	0.89	1.23	0.412	0.154	-	-	-	-	-	-
	0.1923	0.1	-0.76	0.56	0.0981	0.009	-	-	-	-	-	-
BP209	Mid Inter	ln(pop den)	ln(min PD)	ln(max PD)	Cry Num	Vol%	Mid Inter	ln(pop den)	ln(min PD)	ln(max PD)	Cry Num	Vol%
	4.49	-4.56	-4.82	-4.35	0.0216	28.85	1.88	-4.52	-5.25	-4.11	0.00587	1.789
	2.83	-2.46	-2.6	-2.34	0.111	37.14	1.41	-2.44	-2.72	-2.22	0.0353	4.53
	1.788	-0.82	-0.91	-0.73	0.363	30.52	1.055	-0.71	-0.86	-0.58	0.15	8.104
	1.128	0.13	0.03	0.22	0.589	12.44	0.791	0.7	0.6	0.79	0.459	10.47
	0.712	0.97	0.87	1.07	0.868	4.605	0.593	1.48	1.39	1.57	0.753	7.256
	0.449	2.16	2.07	2.24	1.78	2.379	0.445	1.76	1.65	1.86	0.748	3.039
	0.283	3.45	3.38	3.52	4.13	1.381	0.334	1.97	1.83	2.09	0.689	1.18
	0.1788	4.7	4.64	4.76	9.04	0.76	0.25	2.06	1.86	2.23	0.567	0.41
	0.1128	5.6	5.54	5.66	14.1	0.296	0.188	0.87	-0.35	1.4	0.129	0.039
	0.0712	6.49	6.42	6.55	21.5	0.114	-	-	-	-	-	-
	0.0449	4.55	3.79	4.98	1.96	0.002	-	-	-	-	-	-
BP218	Mid Inter	ln(pop den)	ln(min PD)	ln(max PD)	Cry Num	Vol%	Mid Inter	ln(pop den)	ln(min PD)	ln(max PD)	Cry Num	Vol%
	2.94	-3.9	-4.26	-3.64	0.0228	3.437	1.262	-3.39	-4.11	-2.97	0.0163	1.084
	2.005	-1.46	-1.6	-1.34	0.178	8.502	0.86	-0.87	-1.11	-0.67	0.139	2.913
	1.366	0.15	0.05	0.23	0.606	9.139	0.586	1.1	0.97	1.21	0.672	4.458
	0.93	1.73	1.67	1.79	2.02	9.626	0.399	2.95	2.88	3.02	2.93	6.138

	0.634	2.95	2.91	3	4.66	7.027	0.272	3.72	3.65	3.79	4.33	2.869
	0.432	3.48	3.42	3.53	5.38	2.566	0.185	3.63	3.5	3.75	2.69	0.563
	0.294	3.65	3.56	3.72	4.32	0.652	-	-	-	-	-	-
	0.2005	2.72	2.42	2.95	1.16	0.055	-	-	-	-	-	-
BP224	Mid Inter	ln(pop den)	ln(min PD)	ln(max PD)	Cry Num	Vol%	Mid Inter	ln(pop den)	ln(min PD)	ln(max PD)	Cry Num	Vol%
	2.74	-4.88	-5.78	-4.42	0.00798	2.032	1.469	-3.25	-4.11	-2.8	0.0218	1.621
	1.869	-1.36	-1.52	-1.22	0.184	14.78	1.001	0.26	0.1	0.4	0.499	11.71
	1.273	0.54	0.45	0.62	0.837	21.32	0.682	2.53	2.45	2.59	3.27	24.31
	0.867	2.28	2.22	2.33	3.25	26.14	0.465	3.63	3.57	3.69	6.75	15.85
	0.591	3.1	3.05	3.16	5.06	12.88	0.317	4.12	4.04	4.19	7.49	5.557
	0.403	3.72	3.66	3.77	6.35	5.115	0.216	2.25	1.53	2.67	0.788	0.185
	0.274	4.18	4.11	4.25	6.9	1.758	-	-	-	-	-	-
	0.1869	4.54	4.45	4.63	6.72	0.541	-	-	-	-	-	-
	0.1273	4.51	4.34	4.65	4.43	0.112	-	-	-	-	-	-
	0.0867	5.15	4.98	5.3	5.76	0.046	-	-	-	-	-	-
	0.0591	6.14	6.01	6.26	10.5	0.026	-	-	-	-	-	-
	0.0403	5.44	5.07	5.71	3.56	0.002	-	-	-	-	-	-
BP229	Mid Inter	ln(pop den)	ln(min PD)	ln(max PD)	Cry Num	Vol%	Mid Inter	ln(pop den)	ln(min PD)	ln(max PD)	Cry Num	Vol%
	4.33	-7.25	-8.47	-6.71	0.00142	4.265	2.19	-4.22	-4.66	-3.91	0.0124	2.572
	2.73	-4.55	-4.9	-4.3	0.0132	9.965	1.495	-1.64	-1.79	-1.5	0.112	7.312
	1.72	-2	-2.14	-1.87	0.108	20.39	1.018	0.1	0	0.19	0.431	8.923
	1.088	-0.03	-0.11	0.05	0.488	23.17	0.694	1.02	0.93	1.1	0.739	4.837
	0.686	1.35	1.28	1.41	1.22	14.51	0.473	1.81	1.72	1.9	1.11	2.3
	0.433	2.05	1.97	2.13	1.55	4.655	0.322	1.61	1.42	1.77	0.618	0.404
	0.273	2.42	2.3	2.52	1.41	1.06	-	-	-	-	-	-
BP235	Mid Inter	ln(pop den)	ln(min PD)	ln(max PD)	Cry Num	Vol%	Mid Inter	ln(pop den)	ln(min PD)	ln(max PD)	Cry Num	Vol%
	3.18	-4.04	-4.33	-3.81	0.0216	11.61	1.88	-3.32	-3.64	-3.07	0.0261	5.601
	2.17	-1.84	-1.97	-1.72	0.132	22.49	1.278	-1.4	-1.57	-1.25	0.121	8.194
	1.476	-0.34	-0.44	-0.26	0.401	21.62	0.87	0.36	0.26	0.46	0.481	10.3

	1.006	0.43	0.34	0.52	0.596	10.15	0.593	1.6	1.52	1.68	1.13	7.651
	0.685	0.69	0.55	0.81	0.523	2.82	0.404	2.14	2.04	2.23	1.32	2.828
	0.467	0.73	0.5	0.92	0.372	0.633	0.275	2.45	2.32	2.57	1.23	0.83
	0.318	0.17	-0.5	0.57	0.144	0.077	0.188	1.09	0.04	1.6	0.215	0.046
	-	-	-	-	-	-	-	-	-	-	-	-
BP239	Mid Inter	ln(pop den)	ln(min PD)	ln(max PD)	Cry Num	Vol%	Mid Inter	ln(pop den)	ln(min PD)	ln(max PD)	Cry Num	Vol%
	2.671	-1.67	-1.94	-1.46	0.23	25.09	1.011	-0.77	-1.16	-0.49	0.215	3.775
	1.685	0.46	0.32	0.58	1.23	33.65	0.638	2.11	1.98	2.23	2.43	10.72
	1.063	2.19	2.1	2.27	4.36	29.99	0.403	4.05	3.97	4.12	10.6	11.8
	0.671	3.03	2.94	3.12	6.42	11.08	0.254	4.52	4.41	4.61	10.7	2.986
	0.423	3.65	3.53	3.75	7.47	3.24	0.1603	3.24	2.5	3.66	1.88	0.131
	0.2671	2.69	2.18	3.03	1.82	0.197	0.1011	3.84	3.39	4.15	2.18	0.038
	-	-	-	-	-	-	-	-	-	-	-	-
BP243	Mid Inter	ln(pop den)	ln(min PD)	ln(max PD)	Cry Num	Vol%	Mid Inter	ln(pop den)	ln(min PD)	ln(max PD)	Cry Num	Vol%
	4.03	-5.05	-5.3	-4.85	0.00987	7.948	1.74	-4.28	-4.81	-3.94	0.00924	1.626
	2.74	-2.96	-3.08	-2.85	0.0545	13.86	1.186	-1.74	-1.93	-1.59	0.0796	4.432
	1.869	-1.37	-1.45	-1.3	0.182	14.62	0.808	0.12	0.01	0.21	0.349	6.138
	1.273	-0.06	-0.12	0	0.46	11.71	0.551	1	0.9	1.09	0.575	3.199
	0.867	0.58	0.51	0.64	0.595	4.788	0.375	1.56	1.44	1.67	0.688	1.211
	0.591	1.33	1.26	1.39	0.858	2.185	0.256	1.53	1.32	1.71	0.453	0.252
	0.403	1.66	1.57	1.74	0.81	0.652	-	-	-	-	-	-
	0.274	2.6	2.52	2.67	1.42	0.36	-	-	-	-	-	-
	0.1869	3.65	3.58	3.72	2.76	0.222	-	-	-	-	-	-
	0.1273	4.91	4.85	4.96	6.6	0.168	-	-	-	-	-	-
	0.0867	5.32	5.25	5.38	6.78	0.054	-	-	-	-	-	-

APPENDIX – SUPPLEMENTARY MATERIAL

CHAPTER 5. GEOCHEMICAL-ISOTOPIC SIGNATURE OF THE MESOZOIC THOLEIITIC MAGMATISM EXPOSED ON THE EASTERN FLANK OF THE PARNAÍBA BASIN

Table A1. Geochemical and isotopic data set of the sill complexes of eastern border of Parnaíba Basin

Site	Sample	Major elements (wt.%)											
High-Ti tholeiites (HT1)	Sample	SiO_2	Al_2O_3	Fe_2O_{3T}	MnO	MgO	CaO	Na_2O	K_2O	TiO_2	P_2O_5	LOI	SUM
Dikes - Baú	BP-186	52.20	12.80	13.8	0.20	3.65	7.27	2.94	1.99	3.23	0.73	0.53	99.34
Dikes - Monsehnhor Gil	BP-188A	51.90	12.90	13.8	0.21	3.51	6.34	3.57	2.45	3.15	0.72	0.79	99.34
Dikes - Monsehnhor Gil	BP-188B	53.70	12.80	13.2	0.20	2.92	6.29	3.15	2.40	2.75	0.86	1.12	99.39
Picos-Wall Ferraz	BP-190	51.00	12.90	14.0	0.19	3.86	7.25	3.37	1.99	3.42	0.68	0.65	99.31
Picos-Wall Ferraz	BP-270	52.30	12.50	14.2	0.19	3.55	7.13	2.86	2.09	3.34	0.76	0.74	99.66
Picos-Wall Ferraz	BP-271	50.50	15.00	12.7	0.16	3.86	8.53	3.26	1.47	3.55	0.47	0.46	99.96
Picos-Wall Ferraz	BP-272	49.10	13.30	14.6	0.18	5.01	8.73	2.63	1.45	4.10	0.47	0.28	99.85
Picos-Wall Ferraz	23.01	53.00	12.90	14.2	0.20	3.43	6.76	3.44	2.10	3.21	0.77	0.51	100.52
Elesbão Veloso	BP-252	49.80	12.30	14.1	0.18	5.74	9.09	2.49	1.38	3.36	0.47	0.27	99.18
Elesbão Veloso	BP-254	51.40	11.70	14.6	0.20	4.91	7.50	3.25	2.01	3.23	0.64	0.31	99.75
Elesbão Veloso	BP-263	52.50	12.70	13.7	0.20	3.60	7.16	2.90	1.98	3.24	0.76	1.23	99.97
Elesbão Veloso	BP-267	51.70	12.90	14.1	0.19	4.10	6.07	3.73	2.44	3.34	0.69	0.78	100.04
Elesbão Veloso	BP-268	53.20	12.80	14.0	0.20	3.26	6.24	3.29	2.45	2.87	1.23	0.68	100.22
Elesbão Veloso	30.04	49.60	12.90	14.5	0.20	4.99	7.88	2.69	1.69	3.36	0.55	0.94	99.30
São Felix	BP-258A	52.20	12.40	14.2	0.19	3.79	6.92	3.00	2.07	3.39	0.72	0.84	99.72
São Felix	BP-260B	52.40	12.40	14.0	0.18	4.15	6.73	2.99	2.07	3.26	0.72	0.89	99.79
São Felix	BP-260C	52.50	12.60	14.1	0.19	3.82	6.74	3.11	2.27	3.28	0.72	0.86	100.19
São Felix	BP-260D	49.80	12.60	14.9	0.19	4.48	8.11	2.88	1.63	4.25	0.52	0.45	99.81
São Felix	BP-261	51.80	12.90	13.9	0.18	4.90	6.17	2.95	1.18	3.39	0.74	1.88	99.99
Isaias Coelho	BP-209	49.10	13.10	14.8	0.19	4.54	8.21	3.01	1.57	4.20	0.53	0.59	99.84
Isaias Coelho	23.06	53.80	13.80	12.2	0.16	3.30	5.64	2.98	2.49	2.62	0.82	1.70	99.51
Isaias Coelho	BP-215	49.40	12.80	14.7	0.20	4.34	7.79	2.59	1.84	3.99	0.53	1.57	99.75
Isaias Coelho	24.04	50.62	12.96	15.0	0.21	4.55	8.06	2.55	1.69	3.76	0.58	0.01	99.98
Isaias Coelho	24.05	54.09	13.39	13.5	0.20	3.26	6.51	3.00	2.30	2.93	0.83	0.01	100.01
Campinas do Piauí	BP-216	49.00	13.90	13.5	0.18	4.53	8.29	2.80	1.56	4.19	0.43	0.63	99.01
Campinas do Piauí	BP-273	50.50	11.30	14.5	0.20	6.17	9.22	2.33	1.44	3.14	0.54	0.42	99.76
Campinas do Piauí	23.03	51.20	12.70	13.9	0.17	4.02	6.89	2.70	1.98	3.19	0.69	1.91	99.35
Campinas do Piauí	23.04	49.60	11.10	14.8	0.21	7.09	9.29	2.01	1.28	2.92	0.46	0.69	99.45
Campinas do Piauí	23.05	49.90	10.40	14.9	0.23	7.34	9.52	1.92	1.36	2.81	0.48	0.82	99.68
Simplício Mendes	BP-217A	50.90	13.00	13.2	0.13	4.65	6.87	2.63	1.86	3.13	0.68	1.95	99.00
Simplício Mendes	BP-217B	50.80	12.30	13.9	0.18	4.77	7.82	2.53	1.77	3.11	0.62	1.25	99.05
Simplício Mendes	BP-218	52.50	12.90	13.4	0.17	4.34	7.64	2.88	1.88	3.17	0.71	1.18	100.77

Dike - Floriano	BP-229	51.60	13.10	13.7	0.19	3.73	6.95	2.78	1.98	3.20	0.76	1.15	99.14
Floriano	BP-230A	54.30	12.80	13.1	0.20	2.64	5.81	3.18	2.56	2.55	0.91	0.99	99.04
Floriano	BP-230B	54.10	12.80	13.0	0.21	2.72	5.91	3.20	2.52	2.52	1.05	1.20	99.23
Floriano	BP-237	52.50	12.70	14.0	0.21	3.15	6.44	3.01	2.21	3.00	0.84	1.15	99.21
Floriano	BP-277	50.80	12.50	14.6	0.20	5.28	8.50	2.56	1.66	3.16	0.58	0.32	100.16
Floriano	BP-278	51.30	12.20	14.7	0.19	5.05	7.99	2.54	1.86	3.20	0.63	0.46	100.12
Teresina	BP-281	51.20	12.20	14.8	0.20	5.28	8.36	2.58	1.69	3.17	0.60	0.28	100.36
Teresina	BP-282A	53.80	12.80	13.4	0.20	3.08	6.59	3.04	2.38	2.94	0.86	0.54	99.63
Teresina	BP-282B	51.90	12.80	14.1	0.19	4.23	7.39	2.82	1.89	3.25	0.71	1.25	100.53
Teresina	BP-283	50.40	12.20	15.1	0.19	5.19	8.04	2.77	1.74	3.32	0.58	0.69	100.22
Teresina	BP-284A	52.40	13.00	14.0	0.19	3.59	7.23	2.88	2.14	3.37	0.75	0.51	100.06
Teresina	BP-284B	52.90	13.10	14.0	0.18	3.76	6.56	3.17	2.16	3.24	0.76	0.86	100.69
Amarante	BP-231	52.70	12.70	13.7	0.21	3.16	6.53	3.18	2.25	3.04	0.79	1.00	99.26
Amarante	BP-232	51.50	12.50	14.6	0.20	4.70	7.60	2.94	1.89	3.14	0.66	0.49	100.22
Amarante	BP-233	51.30	12.20	14.8	0.20	5.34	8.16	2.49	1.79	3.11	0.59	0.90	100.88
Amarante	30.02	50.60	12.10	14.7	0.21	5.15	8.00	2.37	1.74	3.08	0.61	1.11	99.67
Amarante	BP-234	51.30	12.30	14.5	0.19	5.25	7.89	2.98	1.82	3.10	0.62	0.38	100.33
Amarante (São Francisco do Maranhão)	19.02	51.10	12.20	14.7	0.20	5.04	8.13	2.55	1.74	3.17	0.63	0.62	100.08
Amarante	BP-244	49.00	13.30	14.7	0.19	4.67	8.85	2.66	1.41	4.52	0.48	0.40	100.18
Amarante	BP-245	50.50	11.40	14.7	0.19	5.78	8.95	2.52	1.42	3.06	0.49	0.49	99.50
Amarante	BP-246	53.40	11.40	14.2	0.22	3.17	6.33	3.00	2.34	2.96	0.92	1.11	99.05
Amarante	BP-279	52.50	12.90	14.0	0.19	3.92	5.82	3.39	2.63	3.19	0.77	0.80	100.11
Amarante	BP-280	51.80	12.60	14.5	0.20	4.83	7.04	2.79	1.96	3.25	0.68	0.85	100.50
Amarante	30.01	52.80	12.50	14.1	0.21	3.30	6.31	2.96	2.23	3.00	0.89	0.97	99.27
Dikes - Barrocão	BP-235	50.20	11.90	15.2	0.21	5.68	8.26	2.86	1.64	3.11	0.58	0.21	99.85
Dikes - Barrocão	BP-236	49.70	12.80	14.9	0.21	4.39	7.73	2.46	1.69	3.80	0.56	0.99	99.23
Dikes - Baixa Grande	30.05	50.60	12.40	14.3	0.21	4.55	7.85	2.46	1.72	3.16	0.65	1.38	99.28
Dikes - Baixa Grande	BP-240	50.90	12.60	14.2	0.19	4.43	7.31	2.51	1.99	3.14	0.65	1.32	99.24
Dikes - Baixa Grande	BP-241	50.50	12.30	14.7	0.19	4.79	8.12	2.76	1.68	3.16	0.60	0.70	99.50
Dikes - Monsenhor Gil	19.01	53.20	12.90	13.5	0.20	3.17	6.73	2.93	2.32	2.89	1.07	1.00	99.91
Dikes - Curralinhos	BP-242	54.60	12.90	12.9	0.21	2.74	5.81	2.96	2.69	2.45	1.02	1.50	99.78
Dikes - Curralinhos	BP-243	51.80	13.00	13.4	0.20	3.33	6.97	2.77	2.09	3.01	0.73	2.00	99.30
Dikes - Wall Ferraz	23.02A	49.00	13.20	15.1	0.21	4.80	8.31	2.66	1.43	3.52	0.47	0.85	99.55
Dikes - Wall Ferraz	23.02B	50.90	11.70	14.1	0.20	5.39	8.32	2.33	1.72	3.03	0.63	1.10	99.42
Colinas	29.04	49.80	12.90	14.6	0.19	4.61	8.03	2.68	1.64	3.76	0.57	1.08	99.86
Colinas	29.05	52.50	13.00	13.1	0.19	3.16	6.32	2.91	2.23	2.84	0.81	2.24	99.30
Mimoso	BP-247	54.80	11.90	12.9	0.19	2.77	6.10	3.16	2.71	2.54	1.15	1.11	99.33
Mimoso	BP-249	55.20	12.10	12.8	0.19	2.85	6.08	3.10	2.74	2.33	1.17	1.00	99.56
Mimoso	BP-250	51.90	11.90	14.2	0.18	4.40	6.72	3.27	2.05	3.25	0.70	0.84	99.41

Evolved High-Ti tholeiites (eHT1)	Sample	SiO_2	Al_2O_3	Fe_2O_{3T}	MnO	MgO	CaO	Na_2O	K_2O	TiO_2	P_2O_5	LOI	SUM
Elesbão Veloso	BP-269	60.50	13.40	10.5	0.17	1.21	4.13	3.72	3.46	1.43	0.45	1.26	100.23
Elesbão Veloso	BP-262	60.60	12.90	10.7	0.17	1.27	4.11	3.67	3.64	1.48	0.49	1.17	100.20
Elesbão Veloso	BP-255	61.50	12.60	9.8	0.16	1.22	3.92	3.48	3.76	1.40	0.44	1.23	99.48
Elesbão Veloso	BP-197*	57.10	12.90	11.8	0.20	1.78	4.59	3.38	3.14	1.78	0.65	1.71	99.03
Elesbão Veloso	BP-199*	62.80	13.40	9.0	0.17	0.88	3.21	3.64	3.89	1.08	0.26	1.86	100.14
Elesbão Veloso	BP-201	55.80	13.10	13.1	0.22	2.38	4.86	3.41	2.83	2.05	0.82	1.59	100.16
Elesbão Veloso	BP-257	56.20	12.40	12.9	0.19	2.27	5.41	3.23	2.97	2.25	0.94	1.07	99.83
Mimoso	BP-248	56.70	11.80	12.7	0.19	2.23	5.27	3.16	3.09	2.29	0.87	1.33	99.63

Low-Ti tholeiites (LT)	Sample	SiO_2	Al_2O_3	Fe_2O_{3T}	MnO	MgO	CaO	Na_2O	K_2O	TiO_2	P_2O_5	LOI	SUM
Lagoa de São Francisco	BP-109A	51.10	12.50	16.2	0.23	5.37	8.94	2.16	0.72	1.95	0.17	0.33	99.67
Lagoa de São Francisco	BP-109B	52.60	13.70	12.5	0.19	6.19	9.49	2.35	0.73	1.38	0.17	0.53	99.83
Lagoa de São Francisco	BP-111	52.40	13.30	13.6	0.20	5.41	9.16	2.25	0.75	1.59	0.18	0.58	99.42
Lagoa de São Francisco	BP-112	52.20	13.20	13.8	0.20	5.60	9.08	2.26	0.85	1.62	0.20	0.45	99.46
Lagoa de São Francisco	BP-113	51.90	13.70	12.6	0.20	6.26	9.75	2.26	0.74	1.36	0.16	0.46	99.39
Lagoa de São Francisco	BP-114A1	51.90	13.80	12.6	0.19	6.28	9.75	2.04	0.73	1.34	0.16	0.52	99.31
Lagoa de São Francisco	BP-115	52.10	13.50	13.8	0.19	5.25	9.09	2.38	0.70	1.58	0.19	0.59	99.37
Lagoa de São Francisco	BP-116	52.10	13.60	12.9	0.20	6.02	9.48	2.19	0.78	1.44	0.16	0.42	99.29
Itaueira	BP-227	51.60	13.60	12.4	0.19	6.34	9.79	2.25	0.62	1.37	0.12	1.01	99.29
Itaueira	BP-228	51.90	13.70	12.3	0.18	6.29	10.10	2.21	0.55	1.35	0.12	0.67	99.37
Itaueira	BP-275A	52.50	13.50	12.8	0.18	5.60	9.74	2.53	0.90	1.48	0.16	0.92	100.31
Itaueira	BP-275B	52.00	13.40	12.9	0.19	6.00	9.79	2.35	0.67	1.51	0.16	1.69	100.66
Itaueira	BP-275C	52.70	13.50	13.1	0.19	6.28	9.83	2.25	0.65	1.50	0.16	0.55	100.71
Itaueira	BP-275D	52.50	13.20	13.0	0.19	5.21	9.51	2.44	0.80	1.63	0.18	1.95	100.61
Itaueira	BP-276	52.30	13.30	13.8	0.19	5.77	9.67	2.29	0.69	1.63	0.16	0.63	100.43
Itaueira	24.02	52.00	13.60	12.5	0.19	6.41	10.10	2.09	0.55	1.37	0.14	0.78	99.73
Itaueira	24.01	52.00	13.60	12.5	0.19	6.35	10.10	2.05	0.59	1.38	0.14	0.58	99.48
Elesbão Veloso	BP-200	51.50	13.70	12.6	0.19	6.42	9.75	2.44	0.70	1.37	0.12	0.85	99.64
Elesbão Veloso	BP-253	52.40	12.70	12.8	0.18	6.24	9.86	2.31	0.52	1.50	0.15	0.96	99.62
Elesbão Veloso	BP-256	52.10	13.10	12.8	0.22	6.56	9.71	2.29	0.74	1.41	0.14	0.87	99.94
Elesbão Veloso	BP-264	51.80	13.30	12.7	0.18	6.34	10.20	2.39	0.62	1.42	0.14	0.47	99.56
Elesbão Veloso	BP-265	51.50	13.30	13.4	0.20	6.07	7.74	4.36	0.98	1.48	0.17	1.48	100.68
Elesbão Veloso	BP-266	52.40	13.30	13.0	0.20	6.30	9.76	2.29	0.65	1.48	0.15	0.76	100.29
Batalha (Caraúbas do Piauí)	16.01	52.10	14.40	10.7	0.16	7.44	11.10	2.17	0.55	1.01	0.11	0.09	99.83
Batalha (Caraúbas do Piauí)	16.02	52.90	13.40	13.6	0.19	5.75	9.38	2.49	0.77	1.58	0.17	0.32	100.55
Batalha (Matias Olímpio)	18.01	52.50	14.00	11.8	0.17	7.16	10.60	2.23	0.59	1.24	0.12	0.33	100.74
Batalha (Morro do Chapéu do Piauí)	18.02	51.80	14.40	10.8	0.16	7.64	11.00	2.13	0.63	1.06	0.12	0.24	99.98

Batalha	18.03	52.40	13.20	13.9	0.20	5.63	9.41	2.39	0.81	1.63	0.17	0.33	100.07
Dikes - Jatobá do Piauí	18.06	52.30	14.90	11.3	0.17	6.37	9.96	2.39	0.88	1.22	0.13	0.47	100.09
Dikes - José de Freitas	18.07	51.90	13.50	12.2	0.18	6.28	10.10	2.25	0.92	1.35	0.14	1.77	100.59

High-Ti tholeiites two (HT2)	Sample	SiO_2	Al_2O_3	Fe_2O_{3T}	MnO	MgO	CaO	Na_2O	K_2O	TiO_2	P_2O_5	LOI	SUM
Batalha (Estreito)	16.03	49.50	14.00	14.5	0.20	6.23	10.40	2.49	0.37	1.99	0.17	0.14	99.99
Canto do Buriti	BP-224	48.0	13.10	15.9	0.23	5.75	10.00	2.29	0.34	2.46	0.18	0.75	99

Sample — Trace elements (ppm)

HT1	V	Cr	Co	Ni	Cu	Pb	Zn	Rb	Sr	Cs	Y	Zr	Nb	Ba	Hf	Ta	Th	U
BP-186	154.0		17.2	3.3		1.4		45.9	685.9	0.9	44.5	349.7	29.3	641.0	9.1	2.0	4.7	1.1
BP-188A	198.0		17.7	10.1		6.6		56.8	605.4	0.6	44.6	353.7	27.8	662.0	8.6	2.0	4.9	1.0
BP-188B	132.0		16.2	3.7		2.2		54.0	662.8	1.3	48.0	411.7	34.9	748.0	10.6	2.2	6.0	1.4
BP-190	178.0		17.3	12.5		3.9		43.5	603.8	0.5	42.1	341.6	29.0	663.0	8.6	1.9	4.7	1.1
BP-270	251.0		29.3	8.3	78.9	1.5		42.3	541.5	0.6	41.3	333.5	28.6	545.0	8.6	1.7	4.5	1.0
BP-271	332.0		31.0	17.9	139.4	1.3		27.6	635.4	0.5	25.9	211.0	19.1	476.0	5.2	1.2	2.9	0.6
BP-272	402.0		39.5	41.6	140.5	1.2		28.5	571.7	0.4	28.2	212.3	19.5	410.0	5.5	1.2	2.6	0.6
23.01	232.0		27.4	3.2		2.9		41.2	536.3	0.5	42.2	334.5	28.5	573.0	8.5	1.8	4.5	0.9
BP-252	367.0		41.2	44.9	100.0	1.3	71.0	28.3	564.5	0.5	27.7	214.4	19.2	399.0	5.3	1.3	2.8	0.6
BP-254	311.0		38.0	25.9	91.4	4.0	93.0	46.9	507.6	0.7	35.3	284.2	23.9	525.0	6.9	1.4	3.9	1.0
BP-263	241.0		29.7	9.3	67.0	2.1	99.0	41.9	523.3	1.0	39.7	329.6	26.7	564.0	8.2	1.7	4.8	1.2
BP-267	277.0		31.7	12.5	65.4	3.4	59.0	52.1	461.8	0.6	38.4	299.1	25.8	717.0	7.3	1.6	4.3	1.0
BP-268	175.0		25.7	0.9	23.3	4.9	86.0	47.7	499.2	0.7	46.2	356.9	30.1	649.0	9.0	2.0	4.8	1.1
30.04	355.0		38.6	34.4		5.5		32.7	594.0	0.7	33.5	241.7	21.2	464.0	6.2	1.4	3.2	0.6
BP-258A	274.0		31.9	10.0	82.5	3.3	100.0	43.8	533.2	0.5	38.7	326.1	27.8	586.0	8.1	1.7	4.6	0.9
BP-260B	272.0		32.5	15.8	86.9	1.9	103.0	43.5	589.8	0.8	38.0	313.2	25.9	801.0	8.1	1.5	4.3	1.0
BP-260C	263.0		31.6	14.3	76.1	2.7	95.0	47.7	580.2	0.7	38.8	317.5	27.1	582.0	7.8	1.5	4.3	1.1
BP-260D	425.0		38.1	19.8	149.1	1.7	83.0	34.2	566.0	0.6	31.5	248.9	22.5	446.0	6.4	1.5	3.1	0.7
BP-261	295.0		34.5	22.6	82.5	3.2	98.0	25.9	474.1	0.7	36.8	310.9	26.6	357.0	7.7	1.7	4.5	1.0
BP-209	281.0		21.4	27.7		1.6		35.3	678.6	0.7	33.5	276.1	24.8	487.0	7.3	1.5	3.6	0.9
23.06	162.0		23.1	5.4		2.1		47.8	483.6	0.9	40.1	328.6	27.5	920.0	8.3	1.6	5.0	1.1
BP-215	277.0		21.2	23.1		1.3		41.1	613.7	1.1	35.2	277.4	25.2	532.0	6.9	1.7	3.4	0.9
24.04																		

24.05																	
BP-216	246.0		18.4	37.5		1.3		34.4	742.2	0.7	31.0	246.5	21.6	485.0	6.4	1.5	3.2	0.7
BP-273	332.0		39.3	45.9	180.7	1.5	87.0	27.6	450.0	0.3	32.0	238.0	20.3	396.0	5.8	1.2	3.0	0.7
23.03	199.0		23.4	21.6		3.4		28.9	533.0	0.1	41.7	321.6	27.8	670.0	8.0	1.8	4.8	1.1
23.04	350.0		44.0	53.8		1.2		24.2	472.4	0.3	30.7	216.2	17.5	395.0	5.5	1.2	2.7	0.5
23.05	341.0		45.7	71.2		1.4		27.4	411.8	0.4	31.0	208.3	17.3	407.0	5.5	1.1	2.8	0.5
BP-217A	202.0		23.1	26.0		1.2		42.0	623.4	0.5	44.9	341.7	28.3	589.0	8.9	2.0	4.5	0.9
BP-217B	216.0		19.5	26.6		1.0		38.6	621.7	0.4	40.1	305.3	25.9	585.0	7.9	1.6	3.9	1.0
BP-218	200.0		24.6	27.1		0.9		33.6	660.4		42.9	332.9	27.5	673.0	8.6	1.8	4.6	1.1
BP-229	174.0		19.2	1.8		3.0		44.1	695.5	0.8	46.9	346.7	29.8	747.0	9.1	2.0	4.6	1.1
BP-230A	109.0		17.3	1.2		9.0		62.8	713.5	1.4	56.6	456.0	37.3	824.0	11.4	2.4	6.3	1.3
BP-230B	113.0		15.0	0.9		4.5		62.5	652.1	1.0	55.7	451.0	33.8	797.0	11.8	2.3	6.3	1.5
BP-237	173.0		19.8	2.2		2.5		51.2	679.7	1.0	50.5	401.9	32.2	749.0	10.8	2.2	5.8	1.5
BP-277	364.0		40.9	32.1	88.9	1.4	87.0	36.0	571.6	0.7	34.4	268.5	22.5	507.0	6.9	1.5	3.6	0.7
BP-278	357.0		40.1	32.4	107.2	1.8	101.0	41.0	516.7	0.6	38.5	295.7	25.0	571.0	7.5	1.5	3.9	0.9
BP-281	360.0		40.4	32.7	100.5	1.0	80.0	36.2	531.6	0.5	36.9	279.3	23.7	511.0	7.1	1.5	3.7	0.8
BP-282A	203.0		27.3	2.5	30.7	1.7	103.0	53.0	573.2	0.8	47.4	395.1	33.1	718.0	9.6	1.9	5.7	1.4
BP-282B	305.0		35.0	18.4	91.7	1.1	99.0	47.9	563.3	1.6	40.2	325.8	27.4	597.0	8.1	1.6	4.9	1.0
BP-283	420.0		43.0	34.6	139.3	3.5	105.0	38.8	519.8	0.8	35.6	275.2	23.6	501.0	7.1	1.4	3.7	0.9
BP-284A	281.0		32.4	11.0	71.6	4.0	104.0	49.0	602.5	1.0	43.3	343.5	30.1	697.0	8.7	1.9	4.6	1.1
BP-284B	266.0		31.8	12.4	75.0	4.5	104.0	45.5	557.3	0.6	42.5	336.4	28.2	655.0	8.5	1.9	4.7	1.0
BP-231	171.0		17.3	4.7		4.2		51.4	663.0	1.2	48.2	402.8	31.9	712.0	10.2	2.0	5.7	1.4
BP-232	236.0		35.1	56.8		1.1		43.5	598.7	0.9	43.3	315.0	24.1	577.0	8.1	1.6	4.4	1.0
BP-233	225.0		20.6	32.6		1.3		39.2	589.8	0.5	39.6	297.2	22.8	575.0	7.7	1.5	4.0	1.0
30.02	212.0		20.6	24.0		1.4		38.3	540.0	0.5	38.4	288.0	24.8	552.0	7.3	1.4	4.0	0.9
BP-234	239.0		26.5	41.0		1.6		39.6	567.8	0.4	39.3	299.4	23.6	579.0	7.9	1.9	4.0	1.1
19.02																		
BP-244	423.0		40.5	41.8	187.4	1.9	72.0	29.4	601.6	0.5	29.0	234.3	22.3	427.0	5.3	1.4	3.0	0.8
BP-245	376.0		43.1	45.4	100.4	0.8	70.0	28.8	548.1	0.5	29.4	227.9	18.8	421.0	5.6	1.1	3.1	0.7
BP-246	195.0		30.6	2.7	25.8	1.5	100.0	50.7	538.5	0.8	45.9	374.9	31.7	665.0	9.2	2.0	5.4	1.4
BP-279	266.0		31.0	10.7	67.2	4.9	110.0	56.1	488.2	0.7	43.2	336.5	29.1	699.0	8.4	2.0	4.7	1.0
BP-280	340.0		39.7	29.0	96.1	2.9	129.0	44.8	514.2	1.2	40.6	310.1	26.3	551.0	7.9	1.7	4.6	1.0
30.01	232.0		27.4	3.2		2.9		41.2	536.3	0.5	42.2	334.5	28.5	573.0	8.5	1.8	4.5	0.9
BP-235	239.0		25.0	45.1		1.7		35.0	545.7	0.5	36.9	261.4	23.0	511.0	7.2	1.5	3.7	0.9
BP-236	238.0		24.4	18.5		2.2		36.8	637.4	0.5	41.2	288.8	24.4	541.0	7.2	1.5	4.2	0.9
30.05	191.0		20.6	24.0		0.9		39.0	580.0	0.7	39.4	297.0	25.3	519.0	7.5	1.6	3.9	1.1
BP-240	193.0		22.7	22.3		2.6		45.4	621.6	0.7	42.4	337.9	25.4	660.0	8.7	1.8	4.6	1.1
BP-241	280.0		23.2	34.5		0.9		38.5	613.9	0.6	41.5	307.9	22.7	559.0	7.7	1.7	4.4	1.0

19.01	174.0		25.4	2.3		2.2		47.5	547.4	0.7	46.1	350.3	29.3	645.0	8.7	1.8	5.0	0.9
BP-242	98.0		14.9	1.2		3.2		59.5	593.0	1.0	54.9	445.4	35.8	988.0	11.5	2.4	6.8	1.4
BP-243	153.0		18.4	5.1		3.4		44.9	691.1	0.6	44.5	365.0	29.2	744.0	9.3	1.9	4.9	1.0
23.02A	297.0		34.7	23.5		1.3		33.1	492.9	0.6	36.9	268.4	21.9	482.0	6.7	1.4	3.6	0.8
23.02B																		
29.04	365.0		36.7	30.1		1.5		32.4	496.1	0.9	31.2	245.7	21.4	461.0	6.9	1.3	3.1	0.6
29.05	194.0		25.9	7.1		2.8		44.9	507.8	0.9	45.3	338.6	28.3	615.0	8.9	1.8	4.9	1.1
BP-247	134.0		23.3	0.4	13.2	2.5	100.0	57.3	542.8	0.9	49.5	416.0	32.0	727.0	10.1	2.1	6.2	1.4
BP-249	114.0		22.2	0.3	15.7	2.8	101.0	56.5	563.4	0.9	50.9	406.0	33.8	941.0	9.8	2.1	5.9	1.3
BP-250	290.0		35.9	23.8	87.2	2.5	98.0	41.7	512.6	0.6	38.8	301.6	25.9	559.0	7.6	1.7	4.2	0.9

eHT1	V	Cr	Co	Ni	Cu	Pb	Zn	Rb	Sr	Cs	Y	Zr	Nb	Ba	Hf	Ta	Th	U
BP-269	15.00		9.60	<0.1	10.80	3.90	114.00	73.60	522.20	1.90	55.40	507.80	42.70	967.00	12.70	2.3	7.60	1.70
BP-262	20.00		11.40	<0.1	10.80	3.20	108.00	76.40	507.50	1.40	52.50	552.20	41.10	882.00	13.50	2.4	7.70	1.80
BP-255	24.00		9.50	<0.1	9.60	3.70	103.00	82.90	446.50	1.80	56.10	568.10	41.80	954.00	13.70	2.5	7.70	2.00
BP-197*	23.00		9.20	0.20		3.40		72.40	627.50	1.30	60.70	550.90	43.00	912.00	14.40	3.0	8.00	1.80
BP-199*	6.00		4.60	<0.1		4.20		92.80	517.60	1.60	62.80	671.60	49.60	1234.00	16.40	2.7	9.80	2.20
BP-201	45.00		13.40	<0.1		9.10		62.40	607.20	1.00	57.60	480.00	40.60	934.00	12.00	2.4	6.70	1.60
BP-257	92.00		20.50	0.40	18.40	2.10	96.00	62.70	528.90	1.00	51.60	446.20	36.50	835.00	11.00	2.2	5.80	1.40
BP-248	80.00		19.70	0.10	11.00	3.20	105.00	65.90	515.60	1.00	51.70	463.90	37.50	815.00	11.60	2.1	6.70	1.60

LT	V	Cr	Co	Ni	Cu	Pb	Zn	Rb	Sr	Cs	Y	Zr	Nb	Ba	Hf	Ta	Th	U
BP-109A	339.00		41.00	26.00		4.10		20.70	199.20	0.50	23.90	99.00	6.40	266.00	2.80	0.4	1.70	0.30
BP-109B	590.00		50.40	25.10		6.60		19.60	163.00	1.10	26.60	113.50	7.00	176.00	3.20	0.6	2.00	0.30
BP-111	374.00		40.40	15.90		6.60		21.90	179.50	0.90	27.30	125.00	7.70	207.00	3.40	0.5	2.20	0.40
BP-112	392.00		40.40	14.90		3.70		24.30	188.00	1.00	28.80	121.70	7.40	203.00	3.20	0.4	2.30	0.30
BP-113	319.00		41.40	25.30		8.00		20.40	166.90	0.90	24.00	104.00	6.30	215.00	3.00	0.4	1.90	0.40
BP-114A1	343.00		40.00	30.00		1.80		23.10	166.90	1.30	24.00	102.50	6.80	164.00	2.90	0.4	1.60	0.30
BP-115	400.00		42.80	23.90		1.60		19.10	194.80	0.80	26.70	115.40	6.80	168.00	3.30	0.5	1.90	0.30
BP-116	352.00		43.20	22.60		3.20		21.90	191.20	0.60	28.90	110.10	6.80	192.00	3.00	0.4	1.90	0.20
BP-227	243.00		17.90	22.70		1.30		18.90	214.20	0.70	27.50	119.10	6.70	175.00	3.30	0.3	2.50	0.70
BP-228	189.00		17.60	27.70		1.90		15.70	204.80	0.60	25.50	113.80	6.90	177.00	2.90	0.5	2.40	0.50
BP-275A	345.00		48.70	86.90	142.10	0.70	155.00	25.50	202.30	0.70	32.00	117.30	7.20	303.00	3.20	0.5	1.90	0.30
BP-275B	376.00		44.40	18.50	167.10	0.80	52.00	20.40	191.90	0.60	26.10	123.10	7.40	175.00	3.40	0.4	2.30	0.60
BP-275C	377.00		45.30	15.10	163.90	1.10	52.00	19.70	196.90	0.40	25.20	117.90	7.10	169.00	3.20	0.4	2.10	0.50
BP-275D	361.00		38.00	17.40	181.80	2.30	87.00	21.90	183.60	0.70	27.30	124.10	7.70	223.00	3.20	0.5	2.40	1.40
BP-276	382.00		41.50	17.50	177.30	1.90	62.00	18.40	172.10	0.60	23.70	110.40	6.80	155.00	2.90	0.4	2.10	0.40
24.02	338.00		39.70	25.60		1.40		13.90	178.40	0.50	23.90	101.00	6.20	160.00	2.90	0.5	1.90	0.30

24.01	334.00		39.70	25.00		2.40		15.50	178.90	0.30	23.70	102.50	6.50	157.00	2.80	0.4	1.70	0.30
BP-200	242.00		17.70	26.30		2.50		21.30	243.90	1.30	25.50	114.30	7.00	165.00	3.20	0.4	2.00	0.50
BP-253	358.00		44.30	24.00	163.10	0.90	45.00	16.90	173.20	0.70	24.50	113.40	7.00	128.00	3.00	0.5	2.00	0.50
BP-256	341.00		43.70	26.70	149.80	2.10	70.00	22.40	168.60	1.40	23.00	106.90	6.40	162.00	2.80	0.4	2.10	0.50
BP-264	350.00		43.40	25.10	150.70	4.00	48.00	17.30	204.40	0.60	23.20	102.60	6.20	133.00	2.60	0.5	1.90	0.40
BP-265	355.00		42.80	22.00	127.20	20.00	73.00	27.20	198.70	4.70	24.60	109.00	6.40	165.00	3.10	0.5	2.10	0.50
BP-266	345.00		41.50	25.20	155.50	3.10	55.00	18.60	170.00	0.90	24.00	108.80	6.60	154.00	3.00	0.4	2.00	0.60
16.01	269.00		39.30	23.30		1.20		15.60	190.90	0.40	17.80	76.40	4.90	134.00	2.10	0.3	1.20	0.20
16.02	374.00		41.70	18.60		2.40		22.20	192.60	0.80	27.00	121.90	7.50	306.00	3.20	0.5	2.10	0.30
18.01	305.00		41.30	26.40		1.70		15.30	184.30	0.50	21.60	90.70	5.30	155.00	2.40	0.4	1.50	0.20
18.02	280.00		41.60	29.30		1.00		16.80	177.20	0.30	22.50	77.80	4.90	130.00	2.20	0.3	1.30	0.20
18.03	374.00		42.20	16.50		12.10		22.30	184.60	1.10	26.50	117.40	7.40	190.00	3.30	0.4	2.00	0.40
18.06	325.00		37.70	17.50		1.30		25.00	189.50	0.50	21.90	86.50	5.60	161.00	2.50	0.4	1.50	0.20
18.07	325.00		38.60	17.00		1.70		16.10	182.90		23.40	97.40	6.10	223.00	2.60	0.4	1.60	0.20

HT2	V	Cr	Co	Ni	Cu	Pb	Zn	Rb	Sr	Cs	Y	Zr	Nb	Ba	Hf	Ta	Th	U
16.03	414.00		44.40	26.50		0.90		7.20	218.70	0.10	27.30	120.60	6.10	93.00	3.40	0.4	0.60	0.15
BP-224	362		22.6	24.6		0.5		5.6	239.5		32.8	156.7	7.9	98	4.3	0.5	0.8	0.2

HT1	La	Ce	Pr	Nd	Sm	Eu	Gd	Tb	Dy	Ho	Er	Tm	Yb	Lu
BP-186	49.50	103.10	13.25	58.20	12.39	3.74	11.68	1.67	9.22	1.67	4.36	0.61	3.73	0.57
BP-188A	48.80	107.20	13.62	59.00	12.54	3.63	11.80	1.67	9.24	1.64	4.63	0.60	4.04	0.54
BP-188B	54.60	126.30	15.59	67.30	14.42	4.28	12.92	1.86	10.64	1.85	4.93	0.65	4.07	0.57
BP-190	47.90	108.50	13.64	58.60	12.16	3.64	11.29	1.63	9.20	1.63	4.34	0.58	3.47	0.52
BP-270	45.90	97.80	12.72	56.50	11.60	3.44	10.49	1.53	8.46	1.58	4.18	0.57	3.31	0.48
BP-271	28.70	60.90	7.84	35.70	7.41	2.33	6.82	1.00	5.47	1.02	2.75	0.36	2.15	0.32
BP-272	28.20	62.60	8.06	35.70	7.47	2.32	7.04	1.04	5.59	1.02	2.73	0.37	2.28	0.33
23.01	46.10	103.40	13.52	58.50	12.52	3.67	11.34	1.66	9.10	1.72	4.58	0.60	3.73	0.52
BP-252	29.50	63.00	8.17	35.80	7.66	2.42	7.03	1.07	5.86	1.07	2.87	0.38	2.32	0.34
BP-254	39.00	84.10	10.94	46.20	10.19	3.03	9.23	1.37	7.68	1.43	3.79	0.50	3.01	0.43
BP-263	45.50	98.90	12.44	53.20	11.08	3.44	10.27	1.53	7.80	1.56	4.11	0.54	3.38	0.48
BP-267	40.60	88.10	11.47	49.70	10.64	3.06	9.67	1.40	7.77	1.44	3.95	0.53	3.08	0.47
BP-268	52.10	114.50	14.74	64.30	13.81	3.97	12.58	1.81	9.42	1.77	4.63	0.63	3.65	0.54
30.04	31.60	72.50	9.83	42.70	9.63	2.92	8.69	1.24	7.20	1.32	3.55	0.44	2.73	0.37
BP-258A	45.00	97.60	12.46	53.40	11.20	3.53	10.58	1.51	8.54	1.55	3.99	0.53	3.28	0.49
BP-260B	42.80	93.90	12.04	52.10	10.84	3.24	10.07	1.47	8.06	1.55	4.00	0.53	3.35	0.47
BP-260C	44.20	93.50	11.97	52.10	11.19	3.26	10.16	1.49	7.95	1.49	4.15	0.54	3.22	0.47

BP-260D	32.90	73.00	9.11	40.10	8.91	2.72	8.14	1.18	6.25	1.23	3.25	0.43	2.57	0.37
BP-261	42.20	93.30	11.85	49.70	10.98	3.25	10.05	1.47	7.94	1.48	3.96	0.52	3.35	0.48
BP-209	36.40	81.60	10.38	46.00	9.93	2.94	9.06	1.27	7.51	1.26	3.41	0.45	2.97	0.42
23.06	43.60	99.90	13.19	55.90	12.01	3.60	10.91	1.64	8.79	1.66	4.30	0.58	3.73	0.49
BP-215	37.10	83.10	10.58	46.20	9.88	3.15	9.27	1.31	7.49	1.32	3.34	0.44	2.75	0.40
24.04														
24.05														
BP-216	32.60	73.00	9.27	40.20	8.83	2.85	8.38	1.16	6.62	1.19	3.02	0.39	2.62	0.37
BP-273	31.80	68.40	9.07	38.90	8.28	2.62	8.19	1.18	6.62	1.23	3.29	0.43	2.60	0.38
23.03				39.03	8.45							0.54		
23.04	27.40	63.40	8.50	39.50	8.40	2.64	8.04	1.16	6.48	1.22	3.24	0.42	2.66	0.36
23.05	28.10	61.10	8.64	39.20	8.54	2.57	8.17	1.17	6.83	1.24	3.17	0.42	2.81	0.37
BP-217A	46.10	107.30	13.20	58.30	12.00	3.54	11.26	1.62	8.97	1.61	4.16	0.58	3.74	0.53
BP-217B	41.60	93.70	11.96	51.70	11.06	3.35	10.25	1.45	8.17	1.40	3.84	0.55	3.28	0.47
BP-218	45.10	103.20	13.13	58.80	11.31	3.66	10.89	1.52	8.88	1.57	4.14	0.54	3.70	0.53
BP-229	46.50	109.70	13.88	59.20	12.38	3.91	11.70	1.65	9.31	1.71	4.52	0.56	3.75	0.55
BP-230A	62.00	140.10	17.52	74.50	16.10	4.59	14.46	2.01	11.28	2.05	5.12	0.69	4.36	0.65
BP-230B	60.50	143.40	17.87	78.20	16.37	4.70	14.78	2.07	11.85	2.05	5.55	0.71	4.59	0.64
BP-237	54.60	126.70	16.12	70.70	14.57	4.35	13.70	1.82	10.76	1.81	5.07	0.67	4.25	0.59
BP-277	35.50	79.30	10.10	45.00	9.38	2.94	9.17	1.31	7.05	1.37	3.63	0.47	2.88	0.42
BP-278	39.90	87.00	11.20	48.60	10.32	3.18	9.76	1.45	8.28	1.50	4.11	0.54	3.21	0.46
BP-281	36.70	81.20	10.43	47.10	9.68	2.92	9.38	1.35	7.63	1.45	3.88	0.50	3.10	0.44
BP-282A	53.60	117.40	14.88	64.30	13.26	3.96	12.60	1.83	9.90	1.88	4.92	0.66	3.97	0.59
BP-282B	44.60	94.70	12.35	54.00	11.09	3.35	10.58	1.56	8.61	1.62	4.28	0.58	3.38	0.49
BP-283	35.90	81.30	10.38	44.90	9.64	2.93	9.36	1.36	7.51	1.34	3.63	0.49	2.94	0.42
BP-284A	47.80	104.30	13.30	58.30	12.19	3.58	11.47	1.66	8.93	1.67	4.42	0.58	3.65	0.53
BP-284B	45.60	98.60	13.06	57.20	12.08	3.49	11.09	1.60	8.88	1.62	4.41	0.58	3.44	0.53
BP-231	52.30	119.80	15.24	66.60	13.57	4.12	12.69	1.76	10.51	1.80	4.38	0.66	3.94	0.55
BP-232	41.00	94.70	11.96	51.90	11.17	3.41	10.71	1.55	9.08	1.58	4.17	0.54	3.56	0.48
BP-233	38.80	89.80	11.38	48.60	10.93	3.31	10.49	1.46	8.40	1.55	3.84	0.51	3.46	0.48
30.02												0.50		
BP-234	38.80	91.10	11.52	49.90	10.81	3.28	10.32	1.42	8.39	1.48	3.89	0.54	3.22	0.44
19.02														
BP-244	30.90	67.20	8.65	37.20	8.03	2.54	7.74	1.14	6.01	1.15	3.11	0.40	2.53	0.36
BP-245	32.10	67.60	8.74	38.50	8.31	2.50	7.90	1.15	6.20	1.19	3.12	0.42	2.45	0.37
BP-246	53.50	115.50	14.71	62.80	13.12	3.88	12.41	1.77	9.66	1.84	4.82	0.66	3.84	0.57
BP-279	46.40	100.10	13.04	55.70	11.73	3.51	10.85	1.61	8.82	1.67	4.41	0.59	3.47	0.51
BP-280	43.40	93.10	11.76	51.30	10.98	3.35	10.55	1.53	8.54	1.58	4.20	0.56	3.38	0.49

30.01	46.10	103.40	13.52	58.50	12.52	3.67	11.34	1.66	9.10	1.72	4.58	0.64	3.73	0.52
BP-235	34.90	84.50	10.58	49.00	9.96	3.11	9.37	1.30	7.92	1.44	3.75	0.49	2.90	0.42
BP-236	41.90	88.40	11.20	49.60	10.50	3.40	10.32	1.43	8.66	1.47	3.78	0.52	3.16	0.48
30.05												0.51		
BP-240	43.40	102.20	13.10	55.40	12.21	3.64	11.43	1.59	8.93	1.62	4.20	0.61	3.72	0.54
BP-241	40.90	92.80	11.78	53.20	11.03	3.33	10.38	1.45	8.64	1.50	4.05	0.56	3.39	0.49
19.01	49.20	109.30	15.10	66.20	14.43	4.08	13.10	1.84	10.12	1.89	4.73	0.61	3.90	0.57
BP-242	59.70	140.40	17.57	76.10	16.06	4.47	14.50	2.04	11.89	2.05	5.64	0.74	4.59	0.64
BP-243	49.40	113.30	14.22	63.00	13.69	3.73	11.90	1.67	9.50	1.62	4.60	0.60	3.73	0.55
23.02A	33.90	79.90	10.67	47.70	10.01	3.01	9.93	1.39	7.83	1.45	3.84	0.50	3.22	0.44
23.02B														
29.04	31.80	75.40	9.96	43.40	9.53	2.96	9.08	1.27	7.46	1.33	3.71	0.46	2.90	0.41
29.05	46.00	100.20	13.90	61.50	12.55	3.61	12.01	1.71	9.37	1.75	4.49	0.59	3.85	0.55
BP-247	58.70	125.60	16.33	69.70	14.35	4.19	13.49	1.93	10.34	1.92	5.27	0.66	4.01	0.62
BP-249	59.40	129.20	16.38	71.70	14.57	4.28	13.38	1.89	10.04	1.97	5.33	0.69	4.23	0.62
BP-250	42.30	89.20	11.80	49.80	10.78	3.16	10.16	1.48	7.91	1.52	4.10	0.54	3.22	0.49

eHT1	La	Ce	Pr	Nd	Sm	Eu	Gd	Tb	Dy	Ho	Er	Tm	Yb	Lu
BP-269	68.10	142.30	18.24	75.90	15.74	4.34	13.85	2.02	10.85	2.17	5.72	0.76	4.81	0.69
BP-262	67.40	142.20	17.99	75.50	15.14	4.22	13.29	2.01	10.60	2.12	5.60	0.77	4.66	0.69
BP-255	70.80	150.00	18.85	77.40	15.63	4.14	13.98	2.05	10.99	2.20	5.99	0.81	4.86	0.74
BP-197*	70.90	155.10	19.28	85.00	16.95	4.55	14.78	2.21	12.24	2.14	5.73	0.78	5.13	0.76
BP-199*	77.80	168.40	20.36	84.10	16.29	4.63	15.12	2.21	12.59	2.22	6.12	0.86	5.59	0.85
BP-201	64.40	145.30	18.50	79.80	16.92	4.65	15.63	2.17	12.26	2.14	5.77	0.74	4.63	0.66
BP-257	62.50	130.60	16.93	72.50	14.73	4.22	13.35	1.98	10.78	2.00	5.31	0.71	4.39	0.62
BP-248	63.50	134.80	17.19	72.60	14.76	4.31	13.81	2.01	10.57	2.03	5.45	0.73	4.41	0.64

LT	La	Ce	Pr	Nd	Sm	Eu	Gd	Tb	Dy	Ho	Er	Tm	Yb	Lu
BP-109A	10.40	24.00	3.22	14.10	3.85	1.22	4.35	0.74	4.46	0.92	2.79	0.36	2.52	0.33
BP-109B	11.00	25.20	3.54	16.40	4.43	1.36	4.89	0.79	5.21	1.05	3.09	0.41	2.83	0.40
BP-111	12.90	27.90	3.85	17.60	4.67	1.48	5.06	0.84	5.09	1.13	3.29	0.42	2.79	0.41
BP-112	13.00	27.70	3.78	18.10	4.59	1.55	5.17	0.86	5.65	1.10	3.27	0.43	2.92	0.42
BP-113	10.20	23.00	3.17	14.70	3.69	1.33	4.24	0.71	4.41	0.93	2.80	0.37	2.50	0.35
BP-114A1	10.90	24.30	3.18	14.70	3.78	1.21	4.30	0.71	4.38	0.95	2.76	0.38	2.48	0.36
BP-115	11.60	26.20	3.62	15.90	4.22	1.44	4.77	0.81	5.09	1.05	3.06	0.40	2.80	0.41
BP-116	11.40	24.70	3.48	16.10	4.14	1.38	4.73	0.80	5.10	1.07	3.11	0.43	2.79	0.42
BP-227	11.80	27.70	3.51	16.40	4.26	1.36	4.65	0.80	5.02	0.96	2.76	0.40	2.65	0.41
BP-228	11.70	26.30	3.37	15.90	3.83	1.21	4.56	0.74	4.57	0.94	2.52	0.39	2.42	0.38

BP-275A	13.70	25.60	3.60	16.00	4.09	1.34	5.13	0.84	4.94	1.08	3.12	0.44	2.75	0.41
BP-275B	13.20	29.80	3.56	15.40	3.89	1.29	4.75	0.81	4.87	1.03	3.02	0.44	2.79	0.42
BP-275C	13.00	28.10	3.56	15.90	4.00	1.28	4.59	0.80	4.88	1.00	2.94	0.42	2.65	0.41
BP-275D	13.70	29.00	3.67	16.10	4.21	1.28	4.63	0.79	4.71	1.03	2.79	0.41	2.59	0.39
BP-276	11.70	24.60	3.27	14.50	3.77	1.22	4.15	0.71	4.40	0.90	2.53	0.37	2.32	0.35
24.02	10.40	23.50	3.22	15.50	3.82	1.18	4.32	0.73	4.26	0.95	2.85	0.37	2.39	0.37
24.01	10.80	23.60	3.14	14.50	3.71	1.14	4.32	0.72	4.45	0.94	2.68	0.38	2.43	0.38
BP-200	11.80	27.20	3.36	14.60	3.81	1.19	4.41	0.74	4.85	0.95	2.64	0.38	2.41	0.36
BP-253	12.50	26.50	3.46	15.50	3.98	1.24	4.41	0.76	4.50	1.00	2.76	0.39	2.51	0.39
BP-256	12.00	24.40	3.15	14.00	3.54	1.22	4.07	0.72	4.24	0.87	2.64	0.35	2.33	0.36
BP-264	10.90	24.10	3.08	14.00	3.57	1.16	4.10	0.68	4.13	0.84	2.58	0.36	2.35	0.35
BP-265	11.60	26.00	3.31	15.20	3.77	1.25	4.46	0.75	4.54	0.91	2.71	0.38	2.44	0.38
BP-266	11.50	25.10	3.26	14.90	3.74	1.18	4.32	0.72	4.49	0.96	2.61	0.37	2.41	0.36
16.01	8.00	17.80	2.43	11.30	2.80	0.94	3.41	0.56	3.57	0.74	2.09	0.28	2.01	0.28
16.02	12.20	26.60	3.85	17.10	4.55	1.36	4.86	0.84	5.44	1.08	3.21	0.44	2.84	0.42
18.01	9.30	20.50	2.90	13.00	3.29	1.07	3.91	0.67	4.12	0.81	2.64	0.35	2.20	0.31
18.02	7.70	18.00	2.43	11.90	2.93	0.99	3.79	0.60	4.01	0.82	2.36	0.31	2.02	0.28
18.03	12.00	27.80	3.67	17.20	4.19	1.37	5.10	0.83	4.99	1.08	3.12	0.41	2.84	0.42
18.06	8.60	19.00	2.83	12.90	3.29	1.11	3.79	0.63	3.96	0.83	2.47	0.34	2.24	0.32
18.07	10.10	22.90	3.03	13.90	3.56	1.14	4.15	0.71	4.20	0.85	2.67	0.37	2.31	0.35

HT2	La	Ce	Pr	Nd	Sm	Eu	Gd	Tb	Dy	Ho	Er	Tm	Yb	Lu
16.03	8.50	22.00	3.27	16.60	4.73	1.61	5.27	0.86	5.33	1.09	2.89	0.39	2.54	0.38
BP-224	10.2	27.2	3.97	21.4	5.64	2.04	6.74	1.02	6.53	1.24	3.6	0.46	3.04	0.47

	$^{87}Sr/$	$^{143}Nd/$	$^{206}Pb/$	$^{207}Pb/$	$^{208}Pb/$	$^{87}Rb/$	$^{147}Sm/$	$^{87}Sr/$	$^{143}Nd/$	ε(Nd)	TDM (Ga)	$^{206}Pb/$	$^{207}Pb/$	$^{208}Pb/$

	^{86}Sr	^{144}Nd	^{204}Pb	^{204}Pb	^{204}Pb	^{86}Sr	^{144}Nd	^{86}Sr	^{144}Nd			^{204}Pb	^{204}Pb	^{204}Pb
	measured (present-day) isotopic ratios					calculated isotopic ratios						calculated (initial) isotopic ratios (130 Ma)		
HT1														
BP-186	0.7061866	0.5124245				0.194	0.129	0.7058289	0.5123150	-3.04	1.11			
BP-188A	0.7066029	0.5124351				0.271	0.129	0.7061014	0.5123257	-2.83	1.09			
BP-188B	0.7061243	0.5124384				0.236	0.130	0.7056888	0.5123282	-2.78	1.10			
BP-190	0.7061055	0.5124400	18.263	15.571	38.576	0.208	0.126	0.7057204	0.5123332	-2.68	1.05	17.905	15.553	38.076
BP-263	0.7060327	0.5124429				0.222	0.129	0.7056221	0.5123328	-2.69	1.09			
BP-267	0.7058960	0.5124408				0.145	0.129	0.7056280	0.5123307	-2.73	1.09			
BP-268	0.7063113	0.5124402				0.267	0.133	0.7058174	0.5123267	-2.81	1.15			
30.04	0.7062257	0.5124424				0.232	0.126	0.7057977	0.5123352	-2.64	1.05			
BP-209	0.7065821	0.5124335				0.326	0.129	0.7059791	0.5123234	-2.87	1.11			
23.06	0.7060748	0.5124504				0.276	0.130	0.7055640	0.5123399	-2.55	1.08			
BP-215	0.7058746	0.5124446				0.159	0.136	0.7055804	0.5123285	-2.77	1.18			
BP-217B	0.7063806	0.5124393	18.213	15.564	38.508	0.150	0.131	0.7061025	0.5123282	-2.78	1.11	17.499	15.530	37.573
BP-218	0.7067453	0.5124389				0.286	0.130	0.7062170	0.5123283	-2.78	1.10			
BP-229	0.7064609	0.5124412	18.234	15.563	38.537	0.194	0.129	0.7061029	0.5123312	-2.72	1.09	17.355	15.520	37.450
BP-237	0.7063139	0.5124421				0.134	0.133	0.7060661	0.5123291	-2.76	1.13			
BP-232	0.7060111	0.5124390				0.157	0.131	0.7057213	0.5123276	-2.79	1.11			
BP-233	0.7058490	0.5124465				0.148	0.129	0.7055752	0.5123371	-2.61	1.07			
30.02	0.7060680	0.5124475				0.192	0.132	0.7057124	0.5123354	-2.64	1.11			
BP-234	0.7060754	0.5124382	18.247	15.567	38.532	0.195	0.125	0.7057153	0.5123323	-2.70	1.04	17.295	15.521	36.974
30.01	0.7060024	0.5124281				0.180	0.129	0.7056705	0.5123180	-2.98	1.11			
BP-235	0.7059601	0.5124362	18.245	15.571	38.544	0.147	0.116	0.7056882	0.5123373	-2.60	0.96	16.694	15.495	36.421
BP-236	0.7062281	0.5124670	18.231	15.566	38.530	0.183	0.126	0.7058892	0.5123594	-2.17	1.01	17.766	15.544	37.893
30.05	0.7063496	0.5124407				0.255	0.131	0.7058791	0.5123295	-2.76	1.11			
BP-240	0.7062341	0.5124407				0.277	0.127	0.7057218	0.5123330	-2.69	1.06			
BP-241	0.7061925	0.5124413	18.292	15.563	38.589	0.218	0.125	0.7057898	0.5123353	-2.64	1.03	17.531	15.526	37.626

eHT1	$^{87}Sr/^{86}Sr$	$^{143}Nd/^{144}Nd$	$^{206}Pb/^{204}Pb$	$^{207}Pb/^{204}Pb$	$^{208}Pb/^{204}Pb$	$^{87}Rb/^{86}Sr$	$^{147}Sm/^{144}Nd$	$^{87}Sr/^{86}Sr$	$^{143}Nd/^{144}Nd$	ε(Nd)	TDM (Ga)	$^{206}Pb/^{204}Pb$	$^{207}Pb/^{204}Pb$	$^{208}Pb/^{204}Pb$
BP-269	0.70702989	0.51243615				0.408	0.125	0.7062765	0.5123295	-2.76	1.05			
BP-262	0.70715623	0.51243985				0.436	0.121	0.7063515	0.5123367	-2.62	1.00			
BP-255	0.70679904	0.51242920				0.537	0.122	0.7058066	0.5123253	-2.84	1.03			
BP-197*	0.70705758	0.51244213	18.229	15.570	38.553	0.334	0.121	0.7064408	0.5123395	-2.56	0.99	17.557	15.538	37.576
BP-199*	0.70669580	0.51243427	18.206	15.561	38.512	0.519	0.117	0.7057374	0.5123346	-2.66	0.97	17.541	15.529	37.543
BP-201	0.70632125	0.51244289	18.231	15.572	38.544	0.297	0.128	0.7057719	0.5123338	-2.67	1.07	18.008	15.561	38.239
BP-257	0.70656202	0.51243461				0.343	0.123	0.7059283	0.5123301	-2.74	1.03			
BP-248														

LT	$^{87}Sr/^{86}Sr$	$^{143}Nd/^{144}Nd$	$^{206}Pb/^{204}Pb$	$^{207}Pb/^{204}Pb$	$^{208}Pb/^{204}Pb$	$^{87}Rb/^{86}Sr$	$^{147}Sm/^{144}Nd$	$^{87}Sr/^{86}Sr$	$^{143}Nd/^{144}Nd$	ε(Nd)	TDM (Ga)	$^{206}Pb/^{204}Pb$	$^{207}Pb/^{204}Pb$	$^{208}Pb/^{204}Pb$
BP-109A	0.70801019	0.51253253				0.301	0.165	0.7074547	0.5123920	-1.53	1.59			
BP-109B	0.70683857	0.51253653				0.348	0.163	0.7061958	0.5123975	-1.43	1.53			
BP-111	0.70682072	0.51253364	18.522	15.667	38.598	0.353	0.161	0.7061686	0.5123971	-1.44	1.45	18.445	15.664	38.460
BP-112	0.70735055	0.51254262				0.374	0.153	0.7066596	0.5124121	-1.14	1.26			
BP-113	0.70668936	0.51252781	18.574	15.709	38.766	0.354	0.152	0.7060360	0.5123987	-1.41	1.27	18.510	15.706	38.667
BP-114A1	0.70699436	0.51254595	18.577	15.714	38.781	0.400	0.156	0.7062545	0.5124136	-1.11	1.30	18.365	15.703	38.411
BP-115	0.70674634	0.51251949				0.284	0.161	0.7062222	0.5123829	-1.71	1.49			
BP-116	0.70719258	0.51252766				0.331	0.156	0.7065803	0.5123954	-1.47	1.35			
BP-227	0.70646563	0.51251923				0.255	0.157	0.7059940	0.5123856	-1.66	1.41			
BP-228	0.70637337	0.51253616	18.518	15.609	38.493	0.222	0.146	0.7059636	0.5124122	-1.14	1.14	18.184	15.593	37.969
24.02	0.70637832	0.51254705				0.225	0.149	0.7059619	0.5124202	-0.98	1.17			
24.01	0.70632461	0.51253718				0.251	0.155	0.7058615	0.5124055	-1.27	1.30			
BP-200	0.70758149	0.51253933	18.578	15.638	38.598	0.253	0.158	0.7071146	0.5124051	-1.28	1.37	18.324	15.626	38.266
BP-253	0.70668687	0.51253869				0.282	0.155	0.7061653	0.5124066	-1.25	1.31			
BP-256	0.70662234	0.51244596				0.384	0.153	0.7059122	0.5123159	-3.02	1.49			
BP-264	0.70750030	0.51221164				0.245	0.154	0.7070478	0.5120804	-7.62	2.13			
BP-265	0.70954078	0.51253125				0.396	0.150	0.7088089	0.5124036	-1.31	1.22			
BP-266	0.70689986	0.51253195				0.317	0.152	0.7063150	0.5124028	-1.32	1.26			
16.01	0.70675384	0.51253948				0.236	0.150	0.7063170	0.5124120	-1.15	1.20			
18.01	0.70636043	0.51253970				0.240	0.153	0.7059167	0.5124095	-1.19	1.26			
18.02	0.70657447	0.51253384	18.530	15.633	38.575	0.274	0.149	0.7060677	0.5124072	-1.24	1.20	18.276	15.621	38.035
18.03	0.70683850	0.51251718	18.336	15.609	38.251	0.349	0.147	0.7061928	0.5123918	-1.54	1.21	18.294	15.607	38.182
18.06	0.70694705	0.51252852				0.382	0.154	0.7062418	0.5123973	-1.43	1.32			

HT2	$^{87}Sr/^{86}Sr$	$^{143}Nd/^{144}Nd$	$^{206}Pb/^{204}Pb$	$^{207}Pb/^{204}Pb$	$^{208}Pb/^{204}Pb$	$^{87}Rb/^{86}Sr$	$^{147}Sm/^{144}Nd$	$^{87}Sr/^{86}Sr$	$^{143}Nd/^{144}Nd$	ε(Nd)	TDM (Ga)	$^{206}Pb/^{204}Pb$	$^{207}Pb/^{204}Pb$	$^{208}Pb/^{204}Pb$
16.03	0.70369549	0.51278744	17.985	15.508	37.926	0.095	0.172	0.7035196	0.5126408	3.3200458	0.95	17.774	15.498	37.649
BP-224	0.70355542	0.51292049	18.405	15.565	38.320	0.068	0.159	0.7034305	0.5127849	6.1310970	0.39	17.897	15.540	37.655

APPENDIX – SUPPLEMENTARY MATERIAL

CHAPTER 6. PETROGENESIS OF A MESOZOIC GIANT DIKE SWARMS IN NE SOUTH AMERICA: INTEGRATION OF GEOCHEMICAL AND ISOTOPIC DATA

Table A1. Geochemical and isotopic data set of the NE-Rio Ceará-Mirim and Canindé dike swarms.

Geochemical group		Major elements (wt.%)											
High-Ti tholeiites (HT)	Sample	SiO_2	Al_2O_3	Fe_2O_{3T}	MnO	MgO	CaO	Na_2O	K_2O	TiO_2	P_2O_5	LOI	SUM
NE-RCM and Canindé dikes	DCE04	50.7	13.20	14.3	0.18	4.40	7.46	3.06	1.72	3.55	0.55	0.92	100.04
	DCE05	51.8	12.80	13.8	0.19	3.92	7.72	2.76	1.61	3.12	0.72	1.25	99.69
	DCE07	52.6	13.00	13.6	0.17	3.62	6.82	3.24	2.10	3.10	0.76	0.72	99.73
	DCE08	52.4	13.00	13.8	0.19	3.88	6.98	3.15	2.01	3.10	0.74	0.52	99.77
	DCE09	52.1	13.00	13.8	0.19	3.96	7.24	3.07	1.89	3.09	0.70	0.75	99.79
	DCE10	50.2	12.40	15.7	0.19	4.34	7.80	2.70	1.57	3.80	0.44	0.52	99.66
	DCE11	52.4	13.20	14.5	0.19	3.63	7.26	2.95	1.88	3.32	0.54	0.41	100.28
	DCE12A	50.3	13.00	14.4	0.18	4.31	7.44	3.02	1.81	3.54	0.54	1.33	99.87
	DCE12B	50.6	13.00	14.6	0.18	4.06	7.13	3.06	1.85	3.41	0.57	1.00	99.46
	DCE14	51.8	12.80	14.1	0.18	4.13	6.72	3.15	2.33	3.14	0.82	0.66	99.83
	DCE18	50.9	13.00	15.0	0.17	4.05	7.70	2.74	1.64	3.54	0.45	0.59	99.78
	DCE19.1	52.5	13.10	13.3	0.18	3.67	6.32	3.33	2.48	2.97	0.78	1.43	100.06
	DCE19.2	51.6	13.20	13.7	0.19	3.93	6.98	3.07	2.23	3.10	0.69	0.90	99.59
	DCE20	52.2	12.80	13.8	0.16	3.81	7.41	2.63	2.12	3.07	0.78	1.42	100.2
	DCE23	52.8	12.90	14.0	0.19	3.78	6.75	3.28	1.94	3.05	0.75	0.70	100.14
	DCE24	51.8	12.80	13.9	0.20	3.96	7.77	2.91	1.57	3.12	0.72	0.97	99.72
	DCE25	52.5	13.20	13.8	0.19	3.73	7.13	3.24	1.87	3.03	0.74	0.41	99.84
	DCE26	52.7	13.00	13.7	0.19	3.81	7.34	2.93	2.02	3.06	0.74	0.71	100.2
	DCE27	51.8	12.70	14.8	0.19	3.97	7.30	3.01	1.98	3.16	0.71	0.58	100.2
	DCE28	52.5	13.20	13.8	0.18	3.75	7.18	2.91	2.17	3.06	0.76	0.68	100.19
	DCE29A	53.9	13.50	12.6	0.16	3.37	6.67	3.23	2.24	2.70	0.72	0.98	100.07
	DCE31	53.1	13.20	13.7	0.18	3.83	6.70	3.42	2.31	3.10	0.74	0.64	100.92
	DCE32A	53.6	16.10	10.4	0.15	2.82	7.11	3.88	1.93	2.36	0.61	1.13	100.09
	DCE35	53.9	16.50	10.5	0.13	2.22	7.26	3.49	2.05	1.98	0.54	0.50	99.07

DCE36.1	51.5	12.80	14.8	0.18	3.55	6.96	3.04	2.11	3.36	0.54	0.66	99.5
DCE36.2	51.2	13.10	14.5	0.17	3.75	7.15	2.88	1.89	3.42	0.54	0.80	99.4
DCE37	51.7	12.50	15.3	0.19	3.91	6.81	3.03	1.98	3.54	0.51	0.69	100.16
DCE38	54.3	16.30	10.6	0.14	2.20	7.27	3.35	1.96	2.07	0.52	0.91	99.62
DCE39	52.2	13.10	13.9	0.21	3.84	6.69	3.25	2.15	3.04	0.70	0.31	99.39
DCE40	52.4	13.70	13.5	0.18	3.77	6.95	3.35	1.93	3.16	0.70	0.56	100.2
DCE43	51.8	12.70	14.2	0.20	4.10	7.84	2.76	1.79	3.17	0.70	0.81	100.07
DCE49	49.6	12.80	14.8	0.18	4.50	7.13	3.17	1.78	3.50	0.53	1.40	99.39
DCE50	52.8	13.30	13.2	0.19	3.63	6.60	3.04	2.25	2.75	0.74	0.79	99.29
DCE51	52.2	12.80	13.7	0.17	3.79	7.29	2.76	2.02	2.95	0.74	0.89	99.31
DCE52	51.9	12.60	14.1	0.20	4.05	7.43	2.66	1.99	3.01	0.73	0.72	99.39
DCE63	52.1	12.70	14.1	0.20	3.90	7.18	2.77	2.10	3.00	0.72	0.79	99.56
DCE64	51.7	12.60	14.1	0.20	3.98	7.10	2.87	2.18	3.06	0.73	1.59	100.11
DCE65	52.6	13.00	13.6	0.19	3.67	7.12	2.98	1.91	2.90	0.74	1.12	99.83
DCE66	52.2	12.70	13.7	0.20	3.80	6.74	3.02	2.21	2.90	0.77	1.23	99.47
DCE67	52.2	12.70	14.0	0.17	3.53	7.10	2.78	1.93	2.93	0.80	1.01	99.15
DPI01	51.7	13.00	13.3	0.17	4.06	6.33	3.04	2.21	3.02	0.77	2.94	100.54
DPI06	51.6	12.90	14.0	0.19	3.93	7.16	2.94	1.93	3.13	0.73	0.66	99.17
DPI07	51.8	13.00	13.7	0.19	3.95	6.45	3.35	2.26	3.09	0.72	0.80	99.31
DPI08	52.0	13.30	13.3	0.18	3.63	7.08	2.96	1.99	2.95	0.72	1.45	99.56
DPI09	52.2	13.10	13.6	0.20	4.05	6.91	2.82	2.13	3.02	0.74	0.96	99.73
DPI10A	52.8	13.30	12.9	0.16	3.70	5.88	3.20	2.27	2.82	0.81	1.50	99.34
DPI11	51.4	12.90	13.7	0.16	4.43	6.82	2.75	1.93	3.17	0.67	1.54	99.47
DPI12	52.5	13.00	13.9	0.20	3.91	7.14	2.87	2.09	3.06	0.79	1.01	100.47
DPI13	52.5	12.80	13.4	0.18	3.77	6.08	2.98	2.38	2.96	0.77	1.41	99.23
DPI14	52.5	12.90	13.8	0.20	4.44	5.46	2.37	3.67	3.05	0.80	1.29	100.48
DPI15	54.2	13.10	13.1	0.20	2.75	5.44	2.96	3.05	2.49	0.91	1.31	99.51
DPI16	51.3	12.90	14.1	0.20	4.28	7.04	2.77	2.08	3.32	0.69	1.27	99.95
DPI17	51.2	12.90	14.2	0.19	4.50	6.42	2.70	2.37	3.34	0.70	1.30	99.82

	DPI18	50.2	13.10	14.1	0.20	4.57	8.10	2.55	1.76	3.48	0.59	0.80	99.45
	DPI19	51.3	13.20	14.0	0.20	3.98	7.22	2.66	2.10	3.36	0.69	0.98	99.69
	DPI20	53.3	13.10	13.3	0.18	3.25	5.94	2.87	2.49	2.70	0.86	1.54	99.53
	DPI21	51.1	13.30	13.8	0.19	3.75	7.31	2.55	2.15	3.33	0.69	1.28	99.45
	DPI22	51.7	12.90	13.9	0.19	3.95	7.16	2.57	2.09	3.22	0.69	1.33	99.7
	DPI23	50.6	13.10	14.9	0.2	4.2	7.7	2.7	1.7	3.7	0.5	0.8	99.94
	DPI24	50.7	12.40	15.1	0.2	4.1	7.5	2.7	1.9	3.5	0.5	0.8	99.22
	DPI26	50.6	12.50	15.3	0.2	4.7	6.4	3.1	1.8	3.5	0.6	0.9	99.49
	DPI27	53.2	12.90	13.9	0.2	3.4	6.9	3.1	2.3	2.9	0.5	1.1	100.45
	DPI29	51.1	12.60	15.1	0.2	4.0	6.9	2.9	1.8	3.5	0.5	0.8	99.25
	DPI35	52.9	13.20	13.5	0.2	3.5	6.5	2.7	2.3	2.9	0.8	1.0	99.31
	DPI41	51.2	12.70	14.8	0.2	4.1	7.3	2.8	1.8	3.4	0.5	0.9	99.57
	DPI51	50.5	13.10	14.5	0.2	4.0	8.0	2.7	1.6	3.4	0.4	0.7	99.06
Evolved High-Ti tholeiites (eHT)													
NE-RCM	DCE32C	61.5	15.20	7.93	0.12	1.08	2.61	4.99	3.87	1.33	0.27	0.84	99.7
	DCE33	62.8	14.10	7.61	0.11	1.18	2.54	4.54	3.89	1.40	0.32	1.66	100.2
	DCE34A	57.6	16.90	7.94	0.13	1.83	5.98	4.23	2.49	1.56	0.56	1.10	100.3
	DCE34B	59.0	14.80	8.57	0.16	1.77	3.94	4.49	3.49	1.61	0.48	1.41	99.7
	DCE46	57.3	13.30	11.8	0.16	2.51	5.16	3.45	3.19	2.23	0.69	0.53	100.3
Low-Ti tholeiites (LT1)													
NE-RCM	DCE02	51.9	16.40	11.5	0.17	4.54	9.73	2.72	0.95	1.25	0.18	0.63	99.97
	DCE03	52.0	17.50	11.2	0.16	3.75	9.40	2.89	1.07	1.30	0.18	0.81	100.26
	DCE13	51.0	14.60	10.4	0.16	7.65	11.4	2.17	0.56	0.93	0.12	1.22	100.21
	DCE15	51.8	16.60	10.9	0.16	4.46	9.92	2.71	0.97	1.19	0.17	0.94	99.82
	DCE16	52.0	17.00	11.5	0.16	3.56	9.17	2.91	1.21	1.35	0.20	1.16	100.22

	DCE17	51.9	16.60	11.4	0.16	4.00	9.35	3.13	1.07	1.28	0.19	0.97	100.05
	DCE21	51.5	16.60	11.0	0.16	4.38	9.57	2.86	1.02	1.21	0.18	0.83	99.31
	DCE22	51.8	16.00	12.0	0.17	4.52	9.36	2.78	1.14	1.32	0.19	0.85	100.13
	DCE30	52.5	16.40	11.2	0.16	4.39	9.42	2.90	1.20	1.23	0.18	0.68	100.26
	DCE47	51.8	15.70	11.3	0.17	5.39	10.04	2.49	0.94	1.15	0.16	0.72	99.86
	DCE48	51.8	16.00	11.8	0.17	4.54	9.67	2.59	1.04	1.30	0.18	0.83	99.92
	DCE70	50.9	15.80	11.6	0.17	4.70	9.72	2.62	1.03	1.24	0.17	2.83	100.78
	DCE72	51.8	15.80	11.8	0.17	4.58	9.58	2.53	1.06	1.24	0.17	0.97	99.7
	DCE73	52.0	16.80	11.7	0.15	3.00	8.94	2.76	1.33	1.42	0.21	1.11	99.42
	DCE74	51.7	15.80	12.6	0.17	3.75	8.68	2.65	1.45	1.50	0.21	0.99	99.5
	DCE75	51.7	16.50	11.2	0.16	4.22	9.72	2.71	1.08	1.22	0.17	0.77	99.45
	DCE77	50.5	16.10	12.1	0.17	4.74	9.91	2.73	1.00	1.40	0.16	0.90	99.71

Low-Ti tholeiites (LT2)		SiO_2	Al_2O_3	Fe_2O_{3T}	MnO	MgO	CaO	Na_2O	K_2O	TiO_2	P_2O_5	LOI	SUM
NE-RCM (Senador Pompeu and Santa Quitéria subswarm	DCE01A	52.3	13.9	13.7	0.19	4.97	9.25	2.77	0.79	1.71	0.19	0.71	100.48
	DCE01B	52	13.8	12.5	0.18	6.49	9.6	2.31	1.02	1.36	0.15	0.61	100.02
	DCE41	52.5	13.8	13	0.19	6.08	9.73	2.36	0.68	1.45	0.16	0.37	100.32
	DCE42	51	13.7	11.9	0.17	6.46	10.2	3.58	0.37	1.29	0.14	0.92	99.73
	DCE44	52.2	13.5	12.5	0.19	6.58	10.3	2.32	0.64	1.36	0.14	0.37	100.1
	DCE45	51.5	13.6	12.3	0.16	6.19	9.52	3.52	0.89	1.37	0.15	0.88	100.08
	DCE53	51.7	14.2	11.4	0.17	6.99	10.3	2.23	0.77	1.18	0.15	0.32	99.41
	DCE54	52	14.2	11.4	0.17	6.89	10.3	2.19	0.98	1.2	0.16	0.44	99.93
	DCE55	52.1	14.2	11.4	0.17	7.04	10.01	2.54	0.78	1.16	0.15	0.63	100.18
	DCE57	51.7	14.1	11.6	0.18	7.01	10.9	2.14	0.67	1.25	0.45	0.18	100.18
	DCE58	52.1	14.2	11.4	0.17	7.08	10.5	2.16	0.86	1.16	0.15	0.23	100.01
	DCE59	52.1	14.3	11.4	0.17	7.18	10.6	2.36	0.55	1.16	0.15	0.2	100.17
	DCE60	52	14.3	11.2	0.17	7.17	10.7	2.41	0.51	1.13	0.15	0.56	100.3

DCE61	51.9	14.3	11.3	0.17	7.15	10.4	2.38	0.66	1.15	0.15	0.48	100.04
DCE62	52.1	14.2	11.3	0.17	7.03	10.5	2.16	0.76	1.16	0.15	0.14	99.67
DCE68	51.7	13.4	12.9	0.19	6.58	10.2	2.27	0.6	1.43	0.14	0.5	99.91
DCE79	51.7	13.5	12.4	0.18	6.64	10.2	2.25	0.72	1.33	0.14	0.82	99.88
DCE86	51.8	14.5	12.8	0.17	2.85	8.01	5.34	1.22	1.74	0.27	0.88	99.58
DPI02	48.9	13.6	12.5	0.18	6.2	9.83	3.83	1.02	1.35	0.18	1.53	99.12
DPI03	50.8	13.6	12.4	0.18	6.09	9.89	3.88	0.85	1.4	0.26	1.19	100.54
DPI04	50.5	13.5	12.6	0.19	6.18	9.67	2.82	0.87	1.42	0.16	1.1	99.01
DPI05	51.2	13.7	12.5	0.18	5.98	9.45	3.34	1.3	1.4	0.16	1.01	100.22
DPI49	49.8	13.1	12.1	0.18	6.3	10.2	2.71	1.02	1.29	0.24	3.19	100.13
DPI50	50.1	13.2	12.4	0.18	6.38	10.2	2.65	1.02	1.33	0.19	2.18	99.83

Sample	Trace elements (ppm)																	
HT	V	Cr	Co	Ni	Cu	Pb	Zn	Rb	Sr	Cs	Y	Zr	Nb	Ba	Hf	Ta	Th	U
DCE04	388		37.8	27.2	170.5	2.8	107	42.6	615	1.8	36	276.8	24.3	534	7	1.5	4.4	1
DCE05	274		32	13.7	63.9	2	79	35.6	700.9	3.7	39.7	328	27.5	573	8.1	1.6	4.1	0.9
DCE07	265		35.1	19.9	77.2	4	111	40.3	546.1	0.2	42.4	336.1	28.8	725	8.5	1.7	4.8	1
DCE08	260		31.7	15.1	65	3	94	41.5	539	0.6	40.1	329.1	27.8	617	8.5	1.7	4.5	0.9
DCE09	266		30.6	17.1	61.3	3.6	90	41.2	514.2	0.8	38	308.7	27	550	7.6	1.6	4.1	1
DCE10	453		40.1	24.9	224.1	1.2	78	34.4	492.8	0.5	33.3	278.3	22.8	446	7.1	1.5	3.2	0.7
DCE11	351		33.6	20.4	188.8	1.5	79	40.8	518.5	0.7	37.9	320.3	25	510	8	1.6	4	1
DCE12A	385		37.6	32	177.5	2.6	98	41.2	568.2	2.2	35.9	280.4	24.9	755	7.2	1.4	3.8	0.9
DCE12B	363		38.4	31.9	122.2	2.2	93	43.1	586.1	1.4	38.6	295.4	24.5	968	7.3	1.4	3.9	0.8
DCE14	284		34.8	14.5	62.4	3.8	99	68.8	538	2.1	40.7	323.8	28.1	655	8.3	1.6	4.3	1.1
DCE18	408		38.4	24.6	206.3	2.1	85	37.2	511.7	0.8	39.4	275.3	22.7	555	7.2	1.4	3.4	0.8
DCE19.1	234		29.6	14.7	53.5	4.2	73	65.2	647.1	1.1	48.5	329.2	27.4	638	8.1	1.9	4.6	0.8
DCE19.2	277		33.6	15.7	65.1	3.4	73	64	659	1.2	39.9	313	26.4	582	8	1.7	4.6	1.1
DCE20	268		32.5	16.7	77.3	1.8	92	54.3	537.5	0.7	43.6	338.8	28.6	612	8.6	1.7	4.9	1.1
DCE23	264		35.1	17.3	54.2	2.4	105	45.9	523.3	0.7	47.2	342.3	28.3	737	8.8	1.9	5	1

DCE24	286		33.5	13.5	55.6	1.8	83	51.2	785.3	7.5	40.6	317.2	27.5	649	8	1.6	4.5	1.1
DCE25	276		34.8	16	60.4	3.2	101	39.7	577.2	0.3	43.6	330.2	27.9	676	8.5	1.6	4.9	1.1
DCE26	237		30.3	13.7	52.7	2.1	88	42.2	558.3	0.4	41.2	326.5	26.9	597	7.9	1.6	4.1	0.9
DCE27	271		37.8	69.7	372.9	2.4	100	40.8	522.1	0.6	41.4	317.9	25.5	582	7.6	1.7	4.2	0.9
DCE28	271		32.7	15.6	62.6	3.2	104	52.1	553.7	0.7	41.5	325.9	27.8	626	8.4	1.7	4.8	1
DCE29A	211		27.7	12.6	50.6	1.9	95	52.1	544	0.6	44.9	358.7	28.1	714	8.9	1.9	4.8	0.9
DCE31	257		37.4	37.8	66	2	85	57	553.4	0.6	47.7	326	27.2	698	8.3	1.7	4.3	1
DCE32A	192		21.6	9.5	52.3	4	51	42.6	835.7	0.6	37.3	286.8	24.2	625	7.1	1.5	4.2	0.8
DCE35	145		20.8	6.3	93.6	2.3	78	49	646.7	1.1	38	321.6	22.9	573	7.9	1.3	5.1	1.1
DCE36.1	349		37.4	23.1	191.9	3.3	84	50.1	522.6	0.6	42.4	325.1	26.6	602	8.1	1.6	4.5	0.9
DCE36.2	352		38.6	27.3	185.5	2.5	95	46.5	544.1	0.5	41.5	302.1	25.2	609	7.9	1.5	4.3	0.9
DCE37	378		37.7	23.5	219.2	4.4	100	48.1	463.7	0.7	40.8	320.1	25	611	8.3	1.6	4.2	1.1
DCE38	155		22.2	6.9	105.7	2.4	85	45.5	666.2	0.5	38.5	328	24.2	649	8.4	1.4	4.8	1.1
DCE39	263		38.4	25.5	62.1	2	85	45.1	530.4	0.5	53.1	328.7	27.9	700	8.2	1.7	4.6	1.2
DCE40	258		31.6	16	66.2	2.3	76	36.5	562.9	0.4	37.8	309.6	25.8	696	7.6	1.6	4.1	0.9
DCE43	302		34.4	17.2	83.8	1.3	95	33.4	754.8	2.3	40.7	319	26.9	617	8.2	1.6	4.5	1.1
DCE49																		
DCE50																		
DCE51																		
DCE52																		
DCE63								54	483									
DCE64								35	463									
DCE65																		
DCE66								127	488									
DCE67								42	536									
DPI01	254	11	33	13	54.3	2.4	99	48.2	563.3	0.8	45.6	355.7	30.5	640	9.2	1.8	4.8	1.3
DPI06	290	19	36.4	20	72.6	2.3	89	43.7	594.7	0.5	43.4	341.3	28.2	708	7.8	1.7	4.7	1
DPI07	259	13	33.9	14.4	61.7	2.9	84	44	506.7	0.5	43.3	330.8	27.9	652	8	1.6	4.6	0.9
DPI08	256	16	32.6	12.4	51.7	0.8	92	45.4	620.8	0.7	43.5	337.9	28.7	604	8.2	1.6	4.4	1.1
DPI09	257	12	33.5	12.3	57.8	2.9	98	43.6	565.7	0.8	42.1	337.7	28.4	613	8.6	1.7	4.3	1
DPI10A	203	8	30.1	10	40.8	0.8	91	49.7	532.3	0.7	44.9	369.2	30.9	611	9.2	1.8	4.9	1.1
DPI11	283	15	36.9	17.1	72.4	1	81	42.3	574.3	1	40.3	328.6	28.4	548	7.8	1.8	4.3	1
DPI12	248	11	33.4	11.5	62.2	1.3	101	47.7	580.5	0.6	45.3	352.1	29.7	621	8.9	1.9	5.1	1.2
DPI13	233	8	32	11.4	55.9	2.4	108	54.2	515.8	1.3	45.7	359	29.3	660	9	1.8	4.7	1.1
DPI14	230	9	32.7	10.8	59.9	3	118	84.6	624.2	1.8	44.8	347.7	29.1	672	8.7	1.7	5.2	1.2
DPI15	150	<1	24.3	1.1	24.9	2.4	104	65.7	515.8	0.9	49.9	417	34.1	773	10.9	2.2	5.9	1.4
DPI16	305	11	36.2	21.8	142.1	1.7	101	48.1	494.2	1	40.2	317.3	26.9	580	8.2	1.7	4.2	1
DPI17	314	13	34.8	19.5	83.5	3.1	144	47.9	534.5	0.7	40.5	323.9	28.3	653	8.5	1.8	4.7	1.1
DPI18	372	27	38.6	25.8	101.5	0.9	80	28.4	603.3	0.1	35.8	292.8	24.6	523	7.5	1.7	3.9	0.9

DPI19	299	6	33.8	13.8	82.8	1.5	89	39.8	596.4	0.2	38.6	323.8	28.4	611	7.8	1.7	4.7	1
DPI20	195	1	26.6	4.9	45.6	2.3	112	58	520.6	0.9	47.8	405.7	33.8	702	9.9	1.9	5.9	1.4
DPI21	291	8	34.7	16.2	86.6	2.2	103	36.9	599	0.2	38.6	323.3	27.8	605	7.9	1.7	4.5	1
DPI22	291	10	34.1	15.4	77	2.8	99	34.1	592.1	0.1	40.8	325.9	28	699	8.1	1.9	4.8	1.1
DPI23	423	17	40.4	18.6	191.2	1.8	94	35.6	518.2	0.5	36.9	288.4	24.2	484	7.1	1.5	4.1	0.9
DPI24																		
DPI26																		
DPI27																		
DPI29								45	459									
DPI35																		
DPI41																		
DPI51																		

eHT	V	Cr	Co	Ni	Cu	Pb	Zn	Rb	Sr	Cs	Y	Zr	Nb	Ba	Hf	Ta	Th	U
DCE32C	28		10.6	3.6	21.8	6.2	56	105.7	618.9	1.1	57	477	33.2	1432	11.9	2	7.2	1.5
DCE33	83		10.7	6.3	62.4	10.3	58	105.6	485.4	1.3	51.6	568.9	34.9	1678	14	2.1	10.2	1.9
DCE34A	81		14	2.5	20.9	2.2	42	58.6	813.6	0.8	40	367	29.2	752	9.2	1.7	5.8	1.3
DCE34B	72		15	3.3	19.9	2.2	34	82.2	587.4	0.4	50	465.9	34.3	1028	11.2	2.2	7.4	1.6
DCE46	175		24.5	9.3	54.4	4.1	87	81.9	456.3	0.8	52.6	519.9	33.2	875	13.3	2.1	8.7	1.8

LT1	V	Cr	Co	Ni	Cu	Pb	Zn	Rb	Sr	Cs	Y	Zr	Nb	Ba	Hf	Ta	Th	U
DCE02	318		37.5	11.2	134.7	3.3	52	30.9	269.3	0.6	24.5	117.4	9.2	260	2.9	0.5	3.6	0.8
DCE03	319		33.8	7.9	134.2	3.2	50	36.6	297	1	25.3	119.8	9.5	277	3.2	0.7	3	0.8
DCE13	269		40.7	39.4	112.1	1.1	35	24.2	213.9	0.6	19.3	81.1	6	175	2.2	0.5	1.8	0.3
DCE15	297		34.8	11.1	126.1	2.6	50	30.1	260.5	1.1	22.7	106.4	8.4	232	2.5	0.5	2.9	0.5
DCE16	285		33	10.2	140	4.3	61	37.4	274.7	2.1	26.5	132.4	9.9	306	3.6	0.5	3.4	0.7
DCE17	318		37.3	9.4	144.3	3.1	60	34.6	270.8	0.9	27.7	126	9.8	361	3.3	0.6	3.5	0.9
DCE21	295		36.1	10.3	128.4	2.6	51	32.3	303.2	0.8	24.6	110	8.8	251	2.7	0.5	2.9	0.6
DCE22	308		38.3	14.8	150.4	2.4	56	34.4	286.6	0.9	24.5	127.2	9.6	263	3.1	0.6	3.1	0.7
DCE30	315		38.9	11.4	139.7	2.7	59	42.2	277	1.2	30.5	120.9	9.3	308	3.2	0.7	3.4	0.8
DCE47																		
DCE48																		
DCE70																		
DCE72																		
DCE73																		
DCE74																		
DCE75																		

DCE77

LT2	V	Cr	Co	Ni	Cu	Pb	Zn	Rb	Sr	Cs	Y	Zr	Nb	Ba	Hf	Ta	Th	U
DCE01A	380		38.4	19.4	211.2	4.3	76	24	209.6	0.7	29.6	131	8.3	230	3.5	0.4	2.5	0.5
DCE01B	329		40.1	20.6	151.9	1.1	48	45	243.9	0.6	23	98.8	6.1	547	2.7	0.3	1.7	0.3
DCE41	379		46.3	18.1	166.8	2.3	55	21.6	186.4	0.6	28.2	116.2	7.2	181	3.1	0.4	1.9	0.5
DCE42	320		41.2	14.9	109.8	1.5	34	10.8	219.2	0.2	21	103.8	6.1	158	2.7	0.4	2	1
DCE44	343		44.6	17.4	157.3	5.9	60	16.3	191.1	0.6	23.7	103.3	6.4	215	2.8	0.4	1.7	0.3
DCE45	359		46.6	14.2	166.7	3	50	32.4	232.7	0.8	26.7	112.2	6.8	260	3	0.4	2.7	0.5
DCE53																		
DCE54																		
DCE55																		
DCE57									223									
DCE58																		
DCE59																		
DCE60																		
DCE61								7	191									
DCE62								30	186									
DCE68								57	188									
DCE79									199									
DCE86																		
DPI02	375	5	48	11.3	277	2.9	43	15.5	217.3	<0.1	32.3	96.6	6.8	169	2.9	0.5	10.4	6.4
DPI03	467	4	49.2	11.7	76.4	3.9	39	11.6	245	0.3	30	115.5	7.1	168	2.9	0.4	3.9	0.5
DPI04	377	5	47.8	16.7	153	1.6	52	22.5	242.7	0.3	26.7	116.4	7.5	188	2.9	0.4	3.5	8.2
DPI05	463	5	48.6	18.3	132.1	2.1	56	38.2	204.5	0.3	28.2	132.6	6.8	568	2.9	0.4	3.4	1.9
DPI49																		
DPI50																		

HT	La	Ce	Pr	Nd	Sm	Eu	Gd	Tb	Dy	Ho	Er	Tm	Yb	Lu
DCE04	39.3	85.6	10.81	46.1	9.6	2.97	8.97	1.31	7.4	1.37	3.59	0.48	3.02	0.44
DCE05	41.2	92.9	12.91	55.8	11.86	3.38	10.46	1.57	8.77	1.59	4.13	0.59	3.34	0.47
DCE07	46.2	103.5	12.76	57	11.37	3.54	11.2	1.64	8.93	1.67	4.54	0.6	3.48	0.52
DCE08	44.4	97.5	12.4	53.7	11.24	3.45	10.96	1.55	8.48	1.53	4.26	0.56	3.36	0.51
DCE09	39.9	91.3	11.85	51.6	11.01	3.39	9.97	1.45	7.99	1.53	3.99	0.51	3.26	0.46
DCE10	30.8	69.8	9.59	42.6	9.08	2.74	8.51	1.29	7.07	1.36	3.82	0.5	3.08	0.42
DCE11	36.7	83	11.15	45.8	10.75	3	9.57	1.44	8.03	1.59	4.05	0.54	3.42	0.46

DCE12A	38.2	83.9	10.97	46.4	9.68	3.08	9.03	1.34	7.55	1.41	3.91	0.46	3	0.43
DCE12B	38.9	84.8	11.46	48.4	10.28	3.16	9.75	1.4	8.07	1.5	3.98	0.51	3.22	0.47
DCE14	45.3	97.9	12.3	52.5	11.18	3.37	10.65	1.59	8.7	1.59	4.3	0.56	3.49	0.51
DCE18	35.5	74.9	10.17	45.1	9.88	2.95	9.33	1.4	7.75	1.53	4.03	0.55	3.16	0.48
DCE19.1	45.6	97.9	13.26	57	11.77	3.59	11.08	1.65	8.88	1.7	4.53	0.55	3.72	0.51
DCE19.2	43.1	91.6	12.15	51.2	10.82	3.32	10.35	1.52	8.33	1.58	4.23	0.58	3.35	0.51
DCE20	48.1	103.4	13.21	57.3	12	3.6	11.47	1.65	9.15	1.69	4.66	0.61	3.6	0.52
DCE23	48.5	103.7	13.31	57	11.81	3.57	11.79	1.67	9.23	1.7	4.67	0.6	3.74	0.55
DCE24	44.8	94.6	12.41	52.2	11.06	3.35	10.89	1.55	8.3	1.61	4.39	0.56	3.47	0.47
DCE25	45.3	99.7	12.9	55.4	11.36	3.47	11.12	1.65	8.86	1.62	4.28	0.56	3.57	0.52
DCE26	42.1	96.6	12.77	55.3	11.87	3.54	10.68	1.55	8.49	1.63	4.32	0.55	3.48	0.48
DCE27	41.1	91.8	12.38	53.2	11.24	3.39	10.29	1.51	8.39	1.55	4.4	0.54	3.37	0.49
DCE28	46.7	100.6	12.79	55.5	11.7	3.5	11.18	1.56	8.49	1.62	4.38	0.6	3.55	0.52
DCE29A	45.8	101.3	13.66	56.8	12.64	3.69	11.18	1.62	9.08	1.73	4.52	0.58	3.74	0.53
DCE31	44.7	95.4	13.24	57.4	12.29	3.73	11.66	1.68	9.74	1.87	4.92	0.63	3.96	0.56
DCE32A	40.4	89.6	11.75	51.6	10.04	3.32	9.47	1.37	7.45	1.36	3.84	0.5	3.11	0.43
DCE35	40.6	88.9	12.11	50.7	10.74	3.34	9.48	1.4	7.81	1.5	3.95	0.52	3.32	0.42
DCE36.1	41.5	87.6	11.76	50.7	10.74	3.3	10.53	1.62	8.67	1.69	4.49	0.6	3.61	0.55
DCE36.2	40.5	85	11.13	48	10.43	3.2	10.16	1.54	8.58	1.63	4.58	0.6	3.66	0.53
DCE37	41.2	87.6	11.3	48.1	10.54	3.12	10.29	1.51	8.25	1.63	4.39	0.58	3.63	0.51
DCE38	43.2	92.2	11.83	50.1	10.76	3.39	10.04	1.45	8.15	1.54	4.04	0.56	3.28	0.49
DCE39	48.5	102.6	13.14	57.4	12.13	3.68	11.95	1.71	9.81	1.86	5.09	0.66	3.89	0.6
DCE40	39.1	84.2	11.81	51	10.81	3.34	10.1	1.48	7.87	1.56	3.96	0.53	3.43	0.47
DCE43	43.5	96.6	12.41	52.5	10.9	3.43	10.83	1.59	8.43	1.6	4.1	0.56	3.43	0.51
DCE49														
DCE50														
DCE51														
DCE52														
DCE63														
DCE64														
DCE65														
DCE66														
DCE67														
DPI01	51.1	112.4	14.16	61.4	12.69	3.82	11.89	1.74	8.99	1.71	4.74	0.61	3.64	0.53
DPI06	47.9	105.5	13.35	55.9	12.08	3.54	11.1	1.62	8.72	1.67	4.42	0.56	3.46	0.49
DPI07	47.7	103.2	12.91	55.5	11.45	3.47	10.82	1.57	8.48	1.58	4.19	0.59	3.35	0.49
DPI08	47.9	105.3	13.35	55.9	11.91	3.54	10.96	1.55	8.44	1.62	4.11	0.56	3.49	0.48
DPI09	48.3	106	13.28	57.1	12.16	3.59	10.99	1.6	8.58	1.61	4.31	0.57	3.56	0.5
DPI10A	54.6	117.7	14.73	62.6	13.39	3.74	11.85	1.67	9.48	1.72	4.67	0.61	3.84	0.51

DPI11	46	100	12.56	54.5	11.31	3.31	10.51	1.51	8.19	1.53	4	0.52	3.36	0.46
DPI12	50.7	110	13.97	58.9	12.65	3.67	11.74	1.67	8.88	1.72	4.5	0.6	3.72	0.53
DPI13	51	109.6	13.89	59.2	12.42	3.67	11.35	1.65	9.13	1.73	4.75	0.55	3.47	0.5
DPI14	49.5	109.1	13.82	59.8	12.26	3.57	11.59	1.64	8.87	1.68	4.48	0.57	3.65	0.51
DPI15	57.8	121.5	16.13	68.3	13.94	4.12	13.06	1.91	10.17	1.94	5.06	0.69	4.05	0.57
DPI16	44.5	93.3	12.2	52.3	10.96	3.36	10.56	1.52	8.14	1.55	4.07	0.53	3.37	0.48
DPI17	44.4	96.5	12.5	54.5	11.09	3.41	10.69	1.54	8.14	1.57	4.29	0.56	3.4	0.48
DPI18	39	84	11.06	47.7	10.21	3.12	9.49	1.39	7.46	1.39	3.67	0.48	3.06	0.43
DPI19	45.2	97.6	12.69	53.7	11.25	3.47	10.79	1.53	7.78	1.52	4.05	0.54	3.3	0.45
DPI20	56.1	121.9	15.57	66.8	13.55	3.97	12.87	1.83	9.81	1.83	4.97	0.67	3.92	0.58
DPI21	44.7	98.4	12.57	53.7	10.98	3.38	10.58	1.52	8.07	1.56	4.03	0.55	3.31	0.48
DPI22	45.7	98.5	12.44	55.1	11.39	3.39	10.75	1.55	8.32	1.58	4.08	0.56	3.4	0.5
DPI23	36	78.8	10.05	43.8	9.51	2.95	9.18	1.37	7.09	1.48	4.05	0.54	3.21	0.47
DPI24														
DPI26														
DPI27														
DPI29														
DPI35														
DPI41														
DPI51														

eHT	La	Ce	Pr	Nd	Sm	Eu	Gd	Tb	Dy	Ho	Er	Tm	Yb	Lu
DCE32C	68.7	136.7	18.05	75.8	15.09	5.63	13.62	2.01	10.95	2.16	5.78	0.76	4.63	0.7
DCE33	70.2	143.4	18.65	73.1	13.75	3.96	12.47	1.81	10.03	1.94	5.37	0.73	4.53	0.71
DCE34A	50.4	107.4	14.31	60.1	12.17	3.78	10.44	1.52	8.44	1.58	4.39	0.58	3.71	0.53
DCE34B	64.4	142.5	17.83	75	14.48	4.29	12.68	1.91	10.69	1.98	5.35	0.71	4.64	0.65
DCE46	73.1	149.3	18.96	78.1	15.17	4.2	13.92	1.98	11.15	2.09	5.47	0.75	4.43	0.66

LT1	La	Ce	Pr	Nd	Sm	Eu	Gd	Tb	Dy	Ho	Er	Tm	Yb	Lu
DCE02	16.5	32.6	4.22	17.9	4.13	1.26	4.28	0.76	4.53	0.92	2.86	0.4	2.45	0.38
DCE03	15.7	33.1	4.32	18.1	3.94	1.27	4.46	0.72	4.52	0.91	2.46	0.38	2.49	0.37
DCE13	10.4	21.8	2.9	12.4	2.73	0.94	3.14	0.52	3.44	0.72	2.21	0.3	1.84	0.28
DCE15	14.5	30.2	3.96	16.7	3.89	1.13	4.16	0.68	4.26	0.88	2.53	0.36	2.24	0.33
DCE16	17.6	37.1	4.79	19.7	4.63	1.38	4.79	0.79	5.12	1.05	3.12	0.42	2.71	0.38
DCE17	18.2	37.3	4.62	19.5	4.33	1.29	4.79	0.8	4.95	1.02	3	0.43	2.49	0.38
DCE21	15.7	31.8	4.1	17.4	4.13	1.24	4.23	0.73	4.3	0.96	2.66	0.37	2.31	0.34
DCE22	16.8	35.1	4.46	19.5	4.48	1.32	4.54	0.76	4.53	0.99	3.01	0.39	2.51	0.39

DCE30	18.3	36	4.44	18.9	4.31	1.31	4.99	0.79	4.92	1.02	3.03	0.42	2.62	0.39
DCE47														
DCE48														
DCE70														
DCE72														
DCE73														
DCE74														
DCE75														
DCE77														

LT2	La	Ce	Pr	Nd	Sm	Eu	Gd	Tb	Dy	Ho	Er	Tm	Yb	Lu
DCE01A	13.3	30.8	4.05	18.6	4.68	1.5	5.56	0.91	5.5	1.18	3.36	0.46	3.11	0.44
DCE01B	10.3	23.2	3.13	14.6	3.91	1.21	4.29	0.72	4.46	0.94	2.68	0.37	2.49	0.36
DCE41	13.1	27	3.6	16	4.09	1.37	4.71	0.81	5.07	1.04	3.13	0.42	2.72	0.41
DCE42	10.3	22.9	3.08	13.5	3.48	1.19	3.87	0.68	4.21	0.89	2.52	0.34	2.37	0.33
DCE44	10.9	24.1	3.22	14.1	3.69	1.19	4.13	0.7	4.3	0.92	2.56	0.36	2.38	0.36
DCE45	12.6	25	3.38	14.7	3.92	1.21	4.59	0.78	4.55	0.99	2.88	0.39	2.46	0.36
DCE53														
DCE54														
DCE55														
DCE57														
DCE58														
DCE59														
DCE60														
DCE61														
DCE62														
DCE68														
DCE79														
DCE86														
DPI02	12.5	28.1	3.7	16.6	4.69	1.49	5.94	1.01	6.14	1.24	3.53	0.49	2.78	0.44
DPI03	12.7	27.2	3.51	15.7	3.82	1.25	4.67	0.78	5.11	1.13	3.31	0.48	3.2	0.5
DPI04	13	29.5	3.66	15.8	4.06	1.34	4.8	0.8	4.82	1.01	3.01	0.4	2.56	0.37
DPI05	12.8	26.9	3.48	15.4	3.94	1.28	4.59	0.77	4.96	1.11	3.06	0.4	2.52	0.38
DPI49														
DPI50														

Isotopic data

Sample	$^{87}Sr/^{86}Sr$	$^{143}Nd/^{144}Nd$	$^{206}Pb/^{204}Pb$	$^{207}Pb/^{204}Pb$	$^{208}Pb/^{204}Pb$	$^{87}Rb/^{86}Sr$	$^{147}Sm/^{144}Nd$	$^{87}Sr/^{86}Sr$	$^{143}Nd/^{144}Nd$	ε(Nd)	TDM (Ga)	$^{206}Pb/^{204}Pb$	$^{207}Pb/^{204}Pb$	$^{208}Pb/^{204}Pb$

	measured (present-day) isotopic ratios					calculated isotopic ratios		calculated (initial) isotopic ratios (127 Ma)						
HT	$^{87}Sr/^{86}Sr$	$^{143}Nd/^{144}Nd$	$^{206}Pb/^{204}Pb$	$^{207}Pb/^{204}Pb$	$^{208}Pb/^{204}Pb$	$^{87}Rb/^{86}Sr$	$^{147}Sm/^{144}Nd$	$^{87}Sr/^{86}Sr$	$^{143}Nd/^{144}Nd$	ε(Nd)	TDM (Ga)	$^{206}Pb/^{204}Pb$	$^{207}Pb/^{204}Pb$	$^{208}Pb/^{204}Pb$
DCE04	0.7077013	0.51242426				0.20041	0.12597	0.707340	0.512320	-3.02	1.08			
DCE05	0.7082998	0.51244322				0.14696	0.12857	0.708035	0.512336	-2.70	1.08			
DCE07	0.7069002	0.51243335	18.248	15.574	38.545	0.21349	0.12066	0.706515	0.512333	-2.76	1.00	17.94	15.56	38.06
DCE08	0.7067777	0.51244526				0.22274	0.12661	0.706376	0.512340	-2.62	1.05			
DCE09	0.7067591	0.51243751				0.23180	0.12907	0.706341	0.512330	-2.82	1.09			
DCE10	0.7061885	0.51245959	18.297	15.582	38.570	0.20193	0.12893	0.705824	0.512352	-2.38	1.05	17.57	15.55	37.49
DCE12B	0.7079245	0.51242479				0.21277	0.12848	0.707540	0.512318	-3.05	1.11			
DCE14	0.7094889	0.51243730				0.37006	0.12881	0.708821	0.512330	-2.82	1.09			
DCE18	0.7070487	0.51241992				0.21032	0.13251	0.706669	0.512310	-3.21	1.17			
DCE27	0.7065306	0.51243355	18.234	15.583	38.553	0.22607	0.12780	0.706122	0.512327	-2.87	1.08	17.77	15.56	37.84
DCE31	0.7081231	0.51243113				0.29802	0.12952	0.707585	0.512324	-2.95	1.11			
DCE35	0.7062397	0.51244997				0.21919	0.12814	0.705844	0.512344	-2.56	1.06			
DCE36.1	0.7070333	0.51244501				0.27735	0.12814	0.706533	0.512339	-2.65	1.07			
DCE37	0.7070984	0.51244760				0.30010	0.13255	0.706557	0.512337	-2.68	1.12			
DCE38	0.7058962	0.51244306				0.19757	0.12991	0.705540	0.512335	-2.72	1.09			
DCE39	0.7065737	0.51243613				0.24599	0.12783	0.706130	0.512330	-2.82	1.08			
DCE40	0.7068122	0.51244101				0.18759	0.12822	0.706474	0.512334	-2.73	1.08			
DPI07	0.7070902	0.51244362				0.25122	0.12479	0.706637	0.512340	-2.63	1.03			
DPI08	0.7060580	0.51243289	18.276	15.588	38.623	0.21155	0.12888	0.705676	0.512326	-2.90	1.10	16.57	15.51	36.39
DPI11	0.7062891	0.51243484	18.366	15.588	38.752	0.21307	0.12553	0.705904	0.512331	-2.81	1.05	17.13	15.53	37.01
DPI12	0.7061545	0.51244324				0.23770	0.12991	0.705725	0.512335	-2.72	1.09			
DPI18	0.7060040	0.51243997	18.208	15.567	38.512	0.13618	0.12948	0.705758	0.512332	-2.77	1.09	16.97	15.51	36.75
DPI19	0.7060576	0.51243877				0.19305	0.12672	0.705709	0.512333	-2.75	1.06			
DPI23	0.7058296	0.51245111	18.309	15.578	38.571	0.19873	0.13134	0.705471	0.512342	-2.59	1.10	17.69	15.55	37.65

eHT	$^{87}Sr/^{86}Sr$	$^{143}Nd/^{144}Nd$	$^{206}Pb/^{204}Pb$	$^{207}Pb/^{204}Pb$	$^{208}Pb/^{204}Pb$	$^{87}Rb/^{86}Sr$	$^{147}Sm/^{144}Nd$	$^{87}Sr/^{86}Sr$	$^{143}Nd/^{144}Nd$	ε(Nd)	TDM (Ga)	$^{206}Pb/^{204}Pb$	$^{207}Pb/^{204}Pb$	$^{208}Pb/^{204}Pb$
DCE32C	0.7098613	0.51241973				0.49423	0.12042	0.708969	0.512320	-3.02	1.02			
DCE33	0.7087257	0.51241425	18.365	15.594	38.663	0.62950	0.11378	0.707589	0.512320	-3.02	0.96	18.14	15.58	38.26
DCE34B	0.7093878	0.51240465	18.664	15.614	38.924	0.40494	0.11679	0.708657	0.512308	-3.26	1.01	17.76	15.57	37.56

LT1	$^{87}Sr/^{86}Sr$	$^{143}Nd/^{144}Nd$	$^{206}Pb/^{204}Pb$	$^{207}Pb/^{204}Pb$	$^{208}Pb/^{204}Pb$	$^{87}Rb/^{86}Sr$	$^{147}Sm/^{144}Nd$	$^{87}Sr/^{86}Sr$	$^{143}Nd/^{144}Nd$	ε(Nd)	TDM (Ga)	$^{206}Pb/^{204}Pb$	$^{207}Pb/^{204}Pb$	$^{208}Pb/^{204}Pb$
DCE02	0.7096413	0.51236004				0.33204	0.13957	0.709042	0.512244	-4.50	1.40			
DCE03	0.7091561	0.51235846	18.758	15.669	38.907	0.35659	0.13167	0.708512	0.512249	-4.40	1.27	18.45	15.65	38.53
DCE16	0.7092117	0.51236035				0.39397	0.14217	0.708501	0.512242	-4.53	1.45			

DCE21	0.7110120	0.51236297				0.30832	0.14358	0.710455	0.512244	-4.51	1.47			
DCE22	0.7110343	0.51235160				0.34738	0.13897	0.710407	0.512236	-4.65	1.41			
DCE30	0.7095281	0.51236512	18.740	15.669	38.870	0.44086	0.13794	0.708732	0.512251	-4.37	1.36	18.37	15.65	38.36
LT2	$^{87}Sr/^{86}Sr$	$^{143}Nd/^{144}Nd$	$^{206}Pb/^{204}Pb$	$^{207}Pb/^{204}Pb$	$^{208}Pb/^{204}Pb$	$^{87}Rb/^{86}Sr$	$^{147}Sm/^{144}Nd$	$^{87}Sr/^{86}Sr$	$^{143}Nd/^{144}Nd$	ε(Nd)	TDM (Ga)	$^{206}Pb/^{204}Pb$	$^{207}Pb/^{204}Pb$	$^{208}Pb/^{204}Pb$
DCE01A	0.7097788	0.5125271				0.3313559	0.1522006	0.709181	0.512401	-1.44	1.28			
DCE01B	0.7147423	0.5125355				0.5341805	0.1619972	0.713778	0.512401	-1.44	1.49			
DCE41	0.7070574	0.5125404	18.477	15.619	38.497	0.3352479	0.1546276	0.706452	0.512412	-1.22	1.29	18.21	15.61	38.16
DCE44	0.7072728	0.5125505	18.416	15.629	38.772	0.2467711	0.1583036	0.706827	0.512419	-1.08	1.35	18.35	15.63	38.65
DCE45	0.7102491	0.5125366				0.4029429	0.1613067	0.709522	0.512403	-1.40	1.47			
DPI03	0.7079179	0.5125399				0.1369894	0.1471795	0.707671	0.512418	-1.11	1.15			
DPI05	0.7097317	0.5125368				0.5405587	0.1547601	0.708756	0.512408	-1.29	1.31			

Table A2. Microprobe analysis data for feldspars of the Rio Ceará-Mirim and Canindé dike swarms. Abrev.: C - core, I - intermediate position, R - rim.

Geochemical group	Size (mm)	Position	Spot	SiO_2	TiO_2	Al_2O_3	Fe_2O_3	MgO	CaO	Na_2O	K_2O	SrO	MnO	BaO	Total	An	Ab	Or

High-Ti tholeiites (HT)																		
DCE10	0.85	C	Pl_11_1C	55.93	0.003	27.58	0.601	0.016	10.07	5.32	0.5	0.22	0	0	100.2	66.3	31.7	2.0
		I	Pl_11_2	56.45	0.037	27.19	0.509	0.025	9.33	5.55	0.597	0.164	0	0.016	99.9	63.4	34.1	2.4
		I	Pl_11_3	59.13	0.061	25.81	0.487	0	7.3	6.92	0.644	0.25	0.008	0.186	100.8	52.3	44.9	2.7
		I	Pl_11_4	65.3	0.026	19.7	0.105	0	0.455	3.93	9.96	0.087	0	1.108	100.7	4.6	35.8	59.7
		I	Pl_11_5	65.15	0.007	18.9	0.074	0	0.092	0.944	14.77	0.066	0.008	0.557	100.6	0.9	8.8	90.3
		R	Pl_11_7	66.45	0.003	19.33	0.102	0.03	0.381	4	10.48	0.005	0	0	100.8	3.7	35.3	60.9
	1.82	C	Pl_12_2	59.35	0.028	25.6	0.443	0	7.32	6.69	0.703	0.199	0	0.036	100.4	53.1	43.9	3.0
		R	Pl_12_3B	66.53	0.01	19.32	0.128	0.002	0.404	4.4	10	0.02	0.018	0.044	100.9	3.9	38.5	57.6
	0.63	C	Pl_13_1C	66.32	0	19.31	0.097	0	0.544	4.54	9.34	0.057	0	0.033	100.2	5.3	40.2	54.4
		I	Pl_13_2	66.62	0.031	19.23	0.169	0	0.448	4.08	10.28	0.019	0.007	0	100.9	4.4	36.0	59.7
		I	Pl_13_3	65.84	0.036	18.99	0.54	0.006	0.34	3.98	10.59	0.01	0	0.051	100.4	3.3	35.1	61.5
		R	Pl_13_4	64.9	0	18.75	0.027	0.008	0	0.122	16.51	0.056	0	0.176	100.5	0.0	1.1	98.9
	1.02	C	Pl_14_1C	58.23	0.053	25.93	0.505	0.006	7.71	6.4	0.706	0.266	0.001	0.075	99.9	55.4	41.6	3.0
		I	Pl_14_2	59.45	0.024	25.31	0.425	0	6.83	6.8	0.958	0.196	0	0.242	100.2	50.4	45.4	4.2
		I	Pl_14_3	60.19	0	24.45	0.437	0	5.94	7.34	0.942	0.219	0.004	0.261	99.8	45.2	50.5	4.3
		R	Pl_14_4	66.04	0	19.24	0.315	0.007	0.326	4.4	9.81	0.118	0	0.222	100.5	3.2	39.2	57.6
	0.05	C	Pl_15	60.17	0	24.18	1.77	0.136	5.82	7.41	0.625	0.171	0.016	0.203	100.5	45.1	52.0	2.9
	0.06	C	Pl_16	66	0.042	19.18	0.649	0	0.37	4.18	10.24	0.062	0	0.226	100.9	3.6	36.9	59.5
	0.60	I	Pl_17_1	66.28	0	19.34	0.098	0	0.397	4.25	9.82	0.086	0.019	0.307	100.6	3.9	38.1	57.9
		I	Pl_17_2	65.82	0	19.52	0.193	0.01	0.535	4.48	9.28	0.015	0	0.244	100.1	5.3	40.1	54.6
	0.23	C	Pl_19	66.13	0.003	19.43	0.186	0	0.415	4.43	9.43	0.08	0	0.272	100.4	4.1	39.9	55.9
	0.14	C	Pl_20	66.41	0.045	19.22	0.226	0.002	0.426	4.32	9.66	0.065	0.014	0.043	100.4	4.2	38.8	57.0
	0.19	C	Pl_21	66.06	0	19.14	0.088	0	0.394	3.94	10.1	0	0.016	0.003	99.7	4.0	35.8	60.3
	0.26	C	Pl_22_1	65.91	0	19.18	0.101	0	0.434	4.03	10.06	0.012	0.014	0.034	99.8	4.3	36.2	59.5
	0.62	C	Pl_23_1C	55.25	0.123	27.98	0.614	0.014	10.24	5.23	0.503	0.138	0	0.074	100.2	67.1	31.0	2.0
		I	Pl_23_3	55.5	0.036	27.78	0.679	0.022	9.82	5.39	0.481	0.186	0.001	0	99.9	65.5	32.5	1.9

		I	Pl_23_4	55.67	0.023	27.61	0.678	0.012	9.63	5.49	0.421	0.132	0	0.022	99.7	64.9	33.5	1.7
		I	Pl_23_5	64.56	0.038	21.8	0.176	0	2.87	8.56	1.53	0.084	0.016	0.087	99.7	24.9	67.2	7.9
		I	Pl_23_6	65.84	0.077	19.34	0.105	0.014	0.354	3.7	11.1	0.096	0	0.036	100.7	3.4	32.5	64.1
		R	Pl_23_7	64.47	0	18.89	0.038	0	0.036	0.103	16.17	0.067	0.007	0.296	100.1	0.4	1.0	98.7
	0.86	C	Pl_24_1C	55.38	0.091	28.2	0.704	0.04	10.41	5.09	0.432	0.177	0.012	0	100.5	68.2	30.2	1.7
		I	Pl_24_2	55.19	0.079	28.08	0.7	0.014	10.41	5.06	0.49	0.185	0	0.012	100.2	68.1	30.0	1.9
		I	Pl_24_3	56.08	0.045	27.54	0.596	0	9.7	5.58	0.458	0.225	0	0.098	100.3	64.6	33.6	1.8
		R	Pl_24_3	63.89	0.014	22.42	0.226	0	3.59	8.23	1.46	0.078	0.005	0.066	100.0	30.2	62.5	7.3
		C	Pl_24_4	65.84	0.004	19.28	0.136	0	0.432	4.32	9.81	0.025	0.008	0.128	100.0	4.2	38.4	57.4
		I	Pl_24_5	65.99	0.018	19.23	0.155	0	0.34	4.03	10.43	0.067	0	0.116	100.4	3.3	35.8	60.9
		R	Pl_24_6	65.19	0.003	18.8	0.023	0	0.019	0.224	16.45	0.054	0.009	0.264	101.0	0.2	2.0	97.8
DCE12B	0.50		DCE12B_PL1_1,	66.25	0.025	18.87	0.128	0.001	0.18	4	10.38	0.047	0.007	0	99.9	1.8	36.3	61.9
			DCE12B_PL1_2,	62.64	0.003	19.44	0.003	0.004	0	0.812	14.07	0.044	0	3.24	100.3	0.0	8.1	91.9
			DCE12B_PL1_3,	66.62	0	18.89	0.211	0	0.128	3.87	10.66	0.031	0	0.023	100.4	1.3	35.1	63.6
			DCE12B_PL1_4,	64.7	0.018	18.59	0.065	0.016	0	0.037	16.52	0.046	0.009	0.32	100.3	0.0	0.3	99.7
	0.20	C	DCE12B_PL2_1C,	67.29	0.007	18.93	0.15	0	0.153	4.59	9.45	0.056	0	0.034	100.7	1.5	41.8	56.6
		R	DCE12B_PL2_1B,	77.82	0.028	13.27	0.191	0	0.314	3.36	6.41	0.036	0.006	0.012	101.4	4.4	42.4	53.2
	0.20	R	DCE12B_PL3_2B,	64.68	0.054	21.75	0.235	0	2.67	7.63	3.09	0.09	0	0.364	100.6	23.4	60.5	16.1
		C	DCE12B_PL3_1C,	57.18	0.032	26.87	0.656	0.031	8.67	5.94	0.563	0.238	0.005	0.071	100.3	60.3	37.4	2.3
		R	DCE12B_PL3_2B,	68.51	0.062	18.19	0.305	0.018	0.346	4.19	9.12	0.065	0	0.019	100.8	3.6	39.6	56.8
		I	DCE12B_PL3_3,	58.44	0.047	26.12	0.644	0.022	7.6	6.32	0.707	0.305	0.009	0.115	100.3	55.3	41.6	3.1
		R	DCE12B_PL3_4,	68.64	0.083	18.31	0.403	0.034	0.369	4.21	9.17	0.038	0.009	0	101.3	3.8	39.5	56.6
		I	DCE12B_PL3_1C,	58.23	0.022	26.19	0.592	0.024	7.64	6.49	0.719	0.28	0	0.142	100.3	54.8	42.1	3.1
	0.30	C	DCE12B_PL4_1C,	54.62	0.041	27.19	2.27	0.291	9.62	5.24	0.427	0.226	0.009	0.034	100.0	65.8	32.4	1.7
		R	DCE12B_PL4_2B,	56.82	0.019	26.75	0.72	0	8.66	5.97	0.56	0.228	0.006	0.131	99.9	60.2	37.5	2.3
	0.10	R	DCE12B_PL5_2B,	65.46	0.013	19.04	0.194	0	0.488	2.76	12.65	0.118	0	0.114	100.8	4.6	23.7	71.6
		C	DCE12B_PL5_1C,	66.44	0.008	19.07	0.259	0	0.343	3.91	10.74	0.023	0.007	0.054	100.9	3.3	34.4	62.2

	0.04	C	DCE12B_PL6_1C,	66.25	0.1	19.68	0.603	0	0.515	4.75	9.08	0.082	0	0.277	101.3	5.0	42.1	52.9
		C	DCE12B_PL7_1C,	56.77	0.001	27.41	0.694	0.012	9.38	5.73	0.503	0.227	0	0.075	100.8	63.1	34.9	2.0
		I	DCE12B_PL7_2,	57.9	0	26.7	0.633	0.03	8.32	6.09	0.617	0.319	0	0.093	100.7	58.6	38.8	2.6
		R	DCE12B_PL7_3B,	62.44	0	23.62	0.422	0.002	4.67	7.7	1.46	0.242	0.008	0.374	100.9	37.3	55.7	6.9
	0.40	C	DCE12B_PL8_1C,	66.36	0	19.76	0.282	0	0.611	5.42	8.01	0.121	0.013	0.681	101.3	5.9	47.7	46.4
		R	DCE12B_PL8_2B,	71.08	0.052	15.58	0.77	0.187	0.12	1.37	11.42	0.075	0	0.113	100.8	1.5	15.2	83.3
	0.10	C	DCE12B_PL9_1C,	60.41	0.015	25.1	0.583	0.013	6.36	7.05	0.948	0.291	0	0.198	101.0	47.8	47.9	4.2
		R	DCE12B_PL9_2B,	67.25	0.007	19.73	0.367	0.022	0.599	4.85	8.83	0.084	0.007	0.079	101.8	5.8	42.8	51.3
			DCE12B_PL10_1C,	65.32	0	22.48	0.27	0	3.18	9.07	1.06	0.066	0.005	0	101.5	26.5	68.3	5.3
	0.08		DCE12B_PL11,	66.37	0	19.94	0.342	0	0.917	5.76	7.68	0.077	0.014	0.163	101.3	8.6	48.7	42.7
	0.04		DCE12B_PL12,	64.45	0.037	22.19	0.42	0.006	3.13	8.78	0.768	0.036	0	0.029	99.8	27.1	68.9	4.0
	0.05		DCE12B_PL14,	63.72	0.083	19.61	0.794	0.002	0.023	1.56	13.35	0.036	0.014	2.8	102.0	0.2	15.0	84.7
	0.04		DCE12B_PL15,	65.7	0	19.76	0.378	0	0.656	5.1	8.21	0.104	0	1.007	100.9	6.5	45.4	48.1
	0.05		DCE12B_PL16,	67.01	0	19.5	0.287	0	0.531	5.09	8.61	0.069	0	0.186	101.3	5.2	44.9	49.9
DPI23	1.05	C	DPI23_Pl_1_1C	55.85	0.058	27.86	0.751	0.074	10.24	5.11	0.553	0.17	0.009	0	100.7	67.4	30.4	2.2
		I	DPI23_Pl_1_2	53.76	0.047	29.37	0.798	0.073	11.56	4.31	0.386	0.129	0.012	0.082	100.5	73.7	24.9	1.5
		I	DPI23_Pl_1_3	55.15	0.021	27.73	1.63	0.124	10.13	4.79	0.498	0.111	0	0	100.2	68.6	29.4	2.0
		I	DPI23_Pl_1_4	55.44	0.015	28.24	0.771	0.072	10.83	4.87	0.452	0.152	0	0.068	100.9	69.8	28.4	1.7
		I	DPI23_Pl_1_5	55.08	0	28.47	0.854	0.069	10.88	4.73	0.405	0.157	0.025	0.074	100.7	70.6	27.8	1.6
		R	DPI23_Pl_1_6B	58.86	0.01	26.37	0.627	0.025	7.81	6.1	0.773	0.179	0	0.021	100.8	56.6	40.0	3.3
	0.18	C	DPI23_Pl_2_1C	54.45	0.048	28.66	1.039	0.073	11.24	4.83	0.449	0.103	0	0.025	100.9	70.8	27.5	1.7
		R	DPI23_Pl_2_2B	53.66	0.068	28.47	1.69	0.177	11.27	4.52	0.373	0.109	0.003	0.013	100.4	72.3	26.2	1.4
	1.12	C	DPI23_Pl_3_1C	55.42	0.114	28.41	0.759	0.046	10.75	4.84	0.452	0.135	0	0.03	101.0	69.8	28.4	1.7
		I	DPI23_Pl_3_2	54.01	0.091	29.11	0.788	0.069	11.36	4.5	0.378	0.158	0	0.094	100.6	72.6	26.0	1.4
		I	DPI23_Pl_3_3	53.76	0.056	29.18	0.766	0.052	11.74	4.36	0.338	0.184	0	0	100.4	73.9	24.8	1.3
		I	DPI23_Pl_3_4	57.03	0.061	26.95	0.685	0.042	9.06	5.59	0.604	0.164	0.011	0.103	100.3	62.6	34.9	2.5
		I	DPI23_Pl_3_5	57.79	0.007	26.35	0.586	0.035	8.5	5.91	0.659	0.213	0.02	0.148	100.2	59.7	37.6	2.8

		R	DPI23_Pl_3_6	58.91	0.034	25.93	0.58	0.008	7.67	6.28	0.83	0.178	0.007	0.108	100.5	55.4	41.0	3.6
	0.14		DPI23_Pl_4	59.43	0.049	25.4	0.632	0	7.3	6.69	0.843	0.205	0	0.077	100.6	52.7	43.7	3.6
	1.42		DPI23_Pl_4_1C	54.87	0.078	28.38	0.798	0.072	10.95	4.7	0.405	0.123	0.005	0	100.4	70.9	27.5	1.6
			DPI23_Pl_4_2	53.73	0	28.85	0.786	0.062	11.47	4.47	0.381	0.198	0.023	0.009	100.0	72.9	25.7	1.4
			DPI23_Pl_4_3	54.69	0.081	28.43	0.836	0.072	10.88	4.71	0.455	0.181	0.018	0.056	100.4	70.6	27.7	1.8
	0.16		DPI23_Pl_5	53.93	0.052	29.08	0.877	0.091	11.7	4.31	0.366	0.176	0.019	0.048	100.6	74.0	24.7	1.4
	1.09	C	DPI23_Pl_6_1C	55.66	0.155	27.85	0.782	0.069	10.24	4.98	0.49	0.108	0	0.027	100.4	68.1	30.0	1.9
		I	DPI23_Pl_6_2	54.6	0.058	28	0.908	0.099	10.9	4.79	0.474	0.071	0	0.024	99.9	70.2	27.9	1.8
		I	DPI23_Pl_6_3	54.33	0.106	28.6	0.802	0.061	11.05	4.62	0.426	0.157	0	0	100.2	71.4	27.0	1.6
		I	DPI23_Pl_6_4	54.36	0.001	28.43	0.789	0.076	11.12	4.62	0.446	0.199	0	0.023	100.1	71.4	26.9	1.7
		I	DPI23_Pl_6_5	55.13	0.047	27.9	0.635	0.037	10.38	5.03	0.498	0.197	0.002	0.036	99.9	68.2	29.9	1.9
		I	DPI23_Pl_6_6	56.47	0.035	26.94	0.759	0.059	9.44	5.45	0.615	0.143	0.004	0.076	100.0	64.1	33.5	2.5
		R	DPI23_Pl_6_7B	55.9	0.207	24.13	3.35	1.248	9.85	5.05	0.564	0.188	0.043	0.123	100.7	66.8	31.0	2.3
Evolved high-Ti tholeiites (eHT) (SiO_2 > 56.5 wt.%)																		
DCE32C	<0.5	C	Pl_3_1C	54.21	0.083	28.4	0.652	0.051	11.04	4.8	0.46	0.166	0	0.028	99.9	70.5	27.7	1.7
	<0.5	C	Pl_4_1MATRIZ2	59.4	0.029	24.92	1.043	0.029	6.62	6.89	0.862	0.143	0.022	0.138	100.1	49.5	46.6	3.8
	0.60	C	Pl_01_1C	59.08	0	25.65	0.521	0	7.03	6.6	0.881	0.292	0	0.166	100.2	52.0	44.1	3.9
		I	Pl_01_2	58.61	0.053	25.79	0.501	0.007	7.54	6.55	0.81	0.321	0	0.133	100.3	54.1	42.5	3.5
		I	Pl_01_3	67.73	0	20.27	0.034	0.001	0.665	10.96	0.234	0.117	0	0	100.0	6.2	92.5	1.3
		I	Pl_01_4Br	64.67	0	18.82	0.088	0.003	0.015	0.652	15.25	0.094	0	0.769	100.4	0.2	6.1	93.8
		R	Pl_01_5Br	67.32	0.033	20.67	0.058	0.019	1.052	10.77	0.21	0.138	0.005	0	100.3	9.6	89.2	1.1
	0.36	C	Pl_02_1C	58.7	0.051	25.96	0.496	0	7.31	6.56	0.762	0.244	0	0.113	100.2	53.4	43.3	3.3
		I	Pl_02_2	58.38	0.058	25.78	0.502	0.002	7.46	6.67	0.756	0.249	0	0.151	100.0	53.5	43.3	3.2
		I	Pl_02_3	62.92	0.052	23.07	0.3	0.026	4.03	8.45	0.799	0.214	0.007	0.249	100.1	33.2	62.9	3.9
			Pl_02_4	67.19	0.002	20.94	0.017	0	1.344	10.8	0.216	0.139	0	0	100.6	12.0	86.9	1.1
	0.19	C	Pl_03_1C	57.98	0.072	26.51	0.602	0.01	8.13	6.24	0.571	0.294	0.008	0.077	100.5	57.6	40.0	2.4
	0.38	C	Pl_04_1C	58.28	0.059	25.86	0.548	0.001	7.6	6.51	0.808	0.245	0.006	0.115	100.0	54.4	42.2	3.4
			Pl_04_2	59.76	0.025	25.09	0.442	0	6.52	7	0.877	0.226	0.027	0.153	100.1	48.7	47.4	3.9

		R	Pl_04_3B	67.4	0	20.65	0.056	0	0.956	11.05	0.135	0.095	0.011	0.031	100.4	8.7	90.6	0.7
		R	Pl_04_3B2	64.58	0.02	18.9	0.016	0.012	0.083	1.163	14.49	0.04	0	0.723	100.0	0.9	10.8	88.4
	0.17		Pl_05_1	64.63	0	18.99	0	0.012	0.019	0.709	15.25	0.078	0.006	1.061	100.8	0.2	6.6	93.2
			Pl_05_2	68.85	0	19.92	0	0.001	0.136	11.28	0.371	0.069	0.007	0	100.6	1.3	96.6	2.1
	0.29	C	Pl_06_1C	59.1	0	25.94	0.451	0.009	7.44	6.53	0.796	0.298	0	0.176	100.7	53.8	42.7	3.4
		I	Pl_06_2	58.9	0.006	25.88	0.492	0	7.47	6.47	0.798	0.312	0	0.149	100.5	54.1	42.4	3.4
		I	Pl_06_3	58.75	0.043	25.57	0.514	0	7.32	6.51	0.824	0.279	0.021	0.114	99.9	53.4	43.0	3.6
		I	Pl_06_4	59.72	0.059	24.92	0.491	0.006	6.31	6.99	0.937	0.277	0.009	0.178	99.9	47.8	47.9	4.2
			Pl_06_5	60.02	0.038	24.9	0.515	0	6.23	6.96	1.006	0.309	0	0.235	100.2	47.5	48.0	4.6
	0.32		Pl_07_1	58.56	0	25.67	0.57	0.013	7.2	6.57	0.843	0.229	0	0.196	99.9	52.8	43.6	3.7
		I	Pl_07_2	60.19	0.061	24.9	0.458	0.004	6.15	7.14	0.888	0.232	0	0.333	100.4	46.8	49.2	4.0
		R	Pl_07_3B	71.34	0.068	17.93	0.149	0.01	1.53	8.03	1.68	0.079	0.013	0.124	101.0	15.6	74.2	10.2
	0.16	C	Pl_08_1C	66.61	0.031	21.14	0.013	0	1.46	10.62	0.272	0.156	0	0.061	100.4	13.0	85.6	1.4
			Pl_08_2	64.41	0	18.95	0.03	0.014	0.022	0.684	15.05	0.042	0.006	0.989	100.2	0.2	6.4	93.3
	0.57	C	Pl_09_1C															
			Pl_09_2	65	0	18.66	0.027	0	0.02	0.17	16.37	0.051	0.006	0.204	100.5	0.2	1.6	98.2
		R	Pl_09_3B	68	0	20.05	0.07	0	0.495	11.22	0.203	0.153	0	0	100.2	4.6	94.3	1.1
	<0.5		Pl_09_MATRIZ_01	68.37	0	20.18	0	0	0.335	11.32	0.034	0.176	0	0.084	100.5	3.2	96.6	0.2
	<0.5		Pl_09_MATRIZ_02	67.19	0	19.98	0.662	0.176	0.418	11.19	0.027	0.146	0.018	0	99.8	4.0	95.9	0.2
DCE33	0.12		DCE33_PL3	66.84	0.014	20.26	0.23	0.018	0.891	10.4	0.084	0.17	0	0	98.9	8.6	90.9	0.5
	0.09		DCE33_PL4	67.7	0.072	20.3	0.382	0.019	0.603	10.65	0.12	0.142	0.005	0	100.0	5.8	93.5	0.7
	1.89	C	DCE33_PL6_1C	54.61	0.059	29.03	0.635	0.015	11.14	4.67	0.429	0.227	0.006	0.098	100.9	71.3	27.1	1.6
		I	DCE33_PL6_2	55.16	0.064	28.39	0.645	0.034	10.96	4.55	0.474	0.208	0	0.039	100.5	71.4	26.8	1.8
			DCE33_PL6_4	66.02	0.023	19.71	0.874	0.083	0.47	8.9	3.16	0.133	0.001	0.259	99.6	4.5	77.4	18.1
	0.09	C	DCE33_PL8	70.87	0.071	15.65	0.667	0.076	0.217	1.175	11.73	0.064	0	0.358	100.9	2.6	12.9	84.5
	0.19	C	DCE33_PL9	67.76	0	20.75	0.154	0.006	0.897	10.93	0.105	0.137	0	0.01	100.7	8.3	91.2	0.6
	0.05	C	DCE33_PL10	65.31	0	19.09	0.075	0	0.009	0.945	14.97	0.07	0.013	0.617	101.1	0.1	8.7	91.2

Low-Ti tholeiites (LT1)																		
DCE03	0.99	C	Pl_1_1C	53.65	0.005	29.1	1.059	0.103	12.02	4.31	0.209	0.038	0.008	0.007	100.5	74.9	24.3	0.8
		I	Pl_1_2	54.09	0.007	26.97	1.023	0.075	10.53	3.99	1.99	0.04	0.003	0	98.7	68.7	23.6	7.7
		I	Pl_1_3	54.27	0.048	28.54	1.056	0.061	11.51	4.49	0.261	0.061	0.007	0.053	100.4	73.2	25.8	1.0
	0.31	C	Pl_2_1C	54.42	0	28.94	1.175	0.057	11.36	4.6	0.212	0.06	0.007	0	100.8	72.6	26.6	0.8
	0.18	C	Pl_3	54.26	0.055	28.26	1.047	0.066	10.07	5.41	0.341	0.062	0.002	0.099	99.7	66.4	32.3	1.3
	0.55	C	Pl_5_1C	51.46	0.038	30.47	0.935	0.156	13.48	3.37	0.106	0.047	0.011	0.012	100.1	81.2	18.4	0.4
		I	Pl_5_2	51.98	0.043	30.32	0.909	0.16	12.9	3.48	0.128	0.04	0	0	100.0	80.0	19.5	0.5
		R	Pl_5_3B	56.41	0.047	27.49	0.886	0.021	10	5.22	0.291	0.084	0.006	0.02	100.5	67.1	31.7	1.2
	0.09	C	Pl_6	51.97	0.018	30.17	1.26	0.097	12.85	3.68	0.13	0.063	0.003	0	100.2	79.0	20.5	0.5
	0.16	C	Pl_7	55.46	0.092	27.87	0.875	0.036	10.45	5.06	0.259	0.12	0.003	0	100.2	68.8	30.2	1.0
	0.01	C	Pl_8															
	0.06	C	Pl_9	54.03	0.092	28.38	1.245	0.037	11.5	4.67	0.257	0.101	0.013	0.051	100.4	72.4	26.6	1.0
	0.71	C	Pl_10_1C	52.89	0.066	29.44	1.123	0.094	12.49	3.95	0.18	0.056	0	0.051	100.3	77.2	22.1	0.7
		I	Pl_10_2	53.75	0.067	28.89	1.164	0.072	11.76	4.39	0.199	0.095	0	0.05	100.4	74.2	25.1	0.7
Low-Ti tholeiites (LT2)																		
DCE44	1.29	C	DCE44_Pl_1_1C	51.5	0.033	30.43	0.746	0.131	13.71	3.48	0.151	0.061	0.013	0	100.3	80.9	18.6	0.5
		I	DCE44_Pl_1_2	51.66	0.029	30.29	0.939	0.081	13.62	3.53	0.145	0.074	0.017	0.011	100.4	80.6	18.9	0.5
		I	DCE44_Pl_1_3	53.93	0.106	28.74	1.116	0.091	11.76	4.49	0.207	0.036	0.017	0.056	100.6	73.7	25.5	0.8
		B	DCE44_Pl_1_4															
	0.34	B	DCE44_Pl_2_2B	55.86	0.002	27.71	0.923	0.021	9.98	5.46	0.275	0.114	0.018	0	100.4	66.2	32.8	1.1
	0.20		DCE44_Pl_3	58.64	0.003	26.03	0.697	0	8.12	6.57	0.402	0.106	0	0.029	100.6	56.8	41.6	1.7
	0.14		DCE44_Pl_4	54.34	0.128	27.08	2.01	0.518	10.25	4.94	0.254	0.039	0.013	0.029	99.6	68.9	30.1	1.0
	1.17	C	DCE44_Pl_6_1C	52.84	0.028	29.75	0.989	0.111	12.73	3.86	0.17	0.056	0	0.025	100.6	78.0	21.4	0.6
		I	DCE44_Pl_6_2	53.34	0.034	29.57	1.036	0.098	12.54	4.06	0.173	0.082	0.005	0.059	101.0	76.9	22.5	0.6
		B	DCE44_Pl_6_3B	56.31	0.034	27.52	0.812	0.03	10	5.42	0.268	0.094	0.009	0.069	100.6	66.4	32.6	1.1
	0.19	C	DCE44_Pl_7	53.72	0.004	28.67	1.082	0.043	11.73	4.41	0.22	0.052	0.008	0	99.9	74.0	25.2	0.8
	0.11	C	DCE44_Pl_8	59.51	0	25.44	0.719	0	7.09	7.01	0.553	0.1	0.005	0.049	100.5	51.5	46.1	2.4

	1.59	C	DCE44_Pl_9_1C	50.85	0	31.22	0.7	0.095	14.31	3.2	0.138	0.036	0.016	0	100.6	82.8	16.7	0.5
		I	DCE44_Pl_9_2	53.27	0.074	29.48	0.812	0.187	12.23	4.16	0.373	0.041	0.001	0.013	100.6	75.4	23.2	1.4
		I	DCE44_Pl_9_3	52.59	0.051	29.72	0.96	0.108	12.91	3.91	0.154	0.065	0.005	0.051	100.5	78.1	21.4	0.6
		I	DCE44_Pl_9_4	54.71	0.082	28.39	0.823	0.031	11.33	4.86	0.244	0.065	0.014	0.004	100.6	71.4	27.7	0.9
		B	DCE44_Pl_9_5	57.29	0.088	26.94	0.779	0	9.22	5.91	0.308	0.092	0	0.031	100.7	62.5	36.3	1.2
	0.12	C	DCE44_Pl_10_1C	51.7	0.047	30.62	0.95	0.045	13.67	3.46	0.134	0.079	0	0.045	100.8	81.0	18.5	0.5
		B	DCE44_Pl_10_1B	53.27	0.003	29.36	1.147	0.059	12.44	4.24	0.185	0.045	0.035	0.04	100.8	75.9	23.4	0.7
DPI03	2.05	C	DPI03_PL1_1C	53.41	0.051	29.73	0.737	0.066	12.44	4.13	0.308	0.055	0	0	100.9	76.0	22.8	1.1
		I	DPI03_PL1_2	51.44	0.068	30.88	0.819	0.049	13.87	3.39	0.212	0.077	0.015	0	100.8	81.3	18.0	0.7
		I	DPI03_PL1_3	54.25	0.03	29.36	0.925	0.018	11.91	4.46	0.3	0.08	0.01	0	101.3	73.9	25.0	1.1
		I	DPI03_PL1_4	56.46	0	27.87	0.723	0	9.82	5.57	0.412	0.039	0.021	0.054	101.0	65.0	33.4	1.6
		I	DPI03_PL1_6B	66.67	0.056	21.57	0.162	0	2.13	9.73	0.803	0.056	0	0.147	101.3	18.7	77.1	4.2
		B	DPI03_PL1_7B	67.38	0	17.94	0.057	0.003	0	0.468	15.09	0.025	0	0.174	101.1		4.5	95.5
	0.35	C	DPI03_PL2_1C	51.64	0.035	30.78	0.87	0.015	13.65	3.58	0.173	0.079	0	0.014	100.8	80.3	19.1	0.6
		B	DPI03_PL2_2B	64.21	0.006	21.37	0.256	0	3.4	8.66	0.554	0.097	0	0.127	98.7	29.4	67.8	2.9
	0.38	C	DPI03_PL3_1C	50.66	0.026	31.04	0.826	0	13.9	3.23	0.2	0.07	0	0.017	100.0	82.0	17.3	0.7
		B	DPI03_PL3_2B	51.61	0.044	31.21	1.005	0	13.7	3.54	0.195	0.079	0.014	0.06	101.5	80.5	18.8	0.7
	1.55	C	DPI03_PL4_1C	53.35	0.016	27.56	3.61	0.182	9.69	4.96	0.407	0.086	0.028	0.06	100.0	67.2	31.1	1.7
		I	DPI03_PL4_2	52.14	0.047	30.62	0.821	0.004	12.95	3.8	0.253	0.054	0.005	0.024	100.7	78.3	20.8	0.9
			DPI03_PL4_3	51.86	0.035	30.62	0.981	0	13.36	3.76	0.228	0.091	0.004	0	100.9	79.1	20.1	0.8
	0.25	B	DPI03_PL5_2B	56.61	0.015	27.37	0.71	0	9.39	5.62	0.54	0.074	0.004	0.049	100.4	63.5	34.4	2.2
	0.33	C	DPI03_PL6_1C	52.8	0.022	29.74	1.136	0	12.41	4.22	0.251	0.086	0.012	0.027	100.7	75.8	23.3	0.9
		B	DPI03_PL6_2B	52.65	0.096	29.39	1.033	0	12.26	4.02	0.259	0.085	0.011	0.015	99.8	76.4	22.7	1.0
	0.19	B	DPI03_PL7_2B	62.15	0	24.25	0.492	0	5.5	7.65	0.895	0.072	0.001	0.074	101.1	42.5	53.4	4.1
		C	DPI03_PL7_1C	56.67	0.081	27.58	0.708	0	9.52	5.6	0.501	0.141	0.002	0.02	100.8	64.0	34.0	2.0
	0.12	C	DPI03_PL8_1C	58.18	0	26.47	0.573	0	8.22	6.19	0.613	0.041	0.001	0.056	100.3	57.9	39.5	2.6
		B	DPI03_PL8_2B	63.95	0.024	22.94	0.245	0	3.93	8.68	0.796	0.076	0	0.17	100.8	32.1	64.1	3.9

	0.55	C	DPI03_PL9_1C	52.79	0.041	30.31	0.813	0	12.51	4.05	0.245	0.034	0	0.015	100.8	76.7	22.5	0.9
		I	DPI03_PL9_2	51.89	0	30.66	0.792	0.014	13.18	3.59	0.224	0.056	0.01	0	100.4	79.6	19.6	0.8
			DPI03_PL9_3	52.17	0.015	30.48	0.771	0	12.66	3.87	0.211	0.076	0.003	0	100.3	77.7	21.5	0.8
	0.34	B	DPI03_PL10_2B	50.9	0.046	31.25	0.79	0.037	13.49	3.3	0.173	0.027	0.009	0.012	100.0	81.4	18.0	0.6
	0.30	C	DPI03_PL11_1C	53.22	0.052	29.68	1.036	0.03	12.13	4.12	0.284	0.006	0.018	0	100.6	75.7	23.3	1.1
		B	DPI03_PL11_2B	54.23	0.025	28.94	0.957	0.03	11.37	4.62	0.304	0.05	0	0.019	100.5	72.3	26.6	1.2
	0.30	C	DPI03_PL12_1C	51.3	0.021	31.04	0.872	0.063	13.18	3.47	0.198	0.072	0.001	0	100.2	80.2	19.1	0.7
	0.17	C	DPI03_PL13_1C	55.39	0.028	28.41	0.904	0.033	10.76	4.93	0.374	0.12	0	0.002	101.0	69.7	28.9	1.4
	0.09	C	DPI03_PL14_1C	54.51	0.076	27.85	1.276	0.247	10.92	4.76	0.364	0.106	0.01	0.025	100.1	70.7	27.9	1.4
	0.19	C	DPI03_PL15_1C	56.6	0	27.64	0.727	0	9.39	5.5	0.505	0.075	0	0	100.4	64.0	33.9	2.0
		B	DPI03_PL15_1B	58.09	0.044	26.65	0.909	0.007	8.14	6.33	0.571	0.08	0.025	0.159	101.0	57.3	40.3	2.4

Table A3. Microprobe analysis data for pyroxenes of the Rio Ceará-Mirim and Canindé dike swarms. Abrev.: C - core, I - intermediate position, R - rim.

Geochemical group	Size (mm)	Position	Spot	SiO_2	Al_2O_3	FeO_T	MnO	CaO	K_2O	TiO_2	Cr_2O_3	Na_2O	MgO	Total	Mg#	En	Wo	Fe
High-Ti tholeiites (HT)																		
DCE10	1.20	C	DCE10_CPX1_1C	51.01	1.488	17.52	0.482	16.9	0.005	0.671	0.007	0.226	12.1	100.4	55.2	35.51	35.65	28.84
		I	DCE10_CPX1_2	51.2	1.99	14.6	0.378	16.04	0	0.933	0.005	0.238	14.92	100.3	64.6	43.07	33.28	23.64
		I	DCE10_CPX1_3	51.32	1.539	17.06	0.463	15.25	0	0.809	0.007	0.23	13.73	100.4	58.9	40.08	31.99	27.93
		I	DCE10_CPX1_4	50.37	0.319	33.62	0.862	2.54	0.029	0.212	0.053	0.043	12.16	100.2	39.2	37.02	5.56	57.42
	0.94	C	DCE10_CPX2_1C	51.43	1.585	15.51	0.421	16.25	0	0.811	0.034	0.23	13.87	100.1	61.5	40.50	34.10	25.40
		I	DCE10_CPX2_2	51.3	1.482	17.65	0.434	14.95	0.01	0.788	0	0.212	13.7	100.5	58.1	39.89	31.28	28.83
		I	DCE10_CPX2_3	51.02	0.74	27.15	0.675	5.58	0	0.358	0	0.086	14.55	100.2	48.9	43.06	11.87	45.07
		R	DCE10_CPX2_4	50.95	0.861	21.79	0.54	16.2	0.02	0.447	0.02	0.229	9.91	101.0	44.8	29.34	34.47	36.19
	0.32	C	DCE10_CPX3_1C	50.33	0.687	28.69	0.785	5.67	0	0.432	0.009	0.072	13.38	100.1	45.4	39.88	12.15	47.97
		R	DCE10_CPX4_2B	50.05	0.616	30.35	0.751	5.3	0	0.434	0	0.097	12.53	100.1	42.4	37.56	11.42	51.03
DCE12B	0.60	C	DCE12B_CPX1_1C	51.08	2.27	9.96	0.26	19.02	0.00	1.18	0.02	0.30	15.49	99.6	76.3	39.34	44.58	16.08
		I	DCE12B_CPX1_2	50.46	2.83	11.01	0.26	18.19	0.01	1.14	0.02	0.36	15.28	99.6	74.2	37.86	44.25	17.89
		I	DCE12B_CPX1_3	50.48	2.77	10.39	0.27	18.52	0.00	1.31	0.00	0.30	15.15	99.2	75.2	38.82	44.18	17.00
		I	DCE12B_CPX1_4	50.91	2.59	10.15	0.26	19.13	0.00	1.15	0.01	0.26	15.16	99.6	75.6	39.73	43.81	16.45
		I	DCE12B_CPX1_5	50.68	2.63	10.30	0.26	19.21	0.00	1.40	0.02	0.29	14.99	99.8	75.1	39.93	43.36	16.71
		I	DCE12B_CPX1_6	50.85	2.48	10.31	0.28	19.12	0.00	1.25	0.00	0.27	14.93	99.5	75.0	39.88	43.33	16.79
		I	DCE12B_CPX1_7	49.99	3.03	10.88	0.26	18.67	0.00	1.49	0.00	0.30	14.52	99.1	73.5	39.42	42.65	17.93
		I	DCE12B_CPX1_8	50.40	2.66	10.98	0.28	18.79	0.00	1.46	0.02	0.28	14.64	99.5	73.4	39.37	42.68	17.95
		R	DCE12B_CPX1_9	50.47	2.20	11.14	0.34	19.59	0.01	1.26	0.02	0.32	14.59	99.9	73.1	40.32	41.78	17.90
	0.60	C	DCE12B_CPX11_1C	51.07	2.47	10.27	0.26	18.27	0.01	1.21	0.01	0.33	15.65	99.5	76.0	38.01	45.31	16.68
		I	DCE12B_CPX11_2	50.63	2.84	10.59	0.29	18.59	0.00	1.38	0.02	0.29	14.99	99.6	74.6	38.96	43.71	17.32
		I	DCE12B_CPX11_3	50.48	2.72	10.63	0.30	18.73	0.01	1.27	0.01	0.27	14.99	99.4	74.5	39.12	43.56	17.33
		I	DCE12B_CPX11_4	50.66	2.63	11.58	0.36	18.57	0.02	1.17	0.00	0.28	14.58	99.8	72.3	38.77	42.36	18.87
	0.05	C	DCE12B_CPX13	51.12	2.19	11.40	0.33	19.14	0.00	1.13	0.00	0.29	14.49	100.1	72.5	39.71	41.83	18.46
	0.05	C	DCE12B_CPX14	50.79	2.07	12.98	0.45	17.11	0.00	1.13	0.00	0.28	14.86	99.7	70.4	35.71	43.15	21.14
	0.46		DCE12B_CPX15	50.68	2.85	11.40	0.26	18.35	0.01	1.18	0.00	0.31	15.21	100.2	73.5	37.91	43.72	18.38
			DCE12B_CPX16	49.84	3.49	11.11	0.29	19.21	0.00	1.62	0.00	0.31	14.44	100.3	72.9	40.04	41.88	18.08
			DCE12B_CPX17	49.91	3.09	10.97	0.27	19.34	0.00	1.50	0.00	0.31	14.62	100.0	73.4	40.09	42.16	17.75

			DCE12B_CPX18	50.90	2.33	11.90	0.34	19.27	0.00	1.26	0.00	0.28	14.46	100.7	71.6	39.59	41.33	19.08
DPI23	1.50	C	DPI23_CPX1_1C	51.47	2.13	11.35	0.25	18.67	0.003	1.191	0.075	0.236	15.09	100.5	70.3	43.27	38.48	18.26
		I	DPI23_CPX1_2	51.77	2.01	11.79	0.26	18.05	0	1.082	0.056	0.267	15.3	100.6	69.8	43.86	37.19	18.96
		I	DPI23_CPX1_3	51.15	2.18	13.26	0.319	16.9	0.004	1.196	0.058	0.217	15.07	100.4	67.0	43.49	35.05	21.46
			DPI23_CPX1_4	51.4	1.703	13.82	0.374	17.58	0.014	0.855	0.022	0.205	14.2	100.2	64.7	41.06	36.53	22.41
	0.40	C	DPI23_CPX2	50.95	2.25	14.63	0.376	15.57	0.007	1.265	0.049	0.241	15.05	100.4	64.7	43.69	32.49	23.82
	0.08	C	DPI23_CPX3	50.3	3.1	22.05	0.503	11.58	1.082	1.011	0	0.238	9.61	99.5	43.7	31.71	27.47	40.82
	0.26	C	DPI23_CPX4	50.83	1.98	14.76	0.382	17.44	0	1.002	0.016	0.198	13.68	100.3	62.3	39.66	36.34	24.00
	0.13	C	DPI23_CPX5	51.09	1.3	18.76	0.514	14.36	0.021	0.691	0.021	0.189	12.9	99.8	55.1	38.23	30.59	31.19
	0.75	C	DPI23_CPX6	54.18	2.27	11.73	0.289	18.38	0.022	0.999	0	0.21	11.84	99.9	64.3	37.43	41.76	20.80
	0.10	C	DPI23_CPX7	51.65	1.577	13.69	0.344	16.8	0.006	0.883	0.022	0.201	15.03	100.2	66.2	43.21	34.71	22.08
	0.19	C	DPI23_CPX8	51.09	1.98	13.58	0.31	17.62	0	1.19	0	0.223	14.53	100.5	65.6	41.74	36.38	21.88
	0.19	C	DPI23_CPX9	50.07	1.866	15.84	0.404	19.14	0	1.073	0	0.235	11.44	100.1	56.3	33.57	40.36	26.07
	0.07	C	DPI23_CPX10	50.39	1.708	18.01	0.49	15.62	0.005	0.803	0.014	0.2	12.5	99.7	55.3	36.95	33.19	29.86
Evolved high-Ti tholeiites (eHT) (SiO_2 > 56.5 wt.%)																		
DCE32C	0.93	C	CPX_1_1C	51.07	1.97	13.55	0.428	18.12	0.004	0.905	0	0.238	13.48	99.8	63.9	39.53	38.19	22.29
		R	CPX_1_2B	51.71	1.301	14.77	0.591	18.57	0	0.657	0.045	0.259	12.44	100.3	60.0	36.51	39.17	24.32
	0.44	C	CPX_2_1C	50.8	1.684	12.91	0.437	18.68	0	0.819	0.033	0.237	13.15	98.8	64.5	39.53	38.19	22.29
		R	CPX_2_2B	51.32	1.089	16.39	0.66	18.07	0.017	0.518	0	0.286	11.44	99.8	55.4	36.51	39.17	24.32
	0.19	C	CPX_5_1C	51.16	1.164	15.28	0.605	18.95	0	0.563	0	0.285	11.56	99.6	57.4	34.25	40.35	25.40
	0.20	C	CPX_7	51.38	1.334	14.37	0.583	19.26	0.01	0.539	0	0.276	11.91	99.7	59.6	35.22	40.94	23.84
	0.32	C	CPX_12_1C	51.06	1.193	15.34	0.586	18.8	0.007	0.462	0.02	0.287	12.02	99.8	58.3	35.21	39.58	25.21
		B	CPX_12_3B	51.39	0.935	16.8	0.781	17.57	0.035	0.432	0	0.282	11.1	99.3	54.1	33.48	38.09	28.43
		I	CPX_12_2	50.69	1.516	15.15	0.603	18.56	0	0.62	0.013	0.313	11.97	99.4	58.5	35.41	39.46	25.14
	0.18	R	CPX_14	51.5	0.857	17.36	0.732	17.85	0.019	0.378	0.032	0.264	11.02	100.0	53.1	32.81	38.20	28.99
DCE33	0.21	C	DCE33_CPX1_1C	52.01	1.851	11.65	0.337	19.34	0.007	0.905	0	0.275	14.63	101.0	69.1	41.72	39.64	18.64
		I	DCE33_CPX1_2	51.96	1.069	14.9	0.51	19.12	0.01	0.572	0.011	0.255	12.19	100.6	59.3	35.55	40.08	24.37
	0.55	C	DCE33_CPX2	51.19	2.15	12.33	0.348	18.51	0	0.844	0	0.296	14.35	100.0	67.5	41.51	38.48	20.01
		C	DCE33_CPX3_1C	51.59	2.07	11.69	0.338	19.01	0.001	0.969	0	0.282	14.8	100.8	69.3	42.26	39.01	18.72
			DCE33_CPX4_2	51.84	1.613	12.47	0.39	19	0.001	0.685	0.022	0.238	14.22	100.5	67.0	40.78	39.16	20.06

			DCE33_CPX4_3	51.36	0.823	17.33	0.539	17.82	0.015	0.444	0	0.268	11.51	100.1	54.2	33.81	37.63	28.56
	0.10		DCE33_CPX5	51.08	1.536	12.41	0.391	19.26	0.007	0.882	0.009	0.306	14.05	99.9	66.9	40.31	39.72	19.97
	1.20		DCE33_CPX6_1	51.41	1.98	11.89	0.351	19.06	0.009	0.909	0	0.283	14.64	100.5	68.7	41.82	39.13	19.05
	0.78		DCE33_CPX7_1	51.37	1.96	12.16	0.384	18.68	0.01	0.878	0	0.24	14.57	100.3	68.1	41.85	38.56	19.59
Low-Ti tholeiites (LT1)																		
DCE03	0.56	C	DCE03_CPX1_1C	51.75	2.02	11.7	0.254	17.67	0.009	1.031	0.182	0.235	15.62	100.5	70.4	44.78	36.41	18.81
		I	DCE03_CPX1_2	51.99	2.77	8.14	0.205	18.01	0.01	0.407	0.258	0.173	17.52	99.5	79.3	50.01	36.95	13.03
		I	DCE03_CPX1_3	52.75	2.77	8.16	0.2	18.86	0	0.353	0.157	0.239	17.03	100.5	78.8	48.43	38.55	13.02
		I	DCE03_CPX1_4	52.33	2.81	9.19	0.233	17.5	0	0.461	0.072	0.272	17.33	100.2	77.1	49.43	35.87	14.70
		R	DCE03_CPX1_5	52.83	1.96	10.25	0.26	17.72	0.015	0.52	0.016	0.175	16.94	100.7	74.7	47.82	35.95	16.23
	0.09	C	DCE03_CPX2	50.84	1.174	19.63	0.464	15.31	0	0.584	0.05	0.17	11.98	100.2	52.1	35.24	32.37	32.39
	0.05	C	DCE03_CPX3	51.82	0.813	24.14	0.501	4.19	0.002	0.333	0	0.168	18.04	100.0	57.1	52.15	8.71	39.15
	0.06	C	DCE03_CPX4	51.97	2.04	10.9	0.214	15.5	0.032	1.125	0.051	1.67	15.21	98.7	71.3	46.85	34.32	18.83
	1.16	C	DCE03_CPX5_1C	52.65	2.16	8.45	0.211	17.75	0	0.347	0.203	0.911	16.81	99.5	78.0	49.00	37.19	13.82
		I	DCE03_CPX5_2	52.89	2.53	8.41	0.233	17.36	0.006	0.427	0.171	0.176	18.02	100.2	79.3	51.17	35.43	13.40
		I	DCE03_CPX5_3	52.67	2.54	8.06	0.196	17.84	0	0.375	0.1	0.206	17.83	99.8	79.8	50.69	36.45	12.85
		I	DCE03_CPX5_4	52.49	1.856	10.24	0.228	15.78	0.007	0.638	0.013	0.721	17.21	99.2	75.0	50.18	33.07	16.75
		R	DCE03_CPX5_5B	50.67	1.37	18.13	0.447	16.11	0	0.685	0.009	0.148	11.76	99.3	53.6	35.10	34.55	30.35
	0.25	C	DCE03_CPX6_1C	54.69	0.78	14.2	0.341	4.38	0	0.208	0.059	0.069	25.23	100.0	76.0	69.42	8.66	21.92
		I	DCE03_CPX6_2	52.26	1.262	17.68	0.44	6.44	0.018	0.393	0	0.078	20.28	98.9	67.2	58.23	13.29	28.48
	<0.5	C	DCE03_CPX9	50.64	1.603	16.6	0.405	15.45	0.009	0.694	0.016	0.212	13.32	99.0	58.9	39.48	32.92	27.60
Low-Ti tholeiites (LT2)																		
DCE44	1.01	C	DCE44_CPX1_1C	52.42	1.817	12.15	0.309	15.13	0.002	0.508	0.054	0.645	16.72	99.8	71.0	48.59	31.60	19.81
		I	DCE44_CPX1_2	51.2	1.835	15.78	0.365	14.51	0	0.628	0.009	0.179	15.26	99.8	63.3	44.18	30.19	25.63
	0.09	C	DCE44_CPX2	50.41	1.325	19.11	0.455	15.73	0	0.567	0.02	0.201	11.78	99.6	52.4	34.85	33.44	31.71
	0.07	C	DCE44_CPX3	50.21	1.215	21.5	0.492	14.91	0	0.536	0.09	0.157	11.16	100.3	48.1	32.88	31.58	35.54
	0.17	C	DCE44_CPX5	54.51	0.892	14.49	0.347	4.62	0.001	0.126	0.036	0.047	24.86	99.9	75.4	68.47	9.15	22.39
	1.14	C	DCE44_CPX8_1C	52.7	2.74	7.76	0.192	19.63	0.006	0.4	0.129	0.26	16.78	100.6	79.4	47.61	40.03	12.35
		I	DCE44_CPX8_2	53.21	1.776	10.2	0.281	15.56	0	0.295	0.057	0.206	18.9	100.5	76.8	52.79	31.23	15.98
		I	DCE44_CPX8_3	51.98	1.802	11.91	0.302	17.33	0	0.498	0.038	0.241	15.91	100.0	70.4	45.40	35.54	19.06
		I	DCE44_CPX8_4	50.96	1.862	14.65	0.341	18.34	0	0.785	0	0.218	13.04	100.2	61.3	37.86	38.27	23.86
		I	DCE44_CPX8_5	51.09	1.434	16.03	0.366	17.4	0.002	0.605	0	0.197	12.88	100.0	58.9	37.47	36.38	26.16

	0.05		DCE44_CPX9	50.08	1.193	21.59	0.487	17.07	0.005	0.568	0.048	0.193	8.97	100.2	42.6	26.90	36.79	36.32
	0.98	C	DCE44_CPX10_1C	52.28	2.89	9.06	0.228	17.48	0	0.288	0.097	0.283	17.22	99.8	77.2	49.39	36.03	14.58
		I	DCE44_CPX10_2	52.21	2.39	9.99	0.225	17.47	0.02	0.527	0.062	0.52	16.07	99.5	74.1	46.95	36.68	16.37
		I	DCE44_CPX10_3	52.41	2.17	10.75	0.234	17.98	0.013	0.53	0.011	0.315	15.91	100.3	72.5	45.64	37.07	17.30
		I	DCE44_CPX10_4	50.87	2	15.77	0.35	16.67	0.038	0.837	0.036	0.29	12.86	99.7	59.2	38.17	35.57	26.26
		R	DCE44_CPX10_5B	49.84	1.297	22.43	0.541	15.33	0.051	0.55	0.005	0.14	9.58	99.8	43.2	28.87	33.21	37.92
	0.26	C	DCE44_CPX6_1C	52.73	1.19	17.86	0.399	5.88	0	0.317	0.021	0.092	21.12	99.6	67.8	59.72	11.95	28.33
DPI03	2.67	C	DPI03_CPX1_1C	53.83	0.881	16.82	0.449	4.76	0.004	0.208	0.034	0.064	23.03	100.1	70.9	64.17	9.53	26.29
		B	DPI03_CPX1_2B	51.4	0.937	26.33	0.688	4.71	0.013	0.33	0.017	0.047	15.78	100.3	51.7	46.50	9.98	43.52
	0.72	C	DPI03_CPX2_1C	51.28	1.757	15.05	0.421	17.85	0	0.666	0.018	0.271	13.25	100.6	61.1	38.38	37.16	24.46
		B	DPI03_CPX2_2B	47.36	4.42	25.72	0.338	10.37	0.62	0.704	0.019	1.47	7.72	98.7	34.9	26.08	25.18	48.74
	0.32	C	DPI03_CPX4_1C	51.53	2.25	13.74	0.317	17.35	0.005	0.59	0	0.245	14.59	100.6	65.4	41.96	35.87	22.17
	2.52	C	DPI03_CPX5_1C	52.49	1.98	12.66	0.329	16.53	0.006	0.609	0	0.236	15.95	100.8	69.2	45.66	34.01	20.33
		I	DPI03_CPX5_2	51.28	2.02	14.32	0.371	16.12	0	0.541	0.029	0.224	15.35	100.3	65.6	43.90	33.13	22.97
		I	DPI03_CPX5_3	51.82	1.847	14.75	0.363	16.3	0	0.689	0	0.238	14.86	100.9	64.2	42.64	33.62	23.74
		R	DPI03_CPX5_4	50.63	2.18	15.46	0.41	17.35	0.005	2.2	0.002	0.179	12.3	100.7	58.7	36.78	37.29	25.93
	1.14	C	DPI03_CPX6_1C	51.29	2.08	13.96	0.363	16.49	0.005	0.571	0	0.231	15.1	100.1	65.9	43.41	34.07	22.51
		R	DPI03_CPX6_2B	51.29	2.18	12.68	0.305	18	0.004	0.663	0	0.261	14.69	100.1	67.4	42.29	37.24	20.47
	0.18		DPI03_CPX7															
	0.23		DPI03_CPX8	50.48	1.261	20.15	0.535	16.44	0	0.632	0.027	0.153	10.79	100.5	48.8	31.82	34.85	33.33
	1.80	C	DPI03_CPX9_1C	51.24	1.671	13.93	0.384	16.88	0.018	0.561	0	0.241	14.82	99.7	65.5	42.63	34.90	22.48
		I	DPI03_CPX9_2	51.25	1.675	14.81	0.396	16.94	0	0.507	0	0.227	14.33	100.1	63.3	41.16	34.97	23.86
		I	DPI03_CPX9_4	51.39	1.511	15.76	0.407	16.56	0.001	0.589	0.025	0.21	13.79	100.2	60.9	39.93	34.47	25.60
	0.84	C	DPI03_CPX10_1C	51.24	1.486	17.92	0.484	16.16	0	0.548	0	0.196	12.35	100.4	55.1	36.31	34.14	29.55
		I	DPI03_CPX10_2	49.28	0.905	28.1	0.717	13.64	0.007	0.334	0.021	0.164	7.14	100.3	31.2	21.83	29.97	48.19
		B	DPI03_CPX10_3B	49.33	0.745	28.51	0.739	15.02	0.023	0.411	0	0.153	6.02	101.0	27.3	18.35	32.90	48.75

Supplementary Table A4. Composition of endmembers used in geochemical modelling.

Member	Sample	Rb (ppm)	Sr (ppm)	Sm (ppm)	Nd (ppm)	Pb (ppm)	$^{87}Sr/^{86}Sr_{(m)}$	$^{143}Nd/^{144}Nd_{(m)}$	$^{87}Sr/^{86}Sr_{12}$ 7	$^{143}Nd/^{144}Nd_{1}$ 27	εNd_{12} 7	Source
DMM	Stracke av.	5.0	155.0	2.6	9.0	4.50	0.70291	0.51306	0.70274	0.51292	8.62	Stracke et al. (2005)
HIMU	SH-86+149	8.4	277.0	4.9	22.5	0.82	0.70291	0.51287	0.70275	0.51276	5.65	Chaffey et al. (1989); Kawabata et al. (2011); Stracke et al. (2005)
FOZO	AI-66+FOZOextreme	6.9	425.1	7.3	29.7	1.46	0.70300	0.51306	0.70292	0.51294	9.05	Jicha et al. (2013); GEOROC (extr. comp.)
EM2	Stracke av.	-	-	-	-	-	0.70480	0.51280	0.70471	0.51261	2.76	Stracke et al. (2005)
EM1	Stracke av.	-	-	-	-	-	0.70481	0.51263	0.70473	0.51245	-0.43	Stracke et al. (2005)
Gough (EMI)	SO233 DR3-1[a]	33.7	842.0	9.2	44.8	4.01	0.70536	0.51248	0.70515	0.51238	-1.85	Hoernle et al. (2015)
Alkalines - Alto Paranaíba (SCLM derivation)	TR-84	294.0	1995.0	23.5	159.0	15.00	0.70734	0.51213	0.70657	0.51205	-8.23	Araujo et al. (2001)
Mafic to Intermediate crust (Paleoproterozoic)	ZEF8A+ES543B	-	633.0	-	132.0	13.10	0.71298	0.51100	0.71231	0.51092	-30.26	Souza et al. (2016)
Granodioritic crust (Paleoproterozoic)	ZEF28B	93.7	376.4	5.3	35.3	13.59	0.72588	0.51098	0.72458	0.51090	-30.73	Souza et al. (2016)

High-Ti tholeiite used in MELTS modeling	SiO_2	Al_2O_3	Fe_2O_{3T}	MnO	MgO	CaO	Na_2O	K_2O	TiO_2	P_2O_5	LOI

(Sardinha sill complex)											
Sample 23.05	49.90	10.40	14.9	0.23	7.34	9.52	1.92	1.36	2.81	0.48	0.82

APPENDIX – SUPPLEMENTARY MATERIAL

CHAPTER 7. CRYSTAL SIZE DISTRIBUTION OF RIO CEARÁ-MIRIM DIKES AND CORRELATIONS WITH MAFIC INTRUSIONS OF THE PARNAÍBA BASIN

Table 7A1. CSD dataset of plagioclase and pyroxene of the NE-Rio Ceará-Mirim dikes. n represent number of crystals.

DCE03	n= 557				
Mid Inter	ln(pop den)	ln(min PD)	ln(max PD)	Cry Num	Vol%
4.4					
3.3	-4.19	-4.9	-3.78	0.0144	9.61
2.47	-2.37	-2.69	-2.12	0.0668	18.77
1.85	-1.37	-1.63	-1.17	0.135	16.03
1.39	-0.08	-0.25	0.07	0.369	18.45
1.043	0.48	0.31	0.64	0.487	10.26
0.782	1.36	1.21	1.5	0.881	7.828
0.586	2.11	1.97	2.23	1.4	5.233
0.44	2.68	2.54	2.8	1.84	2.913
0.33	2.98	2.81	3.13	1.87	1.243
0.247	3.63	3.47	3.77	2.69	0.756

DCE16	n = 613				
Mid Inter	ln(pop den)	ln(min PD)	ln(max PD)	Cry Num	Vol%
7.06					
5.08	-4.66	-5.11	-4.35	0.0159	23.38
3.66	-3.4	-3.72	-3.16	0.04	22
2.63	-1.7	-1.88	-1.55	0.158	32.36
1.894	-0.76	-0.92	-0.63	0.291	22.2
1.363	0.04	-0.1	0.17	0.468	13.31
0.981	0.95	0.83	1.06	0.836	8.871
0.706	1.52	1.38	1.64	1.06	4.183
0.508	2.29	2.16	2.4	1.65	2.428

DCE21	n = 525				
Mid Inter	ln(pop den)	ln(min PD)	ln(max PD)	Cry Num	Vol%
4.43					
2.79	-2.22	-2.41	-2.07	0.139	23.87
1.763	-0.31	-0.41	-0.21	0.598	25.79
1.112	0.61	0.5	0.71	0.942	10.2
0.702	1.5	1.39	1.6	1.45	3.951
0.443	1.89	1.73	2.03	1.36	0.926
0.279	2.34	2.13	2.52	1.34	0.23

DCE24	n = 547				
Mid Inter	ln(pop den)	ln(min PD)	ln(max PD)	Cry Num	Vol%
6.71					
4.57	-3.94	-4.36	-3.65	0.034	13.73
3.114	-1.71	-1.88	-1.56	0.217	27.73
2.122	-0.05	-0.16	0.05	0.775	31.32
1.446	0.91	0.81	1	1.38	17.59
0.985	1.49	1.38	1.6	1.68	6.81
0.671	1.84	1.69	1.97	1.63	2.077
0.457	2.39	2.21	2.53	1.91	0.77

DCE44	n = 539				
Mid Inter	ln(pop den)	ln(min PD)	ln(max PD)	Cry Num	Vol%
6.71					
4.57	-3.94	-4.36	-3.65	0.034	13.73
3.114	-1.71	-1.88	-1.56	0.217	27.73
2.122	-0.05	-0.16	0.05	0.775	31.32
1.446	0.91	0.81	1	1.38	17.59
0.985	1.49	1.38	1.6	1.68	6.81
0.671	1.84	1.69	1.97	1.63	2.077
0.457	2.39	2.21	2.53	1.91	0.77

DPI01	n = 483				
Mid Inter	ln(pop den)	ln(min PD)	ln(max PD)	Cry Num	Vol%
6.71					
4.23	-4.68	-5.57	-4.22	0.018	5.588
2.671	-2.46	-2.83	-2.19	0.105	8.163
1.685	0.54	0.42	0.64	1.33	25.96
1.063	2.05	1.97	2.13	3.82	18.76
0.671	2.82	2.72	2.9	5.17	6.37

DPI03	n = 455				
Mid Inter	ln(pop den)	ln(min PD)	ln(max PD)	Cry Num	Vol%
2.397	-3.34	-4.57	-2.8	0.028	2.896
1.725	-0.9	-1.25	-0.65	0.23	8.89
1.241	1.16	1	1.29	1.3	18.66
0.893	2.38	2.27	2.49	3.19	17.09
0.643	3.37	3.27	3.46	6.17	12.33
0.463	3.81	3.69	3.91	6.86	5.118

DPI12	n = 468				
Mid Inter	ln(pop den)	ln(min PD)	ln(max PD)	Cry Num	Vol%
2.44	-3.54	-4.77	-3	0.0272	6.694
1.661	-0.77	-1.07	-0.54	0.295	22.99
1.132	0.61	0.4	0.79	0.803	19.78
0.771	1.64	1.44	1.8	1.52	11.86
0.525	2.56	2.38	2.72	2.62	6.453
0.358	3.98	3.86	4.09	7.38	5.752

Mid Inter	ln(pop den)	ln(min PD)	ln(max PD)	Cry Num	Vol%
4.54					
3.41	-4.28	-4.91	-3.9	0.0136	3.477
2.556	-2.11	-2.34	-1.92	0.0891	9.627
1.917	-1.05	-1.23	-0.89	0.194	8.83
1.437	-0.15	-0.31	-0.02	0.355	6.823
1.078	0.48	0.33	0.61	0.501	4.061
0.808	1.4	1.28	1.52	0.948	3.241
0.606	1.99	1.86	2.1	1.27	1.836
0.454	2.5	2.37	2.62	1.6	0.973

DCE35	n = 516				
Mid Inter	ln(pop den)	ln(min PD)	ln(max PD)	Cry Num	Vol%
7.23					
4.56	-4.64	-5.13	-4.32	0.0202	23.74
2.88	-2.31	-2.52	-2.14	0.131	38.71
1.816	-0.64	-0.78	-0.52	0.44	32.61
1.146	0.31	0.16	0.43	0.717	13.34
0.723	1.32	1.18	1.44	1.24	5.803
0.456	2.28	2.14	2.4	2.05	2.4
0.288	3.46	3.34	3.57	4.23	1.246

DCE38	n = 634				
Mid Inter	ln(pop den)	ln(min PD)	ln(max PD)	Cry Num	Vol%
4.97	-4.41	-4.68	-4.19	0.0233	19.58
3.39	-2.35	-2.49	-2.23	0.124	33
2.307	-1.08	-1.19	-0.99	0.3	25.21
1.572	-0.1	-0.2	-0.01	0.546	14.54
1.071	0.59	0.48	0.68	0.739	6.222
0.73	0.87	0.73	1	0.67	1.782
0.244	4.84	4.72	4.95	11.8	2.917
0.1661	5.58	5.45	5.69	16.8	1.311

DPI22	n = 554				
Mid Inter	ln(pop den)	ln(min PD)	ln(max PD)	Cry Num	Vol%
1.038					
0.804	0.21	-0.4	0.59	0.254	5.33
0.622	1.73	1.4	1.98	0.898	8.76
0.482	2.98	2.77	3.16	2.44	11.03
0.373	4.05	3.88	4.18	5.45	11.45
0.289	4.75	4.6	4.88	8.52	8.305
0.224	5.49	5.36	5.61	13.8	6.264
0.173	6.09	5.96	6.2	19.5	4.089
0.134	6.46	6.32	6.59	22	2.142

DPI23	n = 492				
Mid Inter	ln(pop den)	ln(min PD)	ln(max PD)	Cry Num	Vol%
3.09	-3.21	-3.61	-2.92	0.048	13.98
2.104	-1.41	-1.63	-1.22	0.198	18.2
1.433	-0.36	-0.56	-0.19	0.384	11.19
0.977	1.39	1.27	1.49	1.5	13.8
0.665	2.24	2.13	2.34	2.4	7.001
0.453	2.84	2.71	2.95	2.97	2.732
0.309	3.48	3.34	3.6	3.83	1.117

DCE43	n = 515				
Mid Inter	ln(pop den)	ln(min PD)	ln(max PD)	Cry Num	Vol%
3.09					
2.32					
1.738	-2.11	-2.64	-1.77	0.0606	4.731
1.303	-0.14	-0.36	0.04	0.325	10.71
0.977	0.94	0.77	1.08	0.718	9.974
0.733	2	1.87	2.12	1.56	9.154
0.55	2.86	2.74	2.96	2.76	6.818
0.412	3.54	3.43	3.64	4.09	4.255

APPENDIX – SUPPLEMENTARY MATERIAL

CHAPTER 8. GEOCHEMICAL CORRELATIONS AMONG THOLEIITIC PLUMBING SYSTEMS OF SOUTH ATLANTIC-RELATED LIPs

Table A1. Initialization and training parameters used for SiroSOM modeling.

Database		Initialization					Training								
					Map Size			Rough Training			Fine Training			Error	
Processing	Geochemical parameters	Initiation	Lattice	Shape	Rows	Columns	Neighbour	Inial training radius	Final training radius	Training length	inial training radius	final training radius	training length	Final quantitization (QER)	Final topologic
PEMP and EQUAMP combined (whole dataset)	Major oxides, trace elements, REE	random	hexagonal	toroid	58	52	Gaussian	78	20	70	20	1	1400	0.969	0.0189

Major oxides: SiO_2, Al_2O_3, Fe_2O_{3T}, MnO, MgO, CaO, Na_2O, K_2O, TiO_2, P_2O_5
Trace elements: V, Cr, Co, Ni, Cu, Pb, Zn, Rb, Sr, Cs, Y, Zr, Nb, Ba, Hf, Ta, Th, U
REE: La, Ce, Pr, Nd, Sm, Eu, Gd, Tb, Dy, Ho, Er, Tm, Yb, Lu

Table A2. Centroid values of K-means clusters

Processing	Cluster	SiO_2	Al_2O_3	Fe_2O_{3T}	MnO	MgO	CaO	Na_2O	K_2O	TiO_2	P_2O_5
		Centroids									
PEMP and EQUAMP combined	SA4	52.80	13.60	14.30	0.21	4.42	8.25	2.66	1.50	1.98	0.29
	SA1	51.40	13.30	14.20	0.18	4.37	7.74	2.88	1.78	3.55	0.60
	SA2	56.10	13.40	12.50	0.18	2.84	5.88	3.13	2.77	2.52	0.69
	SA3	50.70	14.70	12.40	0.19	6.69	10.50	2.42	0.81	1.44	0.18

Processing	Cluster	V	Cr	Co	Ni	Cu	Pb	Zn	Rb	Sr	Cs	Y	Zr	Nb	Ba	Hf	Ta	Th	U
		Centroids																	
PEMP and EQUAMP combined	SA4	396.0	49.3	46.6	37.1	143.0	6.3	105.0	51.3	253.0	2.0	38.9	187.0	15.4	407.0	4.9	1.0	5.4	1.4
	SA1	350.0	55.3	45.7	45.2	126.0	6.2	107.0	43.9	611.0	1.5	38.0	279.0	27.0	588.0	7.4	1.9	4.5	1.0
	SA2	161.0	15.7	23.2	13.9	53.5	7.4	107.0	73.6	520.0	1.3	52.1	382.0	34.3	823.0	9.9	2.1	7.6	1.9
	SA3	320.0	173.0	50.1	87.6	121.0	3.1	85.3	24.6	245.0	1.9	25.7	113.0	9.5	230.0	3.0	0.6	2.4	0.5

Processing	Cluster	La	Ce	Pr	Nd	Sm	Eu	Gd	Tb	Dy	Ho	Er	Tm	Yb	Lu
		Centroids													
PEMP and EQUAMP combined	SA4	25.7	54.4	6.8	28.6	6.6	1.9	7.1	1.2	7.0	1.4	4.0	0.6	3.8	0.6
	SA1	41.4	89.5	11.2	48.2	10.2	3.2	9.5	1.4	7.6	1.4	3.7	0.5	3.0	0.4
	SA2	58.8	125.0	15.8	65.1	13.4	3.8	12.4	1.8	10.1	1.9	5.1	0.7	4.3	0.6
	SA3	14.1	30.3	3.9	16.9	4.2	1.4	4.6	0.8	4.7	0.9	2.7	0.4	2.4	0.4